

CHALLENGES AND ADVANCES IN
COMPUTATIONAL CHEMISTRY AND PHYSICS

13

Series Editor J. Leszczynski

Volume Editors R. Zaleśny

M.G. Papadopoulos · P.G. Mezey · J. Leszczynski

Linear-Scaling Techniques in Computational Chemistry and Physics

Methods and Applications

 Springer

Linear-Scaling Techniques in Computational Chemistry and Physics

CHALLENGES AND ADVANCES IN COMPUTATIONAL CHEMISTRY AND PHYSICS

Volume 13

Series Editor:

JERZY LESZCZYNSKI

Department of Chemistry, Jackson State University, U.S.A.

For further volumes:

<http://www.springer.com/series/6918>

Linear-Scaling Techniques in Computational Chemistry and Physics

Methods and Applications

Edited by

Robert Zaleśny

Wrocław University of Technology, Wrocław, Poland

Manthos G. Papadopoulos

National Hellenic Research Foundation, Athens, Greece

Paul G. Mezey

Memorial University of Newfoundland, St. John's, NL, Canada

and

Jerzy Leszczynski

Jackson State University, Jackson, MS, USA



Springer

Editors

Dr. Robert Zalesny
Institute of Physical and Theoretical
Chemistry
Wrocław University of Technology
Wyb. Wyspiańskiego 27, 50-370
Wrocław
Poland
robert.zalesny@pwr.wroc.pl

Prof. Manthos G. Papadopoulos
Institute of Organic and Pharmaceutical
Chemistry
National Hellenic Research Foundation
48 Vas. Constantinou Ave.
Athens 116 35
Greece
mpapad@eie.gr

Prof. Dr. Paul G. Mezey
Department of Chemistry and Department
of Physics and Physical Oceanography
Memorial University of Newfoundland
283 Prince Philip Drive
St. John's, NL, A1B 3X7
Canada
paul.mezey@gmail.com

Prof. Jerzy Leszczynski
Department of Chemistry
Jackson State University
P.O. Box 17910
1400 Lynch Street
Jackson, MS 39217
USA
jerzy@icnanotox.org

ISBN 978-90-481-2852-5

e-ISBN 978-90-481-2853-2

DOI 10.1007/978-90-481-2853-2

Springer Dordrecht Heidelberg London New York

Library of Congress Control Number: 2011922660

© Springer Science+Business Media B.V. 2011

No part of this work may be reproduced, stored in a retrieval system, or transmitted in any form or by any means, electronic, mechanical, photocopying, microfilming, recording or otherwise, without written permission from the Publisher, with the exception of any material supplied specifically for the purpose of being entered and executed on a computer system, for exclusive use by the purchaser of the work.

Printed on acid-free paper

Springer is part of Springer Science+Business Media (www.springer.com)

PREFACE

Computational chemistry methods have become increasingly important in recent years, as manifested by their rapidly extending applications in a large number of diverse fields (e.g. computations of molecular structure, properties, the design of pharmaceutical drugs and novel materials, etc). In part as a result of this general trend, the size of the systems which can be studied has also increased, generating even further needs for size increases, since larger molecular systems show interesting phenomena, important in modern biochemistry, biotechnology, and nanotechnology. Thus, it is of great importance to apply and further develop computational methods which provide physically sound answers for large molecules at a reasonable computational cost. An important variety of such approaches is represented by the linear scaling techniques, that is, by methods where the computational cost scales linearly with the size of the system [$O(N)$]. Over the years, satisfactory linear scaling computational approaches have been developed which are suitable to study a variety of molecular problems. However, the latest trends also provide hope that further, substantial breakthrough in this field may be expected, and one might anticipate developments for which even the early indications have not yet appeared. This book is a collection of chapters which report the state-of-the-art in many of the important questions related to the family of linear scaling methods. We hope that it may give motivation and impetus for more rapid developments in the field.

Pulay reviews plane-wave (PW) based methods for the computation of the Coulomb interaction, in HF and DFT methods, introduced in order to decrease the scaling. The author notes that PW methods have not been fully utilized in quantum chemistry, although several groups have shown their advantages. The author discusses various technical difficulties regarding the applications of PW methods and compares PW basis sets with atomic basis sets. He further comments on ways to combine both of them in a single algorithm and discusses reported implementations and results as well as some of the important problems to be solved in this area (e.g. improvement of the efficiency of other major computational tasks to match the performance of the Coulomb evaluation).

Nagata et al. review the fragment molecular orbital (FMO) method, proposed in 1999 and used to reduce the scaling of MO theories from N^3 – N^7 to nearly linear scaling. They discuss the implementation of various methods (e.g. RI-MP2, DFT, MCSCF) within the framework of the FMO method, the formulation of FMO-ROHF, the interface of time-dependent DFT (TDDFT) with FMO. The authors review the implementation of CIS in multilayer FMO as well as the

inclusion of perturbative doubles [CIS(D)] and the inclusion of effective potentials (e.g. model core potentials) due to the environment or inner-shell electrons into FMO calculations. Application of FMO in molecular dynamics simulations, energy decomposition analysis, and property calculations (e.g. chemical shifts) are also discussed.

Saebø reviews some linear scaling approaches based on the second-order Møller-Plesset (MP2) methods and briefly comments on other, more accurate electron correlation techniques. He focuses mainly on methods relying on the local correlation method introduced by Pulay and Saebø and developed further by other co-workers. The RI-MP2 method is discussed, demonstrating that it is an order of magnitude more efficient than MP2. He reviews the RI-LMP2 method, which is a combination of the density fitting approach (RI) with the local MP2 method, providing linear scaling with the size of the system. A new linearly scaling LMP2 approach providing essentially identical results to conventional canonical MP2 is discussed and applications are presented.

Surján and Szabados review perturbative approaches developed to avoid diagonalization of large one-electron Hamiltonians, taking into account that diagonalization of matrices scales with the cube of the matrix dimension. The first order density matrix P is obtained from an iterative formula which preserves the trace and the idempotency of P . If P is sparse, then the method leads to a linear scaling method. It is noted that the procedure is useful for geometry optimization or self-consistent techniques. Electron correlation methods based on the Hartree-Fock density matrix are also discussed.

Kobayashi and Nakai report on recent developments in the linear-scaling divide-and-conquer (DC) techniques, that is, the density-matrix-based DC self-consistent field (SCF) and the DC-based post-SCF electron correlation methods, which they implemented in the freely available GAMESS-US package. It is shown that the DC-based post-SCF calculation achieves near-linear scaling with respect to the system size, while the memory and scratch space are hardly dependent on the system size. The performance of the techniques is shown by examples.

Mezey reviews the common principles of linear scaling methods as well as the locality aspects of these techniques. Fundamental relations between local and global properties of molecules are discussed. The author reviews the Additive Fuzzy Density Fragmentation (AFDF) Principle and the two, related linear scaling approaches based on it: the MEDLA, Molecular Electron Density Loge (or Lego) Assembler method and the ADMA, Adjustable Density Matrix Assembler method. Mezey notes that the ADMA provides the basis for the Combinatorial Quantum Chemistry technique, with a variety of applications (e.g. in the pharmaceutical industry).

Szekeres and Mezey review the role of molecular fragmentation schemes in various linear scaling methods with special emphasis on fragmentation based on the properties of molecular electron densities. They discuss various fragmentation schemes, for example, chemically motivated fragment selection, functional groups as primary fragments, delocalized fragments, Procrustes fragmentation,

multi-Procrustes fragmentation with trigonometric weighting. The authors review computational techniques for the efficient implementation of the above schemes.

Eckard et al. discuss approximations used for the separation of short- and long-range interactions in order to facilitate calculations of large systems. They focus on fragment-based (FB) techniques, and review the approximations leading to linear scaling. In the FB approaches the molecule is divided into two or more parts and the short- and long-range interactions as well as the interactions between the subsystems are calculated employing different methods (embedding schemes) as it is done in QM/MM approaches. They review techniques to solve the border region problem, which arises upon the division of the molecule into subsystems and the resulting cutting of covalent bonds. Many properties (e.g. total energies, partial charges, electrostatic potentials, molecular forces, but also NMR chemical shifts) have been obtained with the aid of the FB methods. Using the fragment-based adjustable density matrix assembler (ADMA) method the advantages and disadvantages of the presented techniques are discussed for some test systems.

Gu et al. review the linear scaling elongation method for Hartree-Fock and Kohn-Sham electronic structure calculations for quasi-one-dimensional systems. Linear scaling is achieved by (i) regional localization of molecular orbitals, and (ii) a two-electron integral cutoff technique combined with fast multipole evaluation of non-negligible long-range integrals. The authors describe the construction of regional localized molecular orbitals with the resulting separation into an active region and a frozen region. They demonstrate that reduction of the variational space does not lead to any significant loss of accuracy. Results for test systems (including polyglycine and BN nanotubes) are discussed, which show the accuracy and timing of the elongation method.

Rahalkar et al. review the Molecular Tailoring Approach (MTA), which belongs to the Divide-and-Conquer (DC) type methods. MTA is a fragment-based linear scaling technique, developed for the ab initio calculations of spatially extended large molecules. The authors discuss procedures for the fragmentation of the molecule and how to judge the quality of fragments. MTA can be used to evaluate the density matrix, one-electron properties such as molecular electrostatic potential, molecular electron density, multipole moments of the charge density, the Hessian matrix, IR and vibrational spectra and accurate energy estimates, to within 1.5 mH (~ 1 kcal/mol) of the actual one. The authors discuss application of MTA to properties of large organic molecules, biomolecules, molecular clusters and systems with charged centers. This method has been incorporated in a local version of GAMESS package and has also been interfaced with GAUSSIAN suite of programs.

Neese reviews several algorithms for the exact or approximate calculation of the Coulomb and Hartree-Fock exchange parts of the Fock matrix. The central thesis of this chapter is that for most current quantum chemistry applications, linear scaling techniques are not needed, however, the author adds, if a really big system (e.g. involving several hundreds of atoms, or with a spatial extent >20 – 25 Å) must be studied by quantum chemical methods, then there is no alternative to a linear scaling technique. As far as the Coulomb part of the Fock/Kohn-Sham matrix is concerned,

various techniques are discussed including analytical approaches, methods based on multipole approximation and the resolution of identity or Cholesky decomposition. Similarly, algorithms for calculating the exchange term are reviewed (e.g. the semi-numerical and the RI-K approximation). The computations have been performed by employing the ORCA package.

Rubensson et al. discuss methods to compute electron densities using computer resources that increase linearly with system size. They focus on the Hartree-Fock and density functional theories. The authors review multipole methods, linear scaling computation of the Hartree-Fock exchange and density functional theory exchange-correlation matrices, hierarchic representation of sparse matrices, and density matrix purification. They discuss error control and techniques to avoid the use of the ad hoc selected parameters and threshold values to reach linear scaling. Benchmark calculations are presented, in order to demonstrate the scaling behaviour of Kohn-Sham density functional theory calculations performed with the authors' linear scaling program. It seems that the error control and the distributed memory parallelization are currently the most important challenges.

Aquilante et al. review methods which employ the Cholesky Decomposition (CD) technique. A brief introduction to the CD technique is given. The authors demonstrate that the CD-based approaches may be successfully applied in electronic structure theory. The technique, which provides an efficient way of removing linear dependencies, is shown to be a special type of a resolution-of-identity or density-fitting scheme. Examples of the Cholesky techniques utilized in various applications (e.g. in orbital localization, gradient calculations, approximate representation of two-electron integrals, quartic-scaling MP2) as well as examples of calibration of the method with respect to various properties (e.g. total energies) are presented. In the authors' opinion the full potential of the Cholesky technique has not yet been completely explored.

Korona et al. discuss local methods which are implemented in MOLPRO quantum chemistry package for the description of electron correlation in the ground and electronically excited states of molecules. The authors review improvements in the implementation of the density fitting method for all electron-repulsion integrals. It is shown how the linear scaling of CPU time and disc space results from the local fitting approximations. Extension to open shell systems and the effect of explicitly correlated terms is discussed and it is shown that they lead to significant improvement in accuracy of the local methods. They review electron excitations by EOM-CCSD and CC2 theories as well as first and second-order properties within the framework of local methods. Some applications are reviewed which show the efficiency of the discussed techniques.

Authors Panczakiewicz and Anisimov discuss the LocalSCF approach, which relies on the variational finite localized molecular orbital (VFL) approximation. VFL gives an approximate variational solution to the Hartree-Fock-Roothaan equations by employing compact molecular orbitals using constrained atomic orbital expansion (CMO). A localized solution is attained under gradual release of the expansion constraints. A number of tests have confirmed the agreement of the Local SCF results with those obtained by using less approximate methods.

Niklasson reviews some recursive Fermi operator expansion techniques for the calculation of the density matrix and its response to perturbations in tight-binding, Hartree-Fock and density functional theory, at zero or finite electronic temperatures. It is shown that the expansion order increases exponentially with the number of iterations and the computational cost scales linearly with the system size for sufficiently large sparse matrix representations, due to the recursive formulation. Applications are presented to demonstrate the efficiency of the methods.

Zeller reviews a Green function (GF) linear-scaling technique relying on the Korringa-Kohn-Rostoker (KKR) multiple scattering method for Hohenberg-Kohn-Sham density functional calculations of metallic systems. The author shows how linear scaling is achieved in the framework of this approach. The KKR-GF method directly determines the Kohn-Sham Green function by using a reference system concept. Applications involving metallic systems with thousands of atoms are presented and the exploitation of parallel computers for the applications of the KKR-GF method is discussed.

We would like to take this opportunity to thank all the authors for devoting their time and hard work in enabling us to complete this volume.

Wrocław, Poland
Athens, Greece
St. John's, NL, Canada
Jackson, MS, USA

Robert Zaleśny
Manthos G. Papadopoulos
Paul G. Mezey
Jerzy Leszczynski

CONTENTS

1	Plane-Wave Based Low-Scaling Electronic Structure Methods for Molecules	1
	<i>Peter Pulay</i>	
1.1.	Introduction	1
1.2.	Calculation of the Coulomb Energy in Plane Wave Basis	5
1.2.1.	Technical Difficulties	7
1.3.	Plane Wave and Atomic Basis Sets	10
1.3.1.	Comparison of PW and Atomic Basis Sets	10
1.3.2.	The Best of Both Worlds?	11
1.4.	Implementations and Results	11
1.5.	Outlook and Perspectives	14
	References	15
2	Mathematical Formulation of the Fragment Molecular Orbital Method <i>Takeshi Nagata, Dmitri G. Fedorov, and Kazuo Kitaura</i>	17
2.1.	Introduction	17
2.2.	Formulation of the Restricted Hartree-Fock Equation	18
2.2.1.	Many-Body Expansion	18
2.2.2.	Restricted Hartree-Fock Equation for a Fragment	21
2.2.3.	Fragment Energy	22
2.2.4.	Expression in Terms of Basis Functions	23
2.2.5.	Fragmentation at Covalent Bonds	25
2.2.6.	Green's Function	27
2.2.7.	Approximations	28
2.3.	Second Order Møller-Plesset Perturbation Theory	30
2.3.1.	MP2 Implementations	31
2.3.2.	Using Resolutions of the Identity in MP2	31
2.4.	Coupled-Cluster Theory	32
2.5.	Density Functional Theory	32
2.6.	Multiconfiguration SCF	33
2.7.	Open-Shell Treatment	34
2.8.	Multilayer Approach	34

2.9.	Excited States	35
2.9.1.	Time-Dependent DFT	35
2.9.2.	Configuration Interaction	37
2.10.	Quantum Monte-Carlo	38
2.11.	Energy Gradient	39
2.11.1.	Derivatives of the Internal Fragment Energy	39
2.11.2.	Differentiation of the Density Matrix	41
2.11.3.	Differentiation of the Electrostatic Potential	41
2.11.4.	Differentiation of the Approximated Electrostatic Potential Energy	42
2.12.	Effective Potential Models	44
2.12.1.	Polarizable Continuum Model	44
2.12.2.	Effective Fragment Potential	46
2.12.3.	Model Core Potential	48
2.13.	Scaling	49
2.14.	Molecular Dynamics	50
2.15.	Energy Decomposition Analyses	51
2.15.1.	Pair Interaction Energy Decomposition Analysis	52
2.15.2.	Configuration Analysis for Fragment Interaction and Fragment Interaction Analysis Based on Local MP2	52
2.16.	Basis Set Superposition Error	53
2.17.	Property Calculations	54
2.17.1.	Definition of Molecular Orbitals	54
2.17.2.	Molecular Electrostatic Potential and Fitted Atomic Charges	55
2.17.3.	Nuclear Magnetic Resonance	55
2.17.4.	Multipole Moments and Dynamic Polarizabilities	56
2.17.5.	Nuclear Wave Function	57
2.17.6.	Drug Design	58
2.18.	Massively Parallel Computers	59
2.19.	Recent Applications	59
2.20.	Summary	60
	References	60
3	Linear Scaling Second Order Møller Plesset Perturbation Theory	65
	<i>Svein Saebø</i>	
3.1.	Introduction	65
3.2.	Orbital Invariant Formulation of Møller Plesset Perturbation Theory	67
3.3.	Local Correlation	69
3.3.1.	Pair Selection	69
3.3.2.	Reduction of the Virtual Space	69

3.4.	Recent Linearly Scaling MP2 Methods	71
3.4.1.	Full Accuracy Local MP2	71
3.4.2.	RI-MP2 Methods	78
3.4.3.	Local RI-MP2	80
3.5.	Conclusions	80
	References	81
4	Perturbative Approximations to Avoid Matrix Diagonalization	83
	<i>Péter R. Surján and Ágnes Szabados</i>	
4.1.	Introduction	83
4.2.	Perturbative Energy Estimation Using Laplace Transform	84
4.3.	Iterative Search for the Density Matrix	89
4.4.	Electron Correlation	92
4.4.1.	E2[P] Functional	92
4.4.2.	The FLMO Approach	93
	References	94
5	Divide-and-Conquer Approaches to Quantum Chemistry: Theory and Implementation	97
	<i>Masato Kobayashi and Hiromi Nakai</i>	
5.1.	Introduction: History of Divide-and-Conquer	97
5.2.	Theories of Divide-and-Conquer Method	100
5.2.1.	DC-HF and DC-DFT Theories	100
5.2.2.	DC-Based Correlation Theories	105
5.3.	Assessments of Divide-and-Conquer Method	111
5.3.1.	Implementation	111
5.3.2.	DC SCF	113
5.3.3.	DC-Based Post-SCF Correlation Calculation	116
5.4.	Conclusions and Perspectives	123
	References	125
6	Linear Scaling Methods Using Additive Fuzzy Density Fragmentation	129
	<i>Paul G. Mezey</i>	
6.1.	Introduction	129
6.2.	Common Principles of Linear Scaling Methods	131
6.3.	Locality Aspects of Linear Scaling Methods	131
6.4.	Fundamental Relations Between Local and Global Properties of Molecules	132
6.5.	A Fuzzy Fragment Approach to Linear Scaling Methods	134
6.6.	The Linear Scaling Properties of the Medla and Adma Methods	136

6.7.	Combinatorial Quantum Chemistry Based on Linear Scaling Fragmentation	141
6.8.	Summary	143
	References	144
7	Fragmentation Selection Strategies in Linear Scaling Methods	147
	<i>Zsolt Szekeres and Paul G. Mezey</i>	
7.1.	Introduction	147
7.2.	Chemically Motivated Fragment Selection	148
7.3.	Functional Groups as Primary Fragments	151
7.4.	Delocalized Fragments	152
7.5.	Procrustes Fragmentation	152
7.6.	Multi – Procrustes Fragmentation with Trigonometric Weighting	153
7.7.	Summary	155
	References	155
8	Approximations of Long-Range Interactions in Fragment-Based Quantum Chemical Approaches	157
	<i>Simon M. Eckard, Andrea Frank, Ionut Onila, and Thomas E. Exner</i>	
8.1.	Introduction	157
8.2.	Short-Range and Long-Range Interactions	158
8.3.	Fragment-Based Quantum Chemical Approaches	159
8.4.	Embedding Schemes	163
8.5.	Border Region	164
8.6.	Results of Fa-Adma and Gho-Fa-Adma	167
8.7.	Conclusion	170
	References	170
9	Elongation Method: Towards Linear Scaling for Electronic Structure of Random Polymers and other Quasilinear Materials	175
	<i>Feng Long Gu, Bernard Kirtman, and Yuriko Aoki</i>	
9.1.	Introduction	175
9.2.	The Key Steps of the Elongation Method	177
	9.2.1. Construction of RLMOs	178
	9.2.2. SCF Elongation Step	181
9.3.	Tests of the Accuracy of the Elongation Method: Polyglycine and Cationic Cyanine Chains	182
9.4.	Integral Evaluation Techniques for Linear Scaling Construction of Fock Matrix	190
	9.4.1. Reducing the Number of ERIs	190
	9.4.2. Combination of ERI Cutoff with QFMM Evaluation of Remaining Small Integrals	191

9.5.	Illustrative Linear Scaling Calculations for the Elongation Method with ERI Cutoff and QFMM Evaluation of Remaining Small Integrals	191
9.5.1.	Model Linear Water Chain	191
9.5.2.	Polyglycine	192
9.5.3.	Nanotubes	194
9.6.	Summary and Future Prospects	196
	References	197
10	Molecular Tailoring: An Art of the Possible for <i>Ab Initio</i> Treatment of Large Molecules and Molecular Clusters	199
	<i>Anuja P. Rahalkar, Sachin D. Yeole, V. Ganesh, and Shridhar R. Gadre</i>	
10.1.	Introduction	199
10.2.	Computational Details of MTA	206
10.2.1.	Outline of Algorithm	206
10.2.2.	Fragmentation	207
10.2.3.	Assessment of Fragments	209
10.2.4.	Cardinality Expressions	211
10.3.	Capabilities	212
10.4.	Benchmarks and Applications	213
10.4.1.	Establishing MTA	213
10.4.2.	HF Level	213
10.4.3.	MP2 Method	217
10.4.4.	DFT Framework	220
10.5.	Comment on Scaling of MTA	221
10.6.	Concluding Remarks	222
	References	224
11	Some Thoughts on the Scope of Linear Scaling Self-Consistent Field Electronic Structure Methods	227
	<i>Frank Neese</i>	
11.1.	Introduction	227
11.2.	Linear Scaling Versus Prefactor	230
11.3.	Self Consistent Field Algorithms	232
11.3.1.	Coulomb Term	233
11.3.2.	Exchange Term	246
11.4.	Discussion	258
	References	259

12	Methods for Hartree-Fock and Density Functional Theory Electronic Structure Calculations with Linearly Scaling Processor Time and Memory Usage	263
	<i>Emanuel H. Rubensson, Elias Rudberg, and Pawel Salek</i>	
12.1.	Introduction	263
12.2.	The Self-Consistent Field Procedure	264
12.2.1.	Overview of a Linearly Scaling Program	265
12.2.2.	Erroneous Rotations	268
12.2.3.	Controlling Erroneous Rotations	269
12.3.	Integral Evaluation	270
12.3.1.	Primitive Gaussian Integrals	270
12.3.2.	Screening	270
12.3.3.	Cauchy-Schwarz Screening	271
12.3.4.	The Coulomb and Exchange Matrices	271
12.4.	Coulomb Matrix Construction	272
12.4.1.	Multipole Approximations	272
12.5.	Exchange Matrix Construction	275
12.6.	The Exchange-Correlation Matrix	276
12.6.1.	Numerical Grids	278
12.6.2.	Evaluation of Sparse Exchange-Correlation Potential Matrix	278
12.7.	Error Control in Fock and Kohn–Sham Matrix Constructions . .	280
12.8.	Density Matrix Construction	281
12.8.1.	Energy Minimization	282
12.8.2.	Polynomial Expansions	284
12.8.3.	Accuracy	287
12.8.4.	Density Matrix Construction in Ergo	289
12.9.	Sparse Matrix Representations	289
12.9.1.	How to Select Small Matrix Elements for Removal . .	290
12.9.2.	How to Store and Access Only Nonzero Elements . . .	291
12.10.	Benchmarks	292
12.11.	Concluding Remarks	298
	References	298
13	Cholesky Decomposition Techniques in Electronic Structure Theory .	301
	<i>Francesco Aquilante, Linus Boman, Jonas Boström, Henrik Koch, Roland Lindh, Alfredo Sánchez de Merás, and Thomas Bondo Pedersen</i>	
13.1.	Introduction	302
13.2.	Mathematical Background	303
13.3.	Applications	308
13.3.1.	Connection Between Density Fitting and Cholesky Decomposition	308
13.3.2.	One-Center CD Auxiliary Basis Sets	309

13.3.3.	Orbital Localization Using Cholesky Decomposition	313
13.3.4.	The LK Algorithm	315
13.3.5.	Quartic-Scaling MP2	320
13.3.6.	Calculation of Molecular Gradients	322
13.3.7.	Method Specific Cholesky Decomposition	323
13.4.	Calibration of Accuracy	329
13.4.1.	Accuracy of Total Energies	330
13.4.2.	Accuracy of Vertical Transition Energies	331
13.4.3.	Auxiliary Basis Set Pruning	332
13.5.	Implementational Aspects	333
13.6.	Outlook and Perspectives	338
13.7.	Summary and Conclusions	339
	References	341
14	Local Approximations for an Efficient and Accurate Treatment of Electron Correlation and Electron Excitations in Molecules	345
	<i>Tatiana Korona, Daniel Kats, Martin Schütz, Thomas B. Adler, Yu Liu, and Hans-Joachim Werner</i>	
14.1.	Introduction	345
14.2.	Local Treatment of Electron Correlation	348
14.2.1.	Local Approximations in the Electronic Ground State	350
14.2.2.	Exploiting Localization in Program Algorithms	357
14.2.3.	Perturbative Triple Excitations	364
14.2.4.	Open-Shell Local Correlation Methods	365
14.2.5.	Explicitly Correlated Local Correlation Methods	367
14.3.	Density Fitting	369
14.3.1.	Local Density Fitting in LMP2	370
14.3.2.	Local Density Fitting in LCCSD(T)	372
14.4.	Local Properties of First and Second Order	374
14.4.1.	Analytical Energy Gradients for Local Wave Functions	375
14.5.	Local Methods for Excited States	377
14.5.1.	Local EOM-CCSD	378
14.5.2.	Local CC2 Response Theory	381
14.6.	Example Applications	388
14.6.1.	Equilibrium Structures, Vibrational Frequencies, and Other Molecular Properties	388
14.6.2.	Reaction Energies and Conformational Energies	389
14.6.3.	QM/MM Calculations of Reaction Barriers in Enzymes	390
14.6.4.	Intermolecular Interactions	391
14.6.5.	Open-Shell Local Coupled Cluster Calculations	392
14.6.6.	Explicitly Correlated Local Coupled Cluster Calculations	397
14.6.7.	Excited States	398
14.7.	Outlook	401
	References	403

15	The Linear Scaling Semiempirical LocalSCF Method and the Variational Finite LMO Approximation	409
	<i>Artur Panczakiewicz and Victor M. Anisimov</i>	
15.1.	Introduction	410
15.2.	Theory	411
15.2.1.	Linear Scaling Problem	411
15.2.2.	VFL Approximation	413
15.2.3.	LocalSCF Method	417
15.2.4.	SCF Convergence Criteria	420
15.2.5.	Quantum-Mechanical Molecular Dynamics	423
15.3.	Validation	424
15.3.1.	Linear Scaling	424
15.3.2.	Accuracy of the Linear Scaling Algorithm	426
15.3.3.	Validation of QM Molecular Dynamics	431
15.4.	Concluding Remarks	435
	References	436
16	Density Matrix Methods in Linear Scaling Electronic Structure Theory	439
	<i>Anders M.N. Niklasson</i>	
16.1.	Introduction	439
16.2.	The Eigenvalue Problem	442
16.3.	Quantum Locality and Disorder	444
16.4.	Fermi Operator Expansion	446
16.4.1.	Chebyshev Expansion	447
16.4.2.	Green's Function Expansion	448
16.4.3.	Recursive Fermi-Operator Expansion at $T_e > 0$	449
16.4.4.	Recursive Fermi-Operator Expansion at $T_e = 0$ by Purification	451
16.4.5.	Convergence and Accuracy	459
16.4.6.	Iterative Refinement Techniques	463
16.5.	Linear Scaling Density Matrix Perturbation Theory	464
16.5.1.	Density Matrix Response by Recursion	465
16.5.2.	Calculating Response Properties From the $n + 1$ and $2n + 1$ Rules	467
16.5.3.	Example	468
16.6.	Summary	469
	References	469
17	Linear Scaling for Metallic Systems by the Korringa-Kohn- Rostoker Multiple-Scattering Method	475
	<i>Rudolf Zeller</i>	
17.1.	Introduction	475
17.2.	Preliminaries	476

17.2.1.	Density Functional Theory	476
17.2.2.	Linear Scaling Strategies	477
17.2.3.	Metallic Systems	479
17.3.	The KKR-GF Method	480
17.3.1.	Properties of the Green Function	481
17.3.2.	Calculation of the Green Function	482
17.3.3.	Complex Energy Integration	485
17.3.4.	Total Energy and Forces	486
17.3.5.	Temperature Error	488
17.4.	Linear Scaling in the KKR-GF Method	490
17.4.1.	Repulsive Reference System	490
17.4.2.	Iterative Solution	493
17.4.3.	Green Function Truncation	494
17.4.4.	Model Study	495
17.4.5.	Scaling Behaviour	498
17.5.	Conclusions and Outlook	500
	References	503
Index		507

CHAPTER 1

PLANE-WAVE BASED LOW-SCALING ELECTRONIC STRUCTURE METHODS FOR MOLECULES

PETER PULAY

*Department of Chemistry and Biochemistry, University of Arkansas, Fayetteville, AR 72701, USA,
e-mail: pulay@uark.edu*

Abstract: This paper reviews the use of plane-wave based methods to decrease the scaling of the most time-consuming part in molecular electronic structure calculations, the Coulomb interaction. The separability of the inverse distance operator allows the efficient calculation of the Coulomb potential in momentum space. Using the Fast Fourier Transform, this can be converted to the real space in essentially linearly scaling time. Plane wave expansions are periodic, and are better suited for infinite periodic systems than for molecules. Nevertheless, they can be successfully applied to molecules, and lead to large performance gains. The open problems in the field are discussed.

Keywords: Basis sets, Density functional theory, Molecular orbitals, Plane waves, Quadrature

1.1. INTRODUCTION

In most routine molecular quantum chemistry calculations, for instance in Hartree-Fock and density functional (DFT) theories, the dominant computational work is the evaluation of the electron repulsion energy and its matrix elements. This chapter focuses on the efficient evaluation of these quantities, in particular the Coulomb component, using expansions in plane waves. This reduces the steep scaling of the electron repulsion terms with molecular and basis set size drastically. Alternative methods are discussed in other chapters. The main advantage of plane wave based low-scaling methods over competing methods, for instance the fast multipole method [1, 2] is that they become efficient for modest-sized molecules already; many alternative methods don't show significant improvement until large system sizes. However, their infinite periodic nature is not a natural fit with molecules.

The overwhelming majority of molecular electronic structure calculations use atomic basis sets, corresponding to the chemists' notion of a molecule consisting of atoms. In this method, the unknown molecular orbitals (MOs) φ_i are represented as linear combinations of atomic-like fixed basis functions χ_p

$$\varphi_i(\mathbf{r}) = \sum_p \chi_p(\mathbf{r}) C_{pi} \quad (1-1)$$

where \mathbf{r} is the position of the electron. The basis functions are often designated as atomic orbitals (AOs), although they are usually not genuine atomic orbitals. The unknown coefficients C_{pi} are determined by minimizing the total energy. In the non-relativistic case, the ultimate building blocks, the spin-orbitals, can be written as the products of an orbital and a spin function, usually simply α or β . The main advantage of the atomic basis set representation is its compactness. By using the atomic nature of the electron distribution, a few hundred basis functions can adequately describe the MOs of a typical drug-sized molecule. This advantage was essential when computer memories were measured in kilobytes, rather than Gigabytes but it is less important now.

Solid state physicists often use a diametrically opposite starting point where the natural basis functions are plane waves. (For a general reference on plane wave methods, see [3].) In the first approximation, the presence of atoms in the elementary cell is neglected. To preserve electrical neutrality, the positive charge of the nuclei is smeared out evenly in space. In this ‘‘jellium’’ model, the natural basis functions are plane waves (PWs), conveniently written in complex form as

$$\chi(\mathbf{r}) = \exp(i\mathbf{a}\mathbf{g}\mathbf{r}), \quad (1-2)$$

using the Euler formula, $e^{ix} = \cos(x) + i\sin(x)$. Here $\mathbf{g} = (g_x, g_y, g_z)$ is a vector of integers, and $a = 2\pi/L$ where L is dimension of the elementary cell. For simplicity, it is assumed here that L is the same in all three spatial dimensions, although in actual calculations this condition is fulfilled only for cubic space groups. For molecules, a box enclosing essentially the whole electron density replaces the elementary cell; the dimensions are adjusted to the size of the molecule. The factor a ensures that the plane waves are commensurate with the dimensions of the elementary cell. To limit the number of plane wave basis functions, the magnitude or the maximum component of \mathbf{g} must be restricted. A plane wave expansion can describe any orbital or electron density to arbitrary accuracy if the upper limit on \mathbf{g} is sufficiently high. However, the number of plane waves required to describe the sharply peaked core orbitals is huge, and in practice core orbitals and core electron densities cannot be adequately represented by plane waves. Even the valence shells of some electronegative atoms, for instance oxygen, are too compact to be easily represented by plane waves. The quantity characterizing the cutoff is usually given as the kinetic energy corresponding to the maximum wave vector, $E_{cutoff} = 2\pi^2(g_{max}/L)^2 E_h$ (atomic unit of energy; this quantity is often quoted in Rydberg units, $1 \text{ Ry} = 0.5 E_h$). Unless specifically noted, we will use atomic units in this chapter, i.e., distances are measured in units of the Bohr radius a_0 , and energies in Hartrees, E_h . A quantity more useful than g_{max} is the grid density, $d = 2g_{max}/L$, i.e. the number of plane wave basis functions per bohr.

Plane wave based methods became popular in the physics community after the introduction of the Car-Parrinello direct dynamics method [4], for which plane

wave basis sets are particularly appropriate. A number of plane-wave based density functional programs have been developed, mainly for the treatment of solid state problems: CASTEP [5], VASP [6], and Quantum Espresso [7] are three representative examples. Plane wave based electronic structure programs are most appropriate to “pure” DFT, i.e., no Hartree-Fock exchange, because including exact (Hartree-Fock) exchange increases the computational work very much. In addition, to keep the number of plane wave basis functions reasonable, the core electrons (and in some cases even the inner valence) have to be represented by alternative means, treating explicitly only the smoother valence electron distribution. Core charge densities can be replaced by pseudopotentials (effective core potentials), or represented as frozen cores in an atomic basis set. The latter Augmented Plane Wave (APW) methods played an important role in solid-state physics [8] but the severe approximations that they used, and their solid-state orientation made them largely irrelevant for chemistry which is a science of small energy differences. The modern version of the augmented plane wave method, the Projector Augmented Wave (PAW) technique of Blöchl [9], employs only the frozen-core approximation, and can be cast in a form closely analogous to the “ultrasoft” pseudopotentials of Vanderbilt [10], as shown by Kresse and Joubert [11]. Even after eliminating the cores, the number of plane waves required for an accurate representation of the orbitals is large. The actual number depends on the size and description of the core, and the desired accuracy but, for high accuracy, can easily exceed a few million. This causes difficulties with the optimization of the wavefunction which scales computationally as the cube of the basis set size.

The periodic nature of the PW basis is appropriate only for 3-dimensional crystals. Lower dimensional systems: layers, polymer chains, and molecules can be treated by the supercell method, i.e. placing the system in a box sufficiently large to eliminate the interaction between the system and its periodic images. However, this leads to inefficiencies because in PW methods, empty space is not free computationally. An alternative method, based on the truncation of the Coulomb operator, will be described below. We will not be able to review physics-based, solid-state oriented PW methods here; there are a number of excellent reviews in the literature. Rather, we will concentrate on the application of an auxiliary PW basis for the calculation of the Coulomb energy in traditional atomic (in practice Gaussian) basis set calculations. Such methods were first suggested by Lippert et al. [12], and have since been implemented in at least three comprehensive programs: Quickstep [13], see Refs. [12, 14–19]; PQS [20, 21], see Refs. [22–27]; and Q-Chem [28], see Refs. [29–32]. The first implementation uses the acronyms GPW and GAPW; the latter two implementations are known as the Fourier Transform Coulomb (FTC) method. In spite of the promising results published by these groups (see the last section), the potential of plane-wave based methods has not yet been fully utilized in mainstream quantum chemistry.

The principal attraction of PW methods in quantum chemistry is that they allow the low-scaling calculation of the electron repulsion energy which is traditionally the most expensive part of routine calculations. The electron repulsion energy of a determinantal (Hartree-Fock) wavefunction can be conveniently written as the

sum of two terms: the classical Coulomb energy, expressed through the charge density as

$$J = \frac{1}{2} \int d\mathbf{r}^3 \int d\mathbf{r}'^3 \rho(\mathbf{r})\rho(\mathbf{r}')|\mathbf{r} - \mathbf{r}'|^{-1} = \frac{1}{2} \sum_{ij}^{occ} (ii|jj), \quad (1-3)$$

and the exchange term

$$K = 1/2 \sum_{ij}^{occ} (ij|ij). \quad (1-4)$$

Here i and j stand for occupied spin-orbitals ψ_i and ψ_j , respectively, ρ is the electron charge density: $\rho(\mathbf{r}) = \sum_i^{occ} |\psi_i|^2$, and the integrals over \mathbf{r} and \mathbf{r}' run over all space. A two-electron integral is defined in general as

$$(ij|kl) = \int d\mathbf{r}^3 \int d\mathbf{r}'^3 \psi_i(\mathbf{r})\psi_j^*(\mathbf{r})\psi_k(\mathbf{r}')\psi_l^*(\mathbf{r}')|\mathbf{r} - \mathbf{r}'|^{-1} \quad (1-5)$$

The Coulomb term is easily visualized as the self-repulsion of the electron cloud with density ρ . The exchange term has no classical analogue. It arises from the antisymmetry of the wavefunction required by the Pauli principle.

Common (also called “pure”) DFT replaces the exchange energy K (and usually also the much smaller correlation energy) by a local or semilocal functional of the electron density, while in “hybrid” DFT a fraction of the Hartree-Fock exchange, Eq. (1-4), is retained. This is important in the present context because most low-scaling methods can be applied readily only to the classical Coulomb term, and are thus largely restricted to pure DFT methods.

In traditional Hartree-Fock theory, both J and K are calculated by substituting the expansion of the orbitals by basis functions, Eq. (1-1), in Eqs. (1-3) and (1-4). This gives equations that contain 4-index AO integrals ($pq|rs$), and scale formally with the fourth power of the AO basis set size N . This “integral catastrophe” was the major hurdle preventing the application of quantum theory to realistic molecular systems in the early phase of quantum chemistry. The problem resolved itself partially with the dramatic expansion of computer power from 1980 on, because, using proper thresholding, the basis function products (usually called charge densities) pq and rs become negligible if the AOs p and q , or r and s are distant. This means that, for large systems, the number of non-vanishing charge densities grows linearly and not quadratically with the size of the system, assuming that the type of the basis set is kept the same. However, the number of necessary two-electron integrals still grows quadratically with the molecular size because the Coulomb operator, $|\mathbf{r} - \mathbf{r}'|^{-1}$, has long range. Although the steep $O(N^4)$ scaling of AO-based MO theory naturally reduces to $O(N^2)$ in the limit of large molecules, it still imposes a stiff limit on the system size that can be treated with traditional quantum chemistry programs.

Of the two components of the electron repulsion energy, Coulomb and exchange, the scaling of exchange is reduced further naturally (at least in insulators) by the

locality of the density matrix [33]. As a consequence, Hartree-Fock exchange should scale linearly with system size in the asymptotic limit [34–37]. In practice, it is difficult to reach the asymptotic scaling regime, even for linear molecules. However, hybrid density functional that use only the short-range component of the electron repulsion, for instance the HSE functional [38] are comparable in accuracy to functional that use the full exact exchange, and converge faster with system size. Guidon et al. [19] extended the Quickstep program to include short-range Hartree-Fock exchange. The exchange terms are calculated in Gaussian basis as in conventional Hartree-Fock theory. PQS [20, 21] can also use exact exchange but with a significant loss of efficiency.

Natural scaling reduction does not help if the basis set is increased while the molecule size is kept constant in AO basis set methods. In this case, the computational effort to generate and process the 2-electron integrals increases roughly as $O(N^4)$.

1.2. CALCULATION OF THE COULOMB ENERGY IN PLANE WAVE BASIS

The main advantage of a plane wave basis is that the Coulomb operator is separable in plane wave basis. The Fourier transform of the inverse distance operator is given by the Fourier integral

$$|\mathbf{r} - \mathbf{r}'|^{-1} = (2\pi^2)^{-1} \int k^{-2} \exp[i\mathbf{k} \cdot (\mathbf{r} - \mathbf{r}')] d\mathbf{k}^3 \quad (1-6)$$

where $k = |\mathbf{k}|$, and \mathbf{k} is a vector in the reciprocal (momentum) space. The integral is over the full reciprocal space. Representing the infinite periodic charge density by a plane wave expansion (see Eq. (1-2)),

$$\rho(\mathbf{r}) = \sum_{\mathbf{g} < g_{max}} D(\mathbf{g}) \exp(i\mathbf{g} \cdot \mathbf{r}) \quad (1-7)$$

yields the Coulomb potential of the infinite periodic charge density $\rho(\mathbf{r})$ as

$$V(\mathbf{r}) = \int \rho(\mathbf{r}') |\mathbf{r} - \mathbf{r}'|^{-1} d\mathbf{r}' = \left(\frac{L^2}{\pi}\right) \sum_{\mathbf{g}} D(\mathbf{g}) g^{-2} \exp(i\mathbf{g} \cdot \mathbf{r}) \quad (1-8)$$

where we made use of the the orthogonality of plane waves:

$$\int_{-\infty}^{\infty} e^{i(k-k')x} dx = 2\pi \delta(k - k'), \quad (1-9)$$

$g = |\mathbf{g}|$, and the factor L^2 comes from $a^{-2} = (2\pi/L)^{-2}$. Associated with the reciprocal space grid, there is a corresponding real-space grid with the same number of grid points, and a spacing $h = d^{-1}$, i.e., the inverse of the reciprocal (momentum) space grid density introduced in the previous section. Using the fast Fourier

transform (FFT), one can switch from one representation to the other. For quantities that can be represented exactly in the plane-wave basis, the two representations are equivalent. The efficiency of the method derives from the ability to perform each operation in the appropriate representation, i.e., in direct space or momentum space. Thus the Coulomb potential in the discrete momentum space is simply $D(\mathbf{g})g^{-2}$ (cf. Eq. 1-8); its Fourier transform gives the potential $V(\mathbf{r})$ at the real space gridpoints \mathbf{r}_p . $V(\mathbf{r})$ is used to calculate the Coulomb energy in real space by numerical quadrature on the real space grid,

$$J = \int V(\mathbf{r})\rho(\mathbf{r})d\mathbf{r}^3 \approx \sum_p V(\mathbf{r}_p)\rho(\mathbf{r}_p)w(\mathbf{r}_p) \quad (1-10)$$

where \mathbf{r}_p is a real-space grid point and w_p is a quadrature weight; for simple rectangular grids, the weights are constants. The summation in Eq. (1-10) is carried out only in the principal unit cell. The evaluation of the matrix elements of the Coulomb operator is similar, except that the total charge density is replaced by an elementary charge distribution, i.e. by the product of two basis functions:

$$J_{pq} = \int \chi_p^*(\mathbf{r})V(\mathbf{r})\chi_q(\mathbf{r})d\mathbf{r}^3 \approx \sum_p V(\mathbf{r}_p)\chi_p^*(\mathbf{r})\chi_q(\mathbf{r})w(\mathbf{r}_p) \quad (1-11)$$

where χ_p and χ_q are (atomic) basis functions.

Neglecting some technical difficulties which will be addressed below, the essence of the plane-wave (or Fourier space) calculation of the Coulomb energy is to use the two equivalent representation of the potential and the charge density: on a direct-space grid with a spacing $h = d^{-1}$ ($d = 2g_{\max}/L$) in a box of size L , and in the reciprocal space of the integer vectors \mathbf{g} where $|\mathbf{g}| < g_{\max}$. Efficient transformation between the direct and reciprocal space representations, using the fast Fourier transform (FFT) technique, is critical to the success of the plane wave method. An N-point FFT (in one dimension) scales as $O(N\log N)$, i.e., the scaling is only slightly higher than linear. (The base of the logarithm is not specified here as it is not relevant for the scaling; it can be assumed to be 2 if the number of grid points is a power of 2.)

Disregarding the complications caused by the presence of compact orbitals and charge densities, the calculation of the Coulomb energy and matrix consists of the following steps:

- (1) Calculate the electron density on the real-space grid
- (2) Use Fast Fourier Transformation (FFT) to obtain a plane wave (reciprocal space) representation of the charge density, Eq. (1-7), on the plane wave grid defined by the reciprocal vectors \mathbf{g}
- (3) Divide values of the charge density in the reciprocal space by g^2 to obtain the Coulomb potential
- (4) Transform the potential back to real space, Eq. (1-8), using FFT
- (5) Evaluate the Coulomb energy in real space by quadrature, Eq. (1-10)

- (6) For each pair of atomic orbitals p and q , integrate their product with the potential to obtain the matrix elements of the Coulomb operator, needed to form the Fock matrix, according to Eq. (1-11).

The efficiency and scaling of this procedure is determined by three time-critical steps: the calculation of the electron density (1), the Fast Fourier Transformation (FFT) steps (2) and (4), and the evaluation of the matrix elements of the J operator, step (6). The first step can be carried out in two different ways: calculating the orbital values first, and forming the sum of their squares, or using a density matrix formalism, $\rho(\mathbf{r}) = \sum_{pq} D_{pq} \chi_p(\mathbf{r}) \chi_q(\mathbf{r})$. Without thresholding, both have fairly high scaling, e.g., the second method scales as $O(N^3)$. However, if the basis functions are local, this scaling reduces to linear. As mentioned above, FFT scales as $O(M \log N)$ where N is the number of grid points. This is evident for a one-dimensional FFT but also holds in the two- and three-dimensional case. For a given spatial resolution, N is proportional to the volume of the system (more precisely, the volume of a box that contains essentially the whole electron density of the system). In the limit of large systems, the volume and therefore N is roughly proportional to the number of atoms, and the scaling is only slightly steeper than linear.

The numerical integration for the evaluation of the Coulomb energy is obviously linear in the number of the grid points. The calculation of the Coulomb matrix elements appears at first to have a steeper scaling. However, the usual atomic basis functions are highly localized, and, for sufficiently large systems, the number of Coulomb matrix elements exceeding a given threshold is linear in the system size. If properly implemented, the integration effort is independent of the system size, depending only on the spatial extent of the basis functions and the grid density, giving an overall linear scaling. However, this limit is reached only for relatively large systems.

1.2.1. Technical Difficulties

1.2.1.1. Divergencies

The recipe given above appears straightforward. However, in actual implementation, a number of technical problems arise. Chief among these is the fact that the Coulomb potential of an infinite periodic charge density diverges if the lower electrical moments (up to quadrupole), of the elementary cell are non-zero. This is of course always the case if the electronic charge is considered by itself, without the cancelling nuclear charges. (A good discussion of the problems with divergence and conditional convergence, which also arise if the dipole moment of the elementary cell is non-zero, is given in [39], and will not be repeated here.) The problem is that the $\mathbf{g} = \mathbf{0}$ component of the density in the reciprocal space, $D(\mathbf{0})$, is non-zero, resulting in division by 0 in Eq. (1-8). Simply omitting $D(\mathbf{0})$ is physically equivalent to the jellium model, i.e. to adding a uniform neutralizing positive charge density to the system which is far from the actual system. Calculating the Coulomb potential in real space can easily avoid singularities, even for charged systems [40] but this procedure has quadratic scaling and its accuracy is limited [23].

An alternative approach is to consider the total (nuclear + electronic) charge, which has no net charge for neutral systems. The problem here is that the self-repulsion energy of pointlike nuclei, Eq. (1-10) diverges to infinity. In addition, the presence of sharp singularities in the potential causes numerical errors in the numerical quadratures. A possible solution [14, 41] is to smear out the nuclear charge, for instance replacing the pointlike nuclei by positive Gaussian charge distributions, calculate the Coulomb energy and its matrix elements with the modified charge distribution, and correct the result for the difference between the smeared-out and real nuclei. This method is viable, although somewhat involved, and the sharp nuclear charge distributions are a source of numerical errors. Neither of these methods can handle ions. This is not a problem in solid-state applications, as a solid should obviously be electrically neutral, but is a limitation for molecular calculations.

A simpler and more general solution to the divergence problem is to modify the Coulomb potential, eliminating its infinite range which is the source of divergence. In a purely numerical fashion, this was introduced by Hockney [42, 43]. The Coulomb potential, $1/r$, can be simply truncated to zero at $r > D$. The limit D should be chosen to exceed the maximum distance between non-negligible charges in the system. If the periodic repeating box is large enough so that the minimum distance between non-vanishing charges in neighboring boxes is larger than D then the spurious Coulomb effect of neighboring boxes vanishes. This requires a box roughly twice as large as the original box that contains all the charges. The truncated $1/r$ function has an exact Fourier transform: $4\pi k^{-2}[1 - \cos(kD)]$ which differs from the Fourier transform of the infinite-range $1/r$ function by the factor in the square bracket. To the knowledge of the current author, this was first described by Pollock and Glosli [44] but it was not widely known or used, and was rediscovered several times [23, 45]. An alternative method, introduced by Martyna and Tuckerman [46], uses the Ewald decomposition of the Coulomb potential in a long-range and a short-range term, and retains only the latter. While not exact, this method can be made arbitrarily accurate by choosing proper thresholds. It has the advantage that there is no discontinuity in the modified Coulomb potential which generate high frequency components in the reciprocal space and slow down convergence. Note that there is no strict need for the existence of an analytical Fourier transform of the modified Coulomb interaction. For instance, a function $v(r) = 1/r$ if $r < D_1$, $p(r)$ if $D_1 < r < D_2$, and zero if $r > D_2$, could be used, in connection with a tabulated numerical Fourier transform. The function $p(r)$ could be chosen as a polynomial that makes the function $v(r)$ and its first, second,.. derivatives continuous. A function like this has no simple analytical Fourier transform but is rigorously zero beyond D_2 and is smooth. Its numerical Fourier transform must be determined only once and can be stored in tabulated form.

The concept of truncated Coulomb potential can be extended from zero-dimensional molecules ("clusters" in the physics literature) to one- and two-dimensional systems, i.e. polymers (or wires) and layers (or slabs). The Coulomb interaction in these systems must be truncated in two dimensions (for polymers and wires), or one dimension (for layers), and retains its infinite range in the periodic dimensions. The analytical derivation of the Fourier transform of these potentials

is tedious but the resulting formulas are quite simple, both for layers [44] and for polymers. The Ewald decomposition method can be similarly generalized for these cases [47].

1.2.1.2. Compact Charge Densities

Another obvious difficulty with plane wave expansions is that they can represent only smooth charge densities at reasonable computational effort. The sharply peaked core regions must be treated by alternative methods. In programs which use plane waves directly as basis functions, this usually means that the cores, and sometimes even the inner valence regions of the atoms must be represented by pseudopotentials (effective core potentials). Modern pseudopotentials provide accurate representation of the effect of the core on the valence electrons, and in some cases are preferable to all-electron treatment because they allow the inclusion of the main relativistic effects in a non-relativistic program. However, they are obviously inappropriate for properties that are strongly dependent on the core orbitals. Transition metals are a particularly difficult problem, as they have incompletely filled compact d or f shells which must be included in the valence orbital set but are difficult to treat using plane waves with moderate cutoffs. Electronegative first-row elements (O, F) likewise have compact valence shells. This problem can be addressed by two techniques: ultrasoft pseudopotentials [48], and the Projector Augmented Wave (PAW) method of Blöchl [9, 49, 50]. In both methods, fixed atomic orbitals are used to describe the bulk of the core charge, with plane waves supplying a smooth correction. Both methods avoid the tedious matching of orbitals on surfaces separating the cores from the valence region.

Methods which retain atomic basis sets and use plane waves only for the calculation of the Coulomb terms must similarly divide the charge density into a diffuse and a compact component [12]. The Coulomb potential of the diffuse component can be calculated efficiently using a plane wave expansion; for the core part, alternative techniques must be used. For Gaussians, charge density components, i.e., products of atomic basis functions, can be classified based on the sum of the exponents of the Gaussians which largely determines the compactness of the resulting charge density. (In some programs, three cases are distinguished: products of two diffuse basis functions, the product of a compact and a diffuse function, and the product of two compact functions. However, there is no advantage in treating the second and third cases differently: the product of a compact and a diffuse basis function gives a compact charge density.) It is worth mentioning that treating compact and diffuse basis functions separately runs contrary to the idea of contracted Gaussian basis sets, i.e., using fixed linear combinations of primitive Gaussians as basis functions. This problem can be easily taken care of by switching to a decontracted (primitive) representation. Decontracting increases the size of the basis set 1.5–3 times and thus requires significantly more memory but this has ceased to be a problem on modern computers.

There are several methods for the calculation of the Coulomb potential originating from the compact core (and semicore) charges, apart from pseudopotentials

and the Projector Augmented Wave method, which presume a frozen core density and are thus not appropriate for phenomena that involve the cores. The simplest method is to use traditional integral-based algorithms. Because of the highly localized nature of the core orbitals, only a small fraction of the integrals (a few percent in a moderately sized molecule) involve core orbitals. We have found, however, that the effort needed to evaluate core Coulomb contributions by this method is comparable to the evaluation of the rest of the Coulomb terms because of the inherently low efficiency of traditional two-electron integral based algorithms. Other alternatives are density fitting (DF), also called resolution of identity, and a multipole expansion of the core potential. The situation is simplified by the fact that the charges involved are sums of largely spherical atomic-like charge densities. This simplifies both the expansion of the basis set in an auxiliary basis, and the truncation of the multipole expansion. While neither method is linearly scaling, they should reduce the computational effort needed for the core electrons sufficiently to make this part computationally insignificant except in huge calculations.

1.3. PLANE WAVE AND ATOMIC BASIS SETS

1.3.1. Comparison of PW and Atomic Basis Sets

In this section, we compare plane wave basis sets with atomic basis sets. As we shall see, both have significant advantages and disadvantages. The main advantage of atomic basis sets is their compactness: a small set of basis functions can adequately represent an atom in a molecule. Their disadvantages are:

- (1) The definitions of basis sets are complex and somewhat arbitrary, leading to a profusion of competing basis sets, and makes comparing calculations difficult
- (2) The formulas for the evaluation of the integrals are complex and computationally expensive
- (3) They are not orthogonal, which may lead to near-linear dependence and numerical problems
- (4) The coupling of the basis function centers to the nuclear positions complicates the evaluation of the forces on the nuclei
- (5) The Basis Set Superposition Error (BSSE) introduces unphysical attractive forces between atoms.

The advantages of plane wave basis sets are

- (1) They are simple and regular, controlled by a single parameter, the cutoff energy or maximum wave vector
- (2) They allow a highly efficient evaluation of the Coulomb potential
- (3) They are orthogonal, and free from linear dependencies
- (4) They are independent of the nuclear positions, simplifying the calculation of forces on the atoms
- (5) They are free of the Basis Set Superposition Error

These advantages are accompanied by significant disadvantages:

- (1) The large number of plane waves makes the optimization of the wavefunction expensive
- (2) The calculation of the exact (Hartree-Fock) exchange is also expensive in a PW basis
- (3) Atomic cores and compact charge densities cannot be represented with a reasonably sized plane wave basis, and must use auxiliary functions or pseudopotentials

1.3.2. The Best of Both Worlds?

The comparison between plane waves and atomic basis sets suggests that a combination of both may be more efficient than either one alone. There are two possible routes:

The first is to use a genuine augmented plane wave basis set, i.e., a basis set that consists of both plane waves and Gaussians. Plane waves would describe only the diffuse part of the electron cloud, and Gaussians the inner valence and core orbitals. In this method, a limited number of plane waves suffices because only the diffuse basis functions are represented by the plane waves. Most of the problems with atomic basis sets (overcompleteness and basis set superposition error) are caused by diffuse basis functions, and a combined basis should eliminate both while still remaining reasonably compact. A combination as described makes most sense for accurate large basis set calculations, and there is no reason why it should be restricted to density functional theory. Configuration-based electron correlation methods should be feasible, as the basis set size remains modest. As yet, there is no general implementation of this method except for initial tests for very small molecules [22], although all tools are available, and it appears a worthwhile goal.

A simpler alternative, introduced by the Parrinello group [12, 14, 15] and implemented in Quickstep [13], PQS [21] and Q-Chem [28] uses simply an atomic Gaussian basis set. However, the most expensive part of the calculation, the evaluation of the Coulomb terms, is carried out in an auxiliary plane wave basis. This results in a significant speed-up, particularly for large basis sets. However, some of the undesirable aspects of atomic basis sets, in particular overcompleteness of large atomic basis sets and its consequence, near linear dependence, and also basis set superposition error, reappear. The rest of this chapter will deal exclusively with this second method.

1.4. IMPLEMENTATIONS AND RESULTS

All three implementations (Quickstep, PQS and Q-Chem) of the GAPW/FTC (Gaussian and Plane Wave or Fourier Transform Coulomb) methods show significant, in some cases spectacular speed-ups compared to conventional Gaussian non-hybrid DFT calculations, particularly for large basis sets. For instance,

VandeVondele et al. [13] report a DFT pseudopotential calculation on a dinucleoside monophosphate crystal with 280 atoms in the unit cell, using a double zeta plus polarization basis set developed specifically for Quickstep (2,712 basis functions). A single optimization cycle (energy plus forces) on a single CPU took only 6 min, making such large calculations feasible on a desktop computer. Calculation using over 40,000 basis functions for 1,024 water molecules are reported in [13]. Unfortunately, our own attempts to use Quickstep were hindered by SCF convergence difficulties, even on molecules with large bandgaps.

The FTC timings obtained by PQS and Q-Chem are less spectacular but still very encouraging. These programs use a more conservative strategy and try to match the total energy of conventional programs to high accuracy, say $10^{-6} E_h/\text{atom}$. Such high accuracy in the total energy is necessary to convince new users about the reliability of the method. However, it is not needed for most problems, as shown by the accuracy tests of VandeVondele et al. on molecular geometries [13].

All three implementations show clearly that, in order to take full advantage of the large speed-ups in the Coulomb contribution, it is necessary to accelerate all other significant parts of the calculation. Both the part of the Coulomb operator that is calculated in the Gaussian basis, and the evaluation of the exchange-correlation contribution must be accelerated significantly to match the performance gained by the improved Coulomb algorithm. This is particularly important for smaller basis sets where the Coulomb evaluation is less dominant computationally. For instance, for a series of diamond-like carbon clusters, Füsti-Molnár and Kong [29] obtain a fourfold speed-up for the Coulomb term over the already very efficient (J-engine+Continuous Fast Multipoles) algorithm for a diamond-like carbon cluster of 150 atoms, using the 6-311G(d,p) basis set. However, the overall speed-up is only 1.71 because of the overhead from the calculation of the exchange-correlation (69% of the total time) and diagonalization (7%). The FTC step itself amounts to only 5% of the total calculational time. The diagonalization step, or its equivalent (e.g., pseudodiagonalization [51] or Orbital Transformation [52]) becomes important only for calculations over $\sim 5,000$ basis functions. Such large systems (several hundred atoms) can be frequently treated by alternative methods, for instance a combination of quantum mechanical techniques and empirical molecular mechanics (QM/MM) methods. As the above example shows, the main overhead steps for moderately large calculations are the exchange-correlation contribution and the Coulomb contributions that FTC cannot calculate (19% in the above example). The timings obtained using PQS and shown below agree with this general picture.

Significant effort has been undertaken to improve the computational steps that are responsible for the non-Coulomb overhead. Quickstep [13] uses a sophisticated multigrid algorithm for the numerical quadrature. The authors of Q-Chem have also developed new grids for integrating the exchange-correlation term [30–32].

A technical aspect of GAPW/FTC calculations that is worth mentioning is that contractions (which typically include basis functions with both high and low exponents) interfere with FTC since only the lower exponent (more diffuse) functions can be treated by FTC. Either a special decontracted basis set must be used, or the basis can be decontracted in the program. The second alternative is preferable, as standard basis sets can be used.

Table 1-1. Timings (in minutes) and total energies for aspirine, $C_9H_8O_4$, on a 2 GHz AMD 246 Opteron processor. The column ERI shows timings calculated using the traditional electron repulsion integral algorithm. The calculations use slightly decontracted versions of the 6-31G(d,p) and 6-311G(2df, 2pd) basis sets. Coulomb, XC and Matrix refer to the calculation of the Coulomb operator and energy, the calculation of the exchange-correlation and miscellaneous (mainly matrix) operations, such as diagonalization, pseudodiagonalization and DIIS. For FTC calculations, the Coulomb timing includes both the plane wave and the traditional integral time, with the latter dominating for large calculations by about a factor of 3

Basis set	6-31G(d,p)-dc (NBF = 295)		6-311G(2df,2pd)-dc (NBF = 555)	
	FTC	ERI	FTC	ERI
Coulomb	2.43	3.47	7.72	51.59
XC	1.59	1.74	6.32	6.47
Matrix	0.06	0.04	0.27	0.22
Total	4.08	5.28	14.30	58.62
Energy	-648.526478	-648.526479	-648.719612	-648.719612

Tables 1-1, 1-2 and 1-3 show timings and accuracy for B-LYP all-electron total energy calculations for three molecules of increasing size: aspirin ($C_9H_8O_4$), sucrose ($C_{12}H_{22}O_{11}$) and taxol ($C_{47}H_{51}NO_{14}$) [23]. Note that the scaling takes its asymptotic value only for rather large systems in FTC because the box must have a significant size, say $10 a_0$ ($\approx 5 \text{ \AA}$) even for the smallest systems to guarantee that it contains the whole electron density. The results in the Tables are similar to the results obtained by Q-Chem. The plane wave method speeds up the calculation of the Coulomb term very much, over a factor of 30 for the largest molecule and large basis set. However, the overall speed-up for taxol is only an order of magnitude for the large basis set, and less than a factor of 4 for the smaller basis because of the overhead, mainly from the traditional integral calculation and from the evaluation of the exchange-correlation contributions.

Figure 1-1 shows the scaling of the evaluation of the Coulomb contributions for polyalanines, $n = 2-15$. Although the FTC method provides significant speed-up compared to a traditional calculation, the timing is dominated by the evaluation of the small fraction of the electron repulsion integrals for the compact basis functions that cannot be treated by FTC. Replacing the traditional electron repulsion integral algorithm by one of the alternatives discussed in Section 1.2.1.2, for instance by a

Table 1-2. Timings and energies for sucrose, $C_{12}H_{22}O_{11}$. See Table 1-1 for explanation

Basis set	6-31G(d,p)-dc (NBF = 569)		6-311G(2df,2pd)-dc (NBF = 1,080)	
	FTC	ERI	FTC	ERI
Coulomb	6.61	20.89	20.69	278.21
XC	5.25	5.73	19.03	19.88
Matrix	0.36	0.29	2.27	1.53
Total	12.22	26.93	42.00	299.76
Energy	-1,297.606133	-1,297.606137	-1,298.000427	-1,298.000425

Table 1-3. Timings and energies for taxol, $C_{47}H_{51}NO_{14}$. See Table 1-1 for explanation

Basis set	6-31G(d,p)-dc (NBF = 1,484)		6-311G(2df,2pd)-dc (NBF = 2,860)	
	FTC	ERI	FTC	ERI
Coulomb	39.56	255.02	127.78	3,038.50
XC	34.42	56.04	126.19	140.85
Matrix	6.45	5.75	41.49	27.70
Total	80.50	317.00	295.68	3,208.27
Energy + 2,928	-0.615108	-0.615114	-1.442401	-1.442376

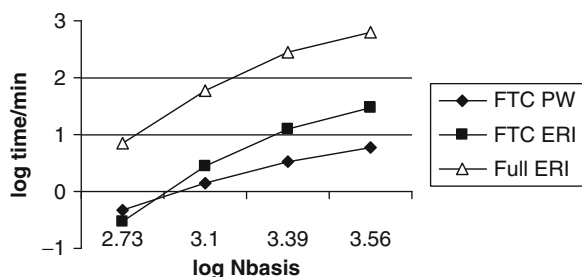


Figure 1-1. The scaling of the Coulomb time with respect to molecular size for a series of polyanilines, $n = 2-15$. FTC PW means the plane wave component of the FTC calculation (diffuse densities). FTC ERI means the remaining (compact) integrals that were calculated using traditional electron repulsion integrals

multipole expansion, should increase the efficiency of the Coulomb part by almost an order of magnitude.

The plane wave parts of both Quickstep [12] and PQS [26, 27] have been implemented in parallel. The factor limiting parallel scaling for a large number of processors is the parallel three-dimensional Fast Fourier Transform, which includes the transposition of a large matrix. Therefore, the parallel scaling of plane-wave methods is limited at this time. However, the inherently high performance of these methods makes up to a certain extent for the limited parallel scalability.

1.5. OUTLOOK AND PERSPECTIVES

Plane wave based methods for the calculation of the Coulomb term in electronic structure calculations accelerate the calculation of these terms, usually the most expensive part of the calculations, by orders of magnitude for large molecules and basis sets. Unlike some of their competitors, they are surprisingly accurate also for relatively small systems, and deserve to be more widely used in chemistry-centered programs.

The most important problems to solve in this field are listed below.

1. Improve the efficiency of the other major computational tasks, for instance to formation of the exchange-correlation matrix, to match the performance of the Coulomb evaluation.
2. Develop improved methods for the calculation of the exact (Hartree-Fock) exchange.
3. Improve the parallel scaling of the method.

ACKNOWLEDGMENTS

This work was supported by the National Science Foundation under grant number CHE-0911541 and by the Mildred B. Cooper Chair at the University of Arkansas. Acquisition of the Star of Arkansas supercomputer was supported in part by the National Science Foundation under award number MRI-0722625.

REFERENCES

1. Greengard L, Rokhlin V (1985) *J Comp Phys* 60:187
2. White CA, Johnson BG, Gill PMW, Head-Gordon M (1994) *Chem Phys Lett* 230:8
3. Payne MC, Teter MP, Allan DC, Arias TA, Joannopoulos JD (1992) *Rev Mod Phys* 64:1045
4. Car R, Parrinello M (1985) *Phys Rev Lett* 55:22
5. Segall MD, Lindan PJD, Probert MJ, Pickard CJ, Hasnip PJ, Clark SJ, Payne MC (2002) *J Phys Condens Matter* 14:2727
6. See: <http://cms.mpi.univie.ac.at/vasp/>
7. Giannozzi P, Baroni S, Bonini N, Calandra M, Car R, Cavazzoni C, Ceresoli D, Chiarotti GL, Cococcioni M, Dabo I, Dal Corso A, de Gironcoli S, Fabris S, Fratesi G, Gebauer R, Gerstmann U, Gougousis C, Kokalj A, Lazzeri M, Martin-Samos L, Marzari N, Mauri F, Mazzarello R, Paolini S, Pasquarello A, Paulatto L, Sbraccia C, Scandolo S, Sclauzero G, Seitsonen AP, Smogunov A, Umari P, Wentzcovitch RM (2009) *J Phys Condens Matter* 21:395502 See also: www.quantum-espresso.org
8. Singh DJ (1994) *Plane waves, pseudopotentials and the LAPW method*. Kluger, Norwell, MA
9. Blöchl PE (1994) *Phys Rev B* 59:1758
10. Vanderbilt D (1990) *Phys Rev B* 41:7892
11. Kresse G, Joubert J (1999) *Phys Rev B* 59:1758
12. Lippert G, Hutter J, Parrinello M (1997) *Mol Phys* 92:477
13. VandeVondele J, Krack M, Mohamed F, Chassaing T, Hutter J (2005) *Comp Phys Comm* 167:103
14. Lippert G, Hutter J, Parrinello M (1999) *Theor Chem Acc* 103:124
15. Krack M, Parrinello M (2000) *Phys Chem Chem Phys* 2:2105
16. Hutter J (2003) *J Chem Phys* 118:3928
17. Iannuzzi M, Chassaing T, Wallman T, Hutter J (2005) *Chimia* 59:499
18. VandeVondele J, Iannuzzi M, Hutter J (2006) *Lect Notes Phys* 703:287
19. Guidon M, Schiffman F, Hutter J, VandeVondele J (2008) *J Chem Phys* 128:214104
20. Parallel Quantum Solutions, LLC, Fayetteville, AR, USA. See: www.pqs-chem.com
21. Baker J, Wolinski K, Malagoli M, Kinghorn DR, Wolinski P, Magyarfalvi G, Saebø S, Janowski T, Pulay P (2009) *J Comput Chem* 30:317
22. Füsti-Molnár L, Pulay P (2002) *J Chem Phys* 116:7795

23. Füsti-Molnár L, Pulay P (2002) *J Chem Phys* 117:7827
24. Füsti-Molnár L, Pulay P (2003) *J Mol Struct (THEOCHEM)* 666:25
25. Füsti-Molnár L (2003) *J Chem Phys* 119:11080
26. Baker J, Füsti-Molnár L, Pulay P (2004) *J Phys Chem A* 108:3040
27. Baker J, Wolinski K, Pulay P (2007) *J Comput Chem* 28:2581
28. Kong J, White CA, Krylov AI et al. (2000) *J Comput Chem* 21:1532
29. Füsti-Molnár L, Kong J (2005) *J Chem Phys* 122:074108
30. Kong J, Brown ST, Füsti-Molnár L (2006) *J Chem Phys* 124:094109
31. Kong J, Brown ST, Füsti-Molnár L (2006) *J Chem Phys* 124:219904
32. Brown ST, Füsti-Molnár L, Kong J (2006) *Chem Phys Lett* 418:490
33. Kohn W (1995) *Int J Quant Chem* 56:229
34. Schwegler E, Challacombe M (1996) *J Chem Phys* 105:2726
35. Burant JC, Scuseria GE, Frisch M (1996) *J Chem Phys* 105:8969
36. Schwegler E, Challacombe M, Head-Gordon M (1997) *J Chem Phys* 106:9708
37. Ochsenfeld C, White CA, Head-Gordon M (1998) *J Chem Phys* 109:1663
38. Heyd J, Scuseria GE, Ernzerhof M (2003) *J Chem Phys* 118:8207
39. Harris F (1975) In: *Electronic structure of polymers and molecular crystals*. Plenum Press, New York, NY, p 453
40. Barnett RN, Landman U (1993) *Phys Rev B* 48:2081
41. DeLeeuw SW, Perram JW, Smit ER (1980) *Proc Roy Soc Lond A* 373:27
42. Hockney RW In: Alder B, Fernbach S, Rothenberg M (1970) *Methods in computational physics*, Academic, New York, NY 9:136
43. Hockney RW, Eastwood JW (1988) *Computer simulation using particle*, Adam Hilger, London
44. Pollock EL, Glosli J (1996) *Comp Phys Comm* 95:93
45. Bylaska EJ, Valiev M, Kawai R, Weare JH (2002) *Comp Phys Comm* 143:11
46. Martyna GJ, Tuckerman ME (1999) *J Chem Phys* 110:2810
47. Mináry P, Moorone JA, Yarne DA, Tuckerman ME, Martyna GJ (2004) *J Chem Phys* 121:11949
48. Vanderbilt D (1994) *Phys Rev B* 50:17953
49. Blöchl PE (1990) *Phys Rev B* 41:5414
50. Blöchl PE, Parrinello M (1992) *Phys Rev B* 45:9413
51. Stewart JJP, Császár P, Pulay P (1982) *J Comp Chem* 3:556
52. VandeVondele J, Hutter J (2003) *J Chem Phys* 118:4365

CHAPTER 2

MATHEMATICAL FORMULATION OF THE FRAGMENT MOLECULAR ORBITAL METHOD

TAKESHI NAGATA¹, DMITRI G. FEDOROV¹, AND KAZUO KITAUURA²

¹ *NRI, National Institute of Advanced Industrial Science and Technology (AIST), 1-1-1 Umezono, Tsukuba, Ibaraki 305-8568, Japan, e-mail: takeshi.nagata@aist.go.jp; d.g.fedorov@aist.go.jp*

² *Graduate School of Pharmaceutical Sciences, Kyoto University, Sakyo-ku, Kyoto 606-8501, Japan; NRI, National Institute of Advanced Industrial Science and Technology (AIST), Tsukuba, Ibaraki 305-8568, Japan, e-mail: kkitaura@pharm.kyoto-u.ac.jp*

Abstract: The fragment molecular orbital (FMO) method is a computational scheme applied to the conventional molecular orbital theories, which reduces their scaling from $N^3 \dots N^7$ to a nearly linear scaling, where N is the system size. FMO provides an accurate treatment of large molecules such as proteins and molecular clusters, and it can be efficiently parallelized to achieve high scaling on massively parallel computers. The main purpose of this chapter is to focus on the derivation of the equations and to provide a concise mathematical description of FMO. A brief summary of the recent applications of FMO is also given.

Keywords: FMO, FMO3, ESP, HOP, AFO, Green's function, ESP-DIM, ESP-PC, MP2, Coupled cluster, DFT, MCSCF, ROHF, Multilayer, TDDFT, CI, CIS, CIS(D), Quantum Monte-Carlo, Gradient, PCM, EFP, MCP, Linear scaling, Molecular dynamics, PIMD, PIE, IFIE, EDA, PIEDA, LMP2, CAFI, BSSE, Counterpoise, FMO-MO, FMO-LCMO, FMO/F, FMO/FX, FMO/XF, RESP, NMR, GIAO, CSGT, Multipole moment, Dynamic polarizability, MCMO, NEO, Drug design, VISCANA, VLS, QSAR, Parallelization, Protein, Ligand, Enzyme, DNA, Solvent, QSAR, Electrostatic potential, Many-body, Fragment, Fragment molecular orbital, RHF, Excited state, Open-shell, Tessera, Cavity, RDM, MO, FILM, Earth Simulator, Energy decomposition analysis, Atomic charge, Massively parallel

2.1. INTRODUCTION

During recent years there has been a considerable progress in the development of quantum-mechanical methods aimed at computing large molecular systems. In addition to the traditional *ab initio* approaches, which frequently rely upon the localized molecular orbitals to describe the electron correlation, there has been a

remarkable development in the methods utilizing in one way or another the idea of fragmentation [1–11].

Typically, these methods operate with small pieces of the system, well defined chemically, such as molecules in molecular clusters, or amino acid residues in proteins, and attempt to reduce the high scaling of ab initio methods to linear scaling (sometimes referred to as $O(N)$). The fragment molecular orbital (FMO) method proposed in 1999 [12] is one of such approaches, which has been considerably developed theoretically as well as applied to a wide variety of systems, including molecular clusters, proteins, DNA, enzymes, small molecules explicitly solvated in water droplets, ionic liquids, molecular crystals, zeolites and nanowires. As the summary of applications and the introductory explanation of FMO have been given elsewhere [8, 13–17], here we focus on the mathematical derivation of the method, followed by a brief summary of recent applications.

2.2. FORMULATION OF THE RESTRICTED HARTREE-FOCK EQUATION

The basic computational scheme of FMO has been described in detail elsewhere [14, 17], and here we only give it very briefly for completeness. The system is divided into pieces (fragments) and each fragment calculation is performed with an ab initio method (such as restricted Hartree-Fock, RHF), in the presence of the electrostatic field of the remaining fragments, determined by their atomic nuclei and the electron density distributions. The fragment (monomer) calculations begin with the field given by some initial guess densities, repeated in a loop self-consistently with respect to the field dependent upon the fragment densities. This loop is called the self-consistent charge (SCC) loop (or monomer self-consistent field, SCF), and it can be accelerated with the direct inversion in the iterative subspace (DIIS) method [18]. Consequently, fragment pairs (dimers), and, optionally, triples (trimers) are computed in the fixed field determined in the previous step (see Figure 2-1). The total properties are computed from those of fragments and dimers (trimers) as shown below.

2.2.1. Many-Body Expansion

In the FMO method, a molecular system is divided into N fragments. The FMO total energy is represented as follows [12, 19, 20]:

$$E^{\text{FMO2}} = \sum_I^N E_I + \sum_{I>J}^N (E_{IJ} - E_I - E_J), \quad (2-1)$$

$$E^{\text{FMO3}} = E^{\text{FMO2}} + \sum_{I>J>K}^N \{ (E_{IJK} - E_I - E_J - E_K) - (E_{IJ} - E_I - E_J) - (E_{JK} - E_J - E_K) - (E_{KI} - E_K - E_I) \}. \quad (2-2)$$

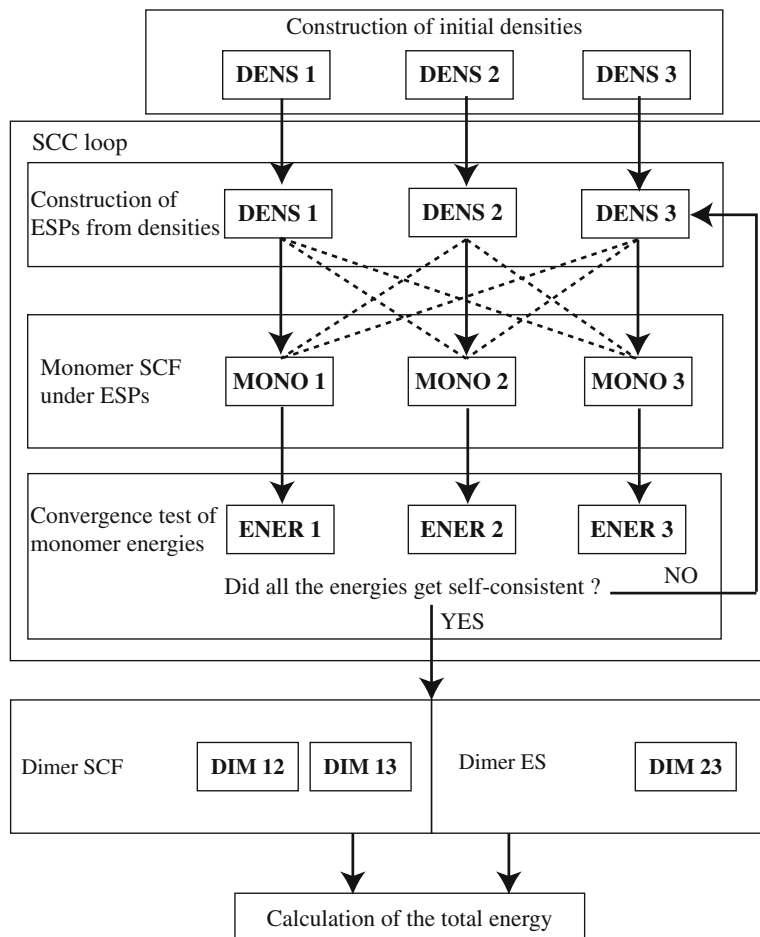


Figure 2-1. Schematic procedure of the FMO energy calculation for a molecule divided into 3 fragments. DENS I , MONO I and DIM IJ ($I, J = 1, 2, 3$) denote monomer density I , SCF calculation for monomer I , and the calculation for dimer IJ , respectively. The dotted lines represent the electrostatic potential due to monomer densities. Dimer SCF and dimer ES show that some dimers can be computed ab initio (SCF) or with an approximation (ES)

The first expression gives the two-body expansion (FMO2) of the total energy E , the second one adds to it the three-body corrections, in terms of the energies of fragments E_I , their pairs E_{IJ} and, optionally, triples E_{IJK} . The one-body energy, if defined in the same manner, would have the electrostatic contribution double-counted [19], however, in some context (e.g., in time-dependent density functional theory, TDDFT) when energy differences are considered, the one-body properties (FMO1) are also useful to consider.

In many places below we give explicit expressions for FMO2, and it is straightforward to extend them into FMO3. It is important to realise that FMO2 includes

many-body effects beyond just the two-body interactions. This is accomplished with the many-body electrostatic interaction explicitly included in all subsystem energies as shown below.

Equation (2-1) can be rewritten as

$$E^{\text{FMO2}} = \sum_{I>J}^N E_{IJ} - (N-2) \sum_I^N E_I, \quad (2-3)$$

and, similarly for FMO3, using combinatorics (see also [7]). The equation in Eq. (2-3) holds, however, if all dimer SCF calculations are performed; because approximations are typically used reducing the number of dimers, the form in Eq. (2-1) is the most convenient one.

The fragment energies, appearing in Eqs. (2-1) and (2-2) can be written using the Hamiltonian H_X and the wave function $|\Psi_X\rangle$ for X (X is fragment I , fragment dimer IJ or fragment trimer IJK), as

$$E_X = \langle \Psi_X | H_X | \Psi_X \rangle. \quad (2-4)$$

To obtain the fragment energy, one has to solve the following Schrödinger equation,

$$H_X |\Psi_X\rangle = E_X |\Psi_X\rangle. \quad (2-5)$$

The explicit form of the fragment Hamiltonian H_X is given by

$$H_X = \sum_{i \in X} \left[-\frac{1}{2} \nabla_i^2 + \sum_C^{\text{all}} \left(-\frac{Z_C}{|\mathbf{r}_i - \mathbf{R}_C|} \right) + \sum_{K \neq X}^{\text{all}} \int \frac{\rho_K(\mathbf{r}')}{|\mathbf{r}_i - \mathbf{r}'|} d\mathbf{r}' \right. \\ \left. + \sum_{j(\in X) > i} \frac{1}{|\mathbf{r}_i - \mathbf{r}_j|} \right] + E_X^{\text{NR}}, \quad (2-6)$$

where the first term is the kinetic energy of electrons (coordinates given by \mathbf{r}), the second term is the one-electron nuclear attraction potential, the third term is the potential due to the electron density $\rho_K(\mathbf{r}')$ of fragment K , and the fourth term is the two-electron potential within X . The nuclear repulsion energy E_X^{NR} is defined as

$$E_X^{\text{NR}} = \sum_{B \in X} \sum_{A(\in X) > B} \frac{Z_A Z_B}{R_{AB}}, \quad (2-7)$$

where Z is the nuclear charge of atoms, and R_{AB} is the distance between atoms A and B . Note here that the sums over C and K describe the potentials due to fragments outside X . Indices C and K run over all atoms (whose coordinates are given by \mathbf{R}) and all fragments, respectively. Integrals over \mathbf{r} go over the whole space.

2.2.2. Restricted Hartree-Fock Equation for a Fragment

A single Slater determinant representation of the wave function is a good starting point to get a more accurate one (such as a correlated wave function). Let us consider RHF, where the restriction is imposed that each molecular orbital is occupied by two electrons with α and β spins. In this case, the wave function for X is represented in the following form,

$$|\Psi_X\rangle = \frac{1}{\sqrt{N_X!}} \begin{vmatrix} \phi_1^X(\mathbf{r}_1) & \bar{\phi}_1^X(\mathbf{r}_1) & \phi_2^X(\mathbf{r}_1) & \bar{\phi}_2^X(\mathbf{r}_1) & \cdots & \bar{\phi}_{N_X/2}^X(\mathbf{r}_1) \\ \phi_1^X(\mathbf{r}_2) & \bar{\phi}_1^X(\mathbf{r}_2) & \phi_2^X(\mathbf{r}_2) & \bar{\phi}_2^X(\mathbf{r}_2) & \cdots & \bar{\phi}_{N_X/2}^X(\mathbf{r}_2) \\ \phi_1^X(\mathbf{r}_3) & \bar{\phi}_1^X(\mathbf{r}_3) & \phi_2^X(\mathbf{r}_3) & \bar{\phi}_2^X(\mathbf{r}_3) & \cdots & \bar{\phi}_{N_X/2}^X(\mathbf{r}_3) \\ \phi_1^X(\mathbf{r}_4) & \bar{\phi}_1^X(\mathbf{r}_4) & \phi_2^X(\mathbf{r}_4) & \bar{\phi}_2^X(\mathbf{r}_4) & \cdots & \bar{\phi}_{N_X/2}^X(\mathbf{r}_4) \\ \vdots & \vdots & \vdots & \vdots & \ddots & \vdots \\ \phi_1^X(\mathbf{r}_{N_X}) & \bar{\phi}_1^X(\mathbf{r}_{N_X}) & \phi_2^X(\mathbf{r}_{N_X}) & \bar{\phi}_2^X(\mathbf{r}_{N_X}) & \cdots & \bar{\phi}_{N_X/2}^X(\mathbf{r}_{N_X}) \end{vmatrix}, \quad (2-8)$$

where ϕ_k^X and $\bar{\phi}_k^X$ are the molecular orbitals (MO) with α and β spins, respectively. N_X is the number of electrons in X , and \mathbf{r}_k is the position of electron k . These MOs are expanded in terms of basis functions on X ,

$$\phi_k^X(\mathbf{r}_1) = \sum_{\mu \in X} C_{\mu k}^X \chi_{\mu}(\mathbf{r}_1), \quad (2-9)$$

where χ_{μ} is the basis function and $C_{\mu k}^X$ is the MO coefficient. We should note that in this chapter the Roman ($ijkl \dots$) and Greek indices ($\mu\nu\rho\sigma \dots$) denote the molecular orbitals (MO) and the atomic orbitals (AO), respectively.

Substituting the wave function of Eq. (2-8) into the Schrödinger equation of Eq. (2-5), one obtains the following RHF equation for X ,

$$f^X(\mathbf{r}_1)\phi_k^X(\mathbf{r}_1) = \epsilon_k^X \phi_k^X(\mathbf{r}_1), \quad (2-10)$$

where the orbital energy ϵ_k^X is the eigenvalue of the Fock operator $f^X(\mathbf{r}_1)$,

$$f^X(\mathbf{r}_1) = \tilde{h}^X(\mathbf{r}_1) + g^X(\mathbf{r}_1), \quad (2-11)$$

including the modified one-electron operator $\tilde{h}^X(\mathbf{r}_1)$,

$$\tilde{h}^X(\mathbf{r}_1) = h^X(\mathbf{r}_1) + V^X(\mathbf{r}_1), \quad (2-12)$$

where $h^X(\mathbf{r}_1)$ and $V^X(\mathbf{r}_1)$ are the internal fragment one-electron Hamiltonian operator and the electrostatic potentials (ESP) due to the nuclei and electron distribution of other fragments, respectively,

$$h^X(\mathbf{r}_1) = -\frac{1}{2}\nabla_1^2 + \sum_{A \in X} \left(-\frac{Z_A}{|\mathbf{r}_1 - \mathbf{R}_A|} \right), \quad (2-13)$$

$$v^X(\mathbf{r}_1) = \sum_{L \neq X}^{\text{all}} \left(-\frac{Z_L}{|\mathbf{r}_1 - \mathbf{R}_L|} \right) + \sum_{K \neq X}^{\text{all}} \int \frac{\rho_K(\mathbf{r}')}{|\mathbf{r}_1 - \mathbf{r}'|} d\mathbf{r}'. \quad (2-14)$$

Unlike $\tilde{h}^X(\mathbf{r}_1)$, the two-electron operator $g^X(\mathbf{r}_1)$ is expressed in terms of operators local to X as

$$g^X(\mathbf{r}_1) = \sum_l^{N_X/2} (2J_l^X(\mathbf{r}_1) - K_l^X(\mathbf{r}_1)), \quad (2-15)$$

where the Coulomb $J_l^X(\mathbf{r}_1)$ and the electron-exchange operator $K_l^X(\mathbf{r}_1)$ are defined as

$$\begin{aligned} J_l^X(\mathbf{r}_1) &= \int d\mathbf{r}_2 \frac{\phi_l^{X*}(\mathbf{r}_2)\phi_l^X(\mathbf{r}_2)}{r_{12}}, \\ K_l^X(\mathbf{r}_1) &= \int d\mathbf{r}_2 \frac{\phi_l^{X*}(\mathbf{r}_2)\wp_{12}\phi_l^X(\mathbf{r}_2)}{r_{12}}, \end{aligned} \quad (2-16)$$

with the distance between electrons 1 and 2 defined as $r_{12} = |\mathbf{r}_1 - \mathbf{r}_2|$ and \wp_{12} is the permutation operator of electrons 1 and 2.

2.2.3. Fragment Energy

Using the above expressions, we derive the fragment energy in Eq. (2-4),

$$\begin{aligned} E_X &= \langle \Psi_X | H_X | \Psi_X \rangle \\ &= \sum_i^{N_X/2} \langle \phi_i^X | \tilde{h}^X | \phi_i^X \rangle + \sum_i^{N_X/2} \langle \phi_i^X | f^X | \phi_i^X \rangle + E_X^{\text{NR}}. \end{aligned} \quad (2-17)$$

$$\begin{aligned} \langle \phi_i^X | f^X | \phi_i^X \rangle &= \langle \phi_i^X | \tilde{h}^X | \phi_i^X \rangle + \langle \phi_i^X | g^X | \phi_i^X \rangle \\ &= -\frac{1}{2} \int \phi_i^{X*}(\mathbf{r}_1) \nabla_1^2 \phi_i^X(\mathbf{r}_1) d\mathbf{r}_1 \\ &\quad + \int \phi_i^{X*}(\mathbf{r}_1) \sum_L^{\text{all}} \left(-\frac{Z_L}{|\mathbf{r}_1 - \mathbf{R}_L|} \right) \phi_i^X(\mathbf{r}_1) d\mathbf{r}_1 \\ &\quad + \int \phi_i^{X*}(\mathbf{r}_1) \sum_{K \neq X}^{\text{all}} \int \frac{\rho_K(\mathbf{r}_2)}{|\mathbf{r}_1 - \mathbf{r}_2|} d\mathbf{r}_2 \phi_i^X(\mathbf{r}_1) d\mathbf{r}_1 \\ &\quad + \int \phi_i^{X*}(\mathbf{r}_1) \sum_l^{N_X/2} (2J_l^X(\mathbf{r}_1) - K_l^X(\mathbf{r}_1)) \phi_i^X(\mathbf{r}_1) d\mathbf{r}_1 \end{aligned} \quad (2-18)$$

$$\begin{aligned}
 &= \langle \phi_i^X | h^X | \phi_i^X \rangle + \langle \phi_i^X | \sum_{L \neq X}^{\text{all}} \left(-\frac{Z_L}{|\mathbf{r}_1 - \mathbf{R}_L|} \right) | \phi_i^X \rangle + 2 \sum_{K \neq X}^{\text{all}} \sum_{k \in K}^{N_K/2} (\phi_i^X \phi_i^X | \phi_k^K \phi_k^K) \\
 &+ \sum_l^{N_X/2} [2 (\phi_i^X \phi_i^X | \phi_l^X \phi_l^X) - (\phi_i^X \phi_l^X | \phi_l^X \phi_i^X)],
 \end{aligned}$$

where the two-electron integral is abbreviated using the chemist's notation:

$$(\phi_i^X \phi_j^X | \phi_k^Y \phi_l^Y) = \int \int \frac{\phi_i^{X*}(\mathbf{r}_1) \phi_j^X(\mathbf{r}_1) \phi_k^{Y*}(\mathbf{r}_2) \phi_l^Y(\mathbf{r}_2)}{r_{12}} d\mathbf{r}_1 d\mathbf{r}_2, \quad (2-19)$$

and the electron density for fragment K defined as

$$\rho_K(\mathbf{r}) = 2 \sum_{k \in K}^{N_K/2} \phi_k^{K*}(\mathbf{r}) \phi_k^K(\mathbf{r}). \quad (2-20)$$

In FMO, the total density can be constructed similar to Eq. (2-1) from the densities of fragments and their pairs,

$$\rho_{\text{FMO}}(\mathbf{r}) = \sum_I^N \rho_I(\mathbf{r}) + \sum_{I>J}^N (\rho_{IJ}(\mathbf{r}) - \rho_I(\mathbf{r}) - \rho_J(\mathbf{r})). \quad (2-21)$$

2.2.4. Expression in Terms of Basis Functions

The RHF equation, Eq. (2-10) can be rederived in terms of basis functions, Eq. (2-9):

$$\mathbf{F}^X \mathbf{C}^X = \mathbf{S}^X \mathbf{C}^X \epsilon^X, \quad (2-22)$$

where the Fock matrix element is

$$F_{\mu\nu}^X = \tilde{h}_{\mu\nu}^X + G_{\mu\nu}^X. \quad (2-23)$$

The two-electron integral matrix element $G_{\mu\nu}^X$ is represented as

$$\begin{aligned}
 G_{\mu\nu}^X &= \langle \chi_\mu | g^X | \chi_\nu \rangle \\
 &= \sum_{\lambda\sigma} D_{\lambda\sigma}^X \left[(\chi_\mu \chi_\nu | \chi_\lambda \chi_\sigma) - \frac{1}{2} (\chi_\mu \chi_\sigma | \chi_\lambda \chi_\nu) \right], \quad (2-24)
 \end{aligned}$$

where the density matrix in Eq. (2-20) is defined in RHF as

$$D_{\lambda\sigma}^X = 2 \sum_i^{\text{occ}} C_{\lambda i}^X C_{\sigma i}^{X*}. \quad (2-25)$$

On the other hand, the one-electron Hamiltonian $\tilde{h}_{\mu\nu}^X$ is composed of

$$\tilde{h}_{\mu\nu}^X = h_{\mu\nu}^X + V_{\mu\nu}^X, \quad (2-26)$$

where $h_{\mu\nu}^X$ is the internal one-electron Hamiltonian matrix element and the external electrostatic matrix element $V_{\mu\nu}^X$ is,

$$V_{\mu\nu}^X = \langle \chi_\mu | V^X | \chi_\nu \rangle = \sum_{K \neq X}^{\text{all}} u_{\mu\nu}^K + \sum_{K \neq X}^{\text{all}} v_{\mu\nu}^K. \quad (2-27)$$

The one-electron $u_{\mu\nu}^K$ and the two-electron $v_{\mu\nu}^K$ terms in Eq. (2-27) are,

$$u_{\mu\nu}^K = - \langle \chi_\mu | \sum_{L \in K} \frac{Z_L}{|\mathbf{r}_1 - \mathbf{R}_L|} | \chi_\nu \rangle, \quad (2-28)$$

$$v_{\mu\nu}^K = \sum_{\lambda\sigma \in K} D_{\lambda\sigma}^K (\chi_\mu \chi_\nu | \chi_\lambda \chi_\sigma). \quad (2-29)$$

The fragment energy of Eq. (2-17) can be written in terms of basis functions,

$$E_X = \frac{1}{2} \sum_{\mu\nu} D_{\mu\nu}^X (\tilde{h}_{\mu\nu}^X + F_{\mu\nu}^X) + E_X^{\text{NR}}. \quad (2-30)$$

An important feature of the FMO method is that the many-body polarization is included at the monomer fragment level. In other words, the monomer electron densities are optimized under the electrostatic potentials due to the densities of all the other fragments until all the densities become self-consistent. On the other hand, SCF calculation for each fragment pair is done once under the electrostatic potentials due to the optimized monomer densities.

The fragment energy can be divided into the internal fragment energy and the external electrostatic potential energy:

$$E_X = E'_X + \text{Tr} [\mathbf{D}^X \mathbf{V}^X], \quad (2-31)$$

where

$$\text{Tr} [\mathbf{D}^X \mathbf{V}^X] = \sum_{\mu\nu \in X} D_{\mu\nu}^X \left(\sum_{K \neq X}^{\text{all}} u_{\mu\nu}^K + \sum_{K \neq X}^{\text{all}} v_{\mu\nu}^K \right). \quad (2-32)$$

There was some discussion [17, 21], as to whether one should add the exchange interaction to ESP in Eq. (2-27):

$$Y_{\mu\nu}^X = -\frac{1}{2} \sum_{K \neq X}^{\text{all}} \sum_{\lambda\sigma \in K} D_{\lambda\sigma}^K (\chi_{\mu}\chi_{\lambda}|\chi_{\nu}\chi_{\sigma}). \quad (2-33)$$

Recently, it was found [22] that when the exchange in Eq. (2-33) is added to ESP, the resultant FMO/X method has a much worse accuracy, as also reported in [21]. The reason is the fact that the fragment wave functions are not mutually orthogonal, and thus the interfragment exchange-repulsion is not accounted for (cf the corresponding terms in the pair interaction energy decomposition analysis, PIEDA [23]). The case of the exchange being useful as a part of ESPs is discussed in Section 2.17.1 below.

Figure 2-2 shows a schematic description [19] of the FMO2 energy, and the FMO diagram in the case of a 3-fragment system. The sum of monomer fragment energies causes the double-counting of the ESPs (i.e., each arc is present twice), which can also be corrected explicitly [5]. By adding the dimer fragment energies into it the orbital mixing and the electrostatic contributions are balanced properly.

2.2.5. Fragmentation at Covalent Bonds

When dividing the system into fragments requires detaching covalent bonds, an additional treatment becomes necessary, which is described at great length elsewhere [14, 17] and here only summarized briefly. In FMO, typically single bonds

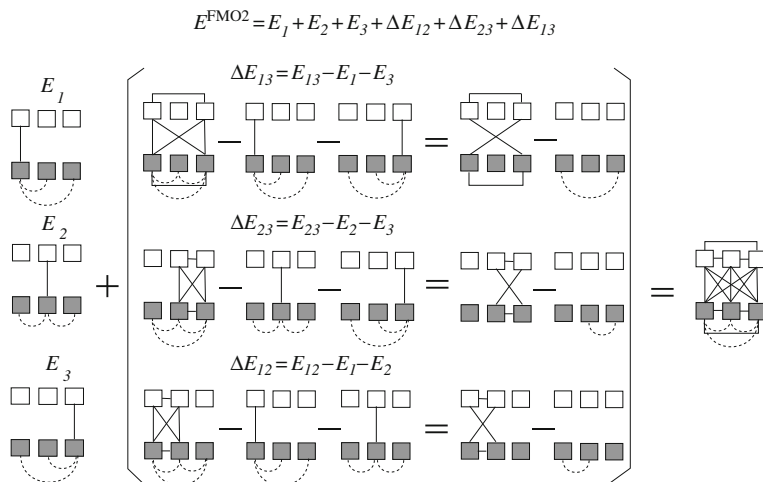


Figure 2-2. FMO diagram for a system divided into 3 fragments. *Solid and open squares* depict the occupied and virtual orbitals, respectively. *Solid lines* represent the orbital mixing in SCF, and the *dotted arcs* show the electrostatic potential. In the diagram on the right representing the total FMO2 energy, each line and arc appears only once

are detached and the two electrons forming a bond are assigned to one fragment, and none to the other. The boundary atom in the latter fragment is called the bond detached atom (BDA). The other atom forming the detached bond is assigned to the other fragment, and this atom is referred to as the bond attached atom (BAA), i.e., schematically, BDA |— BAA, where “—” indicates the detached bond and “|” is the boundary between the two fragments. In order to describe the detached bond in the fragment containing the BAA, one adds BDA in a ghost atom fashion and its basis functions. In order to force the electron density on the BAA fragment to describe the detached bond rather than fall into, for instance, a core orbital state of the BDA, restraints are imposed.

In the first (original) approach, hybrid orbital projectors (HOP) are used and the method is referred to as FMO/HOP. The Fock operator is modified as

$$f^X = \tilde{h}^X + g^X + \sum_k B_k |\theta_k\rangle \langle \theta_k|, \quad (2-34)$$

where B_k is a universal constant equal to 10^{+6} a.u. (so far in all applications independent of k), and θ_k are the hybrid orbitals centered on the BDA. The sum in Eq. (2-34) runs over orbitals in all detached bonds involving X . The projection operators exclude the undesired electronic levels from the variational space. Hybrid orbitals are generated in advance for a small system (e.g., for C—C bonds one computes the localized orbitals of CH_4 , obtaining 1s and four sp^3 orbitals on C). Then in the projection operator on the BDA fragment, one includes the sp^3 orbital describing the detached bond; the operator on the BAA fragment includes the remaining 4 orbitals (which are projected from the variational space). The hybrid orbitals are basis set dependent and have to be generated for each basis set.

In the recently developed adaptive frozen orbital (AFO) scheme (FMO/AFO) [24, 25], in addition to restraining the variational space, one also freezes the occupied MOs describing the detached bonds. This is achieved by precomputing a small model system containing the bond to be detached and obtaining the localized orbitals for this bond as well as the remaining orbitals on the BDA. The detached bond orbital is frozen, and the undesired orbitals are projected out with the Fock matrix transformation technique [26], where the Fock matrix is transformed into the MO basis using the model system orbitals (i.e., 1s and four sp^3) and their orthogonal complement (for the full AO space in X), and then the restraints are imposed by zeroing out off-diagonal matrix elements mixing the frozen orbitals and the rest, as well as adding the constant B to the matrix elements for the projected out orbitals, and then transforming back to the AO basis [24].

The model systems are generated on the fly in the initial step of the FMO calculations, and the AFO preparation is completely automatic, so that the input file preparation is even simpler than for FMO/HOP. In the case of both HOP and AFO, modeling software Facio [27, 28] can be used to either automatically fragment standard systems (peptides, nucleotides, saccharides or any combination thereof) or to detach bonds manually in the graphical user interface otherwise.

It was found that the HOP scheme works best for strongly polar systems such as proteins when medium basis sets (double ζ with polarization) are used, whereas the AFO scheme has a better accuracy in other cases, that is, either when larger basis sets are used or when there are many close detached bonds. In the HOP scheme there is no restraint upon the occupied orbitals and the polarization is well described, where in the AFO scheme the restraints are imposed to freeze the MOs of the detached bonds. FMO/AFO was applied to the adsorption on zeolites [24] and the structure optimization of silicon nanowires [25].

2.2.6. Green's Function

Yasuda et al. [21] reformulated the FMO equation using the cluster expansion of the many-particle Green's function (GF). The perturbation expansion of FMO using GF was given, starting with the electronic state of monomers in FMO as the unperturbed state. This reformation is significant because GF determines the linear response and excitation energy. The one-particle Green's function is defined as

$$g(jt, is) = (-i) \langle \Psi | T [x_j(t)x_i^\dagger(s)] | \Psi \rangle, \quad (2-35)$$

where T and Ψ are the time ordering and the exact ground state, respectively, and x_j and x_i^\dagger are the annihilation and creation operators, respectively. The limit of the zero time interval ($s \rightarrow 0^+, t \rightarrow 0^-$) of g leads to the one and two-particle reduced density matrices, γ (1-RDM) and Γ (2-RDM), respectively:

$$\gamma(j, i) = \langle \Psi | x_i^\dagger x_j | \Psi \rangle \quad (2-36)$$

$$\Gamma^{(2)}(j_1 j_2; i_1, i_2) = \frac{1}{2} \langle \Psi | x_{i_1}^\dagger x_{i_2}^\dagger x_{j_2} x_{j_1} | \Psi \rangle. \quad (2-37)$$

In FMO, the one (γ) and two-particle ($\Gamma^{(2)}$) density matrices can be derived from fragment densities γ_I and γ_{IJ} (here we retain the notation of [21]) as

$$\gamma = \sum_I^N \gamma_I + \sum_{I>J}^N (\gamma_{IJ} - \gamma_I - \gamma_J). \quad (2-38)$$

$$\Gamma_{\text{DM}}^{(2)} = \sum_I^N \Gamma_I^{(2)} + \sum_{I>J}^N (\Gamma_{IJ}^{(2)} - \Gamma_I^{(2)} - \Gamma_J^{(2)}), \quad (2-39)$$

$$\Gamma_{\text{cum}}^{(2)} = \Delta + \gamma \wedge \gamma, \quad (2-40)$$

$$\Gamma_{\text{FMO}}^{(2)} = \Gamma_{\text{DM}}^{(2)} + \frac{1}{2} \sum_{I>J}^N \sum_{K \neq I, J}^N \{ \delta \gamma_{IJ}(j_1, i_1) \gamma_K(j_2, i_2) + \gamma_K(j_1, i_1) \delta \gamma_{IJ}(j_2, i_2) \}, \quad (2-41)$$

$$\Gamma_{\text{SCCE}}^{(2)} = \Gamma_{\text{cum}}^{(2)} - (\gamma - \gamma_0) \wedge (\gamma - \gamma_0), \quad (2-42)$$

$$\Delta = \sum_I^N \Delta_I + \sum_{I>J}^N (\Delta_{IJ} - \Delta_I - \Delta_J), \quad (2-43)$$

and the cumulant $\Delta_X = \Gamma_X^{(2)} - \gamma_X \wedge \gamma_X$, $\gamma \wedge \gamma = 1/2 \{\gamma(j_1, i_1) \gamma(j_2, i_2) - \gamma(j_1, i_2) \gamma(j_2, i_1)\}$, $\gamma_0 = \sum_I \gamma_I$ and $\delta\gamma_{IJ} = \gamma_{IJ} - \gamma_I - \gamma_J$.

The corresponding energies are $E_{DM} = \text{Tr}(v\gamma + w\Gamma_{DM}^{(2)})$, $E_{cum} = \text{Tr}(v\gamma + w\Gamma_{cum}^{(2)})$, $E_{FMO} = \text{Tr}(v\gamma + w\Gamma_{FMO}^{(2)})$ and $E_{SCCE} = \text{Tr}(v\gamma + w\Gamma_{SCCE}^{(2)})$, where v and w are the one- and two-electron integrals, respectively. SCCE is SCC with the exchange (denoted by FMO/X above), and E_{FMO} , E_{SCCE} and E_{cum} are the regular FMO, FMO/X and the FMO-MO [29] energies, respectively. Another important question addressed by the RDMs is the existence of a wave function corresponding to the energy expression, which is affected by the orthogonality condition of the fragment wave functions. Each term in Eq. (2-43) vanishes for RHF.

This formulation can be expanded to the excitation energy, the three-body correction to the density matrices, and the correlation energy. The 3-body correction to 1-RDM is given by

$$\delta\gamma_{3\text{-body}} = \sum_{I>J}^N \sum_{K \neq I, J}^N \delta\gamma_{IK} P \delta\gamma_{KJ}, \quad (2-44)$$

where $P = 2S_0\gamma_0S_0 - S_0$, S_0 is the direct sum of fragment overlap matrices. This correction has the following features: because of the linked-cluster theorem the correction is size-extensive and all the quantities in the correction are available from the pair FMO calculation. A similar correction was derived [21] for 2-RDM. When these corrections are added to the matrices in Eqs. (2-38) and (2-39), one can obtain three-body corrections in FMO using the energy definitions above without having to perform SCF calculations of trimers. The explicit inclusion of trimer terms defined by FMO3 is important in some systems which are characterized by a high degree of electron delocalization [30].

2.2.7. Approximations

The FMO method can be combined with approximations by taking advantages of the local nature of fragments, to further reduce the computational cost and achieve a nearly linear scaling. As discussed later, the approximations are indispensable to the FMO3 treatment involving the trimer calculations.

The approximation of the electrostatic potential with point charges (ESP-PC) replaces the two-electron integral term in Eq. (2-29) by the one-electron integral with the Mulliken atomic population Q_A as follows:

$$v_{\mu\nu}^K = \sum_{\lambda\sigma \in K} D_{\lambda\sigma}^K (\chi_\mu \chi_\nu | \chi_\lambda \chi_\sigma) \rightarrow \sum_{A \in K} \left\langle \chi_\mu \left| \frac{Q_A}{|\mathbf{r}_1 - \mathbf{R}_A|} \right| \chi_\nu \right\rangle, \quad (2-45)$$

if the closest distance between X and K , R_{XK} exceeds a threshold $R_{\text{ESP-PC}}$, i.e.,

$$R_{XK} \geq R_{\text{ESP-PC}}. \quad (2-46)$$

R_{XK} is defined as follows,

$$R_{XK} = \min_{A \in X, B \in K} \left\{ \frac{|\mathbf{R}_A - \mathbf{R}_B|}{W_A + W_B} \right\}, \quad (2-47)$$

where indices A and B run over atoms of X and K , respectively, and W_A and W_B are the corresponding van der Waals radii.

The electrostatic dimer (ES-DIM) approximation replaces the dimer fragment energy with the sum of the monomer energies and the electrostatic interaction energy,

$$\begin{aligned} E'_{IJ} &\simeq E'_I + E'_J + \text{Tr}(\mathbf{D}^I \mathbf{u}^J) + \text{Tr}(\mathbf{D}^J \mathbf{u}^I) \\ &+ \sum_{\mu\nu \in I} \sum_{\lambda\sigma \in J} D'_{\mu\nu} D'_{\lambda\sigma} (\chi_{\mu} \chi_{\nu} | \chi_{\lambda} \chi_{\sigma}) + \Delta E'_{IJ}{}^{\text{NR}}. \end{aligned} \quad (2-48)$$

where $\Delta E'_{IJ}{}^{\text{NR}} = E'_{IJ}{}^{\text{NR}} - E'_I{}^{\text{NR}} - E'_J{}^{\text{NR}}$.

The idea in the approximation in Eq. (2-48) can be extended to FMO3, reducing its computational cost [19]. The trimer IJK calculation can be skipped if the composite measure of the interfragment distances R_{IJ} , R_{JK} and R_{IK} is larger than a threshold value. We note that such a calculation is entirely skipped because the electrostatic approximation in Eq. (2-48) is pairwise additive, and such three-body correction is identically zero. In order to balance out the ESP approximations, the FMO3 energy is reformulated as follows [20]:

$$\begin{aligned} E &= \sum_I^N E'_I + \sum_{I>J}^N \Delta E'_{IJ} + \sum_{I>J>K}^N (\Delta E'_{IJK} - \Delta E'_{IJ} - \Delta E'_{IK} - \Delta E'_{JK}) \\ &+ \sum_{I>J}^N \text{Tr}(\Delta \mathbf{D}^{IJ} \mathbf{V}^{IJ}) \\ &+ \sum_{I>J>K}^N [\text{Tr}(\Delta \mathbf{D}^{IJK} \mathbf{V}^{IJK}) - \text{Tr}(\Delta \mathbf{D}^{IJ} \mathbf{V}^{IJ}) - \text{Tr}(\Delta \mathbf{D}^{IK} \mathbf{V}^{IK}) - \text{Tr}(\Delta \mathbf{D}^{JK} \mathbf{V}^{JK})], \end{aligned} \quad (2-49)$$

where

$$\Delta E'_{IJ} = E'_{IJ} - E'_I - E'_J, \quad (2-50)$$

$$\Delta E'_{IJK} = E'_{IJK} - E'_I - E'_J - E'_K, \quad (2-51)$$

$$\Delta \mathbf{D}^{IJ} = \mathbf{D}^{IJ} - (\mathbf{D}^I \oplus \mathbf{D}^J), \quad (2-52)$$

$$\Delta \mathbf{D}^{IJK} = \mathbf{D}^{IJK} - (\mathbf{D}^I \oplus \mathbf{D}^J \oplus \mathbf{D}^K). \quad (2-53)$$

The expression in Eq. (2-49) has the disadvantage of containing both dimer and trimer ESPs. Due to the nature of the definition of the interfragment distances, the applications of approximations to the ESP due to a fragment may differ, depending on whether this ESP is computed for a dimer or a trimer, resulting in an unbalanced addition of terms in Eq. (2-49). To solve this problem, the blockwise application of approximations was suggested [20] for the computation of $V_{\mu\nu}^{IJ}$ and the distance from external fragment L is defined as

$$\tilde{R}_{IJ,L}(\mu,\nu) = \left\{ \begin{array}{l} R_{I,L} \mu, \nu \in I \\ R_{J,L} \mu, \nu \in J \\ R_{IJ,L} \mu \in I, \nu \in J \text{ or } \mu \in J, \nu \in I \end{array} \right\}. \quad (2-54)$$

And, analogously, for trimers. This approximation enabled a successful use of ESP approximations in FMO3.

2.3. SECOND ORDER MØLLER-PLESSET PERTURBATION THEORY

The dispersion energy is indispensable for the treatment of biological molecules. Especially, the molecular interaction between, for instance, a protein and a ligand cannot be estimated accurately without this type of interaction. Second-order Møller-Plesset perturbation theory (MP2) gives a good description of the dispersion energy and there has been much effort invested in reducing the computational cost for MP2, $O(N^5)$, which is much larger than that of RHF, $O(N^3)$ (N is the system size).

In FMO, the extension of the Hartree-Fock energy expression to the MP2 level is [31–34]

$$E^{\text{MP2}} = \sum_I E_I^{\text{MP2}} + \sum_{I>J} \left(E_{IJ}^{\text{MP2}} - E_I^{\text{MP2}} - E_J^{\text{MP2}} \right), \quad (2-55)$$

where the fragment MP2 energy is

$$E_X^{\text{MP2}} = E_X + E_X^{(2)}. \quad (2-56)$$

$E_X^{(2)}$ is the second-order perturbation energy, which for RHF reference is given by

$$E_X^{(2)} = \sum_{i \geq j \in X}^{\text{occ}} (2 - \delta_{ij}) \sum_{rs \in X}^{\text{vir}} \frac{(\phi_i \phi_r | \phi_j \phi_s) [2(\phi_i \phi_r | \phi_j \phi_s) - (\phi_i \phi_s | \phi_j \phi_r)]}{\epsilon_i + \epsilon_j - \epsilon_r - \epsilon_s}. \quad (2-57)$$

The most time and memory-consuming part in MP2 is the transformation of two-electron AO integrals into the MO basis,

$$(\phi_i\phi_r|\phi_j\phi_s) = \sum_{\mu\nu\lambda\sigma \in X} C_{\mu i}^X C_{\nu r}^X C_{\lambda j}^X C_{\sigma s}^X (\chi_\mu\chi_\nu|\chi_\lambda\chi_\sigma). \quad (2-58)$$

2.3.1. MP2 Implementations

Quantum-chemical program package GAMESS-US [35, 36] has two parallelized closed-shell MP2 implementations, by Fletcher et al. [37] and Ishimura et al. [38]. In the former, the transformation to the MO integrals in Eq. (2-58) is made by distributing the arrays for the occupied pairs ij between nodes with the use of the one-side communication provided by the distributed data interface (DDI) [39].

In the other implementation, one uses the AO shell units to reduce the dimension of the two-electron integrals transformation. The procedure is depicted in Figure 1 of Ref. [38]. The outermost loop M of the AO shells is dynamically distributed between nodes. Then for the two outer AO shells, Λ and Σ one transforms the two indices of the two-electron integrals and stores the data of $o^2sn/2$ in memory of each node, where o is the number of the occupied MOs, s is the number of basis functions in the AO shell and n is the total number of basis functions. This leads to a significant reduction in necessary memory compared with that in the conventional scheme (on^3). At the end of the third transformation, $o^2vn/2$ data are stored on disk. After storing the third-index transformed integrals, the loops of occupied MO pairs ij are statically distributed into nodes, because the amount of the data is the same for each node. The loops accomplish the fourth transformation with the memory usage of $vn + v^2$.

Practically, the main difference between them is that for the DDI-MP2 one has to store all MO-based two-electron integrals ($O(N^4)$) in shared memory, which is impractical for large fragments, while the alternative implementation takes little memory and stores the integral on disk, which works very well if a local disk is present on each node and is problematic otherwise.

2.3.2. Using Resolutions of the Identity in MP2

MP2 based on the resolutions of the identity (RI) is an approximate, but reasonably accurate scheme with a moderate computational cost. The implementation of the RI-MP2 method in FMO is discussed by Ishikawa et al. [40] and we summarize it briefly. As mentioned above, the critical step of MP2 is given in Eq. (2-58), and it is taken care of by RI-MP2. The two-electron AO integrals in Eq. (2-58) can be rewritten as

$$(\chi_\mu\chi_\nu|\chi_\lambda\chi_\sigma) \simeq \sum_{PQ} (\chi_\mu\chi_\nu|\chi_P)V_{PQ}^{-1}(\chi_Q|\chi_\lambda\chi_\sigma), \quad (2-59)$$

with the application of RI,

$$\hat{T} = \sum_{PQ} |\chi_P\rangle V_{PQ}^{-1} \langle \chi_Q| \quad (2-60)$$

where $V_{PQ} = (\chi_P|\chi_Q)$ is the Coulomb metric. Eq. (2-59) is used in Eq. (2-58) to reduce its scaling.

The equality of Eq. (2-59) holds only if the operator \hat{T} is expanded in terms of the products of the two basis functions. In practice, auxiliary basis functions $|\chi_P\rangle$ are determined by minimizing the following equation for atoms except hydrogen [41]:

$$\delta_{\text{RI}} = \frac{1}{4} \sum_{irjs} \frac{(\langle \phi_r \phi_s | | \phi_i \phi_j \rangle - \langle \phi_r \phi_s | | \phi_j \phi_i \rangle_{\text{RI}})^2}{\epsilon_r - \epsilon_i + \epsilon_s - \epsilon_j}, \quad (2-61)$$

with respect to the exponents present in the expansion of the auxiliary basis set χ_P over primitives. $\langle \phi_r \phi_s | | \phi_i \phi_j \rangle = (\phi_r \phi_i | \phi_s \phi_j) - (\phi_r \phi_j | \phi_s \phi_i)$.

2.4. COUPLED-CLUSTER THEORY

The coupled-cluster (CC) theory is often considered the golden standard of accuracy, but it is also very time-consuming. In the application of CC to FMO [42], we use the same energy expression as in MP2:

$$E^{\text{CC}} = \sum_I^N E_I^{\text{CC}} + \sum_{I>J}^N (E_{IJ}^{\text{CC}} - E_I^{\text{CC}} - E_J^{\text{CC}}), \quad (2-62)$$

where E_X^{CC} is the CC energy of X .

Various levels of CC methods have been developed with the compromise between the accuracy and the computational cost. The coupled cluster with singles and doubles (CCSD) [43] can be expanded to include the triples correction, i.e., CCSD(T) [44], which has been widely used.

Recent development in the CC method is remarkable both in the computational performance and the accuracy. Olson et al. [45] have developed a parallel CCSD(T) algorithm. The completely renormalized coupled cluster (CR-CC) methods [46] can describe systems with some open shell character, suitable to study chemical reactions.

2.5. DENSITY FUNCTIONAL THEORY

The density functional theory (DFT) extends the Hartree-Fock method to include the electron correlation via an addition to the Hamiltonian of a density dependent functional. The implementation of FMO-DFT [18, 47] is straightforward,

$$E^{\text{DFT}} = \sum_I^N E_I^{\text{DFT}} + \sum_{I>J}^N (E_{IJ}^{\text{DFT}} - E_I^{\text{DFT}} - E_J^{\text{DFT}}), \quad (2-63)$$

where

$$E_X^{\text{DFT}} = 2 \sum_{i \in X}^{\text{occ}} \left\langle \phi_i^X \left| \left(-\frac{1}{2} \nabla^2 \right) \right| \phi_i^X \right\rangle + \int \mathfrak{N}^X(\mathbf{r}) \rho^X(\mathbf{r}) d\mathbf{r} + \sum_{K \neq X} \int \mathfrak{N}^K(\mathbf{r}) \rho^X(\mathbf{r}) d\mathbf{r} + E_{\text{xc}}[\rho^X(\mathbf{r})] + E_X^{\text{NR}}. \quad (2-64)$$

In Eq. (2-64), the set of potentials $\mathfrak{N}^Y(\mathbf{r})$ due to the nuclear charges and electron densities is described as

$$\mathfrak{N}^Y(\mathbf{r}) = \sum_{A \in Y} \left(-\frac{Z_A}{|\mathbf{r} - \mathbf{R}_A|} \right) + \int \frac{\rho^Y(\mathbf{r}')}{|\mathbf{r} - \mathbf{r}'|} d\mathbf{r}', \quad (2-65)$$

and $E_{\text{xc}}[\rho^X(\mathbf{r})]$ is the electron exchange-correlation energy.

The corresponding Kohn-Sham equation is

$$\left(-\frac{1}{2} \nabla^2 + \mathfrak{N}^X(\mathbf{r}) + \sum_{K \neq X} \mathfrak{N}^K(\mathbf{r}) + v_{\text{xc}}(\mathbf{r}) \right) |\phi_i^X\rangle = \epsilon_i^X |\phi_i^X\rangle, \quad (2-66)$$

where $v_{\text{xc}}(\mathbf{r})$ is the electron-exchange correlation potential.

There are many DFT functionals available. B3LYP [48] is perhaps the most famous functional frequently used in general applications. The long range correction [49] is found to improve the description of charge transfer in DFT. Recently, many new functionals: M06 [50], M08 [51], revTPSS [52] etc have been developed.

2.6. MULTICONFIGURATION SCF

Although DFT and MP2 include the dynamic electron correlation beyond the Hartree-Fock approximation, they are still single reference methods breaking down when several configurations are important, in which case such electronic states can be described with multiconfiguration SCF (MCSCF).

In the current implementation of MCSCF in FMO [53], the MCSCF wave function can be used for only one fragment; all the other fragments are treated by RHF. MCSCF wave function is used also for the dimers containing the MCSCF fragment. For far separated dimers, the ES dimer approximation (see Eq. 2-48) may be applied in the same way as in FMO-RHF; one of monomer densities may be replaced with the MCSCF density. The ESPs in Eq. (2-29) are generated using the MCSCF or RHF density depending on the fragment.

2.7. OPEN-SHELL TREATMENT

A special case of MCSCF is known as the restricted open shell Hartree-Fock method (ROHF), which is based on a single open-shell configuration. While one can of course use MCSCF to perform ROHF calculations as well, but it is much more efficient to develop a special ROHF code, which is nearly the same in terms of the computational cost as the closed shell RHF method. FMO-ROHF was developed for both the two and three-body expansions [54] and it can be used for an arbitrary multiplicity, capable of treating radicals and excited states in large systems.

The formulation of FMO-ROHF is similar to that of FMO-MCSCF, i.e., a single fragment is designated as the open shell fragment, while other fragments are treated as closed shell, consequently, dimer and trimer calculations are performed at the open shell level if they contain the open shell fragment, and as closed shells otherwise. A particular benefit of developing a special method for ROHF is the ability to perform correlated calculations at the MP2 and CC levels. There are several kinds of open shell MP2 and CC, and for FMO so far the Z-averaged perturbation theory [55] and completely renormalized CC(2,3) method [56, 57] were implemented, respectively.

2.8. MULTILAYER APPROACH

In the multilayer FMO (MFMO) [58], each fragment is assigned to a layer, and more important fragments are put to a higher layer treated with a better level of theory. MFMO is designed to significantly reduce the computational cost while retaining high accuracy for the relevant part of the system. The MFMO energy can be written as

$$E = \sum_{L_i=1}^M \left\{ \sum_{I \in L_i}^N \left[E_I^{L_i} + \sum_{L_j=L_i}^M \sum_{J=I+1, J \in L_j}^N \left(E_{IJ}^{L_i} - E_I^{L_i} - E_J^{L_i} \right) \right] \right\}, \quad (2-67)$$

where indices L_i and L_j run over M layers. $E_X^{L_i}$ are the energies in Eq. (2-17) computed at the level of layer i and the sum over J in Eq. (2-67) assumes that fragments are numbered in the increasing order of layers. Alternatively, Eq. (2-67) can be written as

$$E = \sum_I^N E_I^{L_I} + \sum_{I>J}^N \left(E_{IJ}^{L_{IJ}} - E_I^{L_{IJ}} - E_J^{L_{IJ}} \right), \quad (2-68)$$

where L_I is the layer to which fragment I belongs and $L_{IJ} = \min(L_I, L_J)$. For the given layer L_i , the ESPs used for the computation of $E_X^{L_i}$ are constructed as follows:

$$V_{\mu\nu}^{X(L_i)} = - \sum_{K \neq X}^{\text{all}} \left\langle \chi_\mu \left| \sum_{A \in K} \frac{Z_A}{|\mathbf{r}_1 - \mathbf{R}_A|} \right| \chi_\nu \right\rangle + \sum_{K \neq X}^{\text{all}} \sum_{\lambda\sigma \in K} D_{\lambda\sigma}^{K(\tilde{L}_K)} (\chi_\mu \chi_\nu | \chi_\lambda \chi_\sigma), \quad (2-69)$$

where the first term on the right hand side of Eq. (2-69) is not changed from Eq. (2-28) and the second term is obtained from the density, $D_{\lambda\sigma}^{K(\tilde{L}_K)}$ of layer $\tilde{L}_K = \min(L_K, L_i)$.

An MFMO calculation starts by converging the densities of all N fragments in SCC (at the level of layer 1), followed by the dimer calculation at the same level for those dimers where at least one fragment is in layer 1. Consequently, the basis set and wave function for layer 2 are used; the densities of fragments assigned to layer 1 are frozen, and all others are optimized followed by dimer calculations for those dimers where at least one fragment is in layer 2 and the other is in layer 2 or higher; and so on if more layers are present.

The notation for MFMO is to list all wave functions in the increasing order of layers, as in FMO-RHF:MP2 (layer 1: RHF, layer 2: MP2). If necessary, basis sets can be specified: FMO-RHF/6-31G*:MP2/6-311G**. MFMO has been used so far for FMO-based MP2, MCSCF, CI and TDDFT (having RHF as the lower layer), as well as for open-shell MP2 and CC as the two layers. If either the wave function or the basis set is the same in all layers, they can be omitted for brevity in the symbol, e.g. FMO-MCSCF/cc-pVDZ:cc-pVTZ. The use of molecular mechanics is under development [59], and a conceptually multilayer approach was taken to describe the crystal field by point charges in the study of electronic excitations in solid state quinacridone [60].

2.9. EXCITED STATES

Photochemical processes have attracted much attention in recent years, requiring to describe electronic excited states. The photosynthesis, for instance, involves an excitation process, leading to the efficient harvesting of the energy from the sun. Also, excited states determine the structure of measured spectra in spectroscopy and frequently determine the path of chemical reactions.

2.9.1. Time-Dependent DFT

Time-dependent DFT (TDDFT) is a method to study excited states at the low computational cost. Chiba et al. [61–63] interfaced it with FMO. Similarly to FMO-MCSCF, only one fragment M is described by TDDFT. The total energy of an excited state in FMO-TDDFT, E^* can be written as

$$E^* = E_M^* + \sum_{I \neq M}^N (E_{MI}^* - E_M^* - E_I^0) + \sum_{I \neq M}^N E_I^0 + \sum_{I > J (\neq M)}^N (E_{IJ}^0 - E_I^0 - E_J^0), \quad (2-70)$$

where E_X^* is the energy of the excited state ($X = M$ or MI), and E_X^0 ($X = I$, or IJ) is the energy of the ground state (of X). The excitation energy ω is obtained by subtracting the ground state energy from the excited state energy as follows:

$$\omega = E^* - E^0 = \omega_M + \sum_{I \neq M} (\omega_{MI} - \omega_M), \quad (2-71)$$

where $\omega_M = E_M^* - E_M^0$ and $\omega_{MI} = E_{MI}^* - E_{MI}^0$. Eq. (2-71) describes the two-body FMO (FMO2-TDDFT), while the neglect of the second term on the right hand side gives the one-body FMO (FMO1-TDDFT) excitation energy.

To obtain the excitation energy ω_X ($X=M$ or MI), one has to solve the following non-Hermitian eigenvalue equations:

$$\begin{pmatrix} \mathbf{A}^X & \mathbf{B}^X \\ \mathbf{B}^X & \mathbf{A}^X \end{pmatrix} \begin{pmatrix} \mathbf{x}^X \\ \mathbf{y}^X \end{pmatrix} = \omega_X \begin{pmatrix} \mathbf{1} & \mathbf{0} \\ \mathbf{0} & -\mathbf{1} \end{pmatrix} \begin{pmatrix} \mathbf{x}^X \\ \mathbf{y}^X \end{pmatrix}, \quad (2-72)$$

where vectors \mathbf{x}^X and \mathbf{y}^X represent excitation and de-excitation components of the electronic density change, respectively, and

$$A_{ri\sigma, sj\sigma'}^X = \delta_{rs}\delta_{ij}\delta_{\sigma\sigma'} (\epsilon_{ri\sigma}^X - \epsilon_{sj\sigma'}^X) + K_{ri\sigma, sj\sigma'}^X, \quad (2-73)$$

$$B_{ri\sigma, sj\sigma'}^X = K_{ri\sigma, js\sigma'}^X. \quad (2-74)$$

In Eqs. (2-73) and (2-74) σ and σ' are the spin indices, and ϵ is the Kohn-Sham molecular orbital energy. The explicit form of K^X is

$$K_{ab\sigma, pq\sigma'}^X = \left(\phi_{a\sigma}^X \phi_{b\sigma}^X | \phi_{p\sigma'}^X \phi_{q\sigma'}^X \right) - c_x \delta_{\sigma\sigma'} \left(\phi_{a\sigma}^X \phi_{p\sigma}^X | \phi_{b\sigma'}^X \phi_{q\sigma'}^X \right) + f_{ab\sigma pq\sigma'}^{\text{xc}}, \quad (2-75)$$

where $f_{ab\sigma pq\sigma'}^{\text{xc}}$ is the Hessian matrix element of the exchange-correlation energy functional v_{xc} with respect to the electron density in the adiabatic approximation,

$$f_{ab\sigma pq\sigma'}^{\text{xc}} = \frac{\delta^2 v_{\text{xc}}}{\delta \rho_{\sigma}(\mathbf{r}_1) \delta \rho_{\sigma'}(\mathbf{r}_2)}, \quad (2-76)$$

and c_x is a mixing parameter of the HF exchange integral in hybrid functionals.

The FMO-TDDFT energy gradients were implemented by Chiba et al. [64] The gradient expression of the excitation energy is given by (a is an atomic coordinate)

$$\frac{\partial E^*}{\partial a} = \frac{\partial E^0}{\partial a} + \frac{\partial \omega}{\partial a}. \quad (2-77)$$

The first term on the right hand side of Eq. (2-77) is the energy gradient for the ground state at the DFT level. The second term is the excitation energy gradient of FMO-TDDFT.

2.9.2. Configuration Interaction

In ab initio MO theory, the configuration interaction with singles (CIS) is the theoretically and computationally simplest formalism to treat low-lying excited states. An implementation of CIS in multilayer FMO was made by Mochizuki et al. [65], followed by the inclusion of perturbative doubles (CIS(D)) [66–68]. Typically, only one fragment is put into the higher (CI) layer, although some use was made of the CI pair corrections to determine the influence of the environment [69].

The CIS wave function for fragment M is expanded in terms of the Slater determinants in which occupied MO i is replaced with virtual MO r as

$$\left| \Psi_M^{\text{CIS}} \right\rangle = U_1 \left| \Psi_M^0 \right\rangle = \sum_{ir} b_i^r \left| \Psi_M^{i \rightarrow r} \right\rangle, \quad (2-78)$$

where the operator U_1 generates the combination of substituted determinants associated with the amplitudes b_i^r from the reference HF state $\left| \Psi_M^0 \right\rangle$ of fragment M . The corresponding CIS eigenvalue problem is

$$\bar{H}_M \left| \Psi_M^{\text{CIS}} \right\rangle = \omega_M^{\text{CIS}} \left| \Psi_M^{\text{CIS}} \right\rangle, \quad (2-79)$$

where ω_M is the excitation energy and

$$\bar{H}_M = H_M - E_M. \quad (2-80)$$

E_M is the FMO fragment HF ground state energy. One can obtain the excitation energy by solving the eigenvalue problem of Eq. (2-79).

The summary of CIS(D) is as follows. The ground state MP2 wave function of fragment M is described as

$$\left| \Psi_M^{\text{MP2}} \right\rangle = T_2 \left| \Psi_M^0 \right\rangle = \frac{1}{4} \sum_{ijrs} a_{ij}^{rs} \left| \Psi_M^{ij \rightarrow rs} \right\rangle, \quad (2-81)$$

where the operator T_2 generates the double substituted Slater determinant $\left| \Psi_M^{ij \rightarrow rs} \right\rangle$ (or the spin-adapted function) with the corresponding MP2 amplitudes a_{ij}^{rs} ,

$$a_{ij}^{rs} = - \frac{\left\langle \Psi_M^{ij \rightarrow rs} \left| \tilde{V} \right| \Psi_M^0 \right\rangle}{\epsilon_r + \epsilon_s - \epsilon_i - \epsilon_j}. \quad (2-82)$$

and \tilde{V} is the perturbation potential (i.e., the two-electron interaction). The final form of the CIS(D) excitation energy is represented as

$$\begin{aligned}
\omega_M^{\text{CIS(D)}} &= E_M^{\text{CIS(D)}} - E_M^{\text{MP2}} \\
&= -\frac{1}{4} \sum_{ijrs \in M} \frac{(u_M^{ij \rightarrow rs})^2}{\epsilon_r + \epsilon_s - \epsilon_i - \epsilon_j - \omega_M^{\text{CIS}}} + \sum_{ir \in M} b_i^r v_i^r,
\end{aligned} \tag{2-83}$$

where

$$\begin{aligned}
u_M^{ij \rightarrow rs} &= \sum_{t \in M}^{\text{vir}} \left[\langle \phi_r \phi_s | | \phi_t \phi_j \rangle b_i^t - \langle \phi_r \phi_s | | \phi_t \phi_i \rangle b_j^t \right] \\
&\quad + \sum_{k \in M}^{\text{occ}} \left[\langle \phi_k \phi_r | | \phi_i \phi_j \rangle b_k^s - \langle \phi_k \phi_s | | \phi_i \phi_j \rangle b_k^r \right],
\end{aligned} \tag{2-84}$$

$$v_i^r = \frac{1}{2} \sum_{jks t \in M} \langle \phi_j \phi_k | | \phi_s \phi_t \rangle \left[b_i^s a_{jk}^{tr} + b_j^r a_{ik}^{ts} + 2b_j^s a_{ik}^{tr} \right]. \tag{2-85}$$

Note that we used the physicist's notation for the two-electron integrals in Eqs. (2-84) and (2-85) (also see Ref. [66]). While CIS typically overestimates the excitation energies by 1 eV or more [65], due to the lack of the electron correlation (CIS may be viewed as RHF of excited states), CIS(D), which is like MP2 for excited states, shows much improved results [70].

2.10. QUANTUM MONTE-CARLO

The Monte-Carlo simulation is a powerful tool for evaluating the multidimensional integral by sampling the integrand statistically and averaging the sampled values. In the variational Monte-Carlo (VMC) method [71], the total energy is transformed as follows:

$$E_V = \frac{\int \Psi_T^*(\mathbf{R}) H \Psi_T(\mathbf{R}) d\mathbf{R}}{\int \Psi_T^*(\mathbf{R}) \Psi_T(\mathbf{R}) d\mathbf{R}} = \frac{\int |\Psi_T(\mathbf{R})|^2 [\Psi_T(\mathbf{R})^{-1} H \Psi_T(\mathbf{R})] d\mathbf{R}}{\int |\Psi_T(\mathbf{R})|^2 d\mathbf{R}} \geq E_0, \tag{2-86}$$

where Ψ_T is the trial wave function and $\mathbf{R} = (\mathbf{r}_1, \mathbf{r}_2, \dots, \mathbf{r}_N)$ the set of the coordinates of the electrons.

The probability distribution is defined as

$$P(\mathbf{R}) = \frac{|\Psi_T(\mathbf{R})|^2}{\int |\Psi_T(\mathbf{R}')|^2 d\mathbf{R}'}. \tag{2-87}$$

After M steps (the choice of coordinates \mathbf{R}_m is driven by $P(\mathbf{R}_m)$), one has the following expectation value:

$$E_V \approx \frac{1}{M} \sum_{m=1}^M E_L(\mathbf{R}_m), \tag{2-88}$$

where

$$E_L = \Psi_T(\mathbf{R})^{-1} H \Psi_T(\mathbf{R}). \tag{2-89}$$

The FMO many-body expansion (2.1) is applied straightforwardly to the energy in Eq. (2-88) [72].

2.11. ENERGY GRADIENT

In this section, we introduce the derivation of the FMO energy gradients, i.e., the first derivatives of the energy with respect to nuclear coordinates. The first derivation and implementation of the FMO energy gradients were done by Kitaura et al. [73], and the energy derivatives for the electrostatic dimer approximation (see Eq. 2-48) were obtained by Fedorov et al. [59]. Nagata et al. [74] improved the accuracy of the FMO gradient by adding the contributions from the point charge derivatives (for the point charge approximation to ESP) (see Eq. 2-45). Komeiji et al. [75] developed the FMO3 gradient including the ESP derivatives.

2.11.1. Derivatives of the Internal Fragment Energy

To derive the FMO energy gradient, we consider the FMO2 total energy expression in Eq. (2-49),

$$E = \sum_I E'_I + \sum_{I>J} (E'_{IJ} - E'_I - E'_J) + \sum_{I>J} \text{Tr}(\Delta \mathbf{D}^{IJ} \mathbf{V}^{IJ}), \quad (2-90)$$

where the internal energy E'_X is

$$E'_X = \sum_{\mu\nu \in X} D_{\mu\nu}^X h_{\mu\nu}^X + \frac{1}{2} \sum_{\mu\nu\lambda\sigma \in X} \left[D_{\mu\nu}^X D_{\lambda\sigma}^X - \frac{1}{2} D_{\mu\lambda}^X D_{\nu\sigma}^X \right] (\chi_\mu \chi_\nu | \chi_\lambda \chi_\sigma) + E_X^{\text{NR}}. \quad (2-91)$$

Note that the electrostatic potentials V^I due to monomer fragments do not emerge in Eq. (2-90).

The differentiation of the internal fragment energy E'_X with respect to nuclear coordinate a leads to

$$\begin{aligned} \frac{\partial E'_X}{\partial a} &= \sum_{\mu\nu \in X} D_{\mu\nu}^X \frac{\partial h_{\mu\nu}^X}{\partial a} + \frac{1}{2} \sum_{\mu\nu\lambda\sigma \in X} \left[D_{\mu\nu}^X D_{\lambda\sigma}^X - \frac{1}{2} D_{\mu\lambda}^X D_{\nu\sigma}^X \right] \frac{\partial (\chi_\mu \chi_\nu | \chi_\lambda \chi_\sigma)}{\partial a} \\ &+ \sum_{\mu\nu \in X} \frac{\partial D_{\mu\nu}^X}{\partial a} h_{\mu\nu}^X + \frac{1}{2} \sum_{\mu\nu\lambda\sigma \in X} \frac{\partial \left[D_{\mu\nu}^X D_{\lambda\sigma}^X - \frac{1}{2} D_{\mu\lambda}^X D_{\nu\sigma}^X \right]}{\partial a} (\chi_\mu \chi_\nu | \chi_\lambda \chi_\sigma) + \frac{\partial E_X^{\text{NR}}}{\partial a}. \end{aligned} \quad (2-92)$$

The set of the density matrix derivative terms in Eq. (2-92) can be rewritten with the internal Fock matrix in MO basis F_{mi}^X ,

$$\begin{aligned} &\sum_{\mu\nu \in X} \frac{\partial D_{\mu\nu}^X}{\partial a} h_{\mu\nu}^X + \frac{1}{2} \sum_{\mu\nu\lambda\sigma \in X} \frac{\partial \left[D_{\mu\nu}^X D_{\lambda\sigma}^X - \frac{1}{2} D_{\mu\lambda}^X D_{\nu\sigma}^X \right]}{\partial a} (\chi_\mu \chi_\nu | \chi_\lambda \chi_\sigma) \\ &= 4 \sum_{i \in X} \sum_{m \in X}^{\text{occ} \text{ occ} + \text{vir}} U_{mi}^{a,X} F_{mi}^X, \end{aligned} \quad (2-93)$$

where the derivative of the MO coefficient $C_{\mu i}^X$ is expanded in terms of the unknowns, $U_{mi}^{a,X}$ as [76]

$$\frac{\partial C_{\mu i}^X}{\partial a} = \sum_{m \in X}^{\text{occ+vir}} U_{mi}^{a,X} C_{\mu m}^X, \quad (2-94)$$

and

$$F'_{mi}^X = h_{mi}^X + \sum_{j \in X}^{\text{occ}} \left[2 \left(\phi_m^X \phi_i^X | \phi_j^X \phi_j^X \right) - \left(\phi_m^X \phi_j^X | \phi_j^X \phi_i^X \right) \right]. \quad (2-95)$$

It is convenient to transform Eq. (2-93) for the later derivation,

$$\begin{aligned} 4 \sum_{i \in X}^{\text{occ}} \sum_{m \in X}^{\text{occ+vir}} U_{mi}^{a,X} F'_{mi}^X &= -2 \sum_{i,j \in X}^{\text{occ}} S_{ji}^{a,X} F'_{ji}^X + 4 \sum_{i \in X}^{\text{occ}} \sum_{r \in X}^{\text{vir}} U_{ri}^{a,X} (F_{ri}^X - V_{ri}^X) \\ &= -2 \sum_{i,j \in X}^{\text{occ}} S_{ji}^{a,X} F'_{ji}^X - 4 \sum_{i \in X}^{\text{occ}} \sum_{r \in X}^{\text{vir}} U_{ri}^{a,X} V_{ri}^X, \end{aligned} \quad (2-96)$$

where we used $F'_{ri}^X = 0$ and the relation arising from the orthonormality of the molecular orbitals [76],

$$S_{ij}^{a,X} + U_{ij}^{a,X} + U_{ji}^{a,X} = 0, \quad (2-97)$$

is used with the definition

$$S_{ij}^{a,X} = \sum_{\mu\nu \in X} C_{\mu i}^{X*} \frac{\partial S_{\mu\nu}^X}{\partial a} C_{\nu j}^X. \quad (2-98)$$

We collect the unknown terms and define $\bar{U}^{aX,Y}$ as

$$\bar{U}^{aX,Y} = 4 \sum_{i \in X}^{\text{occ}} \sum_{r \in X}^{\text{vir}} U_{ri}^{a,X} V_{ri}^Y. \quad (2-99)$$

Finally, we have the derivative of the internal fragment energy:

$$\begin{aligned} \frac{\partial E'_X}{\partial a} &= \sum_{\mu\nu \in X} D_{\mu\nu}^X \frac{\partial h_{\mu\nu}^X}{\partial a} + \frac{1}{2} \sum_{\mu\nu\lambda\sigma \in X} \left[D_{\mu\nu}^X D_{\lambda\sigma}^X - \frac{1}{2} D_{\mu\lambda}^X D_{\nu\sigma}^X \right] \frac{\partial (\chi_{\mu}\chi_{\nu} | \chi_{\lambda}\chi_{\sigma})}{\partial a} \\ &\quad - 2 \sum_{i,j \in X}^{\text{occ}} S_{ji}^{a,X} F'_{ji}^X + \frac{\partial E_X^{\text{NR}}}{\partial a} - \bar{U}^{aX,X}. \end{aligned} \quad (2-100)$$

2.11.2. Differentiation of the Density Matrix

The differentiation of the electrostatic potential energy in Eq. (2-90) with respect to nuclear coordinate a is

$$\frac{\partial}{\partial a} \text{Tr}(\Delta \mathbf{D}^{IJ} \mathbf{V}^{IJ}) = \sum_{\mu\nu \in IJ} \frac{\partial \Delta D_{\mu\nu}^{IJ}}{\partial a} V_{\mu\nu}^{IJ} + \sum_{\mu\nu \in IJ} \Delta D_{\mu\nu}^{IJ} \frac{\partial V_{\mu\nu}^{IJ}}{\partial a}. \quad (2-101)$$

The first term on the right hand side of Eq. (2-101) can be transformed further:

$$\begin{aligned} \sum_{\mu\nu \in IJ} \frac{\partial \Delta D_{\mu\nu}^{IJ}}{\partial a} V_{\mu\nu}^{IJ} &= -2 \sum_{\mu\nu \in IJ} W_{\mu\nu}^{IJ} \frac{\partial S_{\mu\nu}^{IJ}}{\partial a} + 2 \sum_{\mu\nu \in I} W_{\mu\nu}^I \frac{\partial S_{\mu\nu}^I}{\partial a} \\ &\quad + 2 \sum_{\mu\nu \in J} W_{\mu\nu}^J \frac{\partial S_{\mu\nu}^J}{\partial a} + \bar{U}^{aIJ,IJ} - \bar{U}^{aI,IJ} - \bar{U}^{aJ,IJ}, \end{aligned} \quad (2-102)$$

where

$$W_{\mu\nu}^X = \frac{1}{4} \sum_{\lambda\sigma \in X} D_{\mu\lambda}^X V_{\lambda\sigma}^{IJ} D_{\sigma\nu}^X. \quad (2-103)$$

Collecting the unknown terms in Eqs. (2-100) and (2-102),

$$\begin{aligned} \bar{U}^a &= - \sum_I^N \bar{U}^{aI,I} - \sum_{I>J}^N (\bar{U}^{aIJ,IJ} - \bar{U}^{aI,I} - \bar{U}^{aJ,J}) \\ &\quad + \sum_{I>J}^N (\bar{U}^{aIJ,IJ} - \bar{U}^{aI,IJ} - \bar{U}^{aJ,IJ}) \\ &= - \sum_I^N \bar{U}^{aI,I} + \sum_{I>J}^N (\bar{U}^{aI,I} + \bar{U}^{aJ,J}) - \sum_{I>J}^N (\bar{U}^{aIJ,IJ} + \bar{U}^{aJ,IJ}) \\ &= - \sum_I^N \bar{U}^{aI,I} + \sum_{I>J}^N (\bar{U}^{aI,I(J)} + \bar{U}^{aJ,J(I)}) \\ &= - \sum_I^N \bar{U}^{aI,I} + \sum_I^N \bar{U}^{aI,I} = 0, \end{aligned} \quad (2-104)$$

where the definition,

$$\bar{U}^{aX,X(Y)} = 4 \sum_{i \in X}^{\text{occ}} \sum_{r \in X}^{\text{vir}} U_{ri}^{a,X} (u_{ri}^Y + v_{ri}^Y), \quad (2-105)$$

is used. \bar{U}^a in Eq. (2-104) is equal to zero only if the ESP-PC approximation is used to all or none of ESPs, otherwise the relation holds approximately.

2.11.3. Differentiation of the Electrostatic Potential

The second term on the right hand side of Eq. (2-101) leads to

$$\sum_{\mu\nu\in IJ} \Delta D_{\mu\nu}^{IJ} \frac{\partial V_{\mu\nu}^{IJ}}{\partial a} = \sum_{\mu\nu\in IJ} \Delta D_{\mu\nu}^{IJ} \left(\sum_{K\neq IJ}^{\text{all}} \frac{\partial u_{\mu\nu}^K}{\partial a} + \sum_{K\neq IJ}^{\text{all}} \frac{\partial v_{\mu\nu}^K}{\partial a} \right). \quad (2-106)$$

Since the two-electron integral terms contain the density matrix of fragment K (see Eq. 2-29), the last term on the right hand side of Eq. (2-106) has the following form:

$$\frac{\partial v_{\mu\nu}^K}{\partial a} = \sum_{\lambda\sigma\in K} D_{\lambda\sigma}^K \frac{\partial (\chi_\mu \chi_\nu | \chi_\lambda \chi_\sigma)}{\partial a} + \sum_{\lambda\sigma\in K} \frac{\partial D_{\lambda\sigma}^K}{\partial a} (\chi_\mu \chi_\nu | \chi_\lambda \chi_\sigma). \quad (2-107)$$

Substituting Eq. (2-107) into Eq. (2-106) and then taking only the density derivative term leads to

$$\begin{aligned} & \sum_{\mu\nu\in IJ} \Delta D_{\mu\nu}^{IJ} \sum_{K\neq IJ}^{\text{all}} \sum_{\lambda\sigma\in K} \frac{\partial D_{\lambda\sigma}^K}{\partial a} (\chi_\mu \chi_\nu | \chi_\lambda \chi_\sigma) \\ &= 4 \sum_{\mu\nu\in IJ} \Delta D_{\mu\nu}^{IJ} \sum_{K\neq IJ}^{\text{all}} \sum_{m\in K}^{\text{occ+vir}} \sum_{i\in K}^{\text{occ}} U_{mi}^{a,K} (\chi_\mu \chi_\nu | \phi_m \phi_i) \\ &= -2 \sum_{K\neq IJ}^{\text{all}} \sum_{\mu\nu\in K} \Delta X_{\mu\nu}^{K(IJ)} S_{\mu\nu}^{a,K} \\ & \quad + 4 \sum_{K\neq IJ}^{\text{all}} \sum_{\mu\nu\in IJ} \Delta D_{\mu\nu}^{IJ} \sum_{r\in K}^{\text{vir}} \sum_{i\in K}^{\text{occ}} U_{ri}^{a,K} (\chi_\mu \chi_\nu | \phi_r \phi_i), \end{aligned} \quad (2-108)$$

where

$$\Delta X_{\mu\nu}^{K(IJ)} = \frac{1}{4} \sum_{\lambda\sigma\in K} D_{\mu\lambda}^K \left[\sum_{\zeta\eta\in IJ} \Delta D_{\zeta\eta}^{IJ} (\chi_\zeta \chi_\eta | \chi_\lambda \chi_\sigma) \right] D_{\sigma\nu}^K. \quad (2-109)$$

2.11.4. Differentiation of the Approximated Electrostatic Potential Energy

The two-electron terms of the electrostatic potential energy under the ESP-PC approximation can be written using atomic populations Q_A as

$$\begin{aligned} \sum_{\mu\nu\in IJ} \Delta D_{\mu\nu}^{IJ} \sum_{K\neq IJ}^{\text{all}} v_{\mu\nu}^K &\simeq \sum_{\mu\nu\in IJ} \Delta D_{\mu\nu}^{IJ} \sum_{K\neq IJ}^{R_{IJ,K} < R_{\text{ESP-PC}}} \sum_{\lambda\sigma\in K} D_{\lambda\sigma}^K (\chi_\mu \chi_\nu | \chi_\lambda \chi_\sigma) \\ & \quad + \sum_{\mu\nu\in IJ} \Delta D_{\mu\nu}^{IJ} \sum_{K\neq IJ}^{R_{IJ,K} \geq R_{\text{ESP-PC}}} \sum_{A\in K} \langle \chi_\mu | \frac{Q_A}{|\mathbf{r}-\mathbf{R}_A|} | \chi_\nu \rangle, \end{aligned} \quad (2-110)$$

Since the non-approximated term, i.e., the first term on the right side of Eq. (2-110) is derived in the previous subsection, we focus on the second term. That is,

$$\begin{aligned}
 & \frac{\partial}{\partial a} \sum_{\mu\nu \in IJ} \Delta D_{\mu\nu}^{IJ} \sum_{\substack{R_{IJ,K} \geq R_{\text{ESP-PC}} \\ K \neq IJ}} \sum_{A \in K} \langle \chi_{\mu} | \frac{Q_A}{|\mathbf{r} - \mathbf{R}_A|} | \chi_{\nu} \rangle \\
 &= \sum_{\mu\nu \in IJ} \Delta D_{\mu\nu}^{IJ} \sum_{\substack{R_{IJ,K} \geq R_{\text{ESP-PC}} \\ K \neq IJ}} \left\{ \sum_{A \in K} \left\langle \frac{\partial \chi_{\mu}}{\partial a} \middle| \frac{Q_A}{|\mathbf{r} - \mathbf{R}_A|} \middle| \chi_{\nu} \right\rangle \right. \\
 & \quad + \sum_{A \in K} \left\langle \chi_{\mu} \middle| \frac{Q_A}{|\mathbf{r} - \mathbf{R}_A|} \middle| \frac{\partial \chi_{\nu}}{\partial a} \right\rangle + \sum_{A \in K} \langle \chi_{\mu} | Q_A \frac{\partial |\mathbf{r} - \mathbf{R}_A|^{-1}}{\partial a} | \chi_{\nu} \rangle \\
 & \quad \left. + \sum_{A \in K} \left\langle \chi_{\mu} \middle| \frac{\partial Q_A}{\partial a} \frac{1}{|\mathbf{r} - \mathbf{R}_A|} \middle| \chi_{\nu} \right\rangle \right\} \\
 & \quad + \sum_{\mu\nu \in IJ} \frac{\partial \Delta D_{\mu\nu}^{IJ}}{\partial a} \sum_{\substack{R_{IJ,K} \geq R_{\text{ESP-PC}} \\ K \neq IJ}} \sum_{A \in K} \langle \chi_{\mu} | \frac{Q_A}{|\mathbf{r} - \mathbf{R}_A|} | \chi_{\nu} \rangle.
 \end{aligned} \tag{2-111}$$

The last two sums include the unknown U^a term; the latter sum,

$$\sum_{\mu\nu \in IJ} \frac{\partial \Delta D_{\mu\nu}^{IJ}}{\partial a} \sum_{\substack{R_{IJ,K} \geq R_{\text{ESP-PC}} \\ K \neq IJ}} \sum_{A \in K} \langle \chi_{\mu} | \frac{Q_A}{|\mathbf{r} - \mathbf{R}_A|} | \chi_{\nu} \rangle, \tag{2-112}$$

just replaces the two-electron integral term of Eq. (2-101). The former sum, which includes the derivative of the atomic Mulliken population Q_A , can be further modified as

$$\begin{aligned}
 & \sum_{\mu\nu \in IJ} \Delta D_{\mu\nu}^{IJ} \sum_{\substack{R_{IJ,K} \geq R_{\text{ESP-PC}} \\ K \neq IJ}} \sum_{A \in K} \langle \chi_{\mu} | \frac{\partial Q_A}{\partial a} \frac{1}{|\mathbf{r} - \mathbf{R}_A|} | \chi_{\nu} \rangle \\
 &= \sum_{\mu\nu \in IJ} \Delta D_{\mu\nu}^{IJ} \sum_{\substack{R_{IJ,K} \geq R_{\text{ESP-PC}} \\ K \neq IJ}} \sum_{A \in K} \langle \chi_{\mu} | \sum_{\lambda \in A} \sum_{\sigma \in K} D_{\lambda\sigma}^K \frac{\partial S_{\sigma\lambda}^K}{\partial a} \frac{1}{|\mathbf{r} - \mathbf{R}_A|} | \chi_{\nu} \rangle \\
 & \quad - \frac{1}{2} \sum_{\mu\nu \in IJ} \Delta D_{\mu\nu}^{IJ} \sum_{\substack{R_{IJ,K} \geq R_{\text{ESP-PC}} \\ K \neq IJ}} \sum_{A \in K} \langle \chi_{\mu} | \sum_{\lambda \in A} \sum_{\sigma \rho \zeta \in K} S_{\lambda\sigma}^K D_{\sigma\rho}^K \frac{\partial S_{\rho\zeta}^K}{\partial a} D_{\zeta\lambda}^K \frac{1}{|\mathbf{r} - \mathbf{R}_A|} | \chi_{\nu} \rangle \\
 & \quad + 2 \sum_{\mu\nu \in IJ} \Delta D_{\mu\nu}^{IJ} \sum_{\substack{R_{IJ,K} \geq R_{\text{ESP-PC}} \\ K \neq IJ}} \sum_{A \in K} \langle \chi_{\mu} | \sum_{\lambda \in A} \sum_{\sigma \in K} \sum_{\substack{\text{occ} \\ i \in K}} \sum_{\substack{\text{vir} \\ r \in K}} \frac{(C_{\lambda i}^K C_{\sigma r}^K + C_{\lambda r}^K C_{\sigma i}^K) U_{ri}^{a,K} S_{\lambda\sigma}^K}{|\mathbf{r} - \mathbf{R}_A|} | \chi_{\nu} \rangle.
 \end{aligned} \tag{2-113}$$

To obtain the last term of Eq. (2-108) or (2-113), one must solve the time-consuming CPHF equations for U^a . In the current implementation, this term is simply neglected in the calculation [74], in a compromise between the computational cost and the accuracy.

2.12. EFFECTIVE POTENTIAL MODELS

Additional effective potentials due to the environment or inner-shell electrons can be included into FMO calculations. In this section, we describe the polarizable continuum model (PCM) [77], effective fragment potentials (EFP) [78] and model core potentials (MCP) [79]. While the former two methods are applied to describe the solvent effects on the solute treated with FMO, the latter is designed to compute systems containing heavy atoms. Methodologically, all three methods are similar in presenting an additional term to the one-electron Hamiltonian.

2.12.1. Polarizable Continuum Model

The polarizable continuum model (PCM) can describe solvent effects by representing the solvent as polarizable continuum [80]. Briefly, a cavity surrounding the solute molecule is created in the continuous dielectric medium (representing the solvent). The cavity is made as a union of atomic spheres divided into pieces (frequently, triangular portions) called tesserae, each of which has its own point charge, called the apparent surface charge (ASC). The inclusion of the solvent effect to FMO is made by adding a one-electron Coulomb interaction contribution \mathbf{W}^X into the fragment Fock matrix,

$$\tilde{F}_{\mu\nu}^X = F_{\mu\nu}^X + W_{\mu\nu}^X, \quad (2-114)$$

where $F_{\mu\nu}^X$ is the Fock matrix element in vacuum. The potential $W_{\mu\nu}^X$ exerted by the solvent upon the solute has the following form:

$$W_{\mu\nu}^X = - \sum_i^{N_T} q_i w_{\mu\nu}^i, \quad (2-115)$$

where N_T is the total number of tesserae, whose charges are q_i and $w_{\mu\nu}^i$ describes the one-electron electrostatic interaction of the tessera charge and the solute,

$$w_{\mu\nu}^i = \langle \chi_\mu | \frac{1}{|\mathbf{r} - \mathbf{R}_i|} | \chi_\nu \rangle. \quad (2-116)$$

The electrostatic potential \mathbf{V} exerted on the cavity (the size of vectors \mathbf{V} , \mathbf{V}^I and \mathbf{V}^{IJ} is N_T) by the solute is

$$\mathbf{V} = \sum_I^N \mathbf{V}^I + \sum_{I>J}^N (\mathbf{V}^{IJ} - \mathbf{V}^I - \mathbf{V}^J). \quad (2-117)$$

The contribution \mathbf{V}^X is composed of the potentials due to the electron density and the nuclei in X ,

$$\mathbf{V}^X = \mathbf{V}^{X(e)} + \mathbf{V}^{X(n)}, \quad (2-118)$$

where

$$V_i^{X(e)} = - \sum_{\mu\nu \in X} (D_{\mu\nu}^X w_{\mu\nu}^i), \quad (2-119)$$

$$V_i^{X(n)} = \sum_{\alpha \in X} \frac{Z_\alpha}{|\mathbf{R}_\alpha - \mathbf{R}_i|}. \quad (2-120)$$

The charges \mathbf{q} are obtained by solving the following equation:

$$\mathbf{C}\mathbf{q} = -\mathbf{V}$$

where \mathbf{C} is the geometric matrix ($N_T \times N_T$) including the prefactor $\varepsilon/(\varepsilon - 1)$ following the notation of Ref. [81], where ε is the dielectric constant of the solvent. The interaction energy G between the FMO solute and PCM solvent is represented as

$$G = \frac{1}{2} \mathbf{V}^T \mathbf{q} = -\frac{1}{2} \mathbf{V}^T \mathbf{C}^{-1} \mathbf{V}. \quad (2-121)$$

The FMO/PCM total energy is obtained by adding G and G_{cdr} into the internal solute FMO energy E^{FMO}

$$E^{\text{FMO/PCM}} = E^{\text{FMO}} - \frac{1}{2} \mathbf{V}^T \mathbf{C}^{-1} \mathbf{V} + G_{\text{cdr}}, \quad (2-122)$$

where G_{cdr} is the term describing parametrized values of the cavitation, dispersion and repulsion energies (the former gives the amount of the energy necessary to create a cavity in the solvent occupied by the solute, the latter two describe the corresponding solute-solvent interactions).

The FMO/PCM energy is calculated at various levels, denoted as FMO n /PCM[m] ($n \geq m$). The former number stands for the n -body expanded FMO energy, and the latter means that the electrostatic potential of Eq. (2-117) is truncated up to the m -body contribution. For instance, FMO2/PCM[1] uses the first term of Eq. (2-117) for the monomer calculations as well as the dimer calculations, i.e. the electrostatic potential $\mathbf{V} = \sum_l^N \mathbf{V}^l$ is updated during SCC and then used in the dimer calculations. For FMO n /PCM[2], however, the electrostatic potential has the form of Eq. (2-117) and the FMO2 calculation should thus be repeated with the updated \mathbf{V} until the total energy converges. Because FMO n /PCM[2] is time-consuming, FMO n /PCM[$m(l)$] ($n \geq l > m$) was proposed [77]. In this scheme, first the m -body expansion of the potential \mathbf{V} is adopted to get the ASCs self-consistently and then the ASC is computed using the l -body expanded \mathbf{V} only once.

In the FMO/PCM energy gradient [81], the derivatives of G in Eq. (2-121) or the second term on the right hand side of Eq. (2-122) with respect to nuclear coordinate a are obtained,

$$\frac{\partial G}{\partial a} = \frac{1}{2} \frac{\partial \mathbf{V}^T}{\partial a} (\mathbf{q} + \hat{\mathbf{q}}) + \frac{1}{2} \hat{\mathbf{q}}^T \frac{\partial \mathbf{C}}{\partial a} \mathbf{q}, \quad (2-123)$$

where

$$\hat{\mathbf{q}} = -\left(\mathbf{C}^{-1}\right)^T \mathbf{V}. \quad (2-124)$$

Originally, the derivatives of G_{cdr} were computed numerically (this term does not depend upon the electronic density, but only on the parameters given by the solvent atom types and the cavity shape) and now there are analytic derivatives as well [82].

2.12.2. Effective Fragment Potential

In contrast to PCM, the EFP method is applied to the discrete solvent. We developed a hybrid scheme of FMO and EFP, the FMO/EFP method [78]. In this scheme, the potentials representing the solute and explicit solvent interactions, are added to Eq. (2-26) for subsystem X , composed of the Coulomb, polarization, and the remainder term (that is, charge transfer plus the electron exchange-repulsion):

$$V_X^{\text{EFP}} = V_X^{\text{coul}} + V_X^{\text{pol}} + V_X^{\text{rem}}. \quad (2-125)$$

The Coulomb potential acting on X is represented using the Stone's multipole expansion [83]:

$$V_X^{\text{coul}} = \sum_C^{N_{\text{Coul}}} \left(-\frac{q_C}{r_C} - \sum_a^{x,y,z} \mu_a^C \hat{F}_a(\mathbf{r}_C) - \frac{1}{3} \sum_{ab}^{x,y,z} \Theta_{ab}^C \hat{F}'_{ab}(\mathbf{r}_C) - \frac{1}{15} \sum_{abc}^{x,y,z} \Omega_{abc}^C \hat{F}''_{abc}(\mathbf{r}_C) \cdots \right), \quad (2-126)$$

where index C runs over the N_{Coul} expansion points of the whole solvent system (usually atoms and bond midpoints), and $r_C = |\mathbf{r} - \mathbf{R}_C|$ is the distance between electron in X and point C . μ_a^C , Θ_{ab}^C and Ω_{abc}^C are the dipole, quadrupole, octupole moments at C , respectively. $\hat{F}_a(\mathbf{r}_C) = -(a - a_C)/r_C^3$, $\hat{F}'_{ab}(\mathbf{r}_C)$ and $\hat{F}''_{abc}(\mathbf{r}_C)$ give the electric field due to the QM charge, the field gradient and the field second derivative operators, respectively. To improve the point multipole model accounting for the overlapping electron densities, the first term on the right hand side of Eq. (2-126) can be replaced with

$$-\frac{q_C}{r_C} \rightarrow (1 - \beta_C \exp[-\alpha_C r_C^2]) \left[-\frac{q_C}{r_C} \right], \quad (2-127)$$

where α_C and β_C are fitting parameters [84].

The remainder potential between FMO and EFP fragments is as a one-electron operator,

$$V_X^{\text{rem}} = \sum_m \sum_{i \in X}^{N_{\text{rem}}} V^{\text{rem}}(m, i), \quad (2-128)$$

where m and i run over the EFP remainder expansion points and the electrons in X , respectively, and N_{rem} is the total number of remainder expansion points. For water acting as solvent, the ab initio electron exchange-repulsion plus charge transfer contributions are fitted to Gaussian functions of $V^{\text{rem}}(m, i)$ for water dimer [85].

The polarization energy of EFP is represented by the induced dipoles,

$$E^{\text{pol}} = -\frac{1}{2} \sum_i^{N_{\text{pol}}} (\boldsymbol{\mu}_i - \boldsymbol{\mu}'_i) \cdot \mathbf{F}_i^{\text{tot}}, \quad (2-129)$$

where N_{pol} is the total number of the EFP polarizable points, which are taken to be the centroids of the localized MOs of an effective fragment. The induced dipoles are obtained using the relations:

$$\boldsymbol{\mu}_i = \boldsymbol{\alpha}_i \mathbf{F}_i^{\text{tot}}, \quad (2-130)$$

$$\boldsymbol{\mu}'_i = \boldsymbol{\alpha}_i^T \mathbf{F}_i^{\mu}. \quad (2-131)$$

$\boldsymbol{\alpha}_i$ and $\boldsymbol{\alpha}_i^T$ are the polarizability tensor and its transpose, respectively.

The total field at polarizable point i is due to the QM part of subsystem X , \mathbf{F}_i^{ai} (where ai stands for ab initio, i.e., QM), EFP multipoles ($\mathbf{F}_i^{\text{efp}}$) and the induced dipoles (\mathbf{F}_i^{μ}),

$$\mathbf{F}_i^{\text{tot}} = \mathbf{F}_i^{\text{ai}} + \mathbf{F}_i^{\text{efp}} + \mathbf{F}_i^{\mu}. \quad (2-132)$$

The field due to the FMO fragment X and the field due to the induced dipole are further divided into the electron and nucleus terms, and those due to the dipoles induced by X and the EFP,

$$\mathbf{F}_i^{\text{ai}} = \langle \Psi_X | \hat{\mathbf{f}}_i^{\text{el}, X} | \Psi_X \rangle + \mathbf{F}_i^{\text{nuc}, X}, \quad (2-133)$$

and

$$\mathbf{F}_i^{\mu} = \mathbf{F}_i^{\mu, X} + \mathbf{F}_i^{\mu, \text{EFP}}, \quad (2-134)$$

respectively.

Unlike the Coulomb and the remainder potentials in Eq. (2-125), the induced dipole is influenced by the ab initio density, and should be optimized self-consistently. To do this, the Lagrange multipliers are introduced. The modified SCF equation is

$$\left[H'_X - \frac{1}{2} \sum_i^{N_{\text{pol}}} (\boldsymbol{\alpha}_i \mathbf{F}_i^{\text{tot}} + \boldsymbol{\alpha}_i^T \mathbf{F}_i^{\text{tot}} - \boldsymbol{\alpha}_i^T \mathbf{F}_i^\mu) \cdot \widehat{\mathbf{f}}_i^{\text{el},X} \right] |\Psi_X\rangle = W_X |\Psi_X\rangle, \quad (2-135)$$

and the total electronic fragment energy is,

$$\begin{aligned} E_X &= W_X + \frac{1}{2} \sum_i^{N_{\text{pol}}} (\boldsymbol{\alpha}_i^T \mathbf{F}_i^{\text{tot}} - \boldsymbol{\alpha}_i^T \mathbf{F}_i^{\text{tot}}) \cdot \langle \Psi_X | \widehat{\mathbf{f}}_i^{\text{el}} | \Psi_X \rangle \\ &\quad - \frac{1}{2} \sum_i^{N_{\text{pol}}} \boldsymbol{\alpha}_i \langle \Psi_X | \widehat{\mathbf{f}}_i^{\text{el},X} | \Psi_X \rangle \cdot (\mathbf{F}_i^{\text{nuc},X} + \mathbf{F}_i^{\text{efp}}) \\ &\quad - \frac{1}{2} \sum_i^{N_{\text{pol}}} (\boldsymbol{\alpha}_i \mathbf{F}_i^{\text{nuc},X} + [\boldsymbol{\alpha}_i - \boldsymbol{\alpha}_i^T] \mathbf{F}_i^{\mu,X}) \cdot (\mathbf{F}_i^{\text{nuc},X} + \mathbf{F}_i^{\mu,X} + \mathbf{F}_i^{\text{efp}} + \mathbf{F}_i^{\mu,\text{EFP}}) \\ &\quad - \frac{1}{2} \sum_i^{N_{\text{pol}}} (\boldsymbol{\alpha}_i \mathbf{F}_i^{\text{efp}} + [\boldsymbol{\alpha}_i - \boldsymbol{\alpha}_i^T] \mathbf{F}_i^{\mu,\text{EFP}}) \cdot (\mathbf{F}_i^{\text{nuc},X} + \mathbf{F}_i^{\mu,X}), \end{aligned} \quad (2-136)$$

where

$$H'_X = H_X + V_X^{\text{coul}} + V_X^{\text{rem}}. \quad (2-137)$$

The polarization energy between EFPs,

$$E_{\text{EFP-EFP}}^{\text{pol}} = -\frac{1}{2} \sum_i^{N_{\text{pol}}} (\boldsymbol{\alpha}_i \mathbf{F}_i^{\text{efp}} + [\boldsymbol{\alpha}_i - \boldsymbol{\alpha}_i^T] \mathbf{F}_i^{\mu,\text{EFP}}) \cdot (\mathbf{F}_i^{\text{efp}} + \mathbf{F}_i^{\mu,\text{EFP}}), \quad (2-138)$$

is added into the FMO/EFP energy expression.

2.12.3. Model Core Potential

MCP replaces the particle treatment of some (core) electrons by a potential, retaining N_v explicit (valence) electrons. The MCP Hamiltonian is constructed in FMO-MCP [79] as

$$H_{\text{MCP},X} = \sum_{i \in X} \left[h_{\text{MCP},i} + \sum_{i>j \in X}^{N_v} \frac{1}{|\mathbf{r}_i - \mathbf{r}_j|} \right] + \sum_{B \in X} \sum_{A(\in X) > B} \frac{Z_A^{\text{eff}} Z_B^{\text{eff}}}{R_{AB}}, \quad (2-139)$$

where the one-electron potential modified for MCP is,

$$\begin{aligned}
h_{\text{MCP},i} = & -\frac{1}{2}\nabla_i^2 - \sum_{L \in X} \frac{Z_L^{\text{eff}}}{|\mathbf{r}_i - \mathbf{R}_L|} \\
& \left[1 + \sum_{\substack{k \\ N_{L,c}}}^{n_{L,\alpha}} A_{L,k} e^{(-\alpha_{L,k}|\mathbf{r}_i - \mathbf{R}_L|^2)} + |\mathbf{r}_i - \mathbf{R}_L| \sum_k^{n_{L,\alpha}} B_{L,k} e^{(-\beta_{L,k}|\mathbf{r}_i - \mathbf{R}_L|^2)} \right] \\
& + \sum_{L \in X} \sum_c B_{L,c} |\psi_{L,c}\rangle \langle \psi_{L,c}|,
\end{aligned} \tag{2-140}$$

where the nuclear charge Z_A is replaced by the effective nuclear charge, $Z_A^{\text{eff}} = Z_A - N_{A,c}$ and $N_{A,c}$ is the number of core electrons on atom A . L runs over all atoms. Parameters $A_{L,k}$, $\alpha_{L,k}$, $B_{L,k}$ and $\beta_{L,k}$ are fitted from all-electron calculations when MCP is generated. The last term on the right hand side of Eq. (2-140) is the projection operator that shifts the core orbitals $|\psi_{L,c}\rangle$; it has the same form as the operator used for the bond detachment in FMO, cf Eq.(2-34). Some atoms can be treated without using MCP, in which case the Hamiltonian is trivially modified, cf Eq. (2-6).

Model core potentials are often parametrized to reproduce high level relativistic calculations, and allow one to perform accurate calculations of systems containing heavy atoms, for instance, hydrated mercury ions and platinum-containing compounds [79].

2.13. SCALING

The question of scaling of computational methods is not a very simple one. The label “linear scaling” can be attached with ease without sufficient justification. In many cases the systems used to validate the claim of linear scaling are linear themselves, that is, they look like a wire. The absence of the three-dimensional effects can provide the necessary condition for the linear scaling in the methods, which may not be well discussed.

The intrinsic difficulty in the issue of scaling appears to be in the almost inevitable mixture of scaling regimes, caused by the complicated many-step nature of computational algorithms. In other words, in practice one can find both linear and quadratic scaling parts in a method, for instance, if pairwise distances are to be computed, that alone scales as a square of the system size. In addition, there are other complications such as the use of thresholds and a switch of the approximations, whose efficiency and scaling depend upon the system size N , for instance, in the region of small N the scaling of two-electron integrals is N^4 , but using screening at large N reduces this cost to nearly quadratic.

Finally, even when “manifestly” an algorithm breaks down into N sections, then there may be other issues such as the number of iterations to reach convergence depending upon N or the cost of parallel operations (e.g., global sums) taking more work with respect to N than linear scaling implies. Frequently, there is a dominant part of the algorithm which suppresses other higher scaling aspects, and it may be sufficient in practice if it is linear scaling. With a different N regime the scaling can

change. Although one can aim at “very large N ” when discussing the scaling, infinite N are never used in practice, and the scaling of the whole complex algorithm is thus almost a metaphysical issue (debated at times with ardent zeal), although discussing the scaling of some mathematically well-defined part of an algorithm can certainly be perfectly appropriate.

There is, however, a practical way to estimating the effective scaling, as observed for some specific system and for some specific system size region. This, however, complicates the matters further (perhaps more than is often realized), because then another very complicated factor is brought in, which is the computer. The efficiency of the use of memory including cache and the intrinsic parallelisation in modern CPUs also depend very considerably upon the system type and size. Thus, in our opinion, the question of scaling is not very well defined in most practical cases.

As far the scaling of FMO is concerned, we described it as “nearly linear” [31, 42], demonstrating it by calculating a number of systems which are both linear and globular in shape, and justifying it theoretically from the mathematical grounds [17]. We point out that this is what is observed for “typical” regime of applying FMO, that is, systems sufficiently large so that the approximations reduce the number of the most computationally demanding SCF calculations of monomers and dimers to a value proportional to N , which prevails over other higher scaling parts (e.g., the calculation of the interfragment distances, N^2).

2.14. MOLECULAR DYNAMICS

Molecular dynamics (MD) is an important tool to study protein folding and enzyme reaction in the field of biochemistry. Newton’s equation of motion, in which FMO can be used to compute force \mathbf{F} acting upon atom A , can be represented as [86]

$$m_A \frac{d^2 \mathbf{r}_A}{dt^2} = \mathbf{F}_A = -\nabla_A E^{\text{FMO}}. \quad (2-141)$$

Here a problem arises; as the FMO energy gradient is not fully analytic. The first MD test calculations were done by Komeiji [87], where the validity of FMO-MD was shown with the proper fragmentation and time step. Mochizuki et al. [88] extracted the structures of hydrated formaldehyde obtained from the FMO-MD simulation and then the CIS(D) calculations were carried out for 400 structures to investigate the statistical effect for the lowest $n-\pi^*$ excitation energy. The averaged excitation energy was in good agreement with the corresponding experimental energy. Sato et al. [89] reported on the S_N2 reaction of hydrated CH_3N_2^+ using FMO-MD. Komeiji et al. [90] implemented the blue moon ensemble and performed dynamic fragmentation [75] to describe proton transfers in water solvent.

Ishimoto et al. [91, 92] developed the FMO Hamiltonian algorithm (FMO-HA), which is another approach for the MD simulation. The important feature of FMO-HA is that the geometries in the simulation are rarely trapped at local minima, which improves sampling.

For light atoms, however, the coupling between electrons and protons may be important, and in the path integral MD (PIMD) [93] it is considered via

the partition function in the path integral representation, containing the Born-Oppenheimer electronic energy. The latter can be computed with FMO, resulting in FMO-PIMD [94].

2.15. ENERGY DECOMPOSITION ANALYSES

Because FMO manipulates with subsystems, e.g., monomers and dimers, one can define the pair interaction energies (PIE) between fragments, denoted also by IFIE (interfragment interaction energies). It is particularly easy to define the bulk value of the PIEs. To do this, it is convenient to look at the FMO energy expression in terms of the internal energies, Eq. (2-90), given for RHF, combined with the correlation energy contribution (e.g., the MP2 correlation energy). PIE between fragments I and J can be defined as

$$\Delta E_{IJ} = (E'_{IJ} - E'_I - E'_J) + \text{Tr}(\Delta \mathbf{D}^{IJ} \mathbf{V}^{IJ}) + (E_{IJ}^{\text{corr}} - E_I^{\text{corr}} - E_J^{\text{corr}}). \quad (2-142)$$

The meaning of the three contributions is as follows. The first term, given by the difference of the internal energies is the “internal” PIE, or the interaction of the electronic states of I and J in the field of other fragments but with the explicit effect of the field subtracted (the implicit effect is present via the global polarization). The second term given by the trace is the interaction of the external field with the charge transferred between I and J (as given by the differential density matrix $\Delta \mathbf{D}^{IJ}$). Loosely speaking, it is the explicit coupling of the internal PIE and the external field (i.e., ESP). This second term is not equal to the charge transfer energy, some part of which is included in all terms in Eq. (2-142). The third term arises in correlated methods (i.e., MP2 and CC); in DFT the correlation is included into the internal energies (the first term) and the third term is zero. This term in correlated methods describes the dispersion (or van der Waals) interaction between the fragments I and J , polarized by the field.

It is important to realize that the polarization is included in (a) the internal monomer energies (since the electronic state of monomers is computed in the polarizing external field, ESP), (b) the electrostatic component of PIEs. As shown below, to define the polarization, one should introduce the free state, against which the polarization is measured. PIEs in general include: the attractive component of the polarization, the electrostatic, exchange-repulsion, charge transfer and dispersion interactions.

It should be noted that PIE between connected fragments in FMO (i.e., between which there is a detached covalent bond) is large (for C-C bonds on the order of 15 a.u.), because interactions in BDA are divided into two fragments. Such PIE values can be used directly to study the change of PIE in some process (a chemical reaction) or a BDA correction can be applied [23].

The above discussion pertains to the ground state, and one can also analyze the contributions of fragment to the excitation energies (Eq. 2-71), in the TDDFT [62,

[63] and CIS [69] context. At present, only bulk values of pair corrections to the excitation energies can be obtained.

2.15.1. Pair Interaction Energy Decomposition Analysis

Although the bulk pair interaction energies defined in Eq. (2-142) are already quite useful and have been taken advantage of in many if not most FMO applications (e.g., [95]), it is desirable to define components outlined above. This is accomplished by the interfacing of the Kitaura-Morokuma energy decomposition analysis (EDA) [96] into FMO, resulting in the PIE decomposition analysis (PIE+EDA=PIEDA) [23]. PIEDA allows a very detailed study of the interaction energy components and their couplings (e.g., the coupling of the polarization and the dispersion), and here we only give a very basic outline of the method.

Pair interaction energies are decomposed as

$$\Delta E_{IJ} = \Delta E_{IJ}^{\text{ES}} + \Delta E_{IJ}^{\text{EX}} + \Delta E_{IJ}^{\text{CT+mix}} + \Delta E_{IJ}^{\text{DI}}, \quad (2-143)$$

where $\Delta E_{IJ}^{\text{ES}}$, $\Delta E_{IJ}^{\text{EX}}$, $\Delta E_{IJ}^{\text{CT+mix}}$ and $\Delta E_{IJ}^{\text{DI}}$ are the electrostatic (ES), exchange-repulsion (EX), charge transfer and higher order terms (CT+mix) and dispersion (DI), respectively.

The polarization is divided into two contributions, the destabilization energy (the difference between the internal energy of the polarized state and the free state energies; that is, this component is obtained from E'_I rather than ΔE_{IJ}), and the stabilization energy, extracted as a part of the energy of the interfragment electrostatic interaction. For the fragments connected by the detached bonds, the definition of the free state is somewhat artificial, and in this case one often chooses not to extract the polarization components, but rather to look at the pair interaction energies of the polarized fragments. However, if two systems are compared (e.g., reactants and transition state), then one can look at the internal energies of fragments E'_I and consider the difference in the destabilization polarization.

2.15.2. Configuration Analysis for Fragment Interaction and Fragment Interaction Analysis Based on Local MP2

The components of PIEDA apply to the bulk PIEs. It is, however, often desirable to consider contributions from some subunits of fragments, such as functional groups. The configuration analysis for fragment interaction (CAFI) was developed [97] on the basis of localized orbitals, whereby one can extract some part of the stabilization polarization and charge transfer energies on the basis of orbital pairs of two fragments. By plotting the localized orbitals, one can identify the functional groups associated with contributions.

To supply the dispersion component to CAFI, Ishikawa et al. [98, 99] combined FMO with the local MP2 (LMP2) method [100] to analyze the dispersion interaction between localized orbitals. The correlation part of the interaction energy between fragments I and J is given by

$$\Delta E_{IJ}^{\text{corr}} = E_{IJ}^{\text{corr}} - E_I^{\text{corr}} - E_J^{\text{corr}}. \quad (2-144)$$

In the fragment interaction analysis based on local MP2 (FILM), one replaces $\Delta E_{IJ}^{\text{corr}}$ with the values from LMP2, $\tilde{\Delta E}_{IJ}^{\text{corr}}$, represented in terms of orbital pair correlation energies,

$$\tilde{\Delta E}_{IJ}^{\text{corr}} = \sum_{i(\in I) \geq j(\in J)}^{\text{occ}} \epsilon_{ij}. \quad (2-145)$$

For instance, if the orbital pairs are σ and π , the corresponding ϵ_{ij} represents the CH- π interaction [99]. It should be noted that there sometimes arises a problem in the orbital localization and the assignments of orbitals in dimer IJ to the either monomer. It was argued [98] that the definition in Eq. (2-145) has a much decreased BSSE (see below). The values in Eqs. (2-144) and (2-145) can be considerably different for these reasons.

2.16. BASIS SET SUPERPOSITION ERROR

Basis set superposition error (BSSE) leads to the overestimation of the molecular interactions when an incomplete basis set is applied in the MO method. Therefore, attempts to remove it have been in the mainstream of research for several decades. The most famous and widely used scheme is the counterpoise (CP) method by Boys et al. [101] In the CP scheme, the intermolecular interaction of the molecular complex IJ consisting of subsystems I and J can be calculated as

$$\Delta E_{\text{CP}} = E_{IJ} - \tilde{E}_I - \tilde{E}_J, \quad (2-146)$$

where the tilde means that the energies are obtained with the basis set of the complex IJ using ghost atoms. The value of BSSE can also be defined as

$$\Delta E_{\text{BSSE}} = \Delta E_{\text{CP}} - \Delta E, \quad (2-147)$$

where ΔE is the conventional intermolecular interaction energy:

$$\Delta E = E_{IJ} - E_I - E_J. \quad (2-148)$$

The CP scheme can be applied to the interfragment interaction energy in Eq. (2-142) [79, 102]. ΔE_{BSSE} was computed [102] from the energies appearing in Eq. (2-147) in vacuum (i.e., without the usual ESP in FMO), and thus left room for improvement. Alternatively, Kamiya et al. [103] developed a method which is a particular case of FMO with the ESP-PC approximation for all ESPs. We note that the CP correction is controversial and it was argued that it does not systematically improve the results [104].

2.17. PROPERTY CALCULATIONS

2.17.1. Definition of Molecular Orbitals

In some cases it is desirable to construct molecular orbitals of the whole system. The FMO-MO approach was suggested by Inadomi et al. [29, 105], where the Fock matrix of the whole system is constructed from the density in Eq. (2-21) and then is diagonalized only once to yield the resulting molecular orbitals. If the total energies or improved MOs are desirable, one can do one more SCF iteration for the whole system. This approach shares many problems of conventional ab initio methods, such as the need to diagonalize a large matrix, although they are somewhat reduced because the number of SCF iterations is 1–2 and the initial guess is quite reasonable (the FMO total density).

Sekino et al. [106] suggested taking the union of the monomer MOs and showed that this method produces fairly good orbitals and their energies, although it was later found [22] that especially the virtual orbitals can be inaccurately described in this case, and thus the very important property, the gap between the highest occupied MO (HOMO) and the lowest unoccupied MO (LUMO) is difficult to obtain accurately.

In the FMO-based linear combination of molecular orbital method (FMO-LCMO) [107], the total Fock matrix \mathbf{F} in the basis of a selected set of MO $i(I)$ is computed and diagonalized,

$$F_{i(I),i'(I)} = \sum_{J \neq I} F_{i(I),i'(I)}^{IJ} - (N - 2) \sum_I F_{ii'}^I, \quad (2-149)$$

$$F_{i(I),j(J)} = F_{i(I)j(J)}^{IJ}, \quad (2-150)$$

where the Fock matrix of dimer IJ is expanded in terms of monomer MOs,

$$F_{k(K),l(L)}^{IJ} = \sum_{ij \in IJ} \langle \phi_k^K | \phi_i^{IJ} \rangle F_{ij}^{IJ} \langle \phi_j^{IJ} | \phi_l^L \rangle, \quad (2-151)$$

and using the Fock matrix of X in its own MO basis,

$$F_{ii'}^X = \epsilon_i^X \delta_{ii'}. \quad (2-152)$$

one can further simplify Eqs. (2-150) and (2-151).

Unlike FMO-MO, the construction of the Hamiltonian matrix in FMO-LCMO is limited to a subset of the MO space, as one can see in Eq. (2-149), where indices i and i' run over a desired subset of orbitals (frequently, a few orbitals around the HOMO-LUMO gap in each fragment).

Alternatively, the FMO/F [22] method was suggested, where the total Fock matrix $\mathbf{F}^{\text{FMO/F}}$ is constructed from the monomer \mathbf{F}_I and dimer \mathbf{F}_{IJ} matrices, and diagonalized once.

$$\mathbf{F}^{\text{FMO/F}} = \sum_I^N \oplus \mathbf{F}^I + \sum_{I>J}^N \oplus [\mathbf{F}^{IJ} - (\mathbf{F}^I \oplus \mathbf{F}^J)]. \quad (2-153)$$

The symbol \oplus here indicates the direct matrix summation, that is, adding the block matrix contributions (e.g., \mathbf{F}_I) into the appropriate blocks of the total matrix $\mathbf{F}^{\text{FMO/F}}$.

It was found that adding the exchange post factum works best, i.e., after the determination of the fragment densities in the presence of ESPs without the exchange, it is added afterwards following Eq. (2-33) to the conventional Fock matrix in FMO, Eq. (2-23), resulting in the FMO/FX method. The other alternative, using the exchange both in SCF and in the total Fock matrix construction (FMO/XF) fails to work for the same reason as FMO/X, as described above.

2.17.2. Molecular Electrostatic Potential and Fitted Atomic Charges

Atomic charges is the important property extensively used in many ways. The molecular electrostatic potential has been also widely used in particular, in biochemistry to explain the affinity of ligands, see e.g., [108]. The electrostatic potential at position \mathbf{r} due to nuclear charges of all atoms and the total electron density $\rho_{\text{FMO}}(\mathbf{r}')$ in Eq. (2-21) can be written as

$$V_{\text{FMO}}(\mathbf{r}) = \sum_A^{\text{all}} \frac{Z_A}{|\mathbf{r} - \mathbf{R}_A|} - \int \frac{\rho_{\text{FMO}}(\mathbf{r}')}{|\mathbf{r} - \mathbf{r}'|} d\mathbf{r}'. \quad (2-154)$$

The atomic charges q_A are fitted to minimize the deviations of $V_{\text{FMO}}(\mathbf{R}_i)$ in Eq. (2-154) to the electrostatic potential (ESP) V_i of the atomic charges at point i :

$$V_i = \sum_A \frac{q_A}{|\mathbf{R}_i - \mathbf{R}_A|}, \quad (2-155)$$

where the points i are chosen on some grid surrounding the system and frequently some additional restraints are imposed, producing restrained ESP (RESP) charges [109] within the FMO formalism [110, 111].

2.17.3. Nuclear Magnetic Resonance

Recently, the resolution of nuclear magnetic resonance (NMR) spectroscopy has improved so that the structure of biological molecules can be determined with an accuracy similar to that of X-ray crystal structure resolution. NMR shifts are often used for the validation of structures; for example, one can optimize the structure with an ab initio method, compute the NMR shifts and compare them to the experimental measurements. FMO can be used [112, 113] to calculate the chemical shifts of biomolecules in combination with the gauge-including atomic orbital (GIAO) [114, 115] or continuous set of gauge transformations (CSGT) [116].

The chemical shifts δ are given by

$$\delta = \frac{\sigma^0 - \sigma^{\text{iso}}}{1 - \sigma^0} \times 10^6 \approx (\sigma^0 - \sigma^{\text{iso}}) \times 10^6, \quad (2-156)$$

where $\sigma^{\text{iso}} = \text{Tr}(\sigma)/3$ is the absolute isotropic shielding constant and the reference standard σ^0 . In the GIAO method the magnetic shielding tensor σ is given by the second derivatives of the energy with respect to the magnetic moment of nucleus and the external magnetic field \mathbf{B} ,

$$\sigma_{\alpha\beta} = \frac{\partial^2 E}{\partial \mu_\alpha \partial B_\beta}. \quad (2-157)$$

In the CSGT method, the magnetic tensor is expressed in terms of the induced current density as

$$\sigma_{\alpha\beta} = -\frac{1}{cB} \int d\mathbf{r}_N \left[\mathbf{r}_N \times \mathbf{j}_\beta^{(1)}(\mathbf{r}_N)/r_N^3 \right]_\alpha, \quad (2-158)$$

where $\mathbf{j}_\beta^{(1)}(\mathbf{r}_N)$ is the induced first-order current density and \mathbf{r}_N is the position vector of electron from nuclear N .

In either case, one has to solve CPHF equations to determine the values of shifts. The GIAO method requires the computation of the ESP in FMO in the basis of GIAO, which is tedious, whereas in the case of CSGT only the regular ESP is necessary. There were two different approaches taken to compute the NMR shifts in FMO: (a) the synthetic FMO1-NMR approach [112], where the shifts are computed for the atoms located in the middle of connected dimers (i.e., away from the bond detachment points), combining the results from two fragmentations shifted relatively to each other, and (b) the regular FMO2-NMR approach [113], where shifts are computed in the many-body FMO expansion.

2.17.4. Multipole Moments and Dynamic Polarizabilities

The calculation of dipole, quadrupole or higher order momenta in FMO is straightforward.

$$M_\mu = \sum_I^N M_\mu^I + \sum_{I>J}^N (M_\mu^{IJ} - M_\mu^I - M_\mu^J). \quad (2-159)$$

where M_μ is the μ component of a multipole moment M (e.g., the x -element of the dipole moment \mathbf{d}). The dipole moments were very extensively used in the validation tests establishing the accuracy of FMO (e.g., [19, 31, 47, 53]), and quadrupole moments were also computed for FMO-DFT [106].

The polarizability is a measure of response of a dipole to the external field that can be described by perturbation theory. It is important because it plays a crucial role in the properties of the low-lying excited states. To obtain the polarizability, one has to solve the following CPHF equations [117] similar to those for TDDFT (see Eq. 2-72),

$$\begin{pmatrix} \mathbf{A}^X - \omega \mathbf{1}^X & \mathbf{B}^X \\ \mathbf{B}^X & \mathbf{A}^X + \omega \mathbf{1}^X \end{pmatrix} \begin{pmatrix} \mathbf{N}_\mu^+ \\ \mathbf{N}_\mu^- \end{pmatrix} = -\mathbf{V}_\mu^X, \quad (2-160)$$

where \mathbf{N} is the response vector, \mathbf{V} is the electric field perturbation vector with $\mu = x, y, z$, and the \mathbf{A} and \mathbf{B} are very similar to those in TDDFT,

$$A_{ri,sj}^X = \delta_{rs} \delta_{ij} (\epsilon_r^X - \epsilon_i^X) + 2(\phi_r^X \phi_i^X | \phi_s^X \phi_j^X) - (\phi_r^X \phi_s^X | \phi_i^X \phi_j^X), \quad (2-161)$$

$$B_{ri,sj}^X = 2(\phi_r^X \phi_i^X | \phi_j^X \phi_s^X) - (\phi_r^X \phi_j^X | \phi_i^X \phi_s^X). \quad (2-162)$$

$$\alpha_{\mu\nu}^X = 2(\mathbf{N}_\mu^+, \mathbf{N}_\mu^-) \cdot \mathbf{V}_\nu^X. \quad (2-163)$$

The polarizability tensor is computed in the FMO formalism [117] as

$$\alpha_{\mu\nu} = \sum_I^N \alpha_{\mu\nu}^I + \sum_{I>J}^N (\alpha_{\mu\nu}^{IJ} - \alpha_{\mu\nu}^I - \alpha_{\mu\nu}^J). \quad (2-164)$$

2.17.5. Nuclear Wave Function

The multicomponent molecular orbital method (MCMO) was developed by Tachikawa et al. [118–120] to treat the nuclear quantum phenomena. Ishimoto et al. [121] combined MCMO with FMO and discussed the geometrical relaxation induced by the H/D isotope effect. The Hamiltonian in Eq. (2-6) is modified as

$$\begin{aligned} H_X = & \sum_{T \in X}^M \sum_{i \in T}^{N_T} \left\{ -\frac{1}{2m_T} \nabla_i^2 + \sum_{j \in T < i}^{N_T} \frac{Z_T^2}{|\mathbf{r}_i - \mathbf{r}_j|} + \sum_A^{N_A} \frac{Z_T Z_A}{|\mathbf{r}_i - \mathbf{R}_A|} \right. \\ & \left. + \sum_{K \neq X}^{\text{all}} \int \frac{\rho_K(\mathbf{r}')}{|\mathbf{r}_i - \mathbf{r}'|} d\mathbf{r}' \right\} + \sum_{(S \in X) < T}^M \sum_{i \in T}^{N_T} \sum_{j \in S}^{N_S} \frac{Z_i Z_j}{|\mathbf{r}_i - \mathbf{r}_j|}, \end{aligned} \quad (2-165)$$

where T and S run over M types of particles (electron, proton and deuteron), while particles are labelled i and j . m_T and Z_T are the mass and charge of T -th type of particle, respectively. A denotes heavy atoms, whose number is N_A . The corresponding wave function is regarded as the product of the wave functions of all particles,

$$|\Psi_X\rangle = |\Phi_A\rangle |\Phi_B\rangle \cdots |\Phi_M\rangle. \quad (2-166)$$

Alternatively, one can consider the full quantum-mechanical treatment of protons in the nuclear-electronic orbital (NEO) method [122], where specifically, NEO-RHF, NEO-DFT and NEO-MP2 were interfaced with FMO. In the FMO-NEO calculation, two types of RHF equations are obtained for electrons and quantum nuclei. The modification of NEO equations is made for the external ESPs due to FMO, whereby some nuclear charges in Eq. (2-28) are replaced by the density distributions (derived from the nuclear wave function), i.e., those terms are moved from

Eq. (2-28) to Eq. (2-29). The additional contributions to ESPs for electrons $v_{\mu\nu}^e$ and quantum nuclei $v_{\mu'\nu'}^n$ (cf Eq. 2-29) are thus defined by

$$v_{\mu\nu}^e = \sum_{K \neq X}^{\text{all}} \sum_{\lambda\sigma \in K} D_{\lambda'\sigma'}^{n,K} (\chi_{\mu}^e \chi_{\nu}^e | \chi_{\lambda'}^n \chi_{\sigma'}^n), \quad (2-167)$$

$$v_{\mu'\nu'}^n = \sum_{K \neq X}^{\text{all}} \sum_{\lambda\sigma \in K} D_{\lambda\sigma}^{e,K} (\chi_{\mu'}^n \chi_{\nu'}^n | \chi_{\lambda}^e \chi_{\sigma}^e), \quad (2-168)$$

where $D_{\lambda'\sigma'}^{n,K} = \sum_{i \in X}^{N_n^K} C_{\lambda'i}^{n,K} C_{\sigma'i}^{n,K*}$ and $D_{\lambda\sigma}^{e,K}$ are the nuclear and electronic density matrices obtained from the corresponding orbital coefficients C , respectively. χ_{μ}^e and $\chi_{\mu'}^n$ are the basis functions for electrons and quantum nuclei, respectively. N_n^K is the number of quantum nuclei for fragment K .

For the covalent bond fragmentation, the contribution from nuclear orbitals are negligible, because the nuclear orbitals are much more localized than MOs. The localized feature of the nuclear orbitals allows some ways to neglect the nuclear-nuclear exchange and the nuclear correlation effects, but the strong electron-proton correlations necessitate the explicitly correlated geminal treatment [123].

2.17.6. Drug Design

Visualized cluster analysis of protein-ligand interaction (VISCANA) was developed for the virtual ligand screening (VLS) based on FMO [124], useful for docking simulations. The dissimilarity of interfragment interactions (PIE) between the two ligand compounds I and J is expressed by

$$d_{IJ} = \sum_K^N (\Delta E_{IK} - \Delta E_{JK})^2, \quad (2-169)$$

where K runs over residues of the target protein.

On the other hand, one can define the protein-ligand interaction energy table in the matrix form by arranging the appropriate PIE values as

$$\begin{pmatrix} \Delta E_{\text{ligand}1,1} & \Delta E_{\text{ligand}1,2} & \cdots & \Delta E_{\text{ligand}1,N} \\ \Delta E_{\text{ligand}2,1} & \Delta E_{\text{ligand}2,2} & \cdots & \Delta E_{\text{ligand}2,N} \\ \vdots & \vdots & \ddots & \vdots \\ \Delta E_{\text{ligand}L,1} & \Delta E_{\text{ligand}L,2} & \cdots & \Delta E_{\text{ligand}L,N} \end{pmatrix}, \quad (2-170)$$

where L is the number of ligands and N is the number of amino acid residues of the protein. The order of ligand compounds is sorted by a hierarchical clustering procedure.

The quantitative structure-activity relationship (QSAR) method is a powerful tool for drug design. Yoshida et al. [95] developed a QSAR scheme taking advantage of

the properties from FMO calculations (atomic charges, interfragment interaction energies etc) as descriptors and successfully applied it to the complexes of HIV-1 protease with a few inhibitors. Fischer et al. [125] used atomic charges from FMO to improve scoring functions. QSAR circumvents the difficulties in a fully ab initio calculation of biological activities by fitting parameters, which connect the activities with the computed descriptors for several experimentally measured ligands and then the activity of new substances can be predicted using the prefitted parameters from the properties computed by FMO.

2.18. MASSIVELY PARALLEL COMPUTERS

In 2006, FMO was applied to the photosynthetic reaction center of *blastochloris viridis* containing 20,581 atoms (1,398 fragments) at the RHF/6-31G(d) level [126]. The calculation was performed using GAMESS on the P-32 subsystem of the AIST Super Cluster and took 86.8 hours on 300 nodes (600 CPUs), taking advantage of the generalized DDI (GDDI) [127]. Ikegami et al. [69] discussed the fragment excitation energies of the chromophore in the electrostatic potentials due to the monomer fragment densities of the surrounding protein cage at the CIS level.

Mochizuki et al. [128] adapted ABINIT-MP program to the parallel vector super-computer, the Earth Simulator. The integral transformation in Eq. (2-58) vectorized using DGEMM, which was found to accelerate the computation by the factor of 6 relative to DAXPY and DDOT. The FMO-MP2 calculations were done for the complex of hemagglutinin protein (HA) with the antibody, which contains 14,086 atoms (911 fragments), taking 91.4 min with 2,048 vectorized processing units (VPUs) and 53.4 min with 4,098 VPUs.

2.19. RECENT APPLICATIONS

Driven by the physical nature of a particular problem, one can choose an appropriate model to perform calculations. An increasing number of researchers including experimentalists have used FMO for the practical applications [13]. Tada et al. [129] analyzed interfragment interactions at the active site of Gelsolin with FMO-MP2/6-31G*, Sawada et al. [130] studied the solvated structure of the helical oligosaccharide heparin at the FMO/PCM/6-31G* level.

There is also considerable interest in the application of FMO to photochemical phenomena involving excited states: Taguchi et al. [131] reported FMO-CIS(D)/6-31G* calculations of the excitations in red fluorescent proteins while Tagami et al. [70] applied FMO-CIS(D)/6-31G to the spectra of bioluminescent luciferases. Kistler et al. [132] used FMO-MCSCF/cc-pVDZ:cc-pVTZ to compute the solvatochromic shifts of explicitly solvated uracyl and cytosine.

Influenza is one of the most contagious diseases in the world and several groups [133, 134] applied FMO to its studies; Takematsu et al. [134] computed the complex having more than 14,000 atoms quantum-mechanically at the FMO-MP2/6-31G* level. He et al. [135] applied FMO-MP2/PCM/6-31G* to the protein folding and

reported that the dispersion dominant protein can reproduce the energy-based scoring function correctly using MP2 as well as the Lenard-Jones dispersion potential with the proper parameters. Nagase et al. [136] studied the binding of urokinase-type plasminogen activator (uPA) with uPA receptor (which is deeply related to the cancer spreading) using FMO-MP2/6-31G.

Nakamura et al. elucidated the reaction mechanism of L-2-haloacid dehalogenase from *Pseudomonas* sp. YL (L-DEX YL) catalyzing the hydrolytic dehalogenation of L-2-haloalkanoic acids using MD and FMO-MP2/6-31G [137]. Halogenated compounds are widely used, but cause environmental pollution and health problems due to their toxicity. The complex structure of L-DEX YL with L-2-chloropropionate (2-CPA) in explicit water solvent was determined using MD, followed by FMO-MP2/6-31G calculations to analyze the pair interactions. It was found that the enzyme activity of L-DEX YL correlates with the pair interactions between residues and molecules at some stages of the reaction.

2.20. SUMMARY

In this chapter, we have mainly discussed the FMO method from a mathematical point of view and briefly introduced recent applications of FMO. The computational schemes are frequently interusable, for example, MCP can be combined with EFP. The combination of various levels such as PCM realizes a multiscale physical approach, where quantum-chemical description is used with a continuum model for solvation.

In the multiscale approach, the FMO method can be used in chemically important molecular regions, in which the electronic treatment is required. On the other hand, the EFP method can be applied to the explicit solvent molecules around the FMO region. PCM can be added to describe to the bulk solvent surrounding both the FMO and EFP molecules. This type of multiscale approach is promising, because the moderate change of interactions in borders would be naturally described with the significant reduction of computational cost. The FMO method developed by a number of research groups is expected to be useful in studying various practical problems.

ACKNOWLEDGMENTS

This work was funded in part by the Next Generation SuperComputing Project, Nanoscience Program (MEXT, Japan).

REFERENCES

1. Hua W, Fang T, Li W, Yu J-G, Li S (2008) *J Phys Chem A* 112:10864
2. Rahalkar AP, Ganesh V, Gadre SR (2008) *J Chem Phys* 129:234101
3. He J, Di Paola C, Kantorovich L (2009) *J Chem Phys* 130:144104
4. Söderhjelm S, Ryde U (2009) *J Phys Chem A* 113:617
5. Xie W, Orozco M, Truhlar DG, Gao J (2009) *J Chem Theory Comp* 5:459

6. Leverentz HR, Truhlar DG (2009) *J Chem Theory Comput* 5:1573
7. Suárez E, Díaz N, Suárez D (2009) *J Chem Theory Comput* 5:1667
8. Gordon MS, Mullin JM, Pruitt SR, Roskop LB, Slipchenko LV, Boatz JA (2009) *J Phys Chem B* 113:9646
9. Mata RA, Stoll H, Cabral BJC (2009) *J Chem Theory Comput* 5:1829
10. Le H-A, Lee AM, Bettens RPA (2009) *J Phys Chem A* 113:10527
11. Pomogaev V, Pomogaeva A, Aoki Y (2009) *J Phys Chem A* 113:1429
12. Kitaura K, Ikeo E, Asada T, Nakano T, Uebayasi M (1999) *Chem Phys Lett* 313:701
13. Fedorov DG, Kitaura K (2007) *J Phys Chem A* 111:6904
14. Fedorov DG, Kitaura K (2006) In: Starikov EB, Lewis JP, Tanaka S (eds) *Modern methods for theoretical physical chemistry of biopolymers*, Elsevier, Amsterdam, pp 3–38
15. Nakano T, Mochizuki Y, Fukuzawa K, Amari S, Tanaka S (2006) In: Starikov EB, Lewis JP, Tanaka S (eds) *Modern methods for theoretical physical chemistry of biopolymers*, Elsevier, Amsterdam, pp 39–52
16. Goto H, Obata S, Kamakura T, Nakayama N, Sato M, Nakajima Y, Nagashima U, Watanabe T, Inadomi Y, Ito M, Nishikawa T, Nakano T, Nilsson L, Tanaka S, Fukuzawa K, Inagaki Y, Hamada M, Chuman H (2006) In: Starikov EB, Lewis JP, Tanaka S (eds) *Modern methods for theoretical physical chemistry of biopolymers*, Elsevier, Amsterdam, pp 227–248
17. Fedorov DG, Kitaura K (eds) (2009) *The Fragment Molecular Orbital Method, Practical Applications to Large Molecular Systems*, CRC Press, Boca Raton, FL
18. Sugiki S, Kurita N, Sengoku Y, Sekino H (2003) *Chem Phys Lett* 382:611
19. Fedorov DG, Kitaura K (2004) *J Chem Phys* 120:6832
20. Fedorov DG, Kitaura K (2006) *Chem Phys Lett* 433:182
21. Yasuda K, Yamaki D (2006) *J Chem Phys* 125:154101
22. Fedorov DG, Kitaura K (2009) *J Chem Phys* 131:171106
23. Fedorov DG, Kitaura K (2007) *J Comput Chem* 28:222
24. Fedorov DG, Jensen JH, DeKa RC, Kitaura K (2008) *J Phys Chem A* 112:11808
25. Fedorov DG, Avramov PV, Jensen JH, Kitaura K (2009) *Chem Phys Lett* 477:169
26. Kairys V, Jensen JH (2000) *J Phys Chem A* 104:6656
27. Suenaga M (2008) *J Comput Chem Jpn* 7:33 [in Japanese]
28. Facio can be downloaded from <http://www1.bbiq.jp/zzzfelis/Facio.html>
29. Inadomi Y, Nakano T, Kitaura K, Nagashima U (2002) *Chem Phys Lett* 364:139
30. Fujita T, Fukuzawa K, Mochizuki Y, Nakano T, Tanaka S (2009) *Chem Phys Lett* 478:295
31. Fedorov DG, Kitaura K (2004) *J Chem Phys* 121:2483
32. Mochizuki Y, Koikegami S, Nakano T, Amari S, Kitaura K (2004) *Chem Phys Lett* 396:473
33. Mochizuki Y, Nakano T, Koikegami S, Tanimori S, Abe Y, Nagashima U, Kitaura K (2004) *Theor Chem Acc* 112:442
34. Fedorov DG, Ishimura K, Ishida T, Kitaura K, Pulay P, Nagase S (2007) *J Comput Chem* 28:1476
35. Schmidt MW, Baldrige KK, Boatz JA, Elbert ST, Gordon MS, Jensen JJ, Koseki S, Matsunaga N, Nguyen KA, Su S, Windus TL, Dupuis M, Montgomery JA (1993) *J Comput Chem* 14:1347
36. Gordon MS, Schmidt MW (2005) In: Dykstra CE, Frenking G, Kim KS, Scuseria GE (eds) *Theory and Applications of Computational Chemistry, the first forty years*, Elsevier, Amsterdam, pp 1167–1189, 2005
37. Fletcher GD, Schmidt MW, Gordon MS (1999) *Adv Chem Phys* 110:267
38. Ishimura K, Pulay P, Nagase S (2006) *J Comput Chem* 27:407
39. Fletcher GD, Schmidt MW, Bode BM, Gordon MS (2000) *Comp Phys Commun* 128:190
40. Ishikawa T, Kuwata K (2009) *Chem Phys Lett* 474:195
41. Weigend F, Köhn A, Hättig C (2002) *J Chem Phys* 116:3175
42. Fedorov DG, Kitaura K (2005) *J Chem Phys* 123:134103

43. Purvis GD III, Bartlett RJ (1982) *J Chem Phys* 76:1910
44. Ranghava-chari K, Trucks GW, Pople JA, Head-Gordon M (1989) *Chem Phys Lett* 157:479
45. Olson RM, Bentz JL, Kendall RA, Schmidt MW, Gordon MS (2007) *J Theor Comput Chem* 3:1312
46. Kowalski K, Piecuch P (2000) *J Chem Phys* 113:18
47. Fedorov DG, Kitaura K (2004) *Chem Phys Lett* 389:129
48. Becke AD (1993) *J Chem Phys* 98:5648; Stephens PJ, Devlin FJ, Chabrowski CF, Frisch MJ (1994) *J Phys Chem* 98:11623; Hertwig RH, Koch W (1997) *Chem Phys Lett* 268:345
49. Tawada Y, Tsuneda T, Yanagisawa S, Yanai Y, Hirao K (2004) *J Chem Phys* 120:8425
50. Zhao Y, Truhlar DG (2008) *Acc Chem Res* 41:157
51. Zhao Y, Truhlar DG (2008) *J Chem Theory Comput* 4:1849
52. Perdew JP, Ruzsinsky A, Csonka GI, Constantin LA Sun J (2009) *Phys Rev Lett* 103:026403
53. Fedorov DG, Kitaura K (2005) *J Chem Phys* 122:054108
54. Pruitt SR, Fedorov DG, Kitaura K, Gordon MS (2010) *J Chem Theory Comput* 6:1
55. Aikens CM, Fletcher GD, Schmidt MW, Gordon MS (2006) *J Chem Phys* 124:014107
56. Piecuch P, Włoch M (2005) *J Chem Phys* 123:224105
57. Włoch M, Gour JR, Piecuch P (2007) *J Phys Chem A* 111:11359
58. Fedorov DG, Ishida T, Kitaura K (2005) *J Phys Chem A* 109:2638
59. Some preliminary results can be found in, Fedorov DG, Ishida T, Uebayasi M, Kitaura K (2007) *J Phys Chem A* 111:2722
60. Fukunaga H, Fedorov DG, Chiba M, Nii K, Kitaura K (2008) *J Phys Chem A* 112:10887
61. Chiba M, Fedorov DG, Kitaura K (2007) *Chem Phys Lett* 444:346
62. Chiba M, Fedorov DG, Kitaura K (2007) *J Chem Phys* 127:103108
63. Chiba M, Fedorov DG, Kitaura K (2008) *J Comput Chem* 29:2667
64. Chiba M, Fedorov DG, Nagata T, Kitaura K (2009) *Chem Phys Lett* 474:227
65. Mochizuki Y, Koikegami S, Amari S, Segawa K, Kitaura K, Nakano T (2005) *Chem Phys Lett* 406:283
66. Head-Gordon M, Rico RJ, Oumi M, Lee TJ (1994) *Chem Phys Lett* 219:21
67. Mochizuki Y, Tanaka K, Yamashita K, Ishikawa T, Nakano T, Amari S, Segawa K, Murase T, Tokiwa H, Sakurai M (2007) *Theor Chem Acc* 117:541
68. Mochizuki Y, Tanaka K (2007) *Chem Phys Lett* 443:389
69. Ikegami T, Ishida T, Fedorov DG, Kitaura K, Inadomi Y, Umeda H, Yokokawa M, Sekiguchi S (2010) *J Comput Chem* 31:447
70. Tagami A, Ishibashi N, Kato D, Taguchi N, Mochizuki Y, Watanabe H, Ito M, Tanaka S (2009) *Chem Phys Lett* 472:118
71. Foulkes WMC, Mitas L, Needs RJ, Rajagopal G (2001) *Rev Mod Phys* 73:33
72. Maezono R, Watanabe H, Tanaka S, Towler MD, Needs RJ (2007) *J Phys Soc Jpn* 76:064301
73. Kitaura K, Sugiki SI, Nakano T, Komeiji Y, Uebayasi M (2001) *Chem Phys Lett* 336:163
74. Nagata T, Fedorov DG, Kitaura K (2009) *Chem Phys Lett* 475:124
75. Komeiji Y, Mochizuki Y, Nakano T (2010) *Chem Phys Lett* 484:380
76. Yamaguchi Y, Schaefer HF III, Osamura Y, Goddard J (1994) *A New Dimension to Quantum Chemistry, Analytical Derivative Methods in Ab Initio Molecular Electronic Structure Theory*, Oxford University Press, New York
77. Fedorov DG, Kitaura K, Li H, Jensen JH, Gordon MS (2006) *J Comput Chem* 27:976
78. Nagata T, Fedorov DG, Kitaura K, Gordon MS (2009) *J Chem Phys* 131:024101
79. Ishikawa T, Mochizuki Y, Nakano T, Amari S, Mori H, Honda H, Fujita T, Tokiwa H, Tanaka S, Komeiji Y, Fukuzawa K, Tanaka K, Miyoshi E (2006) *Chem Phys Lett* 427:159
80. Tomasi J, Mennucci B, Cammi R (2005) *Chem Rev* 105:2999

81. Li H, Fedorov DG, Nagata T, Kitaura K, Jensen JH, Gordon MS (2010) *J Comput Chem* 31:778
82. Su P, Li H (2009) *J Chem Phys* 130:074109
83. Stone AJ (1981) *Chem Phys Lett* 83:233
84. Day PN, Jensen JH, Gordon MS, Webb SP, Stevens WJ, Krauss M, Gramer D, Basch H, Cohen D (1996) *J Chem Phys* 108:1968
85. Chen W, Gordon MS (1996) *J Chem Phys* 105, 11081
86. Komeiji Y, Mochizuki Y, Nakano T, Fedorov DG (2009) *J Mol Struct (THEOCHEM)* 898:2
87. Komeiji Y, Nakano T, Fukuzawa K, Ueno Y, Inadomi Y, Nemoto T, Uebayasi M, Fedorov DG, Kitaura K (2003) *Chem Phys Lett* 372:342
88. Mochizuki Y, Komeiji Y, Ishikawa T, Nakano T, Yamataka H (2007) *Chem Phys Lett* 437:66
89. Sato M, Yamataka H, Komeiji Y, Mochizuki Y, Ishikawa T, Nakano T (2008) *J Am Chem Soc* 130:2396
90. Komeiji Y, Ishikawa T, Mochizuki Y, Yamataka H, Nakano T (2008) *J Comput Chem* 30:40
91. Ishimoto T, Tokiwa H, Teramae H, Nagashima U (2004) *Chem Phys Lett* 387:460
92. Ishimoto T, Tokiwa H, Teramae H, Nagashima U (2005) *J Chem Phys* 122:094905
93. Shiga M, Tachikawa M, Miura S (2001) *J Chem Phys* 115:9149
94. Fujita T, Watanabe H, Tanaka S (2009) *J Phys Soc Jpn* 78:104723
95. Yoshida T, Fujita T, Chuman H (2009) *Curr Comp-Aided Drug Des* 5:38
96. Kitaura K, Morokuma K (1976) *Int J Quantum Chem* 10:325
97. Mochizuki Y, Fukuzawa K, Kato A, Tanaka S, Kitaura K, Nakano T (2005) *Chem Phys Lett* 410:247
98. Ishikawa T, Mochizuki Y, Amari S, Nakano T, Tokiwa H, Tanaka S, Tanaka K (2007) *Theor Chem Acc* 118:937
99. Ishikawa T, Mochizuki Y, Amari S, Nakano T, Tanaka S, Tanaka K (2008) *Chem Phys Lett* 463:189
100. Rauhut G, Pulay P, Werner H-J (1998) *J Comput Chem* 19:1241
101. Boys SF, Bernardi F (1970) *Mol Phys* 19:533
102. Ishikawa T, Ishikawa T, Kuwata K (2009) *J Comput Chem* 30:2594
103. Kamiya M, Hirata S, Valiev M (2008) *J Chem Phys* 128:074103
104. Schwenke DW, Truhlar DG (1985) *J Chem Phys* 82:2418; (1986) 84:4113; (1987) 86:3760
105. Tamura K, Watanabe T, Ishimoto T, Umeda H, Inadomi Y, Nagashima U (2008) *Bull Chem Soc Jpn* 81:254
106. Sekino H, Sengoku Y, Sugiki S-I, Kurita N (2003) *Chem Phys Lett* 378:589
107. Tsuneyuki S, Kobori T, Akagi K, Sodeyama K, Terakura K, Fukuyama H (2009) *Chem Phys Lett* 476:104
108. Watanabe T, Inadomi Y, Fukuzawa K, Nakano T, Tanaka S, Nilsson L, Nagashima U (2007) *J Phys Chem B* 111:9621
109. Bayly CI, Cieplak P, Cornell W, Kollman PA (1993) *J Phys Chem* 97:10269
110. Okiyama Y, Watanabe H, Fukuzawa K, Nakano T, Mochizuki Y, Ishikawa T, Tanaka S, Ebina K (2007) *Chem Phys Lett* 449, 329
111. Okiyama Y, Watanabe H, Fukuzawa K, Nakano T, Mochizuki Y, Ishikawa T, Ebina K, Tanaka S (2009) *Chem Phys Lett* 467, 417
112. Gao Q, Yokojima S, Kohno T, Ishida T, Fedorov DG, Kitaura K, Fujihira M, Nakamura S (2007) *Chem Phys Lett* 445:331
113. Sekino H, Matsumura N, Sengoku Y (2007) *Comput Lett* 3:423
114. Ditchfield R (1974) *Mol Phys* 27:789
115. Wolinski K, Hinton JF, Pulay P (1990) *J Am Chem Soc* 112:8251
116. Keith TA, Bader RWF (1993) *Chem Phys Lett* 210:223

117. Mochizuki Y, Ishikawa T, Tanaka K, Tokiwa H, Nakano T, Tanaka S (2006) *Chem Phys Lett* 418:418
118. Tachikawa M, Mori K, Suzuki K, Iguchi K (1998) *Int J Quant Chem* 70:491
119. Tachikawa M (2002) *Chem Phys Lett* 360:494
120. Ishimoto T, Tachikawa M, Nagashima U (2009) *Int J Quant Chem* 109:2677
121. Ishimoto T, Tachikawa M, Nagashima U (2006) *J Chem Phys* 124:014112
122. Auer B, Pak MV, Hammes-Schiffer S (2010) *J Phys Chem C* 114:5582
123. Chakraborty A, Pak MV, Hammes-Schiffer S (2008) *Phys Rev Lett* 101:153001
124. Amari S, Aizawa M, Zhang J, Fukuzawa K, Mochizuki Y, Iwasawa Y, Nakata K, Chuman H, Nakano T (2006) *J Chem Inf Comput Sci* 46:221
125. Fischer B, Fukuzawa K, Wenzel W (2008) *Proteins Struct Funct Bioinf* 70:1264
126. Ikegami T, Ishida T, Fedorov DG, Kitaura K, Inadomi Y, Umeda H, Yokokawa M, Sekiguchi S (2005) In: *Proceedings of Supercomputing 2005*, IEEE Computer Society, Seattle, WA
127. Fedorov DG, Olson RM, Kitaura K, Gordon MS, Koseki S (2004) *J Comput Chem* 25:872
128. Mochizuki Y, Yamashita K, Murase T, Nakano T, Fukuzawa K, Takematsu K, Watanabe H, Tanaka S (2008) *Chem Phys Lett* 457:396
129. Tada M, Nagasima T, Udagawa T, Tachikawa M, Sugawara H (2009) *J Mol Struct (THEOCHEM)* 897:149
130. Sawada T, Fedorov DG, Kitaura K (2009) *Int J Quant Chem* 109:2033
131. Taguchi N, Mochizuki Y, Nakano T, Amari S, Fukuzawa K, Ishikawa T, Sakurai M, Tanaka S (2009) *J Phys Chem B* 113:1153
132. Kistler KA, Matsika S (2009) *J Phys Chem A* 113:12396
133. Takematsu K, Fukuzawa K, Omagari K, Nakajima S, Nakajima K, Mochizuki Y, Nakano T, Watanabe H, Tanaka S (2009) *J Phys Chem B* 113:4991
134. Sawada T, Hashimoto T, Tokiwa H, Suzuki T, Nakano H, Ishida H, Kiso M, Suzuki Y (2009) *J Mol Genet Med* 3:133
135. He X, Fusti-Molnar L, Cui G, Merz KM Jr (2009) *J Phys Chem B* 113:5290
136. Nagase K, Kobayashi H, Yoshikawa E, Kurita N (2009) *J Mol Graph Mod* 28:46
137. Nakamura T, Yamaguchi A, Kondo H, Watanabe H, Kurihara T, Esaki N, Hirono S, Tanaka S (2009) *J Comput Chem* 30:2625

CHAPTER 3

LINEAR SCALING SECOND ORDER MØLLER PLESSET PERTURBATION THEORY

SVEIN SAEBØ

*Department of Chemistry, Mississippi State University, Mississippi State, MS 39762, USA,
e-mail: ssaebo@chemistry.msstate.edu*

Abstract: All traditional methods for electron correlation share a steep power law dependence on the molecular size. This high scaling prohibits the use of these methods to large systems in spite of the very impressive advances in computer technology over the past decades. Clearly, this problem cannot be solved with improvements of computers alone, and new methods reducing the power law scaling to one or near one must be developed. In this chapter some linear of low scaling methods for electron correlation will be reviewed. The focus will be on the linear scaling MP2 methods, but other more accurate correlation methods will also be briefly discussed. In addition, the very efficient RI-MP2 will be discussed even though the high power law scaling of conventional MP2 has not been reduced. A discussion of the RI-MP2 method has been included since it is perhaps an order of magnitude more efficient than other efficient MP2 methods. The RI or density fitting approach has now been combined with the local correlation method, and the RI-LMP2 method exhibits linear scaling with the size of the system. Most of the methods discussed herein are based on the local correlation method introduced by Pulay and Saebø in the early eighties and developed further by Schütz, Werner and co-workers. The topic was reviewed in 2002 and this review will focus on the more recent advances in this field. A new linearly scaling LMP2 approach yielding essentially identical results to conventional canonical MP2 will be described, and MP2 calculations with around 5,000 contracted basis functions have been performed without density fitting using this approach.

Keywords: Electron correlation, Møller-Plesset perturbation theory, Local correlation, Linear scaling

3.1. INTRODUCTION

Over the past decades we have witnessed tremendous advances in computer technology, and this trend is expected to continue in the future. It has been suggested that an increase in computer power of a factor of 1,000 should be expected every decade in the foreseeable future. However, improvements in computer technology alone are not sufficient to make conventional methods for electron correlation applicable to

large systems. Conventional methods for electron correlation share a steep power law dependence with the size of the system and assuming a sixth-order scaling shared by many commonly used methods for electron correlation, an increase in computer power of a factor of 1,000 will only allow study of systems about three times larger than one could study with today's hardware. The only way computational chemists can take full advantage of the advances in computer technology, and move quantum chemistry into new and exciting areas of science, is by reducing the high power-law scaling of conventional quantum mechanical methods.

As pointed out decades ago, this steep computational scaling is also unphysical [1–4] and it is the result of the use of delocalized canonical orbitals. Electron correlation should asymptotically be more efficient than SCF since the latter method is dominated by long-range Coulomb type interactions while electron correlation effects are relatively short ranged, and the only way the steep computational dependency can be reduced or eliminated is by exploring the localized nature of electron correlation.

The local correlation method was introduced in the early eighties by Pulay and Saebø. This method will be referred to as the Pulay-Saebø local correlation method [1–5]. Several other groups have contributed to the field, and the topic has been reviewed by us [6–8] and by Carter and Walter [9]. References to local correlation approaches developed before 2001 can be found in Ref. [6–8]. As discussed in our 2002 review [8] many groups have contributed to this field including Friesner [10], Ayala and Scuseria [11], Carter [12, 13], Head-Gordon [14], and Schütz, Werner, and coworkers [15–22].

The first implementation of the local correlation method was designed for correlation methods beyond MP2 and provided no savings at the MP2 level [2, 4, 5]. It was implemented for several common correlation methods like MP2 [5], MP3 [5], MP4(SDQ) [3, 5], CI-SD [2], ACCD [23], and CEPA-1 [2] and CEPA-2 [2], and variational CEPA [24] and it provided quite significant computational savings for medium sized systems [25–27]. Unfortunately, the computational resources available ~25 years ago only allowed applications on medium sized systems. The local correlation method was also introduced roughly at the same time as vector machines became readily available and the size of the calculation that could be performed was often limited by disk space. This stimulated a semi direct implementation of the local correlation method [6, 28]. Clearly, the advantages of the local correlation approach become greater the larger the system, and in some respect the local correlation method was introduced too early, since with the computational facilities available at the time did not allow employment of the method to the large system for which the method was designed.

This situation changed dramatically during the following decades both with respect to computer technology and new computational algorithms, and this resulted in a renaissance of local correlation methods in the late nineties and early two thousands. Several groups developed low-scaling methods for electron correlation [9–27] and the majority of these methods were based on the original Pulay Saebø method. Most of these methods were discussed in the earlier review of this topic [8]. Werner, Schütz and coworkers have provided very significant contributions to

the local correlation method. They have achieved linear or near linear scaling for LMP2 [15, 16], LCCSD [17–19] and LCCSD(T) [20–22] where the L means that the method is formulated in terms of localized orbitals.

As the title of this chapter implies, linear or low-scaling methods for electron correlation will be reviewed with emphasis on the simplest correlation method, MP2. In Section 3.2 we will give a brief review the orbital invariant formulation of Møller Plesset perturbation theory [3], since this is needed for description of the methods. In Section 3.3 the local correlation method [2–5, 8] and the two different methods for restricting the dimension of the virtual space will be discussed [2, 4, 5, 8, 29]. In Section 3.4 recent low scaling methods will be discussed, including the ‘full accuracy’ LMP2 method by Saebø and Pulay [29] as well as methods based on the resolution of identity approximation [30, 31], RI-MP2 [32–40]. Even though the high power law scaling of conventional MP2 has not been eliminated in RI-MP2, it is probably the most efficient MP2 approach at least for medium sized systems. Recently, the RI-MP2 method has been combined with the local MP2 approach yielding essentially linear scaling with respect to the size of the system and significantly better scaling with the size of the basis set compared to other MP2 methods [40].

3.2. ORBITAL INVARIANT FORMULATION OF MØLLER PLESSET PERTURBATION THEORY

The focus of this chapter is linear scaling MP2 methods and the only way the formal $O(N^5)$ scaling can be reduced is by formulating the MP2 energy expression in terms of local quantities like localized orbitals or directly in terms of atomic orbitals. For reference, we will begin with a brief review of the orbital invariant formulation of MP2. This method was initially implemented by Saebø and Pulay in 1986 using localized orbitals [3]. Analytical gradients using this formulation have been implemented by Saebø and coworkers [41] and by Werner, Pulay and coworkers for local MP2, LMP2 [42]. Throughout this paper i, j, k, \dots are used to describe occupied orbitals and a, b, c, \dots to describe virtual orbitals. Furthermore, Greek letters $\mu, \nu, \lambda, \sigma$ are used for atomic orbitals.

Møller Plesset perturbation theory [43] was first cast in a formulation suited for computer implementation in the late seventies by Bartlett and Purvis [44], and Pople and coworkers [45]. In the original MO formulation, the energy formula is quite simple, and using the spin-adapted generator state formalism [3, 46] the MP2 energy expression is:

$$E_{\text{MP2}} = - \sum_{i \geq j} (2 - \delta_{ij}) \sum_{ab} \mathbf{K}_{ij}^{ab} (2\mathbf{K}_i^{ab} - \mathbf{K}_{ji}^{ab}) / (\epsilon_a + \epsilon_b - \epsilon_i - \epsilon_j) \quad (3-1)$$

The ϵ 's are orbital energies, and \mathbf{K}_{ij} is the internal exchange matrix for pair (\mathbf{i}, \mathbf{j}) for which the element (\mathbf{a}, \mathbf{b}) is the integral

$$\mathbf{K}_{ij}^{ab} = (i, \mathbf{a} | j, \mathbf{b}) = \iint i(1)\mathbf{a}(1)1/r_{12}j(2)\mathbf{b}(2)d\tau_1 d\tau_2 \quad (3-2)$$

where \mathbf{r}_{12} is the distance between electron 1 and 2. The main computational task for calculating the MP2 energy in the canonical formulation as well as in the local formulation, is to generate the integrals in MO basis. This is formally a $O(N^5)$ procedure regardless of the type of orbitals used. The use of localized (internal) orbitals has several potential advantages, and if insignificant contributions are omitted from the calculation it yields a better scaling than a canonical formulation. However, when localized orbitals are used, the energy formula, Eq. (3-1), cannot be used since the denominator is a sum of orbital energies, which are only defined in terms of canonical orbitals. This problem can be solved by two approaches, the orbital invariant formulation of Møller Plesset perturbation theory introduced by Pulay and Saebø [3, 4] and the Laplace transform of the energy denominator introduced by Almlöf and Häser [47–49].

In the spin adapted generator state formulation [46] of the self-consistent electron pair theory the pair amplitudes, collected in matrices \mathbf{T}_{ij} , are determined from the equation:

$$\mathbf{R}_{ij} = \mathbf{K}_{ij} + \mathbf{F}\mathbf{T}_{ij}\mathbf{S} + \mathbf{S}\mathbf{T}_{ij}\mathbf{F} - \sum_{\mathbf{k}} \mathbf{S}(\mathbf{f}_{ik}\mathbf{T}_{kj} + \mathbf{f}_{kj}\mathbf{T}_{ik})\mathbf{S} = 0 \quad (3-3)$$

\mathbf{F} is the Fock-matrix, \mathbf{S} the overlap matrix and $\mathbf{f}_{\mathbf{ki}}$ are the non-diagonal Fock-matrix elements, which are non-zero when non-canonical orbitals are used. These introduce coupling between the pair-coefficients and Eq. (3-3) has to be solved iteratively. All matrices in Eq. (3-3), represented with capitals letters, are defined in a projected AO basis (\mathbf{p}, \mathbf{q}). The projection makes the AOs used to describe the virtual space orthogonal to the occupied space. The projection of the matrices is illustrated below for the internal exchange matrix:

$$\mathbf{K}_{ij}^{\mathbf{pq}} = (\mathbf{p}, \mathbf{i} | \mathbf{j}, \mathbf{q}) = \sum_{\mu\lambda} \mathbf{P}^{\mu\mathbf{p}} \mathbf{K}_{ij}^{\mu\lambda} \mathbf{P}^{\lambda\mathbf{q}} \quad (3-4)$$

and the projection matrix \mathbf{P} is defined by:

$$\mathbf{P} = \mathbf{I} - 1/2\mathbf{D}\mathbf{S} \quad (3-5)$$

where \mathbf{I} is the unit matrix, \mathbf{D} is the doubly-occupied density matrix. All matrices in Eq. (3-5) are in the original (unprojected) AO basis.

Once the pair amplitudes have been determined by solving Eq. (3-3) iteratively, the MP2 energy can be calculated from the formula:

$$E_{\text{MP2}} = - \sum_{i \geq j} (2 - \delta_{ij}) \sum_{\mathbf{pq}} \mathbf{K}_{ij}^{\mathbf{pq}} (2\mathbf{T}_{ij}^{\mathbf{pq}} - \mathbf{T}_{ji}^{\mathbf{pq}}) = \sum_{i \geq j} \mathbf{e}_{ij} \quad (3-6)$$

The energy formula, Eq. (3-6), expresses the correlation energy as a sum of physically meaningful contributions, pair energies. It should also be noted that Eq. (3-6) yields exactly the same energy as the canonical formulation unless additional approximations are introduced.

As mentioned, Almlöf and Häser proposed a Laplace-transform of the energy denominators [47–49] as an alternative approach to theory to eliminate the energy denominators in non-canonical formulations of Møller Plesset perturbation theory. The Laplace transform technique has been used in an effective MP2 method developed by Ayala and Scuseria [11], and the method was discussed in our earlier review [8].

3.3. LOCAL CORRELATION

The Pulay Saebø local correlation method employs localized internal orbitals while the virtual space is described directly in AO basis. This provides two sources of computational savings:

- 1) The contribution to the correlation energy from pairs of distant localized orbitals can either be neglected or approximated.
- 2) The virtual space is described by a subset of the atomic basis set.

3.3.1. Pair Selection

As mentioned, the local correlation method provides two sources of computational savings. The only way the power law scaling of MP2 or other methods for electron correlation can be reduced is by limiting the number of configuration included in the calculation. This is difficult when canonical orbitals are used since in a canonical formulation the number of correlated pairs scales quadratically with the size of the system ($\mathbf{n}*(\mathbf{n} + \mathbf{1})/2$) where \mathbf{n} is the number of correlated orbitals). One almost trivial way to reduce the configurational space, shared by most local correlation methods, is the neglect of pair correlation between pairs of distant localized orbitals and this represents the most important source of computational savings for large systems provided by localized orbitals. When localized orbitals are used the pairs can be divided into groups and each group of pairs is treated computationally different. Pair selection is an essential part of all linearly scaling schemes for electron correlation and this will be discussed in more details in Section 4 below.

3.3.2. Reduction of the Virtual Space

The second source of computational savings provided by the use of localized correlated orbitals is the reduction of the dimension of the virtual space. This can be achieved by expressing the virtual space in terms of local quantities either by using localized virtual orbitals or by expressing the virtual space directly in AO basis which are normally localized on the atoms. The Pulay Saebø local correlation method as well as methods developed by the Stuttgart group (Werner, Schütz and coworkers) [15–22, 40] use the AO approach mainly because virtual orbitals do normally not localize as well as the occupied ones. Some of the early local correlation methods used localized orbitals for both the occupied and virtual spaces and these methods were discussed briefly in an earlier review [8].

There are two philosophically different methods to select the AOs to describe the virtual space for a particular pair of localized orbitals. Both approaches have their advantages and disadvantages and these will be discussed below. The first approach that will be described is the method used in the original formulation of local correlation by Saebø and Pulay, and this approach was also adopted by the Stuttgart group.

When a standard localization method, like the Boys [50] or Pipek-Mezey [51] localization method, is used most internal orbitals localize into core orbitals, lone-pairs, and bicentric bonds. This means that most internal orbitals are localized on either one or two atoms. Subsets, $\mathbf{D}(\mathbf{i})$, of the atomic orbitals, called domains, are assigned for each correlated orbital \mathbf{i} . For diagonal pairs, (\mathbf{ii}) , $\mathbf{D}(\mathbf{i})$ is used as to describe the virtual space while for non-diagonal pairs, (\mathbf{ij}) , the union of the two domains $\mathbf{D}(\mathbf{i}) \cup \mathbf{D}(\mathbf{j})$ is used. In the initial implementation of the local correlation program the local domains were assigned as follows: For lone-pairs $\mathbf{D}(\mathbf{i})$ consisted of all valence AO for the atom on which the lone pair was localized, and for bicentric bonds $\mathbf{D}(\mathbf{i})$ consisted of all valence AOs for the two atoms involved. Core orbitals were normally not correlated mainly due to the lack of proper basis functions when standard basis sets were used. This scheme was later refined and made automatic by Boughton and Pulay [52], and essentially the same selection method was also used in later implementations and by the Stuttgart group. The local domains generated by the Boughton-Pulay scheme are based on numerical criteria, and allowed for contributions from close neighbors and imperfect localization. Clearly, there are many systems where some of the orbitals are delocalized over several atoms, but this will not introduce a big problem since it only results in larger local domains for these particular delocalized orbitals, and the relatively small local domains could be retained for the remaining well localized correlated orbitals of the system.

The dimension of the virtual space defined this way is independent on the size of the system but it does depend on the basis set. We have demonstrated that when basis sets appropriate for electron correlation calculations are used 95–99% of the pair correlation energy is recovered using this scheme [4, 5, 7, 8] The main advantage with this approach is the efficiency since using these relatively small subspaces of the virtual space yields very significant computational savings for large systems. Since the local domains are independent on the size of the system the approach also scales linearly with the size of the system for large systems, at least for the part of the program that depends on the dimension of the virtual space (LMP2-iterations). The error introduced to the correlation energy is significant ($\sim 1\%$), but very systematic. It has also been argued by us and others that at least a large part of the difference in correlation energy between conventional methods and with a type of local basis described above can be attributed to basis set superposition errors of the full (canonical) case. In fact, one of the earliest local correlation like methods was introduced not with the motivation of computational savings but to eliminate basis set superposition errors in studies of weakly interacting systems [53].

In the second approach, which we have called ‘full accuracy’ LMP2, the dimension of the virtual space is determined by purely numerical means and *all* significant contributions to the MP2 energy are retained [29] This scheme yields results that

are within a few micro-Hartrees of the results using the conventional canonical formulation. There are obvious computational advantages in knowing the AOs that are contributing to the correlation energy prior to the calculation, but the main difference between this approach and methods using pre-selected local domains, is that the dimension of the local domains are significantly larger. The ‘full accuracy’ LMP2 scheme is therefore more accurate, but also more expensive than the methods introduced by the Stuttgart group. The error is much smaller but also more random than in the first approach, and the error cannot be attributed to basis set superposition errors. The advantage is, obviously, that the method yields results that are practically identical to conventional MP2 results, and thus does not introduce a new model chemistry. The ‘full accuracy’ LMP2 method will be described in more detail in Section 3.4 below and the discussion will include some recent advances in the treatment of distant pairs.

3.4. RECENT LINEARLY SCALING MP2 METHODS

In this section some of the recent advances in the field will be discussed. Most of the linearly scaling methods for electron correlation were developed in the late nineties or early two thousands and advances that were not included in our 2002 review on this topic will be discussed in this section. We will first discuss the ‘full accuracy’ LMP2 method introduced by Saebø and Pulay. The treatment of the strong pairs in this method is described in Ref. [29] and also discussed in our earlier review [8]. Weak pairs have now been included in the ‘full accuracy’ LMP2 method and the method will be discussed below.

3.4.1. Full Accuracy Local MP2

This method exhibits linear scaling with the size of the system, but it is less efficient than methods based on the Boughton Pulay selection scheme. The main advantage of this approach is that the results are essentially identical to the conventional canonical MP2 results. Conventional MP2 and most of the low-order scaling schemes developed in other groups are dominated by the integral transformation part, transforming electron repulsion integrals from AO basis to MO basis. This is not the case for our approach, and the reason for this is that we are not using pre-selected local domains. Our domains are determined from purely numerical criteria, retaining essentially *all* significant contributions to the correlation energy.

For any low-order scaling scheme designed for very large systems it is essential that *all* parts of the program exhibit this low-order scaling and we will describe the various steps of our method and explain how linear scaling is achieved in each step. Linear scaling with respect to the number of calculated two-electron integrals was achieved by adopting the prescreening procedure suggested by Rauhut et al. [54]. A test density matrix \mathbf{D}_{\max} in which the (μ, λ) element contains the maximum value of the product of MO coefficients for all pairs included in the transformation (see below) is constructed prior to the transformation and integrals are only calculated when

$$(\mu, \nu | \lambda, \nu)^* D_{\max}(\nu, \lambda) > \text{threshold} \quad (3-7)$$

In Eq. (3-7) $(\mu, \nu | \lambda, \nu)$ is an estimate of the absolute value of the integral. This procedure reduces the number of calculated integrals in LMP2, and the integral calculation exhibits a near linear scaling with the size of the system. Interestingly, this pre-screening scheme can also be applied to conventional canonical MP2 since AO integrals with negligible contribution to the MP2 energy are negligible regardless of the formulation. We have implemented a similar prescreening in our canonical MP2 program, and it provides significant savings in CPU time without loss of accuracy [55, 56].

With conventional localization methods only a few MO coefficients for a given MO are large in a large, well localized, system. The remaining coefficients are not negligible; however, most of them do not exceed 10^{-4} in magnitude. The contribution to the internal exchange matrix, \mathbf{K}_{ij} , from an AO integral is the integral multiplied by a product of two MO coefficients and the *majority* of the contributions are therefore negligible, and only a small fraction of the contributions needs to be calculated. To take advantage of this effectively, the coefficients must be processed in order of decreasing magnitude and this is achieved by sorting the MO coefficients prior to the calculation. The local basis for each pair (\mathbf{ij}) is also determined during the integral transformation, essentially as *all* AOs contributing significantly to the external exchange matrix \mathbf{K}_{ij} [29].

As mentioned above, the local domains constructed this way are quite large often around 300 projected AOs (PAO) with a decent basis set, and the ‘full accuracy’ of this scheme is obtained on the expense of reduced efficiency compared to other methods, however, the linear scaling is still retained.

3.4.1.1. Pair Selection

The most important source of computational savings for large systems provided by localized orbitals is the neglect of pair correlation for pairs of very distant localized orbitals. The pair correlation energy decreases very rapidly with the distance between the orbitals (approximately with the inverse sixth power), and the majority of the pairs of a large system do not contribute significantly to the correlation energy. Several different criteria could be used to determine which pairs of localized orbitals that should be included in the calculation, but regardless of the particular criterion chosen, the pairs included in the calculation will only grow linearly with the size of the system; and only the number of negligible pairs will grow quadratically. The asymptotic scaling of the method is therefore not affected by the pair-selection criteria but of course the criterion is very important for the efficiency of the approach.

The magnitude of the pair correlation energy for a non-diagonal; pair is estimated by using the dimensionless quantity \mathbf{E}_{ij} [29]:

$$E_{ij} = Cr_i^3 r_j^3 / d^6 \quad (3-8)$$

where \mathbf{r}_i is the orbital radius of localized orbital \mathbf{i} , and \mathbf{d} is the distance between the two orbital centers, and C is a constant related to the HOMO-LUMO gap. Equation (3-8) corresponds to London's formula for dispersion interaction between two systems, and the estimate E_{ij} depends both on the distance and the degree of localization of the two orbitals. The quantity E_{ij} is calculated for all non-diagonal pairs prior to the calculation (diagonal pairs are obviously always strong and included in the calculation) and based on the value of E_{ij} the pairs are divided into three groups, strong, weak, and negligible pairs. This partitioning of the pairs is somewhat different from that of the Stuttgart group, and as advocated by Hetzer et al. [16], it is probably useful to introduce a fourth category, distant pairs, in particular for methods beyond MP2. In the 'full accuracy' LMP2 approach the strong pairs are calculated as described above and *all* significant contributions are included. Test calculations with all pairs treated this way yield correlation energies that differ only by a few μ -Hartrees from the canonical result.

Furthermore, the negligible pairs are simply omitted from the calculation. For a large system most pairs are in fact negligible and this represents the most important saving provided by localized orbitals. On the other hand, since the number of negligible pairs is very large in large systems, their collective contribution may not be insignificant. In our current implementation an estimate of the contribution from the neglected pairs, calculated using Eq. (3-8) is added to the MP2 energy for the strong and weak pairs. The result below for (glycine)₅₀ show that 92% of the pairs are neglected and the estimated collective contribution to the correlation energy from these pairs is less than 0.01%.

Physically, there is a large difference between strong and weak pairs. Strong pair correlation, which includes intrapair correlation, and correlation between neighboring localized orbitals that overlap significantly, is dominated by short-range interactions. Weak pair correlation is dispersion attraction between non-overlapping charge densities, and its magnitude is much smaller. The number of both strong and weak pairs scales linearly with the size of the system. This is obvious for strong pairs but it is also true for weak pairs since the number of weak pairs is limited by the fact that the pair correlation energies decrease rapidly with the distance between the orbitals, asymptotically as \mathbf{d}^{-6} where \mathbf{d} is the distance between the centers of the localized orbitals. Therefore only orbitals within a certain distance of each other contribute significantly to the correlation energy. For one-dimensional (chain-like) systems the number of weak pairs is similar or slightly larger than the number of strong pairs while for two or three-dimensional systems, the number of weak pairs is usually much larger than the number of strong pairs.

In our preliminary implementation, we used a fixed domain for a given occupied orbital, regardless of its pair partner, i.e. whether it was participating in a strong or weak correlation. We also used symmetrical pair domains (unions of orbital domains) as described above. Thus our pair domains became quite large. The number of basis functions in a pair domain depends on the basis set but typically the number of projected atomic orbitals (PAO) is around 300. As a result, most of the computational effort was spent in the iterative cycles of Eq. (3-3) involving the weak pairs, in spite of their modest contribution to the correlation energy. Compared

to our highly efficient canonical MP2 [55, 56], the local MP2 program was only significantly faster if weak pairs were omitted when applied to medium sized systems. Its main advantage was that it could be applied to very large systems without introducing additional approximations, such as density fitting (see below).

The solution to this problem is to treat the weak pairs different from the strong ones and this is justified by the physical difference between the two types of pairs as discussed above. Treating the weak pairs with full accuracy is wasteful and, increases the expense of the method significantly, and it is obvious that the large local basis sets used in our preliminary implementation are not required for the distant pairs. A more efficient solution is to exploit the physical nature of weak correlation as dispersion energy between distant, non overlapping orbitals to reduce the size of the virtual space. We have demonstrated that a relatively small number of well-chosen MOs are sufficient to accurately describe weak pairs. The details will be described in a forthcoming paper [57]. It is shown that a small MO basis, possibly as small as 5–10 orbitals, determined individually for each localized internal orbital, is capable of describing essentially all dispersion interaction in the virtual space. These orbitals are referred to as the dispersion basis and a different set of virtual orbitals are needed for each localized occupied orbital. The MOs for describing the virtual space for weak pairs, or dispersion orbitals, can be constructed simply by determining the orbitals in the virtual space that maximizes the square of the transition dipole (or higher moments) components. The number of MOs required depends on the distance between the orbitals. At long distances three dispersion orbitals corresponding to the three dipole moment components is sufficient and at shorter distances higher moments and thus more orbitals will be required.

The new treatment for weak pairs has been implemented as an addition to the “full accuracy” LMP2 program reported earlier [29]. The pairs of localized orbitals are initially partitioned into strong, weak, and negligible pairs as described above. The strong pairs are treated as described in Ref. [29]. This part was also described in our earlier review on this topic and the details will therefore not be repeated here, and we will only describe the strategy for the new (and unpublished) treatment of weak pairs. As mentioned above, the details will be provided in a forthcoming paper.

3.4.1.2. *Implementation*

The MO bases for all weak are constructed and written to external storage before the integral transformation. In our current implementation, the virtual space for each weak pair is described with 32 MOs, and each weak pair has its own MO basis. The MO matrix for a single pair is formally $\mathbf{N} \times \mathbf{32}$ matrix where \mathbf{N} is the number of basis functions. The transformation of a single \mathbf{T} or \mathbf{K} from AO to MO basis is thus formally a $\mathbf{32} \mathbf{N}^2$ procedure, and since the number of \mathbf{K} 's and \mathbf{T} 's, or the number of weak pairs included, increases linearly with the system, the transformation exhibits a formal cubic scaling with the size of the system. However, in the spirit of the local correlation method, only a small fraction of the AOs are needed to describe these MOs, and in analogy with the treatment of the strong pairs AOs with insignificant contribution to the correlation energy are neglected by creating local bases for the

orbital matrices and thus reducing their dimensions from $\mathbf{N} \times \mathbf{32}$ to $\mathbf{L} \times \mathbf{32}$ where \mathbf{L} is independent of the size of the system. For large systems \mathbf{L} is only a small fraction of \mathbf{N} for example for (glycine)₅₀ (Table 3-1) \mathbf{N} is 3,118 while the average value of \mathbf{L} is only 263. This reduces the scaling of the transformation of the internal exchange matrices from AO to the dispersion basis and vice versa basis from cubic to linear.

The first half-transformation is carried out for all strong and weak pairs as described in Ref. [29], and a two phase Yoshimine bin sort [58] yields internal exchange matrices \mathbf{K}_{ij} in AO basis. If ij is a weak pair this matrix is transformed to dispersion basis and written to external storage. The disk space needed for these matrices is only $\mathbf{nwp} \times \mathbf{32}^2$ words (\mathbf{nwp} =number of weak pairs) representing less than 1% of the total disk-space requirement for a calculation on a large system. The transformation itself scale as $\mathbf{32} \times \mathbf{nwp} \times \mathbf{L}^2$ as discussed above and since \mathbf{nwp} increase linearly with the size of the system and \mathbf{L} is independent of the size of the system this transformation will exhibit linear scaling. Calculations of the second and third terms of Eq. (3-3) are trivial when the canonically orthogonalized symmetrical MO basis is used since \mathbf{F} is simply the diagonal matrix of eigenvalues and \mathbf{S} in the identity matrix in the dispersion basis.

The major part of the calculation of the residuum matrices is the calculation of the coupling terms, the last term in Eq. (3-3) with the summation over correlated orbitals \mathbf{k} . In a LMP2 calculation there are four different types of coupling terms contributing to a given residuum matrix: Contributions from strong pairs to the residuum for strong pairs, contribution from weak pairs to the residuum for strong pairs, contribution from strong pairs to the residuum for weak pairs, and contributions from weak pairs to the residuum for weak pairs. These types of contributions will be referred to as strong-strong, strong-weak, weak-strong and weak-weak contributions, respectively. The algorithm for evaluation of the strong-strong contributions was described in Ref. [29] and only the latter three types will be described here.

The amplitudes for weak pairs are stored in the small MO basis. For the weak-weak and weak-strong interactions, the amplitudes \mathbf{T}_{kj} and \mathbf{T}_{ik} have the same dimensions (32×32), however, each weak pairs has its own MO basis and these amplitudes must be transformed to a common AO basis. The common AO basis is not the full AO basis but a relatively small subset which is different for different pairs. After the summation of \mathbf{k} is completed, the results are contracted to the MO basis for the weak pair ij for weak-weak interactions, or the local AO basis for the strong pair ij for weak-strong contributions. The strong-weak contributions are calculated essentially the same way the strong-strong contributions, as described in Ref. [29]. The only difference is that the final contribution is contracted the dispersion basis for the weak pair ij rather than the local (AO) basis for strong pair ij .

As discussed in Ref. [29] and [8], the multiplication with \mathbf{S} can either be carried out inside the loop over orbitals \mathbf{k} in local dimension or once outside the loop in a somewhat larger dimension. Both algorithms were tested in our original version of the LMP2 program, and at least for long chain-like molecules where significant overlap between all the local bases in the sum exists, multiplication with \mathbf{S} outside the loop is preferred. However, as pointed out by Schütz et al. [15] multiplication

inside the loop is more efficient for large three-dimensional systems. As discussed earlier, both algorithms exhibit a low order or near linear scaling with the size of the system.

The amplitudes for all pairs are updated according to Eq. (3-9):

$$T_{ij}^{ab} \leftarrow T_{ij}^{ab} - R_{ij}^{ab} / (\epsilon_a + \epsilon_b - \epsilon_i - \epsilon_j) \quad (3-9)$$

For the strong pairs (\mathbf{a}, \mathbf{b}) is a temporary, pair adapted, MO basis, and the details are described in Ref [29]. For the weak pairs the updating is performed directly in the small dispersion basis where ϵ_i and ϵ_j are the Coulson energies for localized orbitals \mathbf{i} and \mathbf{j} , respectively and ϵ_a and ϵ_b are the eigenvalues of the Fock-matrix in the small dispersion basis. Thus the computational effort for updating the amplitudes as well as calculation of the pair energies for the weak pairs is insignificant. In addition, the weak pairs converge faster than the strong ones, and calculation of strong-weak and weak-weak interactions can thus be omitted in the last couple of LMP2 iterations.

The treatment of weak pairs described above has been implemented with our LMP2 program which is part of the PQS suite of programs [59]. Examples describing both accuracy and scaling will be included in our forthcoming paper which will also include a detailed discussion of thresholds and a theoretical justification of the approach [57].

3.4.1.3. Results

The examples discussed below are calculations on rod-shaped poly-glycines. The reason for choosing these systems as tests systems is, obviously, that for these ‘one-dimensional’ systems the onset of linear scaling starts for much smaller systems than it would for two or three dimensional systems. It should be pointed out, however, that for large systems of all shapes only the number of neglected pairs will grow quadratically with the size of the system while both the number of strong and weak pairs will grow linearly with the size of the system. The LMP2 scheme will thus ultimately exhibit linear or near linear scaling for molecules of all shapes.

We have chosen the series (glycine)₃₀, (glycine)₄₀, and (glycine)₅₀ to illustrate efficiency and scaling. The results for this series are shown in Table 3-1. It should be noted that the onset of linear scaling starts for much smaller systems. For the poly-glycine series near linear scaling started around (glycine)₁₃, and for (glycine)₁₃ and larger poly-glycine chains the program exhibited near linear scaling with the size of the system both with respect to elapsed time and disk-space requirements.

From the results in Table 3-1 it can be seen that one of the main advantages of the LMP2 scheme is the very modest disk-space requirements and (glycine)₅₀ with 3,118 contracted basis functions and 554 correlated orbitals required less than 15 GB of disk-storage. The results in Table 3-1 demonstrate the linear growth of strong and weak pairs with the size of the system. The disk-space requirements also scale linearly with the size of the system while the elapsed times exhibit a low and near linear scaling. All calculations in Table 3-1 were performed using a single

Table 3-1. Scaling of the parameters of local LMP2 calculations for a series of poly-glycines^{a,b}

Number of	(Glycine) ₃₀	(Glycine) ₄₀	(Glycine) ₅₀	Scaling1	Scaling2
Contracted functions	1,878	2,498	3,118		
Correlated orbitals	334	444	554		
Strong pairs	3,533	4,713	5,893	1.00	1.00
Weak Pairs	3,609	4,859	6,109	1.03	1.03
Neglected pairs	48,803	89,218	141,733	2.10	2.07
Disk Storage in GB	8.6	11.5	14.6	1.01	1.07
Elapsed times in min ^c					
1-st half transformation	138	216	307	1.56	1.58
LMP2-iterations	126	174	219	1.12	1.03
Total LMP2	309	458	613	1.37	1.31
Energies (Hartrees)					
-E(MP2) strong	17.6074904	23.4133737	29.2192614		
-E(MP2) weak	0.029756	0.039835	0.049913		
-E(MP2) total	17.6386548	23.4551220	29.2715935		

^aGeometries: rod-shaped poly-glycines terminated as zwitter ions.

^b6-31G* basis set using spherical harmonic (5-component) d functions.

Scaling1 of a quantity Q is $\log(Q_{40}/Q_{30})/\log(40/30)$ where Q_{40} and Q_{30} are the values in the (glycine)₄₀ and (glycine)₃₀ calculations, respectively. *Scaling2* is the analogous quantity for (glycine)₅₀/(glycine)₄₀.

^cCPU times are identical to elapsed times when rounded to whole minutes.

2.80 GHz Intel Xeon-EP Nehalem processor. The calculations in Table 3-1 were carried out using the 6-31G* basis. This basis set is too small for accurate MP2 calculations and, if possible, basis set of triple zeta plus polarization quality (or larger) should be used. We have also performed a calculation on (glycine)₃₀ using the more realistic cc-pvtz basis set. This MP2 calculations with 4,918 contracted basis functions is one of the largest MP2 calculations reported to date and the total elapsed time for this MP2 calculation was about 108 h on a single 2.80 GHz Intel Xeon Nehalem processor.

3.4.1.4. Future Work

At the moment, only a single processor implementation of the ‘full accuracy’ LMP2 has been completed, and the method will only be useful when analytical gradients as well as parallelization of the program has been completed. Analytical gradients have been implemented for canonical MP2 and this is included in the PQS-program [59] using the orbital invariant formulation [3, 41]. Werner, Pulay and coworkers have also implemented analytical gradients for LMP2 using the same formalism [42]. The algorithm for calculation of analytical gradients has been worked out in detail and a large part of the work has already been completed. Parallelization of the program is also relatively straight forward. PQS already has a very efficient parallel implementation of canonical MP2 [56] and the strategy for parallelization of the LMP2 program will be essentially identical to the strategy used for canonical MP2.

3.4.2. RI-MP2 Methods

As demonstrated above linear scaling can be achieved for local correlation method, but, depending on the particular local correlation approach applied, linear scaling is achieved only for quite large systems in particular for three-dimensional systems. Another problem is that electron correlation calculations require large atomic basis sets and since the dimension of the local domains increase with the size of the basis set, local correlation methods still has a close to a fourth order dependence on the number of basis functions.

This has limited the use of the local correlation methods, and the majority of MP2 calculations on large systems reported in the literature, are performed using the so-called RI-MP2 approach [32–40]. This approach is also referred to as auxiliary basis set expansion or density fitting approach. Werner and coworkers suggested [40] the name density-fitting or DF-MP2 for this method but the name RI-MP2 is still used by most authors. RI-MP2 is more efficient than conventional MP2, in particular for large systems. However, the formal $O(N^5)$ scaling of conventional MP2, has not been eliminated in RI-MP2, even though the pre-factor is much smaller compared to conventional MP2. The only reason this approach is included in a chapter on linear scaling correlation method is that DF-MP2 scheme has now been combined with the local correlation approach and in the DF-LMP2 or RI-LMP2 approach [40] and in the DF-LMP2 approach the asymptotic scaling is reduced to near $O(N)$ for large systems.

The basic idea of the RI or density fitting approach is that four-index two-electron integrals are approximated by two three-index integrals by expanding the electron charge densities in linear expansion of AOs or auxiliary basis sets. The pseudospectral approach by Friesner [10] and Carter [60] is based on similar ideas. These methods were briefly discussed in our earlier review and will not be discussed here. Auxiliary basis expansions were first introduced by Boys and Shavitt [61] and early work in this field was reviewed by van Alsenoy in 1988 [62]. Auxiliary basis expansions have been used for many different ab initio methods but only the RI-MP2 methods will be discussed here. The RI-MP2 method was first introduced by Feyereissen et al. [30, 32]. These authors also introduced the name resolution of the identity, and this name is still in use today in spite of the fact that other authors have used more descriptive names like auxiliary basis approximation and density fitting approximation. The term resolution of identity originates from the expression of the identity matrix, \mathbf{I} , in an orthonormal basis $|\mathbf{A}\rangle$:

$$\mathbf{I} = \sum_{\mathbf{A}} |\mathbf{A}\rangle \langle \mathbf{A}| \quad (3-10)$$

If Eq. (3-10) is inserted into an electron repulsion integral, this can be written as:

$$(\mu\nu|\lambda\sigma) = \sum_{\mathbf{A}} (\mu\nu\mathbf{A})(\mathbf{A}|\lambda\sigma) \quad (3-11)$$

where $(\boldsymbol{\mu}, \mathbf{v} \mathbf{A})$ is a three index overlap integral and $(\mathbf{A} | \boldsymbol{\lambda} \boldsymbol{\sigma})$ is a three index two-electron integral. Equation (3-11) is exact if the auxiliary basis set $|\mathbf{A}\rangle$ is complete in the space of the pair $(\boldsymbol{\mu}, \mathbf{v})$. In reality, the auxiliary basis is incomplete and Eq. (3-11) then is an approximation called the resolution of identity approximation.

The MP2 energy expression in the canonical formulation can be obtained simply by substituting Eq. (3-11) into Eq. (3-2):

$$\begin{aligned} E_{\text{MP2}} &= - \sum_{i \geq j} (2 - \delta_{ij}) \sum_{ab} (ia | jb) [2(ia | jb)(ja | ib)] / (\epsilon_a | \epsilon_b - \epsilon_i - \epsilon_j) \\ &\approx - \sum_{i \geq j} (2 - \delta_{ij}) \sum_{ab} \sum_A (iaA)(A | jb) \\ &\quad \times \sum_B \{2(iaB)(B | jb) - (jaB)(B | ib)\} / (\epsilon_a + \epsilon_b - \epsilon_i - \epsilon_j) \end{aligned} \quad (3-12)$$

where \mathbf{A} and \mathbf{B} represent the auxiliary basis set. As mentioned, this approximation introduces an error, and by minimizing this error the two electron integrals used in the RI-MP2 method and the MO integral $(\mathbf{K}_{ij})^{\mathbf{a}, \mathbf{b}}$ (Eq. (3-2)) is approximated as:

$$\mathbf{K}_{ij}^{\mathbf{a}, \mathbf{b}} = (ia | jb) \approx \sum_A H_{ia}^A H_{jb}^A \quad (3-13)$$

where

$$H_{ia}^A = \sum_B (ia | B)(B | A)^{-1/2} \quad (3-14)$$

The auxiliary or fitting basis sets are of course important for the accuracy of the RI-MP2 approach and optimal basis sets have been developed by Ahlrichs [33, 63] and others [34–37]. Normally, atom centered Gaussian basis sets are used and in the first implementation of RI-MP2 the same basis set was used both as atomic and auxiliary basis. In order to obtain sufficiently accurate results the auxiliary basis set must be somewhat larger than the atomic basis set. The ratio between the number of auxiliary basis functions and the size of the atomic basis set is normally between 1.5 and 4 [31].

The RI-MP2 approach is very efficient and since it has been implemented in most of the widely used, commercially available, program packages it has been widely used and MP2 calculations on systems with about 200 atoms and more than 4,000 basis functions have been reported [39]. For medium-sized molecules the efficiency compared to conventional MP2 is about an order of magnitude, and with proper choice of fitting basis functions the RI-approximation is also quite good with errors smaller than other errors in MP2 calculations with standard basis sets [40]. However, the formal $O(N^5)$ scaling of conventional MP2 has not been eliminated.

Clearly, for sufficiently large systems the ‘full accuracy’ LMP2 approach will be more efficient than RI-MP2. The crossover point depends on the shape of the system since LMP2 is more efficient for rod-shaped (one-dimensional) systems than for two- and three-dimensional systems. Determination of the cross-over point

would require benchmark calculations using both the LMP2 and RI-MP2 programs, and even though RI-MP2 programs have been implemented in several commercially available software packages, license agreements normally prohibits direct comparison with other programs.

3.4.3. Local RI-MP2

The RI-MP2 method is clearly not a linearly or low scaling method with respect to the molecular size, and the reason a discussion of this method has been included in this chapter is that due to the small pre-factor it is much more efficient than most low-scaling MP2 methods, at least for medium size systems. Another reason is that the RI-MP2 approach has now been combined with the local correlation method and the RI-LMP2 or DF-LMP2 method developed by Werner and coworkers [40] exhibits the same low order scaling with the molecular size as other methods based on the local correlation approximations. In the DF-LMP2 method pre-selected local domains as discussed above are used. It was demonstrated that the error introduced by the RI-approximation was negligible, significantly smaller than the error introduced by restricting the dimension of the virtual space. Analytical gradients for DF-LMP2 [64] has also been implemented and density fitting is now available for all local correlation methods included in the MOLPRO program [65], e. g. LCCSD, LCCSD(T).

3.5. CONCLUSIONS

The steep power-law dependence on the size of the system shared by all conventional methods for electron correlation prohibits application of these methods to large molecular systems. This steep dependence is also unphysical and electron correlation for large systems should be less expensive than Hartree-Fock since the contributions contributing to the correlation energy are short ranged compared to SCF which is dominated by long ranged Coulomb type interactions. Perhaps the *only* way this steep dependency can be eliminated is by a local approach where the correlation energy is expressed in terms of localized quantities like localized orbitals or directly in atomic orbitals.

The local correlation method by Pulay and Saebø from the early eighties was probably introduced too early since the computational facilities available at that time did not allow application of the method to the large system it was designed for. In addition, the introduction of vector machines around that time, temporarily reduced the need for low scaling methods. A decade later this situation had changed and it led to a renaissance of local correlation methods in the mid to late nineties and early twenties. Most of these advanced were discussed in our earlier review of the topic. However, we have improved our “full accuracy” LMP2 method in particular with respect to the treatment of distant pairs and this method exhibit linear scaling without any significant loss of accuracy. MP2 calculations on systems with more than 200 atoms and about 5,000 contracted basis functions have been performed using this method.

The introduction of RI-MP2 practically eliminated, at least temporarily, the need for low scaling MP2 methods in spite of the fact that the formal $O(N^5)$ scaling has not been reduced. The most promising methods for the future are the combinations of density fitting with local correlation methods as pioneered by the Werner, Manby, and Knowles [40, 66]. However, the errors introduced by the local domains used to describe the virtual space, used in these methods are significant and the combination of density fitting with the “full accuracy” LMP2 method would be efficient approach without a significant reduction of accuracy.

REFERENCES

1. Pulay P (1983) Chem Phys Lett 100:151
2. Saebø S, Pulay P (1985) Chem Phys Lett 113:13
3. Pulay P, Saebø S (1986) Theor Chim Acta 69:357
4. Saebø S, Pulay P (1987) J Chem Phys 86:914
5. Saebø S, Pulay P (1988) J Chem Phys 88:1884
6. Saebø S (1992) Int J Quantum Chem 42:217
7. Saebø S, Pulay P (1993) Annu Rev Phys Chem 44:213
8. Saebø S (2002) In: Leszczynski J (ed) Computational chemistry. Review of current trends, vol 7. World Scientific, Singapore, p 63
9. Carter EA, Walter D (2004) In: von Ragué Schleyer P, Allinger NL, Clark T, Gasteiger J, Kollman PA, Schaefer HF III, Schreiner PR (eds) Encyclopedia of computational chemistry (online edition). Wiley, Chichester
10. Friesner RA, Murphy RB, Beachy MD, Ringnalda MN, Pollard WT, Dunietz RB, Cao Y (1999) J Phys Chem A 103:1913
11. Ayala PY, Scuseria GE (1999) J Chem Phys 110:3660
12. Martínez TJ, Carter EA (1994) J Chem Phys 100:3631
13. Reynolds G, Martínez TJ, Carter EA (1996) J Chem Phys 105:6455
14. Lee MS, Maslen PE, Head-Gordon M (2000) J Chem Phys 112:3592
15. Schütz M, Hetzer P, Werner H-J (1999) J Chem Phys 111:5691
16. Hetzer G, Schütz M, Stoll H, Werner H-J (2000) J Chem Phys 113:9443
17. Hampel C, Werner H-J (1996) J Chem Phys 104:6286
18. Schütz M, Werner H-J (2001) J Chem Phys 114:661
19. Schütz M (2002) Phys Chem Chem Phys 4:3941
20. Schütz M, Werner H-J (2000) Chem Phys Lett 318:370
21. Schütz M (2000) J Chem Phys 113:9986
22. Schütz M (2002) J Chem Phys 116:8772
23. Saebø S, Pulay P (1986) Chem Phys Lett 131:384
24. Pulay P, Saebø S (1985) Chem Phys Lett 117:37
25. Boughton JW, Pulay P (1993) Int J Quantum Chem 47:49
26. Pulay P (1986) J Chem Phys 85:1703
27. Saebø S, Boggs JE, Fan K (1992) J Phys Chem 96:926
28. Saebø S (1990) Int J Quantum Chem 38:641
29. Saebø S, Pulay P (2001) J Chem Phys 115:3975
30. Feyereissen M, Fitzgerald G, Komornicki A (1993) Chem Phys Lett 208:359
31. Kendall RA, Früchtl HA (1997) Theor Chem Acc 97:158
32. Vahtras O, Almlöf J, Feyereissen MW (1993) Chem Phys Lett 213:514
33. Weigen F, Häser M, Patzelt H, Ahlrichs R (1998) Chem Phys Lett 294:143

34. Weigen F, Kohn A, Hättig C (1998) *J Chem Phys* 109: 1593
35. Hättig C (2005) *Phys Chem Chem Phys* 7:59
36. Berthold DE, Harrison RJ (1998) *J Chem Phys* 109:1593
37. Hellweg A, Hättig C, Höfner S, Klopper W (2007) *Theor Chem Acc* 117:587
38. Weigen F, Häser M (1997) *Theor Chem Acc* 97:331
39. Katoda M, Nagase S (2009) *Int J Quantum Chem* 109:2121
40. Werner H-J, Manby FR, Knowles PJ (2003) *J Chem Phys* 118:8149
41. Saebø S, Baker J, Wolinski K, Pulay P (2004) *J Chem Phys* 120:11423
42. El-Azhary A, Rauhut G, Pulay P, and Werner H-J (1998) *J Chem Phys* 108:5185
43. Møller C, Plesset MS (1934) *Phys Rev* 46:618
44. Bartlett RJ, Purvis GD (1978) *Int J Quant Chem* 14:561
45. Pople JA, Krishnan R, Schlegel HB, Binkley JS (1978) *Int J Quantum Chem* 14:545
46. Pulay P, Saebø S, Meyer W (1984) *J Chem Phys* 81:1901
47. Almlöf J (1991) *Chem Phys Lett* 176:319
48. Häser M, Almlöf J (1992) *J Chem Phys* 96:489
49. Häser M (1993) *Theor Chim Acta* 87:147
50. Boys SF (1966) In: Löwdin PO (ed) *Quantum theory of atoms, molecules, and the solid state*. Academic, New York, NY, p 253
51. Pipek J, Mezey PG (1989) *J Chem Phys* 90:4916
52. Boughton JW, Pulay P (1993) *J Comput Chem* 14:736
53. Meyer W, Frommhold L (1986) *Phys Rev A* 33:3807
54. Rauhut G, Pulay P, Werner H-J (1998) *J Comput Chem* 19:1241
55. Pulay P, Saebø S, Wolinski K (2001) *Chem Phys Lett* 344:543
56. Baker J, Pulay P (2002) *J Comput Chem* 23:1150
57. Pulay P, Meyer W, Saebø S unpublished results
58. Yoshimine M (1969) Report RJ-555 IBM Research Laboratory, San Jose, CA
59. Baker J, Wolinski K, Malagoli M, Kinghorn D, Wolinski P, Magyarfalvi G, Saebø S, Janowski T, Pulay P (2009) *J Comput Chem* 30:317
60. Walter D, Szilva KNAB, Carter EA (2002) *J Chem Phys* 117:1982
61. Boys SF, Shavitt I (1959) University of Wisconsin, RepWISAF-13
62. van Alsenoy C (1988) *J Comp Chem* 8:620
63. Eichkorn K, Treutler O, Öhm H, Häser M, Ahlrichs R (1995) *Chem Phys Lett* 240:283
64. Schütz M, Werner H-J, Lindh R, Manby FR (2004) *J Chem Phys* 121:737
65. Werner H-J, Knowles PJ, Lindh R, Manby FR, Schütz M, Celani P, Korona T, Mitrushenkov A, Rauhut G, Adler TB, Amos RD, Bernhardsson A, Berning A, Cooper DL, Deegan MJO, Dobbyn AJ, Eckert F, Goll E, Hampel C, Hetzer G, Hrenar T, Knizia G, Köppl C, Liu Y, Lloyd AW, Mata RA, May AJ, McNicholas SJ, Meyer W, Mura ME, Nicklass A, Palmieri P, Pflüger K, Pitzer R, Reiher M, Schumann U, Stoll H, Stone AJ, Tarroni R, Thorsteinsson T, Wang M, Wolf A (2008) *MOLPRO*, version 2008.1, a package of ab initio programs
66. Rauhut G, Werner H-J (2003) *Phys Chem Chem Phys* 5:2001

CHAPTER 4

PERTURBATIVE APPROXIMATIONS TO AVOID MATRIX DIAGONALIZATION

PÉTER R. SURJÁN AND ÁGNES SZABADOS

Laboratory of Theoretical Chemistry, Institute of Chemistry, Eötvös University, H-1518, Budapest, Hungary, e-mail: surjan@chem.elte.hu; szabados@chem.elte.hu

Abstract: With the aim of developing linear-scaling methods, we discuss perturbative approaches designed to avoid diagonalization of large matrices. Approximate molecular orbitals can be corrected by perturbation theory, in course of which the Laplace transformation technique proposed originally by Almløf facilitates linear scaling. The first order density matrix P corresponding to a one-electron problem can be obtained from an iterative formula which preserves the trace and the idempotency of P so that no purification procedures are needed. For systems where P is sparse, the procedure leads to a linear scaling method. The algorithm is useful in course of geometry optimization or self-consistent procedures, since matrix P of the previous step can be used to initialize the density matrix iteration at the next step. Electron correlation methods based on the Hartree-Fock density matrix, without making reference to molecular orbitals are commented on.

Keywords: Linear scaling, Density matrix, Laplace-transform, Idempotency conserving iteration

4.1. INTRODUCTION

Computational effort required by diagonalization of matrices scales cubically with the matrix dimension. In quantum chemistry, one often meets problems for which the dimension is so large that explicit diagonalization, even with the aid of modern computers, is prohibitive. In electron correlation calculations, if configuration interaction (CI) is used, the dimension of the Hamiltonian matrix shows a factorial dependence on the system size (number of electrons/basis functions). This area was therefore the first where Lanczos-type iterative methods were applied, where one or more eigenvectors of the matrix are sought by acting with the matrix on a trial vector repeatedly. A disadvantage is that it may be difficult to obtain eigenvectors more than a few. Quantum chemical applications to the CI problem became revolutionized when the action of the Hamiltonian on the trial vector was directly formulated, so that the huge Hamiltonian matrix was never explicitly constructed (“direct CI” see Ref. [1]), and when the iterative procedure was accelerated by diagonalizing

the small matrices of the Hamiltonian in the iterative subspace (Davidson's technique [2]).

In standard one-electron theories the diagonalization of a one-electron Hamiltonian (Fockian, Kohn-Sham matrix or a simple Hückel Hamiltonian) is required. Albeit these have much smaller size as compared to CI matrices (their dimension being simply the basis set size), large molecular systems or nanostructures may induce serious computational difficulties making it necessary to avoid explicit matrix diagonalization.

In this paper, we shall review two approximation approaches which avoid the explicit diagonalization of large one-electron Hamiltonians. The Hamiltonian may either be a one-electron operator by construction (Hückel, tight-binding) or may emerge from theories that start with the many-electron Hamiltonian and arrive to an effective one-electron operator (Hartree-Fock, Kohn-Sham) via appropriate approximation steps. The formulae we are going to discuss are applicable in both cases.

The literature of density matrix calculation without making reference to molecular orbitals is huge. We mention Green-function techniques [3, 4], numerical minimization procedures [5–9], divide and conquer algorithms [10–12], renormalization group techniques [13, 14], using the sign matrix of the Hamiltonian [15]. Reviews Refs. [16, 17] may also be consulted for getting an orientation in the field. Here, we do not aim to review all the above methods. Rather, we detail two perturbative schemes developed in our laboratory, discussing only the closely related approaches. We shall also elaborate procedures that step beyond the one-electron model and aim the calculation of electron correlation based on the density matrix obtained at the one-electron level.

4.2. PERTURBATIVE ENERGY ESTIMATION USING LAPLACE TRANSFORM

Let us assume that we have a large molecular system, defined over a basis set of atomic orbitals (AOs) $\{\chi_\mu\}$, and an *approximate* set of molecular orbitals (MOs) $\{\phi_i\}$. On approximate MOs we mean a set of occupied and virtual orbitals selected by chemical intuition, which do not exactly obey the Brillouin theorem. An example is, for a system of two or more interacting nanosystems, the ensemble of the MOs of the isolated subsystems. If the interaction is not too strong, it can be conveniently handled by perturbation theory (PT), leading to the second order formula

$$E^{(2)} = - \sum_i^{occ} \sum_k^{virt} \frac{W_{ik}W_{ki}}{\varepsilon_k - \varepsilon_i}, \quad (4-1)$$

with i, k being MO indices and ε are the respective zero-order one-particle energies. If the number of MOs is very large, computation of the above formula, especially evaluation of the effective matrix elements W_{ik} , is time consuming. The main difficulty is that matrix W in the approximate one-particle MO set is usually not sparse. Expanding the MOs φ as linear combinations of AOs χ :

$$\varphi_i = \sum_{\mu} C_{\mu}^i \chi_{\mu}, \quad (4-2)$$

one might attempt to transform Eq. (4-1) to the original basis of site-centered AOs. However, substituting (4-2) into (4-1) alone is not useful from the computational point of view, since the energy denominator prevents one to perform the summation over MO indices k and i independently.

An ingenious idea for factorizing the energy denominator in PT was proposed by Almlöf [18, 19], who applied the identity

$$\frac{1}{\varepsilon_k - \varepsilon_i} = \int_0^{\infty} e^{-s\varepsilon_k} e^{s\varepsilon_i} ds, \quad (4-3)$$

which is the formula for the inverse Laplace transformation of $(1/x)$, with x standing for the energy denominator. The integral is convergent if the energy gap between the occupied and virtual states, $\varepsilon_k - \varepsilon_i$, is positive. This idea has been applied to the evaluation of electron correlation energy with considerable success [19–21].

Substituting identity (4-3) into (4-1) and using that $W_{ik} = \langle \varphi_i | W | \varphi_k \rangle$, we get the expression

$$E^{(2)} = \int_0^{\infty} e(s) ds \quad (4-4)$$

with

$$e(s) = \sum_{\mu\nu\lambda\sigma} t_{\mu\nu} f_{\nu\lambda}^p(s) t_{\lambda\sigma} f_{\sigma\mu}^h(s), \quad (4-5)$$

where $t_{\mu\nu} = \langle \chi_{\mu} | W | \chi_{\nu} \rangle$ is the effective hopping interaction between localized sites, and we have introduced the notations for the s -dependent energy-weighted density matrices

$$\begin{aligned} f_{\nu\lambda}^p(s) &= \sum_k^{virt} e^{-s\varepsilon_k} C_{\nu}^k C_{\lambda}^k \\ f_{\sigma\mu}^h(s) &= \sum_i^{occ} e^{s\varepsilon_i} C_{\mu}^i C_{\sigma}^i. \end{aligned} \quad (4-6)$$

Since matrix t , in contrast to W , is extremely sparse in several applications, a very fast evaluation of Eq. (4-5) is possible at the price of a quadrature (4-4). This obviously facilitates an $\mathcal{O}(n)$ treatment for large systems if the number of nonzero t and f matrix elements grows linearly with the system size.

As an illustration of the sparseness, we present elements of the Hückel density matrix of carbon nanotubes in Figure 4-1 as a function of the distance between sites

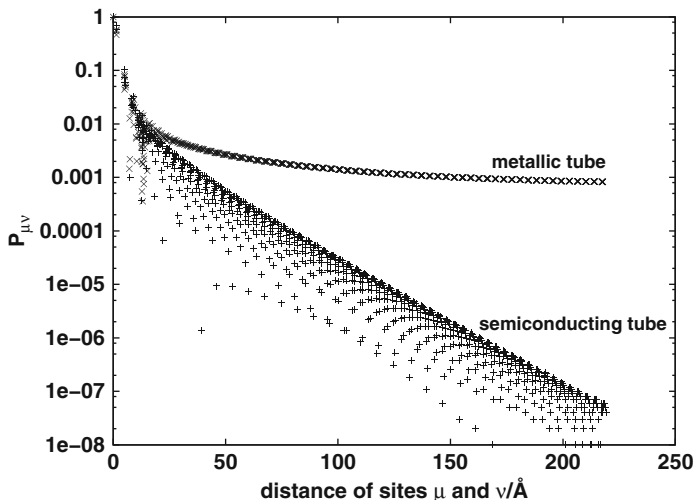


Figure 4-1. Elements of the density matrix obtained at the Hückel level, for finite size carbon nanotubes. A (11, 9) tube is taken as a prototype for a “semiconducting tube”, a (10, 10) tube was computed to illustrate a “metallic tube”

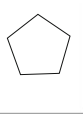
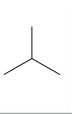
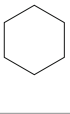
μ and ν . Apparently there is an exponential decay in the case of a semiconducting tube (note the logarithmic scale). Obviously, the same behaviour is inherited by energy weighted density matrices $f^p(s)$ and $f^h(s)$. For these systems calculation of the interaction energy may bring a considerable time gain if exploiting sparsity when multiplying matrices according to Eq. (4-5). Gap-less systems, like the case of a metallic tube shown in Figure 4-1 show a different behaviour. For these systems density matrix elements hardly decay with the distance, hence matrix multiplication in Eq. (4-5) remains formally proportional to N^3 .

The appealing feature of Eq. (4-5) is that only the site-site interaction matrix t depends on the relative position of the interacting partners, while the energy-weighted density matrices are solely characteristic to the zero-order (noninteracting) subsystems. These, therefore, should be evaluated just once when scanning the interaction energy surface. In addition, if the subsystems happen to be identical (cf. a molecular crystal), one can make use of the fact that their matrices f^p and f^h are the same. All of this may result in orders-of-magnitudes saving in computational time, if the second order energy $E^{(2)}$ is to be evaluated at many points in configuration space, provided that the structure of interacting partners is kept rigid.

We illustrate this idea on the example of interacting carbon nanoclusters treated at the Hückel-level. Each carbon atom is considered as a site, and an effective one-electron-per-site model is used with the Hamiltonian

$$\hat{H} = \sum_A \hat{H}^A + \sum_{A < B} \sum_{\mu \in A} \sum_{\nu \in B} t_{\mu\nu} (a_\mu^\dagger a_\nu + \text{h.c.}). \quad (4-7)$$

Table 4-1. Maxima and minima on the interaction energy surface of a C₆₀ molecule advancing and rotating within a piece of a (10,10) carbon nanotube. The face of the C₆₀ as seen looking from the tube end is indicated as table heading. Rotation of C₆₀ is performed around the C₁₀ axis of the nanotube.

			
Maxima [eV]	-9.05	-9.12	-9.12
Minima [eV]	-9.33	-9.23	-9.17
Largest barrier [eV]	0.28	0.12	0.05

Here A runs over the subsystems (in Table 4-1 e.g. $A = 1$ is the C₆₀ molecule, $A = 2$ is the (10,10) nanotube), \hat{H}^A is the Hamiltonian of the isolated subsystem A , while $t_{\mu\nu}$ are the inter-system hopping matrix elements for which we take $t_{\mu\nu} = -t^0 S_{\mu\nu}$ with the overlap integral $S_{\mu\nu}$ between Slater type carbon 2p_z orbitals with an exponent of $\zeta = 2.895 \text{ \AA}^{-1}$ oriented normally to the molecular surface. (Intermolecular Hückel Model, IMH) [22]. The spirit of the model is similar to that of Stafström's [23–25]. Similar models were also applied recently to DWNTs [26, 27].

Solution of the model involves the following steps: (i) the *in vacuo* Hamiltonians H^A are diagonalized separately for both monomers and the energy-weighted density matrices f^h and f^p of Eq. (4-6) are saved; (ii) the inter-system hopping interaction is computed in second order via (4-4) and (4-5); (iii) to describe non-hopping effects, a van der Waals type 6–12 site-site potential is added to the interaction energy with $A_6 = 25.667 \text{ eV}$ and $A_{12} = 154,447.9 \text{ eV}$. (The above values of parameters t_0, ζ, A_6 and A_{12} were obtained by fitting to results of *ab initio* calculations on small systems.)

The time requirement for calculating the interaction energy of a pair of aligned pieces of semiconducting carbon nanotubes is presented in Figure 4-2. For about 1,500 sites the calculation time of second order PT are similar by ordinary means – Eq. (4-1) – and by the Laplace transformed expression – Eq. (4-4). However Eq. (4-1) shows a more drastic increase in computation time with system enlargement if compared with the application of Laplace-transformed denominators in Eq. (4-4).

Formula (4-4) has been applied successfully for the exploration of interaction energy surfaces of weakly interacting nanoclusters like bundles of tubes [28] and double wall nanotubes [29]. Here we present the characteristics of the interaction energy hypersurface of a fullerene molecule encapsulated within a (10,10) nanotube. Relative position of the fullerene and the tube was varied by fixing the tube and pulling and rotating the C₆₀ molecule till a grid of all non-equivalent geometry points were produced. A 2 dimensional cross-section of the interaction surface is plotted in Figure 4-3 for illustration. Here the energy is given as a function of the position of the fullerene and the angle of its rotation around the tube axis. To characterize the hypersurface in numerical terms, energy minima and maxima are collected in Table 4-1 for three specific orientations of the C₆₀ molecule, i.e. when it shows either a 6-membered ring, a 5-membered ring or an apex atom towards the tube end. Based on Figure 4-1 and Table 4-1 we may state that the energetic barriers

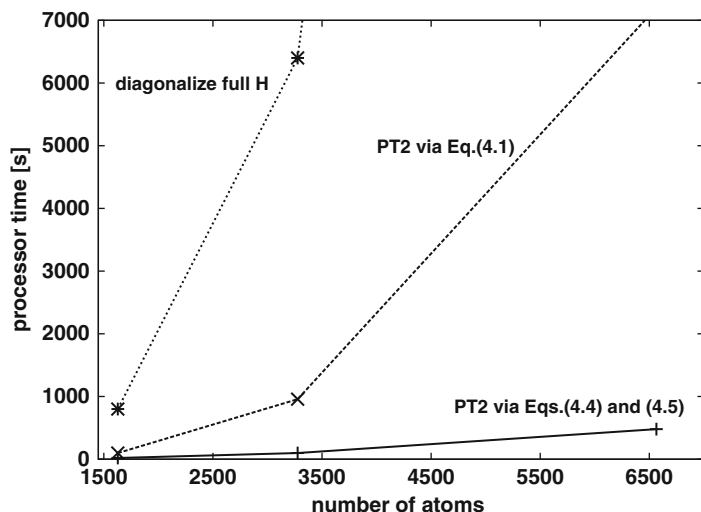


Figure 4-2. Calculation time spent on computing the interaction energy by the intermolecular Hückel model for aligned pairs of finite size carbon nanotubes

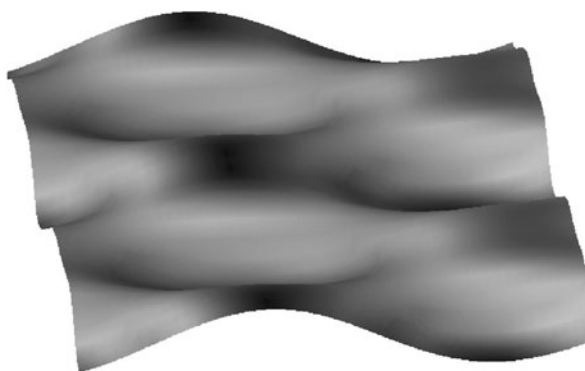


Figure 4-3. Interaction energy of a C_{60} molecule and a piece of a (10,10) nanotube, as a function of the relative orientation of the interacting partners. The fullerene is encapsulated within the tube. Position of C_{60} within the tube is measured on axis x , rotation angle of C_{60} around the tube axis is varied on axis y . Axes x and y span 2.5\AA and 72° respectively while the vertical axis z spans 0.28 eV . The nanotube is kept fixed

to overcome when dragging a fullerene molecule encapsulated in a nanotube along the tube axis range from a few hundredth to a few tenth of an electronvolt. If following the minimum energy path, the molecule would rotate when advancing in the tube.

In concluding, factorization of energy denominators of second order perturbation theory in combination with the application of effective Hamiltonians may result in several orders of magnitude saving of computational work. The key idea is that if

one describes the interaction between two or more subsystems with an effective Hamiltonian at many points in the configuration space, the most demanding part of the computations (namely, the construction of the energy weighted density matrices (4-6)) should be performed only once. The condition under which this drastic simplification is possible is that the interaction should be small enough to justify a perturbative treatment with *rigid* monomers. This also involves that the effective Hamiltonian should be constructed in a way that any overlap between monomers is neglected at the zero order. Since these conditions are quite general, we hope that the idea will induce widespread applications in many areas.

4.3. ITERATIVE SEARCH FOR THE DENSITY MATRIX

Several procedures have been proposed which attempt to find the one-electron density matrix (P) directly, instead of constructing it from the occupied eigenvectors. A direct search of the density matrix, has to take care of the N -representability conditions [30], which are, at the one-electron level, the hermiticity, the idempotency and the correct trace of P . While hermiticity and $\text{Tr}(P) = N$ can usually easily be ensured, idempotency is often violated. To restore idempotency P is usually subjected to purification algorithms [6, 9, 31–33].

We review below a simple iterative formula for P , having the essential feature of idempotency conservation. That is, if one starts with an idempotent initial guess, the idempotency of P is exactly preserved during the iteration so that no purification is needed. The trace of the initial density matrix is also conserved. At convergence, matrix P is fully N -representable and provides the exact energy corresponding to one of the exact wave functions of the model Hamiltonian.

Consider an effective one-electron Hamiltonian matrix H , which is the Hückel Hamiltonian in a noninteracting model or the Fockian in a self-consistent procedure. The exact density P , as represented in an orthogonal basis satisfies the equation [6]

$$[H, P] = 0,$$

which, upon multiplying by P from the right, can be recast to a Bloch-type equation

$$HP - PHP = 0$$

or

$$QHP = 0$$

where $Q = 1 - P$ is the hole density matrix. This equation is essentially equivalent to the Brillouin theorem, and can also be derived from the contracted Schrödinger equation [34]. The latter equation suggests the iterative formula

$$P' = P + \eta (QHP) \tag{4-8}$$

where η is an arbitrary parameter a proper value of which can be selected to facilitate the convergence of the iteration.

It is easy to see that, at any values for η , both the idempotency ($P^2 = P$) and the correct trace ($\text{Tr } P = N$) conditions are preserved upon iterating Eq. (4-8). As to the former property:

$$(\mathcal{P}')^2 = P^2 + \eta PQHP + \eta QHPP + \eta^2 QHPQHP = P + \eta QHP = \mathcal{P}'$$

where we have used that $P^2 = P$ and $PQ = 0$. The trace is conserved since

$$\text{Tr } \mathcal{P}' = \text{Tr } P + \eta \text{Tr } QHP = \text{Tr } P.$$

The latter equation holds as $\text{Tr } QHP = \text{Tr } PQH = 0$.

Apart from idempotency and correct trace, P has to fulfill one further requirement: it has to be self adjoint. Based on this, one can prove that Eq. (4-8) cannot converge to the exact density matrix. The proof is as follows. Assume that starting from an approximate, hermitian one-matrix P_0 and the associated hole-matrix Q_0 , we have arrived at the exact matrix P by iterating Eq. (4-8). One may realize, that every new term appearing in course of this iteration bears a leftmost Q_0 and a rightmost P_0 . Thus the exact one-matrix can be written as

$$P = P_0 + Q_0 h_{\text{eff}} P_0 \quad (4-9)$$

where an effective Hamiltonian h_{eff} is introduced. Now let us multiply Eq. (4-9) by P_0 first from the left, then from the right, to obtain $P_0 P = P_0$ and $PP_0 = P$. Taking the adjoint of this latter equation and utilizing hermiticity of both P and P_0 , we get $P_0 P = P$ which, together with the first of the above two equations involves that $P = P_0$. Therefore, for an approximate, hermitian P_0 we have a contradiction.

The source of the contradiction is clearly that \mathcal{P}' , as defined by Eq. (4-8), is not hermitian and this property is conserved upon iteration. One may correct for this, realizing that the iteration formula

$$\mathcal{P}' = P + \eta (PHQ)$$

has also the same trace- and idempotency conserving properties as Eq. (4-8). It, therefore, facilitates the following double-iteration sequence:

$$\begin{aligned} \mathcal{P}' &= P + \eta (QHP) \\ \mathcal{P}'' &= \mathcal{P}' + \eta (\mathcal{P}' H Q') \end{aligned} \quad (4-10)$$

with $Q' = 1 - \mathcal{P}'$. The above two steps can be combined into one to yield

$$\mathcal{P}'' = P + \eta QHP + \eta (P + \eta QHP)H(Q - \eta QHP). \quad (4-11)$$

Since both steps of Eq. (4-10) conserve the trace and the idempotency, P'' has the correct properties, just like P' . Moreover, upon convergence, conditions $QHP = 0$ and $PHQ = 0$ are satisfied to a given accuracy, which involves that matrix P commutes with H . From this, hermiticity of the converged matrix P automatically follows.

Simple perturbational arguments indicate that hermiticity violation diminishes upon iteration by Eq. (4-11). If one writes $H = h^{(0)} + V$ where V is small, and one starts the iteration with some $P^{(0)}$ which is exact with respect to $h^{(0)}$, one can order the terms coming from the iteration in increasing powers of V . Expanding (4-11) we can write

$$\begin{aligned} P'' &= P^{(0)} + \eta [Q^{(0)}VP^{(0)} + P^{(0)}VQ^{(0)}] \\ &\quad + \eta^2 [Q^{(0)}VP^{(0)}VQ^{(0)} - P^{(0)}VQ^{(0)}VP^{(0)}] \\ &\quad - \eta^3 [Q^{(0)}VP^{(0)}VQ^{(0)}VP^{(0)}]. \end{aligned}$$

Assuming that the initial density matrix $P^{(0)}$ is hermitian, the two terms in the first square bracket are adjoints of each other, while the two terms proportional to η^2 are themselves hermitian. The only violation of hermiticity may come from the last term, which is of order 3, and expected to be very small. Further iteration shifts the violation of hermiticity to higher orders, indicating that non-hermitian terms are gradually eliminated during iteration.

Mazziotti applied an alternative way of correcting for the hermiticity violation of Eq. (4-8): he took the hermitian part of QHP [34]. This way however the idempotency-conserving feature of Eqs. (4-8) or (4-10) is lost and one has to apply a purification procedure at each iteration step.

We tested Eq. (4-10) against a similar, iterative algorithm used by Németh and Scuseria [15] which aims to get the sign matrix of the Fockian. Though the latter often converges much faster, Eq. (4-10) was found to work better for low-gap systems and metals. In addition, Eq. (4-10) has the advantage over sign matrix iterations that (i) it does not need an a priori estimation of the chemical potential; (ii) its intermediate results, being idempotent and having the correct trace, give physically meaningful approximations; (iii) iterations can be started from any good guess, e.g. from the P matrix of a previous SCF cycle or, in course of a geometry optimization procedure, from the converged P matrix of a nearby geometry point.

Numerical experience shows that in SCF or geometry optimization procedures, the sign-matrix iteration is better used at the beginning, while as the density matrix P gets converged, its refinement is more advantageous by Eq. (4-10).

The proper choice of parameter η is crucial [35]: chaotic behavior of the iteration scheme can be expected for a wrongly selected value, since the mapping shown by Eq. (4-8) is closely related to the logistic mapping which is a prototype for chaotic solutions [36]. The sign of η can be determined from the condition that the energy should decrease. Looking at the first equation in (4-10), we can write $E' = E + \eta \text{Tr}(QHPH)$, which tells that the energy change is proportional to η . Thus

the appropriate sign of η can always arrange the energy to decrease in an elementary step. This, if the initial P is properly chosen, will ensure that we converge to the ground state.

In Refs. [37, 38] illustrative applications were presented at the Hückel level as well as for Hartree-Fock calculations. To determine the magnitude of η , the following strategy was applied. For a physically related small system the best η was found by numerical experience. As we observed a great universality in the value η when changing the system size, the same value could be used effectively for the calculation of the larger system. Using sparse matrix technology, one may easily perform each individual iteration in a linear scaling manner. We applied a “flexible” technology, storing only the nonzero elements of all matrices along with two linear arrays for row and column indices. Standard matrix manipulation routines for this technology are available [39]. The effectiveness of this approach clearly depends on the extent of sparsity of the matrices.

In summarizing, we proposed a new iterative solution of the Bloch-type equation for the first order density matrix of a one-electron model. If the number of electrons is known, no prior knowledge of the chemical potential is required, and no purification transformations are needed since the iteration preserves both the trace and the idempotency properties of the one-matrix.

4.4. ELECTRON CORRELATION

4.4.1. E2[P] Functional

Having obtained the density matrix by a linear-scaling procedure directly we do not have a set of molecular orbitals (MOs) in our possession. Standard methods of electron correlation like usual second order Møller-Plesset (MP2) or coupled clusters singles doubles rely on a set of occupied and virtual MOs, hence they are not directly applicable. However, there exist schemes that provide correlation energy merely from the P matrix.

The origin of such an approach may be the observation that the MP2 energy is a functional of the Hartree-Fock density matrix [40]. This functional can be explicitly constructed by the Laplace-transformed version of the MP2 energy formula. Resolving the MP2 energy in a way analogous to Eq. (4-4), the s -dependent energy can be given as [40]

$$e^{[2]}(s) = -\frac{1}{2} \sum_{\mu\nu\lambda\sigma} X_{\mu\rho}(s) Y_{\nu\tau}(s) X_{\lambda\eta}(s) Y_{\sigma\kappa}(s) (\rho\tau|\eta\kappa) [(\mu\nu|\lambda\sigma) - (\mu\sigma|\lambda\nu)] \quad (4-12)$$

in terms of atomic spin orbitals. In this equation $X(s)$ and $Y(s)$ are energy-weighted particle and hole density matrices (EWDMs) defined by matrix P as

$$X(s) = e^{sPF} P. \quad (4-13)$$

and

$$Y(s) = e^{-sQF} Q. \quad (4-14)$$

where $Q = S^{-1} - P$ is the hole density matrix.

If both matrices F and P are sparse, the exponential of their product can be clearly obtained through the Taylor expansion in a linear scaling manner. The expansion is expected to be rapidly convergent for small s , while for large s values one may obtain matrices X, Y by using

$$e^{jsPF} = [e^{sPF}]^j$$

for integer j , which limits merely the choice of quadrature points in course of the numerical integration over s .

It is interesting to note that not only the MP2 energy can be considered as a functional of the HF density matrix. In fact, applying a double resolution, the third order energy is recast as

$$E^{[3]} = \int_0^\infty \int_0^\infty e^{[3]}(s, s') ds ds', \quad (4-15)$$

while the evaluation of the MP4 formula would require a triple integration

$$E^{[4]} = \int_0^\infty \int_0^\infty \int_0^\infty e^{[4]}(s, s', s'') ds ds' ds'' \quad (4-16)$$

with an obvious increase of numerical difficulty throughout the quadrature. Numerical realization of the procedure at order two was performed by Nakai et al. [41, 42].

4.4.2. The FLMO Approach

Even if the full density matrix is not constructed from a set of MOs, there are several ways to construct orbitals based on matrix P . In the frozen localized molecular orbital (FLMO) approach [43], one obtains localized MOs by projecting atomic orbitals $|\chi\rangle$ into the occupied space:

$$|\varphi_i^{\text{occ}}\rangle = \sum_{\mu} (PS)_{\mu i} |\chi_{\mu}\rangle.$$

Similarly, virtuals emerge by projecting AOs with matrix QS . In the FLMO philosophy, AOs of an active site of a large molecule are used for projection, thus the

resulting MOs will be, to a great extent, localized on that site. These active LMOs may be used to compute the correlation energy of the fragment. LMOs falling out of the active site are never explicitly constructed, they serve as a frozen core for the active part of the correlation energy.

In concluding, we have mentioned two alternatives of calculating electron correlation based on the Hartree-Fock P matrix. One may either express the desired correlation energy formula in terms of the density matrix, or utilize P to define a set of molecular orbitals. By the latter approach the number of orbitals, and consequently the calculation time of the correlation energy can be kept under control. Moreover the orbitals are localized on a preselected region of the molecule. These features represent an advantageous starting point for future developments towards efficient calculation of local correlation energies.

ACKNOWLEDGMENTS

This work has been supported by the Hungarian National Research Fund (OTKA), grant numbers NI-67702, K-81588 and K-81590. The European Union and the European Social Fund have also provided financial support to the project under the grant agreement no. TÁMOP 4.2.1./B-09/1/KMR-2010-0003.

REFERENCES

1. Roos BO, Siegbahn PEM (1997) In: Schaefer HF (ed) Modern theoretical chemistry, vol 3, Chapter 7. Plenum, New York, NY
2. Davidson ER (1975) *J Comp Phys* 17:87
3. Abrikosov IA, Niklasson AMN, Simak SI, Johansson B, Ruban AV, Skriver HL (1996) *Phys Rev Lett* 76:4203
4. Reidinger R, Benard M (1991) *J Chem Phys* 94:1222
5. Löwdin P-O (1955) *Phys Rev* 97:1474
6. McWeeny R (1962) *Phys Rev* 126:1028
7. Li X-P, Nunes RW, Vanderbilt D (1993) *Phys Rev B* 47:10891
8. Challacombe M (1999) *J Chem Phys* 110:2332
9. Palser AHR, Manolopoulos DE (1998) *Phys Rev B* 58:12704
10. Yang W (1991) *Phys Rev Lett* 66:1438
11. Yang W (1991) *Phys Rev A* 44:7823
12. Yang W, Lee T-S (1995) *J Chem Phys* 103:5674
13. Baer R, Head-Gordon M (1998) *Phys Rev B* 58:15296
14. Kenoufi A (2004) *J Polonyi Phys Rev B* 70:205105
15. Németh K, Scuseria GE (2000) *J Chem Phys* 113:6035
16. Goedecker S (1999) *Rev Mod Phys* 71:1085
17. Wu SY, Jayanthi CS (2002) *Phys Rep* 358:1
18. Almlöf J (1991) *Chem Phys Lett* 176:319
19. Häser M, Almlöf J (1992) *J Chem Phys* 96:489
20. Ayala PY, Scuseria GE (1999) *J Chem Phys* 110:3660
21. Ayala PY, Kudin KN, Scuseria GE (2001) *J Chem Phys* 115:9698
22. Lázár A, Surján PR, Paulsson M, Stafström S (2002) *Int J Quant Chem* 84:216
23. Tabor S, Stafstrom S (1992) *J Magn Magn Mater* 104:2099

24. Stafstrom S (1993) Phys Rev B 47:12437
25. Paulsson M, Stafstrom S (1999) Phys Rev B 60:7939
26. Hansson A, Stafström S (2003) Phys Rev B 67:075406
27. Ahn KH, Kim Y-H, Wiersig J, Chang KJ (2003) Phys Rev Lett 90:026601
28. Szabados A, Biró LP, Surján PR (2006) Phys Rev B 73:195404
29. Surján PR, Lázár A, Szabados A (2003) Phys Rev A 68:062503
30. Coleman AJ, Yukalov VI (2000) Reduced density matrices: Coulson's challenge. Springer, New York, NY
31. Mazziotti DA (2003) Phys Rev E 68:066701
32. Niklasson AMN (2003) Phys Rev B 68:233104
33. Kryachko ES (2000) Chem Phys Lett 318:210
34. Mazziotti DA (2001) J Chem Phys 115:8305
35. Szakács P, Surján PR (2008) J Math Chem 43:314
36. Ott E (1993) Chaos in dynamical systems. Cambridge University Press, Cambridge
37. Kóhalmi D, Szabados A, Surján PR (2005) Phys Rev Lett 95:13002
38. Szekeres Zs, Mezey PG, Surján PR (2006) Chem Phys Lett 424:420
39. Pissanetzky S (1984) Sparse matrix technology. Academic Press, London
40. Surján PR (2005) Chem Phys Lett 406:318
41. Kobayashi M, Nakai H (2006) Chem Phys Lett 420:250
42. Kobayashi M, Akama T, Nakai H (2006) J Chem Phys 125:204106
43. Surján PR, Kóhalmi D, Rolik Z, Szabados A (2007) Chem Phys Lett 450:400

CHAPTER 5

DIVIDE-AND-CONQUER APPROACHES TO QUANTUM CHEMISTRY: THEORY AND IMPLEMENTATION

MASATO KOBAYASHI^{1,2} AND HIROMI NAKAI^{1,3}

¹ Department of Chemistry and Biochemistry, School of Advanced Science and Engineering, Waseda University, Tokyo 169-8555, Japan

² Department of Theoretical and Computational Molecular Science, Institute for Molecular Science, Okazaki 444-8585, Japan, e-mail: kobayashi@suou.waseda.jp

³ Research Institute for Science and Engineering, Waseda University, Tokyo 169-8555, Japan, e-mail: nakai@waseda.jp

Abstract: Recently, the authors implemented the linear-scaling divide-and-conquer (DC) quantum chemical methodologies into the GAMESS-US package, which is available without charge. In this Chapter, we summarized recent developments in the DC methods, namely, the density-matrix-based DC self-consistent field (SCF) and the DC-based post-SCF electron correlation methods. Especially, the DC-based post-SCF calculation is considerably efficient, i.e., its computational time achieves near-linear scaling with respect to the system size [$O(N^1)$] and the required memory and scratch sizes are hardly dependent on the system size [$O(N^0)$]. Numerical assessments also revealed the reliability of the DC methods.

Keywords: Divide-and-conquer method, Atomic basis function, Self-consistent field calculation, Hartree-Fock theory, Density functional theory, Electron correlation, Møller-Plesset perturbation theory, Coupled cluster method

5.1. INTRODUCTION: HISTORY OF DIVIDE-AND-CONQUER

“Divide each of the difficulties under examination into as many parts as possible, and as might be necessary for its adequate solution.” This is an excerpt from “Discourse on Method” by René Descartes, the famous French philosopher regarded as a founder of modern philosophy. This phrase is none other than the first statement of the divide-and-conquer (DC) approach. The importance of this philosophy has been universal among almost all sciences, especially computer science. Since the invention of the merge sort by von Neumann in 1945 [1], the DC method has been known as the basic strategy for establishing low-scaling efficient algorithms in the field of computer science, e.g., the fast Fourier transformation, quicksort,

Karatsuba multiplication, and binary search algorithms (for details on these algorithms, see Ref. [2] for example). In these algorithms, a complicated problem is divided into two or more (*as many as might be necessary for its adequate solution!*) smaller problems and the solutions of the small problems are combined to obtain the solution of the original problem.

Later on, Yang [3] imported the DC philosophy to the field of the electronic structure calculations, which is regarded as the pioneer in the development of linear-scaling self-consistent field (SCF) electronic structure theories [4, 5] as well as the elongation method of Imamura et al. [6] is. In this original version of the quantum chemical DC method, the local electronic density distribution corresponding to each subsystem region is calculated with the molecular orbitals (MOs) composed of subsystem atomic orbitals (AOs). Then the electronic density of the entire system is constructed by the weighted sum of the local densities with the help of a spatial partition function and uniquely defined Fermi level. The first paper treated only N₂ molecule. Soon after, Yang [7] achieved a breakthrough in the DC method by introducing a *buffer region*, which reduced the limitation of the AOs composing subsystem MOs. This made the applicability of the DC method considerably expand to big molecules [8–10] with a reasonably good accuracy. Further the density-based DC method can provide the density of states [11] and its analytical energy gradient [12], was extended to the treatment of solid-state systems [13] with embedded-cluster calculations, and was derived from the first principle [14]. It has been extended to the use of the discrete variational method [15] or real-space grids [16–19]. Furthermore, Ozaki [20] proposed a different framework that unified DC and his recursion method [21] using Krylov subspace mapping.

Since the density-based DC method only provides the electronic density, its applications had been limited to pure Kohn-Sham density functional theory (DFT) [22]. Yang and Lee [23] achieved the second breakthrough in the DC method that took this limitation away by applying the DC strategy to the one-electron density matrix (DM) since DM can be constructed from a Hartree-Fock (HF) [24] or semiempirical MO calculation. This method is related to the Lego approach [25] or later adjustable density matrix assembler method [26] in the sense of the usage of the partition matrix instead of the partition function. Yang and Lee mentioned another advantage of the DM-based DC formalism over the density-based one that the time-consuming (but still linear-scaling) three-dimensional integrals associated with the partition function can be avoided.

Its application to the HF calculations, however, has been limited because of the requirement of the non-local HF exchange computation. Thus Lee et al. [27] soon applied the DM-based DC method to semiempirical calculations. For treating biological macromolecules with solvent effects, York et al. [28] implemented the conductor-like screening model (COSMO) to the program and they have published a lot of results by the DC calculations of biomolecules including proteins and nucleic acids [29–34]. Dixon and Merz [35, 36] independently developed a semiempirical DC code. They introduced inner and outer buffer regions for improving the SCF convergence as well as reducing the energy error [37] and utilized the Poisson-Boltzmann equation for describing the solvent effect

[38]. Furthermore, van der Vaart and Merz [39, 40] presented an energy decomposition scheme of the intra-molecular interaction and solvation energies like Kitaura-Morokuma analysis [41] within the framework of the DC method, of which the essence had been presented in the earlier work [28] in part. Another example of the semiempirical DC calculation is the work by Cabrera-Trujillo and Robles [42] who applied the method to the calculations of polymerized fullerene clusters. Efficient parallelization schemes of the semiempirical DC method were also proposed [43, 44].

Another candidate for the DM-based DC method was still DFT. St-Amant and coworkers [45, 46] firstly applied the DC strategy to the charge density fitting procedure in the density-fitting DFT implementation [47] for the linear-scaling computation of Coulomb interaction. They soon combined it with DM-based DC-DFT [48, 49], proposed an efficient parallel algorithm [50], and implemented to the DeFT program package [51].

Practically, the first implementation and assessment of the DC method including HF exchange interaction (i.e., DC-HF and DC hybrid DFT) were done in the authors' group [52]. We showed the efficiency and accuracy of the DC-HF and DC hybrid DFT methods, although we also showed that the larger error of the HF exchange term derived from the DC approximation survives in the calculations of delocalized π -conjugated systems [53]. Our ambition, however, was not the development of the linear-scaling HF method but of the entirely linear-scaling post-HF correlation methods based on the DC scheme.

We have proposed two strategies for evaluating the post-HF correlation energy. The first one [54] uses DM of the entire system obtained from the DC-HF calculation for evaluating the second-order Møller-Plesset perturbation (MP2) energy by means of the DM-Laplace MP2 method [55–57]. This post-HF correlation treatment can be categorized into the domain-free approach that uses a linear-scaling trick of the standard MP2 formalism for the entire system. The other one [58–61], which is categorized into the domain-based approach, uses subsystem MOs for evaluating the correlation energy corresponding to the subsystem. The correlation energy of the entire system is recognized as the sum of the subsystem correlation energies. In this approach, we implicitly utilize the idea of the local correlation approach [62, 63], which insists that the interactions contributing to the electron correlation are short ranged. Now, the DC SCF and DC-based correlation methods are implemented in GAMESS-US program package [64–66].

In addition to the DC method described above, many groups have proposed many other “DC-like” methodologies that partition the system under consideration into several fragments to obtain the results of the entire system: e.g., fragment MO (FMO) method [67, 68], molecular fractionation with conjugated caps method [69, 70], systematic molecular fragmentation method [71], molecular tailoring approach [72, 73], incremental correlation method [74, 75], and cluster-in-molecule approach [76, 77]. Furthermore, many types of linear-scaling DM construction methods that rely on the matrix sparsity, instead of dividing into subsystems, have been reported to date [4, 5, 78–85]. In this Chapter, however, we only focus on the DM-based DC method originally introduced by Yang and Lee [23] and its extension to the electron

correlation by the authors. In the following, we first review the theory of the DC SCF and DC-based correlation method. Next, several examples of DC calculations are given. Finally, we would like to mention the current stage and future of the large system calculations using the DC method.

5.2. THEORIES OF DIVIDE-AND-CONQUER METHOD

5.2.1. DC-HF and DC-DFT Theories

5.2.1.1. Formalism

In the DM-based DC method [23, 52], one assumes that each basis function is connected with an atom in the system under consideration, i.e., a basis function is simply called an AO. First, the entire system is spatially divided into disjoint subsystems, where a set of AOs in subsystem α is denoted by $S(\alpha)$ and the union of $S(\alpha)$ becomes a set of AOs in the entire system denoted by T :

$$S(\alpha) \cap S(\beta) = \emptyset \quad \forall \alpha \neq \beta, \quad (5-1)$$

$$\bigcup_{\alpha} S(\alpha) = T. \quad (5-2)$$

From here, this disjoint subsystem is called the *central region*, which is also known as the core region in some literatures. To improve the description of the subsystem, atoms adjacent to the central region, called the *buffer region*, are taken into consideration when constructing subsystem MOs. A set of AOs corresponding to the buffer region of subsystem α is denoted by $B(\alpha)$, and the union of the central and buffer regions of subsystem α is called the *localization region*, of which a set of AOs is denoted by $L(\alpha)$:

$$S(\alpha) \cup B(\alpha) \equiv L(\alpha). \quad (5-3)$$

Hereafter, Greek-letter indices $\{\mu, \nu, \dots\}$ refer to AOs, $\{i, j, \dots\}$ to occupied MOs, $\{a, b, \dots\}$ to virtual MOs, and $\{q, r, \dots\}$ to all MOs. In the DC-HF method, DM of the entire system \mathbf{D} is represented in terms of subsystem DMs \mathbf{D}^{α} :

$$D_{\mu\nu} \approx D_{\mu\nu}^{\text{DC}} = \sum_{\alpha} p_{\mu\nu}^{\alpha} D_{\mu\nu} = \sum_{\alpha} D_{\mu\nu}^{\alpha}, \quad (5-4)$$

with the following partition matrix \mathbf{p}^{α} :

$$p_{\mu\nu}^{\alpha} = \begin{cases} 1 & \text{for } \mu \in S(\alpha) \text{ and } \nu \in S(\alpha) \\ 1/2 & \text{for } \mu \in S(\alpha) \text{ and } \nu \in B(\alpha), \text{ or } \textit{vice versa} \\ 0 & \text{otherwise.} \end{cases} \quad (5-5)$$

When treating a closed-shell n_e -electron system for simplicity, the subsystem DM is given by

$$D_{\mu\nu}^{\alpha} = 2p_{\mu\nu}^{\alpha} \sum_i^{n_e/2} C_{\mu i} C_{v i}^* = 2p_{\mu\nu}^{\alpha} \sum_q \eta(\varepsilon_F - \varepsilon_q) C_{\mu q} C_{v q}^*. \quad (5-6)$$

Here, $\eta(x)$ is the Heaviside step function,

$$\eta(x) = \begin{cases} 1 & (x \geq 0) \\ 0 & (x < 0), \end{cases} \quad (5-7)$$

and ε_F is the Fermi level. In the DC approximation, the subsystem DM is constructed from subsystem orbitals $\{\psi_q^{\alpha}(\mathbf{r})\}$ that are expanded with the local basis functions $\{\phi_{\mu}(\mathbf{r}); \mu \in L(\alpha)\}$:

$$D_{\mu\nu}^{\alpha} \approx 2p_{\mu\nu}^{\alpha} \sum_q^{\text{MO}(\alpha)} \eta(\varepsilon_F - \varepsilon_q^{\alpha}) C_{\mu q}^{\alpha} C_{v q}^{\alpha*}, \quad (5-8)$$

$$\psi_q^{\alpha}(\mathbf{r}) = \sum_{\mu \in L(\alpha)} C_{\mu q}^{\alpha} \phi_{\mu}(\mathbf{r}). \quad (5-9)$$

Here, $\{\varepsilon_q^{\alpha}\}$ and $\{C_q^{\alpha}\}$ are the solutions of the following generalized eigenproblem for subsystem α ,

$$(\mathbf{F}^{\alpha} - \varepsilon_q^{\alpha} \mathbf{S}^{\alpha}) C_q^{\alpha} = \mathbf{0}, \quad (5-10)$$

where \mathbf{F}^{α} and \mathbf{S}^{α} are the Fock and overlap matrices of subsystem α that are the $|L(\alpha)| \times |L(\alpha)|$ Hermitian submatrices of the entire Fock and overlap matrices, \mathbf{F} and \mathbf{S} .

The Fermi level ε_F in Eq. (5-8), which is uniquely defined through the entire system, can be determined by solving the following constraint of the total number of electrons n_e :

$$n_e = \text{Tr} [\mathbf{D}^{\text{DC}} \mathbf{S}] = \sum_{\alpha} \sum_{\mu \in L(\alpha)} (\mathbf{D}^{\alpha} \mathbf{S}^{\alpha})_{\mu\mu}. \quad (5-11)$$

To make the solution of Eq. (5-11) exist, a discrete step function $\eta(x)$ is substituted with the Fermi function,

$$f_{\beta}(x) = \frac{1}{1 + \exp(-\beta x)}, \quad (5-12)$$

with inverse temperature parameter β :

$$D_{\mu\nu}^{\alpha} \approx 2p_{\mu\nu}^{\alpha} \sum_q^{\text{MO}(\alpha)} f_{\beta}(\varepsilon_F - \varepsilon_q^{\alpha}) C_{\mu q}^{\alpha} C_{v q}^{\alpha*}. \quad (5-13)$$

Then the entire density matrix \mathbf{D}^{DC} can be obtained from Eq. (5-4). The constraint Eq. (5-11) can be reduced by introducing the orbital weight w_q^α

$$w_q^\alpha = \sum_{\mu\nu \in \mathbf{L}(\alpha)} p_{\mu\nu}^\alpha C_{\mu q}^\alpha C_{\nu q}^{\alpha*} S_{\nu\mu}^\alpha, \quad (5-14)$$

which is regarded as the maximum occupancy of the orbital q in subsystem α , as the following:

$$n_e = \sum_\alpha \sum_q^{\text{MO}(\alpha)} f_\beta(\varepsilon_F - \varepsilon_q^\alpha) w_q^\alpha. \quad (5-15)$$

The entire Fock matrix \mathbf{F} is constructed in the usual manner: e.g., in the DC-HF calculation,

$$\begin{aligned} F_{\mu\nu} &= H_{\mu\nu}^{\text{core}} + \sum_{\lambda\sigma} D_{\lambda\sigma}^{\text{DC}} \left[\langle \mu\sigma | \nu\lambda \rangle - \frac{1}{2} \langle \mu\sigma | \lambda\nu \rangle \right] \\ &= H_{\mu\nu}^{\text{core}} + \sum_\alpha \sum_{\lambda\sigma \in \mathbf{L}(\alpha)} D_{\lambda\sigma}^\alpha \left[\langle \mu\sigma | \nu\lambda \rangle - \frac{1}{2} \langle \mu\sigma | \lambda\nu \rangle \right], \end{aligned} \quad (5-16)$$

with two-electron integral notation of $\langle \mu\nu | \lambda\sigma \rangle = \iint \mu^*(\mathbf{r}_1) \nu^*(\mathbf{r}_2) r_{12}^{-1} \lambda(\mathbf{r}_1) \sigma(\mathbf{r}_2) d\mathbf{r}_1 d\mathbf{r}_2$ and core Hamiltonian matrix \mathbf{H}^{core} . The Fock-matrix construction of Eq. (5-16) and the DM construction of Eqs. (5-4) and (5-13) are iterated until convergence, in the same manner as the standard SCF procedure. Finally, the DC-HF energy is given as

$$E_{\text{DC-HF}} = \frac{1}{2} \sum_\alpha \sum_{\mu\nu \in \mathbf{L}(\alpha)} D_{\mu\nu}^\alpha (H_{\nu\mu}^{\text{core}} + F_{\nu\mu}) = \sum_\alpha E_{\text{DC-HF}}^\alpha, \quad (5-17)$$

where

$$E_{\text{DC-HF}}^\alpha = \frac{1}{2} \sum_{\mu\nu \in \mathbf{L}(\alpha)} D_{\mu\nu}^\alpha (H_{\nu\mu}^{\text{core}} + F_{\nu\mu}) \quad (5-18)$$

can be recognized as the HF energy corresponding to subsystem α . The schematic of the DC-HF procedure is summarized in Figure 5-1. The same procedure can be adopted in the DC-DFT calculation by substituting the Fock matrix of Eq. (5-16) and the energy expression of Eq. (5-17) with the Kohn-Sham Hamiltonian and energy, respectively.

There are two time-consuming steps in the DC SCF calculation: (i) solving eigenproblems (5-10) for all subsystems, and (ii) constructing Fock matrix by Eq. (5-16). The computational cost of step (i) is $O(|\mathbf{L}(\alpha)|^3)$ for subsystem α , which is independent on the number of AOs in the whole system $|\mathbf{T}|$. Then the cost for solving

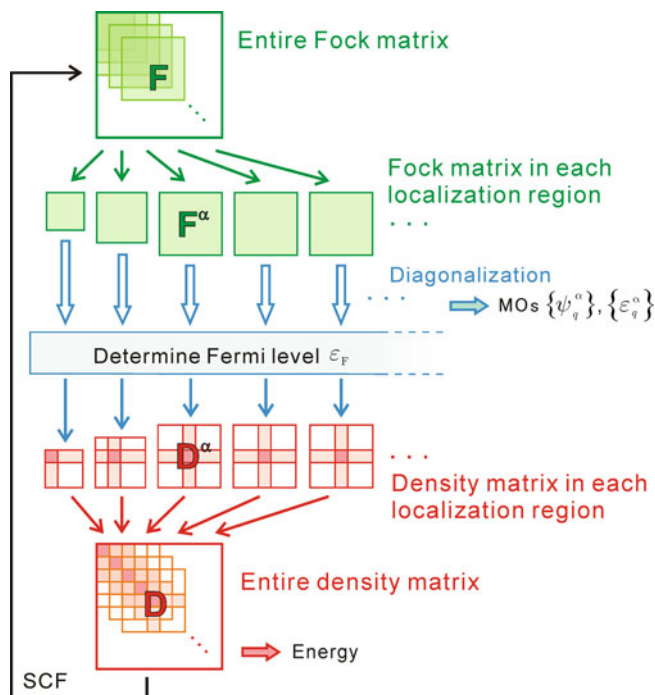


Figure 5-1. Schematic of the DC-HF procedure

Eq. (5-10) in all subsystems becomes $O\left(N_{\text{sub}} \max_{\alpha} |\mathbf{L}(\alpha)|^3\right)$, where N_{sub} denotes the number of subsystems. On the other hand, the cost of step (ii) is reduced to $O(|\mathbf{T}|^2)$ from $O(|\mathbf{T}|^4)$ because (μ, ν) and (λ, σ) in Eq. (5-16) should be in the same subsystem bases. The standard integral screening and the fast Coulomb [86–91] or exchange [92–94] schemes will further diminish the computational cost.

5.2.1.2. Acceleration of DC SCF Procedure

Although the DC method has succeeded in evaluating properties of large molecules, the DC SCF calculation has a problem in its convergence [95]. We have introduced two acceleration methods for the DC SCF procedure.

The first one [52] is based on the direct inversion in the iterative subspace (DIIS) method [96, 97]. The conventional DIIS technique accelerates the SCF convergence by extrapolating several Fock matrices obtained in the SCF process in terms of some error vectors that vanish in the SCF solution,

$$\mathbf{F}_n^{\text{DIIS}} = \sum_{k=1}^n c_k \mathbf{F}_k. \quad (5-19)$$

The usual choice of the error vector of the k th iteration \mathbf{e}_k is

$$\mathbf{e}_k = \mathbf{F}_k \mathbf{D}_k \mathbf{S} - \mathbf{S} \mathbf{D}_k \mathbf{F}_k, \quad (5-20)$$

which is based on the commutation relationship of the Fock matrix and DM in the SCF solution. Shaw and St-Amant [51] noted that the DIIS technique using the error vector of Eq. (5-20) partly works even in DC calculations but leads SCF calculation to oscillating if convergence comes near because slight errors are introduced in the DM by approximation of the DC method. They indicated that the DIIS technique should be turned off when SCF is close to convergence. The alternative choice of the error vectors of

$$\mathbf{e}_k = \mathbf{F}_k - \mathbf{F}_{k-1}, \quad (5-21)$$

which is described in the first DIIS paper [96], will also avoid the oscillation. The extrapolation coefficients c_k in Eq. (5-19) are determined by the least-square criterion together with the condition that the coefficients add up to 1,

$$\begin{pmatrix} 0 & -1 & -1 & \cdots & -1 \\ -1 & B_{11} & B_{12} & & \\ -1 & B_{21} & \ddots & & \\ \vdots & & & B_{kl} & \\ -1 & & & \ddots & B_{nn} \end{pmatrix} \begin{pmatrix} -\Lambda \\ c_1 \\ \vdots \\ c_k \\ \vdots \\ c_n \end{pmatrix} = \begin{pmatrix} -1 \\ 0 \\ \vdots \\ 0 \\ \vdots \\ 0 \end{pmatrix}, \quad (5-22)$$

$$B_{kl} = \langle \mathbf{e}_k | \mathbf{e}_l \rangle, \quad (5-23)$$

where Λ is a Lagrangian multiplier.

We have generalized DIIS to the DC SCF iterations, which is termed DC-DIIS. We assume the commutation relationships between the subsystem Fock matrix and DM at the DC SCF convergence. Therefore, the error vector corresponding to subsystem α is defined as follows:

$$\mathbf{e}_k^\alpha = \mathbf{F}_k^\alpha \mathbf{D}_k^\alpha \mathbf{S}^\alpha - \mathbf{S}^\alpha \mathbf{D}_k^\alpha \mathbf{F}_k^\alpha. \quad (5-24)$$

The Fock matrix of each subsystem can be extrapolated as

$$\mathbf{F}_n^{\alpha, \text{DIIS}} = \sum_{k=1}^n c_k^\alpha \mathbf{F}_k^\alpha, \quad (5-25)$$

where coefficients c_k^α are determined in the same manner as in the total Fock matrix case. The DC-DIIS should be turned on only after the maximum element of \mathbf{e}_k^α becomes sufficiently small after several SCF cycles.

The second SCF acceleration technique [95] is related to the varying fractional occupation number (VFON) method realized by temperature-lowering technique [98]. It is well-known that in standard SCF with finite temperature β , smaller β (higher temperature) leads to faster convergence. We have found this fact holds true even in DC SCF. Smaller β in Eq. (5-13), however, makes the energy error introduced by finite temperature larger. Then we extended the temperature-lowering technique to DC SCF for improving the convergence with keeping the accuracy.

Although several schemes can be considered for lowering the temperature, we have proposed to simply set β increasing linearly ($+\Delta\beta$ per cycle) from an initial smaller value to the final larger value with respect to the SCF iteration, that is, the inverse temperature of k th SCF cycle β_k is represented as

$$\beta_k = \begin{cases} \beta_{\text{ini}} & \text{for } k < k_{\text{ini}} \\ \min[\beta_{\text{ini}} + (k - k_{\text{ini}})\Delta\beta, \beta_{\text{fin}}] & \text{for } k_{\text{ini}} \leq k \leq k_{\text{fin}} \\ \beta_{\text{fin}} & \text{for } k > k_{\text{fin}}, \end{cases} \quad (5-26)$$

where β_{ini} and β_{fin} are the initial and final values of β , respectively. The β value changes from the k_{ini} th to k_{fin} th SCF cycles. The final energy can be obtained with β_{fin} that introduces smaller error than with β_{ini} . Note that there is no extra computational cost in the present method.

5.2.2. DC-Based Correlation Theories

5.2.2.1. Density-Matrix-Based Divide-and-Conquer Møller-Plesset Perturbation

The simplest post-HF correlation theory is the MP2 method. Several groups have reported that the MP2 correlation energy can be written as the functional of HF DM [55–57] with the help of the Laplace-transformed representation [99, 100]. We can thus obtain the MP2 correlation energy from DC-HF DM of Eq. (5-4) although we cannot obtain the canonical (or even localized) MOs of the entire system in the DC-HF calculation. This approach is known as the DC-DM MP2 method [54].

The closed-shell MP2 correlation energy is given by using canonical orbitals as follows:

$$\Delta E_{\text{MP2}} = - \sum_{ij}^{\text{occ}} \sum_{a,b}^{\text{vir}} \frac{\langle ij | ab \rangle [2 \langle ab | ij \rangle - \langle ba | ij \rangle]}{\varepsilon_a + \varepsilon_b - \varepsilon_i - \varepsilon_j}. \quad (5-27)$$

This energy can be rewritten by means of the Laplace transformation as

$$\begin{aligned} \Delta E_{\text{MP2}} &= - \int_0^\infty e_2(s) ds \\ &\approx - \sum_{t=1}^{\tau} w_t e_2(s_t) \end{aligned} \quad (5-28)$$

with τ quadrature points $\{s_t\}$ and their weights $\{w_t\}$. The integrand in Eq. (5-28) is given in AO basis by

$$\begin{aligned} l_2(s_t) &= \sum_{\gamma\delta\kappa\varepsilon} \sum_{\mu\nu\lambda\sigma} X_{\mu\gamma}^t X_{\nu\delta}^t Y_{\kappa\lambda}^t Y_{\varepsilon\sigma}^t \langle \kappa\varepsilon | \gamma\delta \rangle [2 \langle \mu\nu | \lambda\sigma \rangle - \langle \nu\mu | \lambda\sigma \rangle] \\ &= \sum_{\mu\nu\lambda\sigma} \langle \bar{\lambda}\sigma | \underline{\mu\nu} \rangle [2 \langle \mu\nu | \lambda\sigma \rangle - \langle \nu\mu | \lambda\sigma \rangle], \end{aligned} \quad (5-29)$$

where \mathbf{X}^t and \mathbf{Y}^t are the energy-weighted DMs of electron and hole, respectively, and are given by

$$\mathbf{X}^t = \sum_i^{\text{occ}} e^{\varepsilon_i s_t} \mathbf{C}_i \mathbf{C}_i^\dagger = \frac{1}{2} \exp(s_t \mathbf{S}^{-1} \mathbf{F}) \cdot \mathbf{D} = \frac{1}{2} \exp\left(\frac{1}{2} s_t \mathbf{D} \mathbf{F}\right) \cdot \mathbf{D}, \quad (5-30)$$

$$\mathbf{Y}^t = \sum_a^{\text{vir}} e^{-\varepsilon_a s_t} \mathbf{C}_a \mathbf{C}_a^\dagger = \frac{1}{2} \exp(-s_t \mathbf{S}^{-1} \mathbf{F}) \cdot \bar{\mathbf{D}} = \frac{1}{2} \exp\left(-\frac{1}{2} s_t \bar{\mathbf{D}} \mathbf{F}\right) \cdot \bar{\mathbf{D}}. \quad (5-31)$$

$\bar{\mathbf{D}}$ is HF DM of the hole in AO basis,

$$\bar{\mathbf{D}} = 2 \sum_a^{\text{vir}} \mathbf{C}_a \mathbf{C}_a^\dagger. \quad (5-32)$$

The second equalities in Eqs. (5-30) and (5-31) can be derived by only assuming Roothaan equation for the entire system:

$$(\mathbf{F} - \varepsilon_q \mathbf{S}) \mathbf{C}_q = \mathbf{0}, \quad (5-33)$$

and the third equalities by assuming the commutation relationship of $\mathbf{FDS} = \mathbf{SDF}$, idempotency of $\frac{1}{2} \mathbf{DS}$, and

$$\mathbf{D} + \bar{\mathbf{D}} = 2\mathbf{S}^{-1}. \quad (5-34)$$

The DC-HF method defines only the electron DM. We have provided two formalisms for the hole DM, that is,

$$\bar{\mathbf{D}}^{\text{tot}} = 2\mathbf{S}^{-1} - \mathbf{D}^{\text{DC}}, \quad (5-35)$$

and

$$\bar{\mathbf{D}}_{\mu\nu}^{\text{sub}} = \sum_{\alpha} 2p_{\mu\nu}^{\alpha} \sum_q^{\text{MO}(\alpha)} f_{\beta}(\varepsilon_q^{\alpha} - \varepsilon_{\text{F}}) C_{\mu q}^{\alpha} C_{\nu q}^{\alpha*}. \quad (5-36)$$

The numerical results are available in Ref. [54]. Although the DC-DM MP2 method can slightly reduce the computational cost from canonical MP2, its scaling

becomes $O(|T|^3)$ due to the requirement of matrix exponential evaluations in Eqs. (5-30) and (5-31). Furthermore, the available correlation energy functional of the HF DM is only MP2 for the present. Therefore, we moved to the alternative strategy that is sufficiently faster than the DC-DM MP2 approach.

5.2.2.2. Subsystem-Orbital-Based Correlation Method [58–61]

The DC-HF calculation gives MOs in each subsystem (localization region), $\{\psi_q^\alpha(\mathbf{r})\}$, as well as the DM corresponding to the entire system. If occupied and virtual MOs are clearly distinguished among $\{\psi_q^\alpha(\mathbf{r})\}$, the correlation energy corresponding to localization region α will be obtained straightforwardly. However, the sum of the correlation energies over all localization regions would be an inappropriate correlation energy of the entire system because localization regions overlap with each other owing to the existence of the buffer region (a schematic is given in Figure 5-2). Therefore, the correlation energy that corresponds to the central region should be extracted. We have accomplished this task by means of the concept of the energy density analysis (EDA) [101], which have been proposed and developed by the authors' group [102–108].

EDA partitions the energy obtained by the HF calculation into atomic contributions by analogy to Mulliken population analysis [109]. The kinetic energy density for atom A , for example, is represented as:

$$E_{\text{kin}}^A = \sum_{\mu \in A} \sum_{\nu} D_{\mu\nu} \langle \nu | -\nabla^2 / 2 | \mu \rangle = \sum_{\mu \in A} \sum_i^{\text{occ}} C_{\mu i} \langle i | -\nabla^2 / 2 | \mu \rangle. \quad (5-37)$$

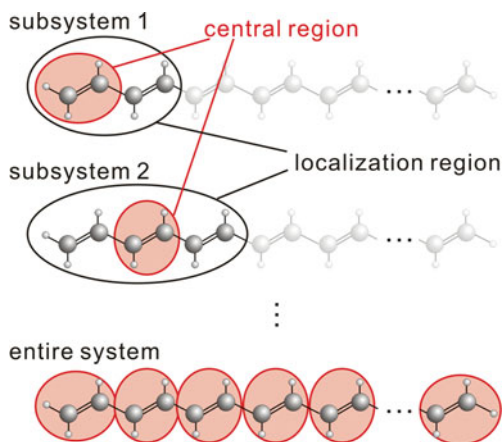


Figure 5-2. Schematic of the DC-based correlation calculation. The subsystem MOs extend to the buffer region. Then, the simple sum of the correlation energies obtained in terms of the subsystem MOs leads to the overlapped counting of the correlation energy. We have solved this issue by evaluating the correlation energy corresponding to the central region of the subsystem using the idea of EDA

Note again that each basis function is connected with an atom. In the same manner, the correlation energy can be partitioned into atomic contributions. Generally, the total correlation energy of a closed-shell system should be represented as the Nesbet's formula [110]:

$$\Delta E_{\text{corr}} = \sum_{ij}^{\text{occ}} \sum_{ab}^{\text{vir}} \langle ij | ab \rangle (2\tilde{t}_{ij,ab} - \tilde{t}_{ij,ba}), \quad (5-38)$$

where $\tilde{t}_{ij,ab}$ represents an effective two-electron excitation coefficient. By leaving the last integral transformation undone, one can rewrite the correlation energy as the sum of the atomic contributions:

$$\begin{aligned} \Delta E_{\text{corr}} &= \sum_A^{\text{atom}} \left[\sum_{ij}^{\text{occ}} \sum_{ab}^{\text{vir}} \left(w_{\text{occ}} \sum_{\mu \in A} C_{\mu i}^* \langle \mu j | ab \rangle \right. \right. \\ &\quad \left. \left. + w_{\text{vir}} \sum_{\lambda \in A} C_{\lambda a} \langle ij | \lambda b \rangle \right) (2\tilde{t}_{ij,ab} - \tilde{t}_{ij,ba}) \right] \\ &\equiv \sum_A^{\text{atom}} \Delta E_{\text{corr}}^A, \end{aligned} \quad (5-39)$$

where w_{occ} and w_{vir} are the linear-combination parameters, which represent the weights of occupied and virtual contributions and are constrained by $w_{\text{occ}} + w_{\text{vir}} = 1$ to reproduce the total correlation energy.

Using this atomic correlation energy, we can define the approximate correlation energy corresponding to the central region of subsystem α as

$$\Delta E_{\text{corr}}^\alpha = \sum_{ij}^{\text{occ}(\alpha)} \sum_{ab}^{\text{vir}(\alpha)} \left(w_{\text{occ}} \sum_{\mu \in \mathcal{S}(\alpha)} C_{\mu i}^* \langle \mu j^\alpha | a^\alpha b^\alpha \rangle + w_{\text{vir}} \sum_{\lambda \in \mathcal{S}(\alpha)} C_{\lambda a}^\alpha \langle i^\alpha j^\alpha | \lambda b^\alpha \rangle \right) (2\tilde{t}_{ij,ab}^\alpha - \tilde{t}_{ij,ba}^\alpha), \quad (5-40)$$

where $\{i^\alpha, j^\alpha, \dots\}$ and $\{a^\alpha, b^\alpha, \dots\}$ refer to the occupied and virtual MOs of subsystem α that have orbital energies smaller than and greater than ε_F , respectively. $\tilde{t}_{ij,ab}^\alpha$ is the effective two-electron excitation amplitude for subsystem α , namely, in the MP2 case [58, 60],

$$\tilde{t}_{ij,ab}^\alpha = -\frac{\langle a^\alpha b^\alpha | i^\alpha j^\alpha \rangle}{\varepsilon_a^\alpha + \varepsilon_b^\alpha - \varepsilon_i^\alpha - \varepsilon_j^\alpha}, \quad (5-41)$$

and in the coupled-cluster (CC) theory with singles and doubles (CCSD) case [59],

$$\tilde{t}_{ij,ab}^\alpha = t_{i,a}^\alpha t_{j,b}^\alpha + t_{ij,ab}^\alpha, \quad (5-42)$$

where T_1 and T_2 amplitudes, $t_{i,a}^\alpha$ and $t_{ij,ab}^\alpha$, are determined by solving the CCSD equations for the localization region of subsystem α .

This post-HF procedure is straightforwardly applicable to the DFT calculations with the double-hybrid exchange-correlation functional like B2PLYP [111] that mixes MP2-type correlation energy expression to the common DFT correlation functional. The energy expression for the B2PLYP functional is given by:

$$E_{xc} = (1 - a_x)E_x^{GGA} + a_x E_x^{HF} + (1 - a_c)E_c^{GGA} + a_c \Delta E_{PT2}, \quad (5-43)$$

where E_x^{GGA} and E_c^{GGA} represent generalized gradient approximation (GGA) exchange and correlation functionals, namely Becke 88 exchange [112] and Lee, Yang, and Parr correlation [113] functionals, respectively, E_x^{HF} is the HF exchange energy, and ΔE_{PT2} is equivalent to ΔE_{MP2} except for using Kohn-Sham orbitals instead of HF ones. The MP2-type energy term is simply omitted for simplicity in the SCF procedure, and ΔE_{PT2} is evaluated *a posteriori*. Grimme [111] proposed the use of $a_x = 0.53$ and $a_c = 0.27$.

Furthermore, this strategy is applicable to wide varieties of correlation theories even if its energy expression does not accord with Nesbet's formula. As an example, we take up the case of the CCSD(T) method [61, 114, 115]. The fourth- and fifth-order connected triples corrections to the CCSD correlation energy are represented as

$$E_{T[4]} = \sum_{ijk}^{\text{occ}} \sum_{abc}^{\text{vir}} \left(\frac{4}{3} t_{ijk,abc}^*(2) - 2t_{ijk,acb}^*(2) + \frac{2}{3} t_{ijk,bca}^*(2) \right) t_{ijk,abc}(2) D_{ijk,abc}, \quad (5-44)$$

$$E_{ST[5]} = \sum_{ijk}^{\text{occ}} \sum_{abc}^{\text{vir}} \left(\frac{4}{3} z_{ijk,abc}^* - 2z_{ijk,acb}^* + \frac{2}{3} z_{ijk,bca}^* \right) t_{ijk,abc}(2) D_{ijk,abc}, \quad (5-45)$$

respectively. The so-called CCSD[T] [115] and CCSD(T) [114] energies are $\Delta E_{CCSD[T]} = \Delta E_{CCSD} + E_{T[4]}$ and $\Delta E_{CCSD(T)} = \Delta E_{CCSD[T]} + E_{ST[5]}$, respectively. Here,

$$D_{ijk,abc} = \varepsilon_i + \varepsilon_j + \varepsilon_k - \varepsilon_a - \varepsilon_b - \varepsilon_c, \quad (5-46)$$

$$t_{ijk,abc}(2) = P_{ijk,abc} \left[\sum_e^{\text{vir}} t_{ij,ae} \langle bc|ek \rangle - \sum_m^{\text{occ}} t_{im,ab} \langle mc|jk \rangle \right] / D_{ijk,abc}, \quad (5-47)$$

$$z_{ijk,abc} = [t_{i,a} \langle bc|jk \rangle + t_{j,b} \langle ac|ik \rangle + t_{k,c} \langle ab|ij \rangle] / D_{ijk,abc}, \quad (5-48)$$

and $P_{ijk,abc}$ is the three-index symmetrizer, e.g.,

$$P_{ijk,abc}[A_{ijk,abc}] = A_{ijk,abc} + A_{jik,bac} + A_{kji,cba} + A_{ikj,acb} + A_{jki,bca} + A_{kij,cab}. \quad (5-49)$$

Considering the energy-partitioning scheme for $t_{ijk,abc}(2)D_{ijk,abc}$, which Eqs. (5-44) and (5-45) have in common, the following correction energy expressions for subsystem α in the DC calculation can be derived:

$$E_{T[4]}^{\alpha} = \sum_{ijk}^{\text{occ}(\alpha)} \sum_{abc}^{\text{vir}(\alpha)} \left(\frac{4}{3} t_{ijk,abc}^{\alpha*}(2) - 2t_{ijk,acb}^{\alpha*}(2) + \frac{2}{3} t_{ijk,bca}^{\alpha*}(2) \right) U_{ijk,abc}^{[X,Y]\alpha}, \quad (5-50)$$

$$E_{ST[5]}^{\alpha} = \sum_{ijk}^{\text{occ}(\alpha)} \sum_{abc}^{\text{vir}(\alpha)} \left(\frac{4}{3} z_{ijk,abc}^{\alpha*} - 2z_{ijk,acb}^{\alpha*} + \frac{2}{3} z_{ijk,bca}^{\alpha*} \right) U_{ijk,abc}^{[X,Y]\alpha}. \quad (5-51)$$

Here, all elements are evaluated in terms of subsystem MOs as

$$t_{ijk,abc}^{\alpha}(2) = P_{ijk,abc} \left[\sum_e^{\text{vir}(\alpha)} t_{ij,ae}^{\alpha} \langle b^{\alpha} c^{\alpha} | e^{\alpha} k^{\alpha} \rangle - \sum_m^{\text{occ}(\alpha)} t_{im,ab}^{\alpha} \langle m^{\alpha} c^{\alpha} | j^{\alpha} k^{\alpha} \rangle \right] / D_{ijk,abc}^{\alpha}, \quad (5-52)$$

$$z_{ijk,abc}^{\alpha} = \left[t_{i,a}^{\alpha} \langle b^{\alpha} c^{\alpha} | j^{\alpha} k^{\alpha} \rangle + t_{j,b}^{\alpha} \langle a^{\alpha} c^{\alpha} | i^{\alpha} k^{\alpha} \rangle + t_{k,c}^{\alpha} \langle a^{\alpha} b^{\alpha} | i^{\alpha} j^{\alpha} \rangle \right] / D_{ijk,abc}^{\alpha}, \quad (5-53)$$

$$D_{ijk,abc}^{\alpha} = \varepsilon_i^{\alpha} + \varepsilon_j^{\alpha} + \varepsilon_k^{\alpha} - \varepsilon_a^{\alpha} - \varepsilon_b^{\alpha} - \varepsilon_c^{\alpha}, \quad (5-54)$$

and $U_{ijk,abc}^{[X,Y]\alpha}$ can be obtained by partitioning $t_{ijk,abc}^{\alpha}(2)D_{ijk,abc}^{\alpha}$ by EDA. Several different expressions are conceivable for $U_{ijk,abc}^{[X,Y]\alpha}$, which are distinguished by $X = 0-2$ and $Y = 0-2$ as follows:

$$U_{ijk,abc}^{[X,Y]\alpha} = u_{ijk,abc}^{[X]\alpha} + v_{ijk,abc}^{[Y]\alpha}, \quad (5-55)$$

$$u_{ijk,abc}^{[0]\alpha} = P_{ijk,abc} \sum_e^{\text{vir}(\alpha)} \sum_{\mu \in S(\alpha)} t_{ij,ae}^{\alpha} C_{\mu k}^{\alpha} \langle b^{\alpha} c^{\alpha} | e^{\alpha} \mu \rangle, \quad (5-56)$$

$$u_{ijk,abc}^{[1]\alpha} = P_{ijk,abc} \sum_e^{\text{vir}(\alpha)} \sum_{\mu \in S(\alpha)} t_{ij,ae}^{\alpha} C_{\mu e}^{\alpha} \langle b^{\alpha} c^{\alpha} | \mu k^{\alpha} \rangle, \quad (5-57)$$

$$u_{ijk,abc}^{[2]\alpha} = P_{ijk,abc} \sum_e^{\text{vir}(\alpha)} \sum_{\mu \in S(\alpha)} t_{ij,ae}^{\alpha} C_{\mu c}^{\alpha*} \langle b^{\alpha} \mu | e^{\alpha} k^{\alpha} \rangle, \quad (5-58)$$

$$v_{ijk,abc}^{[0]\alpha} = P_{ijk,abc} \sum_m^{\text{occ}(\alpha)} \sum_{\mu \in S(\alpha)} t_{im,ab}^{\alpha} C_{\mu k}^{\alpha} \langle m^{\alpha} c^{\alpha} | j^{\alpha} \mu \rangle, \quad (5-59)$$

$$v_{ijk,abc}^{[1]\alpha} = P_{ijk,abc} \sum_m^{\text{occ}(\alpha)} \sum_{\mu \in S(\alpha)} t_{im,ab}^{\alpha} C_{\mu j}^{\alpha} \langle m^{\alpha} c^{\alpha} | \mu k^{\alpha} \rangle, \quad (5-60)$$

$$v_{ijk,abc}^{[2]\alpha} = P_{ijk,abc} \sum_m^{\text{occ}(\alpha)} \sum_{\mu \in S(\alpha)} t_{im,ab}^{\alpha} C_{\mu c}^{\alpha*} \langle m^{\alpha} \mu | j^{\alpha} k^{\alpha} \rangle. \quad (5-61)$$

Then, the DC-CCSD[T] and DC-CCSD(T) energies are expressed as

$$\Delta E_{\text{DC-CCSD(T)}} = \Delta E_{\text{DC-CCSD}} + \sum_{\alpha} E_{\text{T}[4]}^{\alpha}, \quad (5-62)$$

$$\Delta E_{\text{DC-CCSD(T)}} = \Delta E_{\text{DC-CCSD(T)}} + \sum_{\alpha} E_{\text{ST}[5]}^{\alpha}, \quad (5-63)$$

respectively. The authors [61] have also extended to the renormalized CCSD(T) [R-CCSD(T)] method [116, 117] that can reasonably avoid the divergence of the dissociation curve in the CCSD(T) method.

5.2.2.3. Dual-Buffer DC-Based Correlation Method

In DC-based correlation calculations, it is known that the correlation-energy error converges to zero more rapidly with respect to the buffer size than the HF-energy error. Because the computational costs for the correlation energy calculations are generally higher than those for HF, the DC-based correlation calculation can be accelerated with keeping its accuracy by adopting larger and smaller buffers for the HF and correlation calculations, respectively. The procedure of this dual-buffer treatment is as follows [59, 60]:

- 1 Iteratively solve the DC-HF equations adopting larger buffer region and obtain converged total DM and HF energy. This process can be substituted with any accelerated HF methodologies that can provide DM and HF energy, or even with standard HF.
- 2 Solve the DC-HF equations in subsystems with smaller buffer regions once for all and obtain subsystem MOs. The Fermi level, which is required to separate occupied and virtual MOs, may (or may not) be redefined from the constraint of Eq. (5-15).
- 3 Perform the DC-based correlation calculation by using subsystem MOs determined at step 2 and obtain the correlation energy.

5.3. ASSESSMENTS OF DIVIDE-AND-CONQUER METHOD

5.3.1. Implementation

We have implemented the above DC methodologies into the GAMESS-US program package [64–66]. The capabilities of the DC program are summarized in Figure 5-3. All methodologies discussed in Section 5.2 except for DC-DM MP2 are (or will be) available from GAMESS January 2009 version. The DC-CC codes were developed based on the CC program of Piecuch and coworkers [118]. A parallel implementation of the DC-MP2 method has been finished with and without the distributed data interface (DDI) technology [119] in GAMESS. Developments of more efficient parallel codes for the DC methodologies using group DDI (GDDI) [120] are in progress.

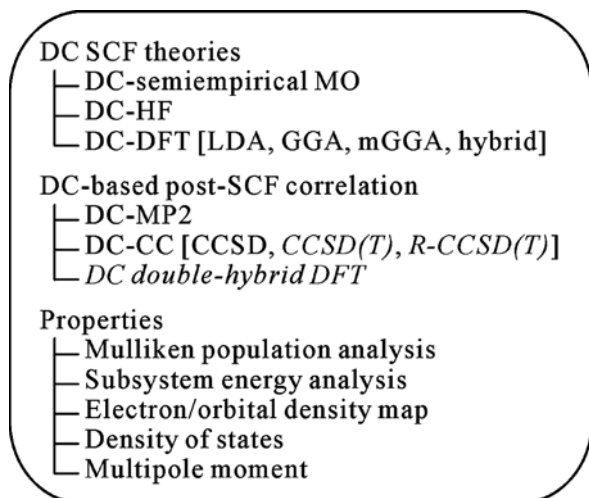


Figure 5-3. Capabilities of the DC program in GAMESS. All methods are available from January 2009 version except for the methods in italic which will be incorporated in the next version

The other notable features in this DC implementation are the followings:

1. Central regions can be defined manually or automatically based on cubic grid.
2. Buffer region can be specified manually or automatically as the union of the spherical regions centered at atoms consisting of the central region.
3. DC extended Hückel DM is applicable as an initial guess.
4. DC Fock construction is compatible with parallel linear-scaling fast multipole method (FMM) [88] implemented in GAMESS.
5. Restart option is available for DC-based correlation methods.

We will show several valuable examples of the DC calculations for assessing its efficiency and accuracy in the following subsections. In the DC SCF calculations, the inverse temperature parameter of the Fermi function β in Eq. (5-13) was fixed to 125.0 a.u. (2526 K) unless otherwise noted. In the post-SCF correlation calculations, chemical core orbitals were frozen. As a comprehensible example, we often use the polyene chain system C_nH_{n+2} , which is one-dimensional but modestly difficult test system for fragmentation methods because of the delocalized character of electrons. We adopted C_2H_2 (or C_2H_3 for the edges) group as a central region and treated several adjacent C_2H_2 (or C_2H_3) as corresponding buffer region, namely the left and right buffer regions in the DC-HF and correlation calculations were up to $C_{n_b}^{HF}H_{n_b}^{HF}$ (or $C_{n_b}^{HF}H_{n_b+1}^{HF}$) and $C_{n_b}^{corr}H_{n_b}^{corr}$ (or $C_{n_b}^{corr}H_{n_b+1}^{corr}$), respectively (see Figure 5-4). In practice, one can adopt the union of the spheres centered at atoms consisting in the central region as the buffer region. This choice will be useful for dynamically selecting the adequate buffer region during geometry optimization and dynamics simulation processes.

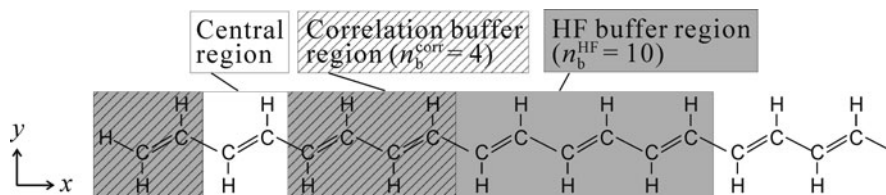


Figure 5-4. Schematic of the central and buffer regions in the DC calculations of polyene chain system C_nH_{n+2} . The x and y axes that are referred to in the quadrupole moment calculation are given together

5.3.2. DC SCF

5.3.2.1. Buffer-Size Dependence

First, we show the buffer-size dependence of the absolute HF energy error in the DC-HF calculations of a polyene chain $C_{60}H_{62}$ in Figure 5-5. The energy error is defined by $E_{DC} - E_{conv}$ through this chapter. The correlation consistent polarized double-zeta (cc-pVDZ) basis set [121] was adopted. The energy error introduced by the DC approximation decays quasi-exponentially with respect to the buffer size. In this system, 1 mHartree or less energy error can be accomplished for $n_b^{HF} \geq 12$. It was found that the DC SCF method can reproduce the conventional SCF energy with the buffer region of appropriate size and that the systematic improvement of the accuracy of the method is possible.

Next, we show the accuracy of the molecular properties. Table 5-1 gives the electrostatic quadrupole moment \mathbf{Q} of a polyene chain $C_{30}H_{32}$ calculated by DC-HF and DC-B3LYP [122, 123] methods with cc-pVDZ basis set. Here, the x and y axes are defined in Figure 5-4 and the z axis is the main axis of the D_{2h} symmetry of the molecule. The quadrupole moment becomes a constant tensor through the system

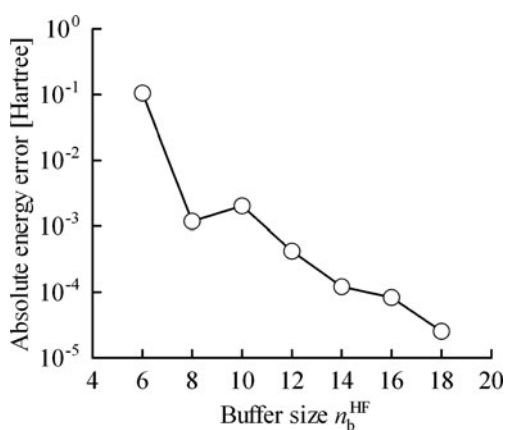


Figure 5-5. Buffer-size dependence of the absolute energy error of polyene chain $C_{60}H_{62}$ obtained by DC-HF/cc-pVDZ calculation

Table 5-1. Electrostatic quadrupole moment \mathbf{Q} (in Buckingham^a) of polyene chain $\text{C}_{30}\text{H}_{32}$ calculated by DC-HF and DC-B3LYP methods with cc-pVDZ basis set. The z axis is the main axis of the D_{2h} symmetry and x and y axes are given in Figure 5-4. The elements that are not given in this table are zero

n_b^{HF}	Q_{xx}		Q_{yy}		Q_{zz}		Q_{xy}	
	HF	B3LYP	HF	B3LYP	HF	B3LYP	HF	B3LYP
6	31.01	29.64	17.29	11.68	-48.30	-41.32	-1.05	1.56
8	20.58	22.40	22.54	15.40	-43.12	-37.80	-0.49	1.66
10	17.92	18.84	23.84	17.16	-41.76	-36.00	-0.30	1.81
12	16.88	16.78	24.36	18.20	-41.24	-34.98	-0.22	1.91
Conv.	16.22	13.53	24.69	19.82	-40.91	-33.35	-0.18	2.00

^a1 Buckingham = $3.33564 \times 10^{-40} \text{ C}\cdot\text{m}^2$.

and satisfies $Q_{xx} + Q_{yy} + Q_{zz} = 0$ by its symmetry. The elements of the tensor that are not given in Table 5-1 are zero. As the buffer-size increases, the quadrupole moments obtained by both DC-HF and DC-B3LYP calculations converge to the values obtained by conventional calculations, which are listed at the bottom of the table. The DC calculation reproduces the sign of Q_{xy} , which differs between HF and B3LYP results. Comparing the difference between conventional and $n_b^{\text{HF}} = 12$ results, DC-B3LYP gives slightly larger error than DC-HF because the small band gap derived from the DFT calculation leads to the contamination of virtual orbitals in DM and introduces large temperature error. However, it was found that the DC SCF calculations sufficiently reproduce not only total energy but also one-electron properties obtained by the conventional calculations.

Even in the large system calculation, the MOs of the entire system (especially frontier MOs) give important information such as the reaction site. For instance, in the FMO method, two schemes for obtaining the frontier MOs have been proposed [124, 125] with an extra computation. Although the DC calculation cannot offer the canonical MOs for the entire system, it can provide the electron density corresponding to each MO. In the closed-shell conventional HF case, the DM corresponding to the k th MO (that is, the MO having the k th lowest orbital energy) can be expressed as:

$$D_{\mu\nu,k} = 2C_{\mu k}C_{\nu k}^* = D_{\mu\nu}(\varepsilon_k) - D_{\mu\nu}(\varepsilon_{k-1}), \quad (5-64)$$

where

$$D_{\mu\nu}(\varepsilon) = 2 \sum_q \eta(\varepsilon - \varepsilon_q) C_{\mu q} C_{\nu q}^*, \quad (5-65)$$

and it clearly reads $\mathbf{D}(\varepsilon_F) = \mathbf{D}$. This scheme can be extended to the DC-HF calculation as the following:

$$D_{\mu\nu,k} \approx D_{\mu\nu}^{\text{DC}}(\varepsilon_k) - D_{\mu\nu}^{\text{DC}}(\varepsilon_{k-1}), \quad (5-66)$$

$$D_{\mu\nu}^{\text{DC}}(\varepsilon) = \sum_{\alpha} 2p_{\mu\nu}^{\alpha} \sum_q f_{\beta}(\varepsilon - \varepsilon_q) C_{\mu q} C_{\nu q}^* \quad (5-67)$$

The orbital energy corresponding to the k th MO of the entire system, ε_k , can be determined by solving the following equation that is analogous to Eq. (5-11):

$$2k = \text{Tr} [\mathbf{D}(\varepsilon_k)\mathbf{S}], \quad (5-68)$$

where the left-hand side represents the number of occupiable electrons up to the k th MO.

Figure 5-6 shows the electron density maps corresponding to highest occupied MO (HOMO) and lowest unoccupied MO (LUMO) obtained by DC and conventional HF calculations of a polyene chain $\text{C}_{30}\text{H}_{32}$ with cc-pVDZ basis set. The DC-HF orbital density fairly reproduces the HF orbital density, although the DC-HF orbital gives theoretically meaningless negative density around orbital nodes in the small buffer ($n_b^{\text{HF}} = 6$) calculation. It is notable that the cost of the computation needed for evaluating orbital density, which is only the determination of ε_k and ε_{k-1} from Eq. (5-68), is negligibly low.

5.3.2.2. System-Size Dependence of the Computational Cost

The efficiency of the DC calculations were assessed by means of the central processing unit (CPU) time. Figure 5-7 shows the CPU times for (a) solving SCF equations for all subsystems, Eq. (5-10), and (b) forming Fock matrix, Eq. (5-16), in the first SCF iteration of DC-HF calculations of polyene chains C_nH_{n+2} . The times in the conventional HF calculations are also shown for comparison. Here, we used 6-31G** basis set [126]. An Intel Pentium4/3.20 GHz processor was used on

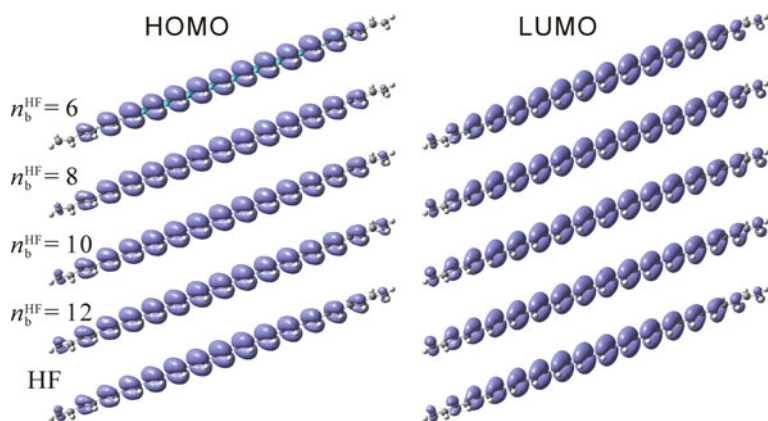


Figure 5-6. HOMO and LUMO density maps of polyene chain $\text{C}_{30}\text{H}_{32}$ obtained by (DC-)HF/cc-pVDZ calculations

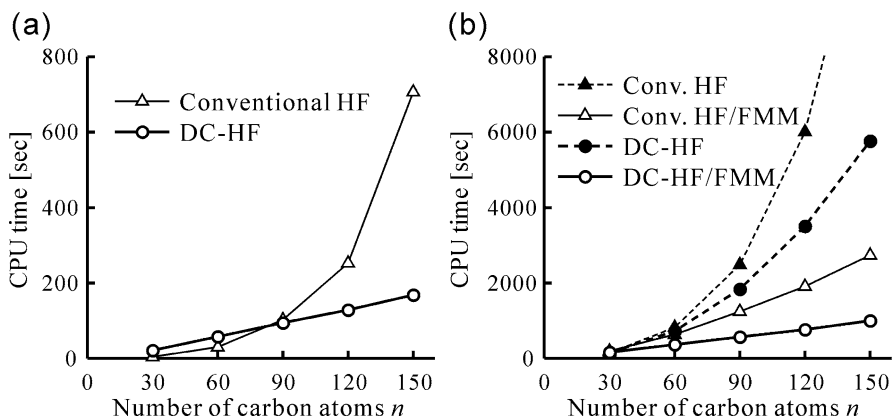


Figure 5-7. System-size dependence of CPU times for (a) solving SCF equation(s) and (b) forming Fock matrix in the first SCF iteration of polyene C_nH_{n+2} calculations at (DC-)HF/6-31G** level of theory. An Intel Pentium4/3.20 GHz processor was used on a single node. The buffer size was fixed at $n_b^{\text{HF}} = 12$. Both with and without FMM option data are presented for (b)

a single node. The buffer size was fixed at $n_b^{\text{HF}} = 12$. For the Fock matrix construction, the results with FMM option in GAMESS [88] are shown together. It is clear that the DC method reduces the computational times of both SCF solution and Fock formation procedures especially for large systems. For example, in the calculation of $C_{150}H_{152}$, the times of DC calculations were 4.2 and 2.2–2.7 times faster than those of conventional ones for (a) and (b), respectively. According to the scaling analysis by the double-logarithmic plot, the times of (a) scale with $O(n^{3.2})$ and $O(n^{1.3})$ for conventional and DC-HF calculations, and those of (b) scale with $O(n^{2.8})$, $O(n^{1.6})$, $O(n^{2.3})$, and $O(n^{1.1})$ for conventional, conventional/FMM, DC, and DC/FMM calculations, respectively. The combination of DC and FMM works quite well because of the sparseness of DC-HF DM and achieves the linear-scaling computational time.

The system-size dependence of the accuracy of the DC calculations was discussed elsewhere [52]. In summary, the energy error linearly increases with respect to the system size for homogeneous systems such as the polyene chain, i.e., the energy error per atom is fairly constant. This behavior is preferable for examining the relative stability of isoelectronic systems.

5.3.3. DC-Based Post-SCF Correlation Calculation

5.3.3.1. Buffer-Size Dependence

In the DC-MP2 and DC-CCSD calculations, the parameter w_{occ} (or w_{vir}) determining the ratio of occupied and virtual contributions in the subsystem correlation energy changes the results. Then, the parameter dependence of the correlation energy error was assessed in the DC-MP2 method. Figure 5-8 shows the buffer-size dependence of the correlation energy error from the canonical MP2 energy in the DC-MP2/cc-pVDZ calculation of a polyene chain $C_{60}H_{62}$. The horizontal

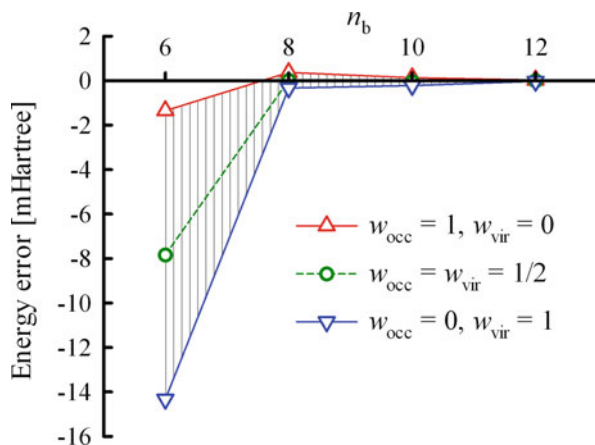


Figure 5-8. Buffer-size dependence of MP2 correlation energy error (in mHartree) in the DC-MP2/cc-pVDZ calculation of polyene chain $C_{60}H_{62}$. Up-triangle, down-triangle, and circle symbols correspond to $(w_{\text{occ}}, w_{\text{vir}}) = (1, 0)$, $(0, 1)$, and $(0.5, 0.5)$, respectively

axis represents the HF and correlation buffer size, i.e., $n_b^{\text{HF}} = n_b^{\text{corr}} = n_b$. Vertical stripes represent the ranges of the correlation energy for $0 \leq w_{\text{occ}} \leq 1$. Up-triangle, down-triangle, and circle symbols correspond to $(w_{\text{occ}}, w_{\text{vir}}) = (1, 0)$, $(0, 1)$, and $(0.5, 0.5)$, respectively. Because w_{occ} (or w_{vir}) is a linear energy coefficient, the energy obtained with $(w_{\text{occ}}, w_{\text{vir}}) = (0.5, 0.5)$ locates at the midpoint between $(w_{\text{occ}}, w_{\text{vir}}) = (1, 0)$ and $(0, 1)$. As the buffer size increases, the energy errors rapidly decrease for both $(w_{\text{occ}}, w_{\text{vir}}) = (1, 0)$ and $(0, 1)$. On the contrary, these differ for small buffer case ($n_b = 6$); the error for $(w_{\text{occ}}, w_{\text{vir}}) = (1, 0)$ is significantly smaller than for $(w_{\text{occ}}, w_{\text{vir}}) = (0, 1)$. Because the occupied MOs are generally more localized than the virtual MOs, the local correlation energy evaluated by partitioning an occupied MO will behave more properly than that by partitioning a virtual MO. We have assessed this type of the parameter dependence for CCSD in Ref. [61] and obtained similar tendency. In the following calculations, we adopted $(w_{\text{occ}}, w_{\text{vir}}) = (1, 0)$.

Next, we assessed the efficiency of the dual-buffer DC-based correlation scheme in the calculations of a polyene chain $C_{60}H_{62}$ at DC-MP2/cc-pVDZ level. Figure 5-9 shows the correlation buffer-size dependences of the user CPU time (solid line) and MP2 energy error from canonical MP2 result (dashed line). HF buffer-size was fixed at $n_b^{\text{HF}} = 12$. Calculations were performed with an Intel Pentium4/3.0 GHz processor on a single node. The time for the DC-HF calculation is included. The results of $n_b^{\text{HF}} = n_b^{\text{corr}} = 12$ correspond to the original DC-MP2. The computational cost can drastically be reduced from the original DC-MP2 by adopting small-size correlation buffer, e.g., the time for $n_b^{\text{corr}} = 6$ is 10.9 times faster than for $n_b^{\text{corr}} = 12$. On the other hand, the energy errors for $6 \leq n_b^{\text{corr}} \leq 12$ are less than 1.4 mHartree (0.87 kcal/mol), which sufficiently achieve the chemical accuracy. The detailed discussions on the accuracy and efficiency of the dual-buffer DC-based correlation method are given in Ref. [60].

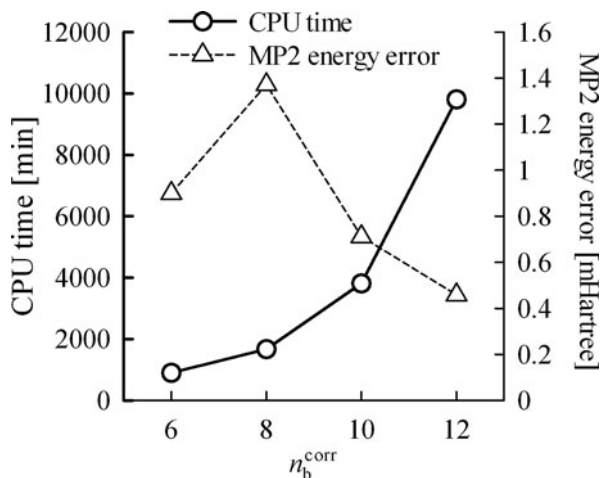


Figure 5-9. Correlation buffer-size dependences of the user CPU time (in min) and MP2 energy error (in mHartree) in the dual-buffer DC-MP2/cc-pVDZ calculation of polyene chain $C_{60}H_{62}$ with $n_b^{\text{HF}} = 12$. Calculations were performed with an Intel Pentium4/3.0 GHz processor on a single node

5.3.3.2. Relative Energy

In practical calculations for chemical phenomena, the relative energies are usually important rather than the total energies. The isomerization energy is a good indicator for assessing the relative energy. We chose the polyhydroacene molecule (Figure 5-10) as the isomer of the polyene. In the calculations of polyenes, the buffer sizes we adopted were $n_b^{\text{HF}} = 14$ and $n_b^{\text{corr}} = 8$. In the calculations of polyhydroacenes, we adopted C_4H_4 (or C_6H_4 for the center, C_4H_6 for the edges) group depicted in Figure 5-10 as a central region and treated three and five adjacent C_4H_4 (or C_6H_4 or C_4H_6) units as corresponding HF and correlation buffer regions.

Table 5-2 gives the total energies of C_nH_{n+2} ($n = 68, 148$; polyhydroacenes and polyenes) and the isomerization energies from polyhydroacene to polyene evaluated by DC-HF, MP2, the spin-component scaled MP2 (SCS-MP2; Ref. [127]), and B2PLYP calculations with 6-31G** basis set. For $n = 68$, the energies obtained from canonical calculations are also listed and the isomerization energy differences between DC and canonical results are in parentheses. The isomerization energy varies according to the methodologies, supposedly because of the fixed geometry. However, the differences between DC and canonical isomerization energies are less than 1.65 kcal/mol. In addition, the isomerization energy per carbon atom is a

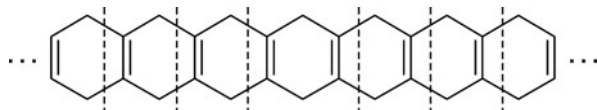


Figure 5-10. Structure of polyhydroacene C_nH_{n+2} . The dashed lines separate the central region

Table 5-2. Total energies (in Hartree) of C_nH_{n+2} (polyhydroarenes and polyenes) and the isomerization energies (in kcal/mol) from polyhydroarene to polyene obtained by DC and canonical HF, MP2, SCS-MP2, and B2PLYP calculations with 6-31G** basis set. The buffer region adopted in DC calculations is given in the main text

n	Method	Polyene (Hartree)		Polyhydroarene (Hartree)		Isomerization energy (kcal/mol)		
		Canonical	DC	Canonical	DC	Canonical	DC	(diff.)
68	HF	-2692.274791	-2692.274498	-2692.747762	-2692.747987	296.794	297.119	(+0.325)
	MP2	-2701.581797	-2701.580011	-2702.143865	-2702.144706	352.703	354.351	(+1.648)
	SCS-MP2	-2701.429552	-2701.428011	-2701.953539	-2701.954253	328.807	330.222	(+1.415)
	B2PLYP	-2707.379827	-2707.377666	-2707.801032	-2707.801445	264.310	265.926	(+1.616)
148	HF		-5767.851824		-5768.876181		642.794	
	MP2		-5787.777887		-5789.006980		771.268	
	SCS-MP2		-5787.441030		-5788.585858		718.391	
	B2PLYP		-5800.188081		-5801.106499		576.316	

good indicator for assessing the scalability of the method. In the B2PLYP case, for instance, the values for $n = 68$ and 148 become 3.911 and 3.894 kcal/mol, respectively. In all methods in the table, the differences of the isomerization energy per carbon atom between $n = 68$ and 148 are less than 0.6% . Thus, the present method can achieve chemical accuracy by adopting the buffer region of sufficient size.

5.3.3.3. Inhomogeneous System

Homogeneous polyenes and polyhydroacenes we have treated so far might seem to be easy cases for the DC treatment. There is no problem to treat inhomogeneous but delocalized systems. We performed the DC-MP2, DC-CCSD, and DC-CCSD(T) calculations of an inhomogeneous $C_{19}FH_{20}N$ system (Figure 5-11), where one hydrogen atom and one CH group in the $C_{20}H_{22}$ polyene chain are substituted with fluorine and nitrogen atoms, respectively. The central and buffer regions are defined in the same manner as the homogeneous polyene chain. HF and correlation buffer sizes were fixed at $n_b^{HF} = 12$ and $n_b^{corr} = 4$, respectively. The 6-31G** basis set was adopted. The DC-CCSD(T) calculation was performed with $U_{ijk,abc}^{[0,0]\alpha}$ partitioning [see Eq. (5-55)], where the dependence of the DC-CCSD(T) energy on the partitioning is discussed in Ref. [61].

Table 5-3 shows the DC subsystem energies [i.e., $E^\alpha DC\text{-HF}$ in Eq. (5-18) and ΔE_{corr}^α in Eqs. (5-40) and (5-63)] for $C_{19}FH_{20}N$ system together with conventional results. To clarify the inhomogeneity of the system, the DC-HF Mulliken charge corresponding to each central region is also listed in the table. The total energy errors from the conventional results are shown in parentheses for HF, MP2, and CCSD. The subsystem energies (both HF and correlation) vary greatly depending on the site of the subsystem, e.g., the subsystem $\alpha = 4$ has large positive charge and then gives higher HF and correlation energies than the other C_2H_2 subsystems. By contrast, the error of the total energy is sufficiently small, namely, 1.2 mHartree or less. Therefore, the DC-based correlation method is greatly expected to work well not only for uniform systems but also for inhomogeneous systems.

5.3.3.4. Computational Cost

Finally, we assessed the computational cost of the DC-based correlation calculations. Figure 5-12 shows the CPU times for DC-MP2, DC-CCSD, and DC-CCSD(T) calculations of polyene chain systems C_nH_{n+2} . Here, we adopted 6-31G basis set [128]. The buffer size was fixed at $n_b^{HF} = 12$ and $n_b^{corr} = 4$. Calculations were

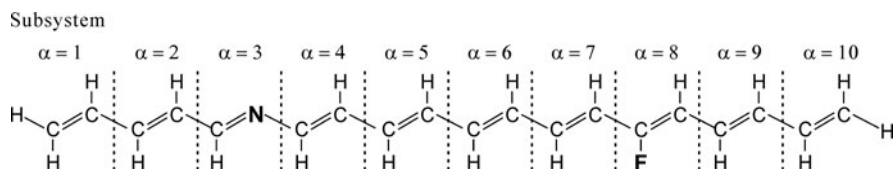


Figure 5-11. Structure and central regions of the inhomogeneous test system $C_{19}FH_{20}N$

Table 5-3. DC-HF, MP2, CCSD, and CCSD(T) subsystem energies of the inhomogeneous chain $C_{10}FH_{20}N$ with the buffer size of $(n_b^{HF}, n_b^{cont}) = (12, 4)$. The 6-31G** basis set was adopted

Subsystem	Charge ^a	E_{DC-HF}^α	ΔE_{DC-MP2}^α	$\Delta E_{DC-CCSD}^\alpha$	$\Delta E_{DC-CCSD(T)}^\alpha$
$\alpha = 1$	(C ₂ H ₃)	-77.460423	-0.271149	-0.292541	-0.304127
2	(C ₂ H ₂)	-76.882436	-0.263082	-0.278071	-0.290902
3	(CNH)	-92.925800	-0.303097	-0.312685	-0.327664
4	(C ₂ H ₂)	+0.223	-0.260911	-0.273410	-0.286561
5	(C ₂ H ₂)	+0.007	-0.265041	-0.279440	-0.292494
6	(C ₂ H ₂)	+0.008	-0.264992	-0.279411	-0.292424
7	(C ₂ H ₂)	-0.004	-0.265043	-0.278950	-0.292045
8	(C ₂ HF)	-0.039	-0.429697	-0.441596	-0.458532
9	(C ₂ H ₂)	+0.023	-0.263778	-0.278248	-0.290943
10	(C ₂ H ₃)	-0.001	-0.271853	-0.293447	-0.305050
	Sum (diff.)	-884.874804 (+0.0000075)	-2.858644 (+0.001140)	-3.007799 (+0.000424)	-3.140742
	Conv.	-884.874880	-2.859784	-3.008223	

^aMulliken charge at DC-HF level.

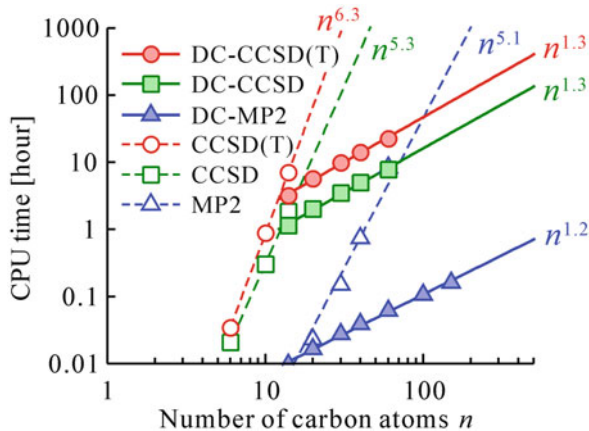


Figure 5-12. System-size dependence of CPU times for DC and conventional MP2, CCSD, and CCSD(T) calculations of polyene chains C_nH_{n+2} with the 6-31G basis set. Calculations were performed with an Intel Pentium4/3.8 GHz processor on a single node

performed with an Intel Pentium4/3.8 GHz processor on a single node. The time for the DC-HF calculation is not included. The gradient of this double-logarithmic plot gives the scaling of each method, which is given in the Figure together. The DC-based correlation methods drastically reduce the CPU times for MP2, CCSD, and CCSD(T) calculations, which theoretically scale $O(n^5)$, $O(n^6)$, and $O(n^7)$, respectively, and achieve near-linear scaling [$O(n^{1.2-1.3})$] computational cost with respect to the system size.

The required computational resources (namely, memory and scratch disk sizes) are the other important elements in assessing the computational cost. Table 5-4 shows the maximum number of CCSD amplitudes N_{amp} and computational resources required for DC and conventional CCSD/6-31G calculation of a polyene chain $C_{20}H_{22}$ with $n_b^{\text{corr}} = 2 - 8$. The ratios with respect to the conventional CCSD values are shown in parentheses. The ratios for the required memory size agree with those for N_{amp} , i.e., the required memory is proportional to N_{amp} , while those for the required scratch-disk capacity are rather large because of the additional terms demanded in the DC scheme. The most important thing we should mention is that

Table 5-4. Maximum number of CCSD amplitudes N_{amp} , required computer memory size, and required scratch-disk capacity for executing DC and conventional CCSD/6-31G calculation of polyene chain $C_{20}H_{22}$. The ratios with respect to the conventional CCSD values are shown in parentheses

n_b^{corr}	Largest subsystem	N_{amp}		Required memory (MB)		Scratch disk (GB)	
2	C_6H_7	1 025 156	(1%)	84	(1%)	2	(1%)
4	$C_{10}H_{11}$	7 488 432	(6%)	607	(6%)	11	(9%)
6	$C_{14}H_{15}$	28 095 300	(24%)	2276	(24%)	39	(34%)
8	$C_{18}H_{19}$	75 768 320	(64%)	6137	(64%)	106	(91%)
Conv.	$C_{20}H_{22}$	118 015 632	(100%)	9649	(100%)	117	(100%)

the DC-based correlation calculations require approximately equal computational resources for different lengths of polyene chains if the same buffer size n_b^{corr} is adopted. We can conclude that the DC-based post-SCF correlation method must be a practical technique for accurate calculations of large systems, including delocalized electronic systems, that costs $O(N)$ computational time and $O(N^0)$ computational resources.

5.4. CONCLUSIONS AND PERSPECTIVES

In this Chapter, we focused on the linear-scaling DM-based DC SCF method firstly proposed by Yang and Lee [23] and DC-based post-SCF correlation method [MP2, CCSD, and CCSD(T)] by the authors [58–61]. Both methods utilize the fact in the quantum chemical calculations that each basis function is connected with an atom in the considered system. Especially, the DC-based post-SCF method utilizes AO-based energy partitioning scheme termed EDA [101]. We have implemented these methods into the GAMESS-US quantum chemistry package [64–66], which is available without charge. Numerical assessments revealed that the combination of these methods achieves totally linear-scaling post-SCF correlation calculations with reasonably good accuracy. In this review, we mainly assessed the methods using the delocalized polyene test systems, not biomolecules or molecular clusters that are expected to be considerably easier than polyenes because of their localized character of electrons.

We hope that the present implementation is sufficiently valuable for the accurate practical calculations of nanomaterials and biomolecules. However, it lacks several important features for material design and mechanism clarification. Especially, the followings are our particular interests and several are in progress.

1. The derivation of the analytical energy gradient is one of the most important tasks for the present-day quantum chemical calculations. The analytical gradient code will enable the geometry optimization and molecular dynamics simulation of large systems. Although Yang and Lee [23] have presented the formalism of the DC-SCF gradient, several preliminary calculations revealed that it has slight error. Further, no analytical Hessian is available, and no analytical gradient of the DC-based correlation method has been proposed so far. The developments of these derivatives will be essential for the practical use of the DC method.
2. There are only few examples of the linear-scaling methods that can deal with the open-shell systems [129, 130]. It is usually difficult for fragmentation-based linear-scaling methods to treat delocalized open-shell systems because the numbers of electrons and excess spins are indefinite. However, in the DC SCF method, the definite numbers of electrons and spins in each subsystem would be needless. Instead, the Fermi level for each spin will determine them (recently, we have applied the DC method to open-shell systems in the unrestricted HF framework [131]). This method and its extension to the post-SCF correlation method will become valuable for *ab initio* treatment of metalloenzymes, biomolecular radicals, nanomagnets, and so on.

3. In addition to the static molecular properties, one of which was assessed in Section 5.3.2.1, the frequency-dependent response properties (i.e., the polarizability and hyperpolarizabilities) are also valuable that implicitly have the information of the electronic excited states and are demanded for optical material calculations. Although the linear-scaling static polarizability calculation is possible by the finite differentiation of the DC energy with respect to the electric field, no dynamic response calculation scheme based on the DC method has been proposed (most recently, we have reported the DC time-dependent HF method [132]). In addition, the DC-based dynamic polarizability calculation has the potential to effectively search the electronic excitation energies of the entire system, which correspond to the poles with respect to the frequency. A linear-response excited-state calculation is also desirable.
4. In the recent computer architecture, the parallelization ratio has become one of the barometers of the computational efficiency of a method. The DC method will be suitable for the parallel computation because the only part we need to gather the results of all subsystems is the determination of Fermi level from Eq. (5-15) in principle, which only demands the communication of orbital energies and weights. However, the efficient parallel implementations to the GAMESS package are undone.

The last thing we would like to introduce again the excerpt from Descartes: “*The long chains of simple and easy reasonings [subsystem calculations]... had led me to imagine that... there is nothing so far removed from us as to be beyond our reach, or so hidden that we cannot discover it.*” The improvements in the feature and computation of the DC method described above will broaden the applications of the accurate quantum chemical calculations to the wide varieties of the systems, not only chemical molecules but biological and solid-physical systems.

ACKNOWLEDGMENTS

We thank Prof. M. S. Gordon and Dr. M. W. Schmidt at Iowa State University for their support when implementing our method to GAMESS program. We are also grateful to many group members, especially Dr. T. Akama, for their contributions. Some of the present calculations were performed at the Research Center for Computational Science (RCCS), Okazaki Research Facilities, National Institutes of Natural Sciences (NINS). The studies were supported in part by a Grant-in-Aid for Scientific Research on Priority Areas “Molecular Theory for Real Systems” “KAKENHI 18066016,” the Next Generation Integrated Nanoscience Simulation Software Project, and the Global COE “Practical Chemical Wisdom” from the Ministry of Education, Culture, Sports, Science and Technology (MEXT), Japan. A project research grant for “Development of high-performance computational environment for quantum chemical calculation and its assessment” from the Research Institute for Science and Engineering (RISE) at Waseda University is gratefully acknowledged. One of the authors (MK) was indebted to the Research Fellowship for Young Scientists from Japan Society for the Promotion of Science (JSPS).

REFERENCES

1. Knuth DE (1973) The art of computer programming, vol. 3: Sorting and searching. Addison-Wesley, Reading, pp 159–170
2. Press WH, Teukolsky SA, Vetterling WT, Flannery BP (1992) Numerical recipes in Fortran 77, 2nd ed. Cambridge University Press, Cambridge
3. Yang W (1991) Phys Rev Lett 66:1438
4. Goedecker S (1999) Rev Mod Phys 71:1085
5. Wu SY, Jayanthi CS (2002) Phys Rep 358:1
6. Imamura A, Aoki Y, Maekawa K (1991) J Chem Phys 95:5419
7. Yang W (1991) Phys Rev A 44:7823
8. Yang W (1992) J Mol Struct Theochem 255:461
9. York D, Lu JP, Yang W (1994) Phys Rev B 49:8526
10. Lu JP, Yang W (1994) Phys Rev B 49:11421
11. Lee C, Yang W (1992) J Chem Phys 96:2408
12. Zhao Q, Yang W (1995) J Chem Phys 102:9598
13. Zhu T, Pan W, Yang W (1996) Phys Rev B 53:12713
14. Zhou Z (1993) Chem Phys Lett 203:396
15. Warschkow O, Dyke JM, Ellis DE (1998) J Comput Phys 143:70
16. Shimojo F, Kalia RK, Nakano A, Vashishta P (2005) Comput Phys Commun 167:151
17. Vashishta P, Kalia RK, Nakano A (2006) J Phys Chem B 110:3727
18. Nakano A, Kalia RK, Nomura K, Sharma A, Vashishta P, Shimojo F, van Duin AC, Goddard WA, Biswas R, Srivastava D (2007) Comput Mat Sci 38:642
19. Shimojo F, Kalia RK, Nakano A, Vashishta P (2008) Phys Rev B 77:085103
20. Ozaki T (2006) Phys Rev B 74:245101
21. Ozaki T, Terakura K (2001) Phys Rev B 64:195126
22. Parr RG, Yang W (1989) Density-functional theory of atoms and molecules. Oxford University Press, New York, NY
23. Yang W, Lee T-S (1995) J Chem Phys 103:5674
24. Szabo A, Ostlund NS (1989) Modern quantum chemistry. McGraw-Hill, New York, NY
25. Walker PD, Mezey PG (1993) J Am Chem Soc 115:12423
26. Mezey PG (1995) J Math Chem 18:141
27. Lee T-S, York DM, Yang W (1996) J Chem Phys 105:2744
28. York DM, Lee T-S, Yang W (1996) Chem Phys Lett 263:297
29. York DM, Lee T-S, Yang W (1996) J Am Chem Soc 118:10940
30. York DM, Lee T-S, Yang W (1998) Phys Rev Lett 80:5011
31. Lewis JP, Liu S, Lee T-S, Yang W (1999) J Comput Phys 151:242
32. Khandogin J, York DM (2002) J Phys Chem B 106:7693
33. Khandogin J, Musier-Forsyth K, York DM (2003) J Mol Biol 330:993
34. Khandogin J, York DM (2004) Proteins 56:724
35. Dixon SL, Merz KM Jr (1996) J Chem Phys 104:6643
36. van der Vaart A, Gogonea V, Dixon SL, Merz KM Jr (2000) J Comput Chem 21:1494
37. Dixon SL, Merz KM Jr (1997) J Chem Phys 107:879
38. Gogonea V, Merz KM Jr (1999) J Phys Chem A 103:5171
39. van der Vaart A, Merz KM Jr (1999) J Phys Chem A 103:3321
40. van der Vaart A, Merz KM Jr (1999) J Am Chem Soc 121:9182
41. Kitaura K, Morokuma K (1976) Int J Quantum Chem 10:325
42. Cabrera-Trujillo JM, Robles J (2001) Phys Rev B 64:165408
43. Pan W, Lee T-S, Yang W (1998) J Comput Chem 19:1101

44. Vincent JJ, Dixon SL, Merz KM Jr (1998) *Theor Chem Acc* 99:220
45. Gallant RT, St-Amant A (1996) *Chem Phys Lett* 256:569
46. Goh SK, St-Amant A (1997) *Chem Phys Lett* 264:9
47. Dunlap BI, Connolly JWD, Sabin JR (1979) *J Chem Phys* 71:3396
48. Goh SK, St-Amant A (1997) *Chem Phys Lett* 274:429
49. Goh SK, Gallant RT, St-Amant A (1998) *Int J Quantum Chem* 69:405
50. Goh SK, Sosa CP, St-Amant A (1998) *Theor Chem Acc* 99:197
51. Shaw DM, St-Amant A (2004) *J Theor Comput Chem* 3:419
52. Akama T, Kobayashi M, Nakai H (2007) *J Comput Chem* 28:2003
53. Akama T, Fujii A, Kobayashi M, Nakai H (2007) *Mol Phys* 105:2799
54. Kobayashi M, Akama T, Nakai H (2006) *J Chem Phys* 125:204106
55. Ayala PY, Scuseria GE (1999) *J Chem Phys* 110:3660
56. Surján PR (2005) *Chem Phys Lett* 406:318
57. Kobayashi M, Nakai H (2006) *Chem Phys Lett* 420:250
58. Kobayashi M, Imamura Y, Nakai H (2007) *J Chem Phys* 127:074103
59. Kobayashi M, Nakai H (2008) *J Chem Phys* 129:044103
60. Kobayashi M, Nakai H (2009) *Int J Quantum Chem* 109:2227
61. Kobayashi M, Nakai H (2009) *J Chem Phys* 131:114108
62. Pulay P (1983) *Chem Phys Lett* 100:151
63. Sæbø S, Pulay P (1993) *Annu Rev Phys Chem* 44:213
64. Schmidt MW, Baldrige KK, Boatz JA, Elbert ST, Gordon MS, Jensen JH, Koseki S, Matsunaga N, Nguyen KA, Su S, Windus TL, Dupuis M, Montgomery JA Jr (1993) *J Comput Chem* 14:1347
65. Gordon MS, Schmidt MW (2005) Advances in electronic structure theory: GAMESS a decade later. In: Dykstra CE, Frenking G, Kim KS, Scuseria GE (eds) *Theory and applications of computational chemistry: the first forty years*. Elsevier, Amsterdam, pp 1167–1189
66. Kobayashi M, Akama T, Nakai H (2009) *J Comput Chem Jpn* 8:1
67. Fedorov DG, Kitaura K (2007) *J Phys Chem A* 111:6904
68. Fedorov DG, Kitaura K (eds) (2009) *The fragment molecular orbital method: practical applications to large molecular systems*. CRC Press, Boca Raton, FL
69. Zhang DW, Zhang JZH (2003) *J Chem Phys* 119:3599
70. Li S, Li W, Fang T (2005) *J Am Chem Soc* 127:7215
71. Deev V, Collins MA (2005) *J Chem Phys* 122:154102
72. Gadre SR, Shirsat RN, Limaye AC (1994) *J Phys Chem* 98:9165
73. Ganesh V, Dongare RK, Balanarayan P, Gadre SR (2006) *J Chem Phys* 125:104109
74. Friedrich J, Dolg M (2008) *J Chem Phys* 129:244105
75. Friedrich J, Dolg M (2009) *J Chem Theory Comput* 5:287
76. Li S, Shen J, Li W, Jiang Y (2006) *J Chem Phys* 125:074109
77. Li W, Piecuch P, Gour JR, Li S (2009) *J Chem Phys* 131:114109
78. Mauri F, Galli G, Car R (1993) *Phys Rev B* 47:9973
79. Ordejon P, Drabold DA, Grumbach MP, Martin RM (1993) *Phys Rev B* 48:14646
80. Kim J, Mauri F, Galli G (1995) *Phys Rev B* 52:1640
81. Scuseria GE (1999) *J Phys Chem A* 103:4782
82. Niklasson AMN, Challacombe M (2004) *Phys Rev Lett* 92:193001
83. Li X-P, Nunes RW, Vanderbilt D (1993) *Phys Rev B* 47:10891
84. Galli G, Parrinello M (1992) *Phys Rev Lett* 69:3547
85. Kóhalmi D, Szabados Á, Surján PR (2005) *Phys Rev Lett* 95:013002
86. Strain MC, Scuseria GE, Frisch MJ (1996) *Science* 271:51
87. White CA, Head-Gordon M (1994) *J Chem Phys* 101:6593

88. Choi CH, Ruedenberg K, Gordon MS (2001) *J Comput Chem* 22:1484
89. Füsti-Molnár L, Pulay P (2002) *J Chem Phys* 117:7827
90. Kurashige Y, Nakajima T, Hirao K (2007) *J Chem Phys* 126:144106
91. Watson MA, Kurashige Y, Nakajima T, Hirao K (2008) *J Chem Phys* 128:054105
92. Schwegler E, Challacombe M (1996) *J Chem Phys* 105:2726
93. Burant JC, Scuseria GE, Frisch MJ (1996) *J Chem Phys* 105:8969
94. Ochsenfeld C, White CA, Head-Gordon M (1998) *J Chem Phys* 109:1663
95. Akama T, Kobayashi M, Nakai H (2009) *Int J Quantum Chem* 109:2706
96. Pulay P (1980) *Chem Phys Lett* 73:393
97. Pulay P (1982) *J Comput Chem* 3:556
98. Rabuck AD, Scuseria GE (1999) *J Chem Phys* 110:695
99. Almlöf J (1991) *Chem Phys Lett* 181:319
100. Häser M (1993) *Theor Chim Acta* 87:147
101. Nakai H (2002) *Chem Phys Lett* 363:73
102. Kawamura Y, Nakai H (2004) *J Comput Chem* 25:1882
103. Nakai H, Kikuchi Y (2005) *J Theor Comput Chem* 4:317
104. Baba T, Takeuchi M, Nakai H (2006) *Chem Phys Lett* 424:193
105. Nakai H, Kurabayashi Y, Katouda M, Atsumi T (2007) *Chem Phys Lett* 438:132
106. Imamura Y, Takahashi A, Nakai H (2007) *J Chem Phys* 126:034103
107. Imamura Y, Nakai H (2008) *J Comput Chem* 29:1555
108. Imamura Y, Baba T, Nakai H (2008) *Int J Quantum Chem* 108:1316
109. Mulliken RS (1955) *J Chem Phys* 23:1833
110. Nesbet RK (1969) Atomic Bethe-Goldstone equations In: LeFebvre R, Moser C (eds) *Advances in chemical physics*, vol. 14. Wiley, Chichester, pp 1–34
111. Grimme S (2006) *J Chem Phys* 124:034108
112. Becke AD (1988) *Phys Rev A* 38:3098
113. Lee C, Yang W, Parr RG (1988) *Phys Rev B* 37:785
114. Raghavachari K, Trucks GW, Pople JA, Head-Gordon M (1989) *Chem Phys Lett* 157:479
115. Urban M, Noga J, Cole SJ, Bartlett RJ (1985) *J Chem Phys* 83:4041
116. Kowalski K, Piecuch P (2000) *J Chem Phys* 113:18
117. Kowalski K, Piecuch P (2000) *J Chem Phys* 113:5644
118. Piecuch P, Kucharski SA, Kowalski K, Musiał M (2002) *Comput Phys Commun* 149:71
119. Fletcher GD, Schmidt MW, Bode BM, Gordon MS (2000) *Comput Phys Commun* 128:190
120. Fedorov DG, Olson RM, Kitaura K, Gordon MS, Koseki S (2004) *J Comput Chem* 25:872
121. Dunning TH Jr (1989) *J Chem Phys* 90:1007
122. Becke AD (1993) *J Chem Phys* 98:5648
123. Stephens PJ, Devlin FJ, Chabalowski CF, Frisch MJ (1994) *J Phys Chem* 98:11623
124. Inadomi Y, Nakano T, Kitaura K, Nagashima U (2002) *Chem Phys Lett* 364:139
125. Tsuneyuki S, Kobori T, Akagi K, Sodeyama K, Terakura K, Fukuyama H (2009) *Chem Phys Lett* 476:104
126. Hariharan PC, Pople JA (1973) *Theor Chim Acta* 28:213
127. Grimme S (2003) *J Chem Phys* 118:9095
128. Hehre WJ, Ditchfield R, Pople JA (1972) *J Chem Phys* 56:2257
129. Xiang HJ, Liang WZ, Yang J, Hou JG, Zhu Q (2005) *J Chem Phys* 123:124105
130. Pruitt SR, Fedorov DG, Kitaura K, Gordon MS (2010) *J Chem Theory Comput* 6:1
131. Kobayashi M, Yoshikawa T, Nakai H (2010) *Chem Phys Lett* 500:172
132. Touma T, Kobayashi M, Nakai H (2010) *Chem Phys Lett* 485:247

CHAPTER 6

LINEAR SCALING METHODS USING ADDITIVE FUZZY DENSITY FRAGMENTATION

PAUL G. MEZEY

Canada Research Chair in Scientific Modeling and Simulation, Editor, Journal of Mathematical Chemistry, Department of Chemistry and Department of Physics and Physical Oceanography, Memorial University of Newfoundland, St. John's, NL, Canada A1B 3X7, e-mail: paul.mezey@gmail.com

Abstract: The Additive Fuzzy Density Fragmentation (AFDF) principle provides the basis for the linear scaling Adjustable Density Matrix Assembler (ADMA) method, developed for detailed, ab initio quality macromolecular electron density computations, directed primarily towards protein studies. The same principle is the basis for novel approaches to the local analysis of electron density fragments, such as functional groups and regions surrounding reactive centers in various biomolecules. The basic theoretical developments as well as the implementation of the ADMA and related methods are subject to the conditions represented by the Holographic Electron Density Theorem: in any non-degenerate ground state, any positive volume local part of the electron density contains the complete information about the entire, boundaryless molecule. This represents a limitation on the transferability of molecular fragments, however, by a fuzzy fragmentation, some of the difficulties can be circumvented. Approximate transferability is a viable option if the relations between local and global properties are properly taken into account. Specifically, the interplay between local and global molecular properties, as manifested, for example, by symmetry properties and the topological shape constraints on molecular features has a strong influence on molecular energies. A better understanding of the interactions between local and global features also leads to fragment-based combinatorial quantum chemistry approaches. A general framework for such studies can be formulated based on the insight obtained by macromolecular quantum chemistry computations using the linear scaling ADMA method.

Keywords: Additive fuzzy density fragmentation principle, Adjustable density matrix assembler (ADMA), Holographic electron density theorem, Combinatorial quantum chemistry (CQC), The ADMA-CQC approach, Quantitative shape-activity relations (QShAR)

6.1. INTRODUCTION

In any modelling approach where an additivity principle is used in order to build up a model of a more complex system from model representations of smaller components, the best outcome one can hope for is a linear dependence of the computational

work on the size of the system. Historically, assuming approximate additivity of smaller constituent components, the associated linear scaling models of chemistry were a natural consequence of the limitations on detailed understanding of molecular structure: it was natural to regard molecules as collections of atoms. Some simple properties, such as mass, did show both additivity and linear scaling, if the goal was the computation of the total molecular mass. Major departures from additivity and linear scaling came when the models used for molecules became more sophisticated. Molecular electronic structure computations based on the LCAO principle, as manifested, for example, in the population analysis technique of Mulliken [1–4], required special weighting of components, such as the linear coefficients of atomic orbitals in a molecular orbital within the LCAO scheme. Even in this approach, the motivation for the use of models with additivity assumptions and linear scaling properties was strong: the somewhat artificial concept of atomic charges, which collectively represent the molecular charge distribution in an additive fashion, summing up to the total charge of the molecule or ion, was introduced to satisfy the need for a classical interpretation of the results of quantum chemical studies. Mulliken's LCAO – MO approach can also be regarded as the origin of all “divide-and-conquer” type techniques, since the basis is the use of local Hamiltonians of smaller systems leading to local representations (the atomic Hamiltonians leading to atomic orbitals), and combining such local representations after some readjustment in order to generate a molecular representation of the complete system (a readjustment by the optimization of coefficients of atomic orbitals within the LCAO representations of molecular orbitals).

Additive models are conceptually simple, however, for a physically realistic additive model of complex systems the choice of the components to be added is non-trivial. If the components themselves are simple, than assuming additivity is often unrealistic if the goal is to generate a good approximation to the complete system, since the interactions between simplistic components are often poorly defined; on the other hand, if in some skilful representation, component additivity can be secured to a good approximation, then the components themselves are likely to have complicated definitions and are difficult to represent properly. Apparently, the two requirements, the simplicity of the components, and the advantage of an additive method to combine them at a reasonable level of reliability, in order to form the model of the large system, often appear contradictory. This has remained the case, for example, within traditional AO and MO methods, even if by skilful representations, relying on orthogonality of molecular orbitals, some aspects of additivity could be recovered [5].

One principal difficulty is the way interactions among the smaller components are described. As the number n of the interacting components increases, the number of pair interactions increases as n^2 , that is, the optimal representation without ignoring some pair interactions must scale at least quadratically. This is the case if only pair interactions and no multicenter interactions are considered; for an inclusion of multicenter interactions, such as the four center integrals of Hartree-Fock theory [6–14], even quadratic scaling is impossible, unless some simplifying approximations are employed, beyond those already inherent in the method.

Such simplifying approximations may be primarily technical, such as those based on ignoring some multicenter integrals below some threshold value, or some general, theoretical principle may be invoked. In fact, in both of the above cases, the formulation of all simplifying assumptions eventually leading to a linear scaling algorithm can be regarded as involving a distance criterion, either directly, or indirectly.

6.2. COMMON PRINCIPLES OF LINEAR SCALING METHODS

In many fields where the complexity of the subject studied requires simplifications, a natural criterion is often used: distance. Sets of objects or objects with parts far apart are less likely to have strong interactions, and this often allows some form of simplification, for example, ignoring interactions beyond some distance threshold.

In the case of molecules, the same principle is often applied: various laws of physics show an inverse square dependence on distance, for example, Coulomb's Law, and even more significant is the fact that atomic electron density functions show an exponential decay by distance.

In fact, whether it is recognized as a guiding principle or it is merely taken as a technical aspect of the approach, all linear scaling methods of quantum chemistry are based on a common principle related to distance. Specifically, the problem of the quantum chemical representation of a large molecule is approached by algorithms setting direct or indirect distance limits on the interactions considered between molecular parts, that allows proportionality of the computational work with molecular size. This principle is at work if some thresholds are applied to molecular integrals, directly or indirectly dependent on distance, or if some fragmentation scheme is considered, where the size of the fragment itself, and the size of the surrounding region included for the representation of intramolecular interactions are both involving a distance criterion that determines these two sizes.

6.3. LOCALITY ASPECTS OF LINEAR SCALING METHODS

The importance of distance as a criterion for the level of approximation represented by a linear scaling quantum chemistry method underlines the role of the concept of locality. Whereas localized orbitals using various criteria for achieving localization [15–18] have been used for a long time to interpret the results of quantum chemistry calculations, they have not provided efficient tools for exploiting another aspect of localization: the identification of local regions in molecules which can be used in an efficient way for the development of linear scaling methods. It is natural to expect that a linear scaling technique, involving distance criteria, may be able to utilize some specific choices for local regions within extended regions of molecules, yet most actual linear scaling approaches take a different route. This is certainly the case if the starting point is a Density Functional approach [19, 20], where the very origin of the theory, the electron gas model, is better suited for a global representation, and localization and local features require some simplifications. Utilizing the simplicity of local Hamiltonians, the typical density functional approaches to linear

scaling algorithm [21–24], such as the so-called “Divide and Conquer” method of Yang, does not involve any density functional analogue of orbital localization, rather a choice of molecular parts to be considered locally, followed by a mutual readjustment step of local representations.

One may take a deliberate choice of using a set of local molecular regions which do not necessarily possess any special chemical or physical significance. If in such an approach the selection of local molecular parts is arbitrary, but it still can provide the basis for a linear scaling scheme that is successful in reproducing conventional computational results for smaller molecules, then one may claim that no bias in the initial assumptions on the relevance of various molecular subdivision can be the source of any fortuitous agreement between the test results, and this eliminates at least some of the questions concerning reliability.

6.4. FUNDAMENTAL RELATIONS BETWEEN LOCAL AND GLOBAL PROPERTIES OF MOLECULES

The interrelations between local and global properties of molecules are encoded in the molecular electron density. As stated by the Hohenberg–Kohn theorem [25], the nondegenerate ground state electron density $\rho(\mathbf{r})$ of a molecule determines the Hamiltonian H of the system within an additive constant, consequently, $\rho(\mathbf{r})$ also determines all ground state and all excited state properties of the system described by the Hamiltonian H .

The generalized and concise “constrained search” proof of density functional theory, as described by Levy [26–28], also provides an elegant proof of the Hohenberg–Kohn theorem.

Among some of the relevant the consequences of this theorem [29–35], we are especially interested in the locality problem. Here, following the discussions in reference [31], we shall consider an alternative argument, a simple, information-theoretical approach that leads to the actual statement of the Hohenberg–Kohn theorem.

The conditions for the Hohenberg–Kohn theorem are rather simple, since the theorem is based on two pieces of information:

- (i) the electronic density as a three-dimensional function given in some form;
- (ii) the additional knowledge that it is a nondegenerate ground state electron density of the system under consideration.

The above conditions and the resulting treatment are equally applicable to any physical system built from nuclei and electrons, however, here we are concerned with molecules.

Based on this information, and on some elementary assumptions on molecules, the following statements can be made:

1. A molecule contains only a set of nuclei and an electron density cloud.
2. Since there is no other material present to encode information, all information concerning the static properties of the molecule must be contained in the nuclear and electron distributions.

3. The location and atomic numbers of the nuclei are fully determined by the nondegenerate ground state electron density $\rho_0(\mathbf{r})$ of the molecule.
4. Consequently, the nondegenerate ground state electron density $\rho_0(\mathbf{r})$ contains all information concerning all static properties of the molecule, including its ground state energy, and any other molecular properties.

The last statement, statement 4, is actually equivalent to the statement of the Hohenberg-Kohn theorem for molecules.

By extending the above argument, among the various molecular properties, the external potential $V(\mathbf{r})$ is also determined by the nondegenerate ground state electron density $\rho_0(\mathbf{r})$. Since the ground state electron density $\rho_0(\mathbf{r})$ determines the molecular Hamiltonian

$$H = \sum V(\mathbf{r}_i) + T + V_{ee}, \quad (6-1)$$

consequently, excited state information is also implied by the nondegenerate ground state electron density. This latter observation suggests that the fundamental constraints on linear scaling methods are the same if they are applied to ground state or to excited electronic states of molecules.

It has been recognized early that the central role of electron density, as established by the Hohenberg-Kohn theorem [25] is likely to provide new approaches to macromolecular quantum chemistry, where the computational methods focus on electron density, even if the method is not directly based on density functional theory. However, if any build-up procedure is used for exploiting small molecular parts in order to build representations of large molecules, the relations between the whole and the parts of molecular electron densities, governed by the quantum mechanical aspects of localization, may imply constraints on any potential linear scaling methods. Consequently, studies addressing the problem of relations between the whole and the parts of electron densities have proven to have special significance.

In a thorough study, Riess and Munch provided a local version of the Hohenberg-Kohn theorem for artificial, bounded systems, with definite boundaries [29]. These authors fully recognized and clearly stated that their result is for closed and bounded models, whereas real molecules are neither bounded nor closed systems. Some subsequent interpretations of their work have overlooked this limitation, assuming that their line of reasoning holds for real molecules, in spite of the well-known fact that treating open, boundaryless systems as if they were closed and bounded may lead to false statements, just as division by zero may. Nevertheless, the controversy surrounding this question has given motivation to search for relations between local and global electron density properties in the case of more realistic models of molecules, not restricted by the closed and bounded conditions.

Some time later, such a relation between local and global properties of electron densities of real, boundaryless molecules has been established by the proof of the holographic electron density theorem [30, 31]. This theorem states that *for any real, boundaryless molecule, any small part of the electron density cloud contains the complete information about the whole electron density of the molecule, as*

long as the part has some positive volume. In fact, the positive volume condition is essential, since a point, a line, or an infinitely thin sheet from the electron density is not sufficient for complete information storage.

Various consequences of the holographic electron density theorem have been studied in some detail, concerning the relations between local and global symmetry properties, its role in potential prediction of both exhibited and latent molecular properties, such as excited state properties “encoded” in ground state electron densities, as well as in the special role of the theorem in the mechanism and reproducibility of molecular recognition [31–35]. The holographic electron density theorem has special significance in the emerging field of molecular informatics [35].

For the purposes of investigating the constraints represented by the fundamental properties of molecular electron densities on the development of linear scaling quantum chemical computational methods, the most important consequence of this theorem is that no molecular part can ever be perfectly transferable, unless they are transferred back to the exact location of the molecule they originate from, or if the new location is related to the old one by perfect symmetry. Consequently, molecular fragments originating from small molecules can never exactly reproduce fragments from large molecules.

The impossibility of exact fit of a molecular part into an environment different from that of its original location also implies that linear scaling quantum chemistry methods based on combinations of smaller entities cannot be exact, unless highly elaborate and additional, and no longer linear scaling processes are also included.

Whereas the holographic electron density theorem describes exact relations, for the exact electron density, the theorem itself does not exclude the possibility for non-exact, but very high levels of approximations for a molecule building approach using molecular fragments within some linear scaling framework.

One approach exploiting a high level of approximate transferability even if exact transferability is impossible, involves a fuzzy set approach [36–37] and a fuzzy electron density fragmentation and subsequent build-up of a macromolecular electron density by a linear scaling algorithm. This family of methods involving the AFDF principle (Additive Fuzzy Density Fragmentation Principle) provided many results for actual macromolecules, including proteins well over the one thousand atom size [38–61]. These methods also provide alternatives to a classically motivated atomic view of molecular pieces [62], extensions of molecular similarity analysis approaches [63–66] to large molecules, the adaptation of the principles of synthetic combinatorial chemistry [67–74] to a quantum chemical combinatorial chemistry approach to molecular design [52, 53, 56], as well as macromolecular generalizations of molecular reactivity studies in terms of potential energy hypersurfaces [75] and molecular shape analysis studies [76].

6.5. A FUZZY FRAGMENT APPROACH TO LINEAR SCALING METHODS

Whereas molecular fragments of various definitions have been used extensively for both theoretical developments and practical approaches, such as structure activity relation studies, not all fragmentation schemes are useful as the source of molecular

pieces or molecular regions involved in linear scaling procedures. The rather natural, classically motivated subdivision of molecules into molecular parts using cuts by various surfaces across the molecules, such as the zero-flux surfaces defined in terms of the density gradient [62], are appealing by their simplicity, however, they cannot, not even accidentally, correspond to viable building blocks for constructing larger molecules. As it follows from the Holographic Electron Density Theorem, each such piece, having sharp boundaries, can fit without a gap or an overlap only to the very same spot of the very same molecule where it originally belongs; a combination with any other such piece of sharp boundary necessarily leads to two kinds of mismatches: a geometrical misfit of the pieces, and a misfit by violating the continuity of the electron density values between the pieces. This is true independently of the choice of the method used to generate the cuts, whether the cuts are based on a criterion of zero flux of the density gradient or on some other idea. Using such surface-bound molecular pieces for constructing models for larger molecules inevitably leads either to density gaps, or density “doubling”, that is, either to a 100% underestimation of the electron density, or to a nearly 100% overestimation of the density (note that, due to a mismatch of the electron density values, such overlaps may lead to slightly less or slightly more than 100% positive error). To make things worse, this happens in a particularly crucial part of the newly built molecular model: in the very regions where the pieces supposedly join, that is, in the regions where one expects the chemically critical bonding between fragments to take place. Such gaps or density doubling can be corrected only by expensive readjustments of the density, causing the loss of any linear scaling property that might have been the motivation for the approach, and also raising serious questions about the reliability of the method.

Besides the above technical considerations, there is another, more fundamental reason why such formal molecular pieces with sharp boundaries should be avoided: the postulates of quantum mechanics, hence the basis of quantum chemistry implies that such pieces with boundaries are very different from actual electron density clouds. Real electron densities beyond some threshold show essentially exponential decay of the density values with distance from the nuclei. A cut, with a discontinuous electron density suddenly becoming zero, where the cutting surface itself shows zero uncertainty in the position variable while moving across the cut, cannot represent a realistic model for a viable electron density cloud, since it is in violation of the Heisenberg relation. This latter limitation by itself does not imply that such models are not applicable for the purposes of analysing features of electron densities, but a better model representation may be expected if the building blocks themselves do not violate some of the fundamental relations of quantum mechanics.

An alternative approach is provided by a fuzzy representation of electron density pieces, in fact, by generating fuzzy electron density “fragments”, inheriting the exponential decay feature of real electron densities (or, in practical computations using Gaussian functions, a composite Gaussian decay imitating an exponential decay by distance). One may regard this approach as a fuzzy decomposition of the electron density cloud into fuzzy, overlapping parts which add up to the complete electron density of the molecule originally considered; a smaller cloud of the fuzzy fragment is “pulled out” from the original larger electron density cloud of the

complete molecule to be partitioned. If such fuzzy pieces, originating from different molecules are combined to generate models of new molecules, then no obvious mismatches, no density gaps or density doubling will appear. The inevitable inaccuracy of the fuzzy fragments in their new locations will not cause any large accumulation of error in any region, and the resulting electron density model will be fully continuous. The numerical inaccuracy of the resulting continuous electron density can be reduced below any positive threshold by increasing the size of the molecules used for generating the fuzzy fragments, if these larger molecules contain larger parts of the macromolecule which is the target of the modelling task where the fuzzy fragments are to be used.

Two actual algorithms to achieve this goal are described in the next section.

6.6. THE LINEAR SCALING PROPERTIES OF THE MEDLA AND ADMA METHODS

The two techniques involving the The Additive Fuzzy Density Fragmentation Principle, or in short, the AFDF Principle [44, 45] is the basis for two, related linear scaling approaches: the MEDLA, Molecular Electron Density Loge (or Lego) Assembler method [38–43] and the ADMA, Adjustable Density Matrix Assembler method [44–61]. From these two, MEDLA is an essentially numerical technique for the construction of macromolecular electron densities, whereas the more advanced ADMA method actually constructs a macromolecular density matrix, and also exploits both the theoretical and computational advantages of the actual knowledge of this approximate, but “ab initio quality” density matrix.

Following the description and notations given in the original references, here we shall give only a brief summary of the various steps involved in the actual linear scaling computation of such a macromolecular density matrix.

Although a similar description can be given for the implementation of the MEDLA and ADMA methods within a density functional framework, here we shall discuss primarily a more conventional molecular orbital implementation.

With respect to a given basis set $\varphi(\mathbf{K})$ of atomic orbitals $\varphi_i(\mathbf{r}, \mathbf{K})$ ($i = 1, 2, \dots, n$), the electronic density $\rho(\mathbf{r}, \mathbf{K})$ of a molecule of nuclear conformation \mathbf{K} can be computed at each point \mathbf{r} by the Hartree-Fock-Roothaan-Hall SCF LCAO ab initio method. Using the $n \times n$ dimensional density matrix $\mathbf{P}(\varphi(\mathbf{K}))$, obtained by such calculations, the electronic density $\rho(\mathbf{r}, \mathbf{K})$ is obtained as

$$\rho(\mathbf{r}, \mathbf{K}) = \sum_{i=1}^n \sum_{j=1}^n P_{ij}(\varphi(\mathbf{K})) \varphi_i(\mathbf{r}, \mathbf{K}) \varphi_j(\mathbf{r}, \mathbf{K}). \quad (6-2)$$

Since beyond some threshold the electron density decreases exponentially with distance from the nuclei, this suggests that an Additive Fuzzy Density Fragmentation (AFDF) approach can be used for both a fuzzy decomposition and construction of molecular electron densities. The simplest AFDF method is the Mulliken-Mezey density matrix fragmentation technique [38, 39], and this is the basis for both the

Molecular Electron Density Loge Assembler (MEDLA) [38–43] and the Adjustable Density Matrix Assembler (ADMA) [44–61] macromolecular quantum chemistry methods.

Following the general Mulliken-Mezey AFDF approach, the set of nuclei of the molecule M are classified into m mutually exclusive families

$$f_1, f_2, \dots, f_k, \dots, f_m. \quad (6-3)$$

For each AO basis function $\varphi_i(\mathbf{r}, \mathbf{K})$ and nuclear family f_k a membership function $m_k(i)$ is defined:

$$m_k(i) = \begin{cases} 1 & \text{if AO } \varphi_i(\mathbf{r}) \text{ is centered on one of the nuclei of set } f_k, \\ 0 & \text{otherwise.} \end{cases} \quad (6-4)$$

One may choose some w_{ij} and w_{ji} weighting factors fulfilling the condition

$$w_{ij} + w_{ji} = 1, \quad w_{ij}, w_{ji} > 0, \quad (6-5)$$

then the elements $P_{ij}^k(\varphi(\mathbf{K}))$ of the $n \times n$ fragment density matrix $\mathbf{P}^k(\varphi(\mathbf{K}))$ for the k -th fragment “anchored” to the nuclear family k are given by

$$P_{ij}^k(\varphi(\mathbf{K})) = [m_k(i) w_{ij} + m_k(j) w_{ji}] P_{ij}(\varphi(\mathbf{K})). \quad (6-6)$$

The simplest choice for the w_{ij} , w_{ji} factors within the Mulliken-Mezey AFDF approach is

$$w_{ij} = w_{ji} = 0.5 \quad (6-7)$$

that follows the principle of the original population analysis scheme of Mulliken.

Based on the above considerations, the k -th additive fuzzy density fragment $\rho^k(\mathbf{r}, \mathbf{K})$ is defined as

$$\rho^k(\mathbf{r}, \mathbf{K}) = \sum_{i=1}^n \sum_{j=1}^n P_{ij}^k(\varphi(\mathbf{K})) \varphi_i(\mathbf{r}, \mathbf{K}) \varphi_j(\mathbf{r}, \mathbf{K}), \quad k = 1, 2, \dots, m. \quad (6-8)$$

A simple substitution shows that the AFDF fragment density matrices $\mathbf{P}^k(\varphi(\mathbf{K}))$ as well as the corresponding fuzzy density fragments $\rho^k(\mathbf{r}, \mathbf{K})$ are exactly additive:

$$\mathbf{P}(\varphi(\mathbf{K})) = \sum_{k=1}^m \mathbf{P}^k(\varphi(\mathbf{K})), \quad (6-9)$$

and

$$\rho(\mathbf{r},\mathbf{K}) = \sum_{k=1}^m \rho^k(\mathbf{r},\mathbf{K}). \quad (6-10)$$

Using the above fuzzy fragmentation for a small molecule M , only a conventional Hartree-Fock computation followed by the application of the AFDF approach are needed to obtain the input information for a detailed study of the shape and the interactions of various parts and local moieties of molecule M .

On the other hand, if the molecule M is large, then a conventional Hartree-Fock computation may no longer be feasible, however, the fuzzy electron density fragments of the large “target” molecule M still can be computed indirectly using the AFDF approach. This can be accomplished with the aid of smaller “parent” molecules, containing various parts of the original large molecule.

For each nuclear family f_k of M , a small parent molecule M_k can be designed, where M_k contains the same nuclear family f_k with the same local arrangement and surroundings as is found in the large target molecule M . A fuzzy density fragmentation can be carried out for the small parent molecule M_k , resulting in a fuzzy density fragment $\rho^k(\mathbf{r},\mathbf{K})$ corresponding to the nuclear set f_k , and other, additional density fragments which are not going to be used for the macromolecular study. By repeating this procedure for each nuclear family f_k of M , the fuzzy fragments

$$\rho^1(\mathbf{r},\mathbf{K}), \rho^2(\mathbf{r},\mathbf{K}), \dots, \rho^k(\mathbf{r},\mathbf{K}), \dots, \rho^m(\mathbf{r},\mathbf{K}) \quad (6-11)$$

obtained from the set of m small “parent” molecules

$$M_1, M_2, \dots, M_k, \dots, M_m, \quad (6-12)$$

can be combined and used to construct the electron density $\rho(\mathbf{r},\mathbf{K})$ of the large target molecule M . The fragment densities can also be used for local analysis of various parts, for example, various functional groups of the macromolecule M .

The first implementation of the simplest version of the AFDF approach was the MEDLA (*Molecular Electron Density “Lego” Assembler*, or *Molecular Electron Density “Lego” Assembler*) method. This method is based on a numerical electron density fragment database of pre-calculated, custom-made electron density fragments $\rho^k(\mathbf{r},\mathbf{K})$, and a subsequent numerical construction of the molecular electron density using Eq. (6-10). As it has been verified by detailed tests [38–43], the MEDLA method generates ab initio quality electron densities for large molecules near the 6-31G** basis set level that has been used for the construction of the fragment density databank. Using the MEDLA method, the first ab initio quality electron densities have been computed for several proteins, including crambin, bovine insulin, the gene-5 protein (g5p) of bacteriophage M13, the proto-oncogene tyrosine kinase protein 1ABL containing 873 atoms and the HIV-1 protease monomer of 1,564 atoms.

Whereas the MEDLA method resulted in several successful quantum chemical studies of macromolecules, nevertheless, the MEDLA method also had some drawbacks: the requirement of a numerical databank and some of the problems associated

with the grid alignment of combined numerical density data. All these difficulties are circumvented in a more advanced application of the AFDF approach relying directly on the fragment density matrices $\mathbf{P}^k(\boldsymbol{\varphi}(K_k))$. This is accomplished by the *Adjustable Density Matrix Assembler* (ADMA) method [44–61], generating a macromolecular density matrix $\mathbf{P}(\boldsymbol{\varphi}(K))$ that can be used for the computation of a variety of molecular properties besides ab initio quality macromolecular electron densities.

When comparing the two methods in electron density computations, the accuracy of the ADMA macromolecular density matrix $\mathbf{P}(\boldsymbol{\varphi}(K))$ corresponds to that of a MEDLA result of an infinite resolution numerical grid.

Within the ADMA method the construction of the macromolecular density matrix is the simplest if the fragment density matrices $\mathbf{P}^k(\boldsymbol{\varphi}(K_k))$ obtained from small parent molecules M_k fulfill the following mutual compatibility requirements:

- (a) The local coordinate systems of AO basis sets of all the fragment density matrices $\mathbf{P}^k(\boldsymbol{\varphi}(K_k))$ have axes that are parallel and have matching orientations with the axes of a common reference coordinate system defined for the macromolecule.
- (b) The nuclear families used in the fragmentation of both the target and the parent molecules are compatible in the following sense: each parent molecule M_k may contain only complete nuclear families from the sets of nuclear families $f_1, f_2, \dots, f_k, \dots, f_m$, present in the large target molecule M . Within each parent molecule additional nuclei, usually H atoms may be involved in order to provide linkages to dangling bonds at the peripheries of these molecules.

As it has been shown, a simple similarity transformation of a fragment density matrix $\mathbf{P}^k(\boldsymbol{\varphi}(K_k))$ using a suitable orthogonal transformation matrix $\mathbf{T}^{(k)}$ of the AO sets, and an appropriate choice of nuclear families f_k for the various fragments within the macromolecule M and within the “coordination shells” of parent molecules M_k can always ensure the fulfillment of these conditions.

The outlined AFDF approach enhanced with these mutual compatibility conditions is referred to as the MC-AFDF approach.

In order to organize the interrelations between various orbital indices within various lists, some notations have been introduced.

The number of AOs in the nuclear family f_k of the target macromolecule M is denoted by n_k . For each pair $(f_k, f_{k'})$ of nuclear families a quantity $c_{k'k}$ is defined:

$$c_{k'k} = \begin{cases} 1, & \text{if nuclear family } f_{k'} \text{ is present in parent molecule } M_k \\ 0 & \text{otherwise,} \end{cases} \quad (6-13)$$

A given AO $\varphi(\mathbf{r})$ is denoted by the symbol $\varphi_{b,k'}(\mathbf{r})$ if its serial number b in the AO set

$$\{\varphi_{a,k'}(\mathbf{r})\}_{a=1, n_{k'}} \quad (6-14)$$

of nuclear family $f_{k'}$ is emphasized. However, the same AO $\varphi(\mathbf{r})$ is denoted by $\varphi_j^k(\mathbf{r})$, if its serial index j in the basis set

$$\left\{ \varphi_i^k(\mathbf{r}) \right\}_i = 1, n_{pk} \quad (6-15)$$

of the k -th fragment density matrix $\mathbf{P}^k(\varphi(K_k))$ is emphasized, where the total number of these AOs is n_{pk} ,

$$n_{pk} = \sum_{k'=1}^m c_{k'/k} n_{k'}. \quad (6-16)$$

Yet, the same AO $\varphi(\mathbf{r})$ is denoted by $\varphi_y(\mathbf{r})$ if its serial index y in the AO set

$$\{\varphi_x(\mathbf{r})\}_{x=1,n} \quad (6-17)$$

of the density matrix $\mathbf{P}(K)$ of the target macromolecule M is emphasized, where for each AO $\varphi_{a,k'}(\mathbf{r}) = \varphi_i^k(\mathbf{r}) = \varphi_x(\mathbf{r})$, the index x is determined by the index a in family k' as follows:

$$x = x(k', a, f) = a + \sum_{b=1}^{k'-1} n_b, \quad (6-18)$$

In index $x(k', a, f)$ the last entry f indicates that k' and a refer to a nuclear family.

In order to be able to determine the index x from the element index i and serial index k of fragment density matrix $\mathbf{P}^k(\varphi(K_k))$, three quantities are introduced for each index k and nuclear family $f_{k''}$ for which $c_{k''k} \neq 0$:

$$a'_k(k'', i) = i + \sum_{b=1}^{k''} n_b c_{bk}, \quad (6-19)$$

$$k' = k'(i, k) = \min\{k'' : a'_k(k'', i) \leq 0\}, \quad (6-20)$$

and

$$a_k(i) = a'_k(k', i) + n_{k'}. \quad (6-21)$$

As follows from the above, the AO index $x = x(k, i, P)$ in the density matrix $\mathbf{P}(K)$ of target molecule M depends on indices i and k and can be expressed using index k' and the function $x(k', a, f)$

$$x = x(k, i, P) = x(k', a_k(i), f), \quad (6-22)$$

where the last entry P in the index function $x(k, i, P)$ indicates that k and i refer to the fragment density matrix $\mathbf{P}^k(\varphi(K_k))$.

If one uses only the nonzero elements of each (usually rather sparse) fragment density matrix $\mathbf{P}^k(\varphi(K_k))$, then the macromolecular density matrix $\mathbf{P}(K)$ is assembled by the following iterative procedure,

$$P_{x(k,i,P),y(k,j,P)}(K) = P_{x(k,i,P),y(k,j,P)}(K) + P_{ij}^k(K_k) \quad (6-23)$$

Since the parent molecules M_k are of limited size, their computation requires computer time that has some upper bound, and the entire procedure depends linearly on the number of fragments and on the size of the target macromolecule M .

Due to its construction, the macromolecular density matrix $\mathbf{P}(K)$ is also a sparse matrix that simplifies its storage and subsequent computations. Using the macromolecular AO basis (that is stored according to a list of appropriate indices referring to a standard list of AO basis sets), the macromolecular electron density is computed according to Eq. (6-2). Using the ADMA method, approximate macromolecular forces and other properties expressible in terms of density matrices can be computed for virtually any molecule, providing a computationally viable approach to macromolecular quantum chemistry.

6.7. COMBINATORIAL QUANTUM CHEMISTRY BASED ON LINEAR SCALING FRAGMENTATION

A macromolecular computational method using electron density fragments to build a model for a large molecule is reminiscent to synthetic methods using smaller structural units and combining them into a larger structure. It is natural then to consider such modeling methods in the context of combinatorial chemistry and to regard these methods as computational realizations of combinatorial quantum chemistry.

The powerful innovation of chemical synthesis called Combinatorial Chemistry, in its first form applicable to the combinatorial synthesis of large numbers of molecules, was invented in 1982 by Arpad Furka [67–70]. The idea of using combinatorial approaches to the production of very large numbers of molecules from specific building blocks has revolutionized synthetic chemistry; for some of the latest advances see Refs. [71–74]. It is not an accident that peptide chemistry was so important in the discovery: the original “portioning – mixing method for the synthesis of combinatorial libraries” by Furka, and subsequent variations on the basic combinatorial chemistry principle were applied primarily to peptides, using individual amino acids as building blocks. Later, these methodologies have also been adapted to other types of molecules and to a much broader family of potential building blocks linked up according to some combinatorial patterns. The advances of combinatorial chemistry and related methods have revolutionized the approaches used by the pharmaceutical industry for the production and selection of new molecules for tests and for the optimization of the pharmacological effectiveness of potential drug molecules.

Although there has been no direct connections, it is an interesting coincidence that within computational quantum chemistry a similar advance has occurred recently. One of the earliest such developments has occurred with the introduction of the MEDLA method [38–43], where fuzzy electron density building blocks have been used within a numerical approach (based on a three-dimensional numerical

grid) to construct electron densities for macromolecules, such as proteins. By a suitable choice of the fuzzy electron density fragments, these building blocks can be combined in a variety of ways, using combinatorial principles, leading to the construction of a large number of molecular electron densities. The development of computer technology apparently provides novel options: if the density construction is carried out using parallel processors, relying on a common fuzzy electron density fragment database, then the combinatorial construction of the electron densities of a large number of molecules can be achieved simultaneously. Such a computational approach is analogous with the synthetic combinatorial chemistry approach. In fact, this approach is an “in silico” version of the original idea of Furka, and the fact that there is no need either for “portioning” or “mixing”, provides important simplifications.

As mentioned above, the MEDLA numerical grid technique was limited to electron density computations in numerical representations, where the variations in local grid alignments when combining two or more fuzzy electron density fragments had disadvantageous effects on the accuracy of the approach. In addition, the MEDLA approach was sensitive to the resolution of the numerical grid, that was important not only in visual displays, but in the very construction process of the numerical electron densities of larger molecules.

The more advanced ADMA (Adjustable Density Matrix Assembler) method [44–61], achieves the combination of fuzzy electron density fragments by building first a macromolecular density matrix from the fuzzy fragment density matrices. In fact, the actual combinatorial step is carried out on the fuzzy fragment density matrices. This matrix representation has several advantages. First, the electron density representation is analytical, relying on the macromolecular density matrix and the associated basis set information, consequently, neither grid alignment problems nor grid resolution problems of the MEDLA method can occur. In addition, with an available macromolecular density matrix, many molecular properties beyond electron density can be calculated, for example, approximate forces acting on individual nuclei of the macromolecule can also be determined, where these forces are suitable for a study of the folding problems in proteins, as well as other conformational problems in various additional macromolecules..

By the construction of a fragment density matrix databank, the ADMA approach can be used for the combinatorial selection and subsequent assembly of fuzzy fragment density matrices, forming approximate density matrices for a large number of macromolecules, where these macromolecules are related to one another by some combinatorial reassignment of local molecular fragments. The resulting approximate macromolecular density matrices are suitable for both electron density computations and for the computation of all other properties determined by density matrices and basis set information. Consequently, the ADMA method provides a versatile basis for a Combinatorial Quantum Chemistry (CQC) approach to novel, systematic modeling studies involving large number of macromolecules. The computational toolbox of fundamental structural biochemistry and biotechnology research will be enhanced by this approach, the ADMA-CQC approach.

There are three main strategies for taking advantage of the computational aspects of the Combinatorial Fragment Assembly Approach:

- (i) No fragment readjustment of databank entries
If one is interested in a fast and only approximate description of a set of combinatorially related target macromolecules, and if there is no need for high accuracy, than fuzzy density fragments taken from a sufficiently detailed fragment density matrix databank might be used directly. If the databank already contains several variants for typical density matrices needed for these macromolecules, where the fragment variants differ in local nuclear geometries and coordination shells, then the optimum choice for each fragment density matrix from the databank, followed by a combinatorial assembly of the required set of related macromolecules is probably suitable to generate a reasonable approximation of the series of macromolecular density matrices and the associated molecular properties.
- (ii) Fuzzy fragment deformation by nuclear rearrangement
In various cases a somewhat higher accuracy is required, and even the optimum fragment density matrices taken from the databank are not accurate enough for the given purpose. In that case the simplest solution is achieved by a simple readjustment of the optimum density matrices from the databank. The most advantageous method for this readjustment is the Löwdin Transform method [48, 57], that converts one density matrix to another one that approximates the density matrix computed at a slightly different nuclear geometry. The Löwdin Transform method also has the advantage of ensuring idempotency for the newly constructed density matrix.
- (iii) Fuzzy fragment recalculation using a new, custom made parent molecule
This approach is not only the most accurate but also the most costly, as it involves a complete recalculation of the fragment density matrix for the actual nuclear geometry and coordination shell, to match those in the actual target macromolecule *M*. One important advantage is the fact that the newly calculated fragment density matrix can be added to the databank, hence it is potentially also beneficial for a possible future calculation, and makes the databank more applicable on the next occasion, even if one then decides to use options (i) or (ii).

In conclusion, if a sufficiently detailed fuzzy density fragment databank is already available, then by choosing the appropriate level of fragment density matrix selection and readjustment, the ADMA-CQC method is applicable for the rapid generation of ab initio quality quantum chemical representations of a large number of macromolecules.

6.8. SUMMARY

Some of the fundamental constraints and some actual realizations of linear scaling quantum chemical approaches have been reviewed, with special emphasis on the emerging field of Combinatorial Quantum Chemistry.

REFERENCES

1. Mulliken RS (1955) Electronic population analysis on LCAO-MO molecular wave functions. I. *J Chem Phys* 23:1833–1840
2. Mulliken RS (1955) Electronic population analysis on LCAO-MO molecular wave functions. II. Overlap populations, bond orders, and covalent bond energies. *J Chem Phys* 23:1841–1846
3. Mulliken RS (1955) Electronic population analysis on LCAO-MO molecular wave functions. III. Effects of hybridization on overlap and gross AO populations. *J Chem Phys* 23:2338–2342
4. Mulliken RS (1955) Electronic population analysis on LCAO-MO molecular wave functions. IV. Bonding and antibonding in LCAO and valence-bond theories. *J Chem Phys* 23:2343–2346
5. Löwdin P-O (1970) On the orthogonality problem. *Adv Quantum Chem* 5:185–199
6. Hartree DR (1928) The wave mechanics of an atom with a non-coulomb central field. Part I. Theory and methods. *Math Proc Camb Philol Soc* 24:89–110
7. Hartree DR (1928) The wave mechanics of an atom with a non-coulomb central field. Part II. Some results and discussion. *Math Proc Camb Philol Soc* 24:111–132
8. Hartree DR (1928) The wave mechanics of an atom with a non-coulomb central field. Part III. Term values and intensities in series in optical spectra. *Math Proc Camb Philol Soc* 24:426–437
9. Hartree DR (1929) The wave mechanics of an atom with a non-coulomb central field. Part IV. Further results relating to terms of the optical spectrum. *Math Proc Camb Philol Soc* 25:310–314
10. Fock V (1930) Naheerungsmethode zur Loesing des quantenmechanischen Mehrkoerperproblems. *Z Phys* 61:126–148
11. Roothaan CC (1951) New developments in molecular orbital theory. *Rev Mod Phys* 23:69–89; *ibid.* (1960) 32, 179
12. Hall GG (1951) The molecular orbital theory of chemical valency. VIII. A method of calculating ionization potentials. *Proc Roy Soc London A*205:541–552
13. Pilar FL (1968) *Elementary quantum chemistry*. McGraw-Hill, New York, NY
14. Szabo A, Ostlund NS (1996) *Modern quantum chemistry: introduction to advanced electronic structure theory*. Dover, Mineola, NY
15. Boys SF (1960) Construction of some molecular orbitals to be approximately invariant for changes from one molecule to another. *Rev Mod Phys* 32:296–299
16. Edmiston C, Ruedenberg K (1963) Localized atomic, molecular orbitals. *Rev Mod Phys* 35:457–464
17. Pipek J, Mezey PG (1989) A fast intrinsic localization procedure applicable for ab initio and semiempirical LCAO wavefunctions. *J Chem Phys* 90:4916–4926
18. Pipek J, Mezey PG (1988) Dependence of MO shapes on a continuous measure of delocalization. *Int J Quantum Chem Symp* 22:1–13
19. Kryachko ES, Ludena EV (1989) *Density functional theory of many-electron systems*. Kluwer, Dordrecht
20. Parr R, Yang W (1989) *Density-functional theory of atoms and molecules*. Oxford University Press, New York, NY
21. Yang W (1991) Direct calculation of electron density in density-functional theory. *Phys Rev Lett* 66:1438–1441
22. Yang W (1991) Direct calculation of electron density in density-functional theory: implementation for benzene and a tetrapeptide. *Phys Rev A* 44:7823–7826
23. Yang W (1992) Electron density as the basic variable: a divide-and-conquer approach to the ab initio computation of large molecules. *J Mol Struct (THEOCHEM)* 255:461–479
24. Lee C, Yang W (1992) The divide-and-conquer density-functional approach: molecular internal rotation and density of states. *J Chem Phys* 96:2408–2411

25. Hohenberg P, Kohn W (1964) Inhomogeneous electron gas. *Phys Rev* 136:B864–B871
26. Levy M (1979) Universal variational functionals of electron densities, first-order density matrices, and natural spin-orbitals and solution of the v -representability problem. *Proc Natl Acad Sci USA* 76:6062–6065
27. Levi M (1982) Electron densities in search of hamiltonians. *Phys Rev A* 26:1200–1208
28. Levy M (1990) Constrained-search formulation and recent coordinate scaling in density functional theory. *Adv Quantum Chem* 21:69–79
29. Riess J, Munch W (1981) The theorem of Hohenberg and Kohn for subdomains of a quantum system. *Theor Chim Acta* 58:295–300
30. Mezey PG (1999) The holographic electron density theorem and quantum similarity measures. *Mol Phys* 96:169–178
31. Mezey PG (1998) Generalized chirality and symmetry deficiency. *J Math Chem* 23:65–84
32. Mezey PG (1999) Holographic electron density shape theorem and its role in drug design and toxicological risk assessment. *J Chem Inf Comp Sci* 39:224–230
33. Mezey PG (2001) The holographic principle for latent molecular properties. *J Math Chem* 30:299–303
34. Mezey PG (2001) A uniqueness theorem on molecular recognition. *J Math Chem* 30:305–313
35. Mezey PG (2007) A fundamental relation of molecular informatics: information carrying properties of density functions. *CCCC (Collection of Czechoslovak Chemical Communications)* 72:153–163 (Volume dedicated to Prof. Koutecky)
36. Zadeh LA (1977) Theory of fuzzy sets. In: *Encyclopedia of computer science and technology*, Marcel Dekker, New York, NY
37. Klir GJ, Yuan B (1995) *Fuzzy sets and fuzzy logic, theory and applications*. Prentice-Hall, Englewood Cliffs, NJ
38. Walker PD, Mezey PG (1993) Molecular electron density lego approach to molecule building. *J Am Chem Soc* 115:12423–12430
39. Walker PD, Mezey PG (1994) Ab initio quality electron densities for proteins: a medla approach. *J Am Chem Soc* 116:12022–12032
40. Walker PD, Mezey PG (1994) Realistic, detailed images of proteins and tertiary structure elements: ab initio quality electron density calculations for bovine insulin. *Can J Chem* 72:2531–2536
41. Walker PD, Mezey PG (1995) A new computational microscope for molecules: high resolution medla images of taxol and hiv-1 protease, using additive electron density fragmentation principles and fuzzy set methods. *J Math Chem* 17:203–234
42. Walker PD, Mezey PG (1995) Towards similarity measures for macromolecular bodies: MEDLA test calculations for substituted benzene systems. *J Comput Chem* 16:1238–1249
43. Mezey PG, Walker PD (1997) Fuzzy molecular fragments in drug research. *Drug Discov Today (Elsevier Trend Journal)* 2:6–11
44. Mezey PG (1995) Shape analysis of macromolecular electron densities. *Struct Chem* 6:261–270
45. Mezey PG (1995) Macromolecular density matrices and electron densities with adjustable nuclear geometries. *J Math Chem* 18:141–168
46. Mezey PG (1996) Local shape analysis of macromolecular electron densities. In: Leszczynski J (ed) *Computational chemistry: reviews and current trends*, vol 1. World Scientific Publishing, Singapore, pp 109–137
47. Mezey PG (1996) Functional groups in quantum chemistry. *Adv Quantum Chem* 27:163–222
48. Mezey PG (1997) Quantum similarity measures and Löwdin's transform for approximate density matrices and macromolecular forces. *Int J Quantum Chem* 63:39–48
49. Mezey PG (1997) Computational microscopy: pictures of proteins. *Pharmaceutical News* 4:29–34
50. Mezey PG (1997) Quantum chemistry of macromolecular shape. *Int Rev Phys Chem* 16:361–388
51. Mezey PG (1998) A crystallographic structure refinement approach using ab initio quality additive fuzzy density fragments. *Adv Molec Structure Res* 4:115–149

52. Mezey PG (1999) Combinatorial aspects of biomolecular shape analysis. *Bolyai Soc Math Stud* 7:323–332
53. Mezey PG (1999) Relations between computational and experimental engineering of molecules from molecular fragments. *Molec Eng* 8:235–250
54. Mezey PG (1999) Local electron densities and functional groups in quantum chemistry. In: Surjan PR (ed) *Correlation and localization. Topics in current chemistry*, vol. 203. Springer, Heidelberg; Berlin, New York, NY, pp 167–186
55. Mezey PG (2000) Transferability, adjustability, and additivity of fuzzy electron density fragments. In: Mezey PG, Robertson B (eds) *Electron, spin, and momentum densities and chemical reactivity*. Kluwer Academic, Dordrecht, The Netherlands, pp 45–69
56. Mezey PG (2001) Computational aspects of combinatorial quantum chemistry. *J Comput Methods Sci Eng (JCMSE)* 1:99–106
57. Exner TE, Mezey PG (2002) A comparison of nonlinear transformation methods for electron density approximation. *J Phys Chem A* 106:5504–5509
58. Exner TE, Mezey PG (2002) Ab initio quality electrostatic potentials for proteins: an application of the ADMA approach. *J Phys Chem A* 106:11791–11800
59. Exner TE, Mezey PG (2003) Ab initio quality properties for macromolecules using the ADMA approach. *J Comput Chem* 24:1980–1986
60. Exner TE, Mezey PG (2004) The field-adapted ADMA approach: introducing point charges. *J Phys Chem* 108:4301–4309
61. Szekeres Zs, Exner TE, Mezey PG (2005) Fuzzy fragment selection strategies, basis set dependence, and HF – DFT comparisons in the applications of the ADMA method of macromolecular quantum chemistry. *Int J Quantum Chem* 104:847–860
62. Bader RFW (1990) *Atoms in molecules: a quantum theory*. Clarendon Press, Oxford
63. Mezey PG (1990) Topological quantum chemistry. In: Weinstein H, Naray-Szabo G (eds) *Reports in molecular theory*, CRC Press, Boca Raton
64. Mezey PG (1990) Three-dimensional topological aspects of molecular similarity. In: Johnson MA, Maggiora GM (eds) *Concepts and applications of molecular similarity*, Wiley, New York, NY
65. Mezey PG (1995) Density domain bonding topology and molecular similarity measures. In: Sen K (ed) *Molecular similarity, topics in current chemistry*, vol. 173. Springer, Heidelberg
66. Mezey PG (1995) Methods of molecular shape-similarity analysis and topological shape design. In: Dean PM (ed) *Molecular similarity in drug design*, Chapman & Hall–Blackie Publishers, Glasgow
67. Furka A (1982) Notarized Notes. see <http://www.win.net/kunagota>, <http://szerves.chem.elte.hu/furka>
68. Furka A, Sebestyen F, Asgedom M, Dibo G (1988) Cornucopia of peptides by synthesis. *Abstracts 14th International Congress Biochemistry, Prague, Czechoslovakia* 5:47–52
69. Furka A, Sebestyen F, Asgedom M, Dibo G (1991) General method for rapid synthesis of multicomponent peptide mixtures. *Int J Peptide Protein Res* 37:487–493
70. Furka A (2002) Combinatorial chemistry: 20 years on. . . . *Drug Discov Today* 7:1–7
71. Darvas F, Dorman G, Urge L, Szabo I, Ronai Z, Sasvari-Szekely M (2001) Combinatorial chemistry. Facing the challenge of chemical genomics. *Pure Appl Chem* 73:1487–1498
72. Darvas F, Dorman G, Papp A (2000) Diversity measures for enhancing ADME admissibility of combinatorial libraries. *J Chem Inf Comput Sci* 40:314–322
73. Jones RV, Godorhazy L, Varga N, Szalay D, Urge L, Darvas F (2006) Continuous-flow high pressure hydrogenation reactor for optimization and high-throughput synthesis. *J Comb Chem* 8:110–116
74. Darvas F, Keseru G, Papp A, Dorman G, Urge L, Krajcsi P (2002) In silico ex silico ADME approaches for drug discovery. *Curr Top Med Chem* 2:1287–1304
75. Mezey PG (1987) *Potential energy hypersurfaces*. Elsevier, Amsterdam
76. Mezey PG (1993) *Shape in chemistry: an introduction to molecular shape and topology*. VCH Publishers, New York, NY

CHAPTER 7

FRAGMENTATION SELECTION STRATEGIES IN LINEAR SCALING METHODS

ZSOLT SZEKERES¹ AND PAUL G. MEZEY²

¹ *Laboratory of Theoretical Chemistry, Institute of Chemistry, Eotvos University of Budapest, H-1518 Budapest, Hungary, e-mail: zsolt.szekeres@gmail.com*

² *Canada Research Chair in Scientific Modeling and Simulation, Editor, Journal of Mathematical Chemistry, Department of Chemistry and Department of Physics and Physical Oceanography, Memorial University of Newfoundland, St. John's, NL, Canada A1B 3X7, e-mail: paul.mezey@gmail.com*

Abstract: The chemical motivation and the role of molecular fragmentation schemes in various linear scaling quantum chemical computational methods are discussed, with special emphasis on fragmentation based on the properties of molecular electron densities. The special significance of functional groups in fragment selection, the concept and use of delocalized fragments, the “Procrustes Fragmentation” and “Multi-Procrustes Fragmentation” schemes, and the utility of trigonometric weighting in reducing potential errors due to the bias introduced by fragment selection are discussed. The special fragmentation possibilities implied by the Additive Fuzzy Density Fragmentation Principle, and their application in the context of the Adjustable Density Matrix Assembler (ADMA) method are also discussed.

Keywords: Molecular fragments, Functional groups, Delocalized fragments, Procrustes fragmentation, Multi-Procrustes fragmentation, Trigonometric weighting, Additive fuzzy density fragmentation principle, Adjustable density matrix assembler (ADMA)

7.1. INTRODUCTION

Most linear scaling methods rely on a threshold for the interactions which are to be included in the model; often this translates into giving special consideration to local ranges within molecules. Such local ranges can be regarded as molecular fragments, hence, fragmentation ideas have important role in various linear scaling approaches. The way these fragments are defined and their actual choices have important implications on the actual algorithms used and the success of the actual linear scaling method. Some of the motivation for the development of rational fragmentation methods originates from the need for reasonably accurate representations of electron densities of important biomolecules, such as hemoglobin [1], where the

special role of fairly rigid molecular entities (such as the heme structure) indicates that compromises may be required between actual, “custom made” fragment selection approaches, and the considerations of some more general, somewhat overly optimistic “universal” fragment selection principles.

7.2. CHEMICALLY MOTIVATED FRAGMENT SELECTION

Since the pioneering work of Mulliken, the ultimate fragmentation scheme, atomic fragmentation, is the basis of many molecular fragmentation schemes within both the Molecular Orbital and Density Functional formalisms. Mulliken’s LCAO principle, leading, for example, to the still very useful Population Analysis techniques [2–5] reflects both a reductionist and a synthetic approach: using local representations, such as Atomic Orbitals, which are eventually combined, or, in fact synthesized into Molecular Orbitals. The global aspects of electron densities, and the special conditions constraining, but not invalidating various fragmentation approaches are well represented by the fundamental relations of Density Functional theory [6–11], especially by the main theorem relevant to electron densities: the Hohenberg-Kohn Theorem [6]. According to this theorem the non-degenerate ground state electron density determines all molecular properties, hence, in a special way, also the “best” fragmentation scheme with respect to a physically realistic computational scheme. Such a scheme must reflect reality even in the following sense: a technical detail, such as the optimality of fragment selection, must also be ultimately dependant on the actual electron density.

Of course, there are many other, also chemically motivated fragment selection possibilities, where groups of atoms within the molecules may be regarded, in the first approximation, as the fragments. Even in such a case, the interplay between local features and their global constraints is of great importance. For artificial models of molecules, confined to a finite and closed range of the three-dimensional space, Munch and Riess have proved an important result [12] that for such systems with boundary, any local electron density range of positive volume determines the electron density within the entire closed and bounded range of space. Although the authors, Riess and Munch have pointed out themselves that their proof holds only for closed and bounded models of molecules, hence not for real molecules which are neither closed systems nor bounded within any finite domain of the three-dimensional space, nevertheless, this aspect of their work has not always been correctly interpreted by other researchers.

By applying a four-dimensional transformation of the molecular electron density to a hypersphere of three-dimensional surface, followed by a step involving a one-point compactification method, Mezey has proved in a later contribution [13] that molecular electron densities follow a holographic principle, and the limitation of the results of Riess and Munch can be circumvented. The resulting Holographic Electron Density Theorem states: for the non-degenerate ground state electron density of any molecule, any positive volume local part of the electron density contains the complete information about the entire molecular electron density, hence, this

local range contains the complete information about all properties of the entire molecule [13]. This Holographic Electron Density Theorem can be regarded as an addition to the Hohenberg-Kohn Theorem [6]; it has several interesting consequences for local symmetry and approximate transferability of molecular fragments [13–18], and in particular, consequences for molecular fragmentation schemes.

Procedures for molecular fragmentation schemes usually rely on some chemically motivated principles. Fragments may provide specific insight to functionality, for example, in a macromolecule like haemoglobin, it is natural to regard the heme region as one of the fragments, since this region is one that is primarily responsible for the main function of this protein: catching Oxygen molecules.

In some other instances, chemical motivation appears to provide more fundamental, or technical conditions.

One condition for a molecular fragmentation approach that provides useful analogies between molecular fragments and complete molecules is the requirement for avoiding cuts and sharp boundaries in the fragment generation process. Real molecules show an eventually exponential decay of the electron density values as one moves away from the molecular center beyond all the nuclei of the molecule, and the treatment of fragments within any model can be made more similar to the treatment of complete molecules if the fragments themselves show a similar, eventually exponential decay of electron density with distance as the position vector moves beyond the nuclei, far away from the center of the molecular fragment.

One such fragmentation scheme is the Additive Fuzzy Density Fragmentation (AFDF) approach [19–22], which may be regarded as a variation of the population analysis approach of Mulliken [2–5], where the integration step that converts the individual molecular orbital contributions to electron density into a formal atomic charge is avoided.

The details of the implementation of this fragmentation approach are described in the original references and have been reviewed elsewhere, here we shall provide only a brief summary, primarily for the purposes of specification of notations.

Within the Hartree-Fock-Roothaan-Hall SCF LCAO ab initio scheme, using a given basis set $\varphi(\mathbf{K})$ of atomic orbitals $\varphi_i(\mathbf{r}, \mathbf{K})$ ($i = 1, 2, \dots, n$), and the $n \times n$ dimensional density matrix $\mathbf{P}(\varphi(\mathbf{K}))$, obtained by such calculations, the electronic density $\rho(\mathbf{r}, \mathbf{K})$ of a molecule of nuclear conformation \mathbf{K} is given at each point \mathbf{r} by

$$\rho(\mathbf{r}, \mathbf{K}) = \sum_{i=1}^n \sum_{j=1}^n P_{ij}(\varphi(\mathbf{K})) \varphi_i(\mathbf{r}, \mathbf{K}) \varphi_j(\mathbf{r}, \mathbf{K}). \quad (7-1)$$

The set of nuclei of the molecule M are classified into m mutually exclusive families

$$f_1, f_2, \dots, f_k, \dots, f_m. \quad (7-2)$$

With respect each nuclear family f_k , a membership function $m_k(i)$ is defined for each AO basis function $\varphi_i(\mathbf{r}, \mathbf{K})$ as follows:

$$m_k(i) = \begin{cases} 1 & \text{if } \varphi_i(\mathbf{r}) \text{ is centered on one of the nuclei of set } f_k, \\ 0 & \text{otherwise.} \end{cases} \quad (7-3)$$

The elements $P_{ij}^k(\varphi(K))$ of the $n \times n$ fragment density matrix $\mathbf{P}^k(\varphi(K))$ for the k -th fragment “anchored” to the nuclear family k are given by

$$P_{ij}^k(\varphi(K)) = [m_k(i)w_{ij} + m_k(j)w_{ji}]P_{ij}(\varphi(K)), \quad (7-4)$$

where the w_{ij} and w_{ji} weighting factors must fulfill the condition

$$w_{ij} + w_{ji} = 1, \quad w_{ij}, w_{ji} > 0, \quad (7-5)$$

with the simplest choice of

$$w_{ij} = w_{ji} = 0.5 \quad (7-6)$$

leading to the Mulliken-Mezey AFDF approach that follows the spirit of Mulliken’s original population analysis scheme.

The k -th additive fuzzy density fragment $\rho^k(\mathbf{r}, K)$ is then defined as

$$\rho^k(\mathbf{r}, K) = \sum_{i=1}^n \sum_{j=1}^n P_{ij}^k(\varphi(K)) \varphi_i(\mathbf{r}, K) \varphi_j(\mathbf{r}, K), \quad k = 1, 2, \dots, m. \quad (7-7)$$

As it is easily verified by simple substitution, both the AFDF fragment density matrices $\mathbf{P}^k(\varphi(K))$ and the corresponding fuzzy density fragments $\rho^k(\mathbf{r}, K)$ are strictly additive:

$$\mathbf{P}(\varphi(K)) = \sum_{k=1}^m \mathbf{P}^k(\varphi(K)), \quad (7-8)$$

and

$$\rho(\mathbf{r}, K) = \sum_{k=1}^m \rho^k(\mathbf{r}, K). \quad (7-9)$$

A good approximation to the fuzzy electron density fragments of a large “target” molecule M can be computed indirectly using the AFDF approach, using smaller “parent” molecules, containing various parts of the original large molecule.

Specifically, for each nuclear family f_k of M , a small parent molecule M_k can be designed, where M_k contains the same nuclear family f_k with the same local arrangement and surroundings as is found in the large target molecule M . The fuzzy density matrix fragmentation (7–4) can be carried out for the small parent molecule M_k , resulting in a fuzzy density fragment $\rho^k(\mathbf{r}, K)$ corresponding to the nuclear set f_k , and other, additional density fragments which are not going to be used for the macro-molecular study. For each nuclear family f_k of M , one may repeat this procedure, and the fuzzy fragment density matrices,

$$\mathbf{P}^1(\varphi(K)), \mathbf{P}^2(\varphi(K)), \dots, \mathbf{P}^k(\varphi(K)), \dots, \mathbf{P}^m(\varphi(K)) \quad (7-10)$$

as well as the fuzzy density fragments

$$\rho^1(\mathbf{r},\mathbf{K}), \rho^2(\mathbf{r},\mathbf{K}), \dots, \rho^k(\mathbf{r},\mathbf{K}), \dots, \rho^m(\mathbf{r},\mathbf{K}) \quad (7-11)$$

obtained from the set of m small “parent” molecules

$$M_1, M_2, \dots, M_k, \dots, M_m, \quad (7-12)$$

can be combined and used to construct good approximations to the macromolecular density matrix $\mathbf{P}(\boldsymbol{\varphi}(\mathbf{K}))$ and the electron density $\rho(\mathbf{r},\mathbf{K})$ of the large target molecule M . The fragment densities themselves can also be used for local analysis of various parts of the macromolecule M , for example, studying various functional groups.

The first applications of this Mulliken-Mezey fragmentation scheme [19–22] within the Hartree-Fock-Roothaan-Hall framework [23–29] were implemented in the two linear scaling methods: Molecular Electron Density Loge Assembler (MEDLA) and the Additive Density Matrix Assembler (ADMA) methods [20–22, 30–38]. The former, numerical method used the computed electron densities (7-11) directly, the more advanced ADMA method uses the computed density matrix, Eq. (7-8).

7.3. FUNCTIONAL GROUPS AS PRIMARY FRAGMENTS

Among the chemically motivated fragmentation schemes, one based on the concept of functional groups is of special importance. Traditionally, functional groups are characterized by nearly identical local structural features and nearly identical reactivities.

On the other hand, the quantum chemical concept of functional groups [39,40] is based on the local properties of electron densities. If a set of nuclei within a molecule is surrounded by an electron density isocontour, then their situation is reminiscent to that of nuclei of one complete molecule placed near, but not yet in any bonding arrangement next to another molecule. The combined electron density cloud of the two molecules must have electron density isocontours which surround all the nuclei of one molecule, without enclosing any of the nuclei of the second molecule. We may regard this condition as a sign of some level of “autonomy” of the nuclei and the surrounding electron density cloud of the first molecule, since the interactions mediated by the electron density among the set of the nuclei of the first molecule are stronger than the interactions mediated by the electron density between the two molecules. The identity and the “autonomy” of the molecules are not yet diminished to any major proportions by placing the molecules into such a relative position.

The same type of argument can also be used within a single molecule, by considering parts of molecules where within one part the local interactions are such that some limited “autonomy” and some “local identity” of the part distinguishes it from other parts of the molecule. If within a single molecule there exists an electron density isocontour that separates one set of nuclei from the rest of the nuclei of the

molecule, then one may regard this set of nuclei and the surrounding electron density cloud as some entity within the molecule where some level of separate identity is meaningful. By applying this concept to actual functional groups, the presence of such isocontours have been confirmed in all the studied instances. Apparently, functional groups do possess special significance, manifested by some electron density isocontours indicated by some degree of limited autonomy within the molecule [39,40]. Note, however, that the above condition also classifies atom groupings as formal, quantum chemical functional groups even if they are not commonly considered as such by more conventional organic chemistry considerations. In the extreme case, most single atoms can be classified as some extreme functional groups, since in most molecules they do possess electron density isocontours separating their nuclei from all the other nuclei of the molecule. Of course, individual atoms can be regarded, even traditionally, as the extreme case of functional groups.

7.4. DELOCALIZED FRAGMENTS

Whereas it makes good sense to chose chemically motivated fragments, such as functional groups [39,40], the Mulliken-Mezey fragmentation scheme does not restrict the fragment choices this way, in fact, by selecting nuclear families (7.2) arbitrarily, the fragmentation scheme remains valid, even if the nuclei in any one family are such that there are no formal bonds between the corresponding “atoms” within the molecule. Such examples have been obtained in early applications, for example, where a bare benzene ring was one of the formal fragments, and five of the H atoms on the ring as another fragment, where this latter single fragment involved five, non-connected nuclei from the molecule. Such delocalized fragments provide considerable flexibility for analysis, and provides direct tools for testing ideas concerning suspected unusual interactions in large molecules. One such problem arises if one is to study the low density ranges, called “Low Density Glue”, within the interior of globular macromolecules, such as some proteins. These studies provide some input to the study of the problem of protein folding. Similarly, the extreme case of single nucleus families have been also used in early test computations [30–38].

7.5. PROCRUSTES FRAGMENTATION

If purely technical aspects of fragmentations are considered, one extreme approach involves complete disregard of chemical properties and a fragmentation where purely geometrical conditions lead to the selection of nuclear families. The simplest of such schemes involves a three-dimensional rectangular grid, with cubic unit cells, and the selection of nuclear families by simply considering the nuclear classification provided by this grid. All nuclei falling within one such cube belong to one family. The main ideas of this approach have been described in ref. [33]. This approach, enforcing a fragmentation based solely on the location and size of the cubes of the grid, is reminiscent to the treatment Procrustes used in ancient Greece

on travellers who crossed his way, and the cubes of the grid are reminiscent to the famous Procrustes bed he used for truncating his visitors: whatever hangs out, it is cut.

Whereas this Procrustes fragmentation is algorithmically simple, it is usually far from optimal if the goal is high accuracy. In the next section we review briefly an extension of the approach that provides some improvement.

7.6. MULTI – PROCRUSTES FRAGMENTATION WITH TRIGONOMETRIC WEIGHTING

One enhancement of the accuracy of the Procrustes fragmentation as applied to ADMA and MEDLA electron densities is based on a method involving multiple tilings of the 3D space domain containing the target macromolecule, by introducing eight separate Procrustes partitionings. This approach is called the Multi-Procrustes approach.

The motivation for this approach is simple: in the process of partially overlapping the fuzzy fragment densities in the target molecule, the electron densities are rather accurate near the centers of the fragments and the more noticeable errors are expected at points at the peripheral ranges of each fragment, where the density contributions from neighboring fragments are approximately the same.

If one considers a rectangular compartmentalization of the nuclei of the target molecule, such as it is in the Procrustes method, then the errors of the ADMA and MEDLA densities are expected to be the largest near the boundaries of these compartments. We should be reminded that these compartment boundaries refer the partitioning of the nuclei of the molecule into boxes, and the actual electronic clouds of the fuzzy density fragments themselves have no boundaries, consequently, they extend beyond the nuclear compartment boundaries.

One approach to further increase the accuracy of the resulting macromolecular electron densities is to take several, different compartmentalizations of the nuclei, ensuring that each boundary point of each compartment becomes an interior point of another compartmentalization, hence a higher accuracy representation is available for those boundary points as well. Then, by properly weighting and combining the computed electron densities obtained from different compartmentalizations, a more accurate overall electron density representation can be computed for the target macromolecule.

Such an accuracy-enhancing scheme is obtained if eight Procrustes fragmentations are combined by a trigonometric weighting scheme, that ensures proper scaling for the various contributions. The approach involves an eightfold increase of the computational work, consequently, just as the ADMA and MEDLA methods themselves, the method is strictly linear scaling.

The actual Multi-Procrustes three-dimensional tiling approach, involves $2^3 = 8$ different tiling schemes, denoted by A, B, C, D, E, F, G, and H. These compartment sets A . . . H are chosen in such a way that each boundary point of each compartment is an interior point of another compartment in another of the eight tiling schemes.

The edge length of each cube is taken as π . The centers of cubes for the eight different tilings are given by the vectors

$$r'_{u,v,w}(i,j,k) = [(i + 0.5u)\pi, (j + 0.5v)\pi, (k + 0.5w)\pi], \quad (7-13)$$

where these A, B, C, D, E, F, G, and H tilings follow the lexicographic order of triples

(u, v, w), with the integers u, v, and w fulfilling the condition

$$0 \leq u, v, w \leq 1, \quad (7-14)$$

for example, the integer triple $u = 1, v = 0$ and $w = 1$ corresponds to tiling scheme F, and where indices i, j, and k refer to the serial numbers of the locations of the centers of the cubes along the x, y, and z coordinate axes, respectively.

The x, y, and z coordinates of the centers of all the cubes in the eight Procrustes tiling schemes are given below:

	A	B	C	D	E	F	G	H
x	$i\pi$	$i\pi$	$i\pi$	$i\pi$	$(i + 0.5)\pi$	$(i + 0.5)\pi$	$(i + 0.5)\pi$	$(i + 0.5)\pi$
y	$j\pi$	$j\pi$	$(j + 0.5)\pi$	$(j + 0.5)\pi$	$j\pi$	$j\pi$	$(j + 0.5)\pi$	$(j + 0.5)\pi$
z	$k\pi$	$(k + 0.5)\pi$	$k\pi$	$(k + 0.5)\pi$	$k\pi$	$(k + 0.5)\pi$	$k\pi$	$(k + 0.5)\pi$

(7-15)

The next step is to carry out an ADMA (or MEDLA) linear scaling computation of the macromolecule M for each of the eight tiling schemes A . . . H the usual way.

As a result, the eight direct ADMA electron densities by fragment generation using tilings A, B, C, D, E, F, G, and H are:

$$\rho_A(x, y, z), \rho_B(x, y, z), \rho_C(x, y, z), \rho_D(x, y, z), \rho_E(x, y, z), \rho_F(x, y, z), \rho_G(x, y, z), \text{ and } \rho_H(x, y, z), \text{ respectively} \quad (7-16)$$

Using these electron densities, a trigonometric weighting ensures, that each boundary location of each tile of each tiling scheme contributes by a factor of zero, whereas each more accurate center location of each tile of each tiling scheme contributes by a factor of 1, with a smooth interpolation for the weights of various contributions for intermediate locations. The actual trigonometric formula for this Multi-Procrustes approach is as follows:

$$\begin{aligned} \rho_{MP}(x,y,z) = & \rho_A(x,y,z)\cos^2x\cos^2y\cos^2z + \rho_B(x,y,z)\cos^2x\cos^2y\sin^2z \\ & + \rho_C(x,y,z)\cos^2x\sin^2y\cos^2z + \rho_D(x,y,z)\cos^2x\sin^2y\sin^2z \\ & + \rho_E(x,y,z)\sin^2x\cos^2y\cos^2z + \rho_F(x,y,z)\sin^2x\cos^2y\sin^2z \\ & + \rho_G(x,y,z)\sin^2x\sin^2y\cos^2z + \rho_H(x,y,z)\sin^2x\sin^2y\sin^2z \end{aligned} \quad (7-17)$$

Although the above Multi-Procrustes approach of linear scaling macromolecular electron density generation requires an approximately eightfold increase in the computer time needed for the same macromolecule, the weighting scheme ensures increased accuracy. Note that, the time needed for the step involving the actual combination of electron densities according to Eq. (7-17) is negligible as compared to

the computer time needed for the actual ADMA or MEDLA computation of individual electron densities for each tiling scheme. The approach provides a possible tool in various applications [41–43].

7.7. SUMMARY

The role of molecular fragmentation principles in linear scaling quantum chemical approaches, theoretical and practical conditions for their implementation, as well as computational methods for efficient fragmentation schemes are discussed.

REFERENCES

1. Szekeres Zs, Exner TE, Mezey PG (2005) Fuzzy fragment selection strategies, basis set dependence, and HF – DFT comparisons in the applications of the ADMA method of macromolecular quantum chemistry. *Int J Quantum Chem* 104:847–860
2. Mulliken RS (1955) Electronic population analysis on LCAO-MO molecular wave functions. I. *J Chem Phys* 23:1833–1840
3. Mulliken RS (1955) Electronic population analysis on LCAO-MO molecular wave functions. II. Overlap populations, bond orders, and covalent bond energies. *J Chem Phys* 23:1841–1846
4. Mulliken RS (1955) Electronic population analysis on LCAO-MO molecular wave functions. III. Effects of hybridization on overlap and gross AO populations. *J Chem Phys* 23:2338–2342
5. Mulliken RS (1955) Electronic population analysis on LCAO-MO molecular wave functions. IV. Bonding and antibonding in LCAO and valence-bond theories. *J Chem Phys* 23:2343–2346
6. Hohenberg P, Kohn W (1964) Inhomogeneous electron gas. *Phys Rev* 136:B864–B871
7. Levy M (1979) Universal variational functionals of electron densities, first-order density matrices, and natural spin-orbitals and solution of the v -representability problem. *Proc Natl Acad Sci USA* 76:6062–6065
8. Levi M (1982) Electron densities in search of Hamiltonians. *Phys Rev A* 26:1200–1208
9. Levy M (1990) Constrained-search formulation and recent coordinate scaling in density functional theory. *Adv Quantum Chem* 21:69–79
10. Kryachko ES, Ludena EV (1989) *Density functional theory of many-electron systems*. Kluwer, Dordrecht
11. Parr R, Yang W (1989) *Density-functional theory of atoms and molecules*. Oxford University Press, New York, NY
12. Riess J, Munch W (1981) The theorem of Hohenberg and Kohn for subdomains of a quantum system. *Theor Chim Acta* 58:295–300
13. Mezey PG (1999) The holographic electron density theorem and quantum similarity measures. *Mol Phys* 96:169–178
14. Mezey PG (1998) Generalized chirality and symmetry deficiency. *J Math Chem* 23:65–84
15. Mezey PG (1999) Holographic electron density shape theorem and its role in drug design and toxicological risk assessment. *J Chem Inf Comp Sci* 39:224–230
16. Mezey PG (2001) The holographic principle for latent molecular properties. *J Math Chem* 30:299–303
17. Mezey PG (2001) A uniqueness theorem on molecular recognition. *J Math Chem* 30:305–313
18. Mezey PG (2007) A fundamental relation of molecular informatics: information carrying properties of density functions. *Collect Czech Chem Commun* 72:153–163
19. Mezey PG (1995) Shape analysis of macromolecular electron densities. *Struct Chem* 6:261–270
20. Mezey PG (1995) Macromolecular density matrices and electron densities with adjustable nuclear geometries. *J Math Chem* 18:141–168

21. Mezey PG (1996) Local shape analysis of macromolecular electron densities. In: Leszczynski J (ed) *Computational chemistry: reviews and current trends*, vol.1. World Scientific Publishing, Singapore, pp 109–137
22. Mezey PG (1997) Quantum similarity measures and Löwdin's transform for approximate density matrices and macromolecular forces. *Int J Quantum Chem* 63:39–48
23. Hartree DR (1928) The wave mechanics of an atom with a non-coulomb central field. Part I. Theory and methods. *Proc Camb Philol Soc* 24:89–110
24. Hartree DR (1928) The wave mechanics of an atom with a non-coulomb central field. Part II. Some results and discussion. *Proc Camb Philolo Soc* 24:111–132
25. Hartree DR (1928) The wave mechanics of an atom with a non-coulomb central field. Part III. Term values and intensities in series in optical spectra. *Proc Camb Philol Soc* 24:426–437
26. Hartree DR (1929) The wave mechanics of an atom with a non-coulomb central field. Part IV. Further results relating to terms of the optical spectrum. *Proc Camb Philol Soc* 25:310–314
27. Fock V (1930) Naeherungsmethode zur Loesing des quantenmechanischen Mehrkoerperproblems. *Z Phys* 61:126–148
28. Roothaan CC (1951) New developments in molecular orbital theory. *Rev Mod Phys* 23:69–89, *ibid.* 32:179 (1960)
29. Hall GG (1951) The molecular orbital theory of chemical valency. VIII. A method of calculating ionization potentials. *Proc Roy Soc London A*205:541–552
30. Walker PD, Mezey PG (1993) Molecular electron density lego approach to molecule building. *J Am Chem Soc* 115:12423–12430
31. Walker PD, Mezey PG (1994) Ab initio quality electron densities for proteins: a MEDLA approach. *J Am Chem Soc* 116:12022–12032
32. Walker PD, Mezey PG (1994) Realistic, detailed images of proteins and tertiary structure elements: ab initio quality electron density calculations for bovine insulin. *Can J Chem* 72:2531–2536
33. Walker PD, Mezey PG (1995) A new computational microscope for molecules: high resolution MEDLA images of Taxol and HIV-1 protease, using additive electron density fragmentation principles and fuzzy set methods. *J Math Chem* 17:203–234
34. Walker PD, Mezey PG (1995) Towards similarity measures for macromolecular bodies: media test calculations for substituted benzene systems. *J Comput Chem* 16:1238–1249
35. Mezey PG, Walker PD (1997) Fuzzy molecular fragments in drug research. *Drug Discov Today (Elsevier Trend Journal)* 2:6–11
36. Mezey PG (1997) Computational microscopy: pictures of proteins. *Pharmaceutical News* 4:29–34
37. Mezey PG (1997) Quantum chemistry of macromolecular shape. *Int Rev Phys Chem* 16:361–388
38. Mezey PG (1999) Combinatorial aspects of biomolecular shape analysis. *Bolyai Soc Math Stud* 7:323–332
39. Mezey PG (1996) Functional groups in quantum chemistry. *Adv Quantum Chem* 27:163–222
40. Mezey PG (1999) Local electron densities and functional groups in quantum chemistry. In Surjan PR (ed) *Correlation and localization. Topics in current chemistry*, vol 203. Springer, Berlin, Heidelberg, New York, NY, pp 167–186
41. Mezey PG (1999) Relations between computational and experimental engineering of molecules from molecular fragments. *Molec Eng* 8:235–250
42. Mezey PG (1998) A crystallographic structure refinement approach using Ab initio quality additive fuzzy density fragments. *Adv Molec Struct Res* 4:115–149
43. Szekeres Zs, Mezey PG, Surjan P (2006) Diagonalization-free initial guess to SCF calculations for large molecules. *Chem Phys Lett* 424:420–424

CHAPTER 8

APPROXIMATIONS OF LONG-RANGE INTERACTIONS IN FRAGMENT-BASED QUANTUM CHEMICAL APPROACHES

SIMON M. ECKARD², ANDREA FRANK¹, IONUT ONILA¹,
AND THOMAS E. EXNER¹

¹*Department of Chemistry and Zukunftskolleg, University of Konstanz D-78457, Konstanz, Germany,
e-mail: andrea.frank@uni-konstanz.de; ionut.onila@uni-konstanz.de; thomas.exner@uni-konstanz.de*

²*Institute of Physical Chemistry, University of Zurich, 8057 Zürich, Switzerland,
e-mail: Simon.Eckard@pci.uzh.ch*

Abstract: Quantum chemical calculations of very large systems still pose major challenges due to the formidable scaling behavior of standard methods with system size. Here, we will describe how the concept of separating short- and long-range interactions can be used to make such calculations possible nonetheless at least in an approximate way. In mixed quantum mechanical/molecular mechanical (QM/MM) and fragment-based quantum chemical methods, the local surroundings are considered explicitly whereas other parts further away are neglected or included with a lower level of theory, e.g. as interactions with point charges. Different methods to combine these two descriptions, so-called embedding schemes, are outlined. Additionally, the border region problem, how subsystems describable by quantum mechanics can be generated by cleaving and saturating bonds connecting atoms located in the different regions, and proposed solutions are discussed. Finally, with the fragment-based adjustable density matrix assembler (ADMA) method as example, the capacities but also some limitations of the presented approaches will be presented using different test systems.

Keywords: Fragment-based approaches, Distance dependence, Linear scaling, Embedding schemes, Border regions, Adjustable density matrix assembler

8.1. INTRODUCTION

Knowledge about the 3D structure (in atomic resolution) and the physico-chemical properties of proteins as well as protein-protein and protein-ligand complexes is a precondition for the in-depth understanding of biological processes and rational manipulation of these. Because of the large size of these molecular systems, the determination of the structure is a playground of experimental methods like X-ray crystallography and NMR spectroscopy. But if such structures are available, theoretical methods come into play. Beside empirical methods, linear-scaling quantum

chemical approaches should be considered for the analysis of such systems since they have, as the name implies, a much better scaling behavior compared to standard quantum chemical methods and a broader field of application without large parameterization compared to e.g. molecular-mechanical force fields. We will concentrate here on one specific type of linear scaling methods, fragment-based quantum chemistry, and describe the approximations leading to linear scaling. Additionally, the limitations of earlier versions as well as possible workarounds will be discussed.

8.2. SHORT-RANGE AND LONG-RANGE INTERACTIONS

Hartree-Fock theory still plays a dominant role in quantum chemistry, due to its relative efficiency as well as being a useful reference for methods which include dynamic electron correlation (except density functional theory). In this theory, the approximate equivalent of the Hamiltonian, the Fock matrix, consists of the kinetic energy term of the electrons, the electron-nucleus interaction and the two-electron interaction matrix \mathbf{G} . The calculation of the latter is the most time-consuming step since it contains the different integrals between any four of all the gaussian basis functions used in the truncated *linear combination of atomic orbitals* (LCAO) expansion series of the atomic (and molecular) orbitals, determined by the basis set in use. These four-center two-electron integrals cause the formidable scaling behavior of $O(n^4)$. In the nowadays mostly applied Kohn-Sham representation of density functional theory, equivalent considerations result in the same scaling behavior just by replacing the Fock matrix with the Kohn-Sham matrix, even though scaling of $O(n^3)$ can be obtained by density-fitting approaches [1–3].

For the case of $1s$ functions (the easiest case in terms of integral evaluation), the integration of the *kinetic terms* $T_{ij} = \langle \varphi_i | -\frac{1}{2}\Delta | \varphi_j \rangle$ yields a distance dependency roughly (i.e., for sufficiently large electron-electron distances r_{ij}) proportional to $r^2 \cdot e^{-qr^2}$. The *electron-nucleus attraction* scales with $\frac{1}{r} \cdot e^{-qe^2} \cdot \text{erf}(r)$ while the matrix elements G_{ijkl} show a distance dependency proportional to $\frac{1}{r_{ijkl}^2} e^{-ar_{ij}^2 - br_{kl}^2}$. The two-electron interaction shows the strongest decrease with increasing distance. Therefore, for these an approximation by only calculating short range interactions seems possible and is highly desirable due to the immense number of matrix elements for large molecules and/or large basis sets. Standard implementations of Hartree-Fock already use this fact by first approximately evaluating all the integrals and then only fully calculate those which are above a specific cut-off resulting in a scaling of roughly $O(n^2 \cdot \log n)$ [4, 5].

Since even the integration of the rather simple interaction between two $1s$ orbitals results in the quite complicated derivation of the above distance dependencies, it is not a trivial task to evaluate the behavior for combinations of functions of higher angular momentum. Furthermore, one has to estimate the absolute values of all the interactions for each pair of particles and then decide which of these should be fully evaluated. Even if there are efficient methods for doing so [6–8], this becomes a too time-consuming process to be of use for very large systems which limits the use of pure quantum mechanics in biochemistry or material science.

If we make the transition to perfectly localized electrons by replacing the Gaussian basis functions by Dirac delta functions (the consequences of which are clearly comprehensible if we let the exponents $q, a, b \rightarrow \infty$ in the derivation of the above formula, equivalent to a view from very far away), we end up with the *classical* Coulomb interaction terms for the electron-nucleus and electron-electron interaction, with the specific “roughness” of the Hamiltonian due to the G_{ijkl} smoothed out. This shows quite clearly that, while one needs to calculate the exact integrals for all the interactions at *short range*, it suffices to consider only the classical Coulomb interactions at *long range* where the $1/r$ behavior falls off significantly slower than the Gaussian functions. The attributes *short-ranged* and *long-ranged* are, of course, subject to discussion and their assignment to the different types of interactions strongly depends on the desired level of accuracy. Hierarchical multipole methods [9–16] generate a smooth transition between the short-range and long-range description. They recursively subdivide a system into a hierarchy of cells. The particle distributions within a cell are approximated by a multipole expansion. Since this expansion becomes increasingly more accurate with separations, larger cells may be used as the interaction distance increases leading to a linear-scaling calculation of the Fock matrix when using fast multipole methods [11, 17–21]. Since this still does not solve the problem of Fock/Kohn-Sham matrix diagonalization needed in the self-consistent cycles of HF or DFT calculations, the even stronger approximation may be applied that the electron-electron interactions are only included up to a specific threshold and from then on they are only implicitly included, described by Coulomb interactions with atomic point charges, or are neglected completely. That this approximation still gives reasonable results is demonstrated by the successful application of mixed quantum mechanical/molecular mechanical (QM/MM) and fragment-based quantum mechanical methods, of which the latter will be described in more detail in the remaining of this chapter.

8.3. FRAGMENT-BASED QUANTUM CHEMICAL APPROACHES

As just described, the long-range interactions have to be approximated to make quantum chemical calculations for large molecules feasible. Here, we will concentrate on fragment-based approaches designed for macromolecular calculations. In these methods, the large molecule is divided into small fragments and independent quantum chemical calculations are performed on each fragment individually. If the fragments are of similar size, and thus the computer time needed for each fragment is almost the same, a linear-scaling quantum chemical method can in principle be obtained due to the fact that the number of fragments scales linearly with the system size. In this way, Hartree-Fock as well as density functional theory (DFT) calculations can be performed even for very large systems.

Probably the best-known fragment-based approach is the divide-and-conquer ansatz by Yang, developed for semiempirical, HF, and density functional theory methods [22–33]. Only the DFT version will be described here [23, 31], in which the part of the electron density of a specific fragment, which contributes to the total electron density of the large system, is calculated according to

$$\rho^k(r) = p^k(r) \cdot \sum_i^N \frac{1}{1 + e^{-\beta(e_F - e_i^k)}} \left| \sum_{\mu}^N C_{\mu i} \varphi_{\mu}(r) \right|,$$

where the atomic orbital coefficients are taken from calculations of small molecules composed of the fragment and additional surroundings in the same geometric arrangement as in the macromolecule. $p^k(r)$ is a positive weighting function for the subsystem k . This function has a large value near the fragment k and decreases with increasing distance to the fragment. In this way, a specific fragment contributes mainly to the region directly surrounding it exploiting the larger importance of short-range interactions. The approximated total electron density is defined as the sum of the electron density of the subsystems, from which the total energy of the system is calculated according to standard density functional theory:

$$E_{KS}(\rho) = T_S(\rho) + \int v(r)\rho(r)dr + E_{XP}(\rho) + \frac{1}{2} \int \frac{\rho(r) \cdot \rho(r')}{|r - r'|} drdr' + V_{NN}$$

The accuracy of the method compared to the direct calculation of the complete molecule is determined by the amount of additional parts of the large molecule, which are included in the fragment calculations, i.e. by the distance up to which local interactions are included in the calculations of the subsystems.

The second approach, the adjustable density matrix assembler (ADMA) [34–37] and its predecessor, the molecular electron density loge assemblers (MEDLA) [38–40], were first introduced in the group of Mezey almost simultaneously to divide-and-conquer and then highly improved and extended in our group. Since the discussion of long-range influences below will be based on this method, it will be discussed in more detail using the Hartree-Fock level of theory here. Analogously DFT can be applied [41]. ADMA combines fragment electron density matrices to approximate the electron density matrix of a large molecule (target molecule) [34–37]. These fragment density matrices are taken from calculations of smaller molecules (parent molecules) having a central region as one of the molecular fragments of the target macromolecule, surrounded by additional regions, called surroundings in the following discussion, with the same local nuclear geometry as in the macromolecule. These additional regions are taken within a selected distance d of the central fragment (see Figure 8-1). Similar to divide-and-conquer, the accuracy of the ADMA method is solely controlled by the distance parameter d and, by using a larger distance parameter, the results of direct quantum chemical calculations can be approximated with greater accuracy. In addition to the directly included surroundings, the field-adapted ADMA (FA-ADMA) version [42, 43] approximates the rest of the target macromolecule with partial charges in the parent molecule calculations. It was shown that the field-adapted approach leads to largely increased accuracy with a fixed parent molecule size [42, 43].

An ADMA calculation is started with the subdivision of the target molecule into a set of m mutually exclusive families of nuclei [34–37;42–45]. Standard quantum chemical calculations following the Hartree-Fock-Roothaan-Hall formalism are

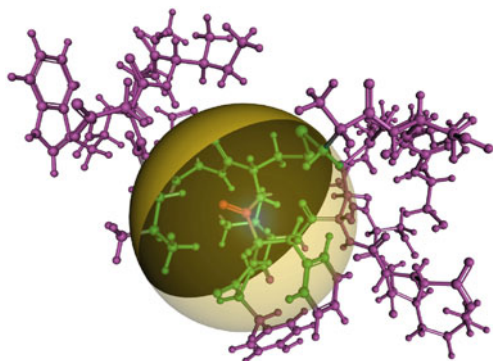


Figure 8-1. Visualization of the fragmentation process: the parent molecule for the red fragment is defined as all atoms (in green) enclosed by a sphere of predefined radius. All other atoms are neglected (ADMA) or included as partial charges (FA-ADMA, see below)

performed for the molecular fragments defined by one of these families, the corresponding quantum mechanical surroundings (defined by the distance parameter d), and eventually also the partial charges at the positions of the rest of the nuclei. The electron density $\rho(\vec{r})$ of a molecule can be expressed in terms of a basis set of n atomic orbitals $\varphi_i(\vec{r})$ ($i = 1, 2, \dots, n$) used for the expansion of the molecular wavefunction and the density matrix P_{ij} determined for the given nuclear configuration using this basis set:

$$\rho(\vec{r}) = \sum_{i=1}^n \sum_{j=1}^n P_{ij} \cdot \varphi_i(\vec{r}) \cdot \varphi_j(\vec{r})$$

Following the *additive fuzzy density fragmentation* (AFDF) scheme [35, 36], the local fuzzy electron density fragments for one of the sets of mutually exclusive families of nuclei denoted by f^k , $k = 1, \dots, m$ can be generated by defining a formal membership function $m^k(i)$ which indicates whether a given atomic orbital (AO) basis function $\varphi_i(\vec{r})$ belongs to the set of AOs centered on a nucleus of the family f^k .

$$m^k(i) = \begin{cases} 1 & \text{if AO } \varphi_i(\vec{r}) \text{ is centered on one nuclei of set } f^k \\ 0 & \text{otherwise} \end{cases}$$

Using this membership function, the elements P_{ij}^k of the density matrix of the k th fragment are calculated according to the Mulliken-Mezey scheme [35, 36]:

$$P_{ij}^k = 0.5 \cdot \left[m^k(i) + m^k(j) \right] \cdot P_{ij}$$

The membership function is designed so that the full and half matrix element value is used, when both nuclei or only one nucleus belongs to the family f^k , respectively. If both nuclei belong to other families, a value of 0 is taken. The resulting fragment

electron density matrices can then be summed up to get the total density matrix and with that the total electron density of the large “target” macromolecule:

$$P_{ij} = \sum_{k=1}^m P_{ij}^k \text{ and } \rho(\vec{r}) = \sum_{i=1}^n \sum_{j=1}^n \sum_{k=1}^m P_{ij}^k \cdot \varphi_i(\vec{r}) \cdot \varphi_j(\vec{r})$$

From this, molecular properties, e.g. the total energy of the target molecule, can be calculated following the standard Hartree-Fock formalism using the renormalized ADMA approximation of the density matrix [42, 43, 45] instead of the ideal, directly calculated exact macromolecular density matrix:

$$E_{HF} = \frac{1}{2} \sum_{i=1}^n \sum_{j=1}^n \left((F_{ij} + H_{ij}^{core}) \cdot \sum_{k=1}^m P_{ij}^k \right) + V_{NN}$$

with:

$$F_{ij} = H_{ij}^{core} + \sum_{r=1}^b \sum_{s=1}^b \left(\left[(ij|rs) - \frac{1}{2} (is|rj) \right] \cdot \sum_{k=1}^m P_{ij}^k \right)$$

Some other methods are based on the same idea as divide-and-conquer and ADMA and will only be listed here: molecular tailoring approach of Gadre and coworkers [46, 47], the central insertion scheme [48], and the fragment energy and localized molecular orbital assembler approach [49, 50]. A different combination of the fragment calculations is applied in the fragment molecular orbital (FMO) method [51–57]. Here, the electronic energy of the fragments and all pairs of fragments are combined using the following equation:

$$E = \sum_I \sum_{J < I} (E_{IJ} - E_I - E_J) + \sum_I E_I$$

E_{IJ} is the energy of the pair of fragments I and J and E_I and E_J the energies obtained from the single fragment calculations on fragment I and J , respectively. In newer versions, energy gradients [54], molecule orbitals of the complete molecule [56], and solvation effects [58] can also be calculated.

Last but not least, we would like to mention that also correlation methods can profit from a fragment-based description. One such approach is the method of increments [59–62]. Like the other local correlation methods, the method of increments starts with localized orbitals obtained from the Hartree-Fock wavefunction. It then reduces the original correlation problem for the total number of electrons to a sum of correlation contributions for smaller numbers of electrons, i.e. the correlation energy is obtained by adding up correlation energy increments in terms of the localized orbitals and in pairs, triples, . . . of the localized orbitals:

$$E_{corr} = \sum_I \varepsilon_I + \frac{1}{2} \sum_I \sum_{J \neq I} \Delta \varepsilon_{IJ} + \frac{1}{6} \sum_I \sum_{J \neq I} \sum_{K \neq I \vee K \neq J} \Delta \varepsilon_{IJK} + \dots$$

All size-extensive correlation methods can be used in this scheme to evaluate the individual increments. Due to the local character of the orbitals it is also possible to calculate the increments in finite embedded clusters, which correspond to the fragments and surroundings in the ADMA jargon. FMO calculations taking correlation effects into account are also possible [63, 64].

8.4. EMBEDDING SCHEMES

If the system is divided into two or more parts and, thus, the short-range and long-range interactions are described by two different theories as done in QM/MM as well as fragment-based quantum chemical approaches, the interactions between the subsystems have to be dealt with in a special way. In the QM/MM literature, these special treatments are called embedding schemes and we will follow this nomenclature here due to the similarities between QM/MM and fragment-based methods. The easiest possibility to combine the two parts (QM and MM region in QM/MM and e.g. fragment plus surroundings and remaining part of the macromolecule in FA-ADMA) is the mechanical embedding scheme. Here, the QM calculations can be performed totally independent on one of the parts without taking the other ones into account, i.e. the calculation is performed on the QM part *in vacuo* without polarization due to the MM part (no point charges of the MM part are included as for the later embeddings). In QM/MM, the QM and MM part interact by a Coulomb potential between fixed point charges (for both the QM and MM part) and steric interactions modeled by a van-der-Waals potential according to the force-field philosophy. The Hamiltonian of the complete system can then be formulated as follows, employing e.g. a Lennard-Jones potential for the van-der-Waals interactions and partial charges taken from empirical force-fields:

$$H_{eff} = H_{QM} + H_{MM} + H_{QM/MM}$$

with

$$H_{QM/MM} = \sum_{i=1}^{QM} \sum_{j=1}^{MM} \left[\frac{q_i \cdot q_j}{r_{ij}} + 4\varepsilon_{ij} \left(\frac{\sigma_{ij}^{12}}{r_{ij}^{12}} - \frac{\sigma_{ij}^6}{r_{ij}^6} \right) \right]$$

In fragment-based methods, all interactions (steric as well as electrostatic as there is no such strict separation between these two types) are calculated for the parent molecules used in the individual QM calculations. Interactions between different fragments are included since the atom sets defining the parent molecules overlap but only as long as the atoms of one fragment are included in the surroundings of the other fragment. In this way, short-range interactions are fully described by the high level of theory but the long-range interactions are totally ignored.

In the electric embedding scheme, molecular parts further away are included as static point charges in the quantum mechanical calculations. Thus, the electron density is polarized by these additional parts. This can be described by an effective QM/MM Hamiltonian:

$$H_{QM/MM} = \sum_{i=1}^{electrons} \sum_{m=1}^{MM} \frac{q_m}{r_{im}} + \sum_{k=1}^{nuclei} \sum_{m=1}^{MM} \left[\frac{Z_k \cdot q_m}{r_{km}} + 4\epsilon_{km} \left(\frac{\sigma_{km}^{12}}{r_{km}^{12}} - \frac{\sigma_{km}^6}{r_{km}^6} \right) \right]$$

The interaction between the partial charges and the electron density as well as between the nuclei is normally calculated in the QM and the van-der-Waals interaction in the MM program. For fragment-based calculations, the application of the electric embedding is not that straightforward. The question here is how to define the partial charges. One useful approximation is to also rely here on empirical force fields and the partial charges defined in these, in which case the long-range interactions are approximated with a lower level of theory.

In the last and most sophisticated approach, the polarized embedding scheme, polarization effects for the complete molecule and all interactions are taken into account. For doing so, polarizable force-fields, which are still subject of ongoing developments, have to be used in QM/MM calculations. Because these force fields have a much higher computational demand, only a limited amount of studies have applied polarized embedding up to now. Full polarizability is much more natural in fragment-based calculations and can be achieved with an iterative, self-consistent cycle. First, a calculation with the mechanical embedding scheme is performed. From this, partial charges are computed for the complete molecule using e.g. Mulliken's definition of partial charges. Then, each fragment calculation is repeated including the charges of the additional regions resulting in new charges. This cycle is terminated if the charges do not change from one iteration to the next.

8.5. BORDER REGION

But even if one has decided on a specific embedding scheme, the combination of two regions treated with different theories, where one is a quantum mechanical method, causes an additional problem for (biological) macromolecules: If the system is divided into subsystems, the border between these subsystems, almost unavoidably in biomolecules, cuts through covalent bonds. For the QM calculation, it is not possible to simply truncate these bonds because this would lead to single-occupied orbitals and would give strong perturbation of the electronic state. To circumvent this problem different approaches were designed ranging from capping hydrogen atoms over specially parameterized atoms or groups of atoms to localized hybrid orbitals and generalized hybrid orbitals.

In most QM/MM and in almost all fragment-based studies, hydrogen atoms are added to saturate dangling bonds. One and probably the most important reason for the widespread use of this approach is its striking simplicity. Since the

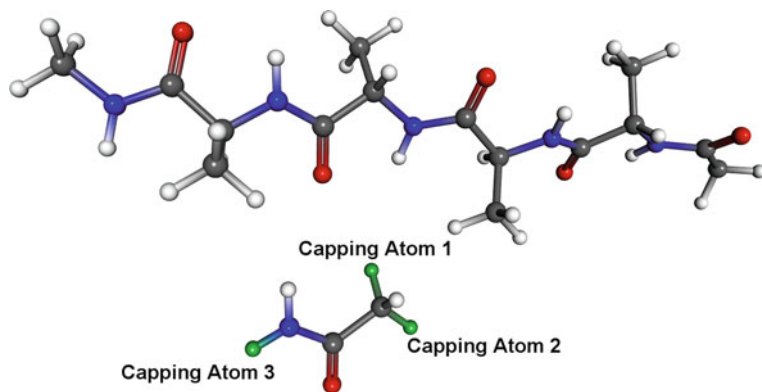


Figure 8-2. Example of a fragment with capping hydrogen atoms: the capping atoms are shown in green. Capping atom 1 replaces the amidic nitrogen, capping atom 2 the C_{β} of the side chain, and capping atom 3 the C_{α} of the next amino acid

hydrogen-capped fragments are normal molecules (see Figure 8-2), any quantum chemical program can be used for the calculations without modification. Hydrogen is also a good choice since the electronegativities of carbon and hydrogen are very similar. Thus, H–C bonds (after adapting the bond length to the standard value) are reasonable substitutes if the bonds through the border region are limited to unpolar C–C bonds between sp^3 carbon atoms. Unfortunately, in contrast to QM/MM methods, this is not possible for most of the many hundreds to thousands of broken bonds generated in fragment-based approaches. Another point to consider is that if partial charges are used to represent the rest of the molecules, the interactions between the ones replacing neighboring atoms and the capping atom are extremely strong because of short distances leading to disturbances of the electronic structure. These unphysical interactions have to be removed by deletion or scaling of selected atomic charges, charge shifting schemes, or Gaussian blurs.

For better agreement, larger capping groups like CH_3 can also be used [65, 66]. The divide-and-conquer and the ADMA approach already take quantum mechanical surroundings into account. Thus, in these cases, larger capping groups are not of much use since the surroundings are just enlarged by the capping groups and the border region problem is moved to the capping groups. In contrast, for methods combining energetic contributions of the fragments and pairs of fragments, e.g. the FMO method described above, larger capping groups can be very valuable due to the better description of the fragments and the possibility to subtract their contributions afterwards. This directly leads to the conjugated caps approach [67, 68]. If a bond is broken in the fragmentation, each atom of the bond belongs to a different fragment and caps are added to both atoms in their corresponding fragments. If the two conjugated caps of a broken bond are combined, a new molecule is generated. The energies or the electron densities of these fused molecular species, called con-caps, are then subtracted from the combined fragments in this way removing the contribution of the caps.

As another way to use the smallest possible cap, one atom, which is even more similar to the replaced group than a hydrogen atom, specifically-designed atoms were proposed. Here, semi-empirical methods have the big advantage that the Coulomb and resonance integrals can be specifically parameterized for the capping atoms as done for a long time in the Hyperchem program [69]. In *ab initio* methods, the special nature must be encoded in the basis set as effective core potentials (ECP). E.g. the pseudobond approach, proposed by Zhang et al. [70], uses a fluorine atom with an adapted ECP to fill the free valence. Zhang [71] then improved on this by designing a special STO-2G basis set in addition to the ECP for the seven-valence atom, which was subsequently used in QM/MM simulations [72]. The quantum capping potential (QCP) [73, 74] combines conventional atom-centered effective core potentials with a shielding potential that moves all but one valence electron into the core. Pauli potentials are also used to prevent the unphysical collapse of other atoms into the QCP atom. Other methods based on the same ideas are the connection-atom method [75], the effective group potential method [76], the minimum principle approach [77], and the multi-centered valence electron effective potential [78].

To avoid additional atoms, it is possible to use orbitals replacing either the broken bond itself or the surrounding of the border atom. These orbitals are not optimized in the SCF procedure but serve as statically occupied charge distributions with a pre-defined electron occupation. Even if these approaches are more physically justified, their implementation in quantum chemical programs needs many modifications and adaptations of the source code so that they are less often used. Nevertheless, since especially the generalized hybrid orbitals show very good results, it is probably worth to invest the time for the additional programming. The earliest method using localized orbitals was the local self-consistent field (LSCF) method by Rivail and Naray-Szabo [79–83] originally invented for semi-empirical calculations. In this, a strictly localized orbital replaces the broken bond (see Figure 8-3), which is optimized in a calculation on a small molecule representing the local surroundings of the border region and is then kept frozen in the fragment calculation. In the group of Friesner [84, 85] the same idea was implemented for Hartree-Fock and DFT calculations. Boys-localized orbitals were parameterized for a number of chemical entities including the 20 naturally occurring amino acids.

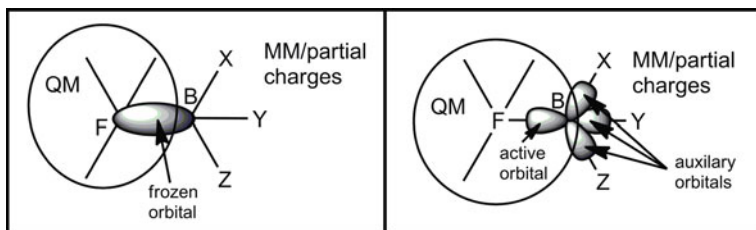


Figure 8-3. Visualization of the local self-consistent field (*left*) and the generalized hybrid orbital (*right*) method to saturate broken bonds between the QM and MM region. In LSCF the bond is replaced by an orbital, which is kept frozen in the QM calculation. In GHO, the MM atom is replaced by four hybrid orbitals. One of these, the active orbital, is optimized while the others, the auxiliary orbitals, are kept constant

In contrast to all approaches described so far, in the generalized hybrid orbital (GHO) method [86] the border between the QM and the MM/partial charge region is placed on the boundary atom **B** and not in the middle of the broken bond (see Figure 8-3). For QM/MM calculations, this means that **B** is a QM as well as a MM atom and, for fragment-based applications, that **B** is fully included in the quantum chemical calculation. This is achieved by constructing an orthonormal set of hybrid orbitals $\{\eta_B, \eta_X, \eta_Y, \eta_Z\}$ on this atom. The orbital η_B is the active hybrid orbital, which replaces the broken bond and is optimized with the orbitals of the QM atoms in the SCF procedure, and the other three, the auxiliary orbitals, are used to provide an additional, fixed electron density distribution for describing, combined with the partial charges, the remaining parts of the molecule not included in the fragment calculation. Besides its good performance in fragment-based calculations (see below), which would already justify its wider application, an advantage of GHO is its dependence on only very few parameters compared to the other localized orbitals.

One interesting method, which should be tested for fragment-based approaches, is the orbital-free effective embedding potential [87, 88]. This local multiplicative potential can be expressed as a functional of two electron densities: that of the investigated fragment (ρ_A) and that of the environment (ρ_B). Even if the analytic form of this functional is not known, this potential can be approximated using some explicit analytical expressions for its kinetic- and exchange-correlation components.

8.6. RESULTS OF FA-ADMA AND GHO-FA-ADMA

In this last section of this chapter, we will show the potential of fragment-based approaches with the adjustable density matrix assembler (ADMA) as an example. ADMA and its extension, the field-adapted ADMA, have demonstrated high accuracy for a number of physicochemical properties.

As described above, the accuracy of the ADMA method is solely controlled by the size of the surroundings, i.e. the additional surroundings of the fragment explicitly included in the fragment quantum chemical calculations. Using a set of polypeptides and small proteins, for which the results can be directly compared to the full calculation, *ab initio* quality could be obtained by varying the distance parameter determining the size of the surrounding. For the electron density, the electrostatic potential, and the partial charges according to the Mulliken or Löwdin definition, very small surroundings of 3 to 5 Å are already sufficient, so that the ADMA approach can be used for the fast and efficient calculation of these properties of macromolecules. These results can then e.g. be used as guidance for the development and improvement of empirical methods like force fields. *Ab initio* quality calculations of dipole moments and especially of energies require larger surroundings. For the protein Crambin, chemical accuracy of lower than 1 kcal/mol was only achieved with 9 Å surroundings. Since the parent molecules for such size of the surroundings are already very large composed out of a few hundreds of atoms, the needed computer resources for such calculations are considerable and limit the possible application. Thus, approaches to reduce the minimal surroundings needed and to make the ADMA approach more efficient had to be developed.

The reason why these large surroundings are needed is the complete neglect of the remaining parts in the fragment calculations. Especially groups with formal charges often occurring in proteins (e.g. arginine or glutamate side chains) close to the border region polarize the electron density in the target molecule. These influences should be also included in the parent molecule calculations, which can be achieved with an electric or even polarized embedding scheme as done in FA-ADMA. Putting point charges on all atoms not explicitly included in the QM calculations resulted in an extreme increase in accuracy for highly polar and formally charged molecules (see Figure 8-4). Additionally, the quality of the results is now less dependent on the properties of the macromolecule. Thus in FA-ADMA a smaller size of the surroundings, that is, smaller parent molecules, can be used to obtain a certain degree of accuracy, which results in a much improved performance. Regarding the used definition for the partial charges only minor influences on the results were seen. On the one hand, if Mulliken or Löwdin charges for the complete molecule are calculated with the FA-ADMA approach in a self-consistent cycle, polarization effects are included in these charges resulting in a fully polarized embedding scheme. On the other hand, an easier approach is to take the charges from a molecular force field like AMBER [89] or CHARMM [90] using the electric embedding scheme. Then only one FA-ADMA calculation is needed with the additional advantage that the charges better represent the electrostatic potential.

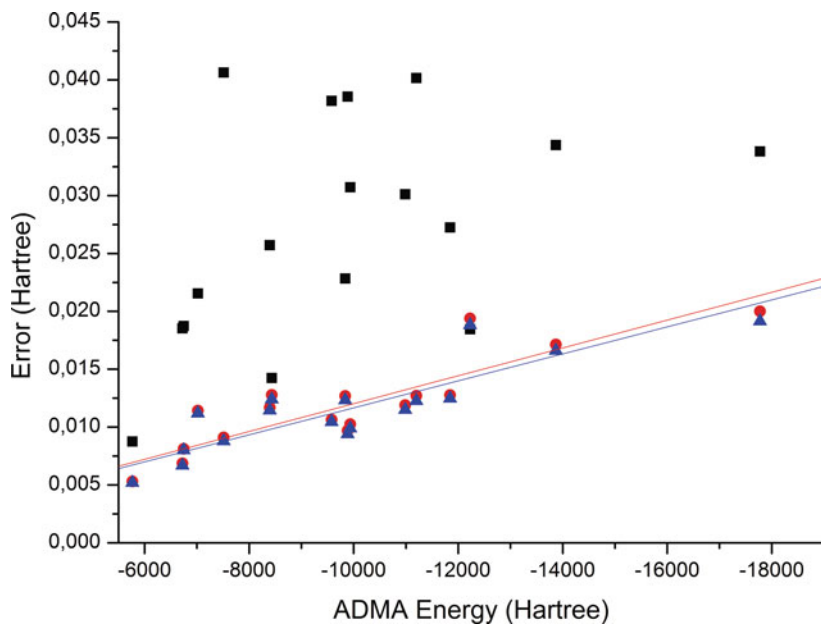


Figure 8-4. Correlation of the energy error of the FA-ADMA (HF/STO-3g, 5 Å surroundings) with Löwdin (blue triangles) and Mulliken (red dots) charges as well as the original ADMA approaches (black squares) with the total energy (in atomic units) for 16 polypeptides [43]. For FA-ADMA a much smaller error can be seen in almost all cases

The next step was to improve the description of the border region between the QM region and the partial charges. As described above, many solutions were proposed. Two of these, the pseudobond approach of Zhang et al. [91] based on effective core potentials (ECP) and generalized hybrid orbitals (GHO) by Pu et al. [86] were tested in the FA-ADMA approach and compared to capping hydrogen atoms used so far. With pseudobonds reasonable accuracy can be obtained for structural as well as electronic features [92]. But when they are further optimized to reproduce specific properties with a higher accuracy, it becomes obvious that the ECP parameters are highly sensitive to the molecules and the molecular properties used in the parameterization and the problem of overfitting easily occurs [92]. Additionally, none of the parameterizations shows significant and consistent improvement over simple capping hydrogen atoms, despite the simplicity of the latter approach. It is also questionable if the resulting potentials are physically meaningful when compared to effective core potentials of first-row elements. In contrast, the generalized hybrid orbital (GHO) method [93, 94] has demonstrated very good transferability from one system to another and gives excellent results for all properties calculated with the fragment-based approach. Especially, the obtainable accuracy with reasonable computational demand of intramolecular forces is now high enough to reliably locally optimize the molecular structures even for large proteins by fragment-based quantum mechanics [94]. Therefore, we would like to see that the GHO method is implemented in additional quantum chemical programs to make it accessible to a larger community interested in QM/MM and fragment-based calculations.

One application which will be pursued intensively in the near future is the quantum chemical calculation of NMR chemical shifts in proteins. We have already performed preliminary calculations on the trp-cage miniprotein [87]. This eicosapeptide (DAYAQLKDGGPSSGRPPPS) adopts (despite of its small size) a well defined 3D structure, which was determined by NMR spectroscopy. Therefore, it is the perfect test example since full quantum chemical calculations are possible, which can be compared to the experiment as well as to the fragment-based calculations. This calculation was mainly meant to see if reasonable results can be obtained with the levels of theory applicable to the AMDA approach. The NMR chemical shifts were determined with the Gauge-Independent Atomic Orbital (GIAO) method [95–98] implemented in GAUSSIAN03 [99]. For protons bound to nitrogen the calculated chemical shifts differ very much from the experimental ones. One explanation for that is that the chemical shift of these atoms is highly dependent on minor variances in the hydrogen bonding network. Since no explicit solvent is present, this network cannot be predicted correctly leading to large deviations from the experiment of up to 5 ppm for solvent exposed protons. For the other protons, a reasonable agreement is observed. The inclusion of correlation effects using B3LYP/6-31g* calculations but especially the use of an implicit solvent model (IEF-PCM [100–102]) additionally improved our results considerably. Taking the NMR chemical shifts from fragment calculations according to the ADMA approach gave the first indication that such calculations could be very valuable for large molecules. With increasing radius of the surroundings better and better agreement with the full calculations are obtained. Especially the maximum error for ^{13}C chemical shifts

drops dramatically when going from 5 Å to 6 Å surroundings. Based on the results presented here, the next step will be the optimization of the fragment-based calculations so that the best agreement with the experiment can be obtained. This will include the combination of fragment calculations with implicit solvent models. Additionally, it will be tried if mixed-basis set could be used to decrease the computational demand and if local optimization of the structures could increase the accuracy with respect to the experiment.

8.7. CONCLUSION

Since their first introduction almost 20 years ago, fragment-based quantum chemical approaches have come a long way and are now mature so that they can be used in real-world problems. A large number of physico-chemical properties, e.g. total energies, partial charges, electrostatic potentials, molecular forces, but also NMR chemical shifts, can be obtained in this way with high accuracy for analysis of large biochemical systems of medicinal interest but also to parameterize more empirical methods like polarizable molecular force fields. Problems exist in the description of the border region between the fragments and additional parts of the macromolecule not included in the fragment. Here, a large number of solutions have been proposed first in the QM/MM methodology and then adapted to fragment-based QM. With the best of these, which can be easily identified in the fragment-based framework, the additional parts (surrounding) explicitly included in the calculations of the fragments can be minimized for a given accuracy highly reducing the computational demand making it acceptable for more and more applications. We therefore hope and are convinced that such calculations will become standard in the near future especially if one takes the always increasing computer power available in high-performance computing facilities but also on the desks of all of us into account.

ACKNOWLEDGMENTS

The authors thank Paul G. Mezey, Raymond A. Poirier, and Peter L. Warburton for fruitful discussions. The work was supported by the Deutsche Forschungsgemeinschaft, Priority Program SPP 1145 “Modern and Universal First-Principles Methods for Many-Electron Systems in Chemistry and Physics” and the Juniorprofessorenprogramm des Landes Baden-Württemberg. Simon Eckard gratefully acknowledges the Fonds der Chemischen Industrie for a PhD fellowship and the German Academic Exchange Service (DAAD) for a short-term PhD student fellowship.

REFERENCES

1. Baerends EJ, Ellis DE, Ros P (1973) *Chem Phys* 2:41–51
2. Sambe H, Felton RH (1975) *J Chem Phys* 62:1122–1126
3. Dunlap BI, Connolly JWD, Sabin JRJ (1979) *Chem Phys* 71:3396–3402

4. Dyczmons V (1973) *Theor Chem Acc* 28:307–310
5. Ahlrichs R (1974) *Theor Chem Acc* 33 157–167
6. Lambrecht DS, Ochsenfeld CJ (2005) *Chem Phys* 123:184101–184114
7. Ochsenfeld C, White CA, Head-Gordon M (1998) *J Chem Phys* 109:1663–1669
8. Maslen PE, Ochsenfeld C, White CA, Lee MS, Head-Gordon M (1998) *J Phys Chem A* 102: 2215–2222
9. Challacombe M, Schwegler E (1997) *J Chem Phys* 106:5526–5536
10. White CA, Johnson BG, Gill PMW, Head-Gordon M (1994) *Chem Phys Lett* 230:8–16
11. White CA, Johnson BG, Gill PMW, Head-Gordon M (1996) *Chem Phys Lett* 253:268–278
12. Scuseria GE (1999) *J Phys Chem A* 103:4782–4790
13. Strain MCG, Scuseria E, Frisch MJ (1996) *Science* 271:51–53
14. Schwegler E, Challacombe M (1999) *J Chem Phys* 111:6223–6229
15. Burant JC, Strain MC, Scuseria GE, Frisch MJ (1996) *Chem Phys Lett* 248:43–49
16. Shao Y, White, CA, Head-Gordon M (2001) *J Chem Phys* 114:6572–6577
17. Greengard L, Rokhlin V (1987) *J Comp Phys* 73:325–348
18. Schmidt KE, Lee MA (1991) *J Stat Phys* 63:1223–1235
19. Petersen HG, Soelvason D, Perram JW, Smith ER (1994) *J Chem Phys* 101:8870–8876
20. White CA, Head-Gordon M (1994) *J Chem Phys* 101:6593–6605
21. White CA, Head-Gordon M (1996) *J Phys Chem* 105:5061–5067
22. Yang W (1991) *Phys Rev Lett* 66:1438
23. Yang W, Lee TS (1995) *J Chem Phys* 103:5674–5678
24. Lee C, Yang W (1992) *J Chem Phys* 96:2408–2411
25. Gogonea V, Westerhoff LM, Merz J (2000) *J Chem Phys* 113:5604–5613
26. Kobayashi M, Nakai H (2009) *Int J Quantum Chem* 109:2227–2237
27. Akama T, Fujii A, Kobayashi M, Nakai H (2007) *Mol Phys* 105:2799–2804
28. Akama T, Kobayashi M, Nakai H (2007) *J Comp Chem* 28:2003–2012
29. Kobayashi M, Akama T, Nakai H (2006) *J Chem Phys* 125:204106–204108
30. He X, Merz KM (2010) *J Chem Theor Comp* 6:405–411
31. St-Amant A (2002) In: Laird BB, Ross RB, Ziegler T (eds) *Chemical applications of density-functional theory*. ACS Symposium Series 629. American Chemical Society, Washington, DC, pp. 70–84
32. Dixon SL, Merz J (1996) *J Chem Phys* 104:6643–6649
33. Dixon SL, Merz KM Jr (1998) In: Schleyer PvR, Allinger NC, Clark T, Gasteiger J, Kollmann PA, Schaefer HF III, Schreiner, PR (eds) *The encyclopedia of computational chemistry*. Wiley, Chichester, pp. 762–776
34. Mezey PG (1996) *Adv Quant Chem* 27:163–222
35. Mezey PG (1997) *Intern Rev Phys Chem* 16:361–388
36. Mezey PG (1995) *J Math Chem* 18:141–168
37. Mezey PG (1997) *Int J Quantum Chem* 63:39–48
38. Walker PD, Mezey PG (1993) *J Amer Chem Soc* 115:12423–12430
39. Walker PD, Mezey PG (1994) *Can J Chem* 72:2531–2536
40. Walker PD, Mezey PG (1994) *J Amer Chem Soc* 116:12022–12032
41. Szekeres Z, Exner TE, Mezey PG (2005) *Int J Quantum Chem* 104:847–860
42. Exner TE, Mezey PG (2004) *J Phys Chem A* 108:4301–4309
43. Exner TE, Mezey PG (2005) *Phys Chem Chem Phys*:7:4061–4069
44. Exner TE, Mezey PG (2002) *J Phys Chem A* 106:11791–11800
45. Exner TE, Mezey PG (2003) *J Comp Chem* 24:1980–1986
46. Gadre SR, Shirsat RN, Limaye AC (1994) *J Phys Chem* 98:9165–9169
47. Babu K, Gadre SR (2003) *J Comp Chem* 24:484–495

48. Gao B, Jiang J, Liu K, Wu Z, Lu W, Luo Y (2008) *J Comp Chem* 29:434–444
49. Li W, Fang T, Li S (2006) *J Chem Phys* 124:154102–154106
50. Li W, Li S (2005) *J Chem Phys* 122:194109–6
51. Kitaura K, Ikeo E, Asada T, Nakano T, Uebayasi M (1999) *Chem Phys Lett* 313:701–706
52. Kitaura K, Sawai T, Asada T, Nakano T, Uebayasi M (1999) *Chem Phys Lett* 312:319–324
53. Nakano T, Kaminuma T, Sato T, Akiyama Y, Uebayasi M, Kitaura K (2000) *Chem Phys Lett* 318:614–618
54. Kitaura K, Sugiki S-I, Nakano T, Komeiji Y, Uebayasi M (2001) *Chem Phys Lett* 336:163–170
55. Nakano T, Kaminuma T, Sato T, Fukuzawa K, Akiyama Y, Uebayasi M, Kitaura K (2002) *Chem Phys Lett* 351:475–480
56. Inadomi Y, Nakano T, Kitaura K, Nagashima U (2002) *Chem Phys Lett* 364:139–143
57. Komeiji Y, Nakano T, Fukuzawa K, Ueno Y, Inadomi Y, Nemoto T, Uebayasi M, Fedorov DG, Kitaura K (2003) *Chem Phys Lett* 372:342–347
58. Fedorov DG, Kitaura K, Li H, Jensen JH, Gordon MS (2006) *J Comp Chem* 27:976–985
59. Stoll H (1992) *Phys Rev B* 46:6700
60. Stoll H (1992) *Chem Phys Lett* 191:548
61. Stoll H (1992) *Chem Phys* 97:8449
62. Paulus B (2006) *Phys Rep* 428:1–52
63. Fedorov DG, Kitaura K (2004) *J Chem Phys* 121:2483–2490
64. Fedorov DG, Kitaura K (2005) *J Chem Phys* 123:134103–134111
65. Ranganathan S, Gready JE (1997) *J Phys Chem B* 101:5614–5618
66. Gready JE, Ranganathan S (1994) *Gre Faraday Trans* 90:2047–2056
67. Zhang DW, Zhang JZH (2003) *J Chem Phys* 119:3599–3605
68. Jiang N, Ma J, Jiang Y (2006) *J Chem Phys* 124:114112–114119
69. Hyperchem 7.5. (2003) Hypercube, Inc., 1115 NW 4th Street, Gainesville, FL 32601, USA. Ref Type: Computer Program
70. Zhang Y, Lee TS, Yang W (1999) *J Chem Phys* 110:46–54
71. Zhang Y (2005) *J Chem Phys* 122:024114
72. Zhang Y (2006) *Theor Chem Acc* 116:43–50
73. Jardillier N, Goursot A (2008) *Chem Phys Lett* 454:65–69
74. DiLabio GA, Hurley MM, Christiansen PA (2002) *J Chem Phys* 116:9578–9584
75. Antes I, Thiel W (1999) *J Phys Chem A* 103:9290–9295
76. Poteau R, Ortega I, Alary F, Ramirez Solis A, Barthelat JC, Daudey J-P (2001) *J Phys Chem A* 105:198–205
77. Yasuda K, Yamaki D (2004) *J Chem Phys* 121:3964–3972
78. Slavicek P, Martinez TJ (2006) *J Chem Phys* 124:084107
79. Assfeld X, Ferre N, Rivail J (1998) In: Combined quantum mechanical and molecular mechanical methods. American Chemical Society, Washington, DC, pp. 234–249
80. Gorb LG, Rivail JL, Thery V, Rinaldi D (1996) *Int J Quantum Chem* 60:1525–1536
81. Rivail JL (1999) *J Mol Struct THEOCHEM* 463:3
82. Thery V, Rinaldi D, Rivail JL, Maigret B, Ferenczy GG (1994) *J Comp Chem* 15:269–282
83. Ferenczy GG, Rivail JL, Surjan PR, Naray-Szabo G (1992) *J Comp Chem* 13:830–837
84. Philipp DM, Friesner RA (1999) *J Comp Chem* 20:1468–1494
85. Murphy RB, Philipp DM, Friesner RA (2000) *J Comp Chem* 21:1442–1457
86. Pu J, Gao J, Truhlar DG (2004) *J Phys Chem A* 108:632–650
87. Pernal K, Wesolowski TA (2009) *Int J Quantum Chem* 109:2520–2525
88. Wesolowski TA (2008) *Phys Rev A* 77:012504
89. Case DA, Darden TA, Cheatham III TE, Simmerling CL, Wang J, Duke RE, Luo R, Crowley M, Walker RC, Zhang W, Merz KM, Wang B, Hayik S, Roitberg A, Seabra G, Kolossvary I, Wong KF,

- Paesani F, Vanicek J, Wu X, Brozell SR, Steinbrecher T, Gohlke H, Yang L, Tan C, Mongan J, Hornak V, Cui G, Mathews DH, Seetin MG, Sagui C, Babin V, Kollman PA (2008) AMBER 10. University of California, San Francisco, CA. Ref Type: Computer Program
90. Brooks BR, Bruccoleri RE, Olafson BD, States DJ, Swaminathan S, Karplus M (1983) *J Comp Chem* 4:187–217
 91. Zhang Y, Lee TS, Yang W (1999) *J Chem Phys* 110:46–54
 92. Exner TE (2010) *Int J Quantum Chem.* doi: 10.1002/qua.22473
 93. Eckard S, Exner TE (2006) *Z Phys Chem* 220:927–944
 94. Eckard S, Exner TE (2009) *Int J Quantum Chem* 109:1451–1463
 95. McWeeny R (1962) *Phys Rev* 126:1028
 96. Ditchfield R (1974) *Mol Phys* 27:789–807
 97. Wolinski K, Sadlej AJ (1980) *Mol Phys* 41:1419–1430
 98. Wolinski K, Hinton JF, Pulay P 1990 *J Amer Chem Soc* 112:8251–8260
 99. Frisch MJ, Trucks GW, Schlegel HB, Scuseria GE, Robb MA, Cheeseman JR, Montgomery JA Jr, Vreven T, Kudin KN, Burant JC, Millam JM, Iyengar SS, Tomasi J, Barone V, Mennucci B, Cossi M, Scalmani G, Rega N, Petersson GA, Nakatsuji H, Hada M, Ehara M, Toyota K, Fukuda R, Hasegawa J, Ishida M, Nakajima T, Honda Y, Kitao O, Nakai H, Klene M, Li X, Knox JE, Hratchian HP, Cross JB, Bakken V, Adamo C, Jaramillo J, Gomperts R, Stratmann RE, Yazyev O, Austin AJ, Cammi R, Pomelli C, Ochterski JW, Ayala PY, Morokuma K, Voth GA, Salvador P, Dannenberg JJ, Zakrzewski VG, Dapprich S, Daniels AD, Strain MC, Farkas O, Malick DK, Rabuck AD, Raghavachari K, Foresman JB, Ortiz JV, Cui Q, Baboul AG, Clifford S, Cioslowski J, Stefanov BB, Liu G, Liashenko A, Piskorz P, Komaromi I, Martin RL, Fox DJ, Keith T, Al-Laham MA, Peng CY, Nanayakkara A, Challacombe M, Gill PMW, Johnson B, Chen W, Wong MW, Gonzalez C, Pople JA (2004) *Gaussian 03 (Revision C.2)*. Wallingford CT, Gaussian, Inc. Ref Type: Computer Program
 100. Cancès E, Mennucci B, Tomasi J (1997) *J Chem Phys* 107:3032–3041
 101. Cossi M, Barone V, Mennucci B, Tomasi J (1998) *Chem Phys Lett* 286:253–260
 102. Mennucci B, Tomasi J (1997) *J Chem Phys* 106:5151–5158

CHAPTER 9

ELONGATION METHOD: TOWARDS LINEAR SCALING FOR ELECTRONIC STRUCTURE OF RANDOM POLYMERS AND OTHER QUASILINEAR MATERIALS

FENG LONG GU^{1,4}, BERNARD KIRTMAN², AND YURIKO AOKI^{3,4}

¹*Center for Computational Quantum Chemistry, South China Normal University, Guangzhou 510631 China, e-mail: gu@scnu.edu.cn*

²*Department of Chemistry and Biochemistry, University of California, Santa Barbara, CA, 93106-9510, USA, e-mail: kirtman@chem.ucsb.edu*

³*Department of Material Sciences, Faculty of Engineering Sciences, Kyushu University, Fukuoka 816-8580, Japan, e-mail: aoki@mm.kyushu-u.ac.jp*

⁴*Japan Science and Technology Agency, CREST, Kawaguchi, Saitama 332-0012, Japan*

Abstract: We present the linear scaling elongation method for Hartree-Fock and Kohn-Sham electronic structure calculations of either periodic or aperiodic quasi-one-dimensional systems. Linear scaling is achieved through two key computational features: (1) regional localization of molecular orbitals; and (2) a two-electron integral cutoff technique combined with quantum fast multipole evaluation of non-negligible long-range integrals. The accuracy and timing of the method is demonstrated for several systems of interest such as polyglycine and BN nanotubes. Future developments of both a technical and methodological nature are noted including the extension to higher dimensionality as well as higher level wave function treatments.

Keywords: Elongation method, Linear scaling, Localization method, Quasi-one-dimensional systems, Cutoff technique

9.1. INTRODUCTION

Quantum chemical calculations have proved to be a reliable and practical tool for investigating the electronic structure and properties of small and medium-size chemical species. There is now great interest in extending the methods used in these calculations to larger systems such as those occurring in materials science and biochemistry. For these systems, the structure/property under investigation can sometimes be satisfactorily studied using a small cluster model, but often that is not the case. The treatment of semiconductors lightly doped with transition metal atoms is just one of many examples. On the other hand, if the system of interest can be adequately approximated as having perfect translational symmetry, then crystal

orbital procedures can be applied. However, in many – if not most – instances the system of interest cannot be modeled in this manner either. An example is a chain of variously arranged amino acids that may play an essential role in the catalytic activity of a particular enzyme.

The major obstacle to treating large systems on the same footing as small/medium-size molecules arises from the fact that the most frequently used electronic structure computational algorithms scale in the range from N^3 to N^7 with the number of electrons, N . Considerable efforts have been devoted in recent years to exploit locality as a means of reducing the power law. For this purpose one can take advantage of the fact that electron-electron interactions between spatially well-separated electron distributions are relatively weak. A number of procedures for doing so have been developed and, when the system is sufficiently extended in space, linear scaling can be achieved. One set of methods utilizes a combination of fragments approach. This set includes the QM/MM [1], “divide and conquer” [2], “local space approximation” [3], and “fragment molecular orbital” [4] treatments. The elongation method (EM), which we present in this chapter, is a treatment of the same general type. It was originally formulated by Imamura, et al. [5] as a Hartree-Fock (HF) procedure for building up the electronic structure of a large quasilinear periodic or aperiodic polymer.

The EM is designed to theoretically mimic the experimental polymerization/copolymerization process. Thus, a polymer chain is (theoretically) synthesized stepwise by adding a monomer unit to a starting cluster. Since the monomer unit is arbitrary any quasilinear structure can be constructed in this manner. Of course, if the individual monomers are identical, then the stereoregular polymer is obtained. For pedagogical and illustrative purposes it is sufficient to consider only the latter case as we have done here. Readers interested in the application to aperiodic and/or defect structures may refer to Refs. [6] and [7].

Subsequent to its initial presentation, the EM has been generalized so that one can treat a local interaction with a periodic system in one, two, or three dimensions (2D or 3D). This includes: (a) a polymer interacting with a small molecule [8]; (b) a local defect or adsorption at a surface [9]; and (c) an impurity or local lattice defect in a crystal [10]. Furthermore the Hartree-Fock treatment has been extended to include Kohn-Sham (KS) DFT [11] as well as MP2. Finally, work is in progress towards development of a full 2D/3D procedure. A working version of the EM has been implemented in the GAMESS program package [12]. In comparison with the other “combination of fragment” methods mentioned here the EM appears to have advantages with regard to efficiency and/or accuracy.

There are two key computational features of the EM that result in linear scaling and determine its efficiency and accuracy. They are: (1) the regional localization scheme [13]; and (2) the two-electron integral cutoff technique which is combined with a quantum fast multipole method (QFMM) for evaluation of non-negligible long-range integrals [14]. Figure 9-1 presents a schematic illustration of the EM. In the next section we describe the construction of regional localized molecular orbitals with the resulting the separation into an active region and a frozen region. The orbitals of the frozen region are discarded in the SCF calculation that is carried out when the monomer is added to the chain. If the size of the active region is

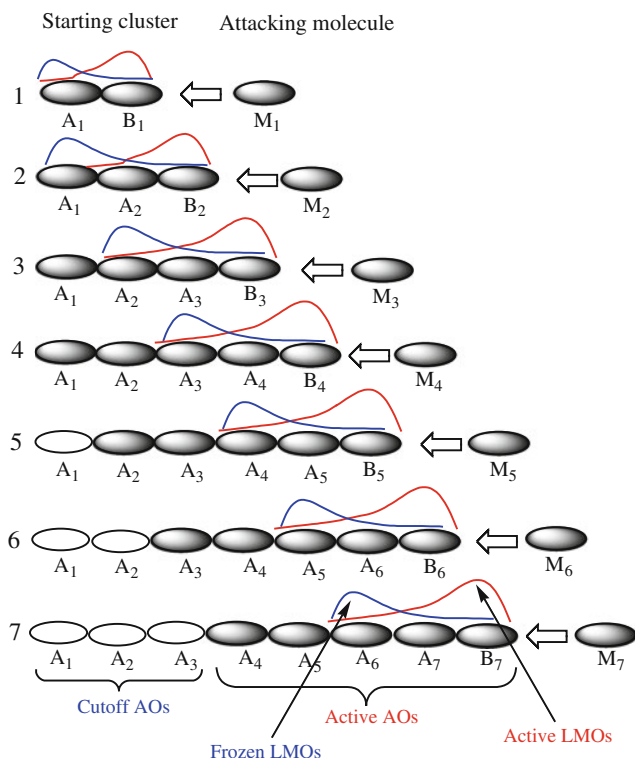


Figure 9-1. Schematic illustration of the elongation method. M_1, M_2, \dots is the attacking monomer; $B_1 + M_1, B_2 + M_2, \dots$ is the active region; and A_1, A_2, \dots are the frozen regions

roughly maintained (with the frozen region increased accordingly), then the size of the Fock matrix that must be diagonalized will remain roughly the same regardless of the chain length. The key steps of the elongation method, namely the construction of regional localized orbitals and solution of the SCF equation for the active space are provided in Section 9.2. In Section 9.3 a number of examples are presented, for several different cases, in order to verify that reducing the variational space as described does not lead to any significant loss of accuracy. Then the technique for eliminating many two-electron integrals is presented in Section 9.4. This procedure leads to overall linear scaling as shown by some test calculations in Section 9.5. Finally, Section 9.6 contains a summary of the EM and prospective extensions of our procedure.

9.2. THE KEY STEPS OF THE ELONGATION METHOD

In this section we describe the construction of regional localized molecular orbitals (RLMOs) and their use in the elongation SCF step. The EM begins with the determination of the Hartree-Fock (HF) or Kohn Sham (KS) canonical molecular orbitals

(CMOs), φ^{CMO} , for an appropriate starting cluster (see later). These CMOs, which are spatially delocalized, are obtained as a linear combination of atomic orbitals (AOs):

$$\varphi^{\text{CMO}} = \chi^{\text{AO}} C_{\text{AO}}^{\text{CMO}} \quad (9-1)$$

where φ^{CMO} and χ^{AO} are row vectors. As shown in Figure 9-1, the CMOs of the starting cluster are localized into two sets in preparation for interaction with an attacking monomer. One set consists of localized molecular orbitals (LMOs) located at the end of the starting cluster that is remote from the point of attack (region A or frozen region); the other set is located in the active region (region B). The choice of active and frozen regions will be discussed in the context of specific examples in Section 9.3. As a general criterion the LMOs of the frozen region must be sufficiently remote from the interaction site that they can be ignored in carrying out the SCF calculation for addition of the monomer. Obviously, this requires LMOs that are as strongly localized as possible. In addition, we desire a localization procedure that is efficient and reliable.

The original localization schemes [5] were based on successive 2×2 rotations of CMOs in a manner similar to the well-known Edmiston and Ruedenberg [15] procedure. This requires an initial assignment of CMOs to one of the two regions, which can be problematic for covalently bonded or pi-conjugated systems. That difficulty was solved by re-expressing the CMOs in terms of hybrid AOs determined from the original AOs by means of an approach due to Del Re [16]. Although this yields adequate localization in many cases, Gu et al. [13] have recently developed a new method that is more efficient and more accurate. Tests on a variety of systems (see Section 9.3) show that the EM results obtained with this new scheme are satisfactory, even for highly delocalized systems, as long as the starting cluster is sufficiently large.

9.2.1. Construction of RLMOs

The RLMO localization scheme relies on the first-order density matrix given by:

$$D^{\text{AO}} = C_{\text{AO}}^{\text{CMO}} \mathbf{d} C_{\text{AO}}^{\text{CMO}\dagger} \quad (9-2)$$

in the AO basis. Here \mathbf{d} is the diagonal occupation number matrix and $C_{\text{AO}}^{\text{CMO}}$ is defined in Eq. (9-1). For a restricted Hartree-Fock wavefunction the occupation number is 2 for doubly-occupied spatial orbitals and 0 for unoccupied orbitals. With the aid of the orthonormality condition

$$C_{\text{AO}}^{\text{CMO}\dagger} S^{\text{AO}} C_{\text{AO}}^{\text{CMO}} = \mathbf{1}, \quad (9-3)$$

wherein S^{AO} is the AO overlap matrix and $\mathbf{1}$ the identity matrix, Eq. (9-2) yields the idempotency relation:

$$D^{\text{AO}} S^{\text{AO}} D^{\text{AO}} = 2D^{\text{AO}}. \quad (9-4)$$

for an ordinary closed shell system.

Next, we transform from the non-orthogonal AO basis to an orthogonalized AO (OAO) basis by adopting Löwdin's symmetric orthogonalization procedure [13], which keeps the new basis least distorted from the original AOs. The transformation matrix

$$X = V\lambda^{1/2}V^\dagger = X^\dagger, (C_{\text{OAO}}^{\text{CMO}} = XC_{\text{AO}}^{\text{CMO}}) \quad (9-5)$$

is obtained by diagonalizing the AO overlap matrix; i.e. V and λ are the eigenvectors and eigenvalues of S^{AO} . Then the density matrix in the OAO basis becomes:

$$D^{\text{OAO}} = XD^{\text{AO}}X^\dagger \quad (9-6)$$

Using Eqs. (9-2) and (9-6), and the fact that $X^\dagger X = XX^\dagger = S^{\text{AO}}$ one can easily verify that

$$D^{\text{OAO}}D^{\text{OAO}} = 2D^{\text{OAO}} \quad (9-7)$$

This is the idempotency relation for the density matrix in the OAO basis. As a consequence, its eigenvalues must be either 2 or 0. Therefore, the eigenvectors of D^{OAO} correspond to orbitals that are either completely occupied or completely vacant. In addition, the OAO density matrix may be unambiguously partitioned into diagonal blocks for the frozen region A and active region B. This avoids the poor localization that was sometimes previously obtained.

The desired RLMOs, which are also simultaneously localized and either completely occupied or vacant in each region, are obtained in two further steps. In the first step, a regional orbital (RO) space is constructed by separately diagonalizing the $D^{\text{OAO}}(\text{A})$ and $D^{\text{OAO}}(\text{B})$ diagonal sub-blocks of D^{OAO} . This yields a set of eigenvectors that span the RO space. The second step is to perform a unitary transformation to undo the mixing between the occupied and unoccupied blocks of D^{RO} in such a way as to preserve the localization as much as possible. The procedure is similar to the construction of natural bond orbitals (NBOs) but suitably modified and generalized for localized regional orbitals.

In the first step, the transformation from OAOs to ROs is given by the direct sum of T^{A} and T^{B} , i.e.

$$T = T^{\text{A}} \oplus T^{\text{B}} \quad (9-8)$$

where T^{A} and T^{B} are the eigenvectors of $D^{\text{OAO}}(\text{A})$ and $D^{\text{OAO}}(\text{B})$, respectively. The eigenvalues may be divided into three sets corresponding to ROs that are approximately doubly-occupied (value close to 2), singly-occupied (eigenvalue close to 1) and empty (eigenvalue close to 0). The singly-occupied orbitals in A and B are hybrid AOs that could be combined to form covalent bonding/antibonding pairs. In order to maintain localization, however, we adopt the alternative procedure of

transferring an electron from each singly-occupied orbital of A to the corresponding singly-occupied orbital of B or *vice versa*, depending upon which region is more electronegative. We thereby create the ionic pair (A^+B^-) or (A^-B^+). For covalently bonded systems, the localization quality from either choice will be essentially the same. For a non-bonded system, such as a water chain, there are only either doubly-occupied or unoccupied orbitals. In terms of T the density matrix in the RO basis is

$$D^{\text{RO}} = T^\dagger D^{\text{OAO}} T \quad (9-9)$$

which corresponds to the transformation

$$C_{\text{RO}}^{\text{CMO}} = T^\dagger X C_{\text{AO}}^{\text{CMO}}. \quad (9-10)$$

Using Eq. (9-7) and the unitarity condition $TT^\dagger = T^\dagger T = 1$, one can verify that

$$D^{\text{RO}} D^{\text{RO}} = 2D^{\text{RO}} \quad (9-11)$$

Except for orthogonalization tails the ROs given above are completely localized to region A or region B. However, they are not completely occupied or unoccupied. Thus, the second, and final, step is to carry out a unitary transformation to remove the coupling between occupied and unoccupied blocks of D^{RO} while retaining the localization as much as possible. This is done using the same Jacobi procedure that is employed in Ref. [17] to convert NBOs into localized molecular orbitals. If U is the complete transformation matrix, then the only non-zero elements of

$$D^{\text{RLMO}} = U^\dagger D^{\text{RO}} U \quad (9-12)$$

will be equal to 2 (cf. Eq. (9-11)) and the resulting RLMO based CMOs will be given by:

$$C_{\text{RLMO}}^{\text{CMO}} = U^\dagger T^\dagger X C_{\text{AO}}^{\text{CMO}} \quad (9-13)$$

Finally, the coefficient matrix for transformation from AOs to RLMOs is (replace φ^{CMO} in Eq. (9-1) with φ^{RLMO})

$$C_{\text{AO}}^{\text{RLMO}} = X^{-1} T U \quad (9-14)$$

From this point on we set $C_{\text{AO}}^{\text{RLMO}} = L_{\text{AO}}^{\text{RLMO}}$ in order to emphasize the localized nature of the transformed orbitals. The RLMOs defined by Eq. (9-14) are completely occupied or vacant, but are not perfectly localized due to the Jacobi rotations. Nonetheless they are sufficiently well-localized so that the following elongation step can be carried out without significant loss of accuracy.

9.2.2. SCF Elongation Step

For a given suitably large starting cluster, the interaction between the frozen region and the attacking monomer is minimized (subject to an occupancy constraint) by using RLMOs. The elongation Hartree-Fock equation is solved self-consistently in a basis consisting of the RLMOs of the active region and modified CMOs of the attacking monomer (M). These CMOs are orthogonalized to the entire set of RLMOs, using the Gram-Schmidt procedure, before proceeding further. In practice, other choice can be made for the monomer. The SCF solution, then, obtained in the reduced space and the resulting CMOs are localized into a new frozen region and a new active region. The new active region is taken to be roughly the same size as the previous one. This entire procedure is repeated until the desired length is reached. The important feature of the elongation method is that the Hartree-Fock equation is solved only for the interactive region instead of the whole system. Each time the system is enlarged, the size of the interactive region remains essentially the same and, thus, the CPU required for the elongation SCF step is more or less constant.

Although we have described the basis set for the SCF elongation calculation we have yet to describe the construction of the Fock matrix for the reduced space defined by the LMOs assigned to the B_1 region together with orthogonalized CMOs of the monomer M_1 . The transformation matrix from AOs to this mixed basis maybe written as:

$$L(B_1 + M_1) = L(B_1) \oplus C(M_1) \quad (9-15)$$

Here $L(B_1 + M_1)$ is a rectangular matrix with as many columns as determined by the reduced space and as many rows as determined by the full space. In practice, instead of CMOs, the molecular orbitals of M_1 are just a convenient arbitrary set of orthonormal orbitals. Then, using Eq. (9-15) the Fock matrix in the LMO-CMO basis obtained through the transformation:

$$F_{ij}^{\text{LMO-CMO}}(B_1 + M_1) = \sum_{\mu} \sum_{\nu} L_{\mu i}(B_1 + M_1) F_{\mu\nu}^{\text{AO}}(A_1 + B_1 + M_1) L_{\nu j}(B_1 + M_1) \quad (9-16)$$

where is the complete Fock matrix in the AO basis. Whereas the AO basis Fock matrix is for the whole system, the LMO-CMO basis Fock matrix is restricted to the interactive region. The overlap matrix in the LMO-CMO basis can be obtained by the same transformation as employed in Eq. (9-16) for the F matrix. Since the overlap matrix in the LMO-CMO basis is the unit matrix, the Hartree-Fock equation for the interactive region becomes:

$$F^{\text{LMO-CMO}}(B_1 + M_1)U(B_1 + M_1) = U(B_1 + M_1)\varepsilon(B_1 + M_1) \quad (9-17)$$

The dimension of the HF equation in Eq. (9-17) is the size of the interactive region (B_1+M_1) instead of the whole space ($A_1+B_1+M_1$). This is the special feature of the

elongation method, which accounts for its efficiency and accuracy when combined with regional localization (already described) and the integral evaluation techniques described in Section 9.4. In connection with the Hartree-Fock equation, we note that the contribution of the frozen orbitals is included in the AO basis Fock matrix of Eq. (9-16). It is important to recognize that the Fock matrix elements coupling the A_1 and M_1 blocks will have a negligible effect (as we will see) if these regions are sufficiently far apart. Moreover, the coupling between the A_1 and B_1 blocks will have little influence on the electron density and total energy. This latter statement follows from the fact that the non-vanishing elements lie entirely within either the occupied or the vacant space by virtue of the regional localization procedure.

After solving Eq. (9-17), the CMOs of the B_1+M_1 region are given by the overall transformation from AOs:

$$C_{\mu i}(B_1 + M_1) = \sum_j L_{\mu j}(B_1 + M_1)U_{ji}(B_1 + M_1) \quad (9-18)$$

Using these coefficients, the total AO density matrix becomes:

$$D_{\mu\nu}^{AO} = 2 \sum_i^{occ} L_{\mu i}(A_1)L_{\nu i}(A_1) + 2 \sum_i^{occ} C_{\mu i}(B_1 + M_1)C_{\nu i}(B_1 + M_1) \quad (9-19)$$

Then, the total AO basis Fock matrix may be obtained in the usual manner as:

$$F_{\mu\nu}^{AO}(A_1 + B_1 + M_1) = H_{\mu\nu}^{core} + \sum_{\lambda\sigma} D_{\lambda\sigma}^{AO} [(\mu\nu | \sigma\lambda) - \frac{1}{2}(\mu\lambda | \sigma\nu)] \quad (9-20)$$

The AO basis Fock matrix in Eq. (9-20) is used to form the updated LMO-CMO basis Fock matrix in Eq. (9-16) and the elongation SCF iterations are repeated until convergence is achieved. The convergence criterion is set so that either the maximum difference in any density matrix element between the previous iteration and the current one is less than a given threshold – normally 10^{-6} – or the difference in the energy is less than 10^{-8} a.u.

After the elongation SCF step is converged, the next elongation step is prepared by localizing the transformation matrix $C(B_1 + M_1)$ of Eq. (9-18) into two regions, a new frozen region A_2 and a new active region B_2 . This new active region is ready to interact with a new attacking monomer M_2 . In such fashion, the elongation procedure is continued until the desired length is reached.

9.3. TESTS OF THE ACCURACY OF THE ELONGATION METHOD: POLYGLYCINE AND CATIONIC CYANINE CHAINS

When a closed-shell oligomer is attacked by a monomer, the reaction corresponds to “substituting” the terminal capping atom(s) by the monomer (with its capping atoms removed). This substitution requires deleting the capping atoms from the Hamiltonian as well as a procedure for replacing the terminal capping atom AO coefficient(s) in the CMOs of A and B. For the latter purpose we use AOs on the

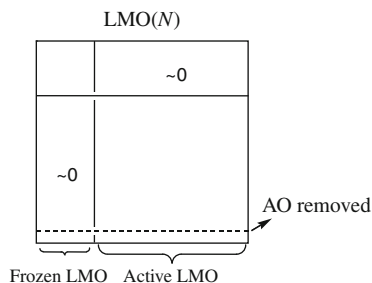


Figure 9-2. Illustration of the terminal atom removal

atom of the monomer that participates in the new bond. The choice of corresponding atomic orbitals is not important because the coefficients are very small for the CMOs of A and the resulting CMOs of B+M are self-consistently corrected during the elongation SCF step. Figure 9-2 illustrates the procedure followed in removing the terminal capping atom(s) of the growing oligomer. For simplicity, we suppose that a hydrogen atom is to be removed. The AO corresponding to the terminal hydrogen is first removed from the basis. Consequently, the $N \times N$ matrix that gives the transformation from AOs to LMOs has one less row and becomes a rectangular $(N - 1) \times N$ matrix. This makes the LMOs linearly dependent and the orthonormalization condition is no longer fulfilled. The linear dependence in the LMOs must be removed and the remaining LMOs re-orthonormalized. This can be done by diagonalizing the overlap matrix for the linear dependent LMOs, that is by following

$$Y^\dagger (\bar{L}^\dagger S \bar{L}) Y = \delta \quad (9-21)$$

where S is the AO overlap matrix, \bar{L} is the transformation matrix after one AO is removed from the basis, and Y and δ are the eigenvectors and eigenvalues of $\bar{L}^\dagger S \bar{L}$, respectively. The eigenvectors corresponding to zero or very small value eigenvalue should be deleted and the re-orthonormalized LMOs are obtained as $L' = \bar{L} Y \delta^{-1/2}$. [18]

As fairly strenuous tests of the elongation method we consider two strongly delocalized and covalently bonded systems, namely polyglycine and cationic cyanine chains. The geometry of both systems is depicted in Figure 9-3. RHF/STO-3G total

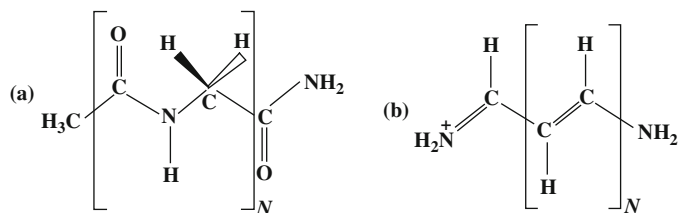


Figure 9-3. Geometrical structure of **a** polyglycine and **b** cationic cyanines. Reprinted with permission from Gu et al. [13]. Copyright [2004], American Institute of Physics

Table 9-1. RHF/STO-3G total energy of polyglycine obtained from conventional calculations and the elongation energy error $\Delta E = E^{\text{elg}} - E^{\text{cvl}}$ for different size starting clusters (N_{st}). Reprinted with permission from

N	E (total, in a.u.)	$\Delta E = E^{\text{elg}} - E^{\text{cvl}}$ (in 10^{-6} a.u.)				
	Conventional	$N_{\text{st}} = 4$	5	6	7	8
4	-856.14997927	0.00				
5	-1,060.26460708	0.13	0.00			
6	-1,264.37928877	0.38	0.16	0.00		
7	-1,468.49397305	0.72	0.43	0.16	0.00	
8	-1,672.60867708	1.11	0.79	0.44	0.17	0.00
9	-1,876.72338190	1.55	1.20	0.82	0.45	0.17
10	-2,080.83809595	2.02	1.66	1.24	0.83	0.46
11	-2,284.95281027	2.51	2.13	1.70	1.25	0.84
12	-2,489.06752962	3.02	2.63	2.18	1.72	1.26
13	-2,693.18224908	3.54	3.15	2.68	2.20	1.73
14	-2,897.29697156	4.07	3.68	3.20	2.71	2.21
15	-3,101.41169409	4.61	4.21	3.73	3.23	2.72
16	-3,305.52641858	5.16	4.76	4.27	3.76	3.24
17	-3,509.64114310	5.72	5.31	4.82	4.30	3.78
18	-3,713.75586896	6.28	5.87	5.37	4.85	4.32
19	-3,917.87059484	6.84	6.43	5.93	5.41	4.87
20	-4,121.98532166	7.41	6.99	6.49	5.96	5.42

Gu et al. [13]. Copyright [2004], American Institute of Physics

energies and elongation errors for different size polyglycine starting clusters (N_{st}) are presented in Table 9-1. Here N_{st} ranges from 4 to 8, where N_{st} counts the number of $(-\text{CO}-\text{NH}-\text{CH}_2-)$ units in the starting cluster. The formula of the starting cluster with $N_{\text{st}} = 4$, for example, is $\text{CH}_3-(\text{CO}-\text{NH}-\text{CH}_2-)_4-\text{H}$, and the attacking monomer is $\text{H}-(\text{CO}-\text{NH}-\text{CH}_2)-\text{H}$. So we have to remove the capping H atoms on the starting cluster and the attacking monomer according to the procedures described above. For the case $N_{\text{st}} = 4$, with one residue in the frozen region and three in the active region, the elongation energy errors compared to a conventional calculation are within a maximum value of 7.5×10^{-6} a.u. for up to 20 residues. The error per unit, $\Delta E(N) - \Delta E(N - 1)$, is plotted *versus* N in Figure 9-4 for different N_{st} . For any given N , the elongation error decreases as the starting cluster size increases, which is what one might expect. Moreover, the difference between starting clusters becomes smaller as the starting number of residues increases. In all instances, the error monotonically approaches a value of roughly 6.0×10^{-7} a.u. This indicates that the elongation error does not accumulate – it saturates to a small asymptotic limit as more and more elongation steps are performed.

It is also of interest to see how our scheme is affected by the choice of basis set. In Table 9-2 RHF/6-31G results from conventional and elongation calculations are given for polyglycine chains containing up to 12 residues. Using this basis set the curves analogous to those in Figure 9-4 are non-monotonic and an upper bound on the error per residue cannot be obtained in the same manner as before. However, for $N_{\text{st}} \geq 6$ the 6-31G basis set error per unit is always much smaller than the

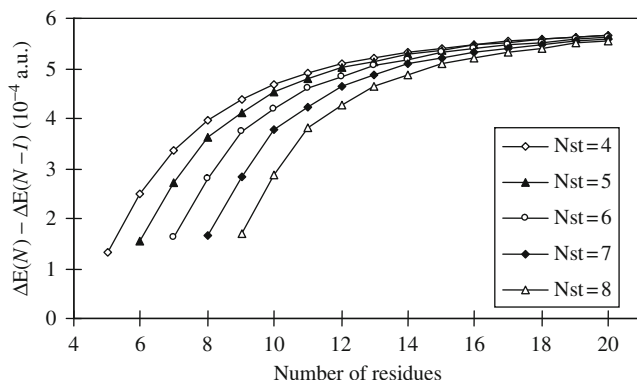


Figure 9-4. The elongation error per unit with respect to the size of starting cluster for polyglycine at HF/STO-3G level. Reprinted with permission from Gu et al. [13]. Copyright [2004], American Institute of Physics

corresponding STO-3G errors. This leads us to believe that an upper bound does exist for these starting clusters and that it is less than the bound for the smaller basis. The same may be true for $N_{st} = 5$ but not for $N_{st} = 4$. This shows in addition, that a larger starting cluster is required for larger basis sets.

For the model cationic cyanine chains shown in Figure 9-3b there is also a resonance form where the charge is localized at the right hand end of the chain and another form with a soliton defect at the center of the chain. These chains are strongly delocalized and we anticipated that a larger starting cluster would be required than for polyglycine. Bearing this in mind we considered starting clusters in the range $10 \leq N_{st} \leq 18$ for the STO-3G basis (see Table 9-3 as well as Figure 9-5 and $10 \leq N_{st} \leq 15$ for the 6-31G basis (see Table 9-4 as well as Figure 9-6). For all starting clusters, the initial frozen region contains 13 atoms: $H_2N^+ = CH - CH = CH - CH = CH -$ with the remainder in the active region. Given a cyanine containing a fixed number of $CH = CH -$ units, the error per unit decreases

Table 9-2. RHF/6-31G total energy of polyglycine obtained from conventional calculations and the elongation energy difference $\Delta E = E^{elg} - E^{cvl}$ for different size of the starting clusters (N_{st})

N	E (total, in a.u.)	$\Delta E = E^{elg} - E^{cvl}$ (in 10^{-6} a.u.)				
	Conventional	$N_{st} = 4$	5	6	7	8
4	-866.98679700	0.00				
5	-1,073.69571468	0.33	0.00			
6	-1,280.40474591	0.84	0.39	0.00		
7	-1,487.11377297	1.57	0.95	0.41	0.00	
8	-1,693.82284353	2.42	1.74	0.99	0.42	0.00
9	-1,900.53191219	3.38	2.63	1.82	1.01	0.42
10	-2,107.24100130	4.41	1.48	0.29	0.10	0.02
11	-2,313.95008940	5.50	1.94	0.43	0.16	0.03
12	-2,520.65918886	6.62	2.45	0.58	0.24	0.06

Table 9-3. RHF/STO-3G total energy of cationic cyanines obtained from conventional calculations and the elongation energy error $\Delta E = E^{\text{elg}} - E^{\text{cvl}}$ for different size starting clusters (N_{st}). All energies are in a.u.

N	E (total)	$\Delta E = E^{\text{elg}} - E^{\text{cvl}}$				
	Conventional	$N_{\text{st}} = 10$	12	14	16	18
10	-907.0294875					
11	-982.9678631	2.643E-04				
12	-1058.9060880	4.585E-04				
13	-1134.8442013	6.290E-04	9.618E-05			
14	-1210.7822352	7.748E-04	1.563E-04			
15	-1286.7202161	8.963E-04	2.052E-04	3.490E-05		
16	-1362.6581659	9.970E-04	2.441E-04	4.839E-05		
17	-1438.5961016	1.081E-03	2.749E-04	5.785E-05	1.264E-05	
18	-1514.5340365	1.155E-03	3.002E-04	6.476E-05	1.126E-05	
19	-1590.4719800	1.223E-03	3.229E-04	7.074E-05	9.739E-06	4.713E-06
20	-1666.4099384	1.289E-03	3.452E-04	7.718E-05	8.761E-06	-1.085E-06
21	-1742.3479152	1.356E-03	3.687E-04	8.504E-05	9.002E-06	-5.577E-06
22	-1818.2859122	1.426E-03	3.945E-04	9.486E-05	1.084E-05	-8.878E-06
23	-1894.2239294	1.500E-03	4.230E-04	1.068E-04	1.435E-05	-1.093E-05
24	-1970.1619663	1.579E-03	4.544E-04	1.207E-04	1.941E-05	-1.178E-05
25	-2046.1000215	1.663E-03	4.887E-04	1.365E-04	2.579E-05	-1.160E-05
26	-2122.0380934	1.751E-03	5.255E-04	1.538E-04	3.319E-05	-1.064E-05
27	-2197.9761805	1.843E-03	5.648E-04	1.725E-04	4.135E-05	-9.121E-06
28	-2273.9142810	1.940E-03	6.062E-04	1.922E-04	5.003E-05	-7.280E-06
29	-2349.8523935	2.040E-03	6.495E-04	2.127E-04	5.903E-05	-5.311E-06
30	-2425.7905166	2.143E-03	6.944E-04	2.339E-04	6.820E-05	-3.360E-06
31	-2501.7286489	2.250E-03	7.408E-04	2.556E-04	7.744E-05	-1.538E-06
32	-2577.6667893	2.359E-03	7.886E-04	2.778E-04	8.670E-05	8.390E-08
33	-2653.6049368	2.471E-03	8.374E-04	3.004E-04	9.590E-05	1.461E-06
34	-2729.5430905	2.584E-03	8.874E-04	3.233E-04	1.050E-04	2.574E-06
35	-2805.4812496	2.700E-03	9.382E-04	3.465E-04	1.141E-04	3.423E-06
36	-2881.4194135	2.817E-03	9.899E-04	3.700E-04	1.231E-04	4.026E-06
37	-2957.3575815	2.936E-03	1.042E-03	3.937E-04	1.320E-04	4.394E-06
38	-3033.2957532	3.056E-03	1.095E-03	4.176E-04	1.409E-04	4.553E-06

Reprinted with permission from Gu et al. [13]. Copyright [2004], American Institute of Physics.

(not unexpectedly) as the size of the starting cluster increases. For a particular starting cluster the error per unit with the 6-31G basis is always largest for the first elongation step. Then, this error decreases monotonically as the chain is lengthened. With the STO-3G basis there is an initial decrease in the error per unit as N increases but, then, for longer chains the error per unit goes through a minimum and increases before ultimately saturating. It is evident, in this case, that the value for large N depends significantly on N_{st} . For either basis set, however, the important point is that, once again, the error does not accumulate as the chain is elongated; instead it levels off to a fairly small value: on the order of 10^{-4} a.u. for $N_{\text{st}} = 10$ as compared to the energy per $-\text{CH}=\text{CH}-$ unit of about 77 a.u. It should also be noted that the limiting error per unit falls off by an order of magnitude when N_{st} is increased from 10 to 15. We judge that the results are satisfactory for

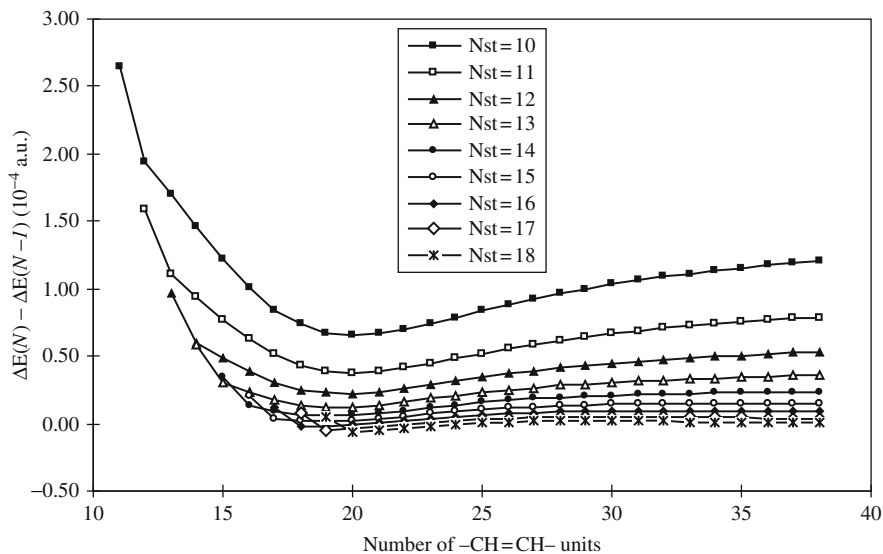


Figure 9-5. Elongation error per unit as a function of N_{st} versus the number of units cells for cyanines at STO-3G level. Reprinted with permission from Gu et al. [13]. Copyright [2004], American Institute of Physics.

$N_{st} \geq 10$. On the other hand, for $N_{st} = 4$ the limiting error per residue is on the order of 10^{-2} a.u.

So far we have been using the energy as the criterion for the accuracy of our elongation treatment. It is of interest to examine other properties as well. Thus, for the cationic cyanines, Mulliken atomic charges computed by the conventional and

Table 9-4. RHF/6-31G total energy of cationic cyanines obtained from conventional calculations and the elongation energy error $\Delta E = E^{elg} - E^{cvl}$ for different size starting clusters (N_{st}). All energies are in a.u.

N	E (total)	$\Delta E = E^{elg} - E^{cvl}$					
	Conventional	$N_{st} = 10$	11	12	13	14	15
10	-917.9884528						
11	-994.8440339	1.773E-04					
12	-1071.6994528	3.373E-04	1.064E-04				
13	-1148.5547423	4.926E-04	1.989E-04	6.432E-05			
14	-1225.4099290	6.382E-04	2.874E-04	1.160E-04	3.899E-05		
15	-1302.2650349	7.702E-04	3.687E-04	1.640E-04	6.589E-05	2.361E-05	
16	-1379.1200784	8.865E-04	4.402E-04	2.065E-04	8.954E-05	3.555E-05	1.423E-05
17	-1455.9750747	9.870E-04	5.012E-04	2.420E-04	1.088E-04	4.466E-05	1.726E-05
18	-1532.8300368	1.073E-03	5.519E-04	2.705E-04	1.233E-04	5.046E-05	1.796E-05
19	-1609.6849756	1.147E-03	5.938E-04	2.928E-04	1.334E-04	5.315E-05	1.631E-05
20	-1686.5398999	1.212E-03	6.287E-04	3.101E-04	1.401E-04	5.339E-05	1.283E-05

Reprinted with permission from Gu et al. [13] Copyright [2004], American Institute of Physics

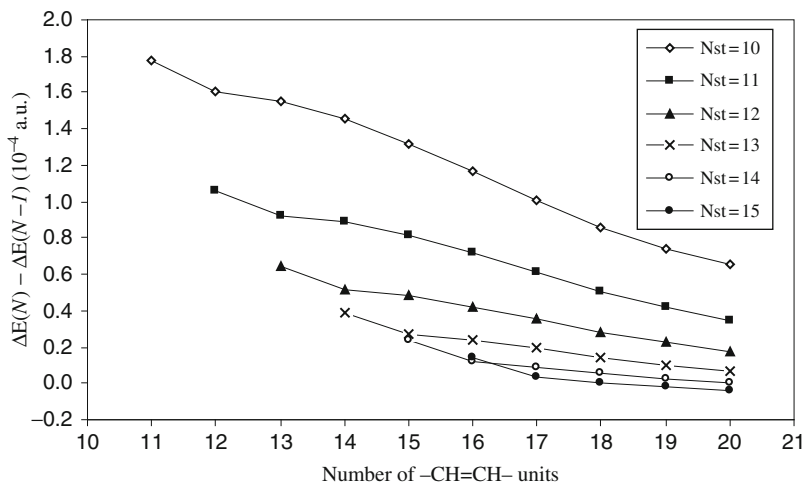


Figure 9-6. Elongation error per unit as a function of N_{st} versus the number of units cells for cyanines at 6-31G level. Reprinted with permission from Gu et al. [13]. Copyright [2004], American Institute of Physics.

elongation methods were compared. Figure 9-7 is a plot of the charge error for the case $N = 20$ obtained using the RHF/6-31G basis. The sizes of the starting cluster for the elongation calculations are $N_{st} = 10$ and $N_{st} = 15$. From Figure 9-7, one can see that the magnitude of the maximum charge error and the range of atoms over which the larger differences occur, both decrease as N_{st} increases. For $N_{st} = 10$ the maximum charge difference is slightly larger than $0.01e$, which we regard as borderline accuracy – i.e. this is the smallest starting cluster that one should use. The

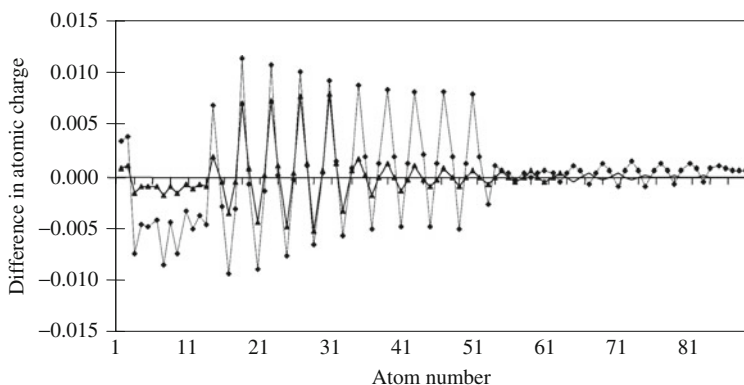


Figure 9-7. Difference in charge distribution between elongation and conventional calculations for two different elongation and conventional calculations for two different Reprinted with permission from Gu et al. [13]. Copyright [2004], American Institute of Physics

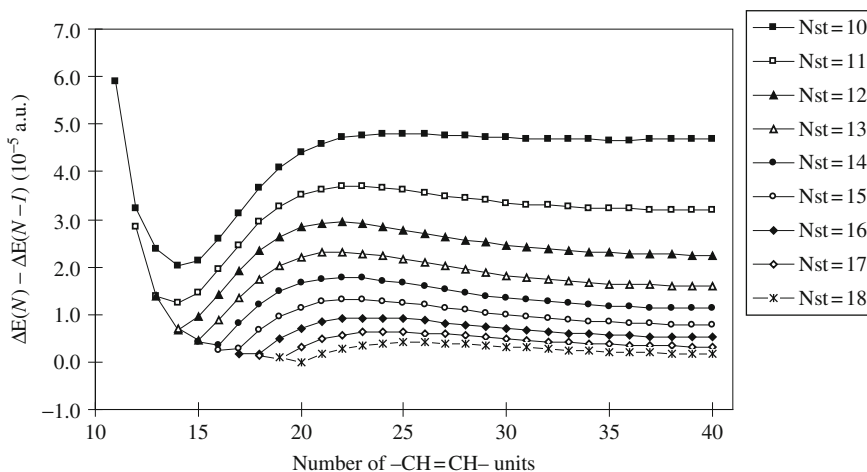


Figure 9-8. Elongation error per unit as a function of N_{st} versus the number of units for cyanines calculated at the PM3 level Reprinted with permission from Gu et al. [13]. Copyright [2004], American Institute of Physics

largest errors are in the vicinity of the border between regions A and B. As noted in Section 9.2.1, in order to have all ROs approximately doubly-occupied or approximately empty, we figuratively transfer an electron from each singly-occupied orbital of region A to the corresponding singly-occupied orbital of region B, which is probably why the largest errors occur near the border. In contrast, for water chains (same basis set; $N_{st} = 5$) no electron transfer is needed in the localization procedure and the atomic charges in the conventional and elongation calculations are almost identical (the maximum difference is less than $10^{-4}e$).

At this point a comment about the negative sign of many ΔE values in the last column of Table 9-3 is in order. Although we have not yet been able to prove that ΔE must be positive (as it would be if the variation principle applied), it has been our experience with the closely related Local Space Approximation [3] that whenever a negative ΔE occurs it is always traceable to some numerical or algorithmic error. Thus, in this case it is likely that the very small negative value is associated with numerical round-off error or incomplete SCF convergence.

For comparison purposes a set of calculations was carried out using the PM3 semiempirical Hamiltonian. As might have been anticipated, the results for the energy error per $-\text{CH}=\text{CH}-$ unit, shown in Figure 9-8, are similar to those obtained using the STO-3G minimum basis set in an *ab initio* treatment (see Figure 9-5). Both sets of curves exhibit a minimum at an intermediate chain length. However, in contrast with the *ab initio* case, the semiempirical curves do not increase monotonically for larger N but go through a small maximum and converge to the long chain limit from above rather than below.

9.4. INTEGRAL EVALUATION TECHNIQUES FOR LINEAR SCALING CONSTRUCTION OF FOCK MATRIX

In the elongation method the variational space on which the RHF or KS molecular orbitals are determined remains more or less constant as the size of the molecule is increased. This is a necessary, but not sufficient, condition to achieve linear scaling. In addition, the construction of the Fock matrix, or the KS potential, must scale linearly. For the Fock matrix we have introduced integral evaluation techniques to accomplish that purpose. In this section these techniques will be described. There are two steps involved – one is to reduce the number of electron repulsion integrals (ERIs) that must be determined and the other is to calculate the remaining small integrals by means of the quantum fast multipole method (QFMM).

9.4.1. Reducing the Number of ERIs

The elongation treatment starts from a conventional calculation performed on a sufficiently large starting cluster followed by a localization procedure whereby the CMOs of the starting cluster are localized into A_1 and B_1 regions. Region B_1 is the orbital space determined by the LMOs that interact significantly with the attacking molecule M_1 , while region A_1 contains the LMOs that have negligible interactions. In the first elongation step the SCF problem is solved on the space defined by the LMOs of B_1 and the CMOs of the attacking monomer (M_1) as shown in the schematic Figure 9-1. All ERIs are retained in forming the Fock matrix on this space. The resulting CMOs from solution of the Fock equation are localized into a new frozen region, A_2 , and a new active region, B_2 . The latter is, then, ready to interact with a new attacking molecule, M_2 . At this point we can check to see whether some of the ERIs involving AOs centered on atoms in region A_1 can be ignored in constructing the Fock matrix for the active space. The quantity used for this purpose should be a measure of the coupling between the frozen region A_1 and the active region B_2 . In the elongation method we use $\sum_{\mu}^{A_1} \sum_{\nu}^{B_n} L_{\mu i}(A_1) S_{\mu\nu}^{AO} L_{\nu j}(B_n)$ to check if a cutoff can be made or not. If this quantity is smaller than a threshold value (the default is 10^{-9}), some ERIs involving the AOs that belong to frozen region A_1 can be eliminated in constructing the Fock matrix for the elongation step. In particular, the ERIs involving 3 or 4 AOs from region A_1 can be ignored since they do not contribute to the Fock matrix in Eq. (9-20) as determined by the reduced density matrix for the active space. In Figure 9-1 the ERI proceeds without any cutoff since the cutoff criterion is not met. In fact, it is not until addition of the 5th monomer that cutoffs are initiated. Subsequently, in each elongation step a new cutoff region is generated while the remaining frozen region is kept more or less the same size. Despite the cutoff used to evaluate the Fock matrix for the active region, it is important to note that all ERIs must be retained when calculating the total energy of the system.

9.4.2. Combination of ERI Cutoff with QFMM Evaluation of Remaining Small Integrals

The elongation method is faster than a conventional HF calculation as far as the localization and, especially, the diagonalization steps are concerned. This is not true, however, for the formation of the Fock matrix. The reduction in number of ERIs afforded by the cutoff procedure described in Section 9.4.1 helps alleviate this situation, so that the overall CPU time favors the elongation method. Nonetheless, the advantage of the latter grows slowly with chain length and our method does not scale linearly without one further development, namely introduction of the quantum fast multipole moment (QFMM) [19] method to evaluate small integrals that survive the cutoff.

The QFMM method for integral evaluation is well-known and will not be reviewed here. Suffice it to say that the implementation in the Gamess [20] suite of programs has been successfully modified to include integral cutoffs. The QFMM divides Coulombic interactions into local and distant contributions. This depends on the extent parameter that characterizes Gaussian charge distributions. Local 2e-integrals are evaluated explicitly by standard methods, while, the 2e-integrals with three- or four-atomic indices belonging to cutoff regions are disregarded. All remaining 2e-integrals are evaluated by the FMM. These are divided into near-field and far-field sets, again based on an extent parameter. Such a procedure defines a tree-like hierarchy of boxes. In the elongation method, during the SCF run, the boxes with charge distributions belonging to cutoff regions are considered as field vectors for the active region.

9.5. ILLUSTRATIVE LINEAR SCALING CALCULATIONS FOR THE ELONGATION METHOD WITH ERI CUTOFF AND QFMM EVALUATION OF REMAINING SMALL INTEGRALS

When the basic elongation method incorporates ERI cutoffs and QFMM evaluation of remaining small integrals, the entire procedure scales linearly with the size of the system. Several illustrative calculations are presented in this section to support this claim. All of these calculations are performed at the HF level of theory using either an STO-3G or 6-31G basis set. [21] The threshold for the density matrix is 10^{-6} . In order to speed up the SCF convergence, the second-order method for orbital optimization [22] as adopted. Our calculations were carried out on computer clusters with 8 nodes for a total of 64 CPUs.

9.5.1. Model Linear Water Chain

For a first demonstration we chose the model system of a linear water chain shown in Figure 9-9. The cutoff calculation is initiated when the interaction between the cutoff region and the active region is less than 10^{-8} . Our results for the overall CPU time of conventional and elongation (with ERI cutoff and QFMM) calculations are

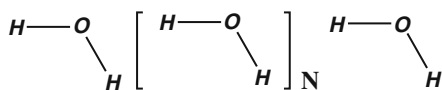


Figure 9-9. Model linear water chain

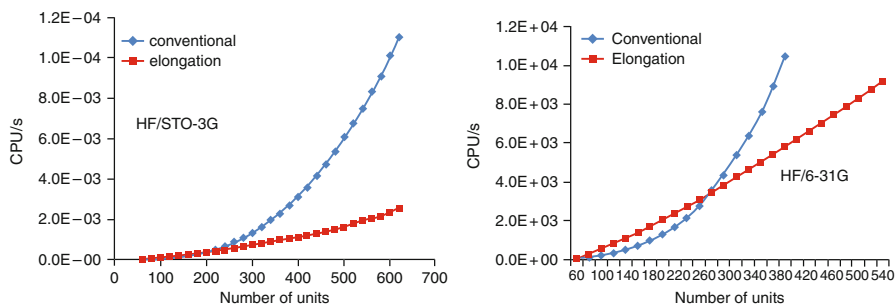


Figure 9-10. Total CPU time for conventional vs. elongation. calculations on model linear water chains, **a** HF/STO-3G and **b** HF/6-31G

shown in Figure 9-10. It is clear that linear scaling is achieved for both STO-3G and 6-31G basis sets, and that the elongation method becomes more efficient than a conventional treatment after about 300 monomer units.

These results also show that linear scaling is achieved only by combining integral cutoff with and QFMM evaluation of remaining non-local integrals.

9.5.2. Polyglycine

The geometrical structure of polyglycine in its C5 conformation is depicted in Figure 9-3a. Chains containing from 20 to 150 glycine units were built by the elongation method. In each elongation step the H atom at the growing end of the chain is removed as is the H atom adjacent to the CO group of the added H-CONH₂-CH₃ unit. A minimal STO-3G basis set was employed in these calculations. Cutoffs were implemented when the interaction between the cutoff fragment and the active region became less than 10⁻⁹. Our starting cluster contains 20 glycine units with three different partitions of the polymer, i.e. the size of the frozen region is taken to contain 4, 8, and 10 glycine units.

Table 9-5 collects the total energies of C5 polyglycine clusters obtained by the conventional and elongation methods, as well as the elongation errors, $\Delta E = E^{\text{elg}} - E^{\text{cvl}}$. It is found that the elongation energies reproduce the exact results very well; the absolute value of ΔE is no more than 5.0×10^{-7} a.u. Cutoff occurs first for the cluster with $N = 32$. The cutoff threshold is a key parameter. When it is set to 10⁻⁵, the error increases to about 10⁻⁶ a.u.

The total elongation CPU time is plotted in Figure 9-11 together with the conventional CPU time for reference purposes. One can observe almost linear dependence for the elongation calculations. However, the curves do not cross until $N = 180$. This

Table 9-5. Conventional RHF/STO-3G total energies (a.u.) for C5 conformer of polyglycine and the energy differences $\Delta E = E^{\text{elg}} - E^{\text{cvl}}$ for $N_{\text{st}} = 20$. All energies are in a.u. In the elongation calculations, $N_{\text{frozen}} = 4(10)$ means four (ten) units are frozen in the starting cluster

N	E (total) (in a.u.)	$\Delta E = E^{\text{elg}} - E^{\text{cvl}}$ (in 10^{-7} a.u.)	
	Conventional	$N_{\text{frozen}}=4$	$N_{\text{frozen}}=10$
40	-8204.27989963	-4.83	1.06
60	-12286.57450490	-4.43	-1.54
80	-16368.86911866	-4.08	-1.10
100	-20451.16374085	-4.19	-0.60
120	-24533.45837184	-4.20	-0.13
140	-28615.75301868	-4.22	-0.21

is due to the large number of intermediate steps. In order to improve that situation we can increase the size of the added units. For illustrative purposes we have performed additional elongation calculations with eight (filled triangles) or ten (filled diamonds) glycine units added in each step while simultaneously using eight or ten frozen units, respectively. These results are also displayed in Figure 9-11. In the first case, the initial cutoff step occurs for $N = 36$, whereas, in the second case, it occurs for $N = 40$. When the polyglycine is enlarged by eight units, the overall elongation time is lower than the conventional one after 80 units. Increasing the size of the building block to ten glycine units slightly reduces the overall CPU time. In both cases the curve of elongation CPU times *versus* number of units is essentially linear.

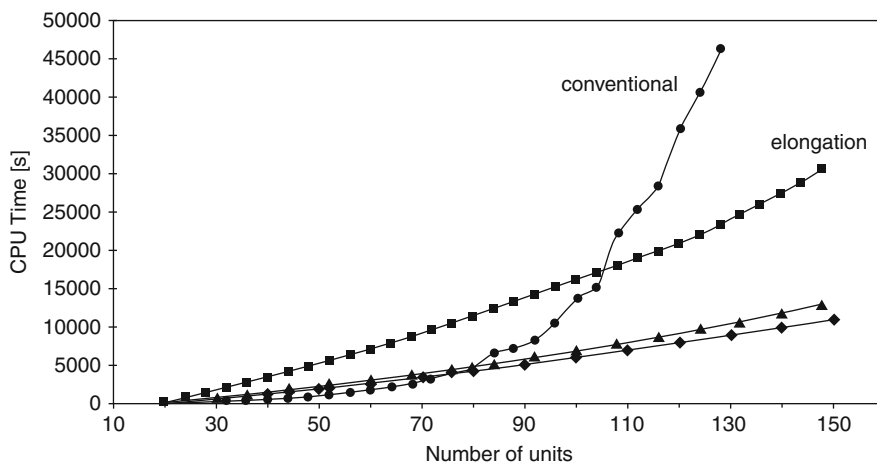


Figure 9-11. Total CPU time vs number of units for the conventional and elongation calculations of C5 polyglycine clusters

9.5.3. Nanotubes

As our third example, we apply the *ab initio* elongation method to the single-wall boron nitride (BN) heterostructured nanotubes [23], depicted in Figure 9-12.

If the localization were perfect the elongation method would reproduce exactly the results of a conventional calculation. However, because chemical bonds are broken when the nanotube is divided into fragments the quality of the localization is at issue. BN nanotubes are usually difficult for methods trying to exploit the local character of the electronic structure because of their strong delocalized nature. Therefore, we compare the elongation method and conventional results to determine the accuracy of the elongation method for different BNNTs. In Tables 9-6 and 9-7, we have collected total energies of (4,4) and (6,0) BNNTs at the HF/STO-3G level for conventional HF, as well as elongation calculations with and without cutoff +QFMM treatment of non-local ERIs.

For (4,4) or (6,0) BNNTs, the starting cluster contains six units, with one unit in frozen region, and the whole system is elongated up to 17 units by adding one unit at a time; the first cutoff step is performed for $N = 13$ units. The elongation error with and without cutoffs ($\Delta E_{\text{elg}}/\text{atom}$ and $\Delta E_{\text{cutoff}}/\text{atom}$ respectively) are defined in the footnotes to Table 9-6. For the (4,4) BNNT containing 17 units, $\Delta E_{\text{elg}}/\text{atom}$ is 1.9×10^{-9} au and $\Delta E_{\text{cutoff}}/\text{atom}$ is 3.1×10^{-9} au. For the (6,0) BNNT containing 17 units, the $\Delta E_{\text{elg}}/\text{atom}$ and $\Delta E_{\text{cutoff}}/\text{atom}$ values are 3.6×10^{-8} . We consider that these errors are small enough as to be completely negligible.

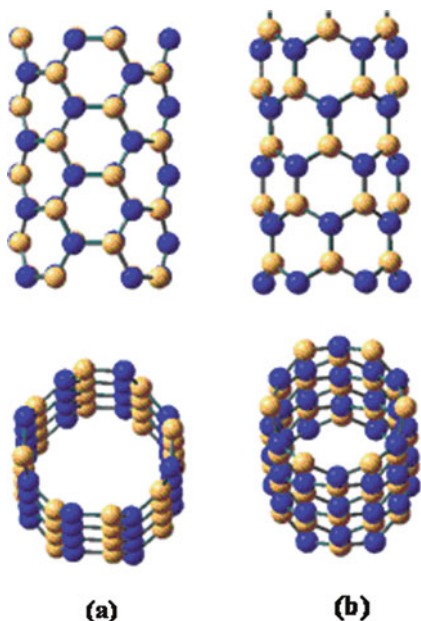


Figure 9-12. The structures of **a** (4,4) BN nanotube and **b** (6,0) BN nanotube. The upper and lower figures are side and top views, respectively Reprinted with permission from Chen et al. [23]. Copyright [2009], American Chemical Society

Table 9-6. The elongation energy error of (4,4) BNNT at the HF/STO-3G level and the error per atom in each elongation step

Number of units	Number of atoms	$\Delta E_{\text{elg}}/\text{atom}^{\text{a}}$	$\Delta E_{\text{cutoff}}/\text{atom}^{\text{b}}$
6	112	0.000E+00	
7	128	2.312E-10	
8	144	4.604E-10	
9	160	6.863E-10	
10	176	8.983E-10	
11	192	1.095E-09	
12	208	1.268E-09	
13	224	1.429E-09	2.919E-09
14	240	1.571E-09	3.045E-09
15	256	1.696E-09	3.080E-09
16	272	1.811E-09	3.111E-09
17	288	1.914E-09	3.145E-09

Reprinted with permission from Chen et al. [23]. Copyright [2009], American Chemical Society

a: $\Delta E_{\text{elg}}/\text{atom} = (E_{\text{elg}} - E_{\text{cvl}})/\text{number of atoms}$

b: $\Delta E_{\text{cutoff}}/\text{atom} = (E_{\text{cutoff}} - E_{\text{cvl}})/\text{number of atoms}$

In order to investigate the basis set effect we repeated our calculations (without cutoff) on the (4,4) BNNT using the 3-21G and 6-31G basis sets. Although the errors (see Table 9-8) do increase somewhat when using the 3-21 G basis set, they are still negligibly small. Note that a larger starting cluster ($N_{\text{st}} = 10$) was needed for the larger basis sets.

Figure 9-13 shows the total computation time for SCF calculations of (4,4) BN nanotube against the number of units with $N_{\text{st}} = 6$ for the STO-3G basis set.

Table 9-7. The elongation energy error of (6,0) BNNT at the HF/STO-3G level and the error per atom in each elongation step

Number of units	Number of atoms	$\Delta E_{\text{elg}}/\text{atom}$	$\Delta E_{\text{cutoff}}/\text{atom}$
6	156	0.000E+00	
7	180	1.463E-09	
8	204	4.513E-09	
9	228	8.351E-09	
10	252	1.246E-08	
11	276	1.653E-08	
12	300	2.044E-08	
13	324	2.409E-08	2.337E-08
14	348	2.747E-08	2.675E-08
15	372	3.059E-08	2.991E-08
16	396	3.346E-08	3.283E-08
17	420	3.610E-08	3.550E-08

Reprinted with permission from Chen et al. [23]. Copyright [2009], American Chemical Society

Table 9-8. STO-3G, 3-21G and 6-31G basis sets are employed to obtain errors per atom introduced by the elongation method for (4,4) BN nanotube. All results are in au

Number of units	Number of atoms	$\Delta E_{\text{elg}}/\text{atom}$		
		STO-3G	3-21G	6-31G
6	112	0.000E+00		
7	128	2.312E-10		
8	144	4.604E-10		
9	160	6.863E-10		
10	176	8.983E-10	0.000E+00	0.000E+00
11	192	1.095E-09	1.757E-08	0.000E+00
12	208	1.268E-09	3.018E-08	0.000E+00
13	224	1.429E-09	4.141E-08	0.000E+00
14	240	1.571E-09	5.116E-08	-4.169E-13
15	256	1.696E-09	5.975E-08	8.781E-10
16	272	1.811E-09	6.736E-08	1.694E-09
17	288	1.914E-09	6.253E-08	2.558E-09

Reprinted with permission from Chen et al. [23] Copyright [2009], American Chemical Society

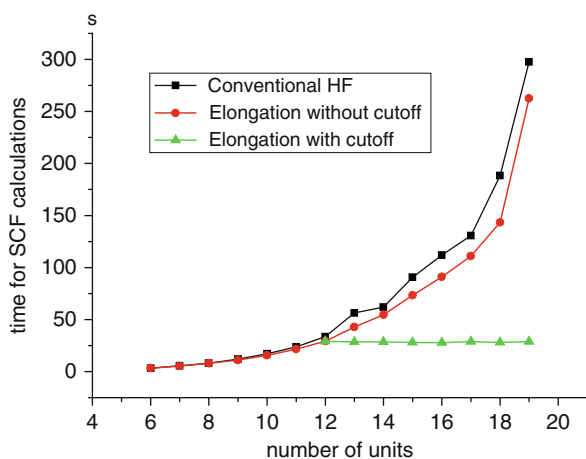


Figure 9-13. Total CPU time required for STO-3G SCF calculations vs. number of units for (4,4) BN nanotube with $N_{\text{st}} = 6$. Reprinted with permission from Chen et al. [23]. Copyright [2009], American Chemical Society

Without cutoff the calculations take somewhat less time than conventional HF, but when the cutoff technique is applied there is a major reduction and linear scaling is essentially achieved.

9.6. SUMMARY AND FUTURE PROSPECTS

In this chapter, we have reviewed the elongation method. The accuracy of the method is illustrated for several examples. When an integral cutoff procedure with

QFMM evaluation of the remaining integrals is included, linear scaling is achieved. This has been substantiated by calculations on model water chains, polyglycine, and BN nanotubes.

Various improvements and extensions are in progress. One technical improvement is to move a carefully selected number of orbitals with long tails from the frozen region to the active region. In initial tests we find that this can improve both the accuracy and efficiency of the method. A second technical improvement, which is easily implemented, will be to add the density for the frozen region to the active region only after the SCF calculation has converged. Finally, a third technical improvement, that will be made shortly, is to also use the multipole expansion method within the cutoff region as well.

The elongation method, as currently constituted, is already suitable for application at the Hartree-Fock and Kohn-Sham DFT levels of theory. In principle, the same general approach can be extended to all *ab initio* wavefunction treatments. An initial elongation-MP2 formalism has been implemented for the final chain length and compared to the standard canonical MP2 approach. [24] Some tests on this elg-MP2 show that it is more efficient than LMP2 with CPU savings from both the Hartree-Fock and MP2 parts of the calculations. In the future, we plan to add a step-by-step MP2 treatment [25] as well as coupled cluster and CI capability.

Based on the achievements of the one-dimensional elongation method, a generalized elongation method for two- and three-dimensional systems has been proposed. [26] In contrast to the original treatment, we add earlier “frozen” units back into the active region if the interaction subsequently becomes strong. In fact, this same procedure can also be applied to quasi-1D systems. Initial tests have been encouraging and work is in progress on the application to large biological systems of interests, such as proteins and DNA as well as 3D molecular crystals.

ACKNOWLEDGMENTS

This work was supported by the Grant-in-Aid for Scientific Research from the Ministry of Education, Culture, Sports, Science and Technology (MEXT) of Japan.

REFERENCES

1. Gao J, Truhlar DG (2002) *Annu rev phys chem* 53:467–505
2. (a) Yang W (1995) *Phys Rev Lett* 66:447; (b) Yang W (1991) *Phys Rev A* 44:7823 ; (c) Yang W, Lee T-S (1995) *J Chem Phys* 103:5674
3. (a) Kirtman B (1999) In: Surjan P, (ed.) *Topics in current Chemistry, localization and correlation –A tribute to Ede Kapuy*, Springer, 203:147; (b) Kirtman B (1982) *J Chem Phys* 86:1059; (c) Kirtman B, de Melo C (1981) *J Chem Phys* 75:4592
4. (a) Kitaura K, Sawai T, Asada T, Nakano T, Uebayasi M (1999) *Chem Phys Lett* 312:319; (b) Kitaura K, Ikeo E, Asada T, Nakano T, Uebayasi M (1999) *Chem Phys Lett* 313:701; (c) Fedorov DG, Olson RM, Kitaura K, Gordon MS, Koseki S (2004) *J Comput Chem* 25:872; (d) Fedorov DG, Kitaura K (2004) *J Chem Phys* 120:6832; (e) Komeiji Y, Inadomi Y, Nakano T (2004) *Comput Biol & Chem*

- 28:155; (f) Stewart JJP (1996) *Int J Quantum Chem* 58:133; (g) Yokojima S, Wang XJ, Zhou DH, Chen GH (1999) *J Chem Phys* 111:10444; (h) Babu K, Gadre SR (2003) *J Comput Chem* 24:484
5. Imamura A, Aoki Y, Maekawa K (1991) *J Chem Phys* 95:5419
 6. Ohnishi S, Gu FL, Naka K, Imamura A, Kirtman B, Aoki Y (2004) *J Phys Chem A* 108:8478
 7. Pomogaeva A, Springborg M, Kirtman B, Gu FL, Aoki Y (2009) *J Chem Phys* 130:194106
 8. Mitani M, Imamura A (1995) *J Chem Phys* 103:663
 9. Mitani M, Aoki Y, Imamura A (1995) *Int J Quantum Chem* 54:167
 10. (a) Mitani M Imamura A (1993) *J Chem Phys* 98:7086; (b) Mitani M, Aoki Y, Imamura A (1994) *J Chem Phys* 100:2346
 11. (a) Aoki Y, Suhai S, Imamura A (1994) *J Chem Phys* 101:10808; (b) Aoki Y, Suhai S, Imamura A (1994) *Int J Quantum Chem* 52:267; (c) Mitani M, Aoki Y, Imamura A (1995) *Int J Quantum Chem* 54:167
 12. Schmidt MW, Baldrige KK, Boatz JA, Elbert ST, Gordon MS, Jensen JH, Koseki S, Matsunaga N, Nguyen KA, Su SJ, Windus TL, Dupuis M, Montgomery JA, Jr. (1993) *J Comput Chem* 14:1347
 13. Gu FL, Aoki Y, Korchowiec J, Imamura A, Kirtman B (2004) *J Chem Phys* 121:10385
 14. Korchowiec J, Lewandowski J, Makowski M, Gu FL, Aoki Y (2009) *J Comput Chem* 30:2515
 15. Edmiston C, Rüdenberg K (1963) *Rev Mod Phys* 35:457
 16. Del Re G (1963) *Theor Chim Acta (Berl)* 1:188
 17. Reed AE, Weinhold F (1985) *J Chem Phys* 83:1736
 18. Imamura A, Aoki Y (1997) *Adv Colloid Interface Sci* 71:147
 19. (a) White CA, Head-Gordon M (1994) *J Chem Phys* 101:6593; (b) White CA, Johnson BG, Gill PMW, Head-Gordon M (1996) *Chem Phys Lett* 253:268
 20. *GAMESS, version 14, January 2003 (R2)*, Iowa State University: Iowa.
 21. Ditchfield R, Hehre WJ, Pople JA (1971) *J Chem Phys* 54:724
 22. Chaban G, Schmidt MW, Gordon MS (1997) *Theoret Chem Acc* 97:88
 23. Chen W, Yu G-T, Gu FL, Aoki Y (2009) *J Phys Chem C*, 113:8447
 24. Makowski M, Korchowiec J, Gu FL, Aoki Y (2009) *J Comput Chem* 31:1733
 25. Kirtman B (1995) *Int J Quantum Chem* 55:103
 26. Gu FL, Aoki Y unpublished results

CHAPTER 10

MOLECULAR TAILORING: AN ART OF THE POSSIBLE FOR *AB INITIO* TREATMENT OF LARGE MOLECULES AND MOLECULAR CLUSTERS

ANUJA P. RAHALKAR^{1,2}, SACHIN D. YEOLE^{1,2}, V. GANESH³,
AND SHRIDHAR R. GADRE^{1,2}

¹*Department of Chemistry, University of Pune, Pune 411007, India,*

e-mail: anuja.rahalkar@gmail.com; sachindyole@gmail.com; gadre@iitk.ac.in

²*Department of Chemistry, IIT Kanpur, Kanpur 208016, India*

³*Department of Computer Science, Australian National University, Canberra ACT-0200, Australia,*
e-mail: tovganesh@gmail.com

Abstract: Divide-and-conquer (DC) type methods are being actively developed in order to break the bottleneck of high scaling order of *ab initio* calculations of large molecules. Molecular Tailoring Approach (MTA) is one of such early attempts, which scissors the parent molecular system into subsystems (fragments). The properties of these subsystems are stitched back in order to estimate those for the parent system. Inclusion-exclusion principle from set theory is incorporated into MTA, which allows accurate estimation of electronic energy, energy-gradients and Hessian. This Chapter summarizes the algorithm, equations as well as basic parameters for obtaining an optimal fragmentation for a given molecule. The fragmentation in MTA is exclusively based on distance-criterion allowing its application to a general class of molecules. Further, the versatility of this method with respect to the level of theory [Hartree-Fock (HF) method, Møller-Plesset second order perturbation theory (MP2) and Density Functional Theory (DFT)] as well as the basis set is illustrated. Apart from earlier benchmarks, a few new test cases including geometry optimization of variety of molecules, benzene clusters, polyaromatic hydrocarbons, metal cluster and a protein with charged centers are presented in this Chapter.

Keywords: Molecular tailoring approach (MTA), Linear scaling methods, Hartree-Fock (HF) Theory, Density functional theory (DFT), Møller-Plesset second order perturbation (MP2) theory, π -conjugation, Large molecules

10.1. INTRODUCTION

Ab initio quantum chemical methods provide a practical means for investigating the electronic structure and properties of moderate-sized molecules. High-performance computing hardware and “black box” suits of programs are further

useful in enhancing the applicability of these methods to large molecular systems. Consequently, theory is being used not only by theoreticians but also by experimentalists. There are several popular packages including GAMESS [1], GAUSSIAN [2], and TURBOMOL [3] etc. which provide efficient codes for calculating energies, geometry optimization, spectra calculation at a desired level of theory. Despite all these developments, the high scaling problem of ab initio methods is inherently insurmountable. For instance, the basic ab initio method, viz. the Hartree-Fock (HF) theory scales as $O(N^4)$, where N is number of basis functions. Møller-Plesset second order perturbation theory (MP2), which accounts for electron correlation to some extent, scales as $O(N^5)$. Thus, the application of ab initio methods is restricted to systems comprising of few hundreds of atoms. The higher-accuracy versions of correlated methods viz. coupled cluster (CC), configuration interaction (CI) are applicable to only few tens of atoms, even with the availability of the powerful supercomputers today.

Though the formal scaling of HF is $O(N^4)$, for spatially extended large molecules, it scales as $O(N^3)$ [4]. Consequently, the memory requirements for HF calculation for large molecules are moderate and can be handled by the contemporary PC-type hardware. However, DFT with similar scaling as HF is more accurate method for ground state properties, as it incorporates exchange-correlation functional. It employs electron density as a basic variable with self-consistency built into Kohn-Sham scheme. Two popular frameworks for exchange correlation functionals are: local density approximation (LDA) and generalized gradient approximation (GGA). Hybrid functionals such as Becke-(3 parameter)-Lee-Yang-Parr (B3LYP) [5], M05, M06 [6] etc. have already become or are becoming popular nowadays, in which the correlation contribution is summed up along with a part of or complete HF exchange. DFT is well-known for providing results at low computational costs, which can be directly compared to experiments. However, it is difficult to choose a functional according to the molecular system and specific molecular property under consideration. For instance, B3LYP is reliable [5] for ground state energies of molecules, while M06, another hybrid functional [6] is parameterized for transition metals and non-metals. Since the exact form of the Hohenberg-Kohn functional is not known, there is generally no clear and systematic way for improving the results within DFT framework. But in the wave-function based methods, HF is the foundational method, onto which variational or perturbative improvements of increasing accuracy can be carried out for obtaining more reliable results. In the former methodology, the higher levels of CC and CI methods, e.g. CCSD(T) and SDTQ CI, although expensive, exemplify highly accurate schemes.

The Hartree-Fock procedure being a basic method lacking electron correlation and higher versions of CC, CI etc. being too expensive to treat large molecules, MP2 is known to provide an affordable alternative that captures substantial part of electron correlation energy. But the scaling of $O(N^5)$ still renders it impossible to treat really large systems such as proteins or large water clusters, to name a few. As an attractive computational alternative, several active groups have been working on parallelization of HF and MP2 methods on a variety of hardware platforms

which have become cost-effective during the last two decades or so. The earlier attempts from our own group [7] included implementation of a parallel algorithm for electron repulsion integrals and HF method [7a,b]. These efforts in the development of parallel codes continued [7c] for effective four-index transformation within MP2 framework. The efficiency of this architecture-independent method was demonstrated with dynamic load balance on few hydrocarbons and cytosine which were considered as 'large molecules' at that time! These parallelization methods aim at exploiting the available low-cost computational resources to the maximum possible extent. With recent improvement in novel hardware technologies such as the cell processor and the graphics processing unit (GPU), researchers have modified the HF algorithm to effectively use the massive computational power offered by them. Notable of these efforts is the work [8] by Martinez et al. which has now resulted into a commercially available package [9]. These efforts have pushed the size of systems that could be handled on a standard PC hardware with commodity add-ons such as a graphics processor.

Another type of attempt to make possible the treatment of large molecular systems by ab initio methods is based on approximations such as localization of molecular orbitals (MO) or neglect of numerically insignificant integrals etc. In a work reported in 1988, Saebo and Pulay [10] exploited the fact that the occupied orbitals in almost all ground-state closed-shell molecules can be very well localized. They demonstrated their method for local correlation treatment of octatetracene molecule. A linear scaling method termed as local second order Møller-Plesset perturbation theory (LMP2) developed in 1999 by Schütz, Hetzer and Werner [11] is also based on localization of MOs. The impressive performance is achieved here by using orbital domains for each electron pair and an effective use of prescreening algorithm in the integral transformations. This method has been benchmarked with test examples of $(\text{Gly})_{n=1,22}$, $\alpha\text{-(Ala)}_{10}$, $(\text{H}_2\text{O})_{n=20-60}$ and small drug molecules such as indinavir and paclitaxel. However, the serious limitations of this method are seen on its application to 'real-life' 3D systems such as water clusters, in which MOs are not localized. Molecules containing ~ 100 atoms and ~ 1000 basis functions can, in general, be readily subjected to MP2-level geometry optimization, using a black-box program, with a small computer cluster made of contemporary off-the-shelf hardware at the time of writing this Chapter. However, due to the inherent N^5 scaling of the MP2 method, on increasing the system size, say to ~ 300 atoms, the memory requirement of the calculation becomes huge (about few hundreds of GB), making it impossible to implement. A technique known as Resolution of Identity (RI) approximation [12-14] is invoked for reducing the effort of MP2 calculation. In this approximation, linear combinations of atom-centered auxiliary basis functions are employed for calculating the two-electron integrals and those with negligible magnitude are skipped during calculation. Recent work by Nagase and co-workers [12], following the earlier studies from other groups [13, 14] has resulted into the development of an efficient RI-MP2-based parallel program. Katouda and Nagase [12c] have recently reported a few benchmarks of their RI-MP2 vis-à-vis the corresponding actual MP2 calculation for single-point energy evaluation. The efficiency and accuracy of RI-MP2 method critically depend on the auxiliary basis set used. The

RI-MP2 approximation is seen to reduce the memory requirements of MP2 method by a factor of ~ 2 , for the molecular systems studied, when a moderate auxiliary basis set is employed [12c].

The real spirit of ab initio methods lies in the determination of electronic structure. This is achieved by geometry optimization of the molecule which normally requires tens or hundreds of such single point energy-gradient steps and is thus seen to be the most time-consuming process. This calls for some alternative solution or modification in ab initio methods for reducing the inherent scaling. As a consequence, a third category of methods for effectively handling large molecules is coming up and is based on divide-and-conquer strategy. The earliest attempt to solve this problem, to the best of the authors' knowledge, was made by Christoffersen and co-workers [15] using a fragmentation-based algorithm. In this method, a large molecule is broken up into fragments, which are individually submitted to ab initio calculation. Admittedly, the calculations reported by Christoffersen et al. were performed employing a very simple model that represented an electron pair with just a single floating Gaussian function due to limitations of computational power available in the early 1970s. However, Christoffersen et al. indeed pioneered the idea of using fragment calculations for treating the large molecular system within ab initio framework. This novel idea was successfully implemented for several spatially extended systems of chemical and biological interest. Many years after this work, another attempt for treating large molecules was reported by Yang et al. [16–18]. In this method, the electron density of the whole molecule was derived from the corresponding fragment densities. The method, later named as “Divide and Conquer” (DC), was tested for polypeptides and large carbon clusters [16–18]. Zhao and Yang reported [18] the first attempt of geometry optimization with their DC-method within DFT framework. However, the systems tested (a glycine unit and a glycine-tetrapeptide) in this work contained less than 30 atoms. These DC-based calculations took more time than the corresponding actual ones. However, more meaningful test cases reflecting time advantage over the actual calculations could not be reported at that time probably due to restrictions of hardware resources.

The next of these DC-based methods, named as Molecular Tailoring Approach (MTA) is being developed in our laboratory in Pune, since 1994. The method has been incorporated in a locally modified version of GAMESS [1] and also been interfaced with GAUSSIAN'03 [2]. To begin with, the method was limited to determining the density matrix (DM) of a spatially extended, large molecule from the respective fragment DM's. Such a synthesized DM was employed for enumeration of one-electron properties such as molecular electron density (MED), dipole moments or molecular electrostatic potential (MESP) [19–21]. These properties, along with the topography of the corresponding scalar fields, were computed for a variety of molecular systems, e.g. tocopherol, ZSM-5 silicalite zeolite and a model polypeptide at HF/6-31G(d,p) level within the MTA framework. A few tests at MP2 level were also performed and led to good results in terms of the accuracy as well as efficiency.

The method was extended [22, 23] to geometry optimization of large systems with qualitative estimates of energies at HF, DFT and MP2 levels. The benchmarks

performed on the chosen systems showed a clear speed-up by factor of 3 or more over that for the corresponding actual calculation [22, 23]. To the best of authors' knowledge, this is one of the earliest systematic attempts of geometry optimization of large molecules using fragment-based strategy. Further, the method has been improved for more accurate energy and gradient estimation by adding a flavor of set theory in terms of cardinality based equations [24]. These new equations were thoroughly benchmarked for single point energy-gradient evaluation as well as geometry optimization. According to this detailed benchmarking studies [24, 25, 26], the energy estimates of MTA were generally to within 1.5 mH (typically ~ 1 kcal/mol, that can be considered as normally accepted chemical accuracy) of the corresponding actual calculations at the same level of theory and basis. Furthermore, the errors in numerically significant gradients were also generally small, viz. $O(10^{-3})$. It was observed that MTA-based geometry optimization closely follows the path followed by the actual calculation as shown [24] by a benchmark performed on a zwitterionic system, $\text{NH}_3^+(\text{CH}_2)_{19}\text{COO}^-$. Also, another remarkable application of MTA was demonstrated by the case study of partial geometry optimization performed [24] on 1prb albumin binding protein consisting of 851 atoms at HF/3-21G level of theory, followed by a few steps at B3LYP/3-21G (4,635 basis functions). This technique was recently employed successfully for investigating structures and energetics of nanotubes of orthoboric acid [26].

In the next step of the development of MTA, it was extended further for Hessian matrix evaluation and IR spectra calculation [27]. The reliability of the MTA-based Hessian was established by a comparison with the corresponding actual Hessian for medium-sized test cases at HF and DFT levels. The RMS deviation in Hessian matrix elements was $O(10^{-4})$ for all the test cases examined [27]. Since Hessian calculation for a large molecule is an expensive and time consuming task, MTA can be gainfully employed, showing a huge time advantage. For instance, in the case of $(\text{H}_2\text{O})_{37}$, MTA calculation was able to get a time advantage factor of 6.86 over the corresponding actual Hessian calculation [27]. MTA was further applied for the determination of vibrational spectra of spatially extended, large molecules for which the corresponding full actual calculations are not feasible [27].

To this end, the work on MTA, the benchmarks and applications of MTA reported so far have unequivocally demonstrated that the method is sufficiently accurate and advantageous for spatially extended large molecules. It has been observed that MTA-based geometry optimization generally follows a path similar to that taken by the actual calculation. MTA-based Hessian is reliable enough to perform IR-spectrum determination as well as has potential use in faster geometry optimization. A limited access to the MTA code is available to users through web-versions viz. WebProp [28] and WebMTA [29]. The algorithm for MTA, fragmentation of the system, cardinality-based equations, parameters in MTA which control the accuracy (R-goodness) and the time advantage factors (Maximum size of a fragment, Scaling Factor) etc. are discussed in detail in the forthcoming section.

Another well-established fragmentation-based procedure for treating large molecules is the fragment molecular orbital (FMO) method, pioneered by Kitaura

et al. [30] in 1999. The method partitions a molecular system into fragments (monomers) and uses many-body decomposition energy analysis for estimating the total energy as given below in Equation (10-1)

$$E = \sum E_I + \sum (E_{IJ} - E_I - E_J) + \sum \{(E_{IJK} - E_I - E_J - E_K) - (E_{IJ} - E_I - E_J) - (E_{JK} - E_J - E_K) - (E_{IK} - E_I - E_K)\} \quad (10-1)$$

Here, E_I , E_{IJ} and E_{IJK} represent the one-, two- and three body energies, respectively. The energy of each fragment (monomer) is calculated in the presence of appropriately defined Coulomb fields of other fragments (monomers). Analytic gradients of the energy were built into the method in 2004 [31]. However, these were utilized [32] later for geometry optimization and the results reported in 2007. Benchmarks for FMO are performed mainly on molecules which are biological in nature viz. α -helix, β -turn, and extended conformers of 10-, 20- and 40-residue polyaniline. All the calculations were performed at HF and higher levels of theory employing 3-21G and 6-31G(d) basis sets. Met-enkephalin dimer was taken as a test case for determination of binding energy at HF/3-21G and 6-31G(d) levels and the errors in the prediction were 1–3 kcal/mol [32]. Chignolin and an agonist polypeptide of erythropoietin receptor protein were optimized at 3-21(+)-G level where the polarization functions were added only on the anionic groups ($-\text{COO}^-$). The RMS deviations in the geometric parameters are reported as 0.2 Å and 0.5° in terms of bond distances and angles respectively showing modest accuracy. The most recent applications of the FMO method include a study of adsorption of toluene and phenol on a faujasite zeolite [33], a structural and interaction analysis of heparin oligosaccharides [34].

FMO is now a part of GAMESS [1] package and is freely distributed for use. FMO provides a choice between desired accuracy and the time advantage to the user by offering two-body (FMO2) and three-body (FMO3) treatments. Clearly, FMO2 is faster and FMO3 is more accurate among these two. However, FMO3 also shows some time advantage over the actual calculation. Further control in FMO2 and FMO3 is achieved by the way in which a fragment is defined. For example, FMO2/2 considers 2-body expansion for 2 molecules/residues per fragment while FMO3/2 accounts for 3-body expansion with 2 molecules/residues per fragment. In principle, contributions from n-body terms, $n \leq$ number of molecules/residues can be taken into account. For $n > 3$, the computational effort becomes huge, normally restricting the value of n to 3 due to practical considerations.

Since FMO is based on many-body analysis, it can be applied to systems where 'bodies' are well-defined. For instance, in case of molecular clusters, each monomer unit or a group of monomers can be treated as a 'body'. In the case of biological systems, amino acid residue(s) can be treated as fragments. However, one cannot readily use FMO for molecules like capreomycin, taxol, cyclodextrin, β -carotene etc. Thus, most of the benchmarks and applications of FMO available were performed on either molecular clusters or biological systems [30–35]. For this, somewhat restricted class of systems, FMO showed outstanding performance especially for biomolecules achieving a sub-milihartree accuracy with large time

advantage over their actual counterparts [35]. FMO estimates for water clusters, on the other hand, were rather poor. The energy estimates for $(\text{H}_2\text{O})_{64}$ by FMO2/2 at MP2/6-31G(d) and MP2/6-311G(d) were in error by ~ 33 mH (~ 20 kcal/mol) and ~ 87 mH (~ 55 kcal/mol), respectively. Despite of the huge time advantage achieved by FMO2/2, these errors are unacceptable. The errors with FMO3/2 (most accurate amongst the reported) were also much beyond chemical accuracy of 1 kcal/mol [35]. FMO method produced better results when 6-31G(d) basis set is employed and the error becomes large when a higher basis set such as 6-311G(d) was used [36]. Yet another constraint of FMO is non-applicability of FMO to calculations employing diffuse functions throughout for the whole system. It is not possible to handle diffuse functions, within FMO, on the boundary atoms of the fragments, whenever a covalent bond is broken during fragmentation of systems (such as polypeptides, proteins). To the best of our knowledge, one cannot readily perform FMO calculations using a routine basis set such as 6-31+G(d) for biological systems. Molecular clusters can, on the other hand, be treated by FMO using diffuse basis functions as only weak bonds are broken during the process of fragmentation.

Since the last decade, fragment-based methods similar in spirit to MTA and FMO have come up in which a molecular system is broken into subsystems (fragments) and the results for the parent system are collated from those of the fragments. A list of such prototype investigations includes works by Li et al. [37, 38], Zhang et al. [39], Collins' systematic fragmentation [40, 41], Bettens et al. [42] and Nakai's DC method [43, 44]. Li and co-workers have recently achieved [38] geometry optimization with their generalized energy-based fragmentation approach. This approach is also based on many-body decomposition of energy. They have benchmarked their method with an $(\text{H}_2\text{O})_{28}$ cluster, a polyglycine containing 12 units and a few more regular systems. The RMS deviations in bond lengths, bond angles and dihedral angles at HF/6-31G(d) were impressive and fall in ranges 0.0003–0.03 Å, 0.1–2° and 0.8–8° respectively [38]. Collins' systematic fragmentation method is based on combining small functional groups in a molecule as fragments. The estimation of energy is again based on many-body expansion in terms of fragments [40]. This method was tested for single point energy-gradient as well as evaluation of second order derivatives of energy for small- to medium-sized molecules [40, 41]. Bettens and co-workers have derived their method from Collin's systematic fragmentation by incorporating an isodesmic approach into the fragmentation process. The method was validated [42] with linamarin, cholesterol, taxol and a BN nanotube. Also, most of the validation has been performed at the B3LYP level, along with a sample calculation performed for cis-3-hexanal at HF, MP2 and MP4 levels as well [42]. In a recent work on the DC-MP2 method, Nakai and co-workers reported that the HF procedure requires [44] a larger buffer zone for capturing sufficient accuracy, as compared to that required for the perturbative correction, E(2). With this in view, a "dual-level" hierarchical scheme for DC treatment for MP2 method [44] has been proposed and tested out.

Despite these fast-developing fragment-based methods, geometry optimization of large molecules at DFT as well as MP2 level still poses a challenge. Moreover, for the methods based on many-body analysis, the applicability is restricted to

molecules wherein ‘bodies’ are well-defined. Thus, most of the benchmarks performed for these methods include polypeptides or proteins (where each amino residue is a body) or molecular clusters, mostly water clusters (where, monomers can be treated as bodies). Also, among all these methods, applications to real life test cases are taken up only by MTA and FMO. Unlike FMO, MTA is applicable to a general class of molecular systems such as taxol, cyclodextrin, water clusters, boric acid clusters as well as metal clusters [45]. Another noteworthy point about MTA is that it can be applied successfully to highly conjugated systems such as β -carotene. The exploratory benchmarks [46] on isomers of heptacene and small graphene model systems achieved a next step of MTA proving its utility for polyaromatic compounds such as a small model of a graphene sheet. In the literature, there are no reports describing application of fragment based methods to these two-dimensional π -conjugated systems and to the best of the authors’ knowledge, MTA has been applied to such systems [46] for the first time.

10.2. COMPUTATIONAL DETAILS OF MTA

10.2.1. Outline of Algorithm

In this Subsection, the basic methodology of MTA is detailed out including the algorithm and programming aspects, as well as a number of terms related to MTA. As mentioned in the previous Section, MTA is a fragment-based linear scaling technique, which is developed for ab initio treatment of spatially extended large molecules. The method is integrated with a locally modified version of GAMESS. An interface with GAUSSIAN, version G03, has also been developed and tested. The important steps in the MTA algorithm are given below.

- (1) The parent molecule under consideration is partitioned into smaller fragments (termed as main fragments), using automatic or manual fragmentation. Binary-, ternary- and higher overlaps (whenever applicable) of these main fragments are generated. These main and overlapping fragments constitute the whole set of fragments.
- (2) Cardinality-based equations are set up for evaluating the energy and its gradients, Hessian etc. of the parent molecule, as per the requirements of the calculation.
- (3) Individual fragments, viz. the main and overlapping fragments, are subjected to ab initio treatment for energy, gradient, Hessian evaluation (as per the requirement) using the available subroutines provided within the GAMESS package [1].
- (4) Fragment results (DM, energy, gradient and/or Hessian) are stitched back in accordance with the cardinality-based equations to estimate those for the parent system. If it is a geometry optimization job, the estimated gradients are used to generate the new geometry of the parent system using standard GAMESS optimizer routine and the above steps are repeated until local minimum/stable geometry is obtained.

10.2.2. Fragmentation

The key step in MTA is clearly the fragmentation of the molecule. This is somewhat subjective step and largely depends on the structure of the molecule. A molecule can be cut in number of ways, each generating a new fragmentation scheme, making it difficult to choose the 'best' one. But using some basic knowledge of chemistry, a general fragmentation routine is developed for automating the process. This routine is a separate routine, which is linked with the locally modified MTA-GAMESS. In the early phases of development of MTA, this fragmentation algorithm developed by Babu et al. [22] was based on recursive scheme, which has now been changed to a new algorithm by Ganesh et al. [23, 24]. This routine first traverses the molecular graph and builds up the connectivity matrix. Then using this information, it finds out the sensitive structures viz. multiple bonds and aromatic rings, which are to be kept intact during fragmentation. Following this, the routine generates the fragments according to the input parameters (RCUT and MXSZ, described below) specified by the user. Out of these parameters, RCUT (abbreviation for Radius Cutoff) in units of Å, is used to generate initial fragments by putting a sphere of radius equal to RCUT value on each atom in the molecular skeleton. Then in various stages these fragments are merged into each other based on the common atoms and unnecessary fragments are deleted. Fragmentor tries to achieve the R-goodness (see the forthcoming discussion in Section 10.2.3.1) value equal to RCUT for the final fragments. Maximum allowed size of a fragment (MXSZ) in terms of number of atoms is another input required by the automatic fragmentation routine. As the name suggests, fragmentation routine tries to restrict the size of main fragments to within this limit while merging the fragments. It is important to note that RCUT and MXSZ are used as guidelines by the fragmentator and these may not be strictly followed due to intricacy of the molecular structure. For instance, input of RCUT = 3.5 and MXSZ = 30 generates 9 main fragments for tocopherol molecule, the largest of which contains 35 atoms (cf. Table 10-1). A better scheme **S2** is obtained by input RCUT = 3.9 and MXSZ = 48, wherein there are only 3 main fragments with R_g of 3.9 Å. Some illustrative fragmentation schemes, generated using this automatic fragmentation code, are given in Table 10-1. Graphical representations of fragmentation schemes listed in Table-10.1 are depicted in Figure 10-1 for tocopherol and cholesterol molecules. Visualization of fragments of water cluster being difficult in 2 dimensions, a graphical representation of fragments for this system is not shown.

The fragmentation program also ensures that every atom in the molecule is present in at least one fragment. Care is taken that unique set of fragments will be generated for a particular set of RCUT and MXSZ, irrespective of the input order of coordinates of the molecule. Whenever a covalent bond is scissored, dummy hydrogen atoms are added to satisfy the valencies of the boundary atoms of the fragments. These dummy atoms are added at the standard bond lengths of C-H, N-H etc. depending on which bond is cut. As a special case, for molecular clusters, there is a keyword introduced in this fragmentation routine for breaking only the weak bonds and to keep all the covalent bonds and the monomers, intact. This

Table 10-1. Illustration of the parameters RCUT, MXSZ, Rg and SF within MTA for tocopherol, cholesterol and a water cluster, (H₂O)₆₃. Rg values in Å and energies in a.u. See text and Figure 10-1 for details

Molecule (no. of atoms)/scheme	Input	Output Parameters ^a		Energy	
	RCUT, MXSZ	N _f , N _{av} , N _{max}	Rg, SF	MTA	Actual
Tocopherol (81)					
S1	3.5, 30	9, 29, 35	3.3, 2.9	-1,276.98211	-1,276.98222
S2	3.9, 48	3, 45, 50	3.9, 1.6	-1,276.98221	
Cholesterol (74)					
S1	3.2, 32	8, 33, 35	2.7, 3.2	-1,124.13094	-1,124.13095
S2	4.1, 52	3, 52, 54	4.1, 2.4	-1,124.13094	
Water Cluster (H ₂ O) ₆₃ (189)					
S1	3.7, 90	7, 82, 90	3.7, 3.0	-4,789.70524	-4,789.70405
S2	4.3, 150	3, 147, 150	4.3, 2.3	-4,789.70445	

^aN_f, N_{av} and N_{max} are the number of main fragments, average size of fragments and size of the largest fragment respectively. Rg and SF are the R-goodness values and scaling factors of the corresponding fragmentation schemes.

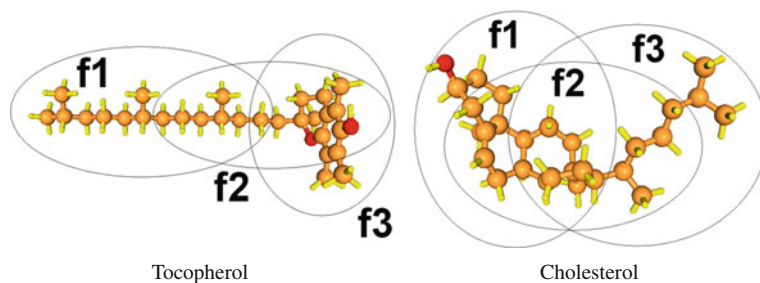


Figure 10-1. Illustration of fragmentation schemes (S2 from Table 10-1) for tocopherol and cholesterol f1, f2 and f3 are the main fragments. See text for details

routine is designed to work for any general molecular system; although due to large diversity in the structures of the molecules, it may not be always possible to produce the ‘best’ scheme for breaking up a molecule/cluster into a set of fragments. An option to feed the fragments externally to the MTA has been provided since it renders flexibility. This manual fragmentation of the molecule can be done with the aid of MeTASstudio [47], a programmable IDE custom-made for computational chemists by Ganesh. With MeTASstudio, the user can visualize the molecule and cut the fragments with a pencil tool. Finally a “key” file for fragments compatible to MTA code can be exported.

10.2.3. Assessment of Fragments

After fragmentation, the next important issue is to judge the quality of fragments. From the vast amount of testing performed, certain parameters viz. R-goodness of the scheme (Rg), Average Size (N_{av}) as well as Scaling factor (SF), are defined for helping the user to anticipate the performance of the scheme. These parameters and their connection with accuracy and computational cost of the calculation are elaborated below with sample test cases of tocopherol, cholesterol and a water cluster of 63 monomers (cf. Table 10-1).

10.2.3.1. R-Goodness (Rg) Value

The success of any fragmentation-based method lies in mimicking the chemical environment of each atom in the fragment as accurately as possible to that in the parent molecule. MTA uses a distance-based criterion for assessing the faithfulness of this representation of the environment for an atom in each fragment. A sphere centered on the atom under consideration in a fragment containing that atom is constructed and the radius is incremented till it touches an atom which is not present in that fragment. The radius of the sphere is termed as the atomic Rg value for the atom in that particular fragment. If an atom is present in more than one fragment, the maximum of the sphere radii (from all the fragments containing that atom) is taken as the atomic Rg. This is exemplified in Figures 10-2 and 10-3, wherein fragmentation schemes of a benzene pentamer and a small model graphene sheet ($C_{56}H_{20}$) are depicted. The benzene pentamer is broken into 3 trimers as main fragments (F1, F2 and F3) by manual fragmentation aided by MeTASstudio [47]. An atom (H) marked by a small square in Figure 10-2 is the atom under consideration. This atom is present in all the three main fragments. As described above, a sphere with increasing radius is drawn centered on H in each fragment. In fragments F1 and F3, the sphere touches an atom outside the fragment at 3.9 Å while, in F2, it finds outside atom at 6.1 Å. The maximum of these radii i.e. 6.1 Å is the atomic Rg for H for this particular fragmentation scheme. This exercise is repeated for every atom in the molecule and a list of atomic Rg values is generated. The minimum of these atomic Rg values is considered as the Rg value of the scheme. Rg of the scheme signifies that chemical environment of each atom is represented to within a sphere of radius Rg in at least one fragment. Evidently, higher the Rg value more is the accuracy of the calculation in general. From the experience gained from the earlier benchmarks, generally a scheme with Rg value greater than or equal to 4 Å is accurate enough for normal chemical structures.

Tocopherol and cholesterol being spatially extended molecules, a sub-milihartree accuracy is readily reached even with small Rg values of 3.3 and 2.7 Å respectively (cf. Table 10-1). For compact or intricate systems such as a water cluster, a higher Rg value is required for achieving accurate results for the molecular energy.

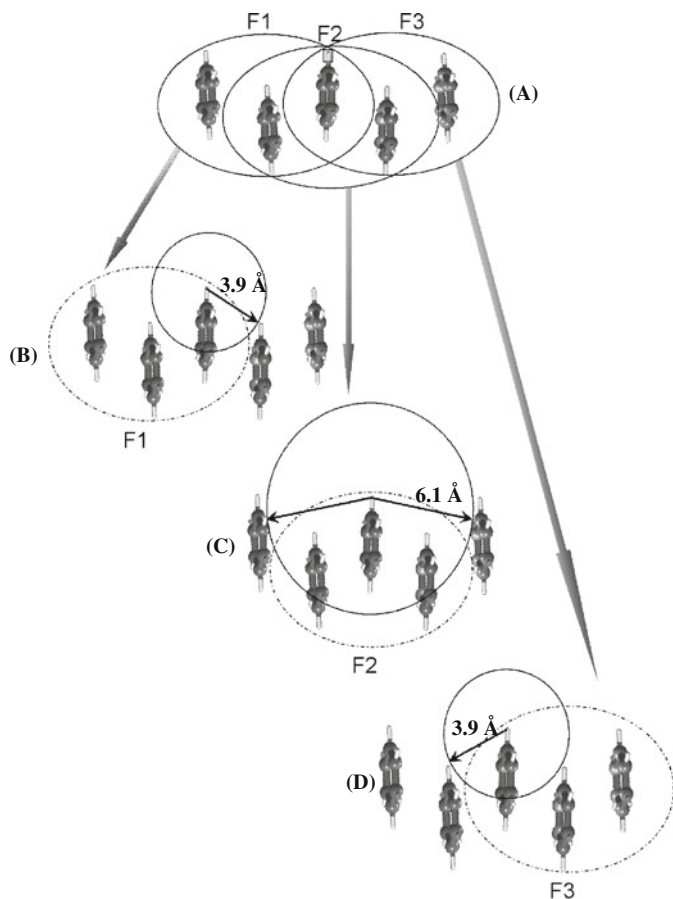


Figure 10-2. A trimer based fragmentation scheme used for a Benzene pentamer. (A) shows main fragments F1, F2 and F3; The atom (H) under consideration is depicted by a small square; (B), (C) and (D) show R_g values of 3.9 Å, 6.1 Å and 3.9 Å for H in F1, F2 and F3, respectively. See text for details

10.2.3.2. Average Size of Fragments (N_{av}) and Scaling Factor (SF)

Average size is the arithmetic mean of sizes of all main fragments in terms of number of atoms. Scaling factor (SF) is calculated as the ratio of sum of atoms in all the main fragments to the total number of atoms in the parent molecule. This parameter has a limited connotation and is to be interpreted along with average and largest size of fragments. This parameter reflects the computational cost required by the calculation. For example, if the average size of several fragments in a large molecule is nearly 75% of the size of the parent molecule, then the MTA-based calculation may not lead to much time advantage over the actual calculation. Learning from earlier benchmarks, SF should be within 2 to 5 for achieving substantial decrease in computational time, provided the average size of fragments is reasonably small.

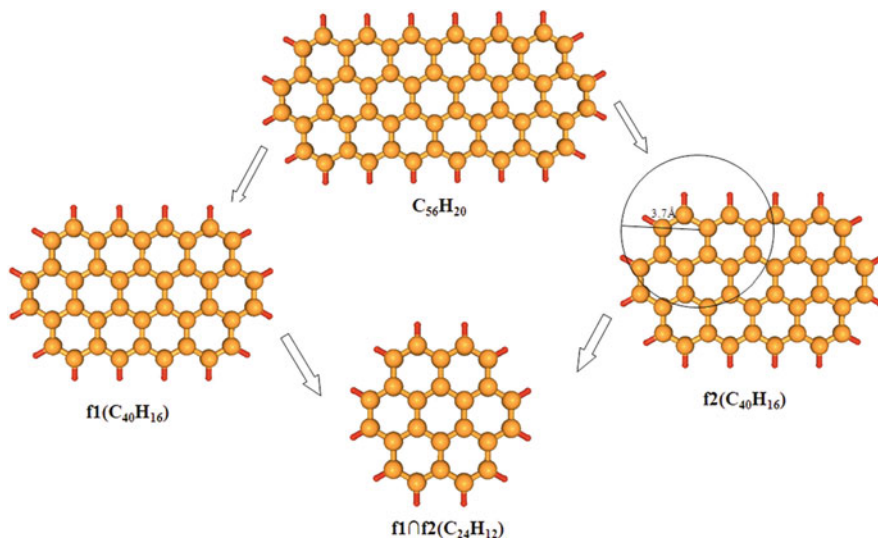


Figure 10-3. A fragmentation scheme used for a small model of graphene sheet, $C_{56}H_{20}$. The main fragments are f_1 and f_2 . The Rg value of a carbon atom in f_2 is illustrated with a circle of radius 3.7 Å

Apart from these, the largest fragment size and uniformity in the sizes of the main fragments are also important factors for guessing the quality of fragments from the point of view of the computational cost.

10.2.4. Cardinality Expressions

Based on the above-mentioned parameters, performance of the fragmentation can be estimated a priori i.e. before performing the fragment calculations. Once a fragmentation scheme is finalized for an MTA-based calculation, the ab initio calculations are performed on individual fragments (both, main and overlapping). Further, the results are stitched back as per the cardinality based equations for energy, gradients, Hessian etc. These equations are based on the inclusion-exclusion principle of set theory. A general equation for determining energy of the parent molecule from those of the fragments can be written as [24, 25]

$$E = \sum E^{f_i} - \sum E^{f_i \cap f_j} + \dots + (-1)^{k-1} \sum E^{f_i \cap f_j \cap \dots \cap f_k} \quad (10-2)$$

Here, E stands for the MTA-based estimate of the energy of the parent molecule, E^{f_i} denotes the energy of fragment i ; $E^{f_i \cap f_j}$ denotes the energy of the binary overlap of fragments i and j and so on. For instance, the cardinality expression set up in the case of scheme S2 (cf. Table 10-1 and Figure 10-1) for cholesterol would be:

$$\begin{aligned}
E(\text{cholesterol}) &= E^{f1} + E^{f2} + E^{f3} - (E^{f1\cap f2} + E^{f2\cap f3} + E^{f1\cap f3}) + E^{f1\cap f2\cap f3} \\
&= E^{f1} + E^{f2} + E^{f3} - (E^{f1\cap f2} + E^{f2\cap f3}) \\
&= -777.15987 - 811.83690 - 701.45928 - (-660.05698 - 506.26813) \\
&= -1124.13094 \text{ a.u.}
\end{aligned}$$

Here, the binary overlap between fragments f1 and f3 is the same as the ternary overlap between the three main fragments (viz. f1, f2 and f3), but have opposite signs of cardinalities. Hence, these get cancelled and there is no need to evaluate the energies of these.

Similar expressions are set up in the case of the gradient or Hessian calculations.

$$\frac{\partial E}{\partial X_\mu} = \sum \frac{\partial E^i}{\partial X_\mu^i} - \sum \frac{\partial E^{i\cap j}}{\partial E_\mu^{i\cap j}} + \dots + (-1)^{k-1} \sum \frac{\partial E^{i\cap j\cap \dots \cap k}}{\partial E_\mu^{i\cap j\cap \dots \cap k}} \quad (10-3)$$

$$\mathbf{H}_{ab} = \sum \mathbf{H}_{ab}^i - \sum \mathbf{H}_{ab}^{i\cap j} + \dots + (-1)^{k-1} \sum \mathbf{H}_{ab}^{i\cap j\cap \dots \cap k} \quad (10-4)$$

Terms in Eqs. (10-3) and (10-4) are respectively the first and second order derivatives of the energy terms, appearing in Eq. (10-2), with respect to nuclear coordinates, with \mathbf{H}_{ab} denoting the element (a, b) of the Hessian matrix. Similar expression is set up for estimating the density matrix of the parent molecule from those of fragments.

10.3. CAPABILITIES

In its earlier days, MTA was developed for determining the Density Matrix (DM) of a large molecule. Further, this DM was employed for evaluating one-electron properties such as Molecular Electrostatic Potential (MESP), Molecular Electron Density (MED) and their topographical features, along with values of the multipole moments of the charge density. It was later extended to geometry optimization based on qualitative estimate of energy and gradients picked from appropriate fragments. The estimation of energy was qualitative. However, it was found that the path followed by MTA-based optimization was in general, similar to that followed by the actual conventional calculation. Later, with cardinality guided (CG) expressions, the MTA method was further developed for accurate energy estimates. With a reasonable fragmentation scheme (with reference to Rg and other parameters discussed in the earlier sections), MTA produces energy estimates to within 1.5 mH (~ 1 kcal/mol) of the actual one, which can be considered as the normally accepted chemical accuracy. Also the numerically significant gradients (norms $\geq 10^{-3}$) are generally found to be accurate enough. Also, for the test cases examined, MTA-based optimization and the actual conventional optimization follow a similar path. On the same lines of cardinality-based treatment, the Hessian may be patched from fragments (cf. Eq. (10-4)). Evaluation of Hessian is an expensive step, especially at DFT and MP2 levels of theory. In DFT, Hessian being numerical, $3N+1$ steps of single-point energy-gradient calculations are required, where N is number of atoms. For large N, the number of basis functions is also large with a reasonable basis set. However, though MTA cannot reduce the number of optimization steps,

it reduces the cost of each step and consequently, the complexity of Hessian calculation as well. This Hessian is employed for calculating the vibrational frequencies and intensities. For intensities, the dipole derivative tensors are patched from those for fragments again based on CG-expressions. The test cases discussed in the present work are based on cardinality expression and are referred, for brevity, as MTA-based calculations. As mentioned in the earlier section, MTA-enabled GAMESS is a locally modified version of GAMESS. A limited access to MTA-enabled GAMESS is provided to the interested users via web-interfaces, WebProp [28] and WebMTA [29]. WebProp evaluates one-electron properties and WebMTA carries out a single point energy-gradient calculation as well as geometry optimization at HF and DFT (for a limited choice of functionals viz. BLYP, B3LYP). These interfaces accept geometry inputs from the user, perform MTA-based calculations on the local clusters where MTA-enabled GAMESS is installed and the outputs are sent to the user via e-mail. In future, it is planned to make these facilities available to the registered users across the world.

10.4. BENCHMARKS AND APPLICATIONS

10.4.1. Establishing MTA

Before presenting the recent applications of MTA, it is necessary to assure the reader about the accuracy of the method. For this purpose, we reproduce some of the earlier benchmarks [25] in which geometry optimization was performed on 4 test cases, viz. γ -cyclodextrin, taxol, folic acid and β -carotene, at the HF and DFT levels. Actual single point energy-gradient calculations were performed on a few randomly selected geometries of these systems in order to assess the accuracy of MTA as well as to gauge the time advantage achieved by fragmentation. A part of the results from Ref. [25] are reproduced in Table 10-2. It is evident that for all the cases examined, the errors in MTA energy estimates are well within 1 mH. MTA calculations are at least twice as fast as the corresponding actual ones as revealed by the T_T values shown in Table 10-2. Thus, it can be stated that for any general molecular system, MTA offers reliable results with less computational time and hardware resources. The forthcoming subsections present some recent results on molecular clusters as well as biological systems with charged centers.

10.4.2. HF Level

On thorough benchmarking and validation performed on MTA, the method is seen to assure a good precision in results on the test systems, typically within limits of chemical accuracy. Hence, a few exploratory investigations were performed with MTA on real-life cases, which cannot be treated otherwise. The initial and final energies of test cases for both MTA as well as actual calculation are given in Table 10-3. One such study [26] done in collaboration with our laboratory assesses energetics and stabilization of orthoboric acid nanotubes with different sizes and diameters. In this work [26], structures composed of 40, 45, 48 and 64 monomers of orthoboric

Table 10-2. A comparison of the actual and MTA-based energy-gradients for test systems at some randomly selected geometries. N and Rg are number of basis functions for the parent system and Rg values of the fragmentation scheme in Å. E_{MTA} and E_{act} are the MTA-based and actual energies in a.u. respectively. G_{RMS} is the RMS gradient norm. T_r is the ratio of time taken by the actual calculation to that for the MTA calculation performed on identical hardware. See text and Ref. [25] for details

System (Level/Basis)	N, Rg	E_{MTA} (G_{RMS})	E_{act} (G_{RMS})	T_r
folic acid HF/6-31G(d)	518, 2.2	-1,560.90931 (0.02174)	-1,560.90939 (0.02158)	3.6
β -carotene HF/6-31G(d)	712, 4.0	-1547.14193 (0.01404)	-1547.14197 (0.01403)	2.1
Taxol B3LYP/6-31G(d)	1185, 4.0	-2,927.89652 (0.0004)	-2927.89660 (0.0005)	2.3
γ -cyclodextrin B3LYP/6-31G(d,p)	1480, 4.1	-4,883.54567 (0.0003)	-4,883.54609 (0.0004)	3.1

acid were investigated (cf. Figure 10-4). The structures were completely optimized at the HF/6-31++G(d, p) level of theory using MTA. It is evident from the results that boric acid can form regular nanotubes, structurally similar to carbon nanotubes, assisted by the extensive network of hydrogen bonds. The stability of these tubes increases due to enhancement in the number of H-bonding interactions with increasing diameter of the tube [26]. An analysis of MESP for a representative case of nanotube of 40 monomers shows that these nanotubes could favorably react with polar systems such as water. It is noteworthy that the largest of these calculations viz. geometry optimization of $(\text{H}_3\text{BO}_3)_{64}$ involved 6,016 basis functions. All these calculations were performed on a cluster of 8 single core nodes with 1 GB RAM each. It is not possible to handle the actual calculation of this system using this hardware configuration.

A small synthetic protein viz. Trp-Cage protein (pdb code: 1L2Y), employed as a test for the FMO method [35], is taken up next (Figure 10-5). This protein comprises of 20 amino acid residues and is known as the fastest folding protein [48]. It has 3 cationic and 2 anionic charge centers and hence, bears an overall unit positive charge. This protein is subjected to MTA-based geometry optimization at HF/3-21G level to start with, following subsequently at the HF/6-31G(d) level of theory. A fragmentation scheme for this system is chosen on the basis of pilot runs, is discussed in detail in Ref. [36]. This scheme consists of 8 main fragments, with Rg value 3.9 Å and SF of 3.5. Number of basis functions involved at HF/3-21G level is 1686 while that at HF/6-31G(d) level is 2610 (cf. Table 10-3). During optimization at HF/3-21G level of theory, the geometry is seen to undergo substantial changes. Because of this, the Rg value is observed to drop down from 3.9 Å to 3.5 Å during the course of optimization (cf. Figures 10.5A, B). Its effect can be seen on the energy accuracy with respect to the actual energy reported in Table 10-3. The error in MTA-energy is ~ 0.9 mH for initial energy, where Rg is 3.9 Å, while for final geometry (Figure 10-5B), the error is increased to ~ 6 mH as the Rg value is 3.5 Å. This clearly shows how Rg value reflects accuracy as described in earlier subsection.

Table 10-3. Results of MTA-based geometry optimization of a few test molecules. N_{at} and N_{BF} denote number of atoms and number of basis functions involved in the calculation. MTA estimates for energy in a.u. (E_{MTA}) and RMS gradient (G_{RMS}) are given for the initial and final geometries. The actual values of single point energy and RMS gradient for initial and final geometries are given in parentheses, wherever possible. See text for details, in particular for the case of IL₂Y and C₅₆H₂₀

Molecule	Level/basis set	Initial			Final		
		N_{at} , N_{BF}	E_{MTA}	G_{RMS}	E_{MTA}	G_{RMS}	G_{RMS}
IL ₂ Y	HF/3-21G	304, 1686	-7,398.26713 (-7,398.26803)	0.0096 (0.0096)	-7,398.61477 (-7,398.62018)	0.0004 (0.0007)	
	HF/6-31G(d)	304, 2610	-7,439.74428 (-7,439.74949)	0.0083 (0.0082)	-7,439.83325 (-7,439.83268)	0.0007 (0.0008)	
(H ₂ O) ₆₃	HF/6-31++G(d,p)	189, 1953	-4,790.60174	0.00389	-4,790.74682	0.00162	
β -cyclodextrin	B3LYP/6-31++G(d,p)	147, 1883	-4,273.32406	0.00154	-4,273.32689	0.00015	
Li ₉₂	B3LYP/6-31G	92, 1748	-692.71667	0.00331	-692.81942	0.00148	
C ₅₆ H ₂₀	B3LYP/6-31+G(d)	76, 1104	-2,145.02273 (-2,145.03209)	0.0102 (0.0084)	-2,145.06000 ^a (-2,145.04607)	0.0003 (0.0007)	
C ₅₆ H ₂₀	MP2/6-31G(d)	76, 880	-2,139.69793	0.01330	-2,139.72237	0.00040	
β -carotene	MP2/6-31G(d)	96, 712	-1,552.38694	0.00184	-1,552.38994	0.00003	
(C ₆ H ₆) ₄	MP2/6-31++G(d,p)	48, 600	-925.87639	0.00040	-925.87654	0.00012	
(C ₆ H ₆) ₅	MP2/6-31++G(d,p)	60, 750	-1,157.63996	0.00108	-1,157.64253	0.0005	
(C ₆ H ₆) ₆	MP2/6-31++G(d,p)	72, 900	-1,389.17402	0.00069	-1,389.18422	0.00047	
(C ₆ H ₆) ₇	MP2/6-31++G(d,p)	84, 1050	-1,620.71545	0.00187	-1,620.71737	0.00056	

^aThis is the final energy of MTA-optimized geometry, which is in error by ~ 13 mH due to inadequate treatment of conjugation and cooperativity effects in the molecule. The actual energy at fully optimized geometry is -2145.04722 a.u. See text for details.

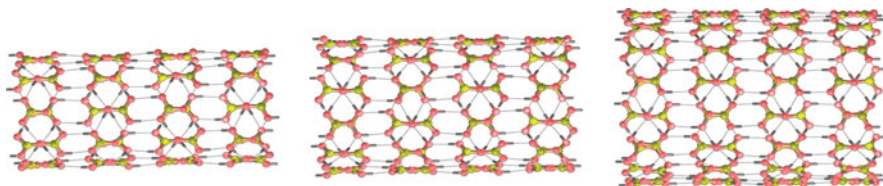


Figure 10-4. Nanotubes of orthoboric acid; **T40**, **T48** and **T64** comprising of 40, 48 and 64 monomers respectively. For details, see text and reference [26]

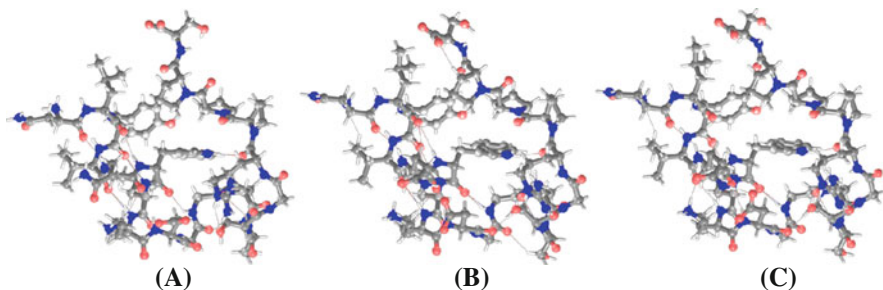


Figure 10-5. Initial geometry (A) of Trp-Cage 1L2Y protein subjected to MTA-based geometry optimization at HF/3-21G level of theory. The final geometry (B) thus obtained from (A) is further subjected to MTA-optimization at HF/6-31G(d) level. (C) depicts the final MTA-optimized geometry at HF/6-31G(d) level

During optimization at HF/6-31G(d), the molecule expands again and the Rg value goes on increasing. Thus, the error of ~ 5 mH (cf. Table 10-3) for initial geometry (Rg of 3.5 \AA) goes down to ~ 0.8 mH for final geometry (Rg of 3.8 \AA). In view of this, dynamic fragmentation strategy during geometry optimization needs to be built into MTA.

MTA-based geometry optimization of this system is performed on a cluster of 7 Core2Quad @ 2.4 GHz with 8 GB RAM each. Distributed mode of MTA is activated for efficient use of computational resource. Each cycle of optimization took merely 15 min at HF/3-21G level. An intermediate geometry from the HF/3-21G optimization run is further subjected to optimization at HF/6-31G(d) level employing the same fragmentation scheme. However, 11 machines (Core2Quads of above-mentioned specification) are used. Each step of optimization took noticeably small time of ~ 55 min for HF/6-31G(d)-level MTA computation. To assure the accuracy as well as time advantage achieved by MTA, the final optimized geometry at HF/6-31G(d) level was subjected to the actual single-point energy-gradient evaluation on the same hardware of 11 Core2Quads. The error in energy of the final geometry is merely 0.3 kcal/mol. Also the actual single point energy-gradient calculation took 13 h as compared to 55 min of that for the MTA calculation.

The above results show that HF level geometry optimization of a system consisting of a few thousand basis functions can be easily handled with the tool of MTA employing a cluster of contemporary off-the-shelf PC hardware.

10.4.3. MP2 Method

Møller-Plesset second order perturbation (MP2) method treats the electron correlation to some extent and is the most affordable post-HF method, albeit with a higher scaling order viz. $O(N^5)$. To examine how far the correlation affects the chemical environments of atoms in highly conjugated systems, β -carotene has been chosen as a test case for MTA-based approach. This highly conjugated system is responsible for the orange color of the carrots. The calculations are performed at MP2/6-31+G(d) level of theory. Firstly, the initial geometry of β -carotene is subjected to MTA-based geometry optimization with a scheme of Rg 3.9 Å. This optimized geometry is taken for further studies. Three fragmentation schemes (**S1**, **S2** and **S3**) are created which have Rg values 3.5, 4.6 and 6.2 Å respectively. Clearly, **S1** is a poor scheme while **S3** is the best scheme among the three. MTA-based geometry optimizations are performed employing these three schemes independently. These calculations involve 872 basis functions, for which it is not possible to perform the actual calculation on identical hardware. Thus, the results of **S1**, **S2** and **S3** are compared with a scheme **S4** having Rg value 7 Å instead of actual results. The initial and final energy-gradients for all the schemes are reported in Table 10-4. A comparison clearly shows that as the Rg value increases, the results become more accurate. As expected, **S1** has produced results which are in error of ~ 5 mH. Clearly, for such a highly conjugated scheme Rg of 3.5 Å is inadequate. The energies of **S2** are in error by ~ 1 mH, in acceptable range, while the best scheme **S3** shows a submilli-hartree accuracy. However, a reasonable accuracy for gradients is achieved even by the moderate scheme **S2**. Thus, it can be concluded that a moderate scheme may be employed for geometry optimization, since it provides reliable enough gradients. This will speed up the process as moderate scheme would give more CPU-time advantage. Final few steps of optimization may be performed with better fragments to ensure reliability of energy as well as gradients.

A study of growth patterns of benzene clusters has recently been investigated with MTA [49]. Since dispersion effects are important in this investigation, the calculations are performed at the MP2 level employing 6-31++G(d, p) basis set. Starting from many possible structures of benzene tetramers, clusters are grown up to benzene heptamers and a few prototype octamers. These clusters are constructed by employing MESP-guided cluster building method discussed in Ref. [45, 50]. All

Table 10-4. Energies and RMS gradient norms (in a.u.) of initial and MTA-optimized geometry of β -carotene with fragmentation schemes **S1**, **S2**, **S3** and **S4** at MP2/6-31+G(d) level of theory. Rg values are in Å. See text for details

Scheme (Rg)	Initial Energy (RMS norm)	Final Energy (RMS norm)
S1 (3.5)	-1,552.47242 (0.00070)	-1,552.47282 (0.00009)
S2 (4.6)	-1,552.47650 (0.00383)	-1,552.47660 (0.00008)
S2 (6.2)	-1,552.47797 (0.00223)	-1,552.47803 (0.00016)
S4 (7.0)	-1,552.47746 (0.00329)	-1,552.47833 (0.00017)

the clusters are fragmented into sets of trimers, as shown in the illustrative fragmentation in Figure 10-2. The density matrices of these fragments are patched as per the cardinality-guided expression similar to Equation (10-2) in order to get the density matrix (DM) for the parent molecule. This final DM is employed for MESP calculation using INDPROP [51] suit of programs developed in our laboratory.

The starting geometries of benzene tetramers are subjected to MTA-based geometry optimization. The growth of a representative tetramer is discussed here. The most stable (**T**) of the tetrameric structures studied, is depicted in Figure 10-6, in which a maximum number of T-shaped interactions is clearly noticed. The tetramer **T** is used for generating the starting structure of benzene pentamer (**P**) by adding a new benzene monomer at the appropriate position and subjecting **P** to MTA-based geometry optimization. The suitable position for adding the ensuing benzene monomer is decided with the aid of MESP-guided method [45, 50] and the cluster is built up further. A representative example is shown in Figure 10-6, wherein MESP isosurfaces at -0.031 a.u. for pentamer **P** are depicted. The addition of new benzene unit at an appropriate position, guided by this isosurface, to generate the corresponding hexamer is exemplified. A hexamer (**Hx**) generated from **P** was further grown to a heptameric structure **Hp** (cf. Figure 10-6) in similar way. The study points out that, T-shaped interactions are somewhat more preferred as compared to parallel shifted interactions and structures incorporating a larger number of T-shaped interactions are hence generated on optimization of the clusters.

In the investigation of benzene oligomers, all the clusters are scissored into trimeric fragments manually with help of MeTASstudio [47]. It is possible to treat tetramers at MP2 using moderate basis set 6-31G(d) by conventional actual calculation. However, from pentamer onwards, the memory requirement is seen to increase drastically making the actual calculation very difficult. Also, with 6-31++G(d,p) basis set, even tetramer is very difficult to treat with the conventional method. In contrast, with the powerful tool of MTA, the memory requirement of any n -mer, $n = 4-8$, or even higher, is exactly identical as all of them are broken up into trimers! More explicitly, memory requirements for actual calculation on a trimer, tetramer, pentamer, hexamer, and a heptamer at MP2/6-31++G(d,p) level, as estimated by GAMESS package are 5, 16, 38, 79 and 146 GB respectively. In contrast, with MTA-enabled GAMESS, any of these clusters requires only 5 GB of RAM for all the calculations.

To ensure the accuracy of the trimer-based calculation, some test calculations are performed on tetramers at MP2/6-31G(d) level. MTA energy for **T** comes out to be -925.85722 a.u. An actual calculation performed on the same geometry using Gaussian'03 [2] package yields an energy value of -925.85714 a.u. The small magnitude of error of 0.1 mH in MTA calculation can be attributed to the fact that a fragmentation scheme used for **T** includes all 2-body and 3-body interactions. In higher clusters with 5 to 7 monomers, it is not possible to include all 2 and 3-body interactions in MTA calculation. However, care is to be taken during fragmentation so as to capture the prominent ones of those. Thus, even though the error introduced in MTA-energy while geometry optimization is relatively higher ($\sim 2-3$ mH), the calculation at least becomes feasible. Also, accurate estimation of MTA energy can

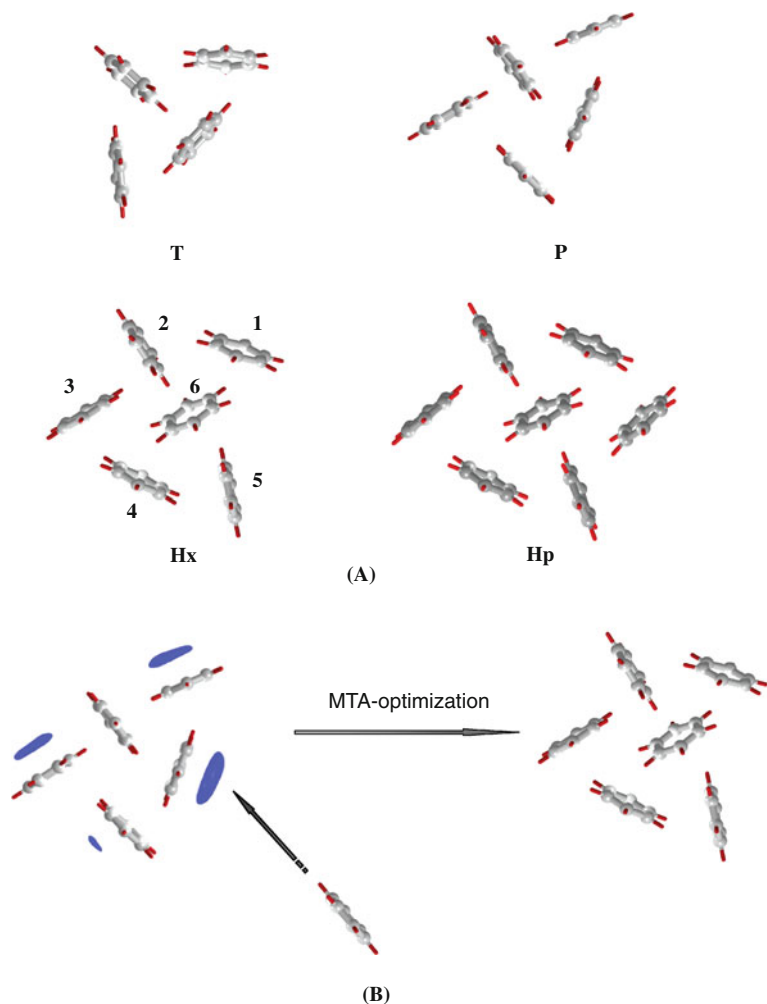


Figure 10-6. (A) MTA-optimized structures of tetramer (**T**), pentamer (**P**), hexamer (**Hx**) and heptamer (**Hp**) of benzene. (B) MESP isosurfaces for pentamer (**P**) at -0.031 a.u. Ensuing benzene monomer is added near the deepest minimum of MESP. See text for details

be easily achieved for the final optimized geometry by adding contributions of the missing 2 and 3-body interaction terms (denoted by ΔE_{ij} and ΔE_{ijk}) as per many body analysis of energy [52]. This is demonstrated for the case of the hexamer **Hx**. As observed from Table 10-5, total missing 2-body contribution ($\Delta 2b$) is significant as compared to total missing 3-body contribution ($\Delta 3b$). The MTA-estimate for **Hx** for the final optimized geometry turns out to be $-1,389.18621$ a.u. after applying the correction instead of $-1,389.18422$ a.u. without correction.

Table 10-5. Energetics of MTA-optimized benzene hexamer, **Hx**. List of missing 2- and 3-body terms, denoted by M_{ij} and M_{ijk} respectively, and their two body (ΔE_{ij}) and three body (ΔE_{ijk}) contributions (all values in a.u.) for a trimer-based fragmentation scheme of benzene hexamer **Hx**. Total contribution due to missing 2-body and 3-body interactions are denoted by $\Delta 2b$ and $\Delta 3b$ respectively. Refer to Figure 10-6 for numbering of benzene units. See text and Table 10-3 for details

Final Energy E_{final}		-1,389.18422	
M_{ij}	ΔE_{ij}	M_{ijk}	ΔE_{ijk}
13	-0.00044	123	+0.00017
14	0.00000	124	-0.00026
15	-0.00074	125	-0.00003
24	-0.00090	134	+0.00009
35	-0.00015	135	-0.00002
		136	+0.00031
		145	-0.00015
		146	+0.00020
		156	-0.00006
		234	-0.00004
		235	+0.00005
		245	+0.00001
		246	-0.00008
		345	+0.00012
		356	-0.00007
($\Delta 2b$)	-0.00223	($\Delta 3b$)	+0.00024
Final corrected energy =		-1,389.18621	
$E_{\text{final}} + \Delta 2b + \Delta 3b$			

Another attempt for testing MTA at MP2 level is made on a small model graphene sheet viz. $C_{56}H_{20}$ (cf. Figure 10-3). This is a part of the studies recently reported from our laboratory [46]. This system is optimized at MP2 level employing 6-31G(d) basis set. The calculation involves 880 basis functions. The memory requirement for each energy-gradient step is ~ 155 GB when a conventional actual calculation is performed, while that for just single point energy is ~ 44 GB. Since actual optimization is not possible on the available hardware, the accuracy of MTA-based energy is compared to actual energy of the final geometry. It is evident that the memory requirements and the computational cost at MP2 level are substantially reduced by MTA. Thus, it clearly demonstrates the feasibility of attempting an MTA-based treatment for the actual calculation that is otherwise not possible.

10.4.4. DFT Framework

It is a well known fact that DFT provides reasonably accurate, yet low cost computational methodology for correlated systems. There is contemporary interest in studying large carbon clusters, fullerenes and graphenes due to their applications in preparation of novel materials. In view of this an exploratory study of some carbon compounds has been performed [46] using MTA within DFT framework. No

such attempt of application of DC-methods to two-dimensional π -conjugated systems has so far been reported in the literature. We have developed a methodology for geometry optimization of one- and two-dimensional π -conjugated systems [46]. Small graphene model system, viz. $C_{56}H_{20}$ is chosen for MTA-based calculation at B3LYP/6-31+G(d) level. MTA optimization is performed in two steps, initially with poorer fragmentation scheme with small R_g value followed by a better fragmentation scheme with higher R_g value. The final MTA-energy is in somewhat larger error (~ 13 mH). However, the geometry produced by MTA matches well with that produced by the conventional actual optimization. The error in MTA energy is probably due to conjugation and cooperative effects which MTA is unable to capture. Therefore, in order to get the correct energy of the MTA-based final geometry, actual single point energy calculation is performed. The actual single point energy of MTA-optimized geometry for $C_{56}H_{20}$ is $-2,145.04607$ a.u. which is in error of 1.15 mH with respect to the actual final optimized energy [46]. The time advantage factor (on 5 parallel Pentium IV machines) for this system comes out to be 1.95. The detailed geometry analysis of the MTA optimized and actual final optimized geometry shows a typical average deviation of 0.0047 \AA for C–C bond lengths and 0.0001 \AA for C–H bond lengths [46]. In this work [46], this method is extended to larger graphene model system $C_{150}H_{30}$ at B3LYP/6-31G level.

Nano-sized cluster materials are recent experimental targets, since they exhibit size dependent chemical and physical properties. MTA has also been applied for building and optimization of atomic and molecular clusters. A locally modified version of MTA-enabled Gaussian'03 is a combination of Gaussian'03 suit of program, fragmentation from MTA and optimizer from GAMESS package. In this version, fragments are generated by MTA code, and fed to Gaussian'03 for calculation. The gradients generated by Gaussian'03 are patched by MTA program and fed to GAMESS optimizer in order to generate a new geometry. We have applied this MTA-enabled Gaussian'03 for geometry optimization of Li_{92} cluster at B3LYP/6-31G, which was previously built with the aid MESP of Li_{72} cluster [45].

10.5. COMMENT ON SCALING OF MTA

The benchmarks reported in the previous subsections clearly show that MTA is successful in reducing the scaling problem of ab initio methods. However, it would be worth to discuss and reason out the extent to which the scaling problem can be overcome with the tool of MTA. Time advantage factor clearly demonstrates the reduction in complexity of a particular calculation. Time advantage factor achieved by MTA is governed mainly by two aspects viz. the level of theory chosen and the type of molecular system under consideration. Consider the order of an ab initio method to be \mathbf{p} , so that the complexity of the calculation is $O(\mathbf{N}^{\mathbf{p}})$, where \mathbf{N} is the number of basis functions for a particular molecule. After applying MTA to the molecule under consideration, let there be \mathbf{m} fragments of comparable size, each containing \mathbf{n} basis functions on an average. The computational cost of the MTA

based calculation would thus be proportional to $\mathbf{m.n^p}$ as against the cost of the actual conventional calculation being proportional to $\mathbf{N^p}$. For $\mathbf{n} \ll \mathbf{N}$, MTA provides advantage over the actual calculation. It is clear that as the power \mathbf{p} for the level of theory increases, MTA would offer higher time advantage factors. This aspect is evident from a recent study [46]. To make this point lucid, advantages achieved by MTA are demonstrated with a case study of benzene hexamer calculation at HF and MP2 theory employing 6-31G(d) basis set. An actual calculation of benzene hexamer at HF/6-31G(d) level of theory takes ~ 6 min on 2 Core2Quad machines @ 2.4 GHz with 8 GB RAM each while the corresponding MTA calculation takes ~ 5 min on the same hardware. When the same actual and MTA based calculations at MP2/6-31G(d) level of theory on the identical hardware the time taken by the actual and MTA calculations is about 236 and 18 min respectively. Evidently the time advantage factor achieved by MTA at MP2 level i.e. 13 is far more, as expected, than the factor of 1.2 attained at the HF level. This may be attributed to the inherent scaling of the HF and MP2 methods.

Further, the structural intricacy and the spatial extent of molecular system can influence the time advantage factor that can be achieved by MTA. As described in the computational details, MTA uses R-goodness parameter to ensure the accuracy of the calculation. If the spatial extent of the molecule is large, the required R-goodness is achieved with smaller fragments. Thus, for linear systems such as β -(ALA) $_n$, (H₃BO₃) $_n$ etc. MTA offers time advantage factors in the range 8–10 [36]. However, for intricate systems such as α -(ALA) $_n$ the same drops down to 2–3. Also for the compact structures such as water clusters, to achieve the required R-goodness value, larger fragments are needed, resulting into very little time saving. However, it may be anticipated that MTA will show its usefulness for a water cluster containing few hundreds of units, where the actual calculation is not possible at all.

Thus, generally one can expect optimum performance of MTA for large and spatially extended systems at higher levels of theory.

10.6. CONCLUDING REMARKS

A versatile fragmentation method is required for ab initio treatment of large molecules. The diverse test cases presented in this Chapter clearly demonstrate that the molecular tailoring approach (MTA) just fits the bill. An attractive attribute of MTA is its applicability at any level of theory including HF and post-HF methods (such as MP2) as well as DFT. In principle, the method can be applied with no restriction on the use of any of the popular basis sets. It has been pointed out by Kohn [53], that the interactions in spatially extended molecular systems are “near-sighted” under certain conditions. Fragmentation-based methods exploit this property although the constant chemical potential condition may not be rigorously satisfied. Another advantage attributed to technical structure of MTA is its compatibility with any package/suit of ab initio methods. The automatic fragmentation routine of MTA and scripts for enabling distributed mode are written independently. Thus, given any ab initio package to run in the backend which actually performs

calculations on individual fragments, a simple script for patching energies and gradients etc. can be written to complete the MTA process. This has been demonstrated in a recent work [36], in which, a small coupler script is written to perform MTA-driven IMS-MP2 and RI-MP2 calculations. This program is benchmarked on some polypeptides, molecular clusters and a small protein.

Apart from these technical aspects, the accuracy and time advantage factors achieved by MTA are noteworthy. In general, a chemical accuracy of 1 kcal/mol (1.5 mH) is achieved by MTA for the cases examined. MTA-based gradients being fairly reliable, geometry engendered by MTA-based optimization is similar to that resulting from the corresponding actual one. For most of the systems, MTA offers a time advantage factor of at least 2 over the actual conventional calculation. It is observed that this factor may enhance up to 10 or more if the spatial extent of the molecular system is large enough. Also, the applications presented in this Chapter show utility of MTA for diverse molecular systems. These include large organic molecules, biomolecules and molecular clusters as well as systems with charged centers. The method of molecular tailoring exploits large spatial extent of the molecules. The MTA methodology is in the spirit of the “nearsightedness principle” of Kohn [53]. No further extraneous artifacts such as re-hybridization, point charges etc. are as yet used.

With the emerging success of MTA, there are some areas requiring improvement. Currently, the application of MTA is restricted only to closed shell systems, which needs to be extended to open shell ones. Also the MTA-driven geometry optimization process requires some improvements, as in the existing algorithm default optimizer from GAMESS package is used. The fact that the MTA-based Hessian calculation is economical than the actual one, it can be utilized towards Hessian-based optimization to speed up the process. Further, the existing fragmentation has been written for general molecules and does not consider any special features of a particular class of molecules. Thus, the specialized automatic fragmentation routines could be gainfully developed for biological systems such as 1L2Y, α -helical structures etc. For effectively handling molecular clusters, a utility for adding missing 2 and 3 body contributions needs to be developed. To add further value to its use, MTA should be combined with newer and faster ab initio codes and other existing packages apart from GAMESS and Gaussian.

In brief, it can be said that the method now stands on a firm footing. With further value addition, it has a potential to be a valuable tool for taking up some grand challenge problems in chemistry, physics and biology.

ACKNOWLEDGMENTS

Authors thank the Center for Development of Advanced Computing (C-DAC), Pune; Naval Research Board (NRB), New Delhi and Center for Advanced Studies (CAS) program in Chemistry supported by the University Grants Commission (UGC), New Delhi for financial assistance and computational resource availability. APR is grateful to the Council of Scientific and Industrial Research (CSIR),

New Delhi for funding. SRG is thankful to Department of Science and Technology (DST), New Delhi for the award of a J. C. Bose Fellowship to him.

REFERENCES

- Schmidt MW, Baldrige KK, Boatz JA, Elbert ST, Gordon MS, Jensen JH, Koseki S, Matsunaga N, Nguyen KA, Su SJ, Windus TL, Dupuis, M, Montgomery JA (1993) *J Comput Chem* 14:1347. For further details, see: <http://www.msg.ameslab.gov/GAMESS/GAMESS.html>
- Gaussian 03, Revision C.02, Frisch MJ, Trucks GW, Schlegel HB, Scuseria GE, Robb MA, Cheeseman JR, Montgomery Jr JA, Vreven T, Kudin KN, Burant JC, Millam JM, Iyengar SS, Tomasi J, Barone V, Mennucci B, Cossi M, Scalmani G, Rega N, Petersson GA, Nakatsuji H, Hada M, Ehara M, Toyota K, Fukuda R, Hasegawa J, Ishida M, Nakajima T, Honda Y, Kitao O, Nakai H, Klene M, Li X, Knox JE, Hratchian HP, Cross JB, Bakken V, Adamo C, Jaramillo J, Gomperts R, Stratmann RE, Yazyev O, Austin AJ, Cammi R, Pomelli C, Ochterski JW, Ayala PY, Morokuma K, Voth GA, Salvador P, Dannenberg JJ, Zakrzewski, VG, Dapprich S, Daniels AD, Strain MC, Farkas O, Malick DK, Rabuck AD, Raghavachari K, Foresman JB, Ortiz JV, Cui Q, Baboul AG, Clifford Cioslowski J, Stefanov BB, Liu G, Liashenko A, Piskorz P, Komaromi I, Martin RL, Fox DJ, Keith T, Al-Laham MA, Peng CY, Nanayakkara A, Challacombe M, Gill PMW, Johnson B, Chen W, Wong MW, Gonzalez C, Pople JA (2004) Gaussian, Inc., Wallingford, CT
- TURBOMOLE V6.0 2009, a development of University of Karlsruhe and Forschungszentrum Karlsruhe GmbH, 1989–2007, TURBOMOLE GmbH, since 2007; available from the website: <http://www.turbomole.com>
- Barden C, Schaefer HF III, Pure J (2000) *Appl Chem* 72:1405
- (a) Becke AD (1993) *J Chem Phys* 98:5648; (b) Lee C, Yang W, Parr RG (1988) *Phys Rev B* 37:785
- Zhao Y, Truhlar DG (2006) *J Phys Chem A* (2006) 110:13126; Valero Z, Costa R, Moreira IPR, Truhlar DG, (2008) *F Illas* 128:114103
- (a) Gadre SR, Kulkarni SA, Limaye AC, Shirsat RN (1991) *Zeit Phys-D : Atoms, Molecules and Clusters* 18:357(b) Shirsat RN, Limaye AC, Gadre SR (1993) *J Comput Chem* 14:445 (c) Limaye AC, Gadre SR (1994) *J Chem Phys* 100 1303
- Ufimtsev IS, Martinez TJ (2009) *J Chem Theory Comput* 5:2619
- The package PetaChem, for quantum chemical calculations on graphics processors, available at <http://www.petachem.com>
- Saebo S, Pulay P (1988) *J Chem Phys* 88:1884
- Schütz M, Hetzer G, Werner H-J (1999) *J Chem Phys* 111:5691.
- (a) Ishimura K, Pulay P, Nagase S (2006) *J Comput Chem* 27:407 (b) Ishimura K, Pulay P, Nagase S (2007) *J Comput Chem* 28:2034(c) Katouda M, Nagase S (2009) *Int J Quant Chem* 109:2121
- Feyereisen M, Fitzgerald G, Komornicki A (1993) *Chem Phys Lett* 208:359
- Weigend F, Häser M, Patzelt H, Ahlrichs R (1998) *Chem Phys Lett* 294:143
- Spangler D, Christoffersen RE (1980) *Int J Quant Chem* 17:1075
- Yang W (1991) *Phys Rev A* 44:7823
- Lee C, Yang W (1992) *J Chem Phys* 96:2408
- Zhao Q, Yang W (1995) *J Chem Phys* 102:9598
- Gadre SR, Shirsat RN, Limaye AC (1994) *J Phys Chem* 98:9165
- Babu K, Gadre SR (2003) *J Comp Chem* 24:484
- Babu K, Ganesh V, Gadre SR, Ghermani NE (2004) *Theor Chem Acc* 111:255
- Gadre SR, Babu K, Ganesh V (2005) In: Maheshwari SN (ed) *Recent trends in practice and theory of information technology: proceedings of nrb seminar*, Viva Books, New Delhi, p 86
- Gadre SR, Ganesh V (2006) *J Theory Comput Chem* 5:835

24. Ganesh V, Dongare RK, Balanarayan P, Gadre SR (2006) *J Chem Phys* 125:104109
25. Gadre SR, Rahalkar AP, Ganesh V (2006) *Indian Assoc Nucl Chem Allied Sci Bull* 4:267
26. Elango M, Subramanian V, Rahalkar AP, Gadre SR, Sathyamurthy N (2008) *J Phys Chem A* 112:7699
27. Rahalkar AP, Ganesh V, Gadre SR (2008) *J Chem Phys* 129:234101
28. WebProp: Web Interface for Ab Initio Calculation of Molecular One-Electron Properties. Available for free academic use at <http://chem.unipune.ernet.in/~tcg/webprop/> See: Ganesh V, Kavathekar R, Rahalkar AP, Gadre SR (2008) *J Comput Chem* 29:488
29. WebMTA: Web interface for Ab Initio Calculations using Molecular Tailoring Approach. Available for free academic use at <http://chem.unipune.ernet.in/~tcg/mtaweb> See: Kavathekar R, Khire S, Ganesh V, Rahalkar AP, Gadre SR (2009) *J Comp Chem* 30:1167
30. Kitaura K, Ikeo E, Asada T, Nakano T, Uebayasi M (1999) *Chem Phys Lett* 313:701
31. Fedorov DG, Kitaura K (2004) *J Chem Phys* 120:6832
32. Fedorov DG, Ishida T, Uebayasi M, Kitaura K (2007) *J Phys Chem A* 111:2722
33. Fedorov DG, Jensen JH, Deka RC, Kitaura K (2008) *J Phys Chem A* 112:11808
34. Sawada T, Fedorov DG, Kitaura K (2009) *Int J Quant Chem* 109:2033
35. Fedorov DG, Ishimura K, Ishida T, Kitaura K, Pulay P, Nagase S (2007) *J Comp Chem* 28:1476
36. Rahalkar AP, Katouda M, Gadre SR, Nagase S (2010) *J Comput Chem* 31:2405
37. Li S, Ma J, Jiang Y (2002) *J Comp Chem* 23:237
38. Huo W, Fang T, Li W, Yu JG, Li S (2008) *J Phys Chem A* 112:10864
39. Zhang DW, Zhang JZH (2003) *J Chem Phys* 119:3599
40. Deev V, Collins MA (2005) *J Chem Phys* 122:154102
41. Collins MA (2007) *J Chem Phys* 127:024104
42. Bettens RPA, Lee AM (2006) *J Phys Chem A* 110:8777
43. Akama T, Kobayashi M, Nakai H (2007) *J Comp Chem* 28:2003
44. Kobayashi M, Nakai H (2009) *Int J Quant Chem* 109:2227
45. Jovan JKV, Gadre SR (2008) *J Chem Phys* 129:164314
46. Yeole SD, Gadre SR (2010) *J Chem Phys* 132:094102
47. The package MeTA Studio available at: <http://code.google.com/p/metastudio/>. See Ganesh V (2009) *J Comp Chem* 30:661
48. Qiu L, Pabit SA, Roitberg AE, Hagen SJ (2002) *J Am Chem Soc* 124:12952
49. Mahadevi S, Rahalkar AP, Gadre SR, Sastry GN (2010) *J Chem Phys* 133:164308
50. Jovan JKV, Gadre SR (2009) *Int J Quant Chem* 109:2238
51. Shirsat RN, Bapat SV, Gadre SR (1992) *Chem Phys Lett* 200:373
52. Kulkarni AD, Ganesh V, Gadre SR (2004) *J Chem Phys* 121:5043
53. Kohn W (1996) *Phys Rev Lett* 76:3168

CHAPTER 11

SOME THOUGHTS ON THE SCOPE OF LINEAR SCALING SELF-CONSISTENT FIELD ELECTRONIC STRUCTURE METHODS

FRANK NEESE

*Lehrstuhl für Theoretische Chemie, Mathematisch Naturwissenschaftliche Fakultät, Institut für Physikalische und Theoretische Chemie, Universität Bonn, D-53115 Bonn, Germany,
e-mail: neese@thch.uni-bonn.de*

Abstract: In this chapter a number of algorithms are described for the exact or approximate calculations of the Coulomb and Hartree-Fock exchange parts of the Fock matrix. Arguments in favor of efficient approximations *without* linear scaling behavior are presented if the goal of the investigation is to solve typical every day computational chemistry problems. “Everyday computational chemistry problems” are, in this context, understood as involving molecules with up to about 100 or 200 atoms. In particular, it is important to test new algorithms with respect to their efficiency in conjunction with basis sets and integral thresholds that are appropriate for actual application work. Some numerical examples for efficiency and accuracy of the methods that are discussed are provided.

Keywords: Linear scaling, Fock matrix, Self-consistent field, Density fitting, Cholesky decomposition, Numerical integration, Pseudospectral approximations

11.1. INTRODUCTION

In the early 1980s Jan Almlöf revolutionized electronic structure theory through the introduction of integral direct methods. Almlöf showed that it is possible to bypass the integral storage bottleneck by recomputing electron-electron repulsion integrals whenever they are needed [1]. In retrospect this proposal was highly courageous because repulsion integral evaluation always strongly dominated the computational effort for molecular self-consistent field (SCF) calculations and the prospect of repeating this step N_{iter} times (typically $N_{\text{iter}} \sim 10\text{--}20$) did not seem to be attractive. However, as Almlöf showed, recursive Fock matrix builds and pre-screening techniques allow one to skip more and more integral batches as the calculation is approaching convergence. The prescreening techniques were improved through the rigorous bounds developed by Häser and Ahlrichs [2] and more recently were further refined by Ochsenfeld and co-workers [3].

It is evident that for large molecules there is a linear number of non-negligible basis function products $\varphi_\mu(\mathbf{r})\varphi_\nu(\mathbf{r})$ that need to be considered. However, the electrostatic interaction integrals between the significant charge distributions, $(\mu\nu|\kappa\tau)$, are only decreasing as the inverse effective distance between the centers of the charge distributions and hence there is an asymptotically quadratic number of non-negligible electron-electron repulsion integrals in large systems.

The two electron contribution to the Fock matrix ($F_{\mu\nu}$) consists of Coulomb ($J_{\mu\nu}$) and exchange ($K_{\mu\nu}$) parts:

$$J_{\mu\nu} = \sum_{\kappa\tau} P_{\kappa\tau}(\mu\nu|\kappa\tau) \quad (11-1)$$

$$K_{\mu\nu} = \sum_{\kappa\tau} P_{\kappa\tau}(\mu\kappa|\nu\tau) \quad (11-2)$$

$$P_{\mu\nu} = \sum_i c_{\mu i} c_{\nu i} \quad (11-3)$$

($c_{\mu i}$ being the molecular orbital coefficients and i refers to occupied spin orbitals). Via Kohn's conjecture one assumes that the decay of the density matrix elements $P_{\mu\nu}$ is exponential with respect to the distance between the centers of basis functions $\varphi_\mu(\mathbf{r})$ and $\varphi_\nu(\mathbf{r})$ as long as the system behaves like an insulator' (i.e. has a sufficiently large HOMO-LUMO gap). Assuming the validity of Kohn's conjecture the asymptotic scaling of the Coulomb matrix is quadratic with system size while the exchange matrix is linearly scaling. A numerical example is shown in Figure 11-1 for a (gly)₁₅ chain. Consistent with Kohn's conjecture, the values of the density matrix drop roughly exponentially with the distance between the orbital

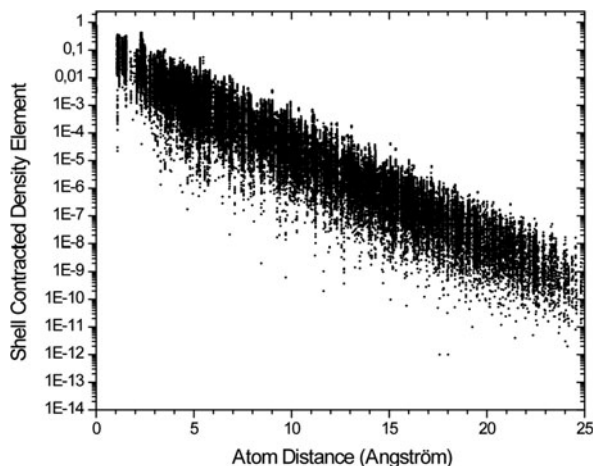


Figure 11-1. Logarithmic plot of the shell contracted density matrix $P(K, L) = \max(|P(k, l)|, k \in K, l \in L)$ versus the distance of the centers of the two orbital shells. The density is a converged RHF density for (gly)₁₅ with the SV basis set

centers – but with a fairly small decay constant (several authors have provided such plots earlier, e.g. [4]). Hence, a distance where the density matrix elements are consistently smaller than 10^{-10} is only reached after well above 25 Å. Consider a large two-center Coulomb integral (AA|BB) that decays just as R_{AB}^{-1} and is thus typically not smaller than 0.01 Eh even in large molecules. To the exchange matrix this integral class contributes as $K_{AB} \leftarrow (AA|BB)P_{AB}$. If the Fock matrix pre-screening threshold is on the order of 10^{-10} Eh, which is certainly required if one wants to obtain an energy correct to at least 10^{-6} Eh and one does not want to interfere with SCF convergence, this estimate indicates that linear scaling cannot set in before the molecule has an extension of more than 25 Å. This situation becomes more favorable in later SCF iterations since the difference density matrices quickly become much smaller and pre-screening becomes more effective. However, the numerical error tends to accumulate and care is required to not spoil convergence by pre-screening. This issues have been carefully discussed by Häser and Ahlrichs [2] (see also the more recent discussion [5]).

The 1990s have seen enormous development activities directed towards developing SCF methods that are linearly scaling with respect to their memory, disk and CPU requirements. Again, Jan Almlöf was at the forefront of these developments [6].

Almlöf recognized early on, that the computation of the Coulomb and exchange matrices are rather different in their computational requirements and the types of integrals that contribute. He then reasoned that it might well be beneficial to calculate these contributions separately making use of the most efficient approximations that are available for each term.

Subsequently, most of the efforts were concentrated towards the efficient computation of the Coulomb term that, owing to its less favorable scaling, was supposed to dominate the computation time. In particular, fast multipole based methods were developed that allowed for the linear scaling computation of $J_{\mu\nu}$ [7–9]. Somewhat less effort was directed towards the exchange term since it is naturally (almost) linear scaling. To achieve actual linear scaling in the exchange formation, however, requires a careful program organization to avoid quadratic prescreening steps [10–12]. With the increasing popularity of density functional theory, a third major computational term, the calculation of the exchange-correlation contribution to the Kohn-Sham matrix, emerged. However, it quickly became evident, that the numerical quadrature required to evaluate this term is not difficult and can be straightforwardly organized in a linear scaling fashion [13].

Following the excitement that arose about linear scaling HF and DFT methods, further efforts were directed towards integral-direct, linear scaling wavefunction based electron correlation methods. These methods are discussed elsewhere in this volume.

Today, highly optimized program packages are abundant that allow for direct HF and DFT calculations on large molecules, including entire proteins (e.g. ref [14] reports calculations with up to 11,650 atoms and 67,204 basis functions) These developments in linear scaling electronic structure theory are highly useful and very

impressive. Nevertheless, a survey of the applied computational chemistry literature reveals that the number of application studies that heavily rely on linear scaling techniques is somewhat limited. Since ultimately, theoretical methods should be developed to be used in actual applications rather than being an end in themselves, it appears appropriate to critically ask what the requirements of computational chemistry are and in which respect further developments could or should be directed. Thus, the present chapter is devoted to the discussion of efficient algorithms for contemporary electronic structure calculations at the SCF level. However, as will be discussed in the concluding section, the points being made apply to correlated wavefunction based calculations even more than to the SCF case.

11.2. LINEAR SCALING VERSUS PREFACTOR

Obviously, in the field of algorithm and method design different researchers have grossly different point of views. Hence, without any claim of generality or universal acceptance, it is attempted here to discuss some points that we have found to be important during our own development efforts that are being closely coordinated with large-scale computational chemistry applications.

In discussing these subjects, the point of view is taken that approximate methods are acceptable as replacements for rigorous implementations as long as they are robust. This means that the errors introduced are so small that they – within reasonable limits – do not affect the outcome of the calculations. What is meant by “reasonable” depends on the context. Typically, one would regard errors of less than 1 kcal/mol in energy differences or 1 pm in bond distances as sufficiently small that they can be ignored relative to other sources of error in the calculations. Furthermore, if one wants to obtain a result that reflects the theoretical method rather than basis set incompleteness artifacts, one has to perform actual computational chemistry studies with sufficiently large basis sets. For HF and DFT calculations this implies at least at triple-zeta basis set with at least one set of polarization functions. For correlation calculations at least three sets of polarization functions (e.g. 2d1f set on main group atoms).

The central hypothesis of this chapter is, that for most present day computational chemistry applications linear scaling electronic structure methods are not required and that it is usually more useful to look for approximate methods that minimize the prefactor.

The arguments in favor of this unconventional view may be summarized as follows:

1. The ultimate goal of an efficient electronic structure method is to minimize the turnaround (e.g. wall-clock) time required to complete a given study. In this respect it is immaterial what the formal scaling of the employed methods is. Much of the linear scaling literature at least implicitly implies short turnaround times *because of* linear scaling. However, the formal scaling does not prove anything about the actual computational efficiency – linear scaling simply implies

that asymptotically such methods are more efficient than non-linear scaling approaches. Thus they are only *potentially* efficient. Yet, the break-even point in terms of molecular or basis set size may be much beyond the actual application that one might envision.

2. Linear scaling methods are typically being tested in conjunction with basis sets that are being too small to be useful for actual computational chemistry applications. For example, MP2 calculations with the 6-31G* basis set are not very useful for application studies. The break-even point between linear scaling methods and methods that minimize the prefactor occurs much later if adequate basis sets are being used.
3. Linear scaling methods heavily rely on sparsity in order to avoid the computation of negligible quantities. For this sparsity to exist, the systems need to have a certain spatial extension. Very many of the molecules presently being studied by the computational chemistry community simply do not fall in the size regime where the thresholding is effective enough to lead to significant savings.
4. If the systems eventually become large enough, there is no doubt that linear scaling approaches are the only feasible choice if a quantum mechanical treatment of the entire system is desired. However, large systems are typically flexible and have many local minima on their potential energy surfaces. Thus one typically would need to study many geometries, not just a few isolated single point calculations.
5. One may ask whether it is always necessary to study a system consisting of hundreds of atoms fully quantum mechanically? In very many cases, it is appropriate to treat a truncated cluster model of perhaps 100–200 atoms quantum mechanically, or – at higher sophistication – resort to QM/MM approaches. The valid question of how to benchmark QM/MM calculations has been addressed for example by Thiel and co-workers as documented in recent reviews [15, 16].
6. Making use of sparsity requires the presence of logic in the innermost loops in order to screen out negligible quantities. This, however, interferes with code optimization since the CPU has to wait for the outcome of the sparsity test before further actions can be taken. For example, a matrix multiplication performs up to fifty times more efficiently if a highly optimized, vendor provided BLAS library is used compared to what one is able to code in a high level language such as Fortran or C. This implies, that screening for sparsity becomes preferable over brute force multiplication if less than about 2% of the contributions are significant. This situation changes continuously with new hardware developments. For example, matrix multiplications proceed on the latest generation of graphics cards up to 10 times faster than in the main CPU. Thus, methods that are dominated by large scale matrix multiplications are immediately accelerated by this factor while a similar speedup is much more difficult to obtain with pre-screening based approaches. Some of the efficiency can be restored, however, with blocked matrix algebra [17, 18].
7. Prescreening necessarily introduces a certain level of numerical noise in the results. This numerical noise becomes larger as the systems get larger. Hence,

one has to use tighter and tighter thresholds as the system size increases and this greatly adds to the computational cost. Linear scaling studies that have been performed (on e.g. a single Fock matrix build) with integral thresholds of $1e-4$ – $1e-7$ Eh are somewhat suspicious in this respect since one would not be able to obtain SCF convergence for large molecules with such cut-offs.

All of the points discussed above are derived from actual experience in computational chemistry applications. They are not meant to distract from the beauty and elegance of linear scaling approaches. As mentioned above, there is no doubt that in the *long* run, if systems of hundreds of atoms are to be treated quantum mechanically, there will be no substitute for linear scaling methods. However, *today* the molecules or cluster models often contain 50–200 atoms and much larger molecules can be studied with QM/MM approaches. In this very significant domain of quantum chemistry – in particular in conjunction with large and accurate basis sets – methods that minimize the prefactor of the calculations are competitive with or superior to linear scaling approaches. This will be illustrated below with some examples.

A strategy that would seem to suggest itself on the basis of this discussion is to *first* optimize the prefactor of a given computational task and *then* to try to linearize it but *without* compromising the efficiency of the underlying algorithm.

One important point in discussing algorithms is the nature of the numerical error that is being introduced. There are several possibilities of why a given result deviates from the exactly computed one. First, there may be random numerical noise, for example introduced by the direct SCF procedure. If too much numerical noise accumulates then the SCF procedure will no longer converge and computed forces will be unacceptably inaccurate. Hence, numerical noise must be kept small, certainly below a level of 10^{-6} Eh in actual applications. A different kind of error is obtained by numerical approximations to the matrix elements that occur in the treatment. These approximations frequently lead to well controlled errors that are systematic and will hence tend to cancel upon taking energy differences or calculating forces. Such systematic errors may be tolerable at the level of 10^{-3} Eh or a little more, provided that error cancellation in taking energy differences is systematic enough such that predicted energies are accurate to the target precision of about 1 kcal/mol. Smooth errors also do not lead to problems in the computation of forces. Experience indicates that methods that involve an auxiliary basis set tend to have very smooth errors while methods that involve real space grids have less smooth errors. This should be taken into account upon judging the numerical results presented below.

11.3. SELF CONSISTENT FIELD ALGORITHMS

In the following, several algorithms for computing the Coulomb- and exchange parts of the Fock or Kohn-Sham matrix are discussed and compared. Throughout semi-local basis sets are assumed. Techniques based on plane waves are outside the scope of this chapter.

11.3.1. Coulomb Term

11.3.1.1. Improved Analytical Evaluation

As mentioned in the introduction, the standard way of computing the Coulomb matrix is:

$$J_{\mu\nu} = \sum_{\kappa\tau} P_{\kappa\tau} (\mu\nu | \kappa\tau) \quad (11-4)$$

Here \mathbf{P} is the one-particle density matrix and

$$(\mu\nu | \kappa\tau) = \iint \frac{\varphi_\mu(\mathbf{r}_1)\varphi_\nu(\mathbf{r}_1)\varphi_\kappa(\mathbf{r}_2)\varphi_\tau(\mathbf{r}_2)}{|\mathbf{r}_1 - \mathbf{r}_2|} d\mathbf{r}_1 d\mathbf{r}_2 \quad (11-5)$$

is an electron-electron repulsion integral (ERI) over real basis functions $\{\varphi\}$. In the McMurchie-Davidson (MD) method [19], the basis function products that appear in Eq. (11-5) are expanded in a linear combination of Hermite Gaussian functions. In an abbreviated notation this expansion can be written [20]:

$$\varphi_\mu^A(\mathbf{r})\varphi_\nu^B = \sum_p E_p^{\mu\nu} \Lambda_p^P(\mathbf{r}) \quad (11-6)$$

$$\Lambda_p^P(\mathbf{r}) = \left(\frac{\partial}{\partial P_x}\right)^{p_x} \left(\frac{\partial}{\partial P_y}\right)^{p_y} \left(\frac{\partial}{\partial P_z}\right)^{p_z} \exp\left(-(\alpha + \beta)(\mathbf{r} - \mathbf{P})^2\right) \quad (11-7)$$

where the E 's are the (scaled) expansion coefficients, the Λ 's are the Hermite Gaussians, α and β are the exponent of the primitive Gaussians. The subscript index p has been used as a compound index containing the three summation variables p_x , p_y , p_z involved in the summation over Cartesian components. The basis functions are attached to centers A and B respectively while the Hermite Gaussians are centered at a point \mathbf{P} along the line joining centers A and B :

$$\mathbf{P} = \frac{1}{\alpha + \beta} (\alpha\mathbf{R}_A + \beta\mathbf{R}_B) \quad (11-8)$$

Excellent publications that describe the details of this approach to ERI evaluation are available [20]. The ERI becomes:

$$(\mu\nu | \kappa\tau) \sum_p E_p^{\mu\nu} \sum_q (-1)^q E_q^{\kappa\tau} R_{pq} \quad (11-9)$$

where R_{pq} is the ERI over Hermite Gaussian functions and the contraction of R_{pq} with the E 's can be regarded as a Hermite to Cartesian Gaussian back transformation. Constant factors like products of contraction coefficients are assumed to be absorbed in the definition of the E 's and the R 's. Both sets of intermediates are easily generated from recursion relations [19, 20]. Thus, the standard approach to the Coulomb matrix can be written as:

$$J_{\mu\nu} = \sum_{\kappa\tau} P_{\kappa\tau} \sum_p E_p^{\mu\nu} \sum_q (-1)^q E_q^{\kappa\tau} R_{pq} \quad (11-10)$$

Explicit reference to integral contraction and transformation to spherical harmonic Gaussian functions and summation of primitive Gaussians are suppressed for simplicity although they are of course executed in actual computer codes.

Since the MD algorithm naturally decouples the coordinates of the two electrons and the density matrix does not connect the two electrons in the Coulomb matrix construction as well, it becomes evident that the standard approach involves a large number of redundant operations in the innermost loops. Almlöf first suggested to form the density in the Hermite Gaussian basis [21]:

$$X_q = \sum_{\kappa\tau} (-1)^q P_{\kappa\tau} E_q^{\kappa\tau} \quad (11-11)$$

Since the number of significant basis function products only grows as $O(N)$, the computation of the vector \mathbf{X} and its storage requirements are negligible. In the second step the vector \mathbf{X} may be contracted with the Hermite basis ERI's to yield the vector \mathbf{Y} :

$$Y_p = \sum_q R_{pq} X_q \quad (11-12)$$

Finally, in the third step the Coulomb matrix is formed by contraction of the Hermite Coulomb “matrix” \mathbf{Y} with the Hermite expansion coefficients of the bra as:

$$J_{\mu\nu} = \sum_p E_p^{\mu\nu} Y_p \quad (11-13)$$

This is essentially the method proposed by Ahmadi and Almlöf [21]. Variations of the same theme have been reported by Schwegler and Challacombe, Shao and Head-Gordon (“J-engine”) [22] and ourselves (“Split-J”) [23].

The main differences in the algorithms probably concern the generation of the integrals R_{pq} and their contraction with the Hermite density X_q in the rate limiting step of the algorithm. In our implementation, an efficient evaluation is obtained by using hand-optimized expressions for most shell pair combinations (all shell pairs with $l_\mu + l_\nu + l_\kappa + l_\tau \leq 6$) and direct formation of the contraction of R_{pq} with X_q without any further intermediate quantities. This approach is devoid of short loops or logic which would spoil computational efficiency, allows for extensive common subexpression elimination and uses no additional central memory. For higher angular momenta the computational overhead due to nested loops is not a major factor and the general recursion relations to form R_{pq} perform well. Compared to the standard algorithm, a substantial amount of overhead, namely the generation of the E coefficients and the contraction with the Hermite integrals, has been removed from the innermost loops. Although not explicitly shown, the transformation to spherical

harmonic Gaussian functions is also done outside the innermost loops in contrast to the standard algorithm

Up to an order of magnitude increase in computational speed has been reported with this algorithm compared to the conventional algorithm despite the fact that no approximation has been introduced [22]. In our hands, the advantages of the improved algorithm are smaller but still significant (*vide supra*).

11.3.1.2. Multipole Approximations

Multipole approximations are important in treatments of large molecules because they allow for a computationally cheap treatment of the long-range interactions that result from the Coulomb part of the electron-electron repulsion while maintaining numerical equivalence to the approximation free calculation [7–9]. The general multipole expansion between two charge distributions $\rho_a(\mathbf{r})$ and $\rho_b(\mathbf{r})$ can be obtained as a special case of the bipolar expansion:

$$\frac{1}{|\mathbf{r}_a - \mathbf{r}_b - \mathbf{R}|} = \sum_{l_a} \sum_{l_b} \sum_{m=l_{<}}^{l_{<}} d_{l_a l_b}^m \frac{r_a^{l_a} r_b^{l_b}}{R^{l_a+l_b+1}} S_{l_a}^m(\hat{r}_a) S_{l_a}^m(\hat{r}_b) \quad (11-14)$$

where $r_a = |\mathbf{r}_a|$, $r_b = |\mathbf{r}_b|$ and $R = |\mathbf{R}|$. The vectors \mathbf{r}_a and \mathbf{r}_b are measured relative to the centers of the corresponding charge distributions. The symbol \hat{r}_a refers to the angular variables of \mathbf{r}_a and the S_l^m are real spherical harmonics ($l_{<}$ is the smaller of l_a and l_b). The equation is valid under the condition $r_a + r_b < R$ which is satisfied if the centers of the two charge distributions are sufficiently well separated and there is no charge penetration. The constant $d_{l_a l_b}^m$ is given by:

$$d_{l_a l_b}^m = \frac{4\pi}{(2l_a + 1)(2l_b + 1)} \frac{(l_a + l_b)! (-1)^{l_a+m}}{\sqrt{(l_a + m)(l_b + m)(l_a - m)(l_b - m)}} \quad (11-15)$$

Thus, if $\rho_a(\mathbf{r}_1)$ is centered at the origin and $\rho_b(\mathbf{r}_1)$ at \mathbf{R} then their repulsion becomes in the large R limit:

$$E_{ab} = \iint \frac{\rho_a(\mathbf{r}_1)\rho_b(\mathbf{R} + \mathbf{r}_2)}{|\mathbf{r}_1 - \mathbf{r}_2 - \mathbf{R}|} d\mathbf{r}_1 d\mathbf{r}_2 = \sum_{l_a} \sum_{l_b} \sum_{m=l_{<}}^{l_{<}} d_{l_a l_b}^m \frac{Q_{l_a,m}^a Q_{l_b,m}^b}{R^{l_a+l_b+1}} \quad (11-16)$$

where $Q_{l_a,m}^a$ and $Q_{l_b,m}^b$ are proportional to the multipole moments of ρ_a and ρ_b :

$$Q_{l_a,m}^a = \int r^{l_a} S_{l_a}^m(\hat{r}) \rho_a(\mathbf{r}) d\mathbf{r} \quad (11-17)$$

The benefit of the multipole approximation is that it leads to a complete separation of the two charge distributions. Thus the scaled multipole moments $Q_{l_a,m}^a$ for each charge distribution can be precomputed and stored and the multipole interactions

can be evaluated with much lower computational effort than the corresponding analytic two electron integrals.

The Coulomb matrix then contains two parts – a short range part of charge distributions which penetrate significantly and where the multipole interaction is not valid and a long-range contribution that can be handled via the multipole expansion. In this case a further speedup of the calculation is possible if the density is summed into the multipoles before the multipole interaction is actually calculated.

The question of the division between the long range and the short range immediately arises since this does not only depend on the separation of the charge distribution centers but also on their size that is determined by the exponents of the basis functions involved. The conditions under which the multipole expansion is allowed (the “MAC”) and the penetration is negligible (the “PAC”) has been extensively studied by Challacombe, Scuseria and others [9]. Both the MAC and the PAC have to be of low computational cost in order to lead to real advantages in actual calculations. Their implementation in terms of a sophisticated tree search algorithm has led to efficient formation of the Coulomb matrix with observed linear scaling for large molecules.

11.3.1.3. The RI Approximation

The so-called “resolution of the identity” (RI) approximation is one of the earliest approximate methods to compute the Coulomb term. It was invented by Baerends and co-workers in the framework of density functional theory (DFT) [24] with a similar, independent suggestion due to Whitten [25]. The proposal consists of fitting the electron density to an auxiliary basis set. This reduced the two-electron integral calculation to two- and three-index integrals and reduces the formal scaling of the calculation by an order of magnitude. The physical content of the approximation was carefully analyzed by Dunlap et al. [26, 27] Vahtras, Almlöf and Feyereisen made an important contribution by showing that the most accurate fitting is obtained by minimizing the self-repulsion of the residual [28].

The method proceeds by expanding each charge distribution $\rho_{\mu\nu}(\mathbf{r}) = \varphi_{\mu}(\mathbf{r})\varphi_{\nu}(\mathbf{r})$ in terms of an atom centered auxiliary basis set $\{\eta\}$:

$$\rho_{\mu\nu}(\mathbf{r}) \approx \sum_P c_P^{\mu\nu} \eta_P(\mathbf{r}) \quad (11-18)$$

The expansion coefficients $c_P^{\mu\nu}$ can be determined in a variety of ways. However, for the approximation of two electron terms Vahtras et al. have shown that the most accurate approximation is obtained by minimizing the self repulsion of the residual [28]:

$$R \equiv \iint \left\{ \rho_{\mu\nu}(\mathbf{r}_1) - \sum_P c_P^{\mu\nu} \eta_P(\mathbf{r}_1) \right\} \frac{1}{|\vec{r}_1 - \vec{r}_2|} \left\{ \rho_{\mu\nu}(\mathbf{r}_2) - \sum_Q c_Q^{\mu\nu} \eta_Q(\mathbf{r}_2) \right\} d\mathbf{r}_1 d\mathbf{r}_2 \quad (11-19)$$

If the three index repulsion integrals $(\mu\nu|P)$ are collected in the vector $\mathbf{t}^{\mu\nu}$, the two index repulsion integrals $(P|Q)$ in the matrix \mathbf{V} and the expansion coefficients in the vector $\mathbf{c}^{\mu\nu}$, the solution is obtained as:

$$\mathbf{c}^{\mu\nu} = \mathbf{V}^{-1}\mathbf{t}^{\mu\nu} \quad (11-20)$$

Any two electron integral can then be approximated by:

$$(\mu\nu|\kappa\tau) \approx \sum_{PQ} c_P^{\mu\nu} c_Q^{\kappa\tau} V_{PQ} \quad (11-21)$$

$$= \sum_{PQ} t_P^{\mu\nu} V_{PQ}^{-1} t_Q^{\kappa\tau} \quad (11-22)$$

$$= \sum_P (\mu\nu|\bar{P})(\bar{P}|\kappa\tau) \quad (11-23)$$

where:

$$(\mu\nu|\bar{P}) = \sum_Q V_P^{-1/2} (\mu\nu|Q) \quad (11-24)$$

In the form Eq. (11-23) the approximation formally looks like as if a resolution of the identity has been inserted between the bra and the ket in a given electron-electron repulsion integral which gives the method its name. Werner and co-workers have argued in favor of the name “density fitting” instead [29, 30]. Using the approximation, Eq. (11-23), for an element of the Coulomb matrix:

$$J_{\mu\nu}^{RI} \approx \underbrace{\sum_P (\mu\nu|P)}_{P_p} \underbrace{\sum_Q V_{PQ}^{-1} \sum_{\kappa\tau} P_{\kappa\tau}}_{g_Q} (\kappa\tau|Q) \quad (11-25)$$

The calculation of the Coulomb term in the RI approximation involves the evaluation of the three-index repulsion integrals to form the intermediate g_Q , the solution of the linear equation system to obtain the auxiliary basis density P_P and finally a second evaluation of the three index repulsion integrals to form $J_{\mu\nu}^{RI}$. The approximation reduces the formal scaling of the Coulomb term from $O(N^4)$ to $O(N^3)$. For large systems the scaling will tend towards $O(N^2)$, similar to the exact treatment of \mathbf{J} . However, the prefactor of the RI approximation is much smaller than for the exact computation because: (a) provided that the number of auxiliary basis functions is not larger than 2–3 times the number of basis functions, there is an order of magnitude fewer three-index than four-index ERIs, (b) the three-index ERIs are much more efficiently evaluated because they are simpler than four-index ERIs (c) owing to the much smaller number of three-index ERIs calculations can often be done in

an integral conventional mode or with pre-computed three-index ERIs in high-speed memory [31, 32].

As shown by Ahlrichs and co-workers, the solution of the linear equation system is best done via the Cholesky decomposition of the \mathbf{V} -matrix [31, 32]. Even for 10,000 auxiliary basis functions this step takes a negligible amount of computer time if the most efficient library routines are used for this task.

Provided the auxiliary basis set $\{\eta\}$ is of sufficient quality and small enough size, up to two or almost three orders of magnitude in computation time can be saved with the RI approximation [31, 32]. Fortunately efficient and accurate auxiliary basis sets for different qualities of the orbital basis set $\{\varphi\}$ have been developed by Eichkorn et al. [31, 32] They have been shown to yield errors of less than 0.1 mEh per atom in DFT calculations. As a rule of thumb these auxiliary basis sets are two to three times larger than the orbital expansion bases. More recently Weigend has reinvestigated the auxiliary basis set problem and has developed improved and accurate Coulomb fitting bases for essentially the entire periodic table (error < 0.01 mEh per atom) [33]. Noteworthy is that the ratio of basis functions to auxiliary basis functions decreases with increasing quality of the orbital basis. For quadruple-zeta quality orbital bases, the Coulomb fitting bases are even *smaller* than the orbital basis this leading to very large advantages of the RI approximation relative to the exact analytical evaluation [33].

The angular moment requirements of the auxiliary basis set can be understood from the expansion of the one center charge distributions $\varphi_{\mu}^A \varphi_{\nu}^A$. For angular momentum l_{max} in the orbital basis the auxiliary basis should have functions up to $l = 2l_{max}$ in order to be able to describe all multipole moments of the orbital basis accurately. In practice it is found that auxiliary bases up to $l = 3 - 4$ for first and second row atoms and $l = 4 - 6$ for transition metals are found to give accurate results. Other strategies for the construction of auxiliary basis sets have been reported in the literature but none have been as systematic as the work of Eichkorn et al. and Weigend.

A favorable feature of the fitting procedure as outlined above is that it is variational [26, 27, 34], i.e. the approximate Coulomb energy is an upper bound to the exact Coulomb energy. This is helpful in assessing the error caused by the approximation and is helpful in the development of new auxiliary basis sets. Another feature of the approximation is that it does not conserve the total number of electrons. A large body of evidence accumulated in thousands of applications proves that the errors in structures, relative energies and other properties due to the RI-J approximation are much smaller than the errors inherent in the present day density functional (provided that appropriate fitting bases are employed) and can be safely disregarded for chemical applications.

Sierka and Ahlrichs have developed a multipole-accelerated version of the RI-J algorithm (MARI-J) and have proven its efficiency [35]. However, they also pointed out that the investigated systems have to be very large in order for the MARI-J method to lead to substantial computational savings relative to the original RI-J method.

11.3.1.4. The Split-RI-J Approximation

It is clearly possible to use the Ahmadi-Almlöf idea to improve on the performance of the RI approximation. This was first discussed by the present author [23] and later re-discovered by Head-Gordon et al. who also developed a linear scaling version of the RI-J algorithm [36].

The three center ERI's can be written in the spirit of the MD algorithm as:

$$(\mu\nu|P) = \sum_p E_p^P \sum_q (-1)^q E_q^{\mu\nu} R_{pq} \quad (11-26)$$

where the auxiliary basis function η_P has also been expanded in terms of Hermite Gaussians. Formally Eq. (11-26) corresponds to a four center ERI in which the fourth (unnormalized) primitive Gaussian has an exponent of zero. Again, it is clear that the computation of the Intermediate g_Q and the matrix $J_{\mu\nu}^{RI}$ (Eq. 11-25) with such an algorithm must be inefficient due to the unnecessary Hermite Gaussian to Cartesian Gaussian transformations in the innermost loops. The RI algorithm can therefore be rewritten as:

$$X_q = \sum_{\kappa\tau} P_{\kappa\tau} E_q^{\kappa\tau} (-1)^q \quad (11-27)$$

$$Y_p = \sum_q R_{pq} X_q \quad (11-28)$$

$$g_Q = \sum_p E_p^Q Y_p \quad (11-29)$$

After formation of the vector \mathbf{g} , the linear equation set is solved using the Choleksy decomposition of \mathbf{V} and the Coulomb matrix is completed by the following three steps:

$$T_p = \sum_Q E_p^Q d_Q \quad (11-30)$$

$$U_q = \sum_p R_{pq} T_p \quad (11-31)$$

$$J_{\mu\nu}^{RI} = \sum_q (-1)^q E_q^{\mu\nu} U_q \quad (11-32)$$

All computational steps are straightforward and short loops that would significantly add to the overhead can be completely avoided. This algorithm has been termed ‘‘Split-RI-J’’ since the computation of the Coulomb matrix has been split into several parts [23]. The most expensive steps are the contractions of the Hermite ERI's with the vectors \mathbf{X} and \mathbf{T} in Eqs. (11-28) and (11-31) which will tend to $O(N^2)$ for large systems. However, the prefactor for the evaluation of the Split-RI-J approximation to the Coulomb matrix is much smaller than for the exact evaluation as will be discussed below.

In conclusion some straightforward manipulations allow one to move the expensive steps of the ERI evaluation in the Coulomb matrix and RI-approximation outside the innermost loops. The intermediate quantities no longer contain the ERI's themselves but instead the density and electron repulsion operator in the intermediate Hermite basis. The back transformation to the orbital basis and the transformation of the density into the Hermite basis can then be executed outside the rate determining loops of the program and high efficiency can be achieved.

11.3.1.5. Cholesky Decomposition Techniques

A method that shares many features with the RI methodology is the Cholesky decomposition of the two-electron integral supermatrix. As was shown early on by Bebe and Linderberg [37], the two-electron integrals can be written in terms of Cholesky vectors:

$$(\mu\nu|\kappa\tau) = \sum_{P=1}^M L_P^{\mu\nu} L_P^{\kappa\tau} \quad (11-33)$$

where M is the number of Cholesky vectors. If there are N basis functions, the maximum number of Cholesky vectors is $M = N(N+1)/2$. However, many of these vectors are essentially zero and can be neglected such that the number of surviving vectors is on the order of, perhaps, $2-4N$. The technique has been pioneered by Bebe and Linderberg [37] and has been further developed by Simons and co-workers [38]. In modern electronic structure theory, the approach has been revived by Koch and co-workers [39] and has since then seen many implementations into major electronic structure packages such as Dalton or MOLCAS [40-49].

Once the Cholesky vectors are available (and stored on disk), they can be used in an exactly analogous way as the orthogonalized RI integrals $(\mu\nu|P)$. This means that a very efficient Coulomb matrix formation is possible.

The Cholesky vectors are determined by an iterative procedure. One first calculates the standard exchange integrals for each charge distribution $\mu\nu$ and sets

$$L_{\mu\nu}^{\mu\nu} = \sqrt{(\mu\nu|\mu\nu)} \quad (11-34)$$

These integrals are sorted into decreasing order and each charge distribution is assigned an address $a_{\mu\nu}$. Then for each $\mu\nu$ one calculates the matrix $I_{\kappa\tau}^{\mu\nu} = (\mu\nu|\kappa\tau)$ for charge distributions $\kappa\tau$ with $a_{\kappa\tau} > a_{\mu\nu}$ and sets:

$$L_{\kappa\tau}^{\mu\nu} = \frac{1}{L_{\mu\nu}^{\mu\nu}} \left((\mu\nu|\kappa\tau) - \sum_{P=1}^{a_{\mu\nu}-1} L_P^{\mu\nu} L_P^{\kappa\tau} \right) \quad (11-35)$$

followed by:

$$(\mu\nu|\mu\nu) \leftarrow (\mu\nu|\mu\nu) - L_{\kappa\tau}^{\mu\nu} \quad (11-36)$$

for $a_{\kappa\tau} > a_{\mu\nu}$. After all $(\mu\nu|\mu\nu) < \delta$, where δ is a threshold, the process can be stopped.

There are several attractive features about the Cholesky approach: (a) the method does not require an auxiliary basis set that must be matched with the orbital basis; (b) the set of Cholesky decomposed charge distributions is, in a sense, the most compact auxiliary basis possible; (c) the method can reach arbitrary precision relative to the canonical calculation.

Thus, provided that the Cholesky vectors can be obtained efficiently and their storage is not problematic (which will be the case up to a few thousand basis functions), the procedure is computationally attractive. One potential efficiency bottleneck might be the iterative determination of the Cholesky vectors that requires the generation of the traditional four index integrals over basis functions, which may become expensive for accurate and highly polarized basis sets. One possible solution to this problem is to only consider charge distributions $\kappa\tau$ of one-center nature. This defines the 1C-CD approach advocated more recently [42]. The efficiency of the Cholesky decomposition and RI approaches has been compared recently by Weigend, Kattannek and Ahlrichs who found timing advantages for the RI algorithm [50]. Nevertheless, the Cholesky approach has a number of attractive properties and will certainly play an important role in the future.

11.3.1.6. Fully Numerical Approximations

Another way to approximate the two electron terms in the Fock matrix comes from the combination of a numerical integration scheme with multipole expansions. Consider an element of the Coulomb matrix:

$$J_{\mu\nu} = \int \varphi_{\mu}(\mathbf{r})\varphi_{\nu}(\mathbf{r})V_C(\mathbf{r})d\mathbf{r} \quad (11-37)$$

where the potential $V_C(\mathbf{r})$ due to the charge distribution $\rho(\mathbf{r}_2)$ at point \mathbf{r} is:

$$V_C(\mathbf{r}) = \int \frac{\rho(\mathbf{r}_2)}{|\mathbf{r} - \mathbf{r}_2|}d\mathbf{r}_2 \quad (11-38)$$

In a fully numerical integration scheme the Coulomb matrix element will be approximated by:

$$J_{\mu\nu}^{FN} \approx \sum_A \sum_g^A \varphi_{\mu}(\mathbf{r}_g)\varphi_{\nu}(\mathbf{r}_g)V_C(\mathbf{r}_g)w_g^A \quad (11-39)$$

The sum A is over all atoms in the molecule and the superscript indicates that the integration points \mathbf{r}_g with weight w_g^A belong to atom A . Likewise the potential is approximated as:

$$V_C(\mathbf{r}) \approx \sum_B \sum_{g'} \frac{\rho(\mathbf{r}_{g'})}{|\mathbf{r} - \mathbf{r}_{g'}|} w_{g'}^B \quad (11-40)$$

The great convenience gained by the numerical integration scheme is that the potential is naturally divided into atomic contributions. This allows one to define a “near-field” contribution which consists of those atoms that are close to the point \mathbf{r} and a “far-field” contribution consisting of the atoms that are far away. The exact criterion for establishing what is meant by “far away” remains to be specified. The near-field contribution should be treated accurately. However, the far-field contribution can be approximated by developing the denominator in a Taylor series around the position $\mathbf{r}_{g'} = \mathbf{R}_B$ of atom B :

$$\frac{1}{|\mathbf{r} - \mathbf{r}_{g'}|} = \frac{1}{|\mathbf{r} - \mathbf{R}_B|} + \frac{\mathbf{r} - \mathbf{R}_B}{|\mathbf{r} - \mathbf{R}_B|^3} (\mathbf{r}_{g'} - \mathbf{R}_B) + \dots \quad (11-41)$$

Inserting this expansion gives:

$$V_C(\mathbf{r}) \approx \sum_B \left\{ \frac{1}{|\mathbf{r} - \mathbf{R}_B|} \sum_{g'} \rho(\mathbf{r}_{g'}) w_{g'}^B + \frac{\mathbf{r} - \mathbf{R}_B}{|\mathbf{r} - \mathbf{R}_B|^3} \sum_{g'} \rho(\mathbf{r}_{g'}) (\mathbf{r}_{g'} - \mathbf{R}_B) w_{g'}^B + \dots \right\} \quad (11-42)$$

$$= \sum_B \left\{ \frac{q_B}{|\mathbf{r} - \mathbf{R}_B|} + \frac{(\mathbf{r} - \mathbf{R}_B) \bar{\mu}_B}{|\mathbf{r} - \mathbf{R}_B|^3} + \dots \right\} \quad (11-43)$$

Here q_B is the charge assigned to atom B by the numerical integration scheme and $\bar{\mu}_B$ is the dipole moment of the same atom. In effect one has removed the dependence of the potential on the numerical integration grid in the far-field and instead obtained a multipole expansion of the far-field interactions. If this multipole expansion is truncated at an appropriate order and the far-field is sufficiently conservatively defined the method should be accurate. In DFT calculations the electron density at each grid point is available from the exchange-correlation integration and the multipole moments for each atom can be precomputed before entering the loop that determines the Coulomb matrix. The size of the numerical integration grid grows only linearly with the size of the system and the number of significant functions per grid point becomes rapidly constant due to the fast decaying nature of Gaussian basis functions. Thus the far-field contributions scales *essentially* linearly with the system size except for a small quadratic component that arises from the evaluation of the multipole interactions. A similar approach is indeed taken in the ADF program and has been demonstrated to show near linear scaling [51–53].

However, the direct numerical integration over the Coulomb singularity leads to somewhat slow convergence with the grid size. Hence, an alternative approach is based on the solution of the Poisson equation on the grid. This also leads to a fully numerical algorithm for the Coulomb potential and the Coulomb matrix. Appropriate algorithms have been developed by Dickson and Becke [54] and Delley [55]. Dickson and Becke used this method to construct a basis set free DFT program while Delley’s DMOL program is based on numerical basis functions. The latter

program is commercial and therefore difficult to benchmark. However, available evidence indicates that the code is highly efficient and competitive with the fastest alternative approaches.

The leading ideas are readily appreciated. As indicated above, one first starts by dividing the density into atomic contributions through the assignment of the grid points to “parent” atoms. The density around each atom is then expanded in the multipole components in spherical coordinates:

$$\rho_A(r, \theta, \phi) = \sum_{lm} \rho_{lm}^{(A)}(r) S_m^l(\theta, \phi) \quad (11-44)$$

with the radial function being obtained by:

$$\rho_{lm}^{(A)}(r) = \int S_m^l(\theta, \phi) \rho^{(A)}(r, \theta, \phi) \sin \theta d\theta d\phi \quad (11-45)$$

The expansion must be terminated at a given maximum angular momentum L_{\max} that is related to the size of the grid. The procedures of Dickson and Becke and Delley differ somewhat in this respect. One then aims at solving the single center Poisson equation:

$$\nabla^2 V_C^{(A)}(\mathbf{r}) = -4\pi \rho^{(A)}(\mathbf{r}) \quad (11-46)$$

for the single center Coulomb potential $V_C^{(A)}(\mathbf{r})$. This is best approached by expanding the potential in spherical coordinates as:

$$V_C^{(A)}(r, \theta, \phi) = \sum_{lm} r^{-1} U_{lm}^{(A)}(r) S_m^l(\theta, \phi) \quad (11-47)$$

Insertion into the Poisson equation then yields an equation for the unknown radial functions $U_{lm}^{(A)}$:

$$\frac{d^2 U_{lm}^{(A)}(r)}{dr^2} - \frac{l(l+1)}{r^2} U_{lm}^{(A)}(r) = -4\pi \rho_{lm}(r) \quad (11-48)$$

This equation can be efficiently solved by numerical standard methods. This yields the radial functions at the radial grid points assigned to atom A. The total Coulomb potential is then reconstructed as:

$$V_C(\mathbf{r}) = \sum_A V_C^{(A)}(\mathbf{r}) \quad (11-49)$$

If this potential is evaluated at a grid point that, say, belongs to atom B, the contributions coming from atoms $A \neq B$ must be obtained by interpolation.

11.3.1.7. Semianalytic and Pseudo-Spectral Approximations

An obvious alternative to the completely numerical approximation described above is to evaluate the integrals that occur in the potential analytically. This, again, essentially restricts the method to Gaussian basis sets for which the required integrals can be efficiently calculated. For the Coulomb matrix elements one obtains:

$$J_{\mu\nu} \approx \sum_A \sum_g A W_g^A \varphi_\mu(\mathbf{r}_g) \varphi_\nu(\mathbf{r}_g) \sum_{\kappa\tau} P_{\kappa\tau} A_{\kappa\tau}(\mathbf{r}_g) \quad (11-50)$$

with:

$$A_{\kappa\tau}(\mathbf{r}_g) = \int \frac{\varphi_\kappa(\mathbf{r}_2) \varphi_\tau(\mathbf{r}_2)}{|\mathbf{r}_g - \mathbf{r}_2|} d\mathbf{r}_2 \quad (11-51)$$

The A integrals are simply nuclear attraction type integrals that can be efficiently evaluated over Gaussian basis functions using standard techniques. This mixed numerical/analytical approach is the essence of Friesner's pseudospectral method that is implemented in the commercial program Jaguar [56–61]. Semi-numerical integration techniques have also been pursued by Termath and Handy [62] and by Van Wüllen [63]. However, it appears that this technique is more beneficial for the treatment of the exchange than of the Coulomb term. Details will be provided below. Using:

$$X_{\mu g} = w_g^{1/2} \varphi_\mu(\mathbf{r}_g) \quad (11-52)$$

The semi-numeric Coulomb approximation can be written as:

$$J_{\mu\nu} \approx \sum_g X_{\mu g} X_{\nu g} J_g \quad (11-53)$$

with:

$$J_g = \sum_{\kappa\tau} P_{\kappa\tau} A_{\kappa\tau}(\mathbf{r}_g) \quad (11-54)$$

It appears to be possible in a straightforward manner to combine the semi-numeric and density fitting strategies through the sequence:

$$F_{\nu g} = \sum_\mu P_{\mu\nu} X_{\mu g} \quad (11-55)$$

$$P_g = \sum_\nu F_{\nu g} X_{\nu g} \quad (11-56)$$

$$g_P \approx \sum_g A_P(\mathbf{r}_g) P_g \quad (11-57)$$

$$P_P = \sum_Q V_{PQ}^{-1} g_Q \quad (11-58)$$

$$J_g = \sum_P A_P(\mathbf{r}_g) P_P \quad (11-59)$$

$$J_{\mu\nu} \approx \sum_g X_{\mu g} X_{\nu g} J_g \quad (11-60)$$

One might anticipate savings from this treatment compared to the original pseudo-spectral or analytic RI methods for the Coulomb matrix but an implementation is so far not available.

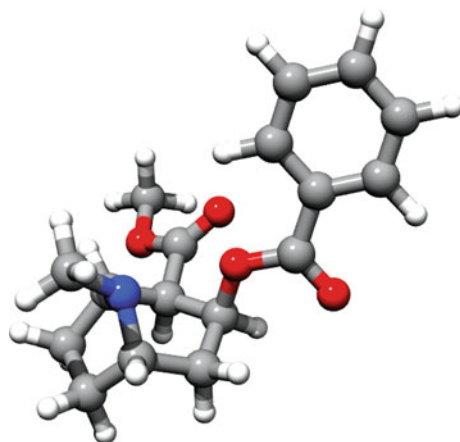
11.3.1.8. A Numerical Comparison

In order to provide some feeling for the approximations discussed above, some actual calculations are reported. Unfortunately, the methods described above are not all implemented in any single electronic structure code and hence a fair comparison is very difficult. The comparison is therefore restricted to the algorithms available in the ORCA program.

As a first calculation, a medium size organic molecule, cocaine, is considered with a variety of basis sets. Such molecules are of typical size for many contemporary applications of quantum chemistry. It is obvious that the RI-J approximation is much more efficient than the (exact) Split-J algorithm (Table 11-1). Interestingly, the best strategy for this type of application is to store the three index integrals. On present day computers this is even efficient for almost 2,000 basis functions (leading to about 12 GB of stored integrals). The advantages of the RI-J algorithm over the conventional integral direct algorithm increase with the quality of the orbital basis set. Speedups of up to a factor of almost 220 are found. Thus, extremely efficient “pure” DFT calculations are possible on the basis of this algorithm. The total wall clock time to complete the largest calculation with a quadruple-zeta basis set and 1,884 basis functions is only 35 min on a single CPU. It is unlikely that a multipole based algorithm with exactly calculated near-field integrals would even be nearly competitive with the timings achieved by the RI-J algorithm.

Secondly, the efficiency of the approaches is compared for a large molecule, Vancomycine (176 atoms). With a modest basis set, def2-SV(P) this molecule is described by ~1,500 basis functions. In this case, the Coulomb formation and the numerical XC integration that together account for the Fock matrix formation in RI-DFT calculations take less time than steps like diagonalization or the integration grid setup. Thus, highly efficient calculations are also possible on large molecules (200 atoms or more) despite the lack of linear scaling. Once more, the integral conventional algorithm proved to be the most efficient variant. This changes for larger basis sets. With the more accurate def2-TZVP(-f) basis (that has a 2d polarization set on non-hydrogens and 1p on hydrogens), there are ~2,900 basis functions (and 5,778

Table 11-1. Comparison of different algorithms for the formation of the Coulomb matrix. Timings (in sec for 15 Coulomb matrix builds) are given for calculations on the cocaine molecule with different basis sets. In parenthesis the speedup to the traditional integral direct Coulomb formation is given



	Def2-SV(P)	6-31G*	6-311G(d, p)	Def2-TZVP(-f)	Def2-TZVPP	Def2-QZVPP
N _{BAS}	350	350	522	654	976	1,884
Exact-J	921	986	2,772	9,084	28,881	271,892
Split-J	513 (1.8)	632 (1.6)	1,603 (1.7)	4,206 (2.2)	22,618 (1.3)	226,576 (1.2)
RI-J (direct)	94 (9.8)	101 (9.8)	155 (17.9)	321 (28.3)	1,346 (21.5)	39,081 (7.0)
RI-J (semi-direct)	58 (15.9)	60 (16.4)	117 (23.7)	191 (47.6)	319 (90.5)	1,795 (151.5)
RI-J (conv)	27 (34.1)	27 (36.5)	63 (44.0)	99 (91.8)	271 (106.6)	1,243 (218.7)
Split-RI-J	62 (14.9)	67 (14.7)	110 (25.2)	164 (55.4)	374 (77.2)	38,591 (7.0)

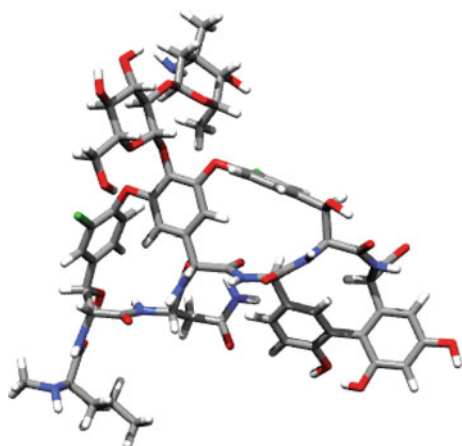
Single CPU of a MacPro 3.1; operating system OS X 10.5, 2 quad-core Intel XEON 3.0 GHZ CPUs that have 12 MB level 2 cache

auxiliary functions). In this case, the conventional RI-J calculation drops in efficiency due to the large I/O penalty (about 46 GB of integrals are stored in this case). Here, the Split-RI-J algorithm is the most efficient choice. Nevertheless, up to about 2,000 basis functions, the integral conventional RI-J algorithm is very attractive (Table 11-2).

11.3.2. Exchange Term

If the exchange term is computed by the integral direct SCF method, already Almlöf [64] has shown that there is only a linear scaling number of contributions to the Fock matrix, provided that Kohn's conjecture holds that the density matrix elements decay exponentially with distance [65]. While this seems to imply that the HF-exchange is inherently linearly scaling, there still is a quadratically scaling pre-screening step that becomes computationally recognizable in large calculations. In practice, one typically observes a scaling around $N^{1.5}$. Perfectly linearly scaling exchange algorithms that proceed via traditional two-electron repulsion integrals

Table 11-2. Comparison of different algorithms for a RI-BP86 DFT calculation on Vancomycine. Timings (in sec for 18 Coulomb matrix builds) are given. In parenthesis the speedup relative to the traditional integral direct Coulomb formation is given



	Def2-SV(P)	Def2-TZVP(-f)
N_{BAS}	1,572	2,886
Exact-J	33,364	–
RI-J (direct)	2,657 (12.6)	8,697
RI-J (semi-direct)	1,671 (20.0)	8,657
RI-J (conv)	855 (39.0)	14,897
Split-RI-J	1,811 (18.4)	5,657
XC integration	229	1,447
Diag+DIIS	473	945
Grid generation	303	317

Single CPU of a MacPro 3.1; operating system OS X 10.5, 2 quad-core Intel XEON 3.0 GHZ CPUs that have 12 MB level 2 cache

have consequently been developed [4, 10]. The only drawback of these procedures is that the calculations are still costly. Note also that the algorithm by Ochsenfeld [10] fully exploits the permutational symmetry of the electron-electron repulsion integrals while that of Challacombe [4] does not and consequently leads to late crossovers with the standard direct SCF algorithm.

The ORCA package has for almost a decade featured a variant in which the Coulomb term is treated by the RI-J algorithm and the exchange is computed via a standard direct SCF treatment (this was called RIJONX [66] and was frequently used in application studies [67–69]; However, RIJONX is an unfortunate name since the exchange treatment is not based on a genuine $O(N)$ procedure. Hence, this is now referred to as RIJDX; DX = “Direct Exchange”). Even for the largest systems that have been treated so far with several hundred atoms, the time to compute

the exchange term strongly dominates the computation time despite its favorable scaling.

Inspired by the success of the RI-J approximation, several attempts have been made to approximate the HF exchange by similar fitting techniques. Initially, the results of Kendall and Früchtl et al. in the framework of the NWChem program indicated that efficiency can indeed be gained in this way [70]. This could not be confirmed in later attempts by the present author [71]. Weigend developed an RI-X algorithm (termed RI-K) that proceeded by large scale matrix multiplications and scaled as $O(N^4)$ [72]. It has been shown to be efficient for compact molecules treated with large and accurate basis sets [72]. Polly et al. used the concept of “fitting-domains” to arrive at a linear scaling RI-X algorithm [73]. More recently, further efforts have been reported by Head-Gordon and co-workers [74] as well as by Lindh et al. [75] who used the closely related Cholesky decomposition technique. In both cases speedups relative to the conventional implementation were obtained but the algorithms were not linearly scaling.

As discussed above, Friesner’s pseudo-spectral methods consist of a semi-numeric approximation to the two-electron integrals [56–58, 60, 61, 76]. From the resulting factorization considerable speedups can be realized for both the Coulomb and the exchange term. The actual computational machinery, as realized in the Jaguar code, is highly sophisticated and acknowledged to be efficient [59–61, 76–79]. In order to realize the full potential of the pseudospectral method, the computational algorithms have been optimized for specific basis sets [59, 61, 77–79].

11.3.2.1. *Semi-numerical Approximations: Pseudospectral and Chain of Spheres*

The semi-numerical approximation to the exchange term can be written as follows:

$$K_{\mu\nu} \approx \sum_g X_{\mu g} \sum_{\tau} A_{v\tau}(\mathbf{r}_g) \sum_{\kappa} P_{\kappa\tau} X_{\kappa g} \quad (11-61)$$

Here the index “g” refers to grid points \mathbf{r}_g and:

$$X_{\kappa g} = w_g^{1/2} \kappa(\mathbf{r}_g) \quad (11-62)$$

Thus, the first integration (over the coordinates of electron 1) is carried out numerically and the second one (over the coordinates of electron 2) analytically. Note that this destroys the Hermitian character of the two-electron integrals. Eq. (11-61) is perhaps best evaluated in three steps:

$$F_{\tau g} = (\mathbf{P}\mathbf{X})_{\tau g} \quad (11-63)$$

$$G_{vg} = \sum_{\tau} A_{v\tau}(\mathbf{r}_g) F_{\tau g} \quad (11-64)$$

$$K_{\mu\nu} = (\mathbf{XG}^+)_{\mu\nu} \quad (11-65)$$

As such the equations are very similar to the pseudo-spectral method extensively developed and discussed by Friesner and co-workers since the mid 1980s and commercially available in the Jaguar quantum chemistry package. The main difference at this point is that instead of $X_{\kappa g}$ there appears a least-square fitting operator $Q_{\kappa g}$ in Friesner's formulation. As Friesner has pointed out, the evaluation of Eq. (11-61) scales as $O(N^3)$ [56–58]. A potentially linear scaling version of Eqs. (11-63–11-65) is presented below.

The COSX algorithm. In order to arrive at an efficient implementation of the semi-numerical exchange treatment, we have developed an algorithm that we have termed the “chain of spheres exchange” (COSX) treatment [80]. The basic idea is simple and consists of constructing small “chains” of shells of basis functions that give non-negligible contributions to the exchange matrix (within the cut-off *Thresh* of the direct SCF procedure). Negligible contributions arise either from negligible differential overlap between pairs of basis functions or from negligible density matrix elements. Two basis functions that are connected by differential overlap are said to be linked by an “S-junction” and pairs that are connected by a density matrix element are said to be linked by a “P-junction”. Finding non-negligible S-junctions is achieved by surrounding each contracted basis function by a sphere outside of which the absolute value of the basis function is considered to be negligible (in practice typically $< BFCut = 10^{-10}$). For valence basis functions of first row-atoms, the spheres typically have a radius of $\sim 3 \text{ \AA}$ [80]. Given the spheres, one can construct for each basis function a list of partners with a significant S-junction. Asymptotically, the list is of constant length for each given basis function. Likewise, one constructs for each basis function a list of partners with significant P-junctions that is expected to become asymptotically constant as long as Kohn's conjecture holds. Furthermore, taking advantage of the fact that the exchange matrix is linear in the density, the second and later SCF iterations are done with the difference density rather than the full density, which greatly diminishes the number of significant P-junctions. The calculation of the intermediate $F_{\tau g}$ proceeds via a BLAS level 3 matrix multiplication of the rectangular matrices $X_{\kappa g}$ and $P_{\kappa\tau}$, both restricted to the list of non-negligible basis functions for a given grid point. In the rate limiting step, the analytical integrals $A_{v\tau}(\mathbf{r}_g)$ are calculated and are immediately contracted with $F_{\tau g}$ to give G_{vg} . Finally, the contribution to the exchange matrix is calculated via another BLAS-level 3 operation in which the matrices $X_{\mu g}$ and G_{vg} are contracted. More details are found in the original publication. Since all matrices used in the intermediate steps are asymptotically of constant size, the entire algorithm is expected to scale linearly with system size. The thresholding procedure is conservative and the accuracy of the approximation is only determined by the size and quality of the integration grid. The efficiency of the algorithm is directly proportional to the number of grid points and the efficiency of the code for the analytic integrals.

Scaling with basis set angular momentum. It is interesting to analyze the computational effort for this method with respect to basis sets that only consist of basis functions with angular momentum L . Friesner and co-workers had already reported

that their speedup over conventional algorithms is increasing for more extended basis sets [61]. If one focuses on the MD integral algorithm a two-electron integral is calculated as shown in Eq. (11-9). There, the loops over p and q are all of a length proportional to L^3 such that the overall scaling of the integrals is $O(L^{10})$ and this carries over to the exchange matrix as well. By contrast, in the pseudo-spectral and COSX algorithms, the steepest scaling intermediate (with respect to L) is $G_{\nu g}$ that shows an $O(L^5)$ behavior. Thus, it is evident that once the higher angular momentum basis functions start to dominate the computational effort the advantages of the semi-numeric algorithms over the conventional treatments become very large. In practice this already occurs for the popular triple- ζ basis sets with 2d1f polarization sets on the heavy atoms and 2p1d on the hydrogens (e.g. TZVPP, or 6-311G(2df,2pd)).

Comparison between COSX and pseudo-spectral methods. In order to arrive at the smallest possible grids, Friesner et al. have implemented a number of sophisticated numerical methods [56–61, 76]. Foremost, in order to realize a truly pseudo-spectral method (as opposed to the semi-numerical treatment pursued here) it is necessary to introduce a least squares fitting operator $Q_{\kappa g}$ that replaces $X_{\kappa g}$ in the second basis function of the bra. Note that this even breaks the permutation symmetry of the basis function product in the bra. In order to evaluate this operator it is furthermore necessary to introduce a set of “dealiasing” functions that supplement the orbital basis set. The set of dealiasing functions is, however, specific for each orbital basis set and must be carefully optimized in order to obtain accurate results [56–61, 76]. It is then necessary to carefully analyze the orbital basis set in terms of short-range and long-range components in order to not destroy the locality that is inherent in $X_{\kappa g}$ [61]. Secondly, Friesner and co-workers have chosen to correct for the errors of the PS method by computing parts of the integrals (one-center, two-center and even part of the three-center integrals) by analytical means [61]. As they rightly point out, this has to be done in a careful way in order to not add significantly to the computation time. It does, however, take some of the favorable L -scaling inherent in the semi-numerical method away. Finally, Friesner et al. have carefully optimized different grids and have developed specific iterative schemes in which different grids are used in different SCF cycles in order to further increase the efficiency of their algorithm. In our work, we do not want to deal with the intricacies of dealiasing functions, basis set dependent integration grids or geometry dependent integral corrections. All of this complicates the implementation of gradients and presumably leads to high code complexity including more complex parallelization. Thus, in ref [80], we accepted to pay the price of somewhat larger integration grids and have demonstrated robustness and computational efficiency.

The combination of the COSX exchange algorithm with the RI-J approximation for the Coulomb term is called RIJCOSX and will be used below.

11.3.2.2. The RI-K Algorithm

In the RI-K approximation [72], the calculation of the exchange matrix proceeds as:

$$X_{\mu P}^i = \sum_{\nu} c_{\nu i}(\mu\nu|P) \quad (11-66)$$

$$Y_{\mu P}^i = \sum_Q V_{PQ}^{-1/2} X_{\mu Q}^i \quad (11-67)$$

$$K_{\mu\nu}^{RI-JK} \approx \sum_{iP} Y_{\mu P}^i Y_{\nu P}^i \quad (11-68)$$

If properly organized all three steps can be done as matrix multiplications making use of the extremely high efficiency of the basic linear algebra subroutine (BLAS) level 3 library functions that are available for all modern computers. Since the memory requirements for the intermediate quantities scale cubically with molecular size it will often be necessary to perform the calculation in batches and generate the three-index integrals repeatedly. Alternatively, one can store the RI integrals on disk and re-read them continuously. The same algorithm can, of course, be realized on the basis of the Cholesky decomposition technique. In fact, Lindh et al. have reported a Cholesky based exchange algorithm that scales as $O(N^2)$ [46] and Head-Gordon et al. have developed a RI exchange method that has the same scaling [74].

Formally the calculation of the Coulomb term scales as $O(N^3)$ and that of the RI-K exchange term as $O(N^4)$. Prescreening of negligible three-index integrals reduces the Coulomb term to $O(N^2)$ while sparsity is not exploited in the RI-K exchange approximation which remains at $O(N^4)$ scaling.

The requirements for the auxiliary basis sets are modest for the Coulomb part but more stringent for the exchange part. Ahlrichs, Weigend et al. have developed suitable basis sets for either Coulomb alone [31–33] or simultaneous Coulomb and exchange fitting [72, 81].

11.3.2.3. Performance of RIJCOSX

In order demonstrate the efficiency and accuracy of the RIJCOSX approximation in “real-life applications” we have studied a test set of 26 medium sized molecules in the range 15–174 atoms and up to ~2,000–4,000 basis functions (Table 11-3) [80].

The data in Table 11-3 demonstrate that the RIJDX approximation provides speedups of less than a factor of two and introduces an error that is always negative. This makes sense of course, since the RI-J approximation always underestimates the true Coulomb energy. The mean error is ~0.5 kcal/mol and only for molecules as large as Vancomycin (176 atoms) exceeds 1 kcal/mol.

The RIJCOSX approximation is similarly accurate but shows errors that are either positive or negative. The trend is to errors of positive sign for more extended basis sets. Importantly, the error remains small for extended basis sets up to TZVPP. For the very flexible QZVP basis set we have preferred to revert to a 302 point final grid and in this case the absolute errors remain very small. This is presumably due to the high angular momentum basis functions in the quadruple- ζ basis set that requires more accurate angular grids for an accurate enough numerical integration to be obtained. There tends to be a cancellation of errors from the RI-J and COSX approximations such that the mean absolute RIJCOSX (0.27 kcal/mol) errors are smaller than the RIJDX ones (0.46 kcal/mol).

Table 11-3. Accuracy and efficiency of the RIJDX and RIJCOSX algorithms for RHF calculations on medium sized molecules with different basis sets. All calculations were done with the default grids and basis set labels refer to the “def2” variants [82]. The speedup refers to the ratio of total wall clock times required to finish the calculation^d

Molecule	N _{Atoms}	Basis	N _{BAS}	ΔRIJDX (kcal/mol)	ΔRIJCOSX (kcal/mol)	Speedup (RIJDX)	SpeedUp (RIJCOSX)	t _{RIJCOSX} (sec) ^b
Vancomycin	176	SV(P)	1,572	-2.9	-1.1	1.7	5.0	1,5278
		TZVPP	4,197	-	-	-	-	121,656
Morphin	40	SV(P)	332	-0.6	-0.3	1.2	3.1	726
		TZVP	765	-0.5	0.3	1.3	30.7	4,907
		TZVPP	917	-0.6	0.4	1.2	32.7	5,644
Beclomethasone	57	SV(P)	454	-0.7	-0.2	1.4	3.4	1,501
		TZVP	1,045	-0.7	0.4	1.6	37.9	9,365
		TZVPP	1,282	-0.7	0.6	1.1	27.3	11,229
Captopril	30	SV(P)	220	-0.5	-0.2	1.1	1.5	278
		TZVP	508	-0.4	0.1	1.2	15.6	1,696
		TZVPP	649	-0.5	0.1	1.2	18.7	2,131
Epinephrine	26	SV(P)	208	-0.4	-0.3	1.1	1.6	217
		TZVP	481	-0.4	0.0	1.1	15.4	1,429
		TZVPP	585	-0.4	0.1	1.2	18.6	1,684
Flutamide	30	QZVP	1,131	-0.5	-0.4	1.2	40.5	13,482
		SV(P)	288	-0.5	-0.4	1.1	2.2	385
		TZVP	655	-0.4	0.3	1.2	20.4	2,566
Nitroglycerine	17	TZVPP	743	-0.4	0.3	1.2	21.2	2,876
		SV(P)	178	-0.4	-0.5	1.1	1.6	133
		TZVP	402	-0.3	-0.2	1.1	15.1	840
Penicillin	42	TZVPP	442	-0.3	-0.2	1.3	16.6	932
		QZVP	834	-0.3	0.2	1.2	33.5	7,305
		SV(P)	376	-0.8	-0.3	1.2	2.5	671
		TZVP	855	-0.7	0.0	1.3	22.2	4,760
		TZVPP	1,004	-0.7	0.1	1.1	19.0	5,394

Table 11-3. Continued

Molecule	N _{Atoms}	Basis	N _{BAS}	ΔR _{UDX} (kcal/mol)	ΔR _{UCOSX} (kcal/mol)	Speedup (R _{UDX})	SpeedUp (R _{UCOSX})	t _{RUCOSX} (sec) ^b
Tetracycline	56	SV(P)	496	-0.9	-0.5	1.4	3.5	1,595
		TZVP	1,136	-0.8	0.1	1.3	30.5	10,466
		TZVPP	1,328	-0.9	0.2	1.4	35.0	11,619
Cholesterol	74	SV(P)	484	-0.7	-0.3	1.2	2.4	1,563
		TZVP	1,144	-0.7	0.4	1.2	24.3	9,630
		TZVPP	1,512	-0.7	0.7	1.6	33.8	12,420
Menthol	31	SV(P)	194	-0.3	-0.2	1.1	1.4	230
		TZVP	461	-0.3	-0.1	1.2	15.4	1,292
		TZVPP	621	-0.3	0.0	1.2	19.2	1,724
Tryptophane	27	QZVP	1,227	-0.4	-0.2	1.4	61.2	14,263
		SV(P)	234	-0.4	0.0	1.1	1.9	296
		TZVP	537	-0.3	0.3	1.2	17.1	1,900
Histidine	20	TZVPP	633	-0.4	0.4	1.2	21.8	2,179
		QZVP	1,215	-0.4	-0.3	1.2	55.0	17,481
		SV(P)	172	-0.3	-0.1	1.1	1.3	135
Cysteine	14	TZVP	395	-0.3	0.1	1.1	14.8	858
		TZVPP	467	-0.3	0.1	1.2	17.3	1,004
		QZVP	897	-0.3	-0.3	1.2	45.5	8,106
Glycine	10	SV(P)	116	-0.3	-0.2	1.0	1.0	60
		TZVP	395	-0.2	-0.1	1.1	10.8	345
		TZVPP	467	-0.3	-0.1	1.0	11.7	417
Tyrosine	24	QZVP	897	-0.3	-0.1	1.2	37.3	3,690
		SV(P)	80	-0.2	-0.2	0.8	0.6	30
		TZVP	185	-0.1	0.0	1.1	7.8	142
Tyrosine	24	TZVPP	225	-0.2	0.0	1.1	9.5	172
		QZVP	435	-0.2	-0.1	1.0	25	1,583
		SV(P)	204	-0.4	-0.1	1.1	1.5	207
TZVP	469	-0.3	0.2	1.2	16.7	1,272		

Table 11-3. Continued

Molecule	N _{Atoms}	Basis	N _{BAS}	ΔRIIDX (kcal/mol)	ΔRIUCOSX (kcal/mol)	Speedup (RIIDX)	SpeedUp (RIJCOSX)	RIUCOSX (sec) ^b
Adenine	15	TZVPP	557	-0.4	0.2	1.2	19.5	1,488
		QZVP	1,071	-0.3	-0.3	1.1	44.1	12,237
		SV(P)	150	-0.3	0.0	0.8	1.4	99
		TZVP	340	-0.2	0.1	1.1	16.4	696
		TZVPP	380	-0.3	0.1	1.1	17.6	754
Cytosine	13	QZVP	720	-0.3	-0.2	1.1	45.5	5,726
		SV(P)	122	-0.1	-0.1	1.0	1.3	64
		TZVP	278	-0.2	0.1	1.1	12.8	425
		TZVPP	318	-0.2	0.1	1.1	14.5	474
		QZVP	606	-0.2	-0.2	1.1	38.4	3,832
Guanine	16	SV(P)	164	-0.3	-0.2	1.0	1.7	119
		TZVP	371	-0.3	0.0	1.0	14.1	831
		TZVPP	411	-0.3	0.0	1.1	17.5	887
		QZVP	777	-0.3	-0.2	1.2	45.9	7,363
		SV(P)	138	-0.3	-0.2	1.0	1.3	86
Thymine	15	TZVP	315	-0.2	0.0	1.1	13.6	583
		TZVPP	363	-0.3	0.1	1.1	15.9	634
		QZVP	693	-0.2	-0.2	1.2	41.0	5,051
		SV(P)	192	-0.4	-0.5	1.1	1.5	184
		TZVP	444	-0.4	-0.3	1.3	16.3	1,128
D-Glucose	24	TZVPP	540	-0.4	-0.2	1.3	18.2	1,383
		QZVP	1,044	-0.4	-0.4	1.3	47.4	11,283
		SV(P)	789	-1.2	-0.1	1.5	4.0	6,814
		TZVP	1,780	-1.1	1.6	1.7	38.9	42,996
		TZVPP	2,087	-1.2	1.8	1.9	41.7	51,005
CO-Heme	86	SV(P)	191	-0.2	-0.2	1.1	2.9	479
		TZVP	415	-0.3	0.3	1.3	13.8	3,157
		TZVPP	514	-0.3	0.4	1.2	14.1	4,256
		QZVP	954	-0.3	-0.5	1.2	42.2	26,825
		SV(P)	191	-0.2	-0.2	1.1	2.9	479

Table 11-3. Continued

Molecule	N _{Atoms}	Basis	N _{BAS}	ΔRIJDX (kcal/mol)	ΔRIJCOSX (kcal/mol)	Speedup (RIJDX)	SpeedUp (RIJCOSX)	t _{RIJCOSX} (sec) ^b
Ni(tren) ₂ (NCS) ₂	35	SV(P)	299	-0.6	-0.1	1.2	2.0	2,123
		TZVP	655	-0.5	0.5	0.9	10.7	13,585
		TZVPP	828	-0.6	-1.8	1.3	10.2	25,195
Dibenzo-Crown18.6	50	SV(P)	412	-0.8	-0.5	1.3	2.3	789
		TZVP	950	-0.7	0.0	1.3	19.1	5,226
		TZVPP	1,142	-0.8	0.0	1.3	21.9	6,121
Mean Error			-0.46	-0.03				
Mean Abs. Error			0.46	0.27				
Min. Error			-2.9	-1.8				
Max. Error			-0.1	1.8				

^a for the QZVP calculations a 302 point final grid has been used.

^b t_{RIJCOSX} is the total wall clock time required to finish the entire SCF calculation including the initial guess and all overhead.

The speedups observed for RIJCOSX range from moderate for small basis sets such as def2-SV(P) (factors of 1–5) and become spectacularly large for extended basis sets such as TZVPP and QZVP (up to a factor of 60). Thus, the RIJCOSX approximation is highly attractive for fast and accurate calculations on large molecules. Note that the largest calculation reported in Table 11-3 involved $\sim 4,200$ basis functions and was completed in ~ 1.5 days on a single CPU.

11.3.2.4. Comparison of COSX and RI-K

In order to compare the efficiency of the RI-JK and RIJCOSX approximations calculations were carried out with a number of basis sets on glycine helices (gly)₂, (gly)₄ and (gly)₈ [83]. The results reproduced in Table 11-4 show some interesting features:

- (1) The absolute error of the two methods is similar and both reproduce the canonical results within the chemical accuracy of ~ 1 kcal mol⁻¹. Interestingly, both methods show the largest errors for the smallest basis set (def2-SVP). However, the error of the RI-JK approximation is always positive while that of the RIJCOSX approximation can have either sign. The error of the RI-JK approximation is therefore seen to be more smooth and energy differences will be slightly more accurate. However, both methods yield errors that are smaller than the typical uncertainties in computational chemistry applications that are due to errors in the structures, the treatment of the environment, the intrinsic errors in density functionals or the basis set incompleteness errors.
- (2) Both approximations perform best for large and accurate basis sets. As discussed earlier [80], this is related to the much better scaling of the two approximations with the highest angular momentum in the basis set. In the standard calculation of four index integrals this scaling is $16/9L^{10} + \dots$ for the McMurchie-Davidson algorithm [19]. In the case of RI-JK this reduces to $2/9L^9 + \dots$ due to the three-index nature of the electron-electron repulsion integrals. In COSX the scaling is even reduced to $O(L^6)$ [80].
- (3) For the small (gly)₂ molecule, the RI-JK approximation is more efficient than RIJCOSX, for (gly)₄ the performance of both approximations is comparable while for (gly)₈ RIJCOSX performs better. This result is, of course, not unexpected due to the less favorable scaling of RI-JK compared to RIJCOSX. However, low-order scaling variants of RI-JK can and have been developed [73].
- (4) This behavior is typical and not affected by the choice of Glycine chains as the test systems. For example, for cholesterol – a more or less 2 dimensional molecule – the times required for RI-JK and RIJCOSX for a RHF calculation with the def2-TZVP basis set (74 atom, 1,144 basis functions) require 16,900 sec (RI-JK) and 7,300 sec (RIJCOSX), in line with the (gly)_n results. The total energies differ by only 0,3 mEh.

Recently the efficiency of the RI-JK and RIJCOSX approximations to the calculation of the Fock matrix was examined and illustrated by some test calculations.

Table 11-4. Comparison of RI-JK and RIJCOSX for RHF calculations on Glycine chains

	BASIS	NBAS	T _{WALL} (min)	SPEEDUP _{RI-JK}	ERROR _{RI-JK} (mEh)	SPEEDUP _{RIJCOSX}	ERROR _{RIJCOSX} (mEh)
(gly)2	def2-SVP	166	1, 8	2, 4	0, 4	1, 5	-0, 6
	def2-TZVP(-df)	219	5, 3	4, 5	0, 2	2, 6	-0, 4
	def2-TZVPP	391	42, 9	7, 9	0, 3	4, 9	-0, 2
	def2-QZVPP	753	464, 3	9, 1	0, 3	4, 5	0, 5
(gly)4	def2-SVP	308	10, 2	1, 8	0, 8	2, 2	-1, 1
	def2-TZVP(-df)	407	32, 0	2, 8	0, 5	3, 4	-0, 5
	def2-TZVPP	723	232, 8	5, 1	0, 5	5, 8	-0, 1
	def2-QZVPP	1,389	2,684, 1	5, 3	0, 6	6, 6	0, 9
(gly)8	def2-SVP	592	57, 2	1, 0	1, 5	2, 9	-1, 7
	def2-TZVP(-df)	783	208, 4	2, 3	0, 9	5, 6	-0, 8
	def2-TZVPP	1387	1,379, 6	5, 0	1, 0	9, 7	-0, 1
	def2-QZVPP	2, 661	12,262, 7	6, 2	1, 2	8, 4	1, 4

NBAS = number of basis functions; T_{WALL} = total wall clock time required to converge the RHF equations to an accuracy of 10⁻⁸ Eh. Typically 13–15 cycles are required for convergence. SPEEDUP_γ = ratio of wall clock times for the standard exact calculation via four index integrals divided by the wall clock time required for approximation γ . ERROR_γ = absolute deviation of the total energy of approximation γ relative to the conventional four index integral calculation.

The comparison reveals that both approximations are efficient and accurate while their performance is overall comparable. For large-scale calculations on smaller molecules RI-JK is probably preferable while RIJCOSX is the method of choice for larger molecules. Several points are noted:

- (1) RI-JK achieves its efficiency through the formulation of the density matrix in the MO basis. This implies that for other exchange type matrices, for example those that arise in electric and magnetic linear response calculations, the approximation is less beneficially employed. In this respect RIJCOSX, that is formulated entirely in the AO basis, is the more general technique for simultaneously approximating Coulomb and exchange type contributions.
- (2) For spin unrestricted calculations the cost of the RI-JK method doubles since the rate limiting step is the first contraction of the MO coefficients with the three-index integrals. This is not true for the COSX approximation where the rate limiting step is the calculation of the $A_{\nu\kappa}(\mathbf{r}_g)$ integrals which is independent on the number of spin cases.
- (3) Energy derivatives are more readily and more efficiently formulated in the RIJCOSX approximation compared to RI-JK [80].
- (4) RI-JK requires much more main memory than RIJCOSX due to the structure of the intermediate quantities. Thus, if memory becomes limiting many passes through the integral list may be necessary in RI-JK with concomitant penalties in the overall performance. However, this is not much of an issue if about 4 GB of main memory are available.
- (5) Since RI-JK is dominated by matrix multiplications it will strongly benefit from the latest hardware developments where matrix operations can be extremely efficiently performed on graphics cards. This will further increase the attractiveness of RI-JK.

In our opinion, both, the RI-JK and RIJCOSX approximations are attractive tools in quantum chemistry. Their efficiency, accuracy, robustness and availability is proven.

11.4. DISCUSSION

In this chapter some contemporary algorithms for the calculations of the Coulomb and Exchange contributions to the Fock matrix were described and discussed. It has been emphasized that highly efficient calculations with essentially saturated basis sets are possible on molecules in the range of up to 200 atoms even with algorithms that do not show linear scaling. The most efficient combination appears to be the RI-J method for the Coulomb term combined with the COSX semi-numerical method for the exchange term (thus defining RIJCOSX). Depending on the basis set and the system, this method is 10–200 times faster than the standard algorithms if no HF exchange is present and 2–60 times faster if the HF exchange is to be computed. The advantages increase with increasing quality of the basis set. Unfortunately, the Hartree-Fock exchange term is still the by far most expensive part of the Fock matrix construction and more efficient algorithms for it need to be found in the future. However, already the algorithms described here will often significantly outperform

linear scaling methods. Thus, the point of view is taken that linear scaling is not an end in itself and should not be mistaken to automatically imply computational efficiency. In fact, linear scaling methods heavily rely upon the sparsity that originates from the spatial extension of molecules. However, true sparsity (to the level of 10^{-10} in the density matrix elements) only sets in for fairly large molecules with a spatial extent $>20\text{--}25$ Å that are not uniformly in the focus of contemporary theoretical investigations. In our opinion, the final proof of usefulness of a given algorithm is its performance in today's real-life chemical applications, irrespective of what the formal scaling might be.

If one considers that models with 50–100 atoms are very often sufficient to solve chemical problems or to model the quantum region in a QM/MM calculation, it may well be argued that even today focusing development efforts on algorithms that reduce the prefactor of the calculation is a good choice. It is equally evident that for even larger molecules one *eventually* has to resort to linear scaling algorithms. However, when one considers the break even point between linear scaling and non-linear scaling algorithms a fair comparison must involve: (a) the use of integral neglect thresholds that lead to actually converged and accurate SCF energies and (b) the use of basis sets that are of sufficient quality to ensure that the chemical problem at hand can actually be successfully addressed. In our opinion, a significant number of linear-scaling development publications fall short of providing a realistic perspective for actual chemical applications because they are either done with insufficiently large basis sets or too loose integral neglect thresholds. The basis set issue might not be particularly pressing in SCF calculations because acceptably good results are often already obtained with singly polarized double-zeta quality basis sets. It does become, however, a significant issue in correlation calculations where basis sets of at least doubly- or triply polarized triple zeta quality are mandatory for chemically meaningful results. A point in case is the recent development of the local pair-natural orbital coupled pair and coupled cluster methods (LPNO-CEPA and LPNO-CCSD) that can be applied to molecules of significant size with meaningful basis sets while not exploding in their computational cost [84, 85]. These methods are not even nearly linear scaling but will outperform other local correlation methods if the requirements of accurate correlation energies and sufficiently saturated basis sets are met to equal extents by the competing algorithms.

For the future it appears to be a promising strategy to first optimize the prefactor of a given algorithm and then to try to linearize it but without compromising the inherent computational efficiency of the original approach.

REFERENCES

1. Almlöf J, Faegri K, Korsell K (1982) *J Comp Chem* 3:385
2. Häser M, Ahlrichs R (1989) *J Comp Chem* 10:104
3. Lambrecht DS, Doser B, Ochsenfeld C (2005) *J Chem Phys* 123:184102
4. Challacombe M, Schwegler E (1997) *J Chem Phys* 106:5526
5. Rudberg E, Rubensson EH, Sałek P (2009) *J Chem Theor Comp* 5:80
6. Challacombe M, Schwegler E, Almlöf J (1996) *J Chem Phys* 104:4685

7. White CA, Head-Gordon MJ (1994) *Chem Phys* 101:6593
8. White CA, Johnson BG, Gill PMW, Head-Gordon M (1994) *Chem Phys Lett* 230:8
9. Challacombe M, Schwegler E, Almlöf J (1995) *Chem Phys Lett* 241:67
10. Ochsenfeld C, White CA, Head-Gordon M (1998) *J Chem Phys* 109:1663
11. Burant JC, Scuseria GE, Frisch MJ (1996) *J Chem Phys* 105:8969
12. Schwegler E, Challacombe M, Head-Gordon M (1997) *J Chem Phys* 106:9708
13. Stratmann RE, Scuseria GE, Frisch MJ (1996) *Chem Phys Lett* 257:213
14. Rudberg E, Rubensson EH, Salek PJ (2008) *Chem Phys* 128:184106
15. Senn HM, Thiel W (2007) Atomistic approaches in modern biology: from quantum chemistry to molecular simulations. *Top Curr Chem* 268:173
16. Senn HM, Thiel W (2007) *Curr Opin Chem Biol* 11:182
17. Challacombe M (1999) *J Chem Phys* 110:2332
18. Saravanan C, Shao Y, Baer R, Ross PN, Head-Gordon M (2003) *J Comp Chem* 24:618
19. McMurchie LE, Davidson ER (1978) *J Comp Phys* 26:218
20. Helgaker T, Taylor PR (1995) In: Yarkony DR (ed) *Modern electronic structure theory*. World Scientific, Singapore, p 725
21. Ahmadi GR, Almlöf J (1995) *Chem Phys Lett* 246:364
22. Shao YY, Head-Gordon M (2000) *Chem Phys Lett* 323:425
23. Neese F (2003) *J Comp Chem* 24:1740
24. Baerends EJ, Ellis DE, Ros P (1973) *Chem Phys* 2:41
25. Whitten JL (1973) *J Chem Phys* 58:4496
26. Dunlap BI (2000) *J Mol Struct Theochem* 529:37
27. Dunlap BI, Connolly JWD, Sabin JR (1979) *J Chem Phys* 71:3396
28. Vahtras O, Almlöf J, Feyereisen MW (1993) *Chem Phys Lett* 213:514
29. Werner H-J, Manby FR, Knowles PJ (2003) *J Chem Phys* 118:8149
30. Schütz M, Manby FR (2003) *Phys Chem Chem Phys* 5:3349
31. Eichkorn K, Treutler O, Ohm H, Haser M, Ahlrichs R (1995) *Chem Phys Lett* 242:652
32. Eichkorn K, Weigend F, Treutler O, Ahlrichs R (1997) *Theor Chem Acc* 97:119
33. Weigend F (2006) *Phys Chem Chem Phys* 8:1057
34. Dunlap BI (2000) *Phys Chem Chem Phys* 2:2113
35. Sierka M, Hogeckamp A, Ahlrichs R (2003) *J Chem Phys* 118:9136
36. Sodt A, Subotnik JE, Head-Gordon M (2006) *J Chem Phys* 125
37. Bebe NHF, Linderberg J (1977) *Int J Quant Chem* 7:683
38. O'Nea DW, Simons J (1989) *Int J Quant Chem XXXVI*:673
39. Koch H, Sanchez de Meras A, Pedersen TB (2003) *J Chem Phys* 118:9481
40. Pedersen TB, Aquilante F, Lindh R (2009) *Theor Chem Acc* 124:1
41. Bostrom J, Aquilante F, Pedersen TB, Lindh R (2009) *J Chem Theo Comp* 5:1545
42. Aquilante F, Gagliardi L, Pedersen TB, Lindh R (2009) *J Chem Phys* 130:154107
43. Boman L, Koch H, de Meras AS (2008) *J Chem Phys* 129:134107
44. Aquilante F, Pedersen TB, Lindh R, Roos BO, De Meras AS, Koch HJ (2008) *J Chem Phys* 129:024113
45. Aquilante F, Lindh R, Pedersen TB (2008) *J Chem Phys* 129:034106
46. Aquilante F, Pedersen TB, Lindh R (2007) *J Chem Phys* 126:194106
47. Aquilante F, Lindh R, Pedersen TB (2007) *J Chem Phys* 127:114107
48. Pedersen TB, de Meras A, Koch HJ (2004) *Chem Phys* 120:8887
49. Cuesta IG, Pedersen TB, Koch H, de Meras A (2004) *Chem Phys Lett* 390:170
50. Weigend F, Kattanneck M, Ahlrichs R (2009) *J Chem Phys* 130:164106
51. Velde GT, Bickelhaupt FM, Baerends EJ, Guerra CF, Van Gisbergen SJA, Snijders JG, Ziegler T (2001) *J Comp Chem* 22:931

52. van Gisbergen SJA, Fonseca Guerra C, Baerends EJ (2000) *J Comp Chem* 21:1511
53. Guerra CF, Snijders JG, te Velde G, Baerends EJ (1998) *Theo Chem Acc* 99:391
54. Becke AD, Dickson RM (1988) *J Chem Phys* 89:2993
55. Delley B (1990) *J Chem Phys* 92:508
56. Friesner RA (1985) *Chem Phys Lett* 116:39
57. Friesner RA (1986) *J Chem Phys* 85:1462
58. Friesner RA (1986) *J Chem Phys* 86:3522
59. Murphy RB, Cao Y, Beachy MD, Ringnalda MN, Friesner RA (2000) *J Chem Phys* 112:10131
60. Ringnalda MN, Belhadj M, Friesner RA (1990) *J Chem Phys* 93:3397
61. Greeley BH, Russo TV, Mainz DT, Friesner RA, Langlois J-M, Goddard III WA, Donnelly ER, Ringnalda MN (1994) *J Chem Phys* 101:4028
62. Termath V, Handy NC (1994) *Chem Phys Lett* 230:17
63. van Wüllen C (1995) *Chem Phys Lett* 245:648
64. Panas I, Almlöf J, Feyereisen MW (1991) *Int J Quant Chem* 40:797
65. Kohn W (1995) *Int J Quant Chem* 56:229
66. Neese F, Olbrich G (2002) *Chem Phys Lett* 362:170
67. Sinnecker S, Svensen N, Barr EW, Ye S, Bollinger JM, Neese F, Krebs C (2007) *J Am Chem Soc* 129:168
68. Ray K, George SD, Solomon EI, Wiegardt K, Neese F (2007) *Chem Eur J* 13:2783
69. Muresan N, Chlopek K, Weyhermüller T, Neese F, Wiegardt K (2007) *Inorg Chem* 46:5327
70. Kendall RA, Früchtl HA (1997) *Theor Chem Acc* 97:158
71. Neese F (2001) *Electronic structure in bioinorganic chemistry: combined spectroscopic/theoretical studies on mononuclear non-heme iron centers and Development of a large scale ab initio and density functional electronic structure package*. Universität Konstanz, Germany
72. Weigend F (2002) *Phys Chem Chem Phys* 4:4285
73. Polly R, Werner HJ, Manby FR, Knowles PJ (2004) *Mol Phys* 102:2311
74. Sodt A, Head-Gordon M (2008) *J Chem Phys* 128:104106
75. Aquilante F, Pedersen TB, Lindh R (2007) *J Chem Phys* 126:194106
76. Won Y, Lee J-G, Ringnalda MN, Friesner RA (1991) *J Chem Phys* 94:8152
77. Ko C, Malick DK, Bradon DA, Friesner RA, Martinez TJ (2008) *J Chem Phys* 128:104103
78. Friesner RA (2005) *Proc Natl Acad Sci USA* 102:6648
79. Friesner RA, Dunietz BD (2001) *Acc Chem Res* 34:351
80. Neese F, Wennmohs F, Hansen A, Becker U (2009) *Chem Phys* 356:98 81. Weigend F (2008) *J Comp Chem* 29:167
81. Weigend F (2008) *J Comp Chem* 29:167
82. Weigend F, Ahlrichs R (2005) *Phys Chem Chem Phys* 7:3297
83. Kossmann S, Neese F (2009) *Chem Phys Lett* 481:240
84. Neese F, Wennmohs F, Hansen A (2009) *J Chem Phys* 130:114108
85. Neese F, Hansen A, Liakos DG (2009) *J Chem Phys* 131:064103

CHAPTER 12

METHODS FOR HARTREE-FOCK AND DENSITY FUNCTIONAL THEORY ELECTRONIC STRUCTURE CALCULATIONS WITH LINEARLY SCALING PROCESSOR TIME AND MEMORY USAGE

EMANUEL H. RUBENSSON¹, ELIAS RUDBERG¹, AND PAWEŁ SALEK²

¹*Division of Scientific Computing, Department of Information Technology, Uppsala University, SE-751 05 Uppsala, Sweden*

²*ul. Zaporoska 8/4, 30-389 Kraków, Poland, e-mail: pawsa@theochem.kth.se*

Abstract: We discuss algorithms that can be used to calculate electron densities using computer resources – memory and processor time – that increase only linearly with system size. We focus on the Hartree-Fock and density functional theories and calculations using Gaussian basis sets. However, many of the approaches discussed here are applicable also for other methods and for any local basis. Particular attention is directed towards error control and how to avoid the use of the ad-hoc selected parameters and threshold values often associated with computational approximations employed to reach linear scaling. The discussed aspects include multipole methods, linear scaling computation of the Hartree-Fock exchange and density functional theory exchange-correlation matrices, hierarchic representation of sparse matrices, and density matrix purification. The article also describes how these different parts are put together to achieve linear scaling for the entire Hartree-Fock or density functional theory calculation, controlling errors in the self-consistent field procedure by considering rotations of the occupied subspace.

Keywords: Density functional theory, Density matrix purification, Multipole approximations, Parametrized minimization, Sparse matrix, Two-electron integrals

12.1. INTRODUCTION

In recent years, there has been great interest in electronic structure calculations for which the computational cost increases only linearly with system size [1–3]. Many methods have been developed that appear to cover all aspects required to indeed perform linear scaling calculations. Despite that, a substantial breakthrough of linear scaling methods is a long time in coming. There may be several reasons for this,

but one important aspect is that typical linear scaling implementations are parameterized with a number of threshold values and parameters that are not easily selected for someone who is not well acquainted with the code. These threshold values and parameters are used to govern the accuracy and efficiency of approximations that are needed to reach linear scaling. Ideally, parameters that control approximations should be set automatically so that the level of accuracy that is needed at each stage of the calculation is reached. We discuss in this article how such control of the accuracy can be obtained. Another aspect that has often been overlooked is the memory usage. The focus has mostly been on achieving linear scaling in time. In this article we share our experiences from the development of Ergo, a research quantum chemistry program for Hartree-Fock and Kohn-Sham density functional theory calculations which uses processor time and memory that both scale only linearly with system size [4, 5]. We are not aware of any other program with linearly scaling memory usage throughout the entire code. Initially, the development of Ergo was part of the PhD thesis works by two of the authors. This article builds in part on those authors' recent dissertations [6, 7].

This article is organized as follows: In the following section, Section 12.2, we discuss the self-consistent field procedure as used in a linear scaling electronic structure calculation. An overview of the different steps involved is given, along with a description of how error control can be achieved by considering desired and erroneous rotations of subspaces occurring in the computational procedures.

A general discussion about four-center Gaussian integral evaluation is given in Section 12.3. In particular, this section explains how the computational complexity can be reduced from $\mathcal{O}(n^4)$ to $\mathcal{O}(n^2)$. When the complexity is to be reduced to $\mathcal{O}(n)$, Coulomb and exchange matrix evaluations must be treated separately. Linear scaling evaluations of the Coulomb and exchange matrices are considered in Sections 12.4 and 12.5 respectively. Linear scaling evaluation of the exchange correlation matrix using numerical integration is discussed in Section 12.6. In Section 12.7, it is discussed how errors due to computational approximations in the Coulomb, exchange, and exchange-correlation steps can be controlled using an extrapolation scheme.

Section 12.8 discusses different ways to construct the density matrix, both algorithms based on energy minimization and polynomial expansion methods. We argue that among these methods, density matrix purification is preferable since it can deliver good performance while errors are strictly controlled. The storage and manipulation of sparse matrices, used not only in density matrix purification but also in intermediate steps throughout the calculation, is described in Section 12.9.

A set of benchmark density functional theory calculations on peptide helix molecules is presented in Section 12.10. Finally, a few concluding remarks are given in Section 12.11.

12.2. THE SELF-CONSISTENT FIELD PROCEDURE

Electronic structure calculations at the Hartree-Fock and Kohn-Sham density functional theory levels are usually performed using the so-called self-consistent field

(SCF) procedure. In the self-consistent field procedure, two steps are used repeatedly; (1) construction of the Fock/Kohn-Sham matrix for a given electron density ($D \rightarrow F$) and (2) calculation of the density matrix for the resulting potential ($F \rightarrow D$). These two steps are repeated until convergence:

$$D_1 \longrightarrow F_2 \longrightarrow D_2 \longrightarrow F_3 \longrightarrow D_3 \longrightarrow \dots \quad (12-1)$$

The electron density at a given time during this optimization is completely described by the so-called *occupied subspace*, the space spanned by the eigenvectors of F that correspond to occupied orbitals [8]. The self-consistent field procedure can be seen as a sequence of rotations of the occupied subspace:

$$\mathcal{D}_1 \longrightarrow \mathcal{D}_2 \longrightarrow \mathcal{D}_3 \longrightarrow \dots, \quad (12-2)$$

where \mathcal{D}_i is the occupied subspace of F_i and D_i . A rotation occurs every time a new Fock/Kohn-Sham matrix is constructed. In the calculation of the density matrix, no rotation would occur if exact arithmetics were used. Before we discuss what happens when approximations and erroneous rotations are introduced, we will describe the different steps of the computational procedure.

12.2.1. Overview of a Linearly Scaling Program

In this article, we focus mainly on calculations where the electron density is expanded in a set of n basis functions $\{\phi_k(r)\}$ built up by combinations of polynomials and Gaussian functions centered at the nuclei of the molecule;

$$\phi(r) = p(r - r_0) \sum_i \beta_i e^{-\alpha_i(r-r_0)^2}. \quad (12-3)$$

Here r_0 is the center of a nucleus and $p(r)$ is a polynomial function of the Cartesian coordinates $r = (x,y,z)$. These basis sets, which are commonly referred to as Gaussian type linear combination of atomic orbital (GT-LCAO) basis sets or simply Gaussian basis sets, are extensively discussed in Ref. [9]. In the following, a vector notation

$$\Phi^T(r) = [\phi_1(r) \phi_2(r) \dots \phi_n(r)] \quad (12-4)$$

is used for the set of basis functions. In Algorithm 1 we give an example of how the main structure of a linear scaling self-consistent field program can look in practice. The sequence of steps illustrated in Algorithm 1 summarizes how a Hartree-Fock or Kohn-Sham density functional theory calculation is carried out in the Ergo quantum chemistry program [4]. Ergo is a research quantum chemistry program that we used to demonstrate many of the methods described in this article. It uses Gaussian basis sets to compute electron densities with linearly scaling processor time and memory usage. The Ergo code has also been used as a testing ground to develop some linear response methods scaling linearly in time.

Algorithm 1 Overview of self-consistent field program

-
- 1: Read molecule and basis set information from input files.
 - 2: Compute overlap matrix S .
 - 3: Compute inverse factor Z such that $Z^T S Z = I$.
 - 4: Compute one-electron Hamiltonian matrix H_1 .
 - 5: Generate starting guess density matrix D_S .
 - 6: **for** $i = 1, 2, \dots$ **do**
 - 7: Compute new Coulomb matrix J .
 - 8: Compute new Hartree-Fock exchange matrix K .
 - 9: Compute new Kohn-Sham exchange-correlation matrix V_{xc} .
 - 10: Compute energy $E = \text{Tr}(D_S H_1) + \frac{1}{2} \text{Tr}(D_S (J + \alpha K)) + E_{xc}$.
 - 11: Compute new Fock/Kohn-Sham matrix $F_S = H_1 + J + \alpha K + V_{xc}$.
 - 12: Compute matrix $F_S D_S S - S D_S F_S$ (needed for DIIS [10, 11]).
 - 13: Compute \tilde{F}_S as a linear combination of new and previous Fock/Kohn-Sham matrices.
 - 14: Compute $F_{\perp} = Z^T \tilde{F}_S Z$.
 - 15: Compute new density matrix D_{\perp} from F_{\perp} .
 - 16: Compute $D_S = Z D_{\perp} Z^T$.
 - 17: **end for**
-

The matrix operations needed in several of the above steps (matrix – matrix multiplication, matrix addition, matrix trace) are performed using sparse matrix algebra. This allows for linear scaling provided that the matrix sparsity is such that the number of non-zero elements per row does not increase with system size. In practice this is usually the case for non-metallic molecular systems.

We will now comment on the different steps and introduce some notation.

- *Step 2:* The overlap matrix

$$S = \int_{\mathbb{R}^3} \Phi(r) \Phi^T(r) dr. \quad (12-5)$$

The overlap matrix can easily be constructed directly in sparse form given the locality of the basis functions. The number of non-negligible contributions scales linearly with system size.

- *Step 3:* The inverse factor Z is needed for the congruence transformations in Steps 14 and 16. The inverse factor can be computed using inverse Cholesky decomposition [12, 13] which is very efficient for small systems. However, for the Cholesky approach it is difficult to achieve linear scaling while keeping errors strictly controlled. An alternative technique is the recursive inverse factorization method [14].
- *Step 4:* The one-electron Hamiltonian matrix depends only on the basis set and positions of the nuclei;

$$H_1 = - \int_{\mathbb{R}^3} \Phi(r) \frac{\nabla^2 \Phi^T(r)}{2} dr - \int_{\mathbb{R}^3} \Phi(r) \sum_A \frac{Z_A}{|r_A - r|} \Phi^T(r) dr. \quad (12-6)$$

Here Z_A and r_A are the charge and position respectively of atom A . For the first term in (12-6), linear scaling is easily achieved by making use of the locality of the basis functions. For the second term, describing the Coulomb attraction between electrons and nuclei, linear scaling is achieved using multipole descriptions of groups of charges in essentially the same way as for the Coulomb matrix, see Section 12.4.

- *Step 7:* The Coulomb matrix

$$J = 2 \int_{\mathbb{R}^6} \frac{\Phi(r_1)\Phi^T(r_2)D_S\Phi(r_2)\Phi^T(r_1)}{|r_1 - r_2|} dr_1 dr_2. \quad (12-7)$$

This step is discussed in Section 12.4.

- *Step 8:* The Hartree-Fock exchange matrix

$$K = - \int_{\mathbb{R}^6} \frac{\Phi(r_1)\Phi^T(r_2)D_S\Phi(r_1)\Phi^T(r_2)}{|r_1 - r_2|} dr_1 dr_2. \quad (12-8)$$

This step is discussed in Section 12.5.

- *Step 9:* The Kohn-Sham exchange-correlation matrix

$$V_{xc} = \int_{\mathbb{R}^3} \Phi(r) \left. \frac{\partial \mathcal{F}}{\partial \rho} \right|_{\rho=\rho(r)} \Phi^T(r) dr \quad (12-9)$$

where $\int \mathcal{F}(\rho) dr$ is the energy functional which in (12-9) for simplicity is assumed to be only density dependent. This step is discussed in Section 12.6 where also gradient dependent energy functionals are discussed.

- *Step 11:* The Fock/Kohn-Sham matrix consists of one-electron (H_1) and two-electron (J , K , V_{xc}) contributions. In case of a Hartree-Fock calculation, $V_{xc} = 0$, $E_{xc} = 0$, and $\alpha = 1$. In case of a pure Kohn-Sham calculation, $\alpha = 0$. For so-called hybrid functionals, V_{xc} and E_{xc} are both nonzero and $0 < \alpha \leq 1$.
- *Step 13:* Usually, some convergence enhancing schemes are used to accelerate and hopefully even ensure convergence, see Refs. [15, 16] for recent reviews. In the Ergo quantum chemistry program either damping [17, 18] or direct inversion in the iterative subspace (DIIS) [10, 11] is used to generate \tilde{F}_S as a linear combination of new and previous Fock/Kohn-Sham matrices.
- *Step 14:* We denote by F_S and F_\perp the Fock/Kohn-Sham matrix before and after this congruence transformation, respectively.
- *Step 15:* The density matrix D_\perp is calculated from the occupied invariant subspace of F_\perp , usually the subspace that corresponds to its n_{occ} smallest eigenvalues, where n_{occ} is the number of occupied orbitals, see Figure 12-1. The $F \rightarrow D$ step is discussed in Section 12.8.
- *Step 16:* We denote by D_\perp and D_S the density matrix before and after this congruence transformation, respectively.

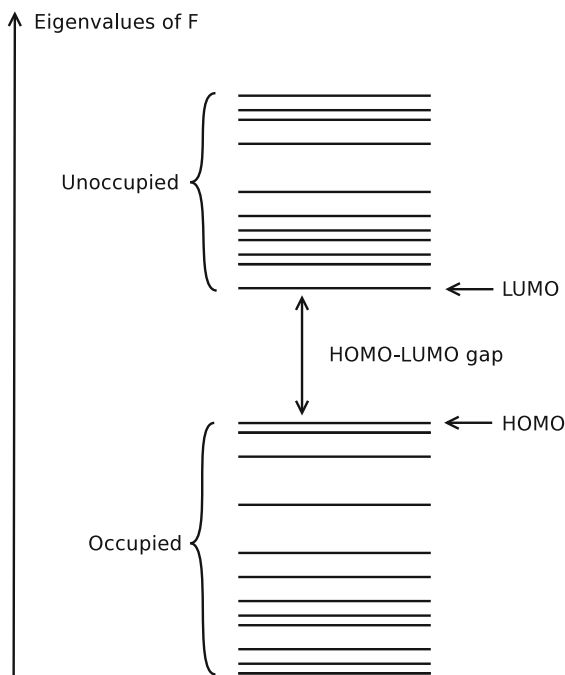


Figure 12-1. Schematic illustration of eigenvalues corresponding to the occupied and unoccupied subspaces of the Fock/Kohn-Sham matrix F

12.2.2. Erroneous Rotations

In practice, both the $D \rightarrow F$ and $F \rightarrow D$ steps are carried out approximately in order to reduce the computational effort. Computational approximations such as Cauchy-Schwarz screening of integrals and truncated multipole expansions are frequently used, as described in Sections 12.3 and 12.4. Consequently, a distorted subspace $\tilde{\mathcal{D}}_{i+1}$ is obtained instead of \mathcal{D}_{i+1} when F_{i+1} and D_{i+1} are computed from D_i . That is, an erroneous rotation

$$\mathcal{D}_{i+1} \dashrightarrow \tilde{\mathcal{D}}_{i+1} \quad (12-10)$$

happens together with the desired

$$\mathcal{D}_i \rightarrow \mathcal{D}_{i+1} \quad (12-11)$$

rotation, see Figure 12-2. Note that in exact arithmetics, \mathcal{D}_{i+1} is the occupied subspace of both F_{i+1} and D_{i+1} . The approximate $\tilde{\mathcal{D}}_{i+1}$ is the occupied subspace of D_{i+1} only, but contains erroneous rotations coming from both the $D_i \rightarrow F_{i+1}$ and $F_{i+1} \rightarrow D_{i+1}$ steps.

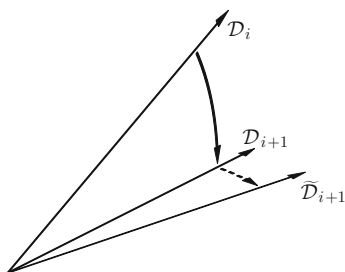


Figure 12-2. When computational approximations are used, erroneous rotations (\dashrightarrow) distort the desired rotation (\rightarrow) so that a perturbed subspace \tilde{D}_{i+1} is obtained instead of the D_{i+1} subspace

12.2.3. Controlling Erroneous Rotations

The erroneous rotations of the occupied subspace should be small compared to the desired self-consistent field rotations. A rotation of a subspace can be measured by the largest canonical angle between the original and rotated subspaces. The largest canonical angle θ is defined as the largest acute angle between any vector in the first subspace and the closest vector in the second subspace. Consider a matrix A , where for example $A = F$ or $A = D$, and its approximation $\tilde{A} = A + E$. Assume that the eigenvalues of A are separated in two groups, corresponding to two subspaces, as in Figure 12-1. Assume also that the gap ξ (the HOMO-LUMO gap in case of $A = F$) between the two groups is larger than $\|E\|_2$. Then, it can be shown that

$$\sin \theta \leq \frac{\|E\|_2}{\xi - \|E\|_2}. \quad (12-12)$$

Moreover, in case A and \tilde{A} are projections onto the subspaces in question,

$$\sin \theta = \|E\|_2. \quad (12-13)$$

This means that controlling the erroneous rotation of an approximation amounts to knowing the band gap and controlling the norm of the error matrix. See Ref. [8] for a more thorough discussion. It should be noted that (12-12) and (12-13) are written in terms of any unitary-invariant norm in Ref. [8].

Controlling erroneous rotations is particularly important in linear scaling self-consistent field calculations where approximations to reduce the computational complexity are frequently employed. In the following sections we will discuss such approximations. We will also discuss methods to improve error control along the lines above.

12.3. INTEGRAL EVALUATION

In a Hartree-Fock or Kohn-Sham density functional theory calculation, much computer time is spent on the task of computing a new Fock/Kohn-Sham matrix for a given density matrix. Much of the work comes down to evaluating two-electron integrals of the type

$$(pq|rs) = \int_{\mathbb{R}^6} \frac{\phi_p(r_1)\phi_q(r_1)\phi_r(r_2)\phi_s(r_2)}{|r_1 - r_2|} dr_1 dr_2. \quad (12-14)$$

There are very many such integrals; if all of them are computed explicitly, the number of integrals that must be evaluated is n^4 , where n is the number of basis functions. Fortunately, there are ways to reduce the needed computational effort. There is some symmetry to take advantage of: it follows from (12-14) that $(pq|rs) = (qp|rs) = (pq|sr) = (rs|pq)$ etc., so that if all four indexes are different, there are eight integrals having the same value. This means that the number of unique integrals is about $\frac{1}{8}n^4$. For large systems, it is possible to reduce the number of integrals that need to be computed even more, provided that localized basis functions are used.

12.3.1. Primitive Gaussian Integrals

When Gaussian basis functions of the form (12-3) are used, each two-electron integral $(pq|rs)$ can be expressed as a sum of primitive integrals of the type

$$\int_{\mathbb{R}^6} \frac{\Psi_A(r_1)\Psi_B(r_2)}{|r_1 - r_2|} dr_1 dr_2 \quad (12-15)$$

where

$$\Psi_A(r) = (x - x_A)^{i_A} (y - y_A)^{j_A} (z - z_A)^{k_A} e^{-\alpha_A(r-r_A)^2} \quad (12-16)$$

$$\Psi_B(r) = (x - x_B)^{i_B} (y - y_B)^{j_B} (z - z_B)^{k_B} e^{-\alpha_B(r-r_B)^2}. \quad (12-17)$$

At this level, each primitive distribution Ψ_A is determined by its exponent α_A , its center coordinates $r_A = (x_A, y_A, z_A)$, and the three integers i_A, j_A and k_A .

Primitive integrals of the type (12-15) can be efficiently computed using the recurrence relations of the McMurchie-Davidson scheme. A thorough explanation of this scheme is given by Helgaker et al. in Ref. [9].

12.3.2. Screening

In this section, the concept of *screening* is used in the context of integral evaluation. What is meant by screening in this context is something like “neglect of small contributions”. As seen from (12-7) and (12-8), the elements of the Coulomb and Hartree-Fock exchange matrices are sums in which each term is of the form

$$D_{ab}(pq|rs) \quad (12-18)$$

where D_{ab} denotes the matrix element (a,b) of the density matrix D_S . Now, if it is known that $|D_{ab}| < \epsilon_1$ and that $|(pq|rs)| < \epsilon_2$, then the contribution to the result matrix is surely smaller than $\epsilon_1\epsilon_2$. The idea of integral screening is to systematically estimate bounds on $|D_{ab}|$ and $|(pq|rs)|$ and use that information to skip evaluation of $|(pq|rs)|$ whenever it is known that the resulting contribution would be smaller than some threshold value τ .

12.3.3. Cauchy-Schwarz Screening

The Schwarz inequality, also known as the Cauchy-Schwarz inequality, is very useful for providing bounds on two-electron integrals [19]:

$$|(pq|rs)| \leq \sqrt{(pq|pq)}\sqrt{(rs|rs)} \quad (12-19)$$

The quantity $\sqrt{(pq|pq)}$ associated with a pair of basis functions $\phi_p(r)$ and $\phi_q(r)$ is therefore of interest. Let D_{max} be the largest absolute density matrix element, and let C_{max} be the largest Cauchy-Schwarz factor $\sqrt{(pq|pq)}$ among all pairs of basis functions. Then a limit for the largest possible contribution to the Coulomb or exchange matrix from a particular basis function pair pq is given by $D_{max}C_{max}\sqrt{(pq|pq)}$. Therefore, once D_{max} and C_{max} are known, many basis function pairs can be neglected; it makes sense to create a list of all non-negligible basis function pairs. When Gaussian basis functions of the type (12-3) are used, the number of non-negligible basis function pairs will scale as $\mathcal{O}(n)$, thanks to locality of basis functions. Using such a list of non-negligible basis function pairs as a starting point, all non-negligible integrals $(pq|rs)$ can easily be computed with $\mathcal{O}(n^2)$ complexity.

12.3.4. The Coulomb and Exchange Matrices

In the previous section, it was discussed how the formal $\mathcal{O}(n^4)$ scaling can be improved to $\mathcal{O}(n^2)$ while still considering all contributions to the Coulomb and exchange matrices on an equal footing. Further improvements can be made if one takes into account the way that density matrix elements are combined with the two-electron integrals. This differs between the Coulomb contribution J and the exchange contribution K , see (12-7) and (12-8):

$$D_{rs}(pq|rs) \quad (\text{Coulomb}) \quad (12-20)$$

$$D_{rs}(pr|qs) \quad (\text{exchange}) \quad (12-21)$$

Therefore, when attempting to improve the scaling beyond $\mathcal{O}(n^2)$, it is helpful to use separate algorithms for the two contributions J and K . In the case of J , one can exploit the fact that pairs of basis functions together with the corresponding density matrix elements can be seen as charge distributions for which simplified descriptions can be generated. In the case of K , improved scaling can be achieved if density matrix elements decay with the distance between the corresponding basis functions, as is normally the case for non-metallic systems. More details about

Coulomb matrix construction using multipoles will be given in Section 12.4, and exchange matrix construction is discussed in Section 12.5.

12.4. COULOMB MATRIX CONSTRUCTION

This section gives a brief description of how and why the scaling of the Coulomb matrix construction step can be improved using multipole expansions. For a more detailed discussion of the implementation of Coulomb matrix construction in the Ergo program, see Ref. [20].

The Coulomb matrix is essential in all self-consistent field quantum chemistry calculations: it is needed in Hartree-Fock as well as in Kohn-Sham density functional theory, for both pure and hybrid functionals. This section focuses on how multipole approximations can be used to accelerate the computation of the Coulomb matrix. The Coulomb matrix J is given by

$$J_{pq} = 2 \sum_{rs} D_{rs}(pq|rs). \quad (12-22)$$

Taking into account the expression (12-14) for the two-electron integrals $(pq|rs)$, this can be rewritten as

$$J_{pq} = 2 \int_{\mathbb{R}^6} \frac{\phi_p(r_1)\phi_q(r_1)\sum_{rs} D_{rs}\phi_r(r_2)\phi_s(r_2)}{|r_1 - r_2|} dr_1 dr_2 = 2 \int_{\mathbb{R}^6} \frac{\phi_p(r_1)\phi_q(r_1)\rho(r_2)}{|r_1 - r_2|} dr_1 dr_2 \quad (12-23)$$

where $\rho(r)$ is the electron density

$$\rho(r) = \sum_{rs} D_{rs}\phi_r(r)\phi_s(r). \quad (12-24)$$

This means that the Coulomb matrix element J_{pq} can be interpreted as follows: J_{pq} is the Coulombic repulsion energy of an electron whose spatial distribution is given by $\phi_p(r)\phi_q(r)$, due to the total charge distribution $\rho(r)$ of all electrons.

To efficiently evaluate Coulomb matrix elements J_{pq} it is useful to have two things precomputed. Firstly, a list of non-negligible basis function products $\phi_p(r)\phi_q(r)$, as described in Section 12.3.3. Secondly, a description of the density $\rho(r)$ that allows one to evaluate repulsion from a group of charges that are far away, without considering interactions of individual pairs of charges. Such a description of $\rho(r)$ can be created using multipole expansions, as discussed in the following section.

12.4.1. Multipole Approximations

The Fast Multipole Method (FMM) was originally developed for calculation of the interaction between classical point charges [21, 22]. Later, much research has

been devoted to the application of multipole approximations in quantum chemistry [23–34]. The basic idea is that a group of charges that are close to each other can be described by a multipole expansion, which includes enough information to accurately evaluate the Coulomb repulsion between that group of charges and some other charge that is well separated from the group. This allows Coulomb interaction to be calculated without taking into account each individual charge separately, thus reducing the computational effort. A hierarchy of groups of charges is used, so that larger groups of charges can be used at long distances. This gives improved scaling.

When multipole approximations are applied in quantum chemistry with Gaussian basis functions, the “charges” are no longer point charges but instead Gaussian charge distributions arising from products of basis functions. Groups of such charge distributions are then described by multipole expansions.

So what is a “multipole expansion”? It is a list of numbers called “multipole moments”, each multipole moment giving the weight of one particular contribution to the expansion. The simplest part is the monopole contribution. Then there are three dipole contributions, one for each coordinate direction. Higher order contributions correspond to more complicated multipoles; quadrupoles, octopoles, etc. See Figure 12-3 for an illustration. The expansion must be truncated at some expansion order, chosen so that the desired accuracy is maintained.

Each Coulomb matrix element J_{pq} is computed as a sum of a near-field (NF) part and a far-field (FF) part:

$$J_{pq} = J_{pq}^{\text{NF}} + J_{pq}^{\text{FF}} \quad (12-25)$$

The near-field part J_{pq}^{NF} is computed by explicit evaluation of the integrals $(pq|rs)$, while the far-field part J_{pq}^{FF} is computed as

$$J_{pq}^{\text{FF}} = 2 \sum_i \int \frac{\phi_p(r_1)\phi_q(r_1)\rho_i(r_2)}{|r_1 - r_2|} dr_1 dr_2 \quad (12-26)$$

where the sum is taken over all far-field groups of charges, each with electron density $\rho_i(r)$. Each term in the sum (12-26) is computed using a truncated multipole expansion of the density $\rho_i(r)$:

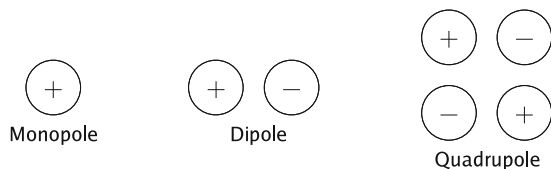


Figure 12-3. Multipole moments

$$\int \frac{\phi_p(r_1)\phi_q(r_1)\rho_i(r_2)}{|r_1 - r_2|} dr_1 dr_2 \approx q_{pq}^T T q_i \quad (12-27)$$

Here, T is the multipole interaction matrix, and q_{pq} and q_i are the multipole expansions (i.e. vectors of multipole moments) for the basis function pair pq and the density ρ_i respectively.

Using (12-27), the interaction between the basis function pair pq and a large part of the electron density can be evaluated at once, saving lots of work compared to the alternative of explicitly computing all needed integrals ($pq|rs$). By using a hierarchy of spatial boxes, one can make sure that larger groups of charges are used at longer distances, see Figure 12-4.

To compute the whole Coulomb matrix J , a large number of interactions of the type (12-27) must be evaluated, and each vector of multipole moments q can be reused many times. The multipole moments (components of the vector q) describing a charge distribution $\rho(r)$ are computed as

$$q_k = \int \rho(r) f_k(r - r_c) dr \quad (12-28)$$

where r_c is the center point chosen for the multipole expansion. The functions $f_k(r)$ are the real regular solid harmonics [9, 33]. The functions of zeroth, first, and second order are as follows:

M	M			M	M	M
M	M			M	M	
M	M	M	M	M	M	M
M	M	x	x			
M	M	x	pq	x	M	
M	M	x	x	x	M	
M	M	M	M	M	M	M
M	M	M	M			

Figure 12-4. Schematic picture of the hierarchy of boxes used to compute the Coulomb matrix element J_{pq} . Multipole descriptions of the electron density are used for boxes marked with M, while interaction with boxes marked with X are treated by explicit evaluation of the corresponding two-electron integrals ($pq|rs$)

$$\begin{aligned}
 f_1(r) = 1 & & f_2(r) = x & & f_3(r) = y & & f_4(r) = z & & f_5(r) = \frac{1}{2}\sqrt{3}(x^2 - y^2) \\
 & & & & & & & & f_6(r) = \sqrt{3}xz \\
 & & & & & & & & f_7(r) = \frac{1}{2}(3z^2 - r^2) \\
 & & & & & & & & f_8(r) = \sqrt{3}yz \\
 & & & & & & & & f_9(r) = \sqrt{3}xy
 \end{aligned}
 \tag{12-29}$$

Thus, the first multipole moment is simply the total charge: $q_0 = \int \rho(r)dr$. Higher order moments involve polynomials of increasing degrees.

In principle, infinitely high order of multipole moments is needed for an exact description of a general charge distribution $\rho(r)$. However, when evaluating Coulomb interaction at long distances, the higher order moments become less important as the distance increases. At very long distances, the monopole contribution (total charge) is the only thing that matters. At intermediate distances, the interaction is well described using a truncated multipole expansion, where only the lower-order moments are included. This is the reason why truncated multipole expansions are so useful for Coulomb interactions: by computing only the lower-order multipole moments q_k , we are extracting the most relevant information about the charge distribution $\rho(r)$.

The multipole interaction matrix T in (12-27) depends on the separation vector $(\Delta x, \Delta y, \Delta z)$ between the interacting multipoles [9]. Therefore, T must be re-evaluated many times. Both the computation of T and the subsequent contraction with multipole moments (12-27) become very time-consuming if a high order of multipole moments is used. Therefore, much efficiency can be gained by choosing as low multipole expansion order as possible for each interaction. On the other hand, when truncated multipole expansions are used to describe the electron density, this approximation introduces errors. An important aspect is therefore how the order of multipole expansion can be selected dynamically, depending on the needed accuracy in each part of the Coulomb matrix computation [20].

12.5. EXCHANGE MATRIX CONSTRUCTION

The Hartree-Fock exchange matrix is needed in both Hartree-Fock and hybrid Kohn-Sham density functional theory calculations. This section contains a brief discussion of how and why linear scaling can be achieved in exchange matrix construction. The exchange matrix K is given by

$$K_{pq} = - \sum_{rs} D_{rs}(pr|qs). \tag{12-30}$$

Note the difference in the order of indexes compared to the Coulomb matrix. There has been much research devoted to efficient computation of the exchange matrix [35–42]. In particular, the so-called LinK algorithm [38, 40] has been very successful and is now used in several quantum chemistry codes. Some details about the exchange matrix evaluation in the Ergo code, including memory usage considerations, can be found in Ref. [5].

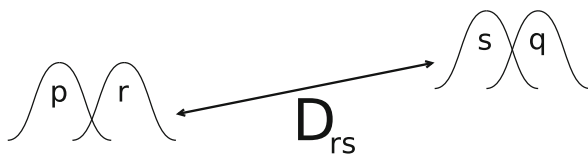


Figure 12-5. Schematic illustration of how the basis function products $\phi_p(r)\phi_r(r)$ and $\phi_q(r)\phi_s(r)$ are coupled through the density matrix element D_{rs} in the exchange matrix evaluation

With the assumption that any density matrix element D_{rs} is negligible when the corresponding basis functions are far enough apart, and recalling the expression (12-14) for the two-electron integrals $(pq|rs)$, one can understand why linear scaling is possible for the exchange by considering the contribution $D_{rs}(pr|qs)$. For such a contribution to be non-negligible, the following conditions must be met (see Figure 12-5):

- The basis functions $\phi_p(r)$ and $\phi_r(r)$ must be close enough to each other so that the product $\phi_p(r)\phi_r(r)$ is non-negligible.
- The basis functions $\phi_q(r)$ and $\phi_s(r)$ must be close enough to each other so that the product $\phi_q(r)\phi_s(r)$ is non-negligible.
- The basis functions $\phi_r(r)$ and $\phi_s(r)$ must be close enough to each other so that the density matrix element D_{rs} is non-negligible.

But then all four basis functions ϕ_p, ϕ_q, ϕ_r , and ϕ_s must be close to each other! So, for a particular density matrix element D_{rs} , the number of non-negligible exchange matrix contributions $D_{rs}(pr|qs)$ that must be evaluated is constant (independent of system size) for large enough systems. Provided that the number of non-negligible density matrix elements scales linearly with system size, the number of non-negligible contributions $D_{rs}(pr|qs)$ needed for the construction of the exchange matrix K also scales linearly with system size.

In order to compute the exchange matrix K in a linear scaling fashion, one must predict the size of contributions $D_{rs}(pr|qs)$ without explicitly computing them. Also, one must be able to skip many contributions at once, without performing work to estimate the size of each individual contribution. This can be done by precomputing the basis function products $\phi_p(r)\phi_q(r)$ and sorting them according to their size as measured by the Cauchy–Schwarz measure $\sqrt{(pq|pq)}$. Given such a sorted list of basis function products, it is possible to skip many exchange matrix contributions at a time. This is one of the key ideas used to improve the scaling of the exchange matrix calculation step.

12.6. THE EXCHANGE-CORRELATION MATRIX

The Kohn-Sham formulation of density functional theory allows one to formulate the framework for density functional theory calculations in a way similar to the Hartree-Fock framework with two important modifications. Hartree-Fock exchange

is scaled down or entirely removed. Instead, an exchange-correlation term is added to the energy and a corresponding contribution is added to the Fock matrix. A Fock matrix with an exchange-correlation contribution is traditionally called a Kohn-Sham matrix.

The exchange-correlation energy E_{xc} within the local-spin-density approximation (LSDA) is given by

$$E_{xc} = \int_{\mathbb{R}^3} \mathcal{F}(\rho_\alpha(r), \rho_\beta(r)) dr. \quad (12-31)$$

LSDA assumes that the non-local exchange and correlation contributions are negligible or cancel out. It also separately considers electron densities with spin up and down. These densities are the same in the special case of closed shell calculations. Practical density functional theory calculations in chemistry demand that a non-local correction is made, giving rise to the so-called Generalized Gradient Approximation (GGA). In this approximation, the exchange-correlation energy is still given by an integral over all space, but the contribution to E_{xc} at each point depends not only on the electronic density but also on its gradient. For simplicity, the rest of this section is restricted to the LSDA case. However, the Ergo program [4] implements both LSDA and GGA.

Matrix elements of the exchange-correlation matrix under the LSDA approximation are expressed as

$$V_{xc;pq} = \int_{\mathbb{R}^3} v_{xc}(r) \phi_p(r) \phi_q(r) dr, \quad v_{xc}(r) = \sum_{\sigma=\alpha,\beta} \left. \frac{\partial \mathcal{F}}{\partial \rho_\sigma} \right|_{\rho_\sigma=\rho_\sigma(r)} \quad (12-32)$$

where $V_{xc;pq}$ denote the elements of the exchange-correlation matrix V_{xc} .

In contrast to the integrals encountered in calculations of Coulomb repulsion and Hartree-Fock exchange, exchange-correlation integrals cannot be expressed in a compact analytical form. Instead, the exchange-correlation energy E_{xc} and the matrix elements $V_{xc;pq}$ are computed using numerical integration over a grid:

$$E_{xc} = \sum_i w_i \mathcal{F}(\rho_\alpha(r_i), \rho_\beta(r_i)), \quad (12-33)$$

$$V_{xc;pq} = \sum_i w_i v_{xc}(r_i) \phi_p(r_i) \phi_q(r_i). \quad (12-34)$$

The choice of grid point locations r_i and associated grid weights w_i determines the quality of the grid. The electron density at a given grid point r_i is computed by contracting the density matrix D_S with basis functions evaluated at r_i :

$$\rho(r_i) = \sum_{pq} D_{pq} \phi_p(r_i) \phi_q(r_i). \quad (12-35)$$

The calculation of the exchange-correlation matrix formally scales cubically with system size. The scaling can be reduced to linear if basis function screening is implemented. The numerical grids used in calculations traditionally make use of the atomic structure of the molecule to distribute the grid points and choose the weights [43] but hierarchical adaptive grids have been devised as well [44].

12.6.1. Numerical Grids

Traditionally, the entire integration grid is constructed as a union of atomic grids, with grid weights w_i adjusted in the overlapping regions [45]. Atomic grids are constructed as outer products of Lebedev grids for angular integration [46] and Gauss-Chebyshev radial grids. Alternative methods have been proposed as well [47]. The weights in overlapping regions are adjusted using Becke partitioning or its variants [48, 49]. Smooth switching functions used in the Becke partitioning process in principle stretch out infinitely. This makes the partitioning process scale cubically with system size. In practice, the right choice of multiplication order used in the grid weight scaling process can make the effort per atom roughly independent of the system size. Other partitioning schemes like SSF [49] choose the partitioning function in a way that allows for trivial screening of atoms far away from the grid point associated with the weight being adjusted.

While such grids are well established, the existence of overlapping regions in multi-atom systems introduces errors that are difficult to control. The high accuracy that is possible for integration of densities or exchange-correlation potentials for spherically symmetric systems like atoms cannot be realized in such cases. The complication of overlapping regions makes the error increase by several orders of magnitude. A grid construction method that in principle allows for integration of the electron density up to any accuracy is the so-called hierarchical cubature (HiCu) [44]. The disadvantage of this scheme is that it generates larger grids for low- and medium-precision integrations as compared to schemes employing atomic grids with space partitioning.

12.6.2. Evaluation of Sparse Exchange-Correlation Potential Matrix

The evaluation of the exchange-correlation matrix as given by (12-34) formally follows the scheme shown in Algorithm 2. An efficient implementation of that algorithm must fulfill a few conditions:

Algorithm 2 Numerical integration algorithm for computation of the exchange-correlation matrix.

```

1:  for each (p,q) giving rise to a nonvanishing  $V_{xc;pq}$  do
2:     $V_{xc;pq} = \sum_i^{\text{grid}} \omega_i v_{xc}(r_i) \phi_p(r_i) \phi_q(r_i)$ 
3:  end for

```

1. Matrix element magnitudes $|V_{xc;pq}|$ are estimated in advance so that memory for $V_{xc;pq} < \tau$ is not allocated and the sum contributing to that element is not computed. Here, τ is a preselected threshold for matrix elements.
2. Terms $v_{xc}(r_i)$, $\phi_p(r_i)$, and $\phi_q(r_i)$, contributing to several matrix elements, are not unnecessarily recomputed.

Depending on the amount of available memory and other considerations, the operations in Algorithm 2 may be performed in a different order. If memory constraints were not present, we could perform the operations as shown in Algorithm 3. This simple algorithm has significant memory requirements. The sparse matrix B needs to be available during the entire integration process. Let us consider for example a system with 10,000 atoms, with 10,000 grid points per atom, and where on average 50 basis functions are non-vanishing at a grid point. In that example, the matrix B would require approximately 60 GB of memory if stored in the compressed sparse row format. One way to reduce the memory demand is to process the grid points in batches. The Ergo implementation follows that approach.

Algorithm 3 Linearly scaling numerical integration algorithm for construction of the exchange-correlation matrix.

- 1: Compute a sparse matrix B with elements $B_{ki} = \phi_k(r_i)$ of basis functions ϕ_k evaluated at grid points r_i .
 - 2: Compute $\rho(r_i)$ by contracting the sparse density matrix D with sparse B on each side: $\rho(r_i) = \sum_{pq} B_{pi} D_{pq} B_{qi}$.
 - 3: Use $\rho(r_i)$ to compute $v_{xc;i} = v_{xc}(r_i)$ and store the result.
 - 4: Compute the exchange-correlation matrix by performing a matrix scaling and a sparse matrix-matrix multiplication: $V_{xc;pq} = \sum_i B_{pi} w_i v_{xc;i} B_{qi}$.
-

At the time of grid generation, grid points are collected in spatial cells. For each cell, we find the basis functions that overlap with that cell. This data is important with respect to both accuracy and performance. A too cautious estimation may result in a dramatic increase in calculation time. On the other hand, a too sloppy criterion for determination of basis functions relevant for a given cell will inadvertently affect the calculation accuracy. The list of non-vanishing basis functions allows us to predict which exchange-correlation matrix elements may have non-zero values and to determine an exchange-correlation matrix sparsity pattern. This pattern in turn permits preallocation of the resulting exchange-correlation matrix $V_{xc;pq}$ so that individual contributions computed later can be added quickly without need to reallocate data. The numerical integration is then performed one cell at a time. For each cell, we follow Algorithm 3 with the exception that the partial contributions computed according to this algorithm are accumulated for all cells.

12.7. ERROR CONTROL IN FOCK AND KOHN-SHAM MATRIX CONSTRUCTIONS

When a contribution J , K , or V_{xc} to the Fock or Kohn-Sham matrix is computed approximately, controlling the error in the occupied subspace amounts to knowing the band gap and controlling the Euclidean norm of the error matrix, as explained in Section 12.2. As seen in Sections 12.4, 12.5, and 12.6, modern algorithms to construct Coulomb, exchange, and exchange-correlation matrices typically employ one or several threshold values controlling the accuracy.

In the following we will use the notation

$$E = \tilde{X} - X \quad (12-36)$$

for the error matrix, where $X \in \{J, K, V_{xc}\}$ and \tilde{X} is the corresponding approximate matrix obtained when small contributions are neglected. Given a requested accuracy ε_{req} , the computations of J , K , and V_{xc} should ideally use as little computational resources as possible while

$$\|E\|_2 < \varepsilon_{\text{req}}. \quad (12-37)$$

Strict, practically useful bounds for the overall error are hard to come by since the error in each matrix element is made up of many small contributions that may or may not cancel each other out. For V_{xc} , the type of grid used for the numerical integration affects the accuracy in a non-trivial way.

However, when the error in J or K is observed by looking at the norm of the whole error matrix rather than at its constituent parts, it can be seen that the error behaves predictably and that the norm of the error matrix ε is related to the threshold value τ as $\varepsilon = c\tau^\alpha$ [50]. This relation can be utilized to achieve error control using an extrapolation scheme.

We regard the constructions of the matrices J and K as black boxes that take the density matrix D and a threshold parameter τ as input, see Figure 12-6. An appropriate threshold value can be obtained by the following procedure illustrated in Figure 12-7. (1) Perform three low accuracy computations using threshold values τ_{ref} , τ_1 , and τ_2 to obtain three matrices X_{ref} , X_1 , and X_2 . (2) Compute error matrices for X_1 and X_2 using X_{ref} as reference: $E_1 = X_1 - X_{\text{ref}}$ and $E_2 = X_2 - X_{\text{ref}}$. Then, a threshold value that gives the desired accuracy can be selected by extrapolation, see Figure 12-7.

This approach has been successfully applied to Coulomb and exchange matrix constructions [50]. An advantage is that existing codes can be used without modification, as long as the accuracy is governed by a single parameter τ . In the case of a Kohn-Sham density functional theory calculation, the use of hierarchical adaptive grids [44] allows the accuracy of the numerical integration needed for V_{xc} to be controlled by a single continuous parameter. Therefore, one can expect that a similar extrapolation scheme can be used for the exchange-correlation matrix V_{xc} as well.

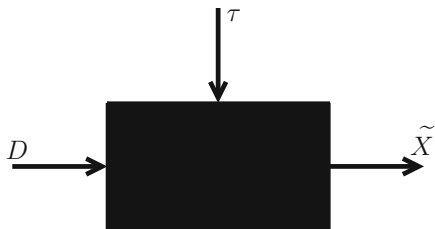


Figure 12-6. Constructions of Coulomb and exchange matrices can be regarded as *black boxes* where a threshold value τ and the density matrix D are taken as input. The *black box* returns the matrix \tilde{X} which is either \tilde{J} or \tilde{K}

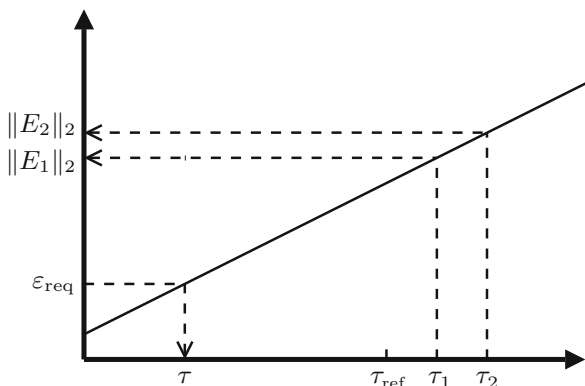


Figure 12-7. Schematic figure that illustrates the accuracy as a function of threshold value and how an appropriate threshold value τ can be selected by extrapolation. Both the x-axis and the y-axis are given in logarithmic scale. First, three low accuracy calculations are performed using threshold values τ_{ref} , τ_1 , and τ_2 . Using the most accurate of these calculations as reference, error matrices E_1 and E_2 can be computed. Taking the norms of these error matrices, we obtain two points on the line and can, given a desired accuracy ϵ_{req} , select an appropriate threshold value τ by extrapolation

12.8. DENSITY MATRIX CONSTRUCTION

One of the key operations in Hartree-Fock and Kohn-Sham density functional theory calculations is to construct the density matrix D_{\perp} for a given Fock or Kohn-Sham matrix F_{\perp} , Step 15 of Algorithm 1. For ease of notation, in this section we drop the subscript \perp and simply write D and F for D_{\perp} and F_{\perp} , respectively.

The density matrix D is the matrix for projection onto the occupied invariant subspace \mathcal{X} of F . This subspace is spanned by the eigenvectors of F that correspond to the n_{occ} smallest eigenvalues, see Figure 12-1. Therefore, it is possible to construct the density matrix via a diagonalization of F :

$$FC_{\mathcal{X}} = C_{\mathcal{X}}\Lambda_{\mathcal{X}} \implies D = C_{\mathcal{X}}C_{\mathcal{X}}^T. \tag{12-38}$$

Here $C_{\mathcal{X}}$ is a $n \times n_{\text{occ}}$ matrix that contains the eigenvectors that span \mathcal{X} and $\Lambda_{\mathcal{X}}$ is a diagonal $n_{\text{occ}} \times n_{\text{occ}}$ matrix with the corresponding eigenvalues. The time needed to perform this operation generally grows cubically with system size. Also, standard diagonalization schemes usually make much effort to obtain accurate eigenvectors. Here, we want an accurate representation of the occupied invariant subspace but do not care about individual eigenvectors; any orthonormal basis $Q_{\mathcal{X}}$ for \mathcal{X} would suffice. Several methods to obtain such a basis without direct diagonalization have been proposed, often based on Krylov subspace iterations [51, 52].

In a linear scaling method, $Q_{\mathcal{X}}$ would need to be sparse. Many possible choices of $Q_{\mathcal{X}}$ exist of which most are likely to be dense. The most difficult part for any method to efficiently construct a representation of the occupied subspace with $\mathcal{O}(n)$ memory and time usage is to bring about sparsity while controlling errors. In this section we will consider methods that employ the density matrix to represent the occupied subspace. Together with careful approaches to bring about sparsity, it is at least with some of these methods possible to control the error in the occupied subspace. The aim of solving the eigenvalue problem in (12-38) is not always to obtain a representation of the occupied subspace. Therefore methods have been developed that avoid the full solution of (12-38) but that do not return the density matrix. Examples include methods to estimate the distribution of eigenvalues [53] and methods to compute a subset of physically relevant eigenvectors, usually in a window around the band gap [54, 55].

Here we focus on self-consistent field calculations where a representation of the whole occupied invariant subspace is needed to compute a new Fock/Kohn-Sham matrix. We consider two classes of methods: energy minimization and polynomial expansion methods. These methods generate a representation of the occupied subspace in terms of the density matrix D without need for computation of any orthonormal basis $Q_{\mathcal{X}}$ for \mathcal{X} . The methods rely on sparse matrix–matrix multiplication. Therefore, linear scaling in time and memory is possible provided that the matrices can be kept sufficiently sparse.

12.8.1. Energy Minimization

The correct density matrix D minimizes

$$\text{Tr}[DF] \tag{12-39}$$

under the constraints $D = D^2$ (hereinafter *the idempotency condition*) and $\text{Tr}[D] = n_{\text{occ}}$ (hereinafter *the trace condition*) [56]. The idea of energy minimization methods is to find a functional based on (12-39), somehow taking the constraints into account, and apply some minimization scheme such as the conjugate gradient method or Newton’s method [57].

12.8.1.1. First Attempts

Li, Nunes, and Vanderbilt suggested to handle the idempotency condition by replacing the density matrix in (12-39) with its so-called McWeeny-purified version,

and the trace condition by shifting the Fock/Kohn-Sham matrix with the chemical potential μ [58]. This results in the functional

$$\Omega_{\text{LNV}}(D) = \text{Tr}[(3D^2 - 2D^3)(F - \mu I)]. \quad (12-40)$$

Later Millam and Scuseria eliminated the need to know the chemical potential by a modification of the LNV functional [59];

$$\Omega_{\text{MS}}(D) = \text{Tr}[(3D^2 - 2D^3)F] + \mu(\text{Tr}[D] - n_{\text{occ}}). \quad (12-41)$$

In this method the initial density matrix is chosen to have correct trace. The trace condition is then satisfied throughout the minimization by choosing μ so that the trace of the gradient $\nabla\Omega_{\text{MS}}(D)$ is equal to zero in each step. Similar methods were presented by Daw [60] and Challacombe [61].

Provided that the idempotency condition is satisfied, both the functionals above properly take the trace condition into account. The problem, however, is that the desired solution is not a global minimum because of the way the idempotency condition is handled. It is easy to construct a matrix that gives a lower functional value than the desired density matrix. As a consequence one has to be careful during the optimization and make sure not to leave the stable region.

12.8.1.2. Parametrized Minimization

The idempotency problem can be avoided by use of an exponential parametrization of the density matrix. Given an approximate density matrix D_i that fulfills the trace and idempotency conditions, a new density matrix that fulfills the conditions as well, can be expressed in terms of an antisymmetric matrix X [62];

$$D_{i+1} = e^X D_i e^{-X}. \quad (12-42)$$

Once again we modify (12-39) by inserting our expression for the density matrix and obtain the functional

$$\Omega(X) = \text{Tr}[F e^X D_i e^{-X}]. \quad (12-43)$$

After improving X according to the used optimization scheme, for example by taking a step in the gradient direction, an improved density matrix D_{i+1} is given by (12-42). Equation (12-42) can be evaluated using the so-called Campbell-Baker-Hausdorff expansion [9];

$$e^X D_i e^{-X} = D_i + [X, D_i] + \frac{1}{2!} [X, [X, D_i]] + \frac{1}{3!} [X, [X, [X, D_i]]] + \dots \quad (12-44)$$

where

$$[A, B] = AB - BA. \quad (12-45)$$

Exponential parametrization was used in Refs. [63–65]. This is a conceptually appealing way of dealing with the idempotency and trace conditions. There are however some difficulties that need to be addressed when the exponential parametrization is applied. For example, it seems difficult to know how many terms of the expansion (12-44) to use. If too few terms are included, the conservation of idempotency could be lost. For this reason, an ad-hoc restriction of the step length, i.e. the magnitude of X , was used in Ref. [65]. If many terms are included, idempotency could anyway be lost due to accumulating errors in the recursive evaluation. Furthermore, it is unclear how sparse the matrix X is and whether that sparsity has to be enforced by truncation of small matrix elements, and what impact that would have on accuracy and convergence.

12.8.2. Polynomial Expansions

The density matrix can be defined using the step function

$$D = f(F) = \theta(\mu I - F) \quad (12-46)$$

where

$$\theta(x) = \begin{cases} 0 & \text{if } x < 0 \\ 1 & \text{otherwise} \end{cases} \quad (12-47)$$

is the Heaviside step function. By applying the step function $f(x)$, eigenvalues corresponding to the occupied and virtual invariant subspaces of F are mapped to 1 and 0 respectively. At first impression the discontinuity at μ may discourage any attempt to approximate this function by a polynomial expansion. However, in cases when there is a gap between the occupied and virtual parts of the eigenspectrum, the density matrix can be accurately computed without high resolution of the step; a polynomial $p(x)$ that varies smoothly between 0 and 1 in the gap may be used [66, 67], see Figure 12-8. We will discuss two different ways to construct such a polynomial $p(x)$: Chebyshev expansion and iterative density matrix purification.

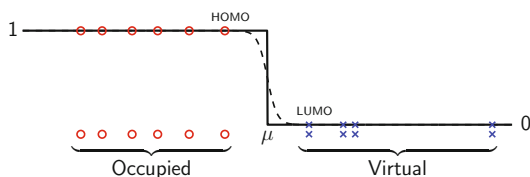


Figure 12-8. Schematic picture illustrating mapping by the step function $f(x)$ (solid line) of eigenvalues corresponding to occupied and virtual subspaces respectively. A function $p(x)$ (dashed line) that varies smoothly between 0 and 1 may be used to approximate $f(x)$. The only requirement on p is that it maps all eigenvalues to their desired values of 0 and 1

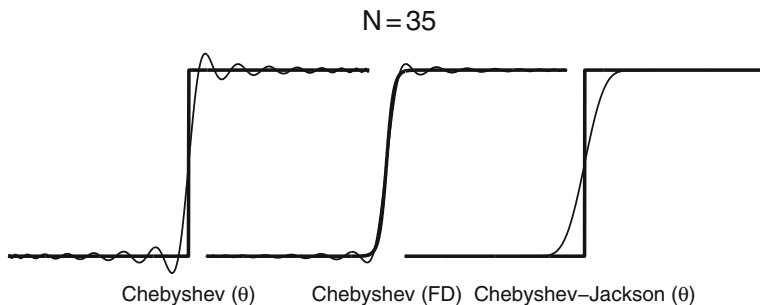


Figure 12-9. Chebyshev approximations of the Heaviside step function (θ) using $N = 35$ Chebyshev polynomials. *Left*: Chebyshev expansion of the Heaviside step function. *Center*: Chebyshev expansion of the Fermi-Dirac function (FD) with $\beta = 50$. *Right*: Chebyshev expansion of the Heaviside step function using the Jackson damping factors

12.8.2.1. Chebyshev Expansion

The Heaviside step function can be approximated by a truncated Chebyshev expansion. Straightforward application of the Chebyshev expansion leads, however, to Gibbs oscillations and errors that spread over the entire interval, see Figure 12-9. A possible remedy is to replace the Heaviside function with some function that varies smoothly between 0 and 1 in the HOMO-LUMO gap [67–70]. One choice is the Fermi-Dirac function

$$\frac{1}{1 + e^{-\beta(\mu - F)}} \quad (12-48)$$

where β depends on the HOMO-LUMO gap; the smaller the HOMO-LUMO gap is, the larger β is needed. In this way the oscillations are reduced, as seen in Figure 12-9. However, the convergence towards 0 and 1 is anyway slow and purification, discussed in the following section, is often needed to get the eigenvalues sufficiently close to their desired values of 0 and 1 [70].

An alternative way to reduce the oscillations is to use some Gibbs damping factors in the Chebyshev expansion [71]. In the rightmost function depicted in Figure 12-9 the so-called Jackson kernel [71] has been used to reduce the oscillations. While the oscillations have been successfully damped, a disadvantage with the Jackson kernel is that the slope at the inflexion point is smaller.

12.8.2.2. Density Matrix Purification

Another way of constructing a polynomial $p(x)$ to approximate the step function, as depicted in Figure 12-8, is to iteratively apply low-order polynomials that push the eigenvalues towards 0 and 1 until convergence. Usually this is done by an initial linear transformation f_0 that maps the eigenvalues of F into the $[0, 1]$ interval, followed by application of a sequence of polynomials f_i , $i = 1, 2, \dots$ with fixed points at 0 and 1:

$$\begin{aligned} X_0 &= f_0(F) \\ X_i &= f_i(X_{i-1}) \end{aligned} \quad (12-49)$$

Already in 1956, McWeeny suggested to use the polynomial $x^2(3 - 2x)$ to refine matrices that are roughly idempotent [56]. During the last decade researchers have realized that purification transforms similar to the McWeeny polynomial can be used to improve the computational complexity of the entire $F \rightarrow D$ step. In 1998, Palser and Manolopoulos presented two purification algorithms that both fit into the general scheme of (12-49) [72]. In the first one, referred to as *grand-canonical purification*, f_0 is such that the occupied and virtual parts of the eigenspectrum of X_0 end up in the $[0.5, 1]$ and $[0, 0.5]$ intervals respectively. After that, the McWeeny polynomial is used to push eigenvalues to their desired values. Because of the fixed point at 0.5, the chemical potential μ is conserved throughout the iterations. Palser and Manolopoulos also propose *canonical purification* which does not require knowledge of the chemical potential for the initial transformation. This method conserves the trace instead of the chemical potential; the initial transformation makes sure that X_0 has the correct trace instead of correct chemical potential. After that, the polynomials are chosen such as to conserve the trace while pushing eigenvalues towards 0 and 1.

Subsequent to the work by Palser and Manolopoulos, a number of purification algorithms have been proposed [73–78]. Most of these proposals focus on finding polynomials that optimize the convergence of eigenvalues. Significant improvements were also made in this respect. The main difficulty with purification lies, however, in preserving the occupied subspace throughout the iterations when small matrix elements are removed to maintain sparsity.

Among the proposed purification polynomials, we would like to recommend the use of the so-called trace-correcting purification polynomials x^2 and $2x - x^2$ suggested by Niklasson [73]. Using these low order polynomials is advantageous because only a single matrix multiply is needed in each iteration. This simplifies error control and reduces the need to store intermediate matrices [79]. How to control errors is further discussed in Section 12.8.3.

12.8.2.3. Polynomial Evaluation

The Chebyshev expansion and density matrix purification methods construct in different ways a high order polynomial that approximates the step function in (12-46). A polynomial like the Chebyshev expansion can be efficiently evaluated using the method proposed by Paterson and Stockmeyer [80]. With this method, a polynomial of order 25 can, for example, be evaluated with 8 matrix–matrix multiplications. Although this represents a significant improvement compared to straightforward evaluation, iterative construction of polynomials as in density matrix purification is much more efficient. By recursive application of low order polynomials, the polynomial degree increases exponentially with the number of matrix–matrix

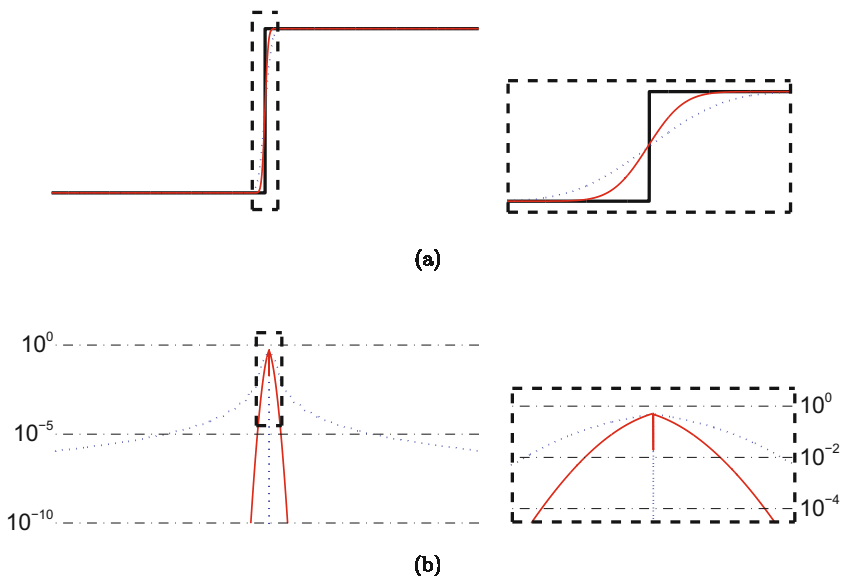


Figure 12-10. Comparison of two different ways to approximate a step function: Chebyshev expansion and purification methods. The methods have been allowed to use 20 matrix – matrix multiplications each. This gave a polynomial degree of 121 for the Chebyshev expansion and $2^{20} = 1,048,576$ for the purification method. The solid lines show the result for purification. The purifying polynomials x^2 and $2x - x^2$ have been applied. The dotted lines show the result for a Chebyshev-Jackson approximation of the step function using the Paterson-Stockmeyer polynomial evaluation method. (a) A step function $f(x)$ approximated by a Chebyshev-Jackson expansion $p_{CJ}(x)$ (dotted lines) and purification $p_P(x)$ (solid lines). The right figure shows a closeup of the step. (b) Absolute errors $(|f(x) - p_X(x)|)$ of the two step function approximations, Chebyshev-Jackson (X=CJ, dotted lines) and purification (X=P, solid lines), depicted in Panel (a)

multiplications. By repeated application of x^2 one can for example generate a polynomial of order 2^m with only m multiplications. The difference between the two methods is illustrated in Figure 12-10.

12.8.3. Accuracy

Some problems are inherently more difficult than others, regardless of the computational method used to solve them. Therefore, the accuracy of a solution to a problem does not only depend on the algorithm used to solve the problem but also on the problem itself. In the following we will first consider the so-called condition number of the $F \rightarrow D$ problem and then analyze the forward error.

12.8.3.1. Conditioning

A problem is said to be well-conditioned if its solution is insensitive to perturbations in the input data. In other words, for a well-conditioned problem, a small change in the input results in a small change in the exact solution. A *condition number*

associated with a problem is a measure of the conditioning of the problem. A problem with low condition number is well-conditioned whereas a problem with high condition number is ill-conditioned. For the problem of computing a new density matrix for a given Fock matrix, the condition number can be defined as

$$\kappa_F = \lim_{h \rightarrow 0} \sup_{A: \|A\|_2 = \|F\|_2} \frac{\|D(F + hA) - D(F)\|_2}{h}. \quad (12-50)$$

Here, we used the notation $D(F)$ for the exact density matrix corresponding to a given Fock/Kohn-Sham matrix F . In Ref. [79] it is shown that

$$\kappa_F = \frac{\|F\|_2}{\xi} \quad (12-51)$$

where ξ is the size of the HOMO-LUMO gap. It is well-known that problems with small HOMO-LUMO gaps, arising for example from metallic systems, are difficult to solve. Equation (12-51) gives a mathematical explanation to these difficulties; as $\xi \rightarrow 0$, $\kappa_F \rightarrow \infty$. If the HOMO-LUMO gap vanishes, the problem does not even have a unique solution. Because of (12-51), we expect all density matrix construction methods to run into difficulties as ξ decreases. The difficulties may just become manifest in different ways. Density matrix purification, for example, will for small gaps require more iterations to converge and tighter threshold values to conserve the occupied subspace. This is thoroughly discussed in Ref. [79]. In energy minimization methods small gaps are likely to result in shallow minima which will make the convergence of for example the conjugate gradient method more sensitive to perturbations. In some cases, however, a small HOMO-LUMO gap should be regarded as a sign of a modeling problem for the studied molecular system. For example, incorrect protonation in protein molecule studies can lead to small gaps and difficulties to converge the whole self-consistent field procedure.

12.8.3.2. Forward Error Analysis

Error analysis can be carried out in different ways. The natural way is to analyze the difference between the computed result and the exact solution. This difference is sometimes referred to as the *forward error*. The *backward error* is the smallest possible change in input for which the exact solution is equal to the approximate solution of the original problem. In other words, the backward error is obtained by analyzing which problem the algorithm actually solved. Here, however, we shall focus on the forward error. Let D denote the exact density matrix corresponding to the Fock/Kohn-Sham matrix F and let \tilde{D} denote the approximate matrix obtained by the applied algorithm. The forward error can be defined as

$$\varepsilon = \|\tilde{D} - D\|_2. \quad (12-52)$$

In Ref. [79], the forward error of density matrix purification is analyzed and schemes to control the forward error are proposed. A key in the analysis is to distinguish

between errors in the occupied invariant subspace $\tilde{\mathcal{X}}$ of \tilde{D} and errors in eigenvalues. The forward error is separated into two parts;

$$\underbrace{\|\tilde{D} - D\|_2}_{\equiv \varepsilon} \leq \underbrace{\|\tilde{D} - P_{\tilde{\mathcal{X}}}\|_2}_{\equiv \varepsilon^\lambda} + \underbrace{\|P_{\tilde{\mathcal{X}}} - D\|_2}_{\equiv \varepsilon^\Theta}, \quad (12-53)$$

where $P_{\tilde{\mathcal{X}}}$ denotes the matrix for orthogonal projection onto the subspace $\tilde{\mathcal{X}}$. The first norm on the right hand side, ε^λ , measures only deviations of the eigenvalues of \tilde{D} from 0 and 1, and the second norm on the right hand side, ε^Θ , measures only errors in the occupied subspace; recall that D is the matrix for projection onto the subspace \mathcal{X} . In density matrix purification, ε^λ is expected to be large in the early iterations and decrease as the polynomial expansion approaches a step function. The subspace error, ε^Θ , is small in the early iterations but grows as the purification proceeds. Note also that (12-53) gives a natural convergence criterion; as soon as the forward error is dominated by ε^Θ , it is time to stop the purification process since no further progress can be made.

The separation of the forward error given by (12-53) is likely to be useful also for error and convergence analysis in other density matrix methods. In particular, the parameterized energy minimization is likely to benefit from such an analysis. In this class of methods, the subspace error is expected to decrease over the iterations whereas the error in eigenvalues is expected to be small. The parameterized energy minimization is in a way opposite to density matrix purification: In purification, one tries to move the eigenvalues to their desired values while conserving the occupied subspace. In parameterized energy minimization, one tries to rotate the occupied subspace while conserving the eigenvalues.

12.8.4. Density Matrix Construction in Ergo

In the Ergo program, linear scaling density matrix construction is performed using the density matrix purification method described in Ref. [79]. This purification method employs the trace correcting purification polynomials x^2 and $2x - x^2$. The most important feature of the purification scheme presented in Ref. [79] is that removal of small matrix elements is performed in such a way that the accuracy in the occupied subspace is strictly controlled, as was briefly discussed in the previous section. Thus, the $F \rightarrow D$ step can be performed with linear scaling processor time and memory usage while controlling erroneous rotations occurring in each self-consistent field iteration as was envisioned in Section 12.2.

12.9. SPARSE MATRIX REPRESENTATIONS

Sparsity in matrices and efficient access to nonzero matrix elements are imperative for the efficiency of the algorithms discussed in the previous sections.

Each element in the Fock/Kohn–Sham matrix F , the overlap matrix S , and the density matrix D corresponds to two basis functions centered at two atom centers of the molecule, see Figure 12-11. The magnitude of a matrix element generally

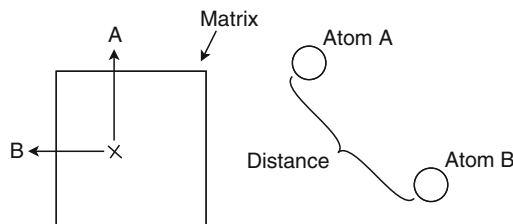


Figure 12-11. Each matrix element corresponds to two basis function centers, usually located at atom centers. Hence, each element is associated with a distance between two atoms

depends on the distance between the two atom centers; if the distance is large, the corresponding matrix element is likely to be of small magnitude. If small matrix elements are removed, we can take advantage of the matrix sparsity that appears for extensive molecular systems. However, the removal of small matrix elements is an approximation which can introduce significant errors, if not done carefully. As discussed in Section 12.2, errors incurred by approximations can be seen as erroneous rotations of the occupied subspace.

Two questions should be addressed when sparse matrix representations are used in self-consistent field calculations: (1) How to remove small matrix elements while being in control of the occupied subspace? (2) How to store and operate on only nonzero matrix elements with high performance?

12.9.1. How to Select Small Matrix Elements for Removal

We wish to remove small matrix elements that contribute little to the overall accuracy. More precisely, we would like to remove elements in such a way that we are in control of errors in the occupied subspace. Removal of small matrix elements (herein often referred to as *truncation*) can be seen as a perturbation E of the original matrix X so that the matrix after truncation

$$\tilde{X} = X + E. \quad (12-54)$$

It is not obvious when a matrix element should be considered to be negligible. One popular approach has been to remove all elements that correspond to an interatomic distance larger than some predefined cutoff radius [58, 64, 65, 69, 70, 72, 81]. If matrix elements are grouped into submatrices, each submatrix corresponds to two groups of atoms. In this case, the submatrix is dropped if the shortest distance between the two groups is greater than the predefined cutoff radius. Another approach to remove small elements is to drop all matrix elements below some predefined threshold value [59, 63, 82]. If elements are grouped into submatrices, a submatrix is dropped when its norm is below the threshold [61, 74]. Unfortunately, a direct relation between threshold value and accuracy in the occupied subspace has not been known for any of these methods. We recall from Section 12.2 that controlling the occupied subspace amounts to controlling some unitary-invariant norm of

the error matrix and knowing the HOMO–LUMO gap [8]. In Ref. [83] we argue that the Euclidean norm is a suitable choice of unitary-invariant norm and propose Euclidean norm based truncation schemes. In these methods, small matrix elements are removed while ensuring that

$$\|E\|_2 \leq \tau \quad (12-55)$$

where the threshold value τ should be chosen based on the HOMO–LUMO gap and the desired accuracy in the occupied subspace, see (12-12).

12.9.2. How to Store and Access Only Nonzero Elements

After removal of small matrix elements according to the previous section, we hopefully have a matrix with many zero matrix elements. The best possible data structure for a sparse matrix depends on several factors such as the number of nonzero elements, the nonzero pattern, and the algorithms used to access the elements. If the matrix has many nonzero elements per row that lie close to each other, it can be advantageous to use a blocked data structure. Often, data locality can be improved by permuting the rows and columns of the matrix.

12.9.2.1. Permutations for Data Locality

The matrices that occur in Hartree–Fock and Kohn–Sham calculations with Gaussian basis sets often have thousands of nonzero elements per row [5, 84]. The matrices are to be regarded as semi-sparse rather than sparse. For this reason, a blocked sparse data structure is usually employed where nonzero matrix elements are grouped into submatrix blocks. The use of a blocked data structure can significantly increase the performance of matrix operations. However, grouping nonzero matrix elements into submatrices without losing sparsity is only possible if the nonzero elements are neighbors. In Figure 12-12, the nonzero patterns of two matrices with 50% nonzero elements each are depicted. The figure shows that for the same sparsity level, the data locality can be quite different. In this case, however,

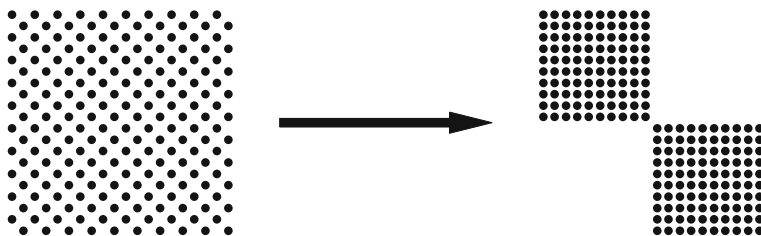


Figure 12-12. This figure illustrates how permutations of matrix rows and columns can result in improved data locality. Each dot corresponds to a nonzero matrix element. The left matrix has perfect non-locality in the sense that no nonzero matrix element is an immediate neighbor of another nonzero matrix element. In the right matrix the data locality has been dramatically improved by a permutation of the rows and columns of the left matrix

the left matrix can be transformed to the right matrix by a permutation of its rows and columns.

The distance–magnitude relation described earlier in this section can be used to achieve data locality in the overlap, Fock/Kohn–Sham, and density matrices. Challacombe grouped basis functions belonging to the same atom and formed in this way *atom blocks* [61]. Later, it was recognized that the performance in submatrix operations, using standard dense matrix linear algebra libraries [85–88], could be improved if basis functions belonging to several neighboring atoms were grouped into larger *multi–atom blocks* [81]. With atom or multi–atom blocks, the block size cannot be chosen at will. Therefore, the use of a uniform block size was suggested in Ref. [13]. This means that basis functions centered on the same atom are not restricted to be in the same block. Using a uniform block size makes it easier to tune the block size with respect to the performance of a dense matrix library. Alternatively, one can tune small dense matrix operations for a single given block size.

Approaches that are not explicitly based on the distance–magnitude relation also exist. In Ref. [14], for example, the matrix is seen as the connection matrix for a weighted network. This allows for network theory to be used to find community divisions of the network which correspond to a permutation and block partitioning of the matrix.

12.9.2.2. *Data Structures*

In the Ergo quantum chemistry program, a hierarchic sparse matrix data structure is used for numerical linear algebra [13]. This data structure consists of a hierarchy of matrices where the matrices at the upper levels consist of lower level hierarchic matrices. At the lowest level a simple column wise dense matrix data structure is used. Sparsity is utilized by not storing or operating on parts of the hierarchy that contain only zero elements. At higher levels the implementation of routines such as matrix–matrix multiplication is straightforward, at the lowest level the program can be linked to some optimized dense linear algebra library.

The main advantage with the hierarchic data structure is that new algorithms are easy to develop and implement. Another advantage is that matrix symmetry can easily be exploited, giving a speedup close to 2 for many operations. Hierarchic data structures have previously been used to reduce cache misses in dense matrix operations, see for example Ref. [89]. Whereas an improved cache hit rate may be a positive side effect of the data structure proposed in Ref. [13], our main motivation for using a hierarchy is to utilize sparsity in an efficient and transparent manner.

12.10. BENCHMARKS

In this section, results from a set of benchmark calculations are presented, in order to demonstrate the performance and scaling behavior of Kohn–Sham density functional theory calculations performed with the Ergo program. The molecular systems used in these tests are glutamic acid–alanine helix molecules of increasing length.

Becke's half-and-half exchange functional with the LYP correlation functional (BHandHLYP) [90] was used, with the 3-21G and 6-31G** basis sets.

The calculations were run on an HP ProLiant DL140 G3 computer with dual Intel Xeon E5345 2.33 GHz Quad Core processors with 4 MB Level 2 cache and 32 GB of shared memory, running the Linux CentOS 5 operating system. The Ergo source code was compiled using the Intel C++ compiler version 10.1 and linked to the Intel Math Kernel Library version 9. In order to reduce the memory usage, data such as sparse matrices and grid points for numerical integration were stored on scratch disk space when not needed.

The glutamic acid-alanine helix molecule files were generated using the "build sequence" function in the Spartan program [91], with the alpha helix option selected. We refer to these systems as $[\text{GluAla}]_n$ where n is the number of repeating glutamic acid-alanine units.

In our implementation of the hybrid Kohn-Sham density functional theory self-consistent field method, there are several parameters that affect the accuracy and computational cost of different parts of the calculation: threshold values for the truncation of matrices (τ_M), density matrix purification (τ_P), Coulomb matrix construction (τ_J), and exchange matrix construction (τ_K), as well as several parameters for the grid used in the exchange-correlation integration: the radial integration threshold (τ_r) and the angular integration order (N_{ang}). In general, we follow Ref. [45] and use radial T2 quadrature with M4 mapping of r , giving 34 radial integration points for carbon atoms. For angular integration, we use Lebedev grids of order 29, pruning them when necessary for small r . This grid has in total 6,428 grid points per carbon atom.

The truncation of matrices is done so that the norm of the error matrix is smaller than τ_M , except for the truncations of matrices inside the density matrix purification routine. Density matrix purification is done as described in [79], with the requested accuracy in the occupied subspace set to τ_P . In the Coulomb and exchange matrix routines, contributions to result matrix elements are neglected if they are smaller than τ_J and τ_K , respectively. In the calculations reported here, we used $\tau_J = \tau_K = 10^{-7}$ for Coulomb and exchange matrix construction, and $\tau_M = 10^{-6}$ and $\tau_P = 10^{-5}$.

Figure 12-13 shows the total wall time needed to complete the whole electronic structure calculation using the 3-21G basis set, including all initialization such as the one-time computation of the core Hamiltonian matrix, Cholesky decomposition to get an inverse factor Z of the overlap matrix, etc. The total wall times for the 6-31G** calculations were five to six times longer for all system sizes. Timings for one SCF cycle, broken down into the different parts, are shown in Figure 12-14.

The most time-critical parts of the code are threaded, using OpenMP for the matrix operations and POSIX threads for parts of the Coulomb and exchange matrix construction steps as well as the exchange-correlation numerical integration. However, some parts of the code are not threaded. In particular, a preparatory step needed before the exchange matrix computation is serial. This part is denoted as "Exchange prep" in Figure 12-14. Clearly, that part should also be threaded in order to make efficient use of a multicore computer system. Instead of the ideal speedup

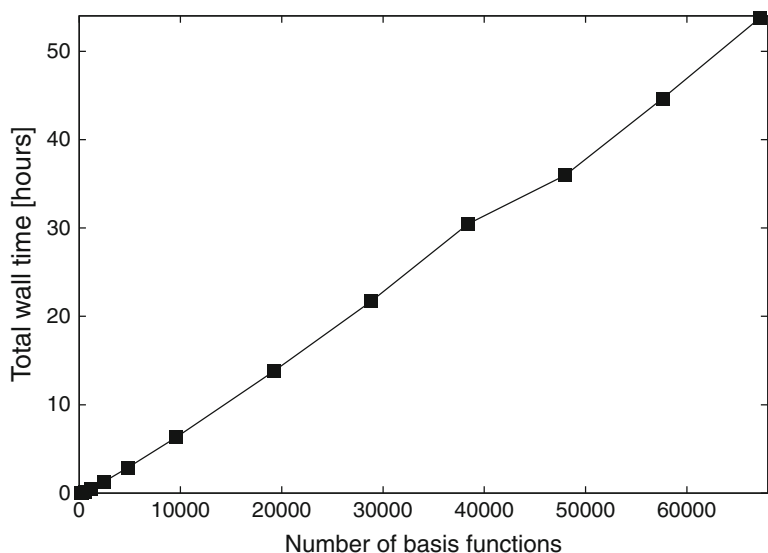


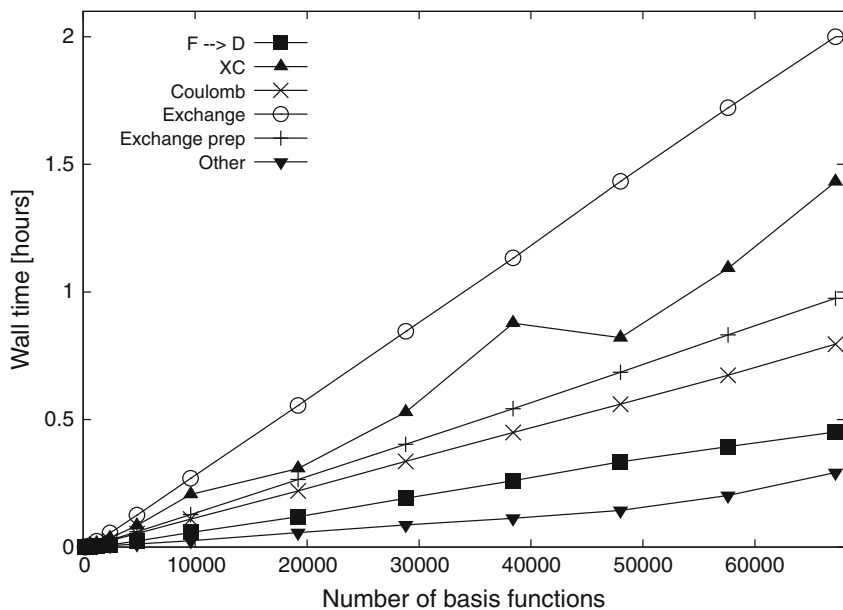
Figure 12-13. Density functional theory BHandHLYP/3-21G calculations on glutamic acid-alanine helix systems of varying size. Total wall times for the whole calculations. This includes all parts, including one-time computation of overlap and core Hamiltonian matrices and evaluation of the inverse Cholesky factor, see Algorithm 1

of 8 for an 8-core computer, in these benchmark calculations the threading gave an overall CPU time vs wall time ratio of around 5.5.

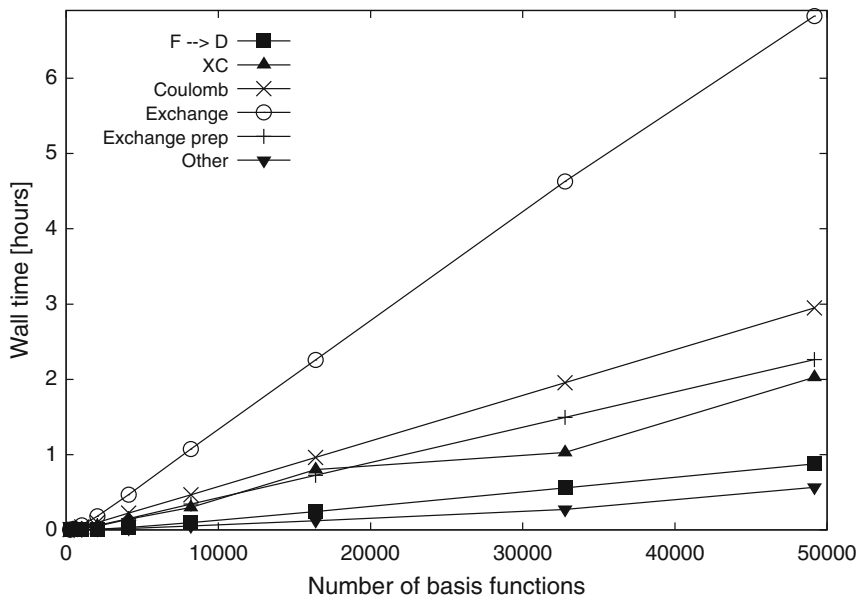
When comparing the timings in Figure 12-14 it should be noted that the threshold values were chosen ad-hoc; the errors from computational approximations in the different parts are probably not well balanced. In order to not waste computational resources, the threshold values should be selected so that the different parts contribute equally to the error in the occupied subspace as outlined in Ref. [8]. However, that has not yet been implemented in the Ergo program, making it difficult to do a fair comparison of the performance of different parts of the code. The irregularities in the exchange-correlation integration timings probably result from a too conservative determination of the exchange-correlation matrix sparsity pattern.

The peak virtual memory usages for the 3-21G and 6-31G** calculations are shown in Figure 12-15. The plotted memory usage is the virtual memory usage as reported by the operating system. The virtual memory usage is an upper limit on the amount of actual resident memory used by the program. The final data point in Figure 12-15(a) shows that the peak virtual memory usage actually went down

Figure 12-14. Density functional theory BHandHLYP calculations on GluAla helix systems of varying size using the basis sets 3-21G and 6-31G**. Timings for the different parts of self-consistent field cycle 4. $F \rightarrow D$: Density matrix purification including congruence transformations.



(a)



(b)

Figure 12-14. (continued) XC: Evaluation of the exchange-correlation matrix. Coulomb: Evaluation of the Coulomb matrix. Exchange: Evaluation of the exchange matrix. Exchange prep: Preparation for the exchange matrix evaluation, see the text. Other: Intermediate steps such as evaluation of the $FDS - SDF$ commutator needed for DIIS and other matrix operations. (a) Basis set 3-21G. (b) Basis set 6-31G**

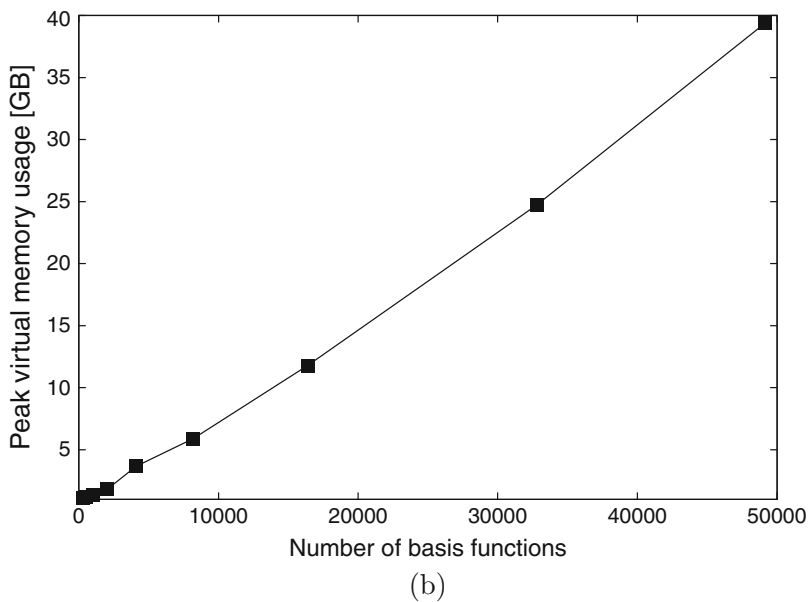
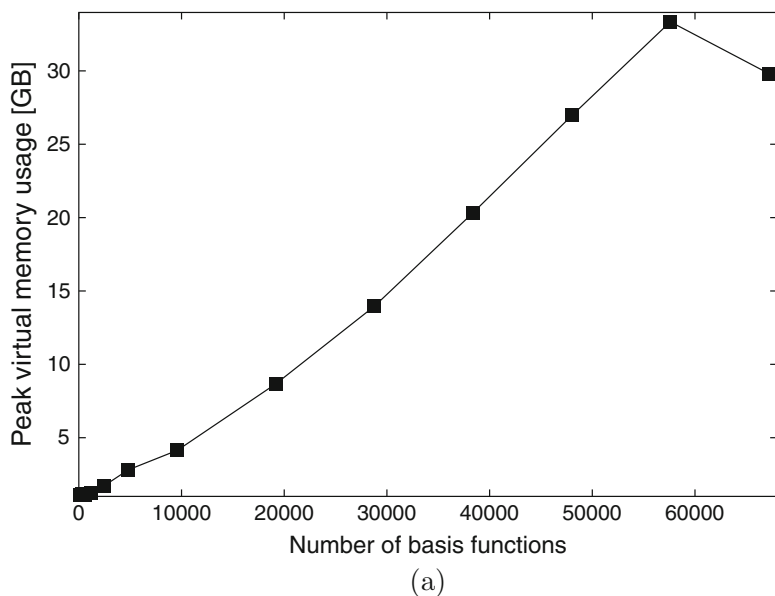


Figure 12-15. Density functional theory BHandHLYP calculations on GluAla helix systems of varying size using the basis sets 3-21G and 6-31G**. Peak virtual memory usage as reported by the operating system. The decrease in virtual memory usage when going from 57,604 to 67,204 basis functions for the 3-21G case is likely due to the operating system reorganizing the memory as the memory usage approaches the amount of physical memory available. (a) Basis set 3-21G. (b) Basis set 6-31G**

as compared to the previous system size. This effect is likely due to the operating system reorganizing the memory as the memory usage approaches the amount of physical memory available.

HOMO-LUMO gaps (band gaps) for the 3-21G calculations are plotted in Figure 12-16. The computed HOMO-LUMO gaps for the larger GluAla systems are around 2.5 eV. For the 6-31G** basis set, the computed HOMO-LUMO gaps for the larger GluAla systems are around 2.8 eV. Note that these values are strongly dependent on the amount of Hartree-Fock exchange included in the chosen hybrid density functional. The BHandHLYP functional used here includes 50% Hartree-Fock exchange. A lower fraction of Hartree-Fock exchange, as in the popular B3LYP functional, would result in much smaller HOMO-LUMO gaps. Hartree-Fock calculations on these GluAla helices give HOMO-LUMO gaps of around 7 eV [5].

The largest calculation we could treat with the 3-21G basis set on the used computer system was [GluAla]₄₄₈, C₃₅₈₄N₈₉₆O₁₇₉₂H₅₃₇₈, corresponding to 67,204 basis functions. The largest system for 6-31G** was [GluAla]₁₉₂, C₁₅₃₆N₃₈₄O₇₆₈H₂₃₀₆, corresponding to 49,162 basis functions. For the 3-21G case, the starting guess was taken as a projection of the density from a previously converged Hartree-Fock STO-2G calculation. The smallest 3-21G calculations up to around 10,000 basis functions converged in 8 SCF iterations, while the larger ones needed 9 iterations.

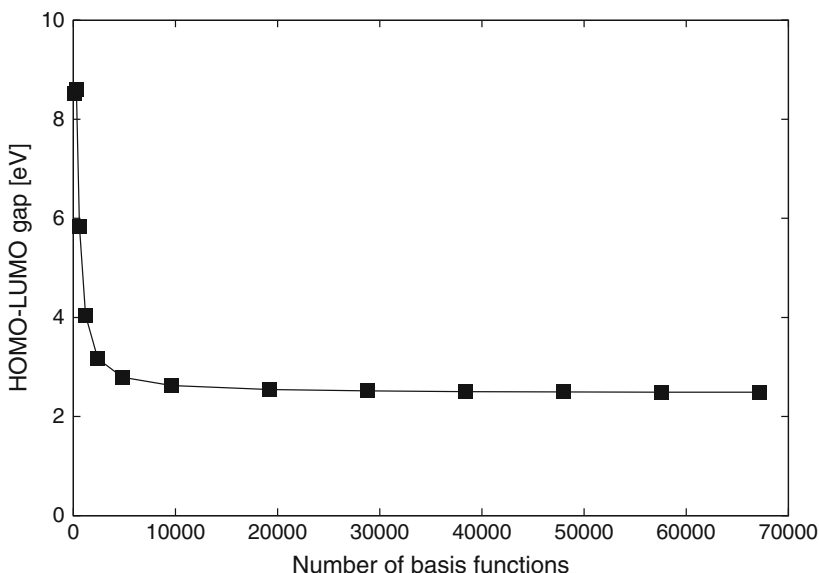


Figure 12-16. Density functional theory BHandHLYP/3-21G calculations on GluAla helix systems of varying size. HOMO-LUMO gaps. It seems that the HOMO-LUMO gap for long helices converges to around 2.5 eV. However, this value is strongly dependent on the density functional, see the text

The converged 3-21G densities were then used as starting guesses for the 6-31G** calculations. Each 6-31G** calculation converged in 7 SCF iterations.

By comparison to calculations with tighter thresholds to achieve higher accuracy, we have found that the choices of threshold values used in these benchmarks give errors in total energies smaller than 2×10^{-5} Hartree/atom for the studied systems.

12.11. CONCLUDING REMARKS

Our experiences from development of the Ergo program show that linear scaling Hartree-Fock and Kohn-Sham density functional theory calculations are indeed possible, not only in theory but also in practice. A whole electronic structure calculation can thus be performed using computational resources – both time and memory – that scale only linearly with the size of the studied molecular system.

Because of the many computational approximations employed in this kind of calculations, they have so far employed a large number of parameters that affect the performance and accuracy. This has limited the usefulness of these methods. In this article we have discussed ways to remedy this problem by automatic selection of threshold values. Such automatic selection procedures have so far only partially been included in the Ergo code, but we plan to implement it fully in the near future. This would not only increase the usefulness of the code for users who are not familiar with the internal workings of the linear scaling algorithms used, but also allow more efficient calculations since balanced accuracy throughout the code would reduce the redundant use of computer resources.

Another important future aspect is parallelization. The linear scaling algorithms discussed here are relatively straightforward to parallelize for shared memory computer architectures, but for distributed memory the task of parallelization is more challenging. Although pioneering work in this respect has been done [34, 92, 93], we are not aware of any complete parallel implementation of a linear scaling Hartree-Fock or hybrid Kohn-Sham density functional theory method. Aside from the issue of error control, we consider distributed memory parallelization as the most important challenge for the future.

REFERENCES

1. Goedecker S (1999) *Rev Mod Phys* 71:1085
2. Bowler DR, Miyazaki T, Gillan MJ (2002) *J Phys Condens Matter* 14:2781
3. Wu SY, Jayanthi CS (2002) *Phys Rep* 358:1
4. Rudberg E, Rubensson EH, Sałek P Ergo (2009) Version 2.0: a quantum chemistry program for large scale self-consistent field calculations. www.ergoscf.org
5. Rudberg E, Rubensson EH, Sałek P (2008) *J Chem Phys* 128:184106
6. Rubensson EH (2008) Matrix algebra for quantum chemistry. PhD thesis, Department of Theoretical Chemistry, Royal Institute of Technology, Stockholm
7. Rudberg E (2007) Quantum chemistry for large systems. PhD thesis, Department of Theoretical Chemistry, Royal Institute of Technology, Stockholm
8. Rubensson EH, Rudberg E, Sałek P (2008) *J Math Phys* 49:032103
9. Helgaker T, Jørgensen P, Olsen J (2000) *Molecular electronic-structure theory* Wiley, Chichester

10. Pulay P (1980) *Chem Phys Lett* 73:393
11. Pulay P (1982) *J Comput Chem* 3:556
12. Benzi M, Kouhia R, Tuma M (2001) *Comput Meth Appl Mech Eng* 190:6533
13. Rubensson EH, Rudberg E, Sałek P (2007) *J Comput Chem* 28:2531
14. Rubensson EH, Bock N, Holmström E, Niklasson AMN (2008) *J Chem Phys* 128:104105
15. Lea Thøgersen (2005) Optimization of densities in Hartree-Fock and density-functional theory, Atomic orbital based response Theory, and Benchmarking for radicals. PhD thesis, Department of Chemistry, University of Aarhus, Aarhus
16. Kudin KN, Scuseria GE (2007) *Math Model Num Anal* 41:281
17. Zerner MC, Hehenberger M (1979) *Chem Phys Lett* 62:550
18. Cancès E, Le Bris C (2000) *Int J Quantum Chem* 79:82
19. Häser M, Ahlrichs R (1989) *J Comput Chem* 10:104
20. Rudberg E, Sałek P (2006) *J Chem Phys* 125:084106
21. Greengard L, Rokhlin V (1987) *J Comput Phys* 73:325
22. Schmidt KE, Lee MA (1991) *J Stat Phys* 63:1223
23. Panas I, Almlöf, J, Feyereisen, MW (1991) *Int J Quantum Chem* 40:797
24. Panas I, Almlöf J (1992) *Int J Quantum Chem* 42:1073
25. White CA, Johnson BG, Gill PMW, Head-Gordon M (1994) *Chem Phys Lett* 230:8
26. White CA, Head-Gordon M (1994) *J Chem Phys* 101:6593
27. Challacombe M, Schwegler E, Almlöf J (1995) *J Chem Phys* 104:4685
28. Challacombe M, Schwegler E (1997) *J Chem Phys* 106:5526
29. White CA, Johnson BG, Gill PMW, Head-Gordon M (1996) *Chem Phys Lett* 253:268
30. Strain MC, Scuseria GE, Frisch MJ (1996) *Science* 271:51
31. Choi CH, Ruedenberg K, Gordon MS (2001) *J Comput Chem* 22:1484
32. Sierka M, Hogeckamp A, Ahlrichs R (2003) *J Chem Phys* 118:9136
33. Watson MA, Sałek P, Macak P, Helgaker T (2004) *J Chem Phys* 121:2915
34. Gan CK, Tymczak C, Challacombe M (2004) *J Chem Phys* 121:6608
35. Schwegler E, Challacombe M (1996) *J Chem Phys* 105:2726
36. Burant JC, Scuseria GE (1996) *J Chem Phys* 105:8969
37. Schwegler E, Challacombe M, Head-Gordon M (1997) *J Chem Phys* 106:9708
38. Ochsenfeld C, White CA, Head-Gordon M (1998) *J Chem Phys* 109:1663
39. Schwegler E, Challacombe M (1999) *J Chem Phys* 111:6223
40. Ochsenfeld C (2000) *Chem Phys Lett* 327:216
41. Lambrecht DS, Ochsenfeld C (2005) *J Chem Phys* 123:184101
42. Aquilante F, Pedersen TB, Lindh R (2007) *J Chem Phys* 126:194106
43. Murray CW, Handy NC, Lamington GJ (1993) *Mol Phys* 78:997
44. Challacombe M (2000) *J Chem Phys* 113:10037
45. Treutler O, Ahlrichs R (1995) *J Chem Phys* 102:346
46. Lebedev VI, vychisl, Zh (1975) *Mat mat Fiz* 45:48
47. Lindh R, Malmqvist PA, Gagliardi L (2001) *Theor Chem Acc* 106:178
48. Becke AD (1988) *J Chem Phys* 88:2547
49. Stratmann RE, Scuseria GE, Frisch MJ (1996) *Chem Phys Lett* 257:213
50. Rudberg E, Rubensson EH, Sałek P (2009) *J Chem Theory Comput* 5:80
51. Sankey OF, Drabold DA, Gibson A (1994) *Phys Rev B* 50:1376
52. Bekas C, Kokipoulou E, Saad Y, SIAM J (2008) *Matrix Anal Appl* 30:397
53. Drabold DA, Sankey OF (1993) *Phys Rev Lett* 70:3631
54. Wang LW, Zunger A (1994) *J Chem Phys* 100:2394
55. Gao B, Jiang J, Liu K, Wu Z, Lu W, Luo Y (2007) *J Comput Chem* 29:434
56. McWeeny R (1956) *Proc R Soc London Ser A* 235:496

57. Heath MT (1997) Scientific computing: an introductory survey. McGraw-Hill, Singapore
58. Li XP, Nunes RW, Vanderbilt D (1993) Phys Rev B 47:10891
59. Millam JM, Scuseria GE (1997) J Chem Phys 106:5569
60. Daw MS (1993) Phys Rev B 47:10895
61. Challacombe M (1999) J Chem Phys 110:2332
62. Helgaker T, Larsen H, Olsen J, Jørgensen P (2000) Chem Phys Lett 327:397
63. Dyan A, Dubot P, Cenedese P (2005) Phys Rev B 72:125104
64. Larsen H, Olsen J, Jørgensen P, Helgaker T (2001) J Chem Phys 115:9685
65. Shao Y, Saravanan C, Head-Gordon M, White CA (2003) J Chem Phys 118:6144
66. Goedecker S, Colombo L (1994) Phys Rev Lett 73:122
67. Goedecker S, Teter M (1995) Phys Rev B 51:9455
68. Baer R, Head-Gordon M (1997) J Chem Phys 107:10003
69. Bates KR, Daniels AD, Scuseria GE (1998) J Chem Phys 109:3308
70. Liang W, Saravanan C, Shao Y, Baer R, Bell AT, Head-Gordon M (2003) J Chem Phys 119:4117
71. Silver RN, Roeder H, Voter AF, Kress JD (1996) J Comput Phys 124:115
72. Palser AHR, Manolopoulos DE (1998) Phys Rev B 58:12704
73. Niklasson AMN (2002) Phys Rev B 66:155115
74. Niklasson AMN, Tymczak CJ, Challacombe M (2003) J Chem Phys 118:8611
75. Holas A (2001) Chem Phys Lett 340:552
76. Mazziotti DA (2003) Phys Rev E 68:066701
77. Xiang HJ, Liang WZ, Yang J, Hou JG, Zhu Q (2005) J Chem Phys 123:124105
78. Pino R, Scuseria GE (2002) Chem Phys Lett 360:117
79. Rubensson EH, Rudberg E, Sałek P (2008) J Chem Phys 128:074106
80. Paterson MS, Stockmeyer L, SIAM (1973) J Comput 2:60
81. Saravanan C, Shao Y, Baer R, Ross PN, Head-Gordon M (2003) J Comput Chem 24:618
82. Maslen PE, Ochsenfeld C, White CA, Lee MS, Head-Gordon M (1998) J Phys Chem A 102:2215
83. Rubensson EH, Rudberg E, Sałek P (2009) J Comput Chem 30:974
84. Rubensson EH, Rudberg E, Sałek P (2007) Proceedings of PARA'06, Springer LNCS 4699:90
85. Gotoblas. <http://www.tacc.utexas.edu/resources/software/#blas>
86. Automatically tuned linear algebra software (ATLAS). <http://mathatlas.sourceforge.net/>
87. Intel math kernel library (Intel MKL). <http://www.intel.com/cd/software/products/asm-na/eng/307757.htm>
88. AMD core math library (ACML). <http://developer.amd.com/cpu/libraries/acml/Pages/default.aspx>
89. Elmroth E, Gustavson F, Jonsson I, Kågström B (2004) SIAM Rev 46:3
90. Becke AD (1993) J Chem Phys 98:1372
91. Spartan'02 (2002) Molecular modeling package by Wavefunction, Inc.
92. Challacombe M (2000) Comp Phys Commun 128:93
93. Bowler DR, Miyazaki T, Gillan MJ (2001) Comp Phys Commun 137:255

CHAPTER 13

CHOLESKY DECOMPOSITION TECHNIQUES IN ELECTRONIC STRUCTURE THEORY

FRANCESCO AQUILANTE¹, LINUS BOMAN², JONAS BOSTRÖM³,
HENRIK KOCH², ROLAND LINDH⁴, ALFREDO SÁNCHEZ DE MERÁS⁵,
AND THOMAS BONDO PEDERSEN⁶

¹ *Department of Physical Chemistry, Sciences II, University of Geneva, 1211 Geneva 4, Switzerland, e-mail: francesco.aquilante@gmail.com*

² *Department of Chemistry, Norwegian University of Science and Technology, N-7491 Trondheim, Norway, e-mail: linus.boman@chem.ntnu.no; henrik.koch@chem.ntnu.no*

³ *Department of Theoretical Chemistry, Chemical Center, University of Lund, S-221 00 Lund, Sweden, e-mail: Jonas.Bostrom@teokem.lu.se*

⁴ *Department of Quantum Chemistry, Uppsala University, SE-751 20, Uppsala, Sweden, e-mail: roland.lindh@kvac.uu.se*

⁵ *Instituto de Ciencia Molecular, Universitat de València, ES-46071 Valencia, Spain, e-mail: sanchez@uv.es*

⁶ *Department of Chemistry, Centre for Theoretical and Computational Chemistry, University of Oslo, Blindern, N-0315 Oslo, Norway, e-mail: t.b.pedersen@kjemi.uio.no*

Abstract: We review recently developed methods to efficiently utilize the Cholesky decomposition technique in electronic structure calculations. The review starts with a brief introduction to the basics of the Cholesky decomposition technique. Subsequently, examples of applications of the technique to *ab initio* procedures are presented. The technique is demonstrated to be a special type of a resolution-of-identity or density-fitting scheme. This is followed by explicit examples of the Cholesky techniques used in orbital localization, computation of the exchange contribution to the Fock matrix, in MP2, gradient calculations, and so-called method specific Cholesky decomposition. Subsequently, examples of calibration of the method with respect to computed total energies, excitation energies, and auxiliary basis set pruning are presented. In particular, it is demonstrated that the Cholesky method is an unbiased method to derive auxiliary basis sets. Furthermore, details of the implementational considerations are put forward and examples from a parallel Cholesky decomposition scheme is presented. Finally, an outlook and perspectives are presented, followed by a summary and conclusions section. We are of the opinion that the Cholesky decomposition method is a technique that has been overlooked for too long. We have just recently started to understand how to efficiently incorporate the method in existing *ab initio* programs. The full potential of the Cholesky technique has not yet been fully explored.

Keywords: Cholesky decomposition, Reduced scaling, Low-rank tensor approximation, Inner projection, Density fitting, Multi-configurational methods, Orbital localization, Linear-scaling correlation methods

13.1. INTRODUCTION

The application of electronic structure methods to large molecular systems using accurate basis sets is limited due to the steep computational scaling many of the methods encounter. The evaluation of two-electron integrals has turned out to be a major bottleneck in most of these methods. Although many different schemes have been devised for calculating two-electron integrals, for instance McMurchie-Davidson, Rys quadrature and Obara-Saika schemes, the algorithms are still demanding, especially for two-electron integrals that contain orbitals with high angular momentum. The altogether best approach to reduce the computational time used for calculating two-electron integrals is to reduce the number of integrals that need to be calculated. The first step in these developments is to avoid calculating integrals that are zero or small and give small contributions to the properties we are calculating. This has led to the development of the so-called linear scaling methods and they have proven highly efficient for small basis sets. Linear scaling formalisms have been developed by many groups. However, these algorithms currently only work efficiently for large systems in very small basis sets. When more accuracy is needed larger basis sets are essential and for these cases the resolution of identity (RI) method [1–8] has been used to reduce the computational effort. The RI method has worked very well for the calculation of the Coulomb contribution to the Fock matrix [9–18], but the exchange contribution is much more difficult to compute with the same benefits [15, 19–22]. We shall discuss these problems in more detail. Another complication using the RI method is that the accuracy of the results is not easily controlled as the approach typically uses atom-centered pre-optimized auxiliary basis sets. The argument found in the literature is that the error due to the incompleteness of the auxiliary basis is smaller than the basis set error speaks in favor of the RI method. However, care should be exercised as size-extensive properties cannot be used to extrapolate to the basis set limit if the errors are larger than the accuracy of the extrapolation procedures.

In this review we report on different approaches similar to the RI method that avoids the use of pre-optimized auxiliary basis sets. We simply determine the auxiliary basis using the decomposition developed by Commandant André-Louis Cholesky (1875–1918) and published by Commandant Benoît in 1924 [23]. The idea to apply the Cholesky decomposition (CD) to the two-electron integral matrix was first suggested by Beebe and Linderberg [24] more than thirty years ago. The CD is the only numerical procedure known to the authors that can remove the zero or small eigenvalues of a positive semi-definite matrix without calculating the entire matrix. This makes the procedure truly unique and the possibilities to obtain tremendous computational savings are apparent. Just consider the two-electron integral matrix. In the limit of a complete basis the number of integrals will scale as N^4 , but the number of non-zero eigenvalues scales as N in the limit of a complete basis (N is the size of the basis). Despite this, the CD does not

seem to have received much attention in the quantum chemistry community. There are notable exceptions, especially the developments by Røeggen and co-workers who have used the Cholesky decomposition of the two-electron integrals in the implementation of geminal models [25–30]. The use of the CD in connection with the calculation of derivative integrals has been discussed by O’Neal and Simons [31]. More recently, Koch, Sánchez de Merás and Pedersen [32, 33] have developed an implementation of the CD of the two-electron integrals aiming at large scale applications. The decomposition was shown to give large savings for large basis sets with a variety of theoretical methods: Hartree-Fock (HF), density functional theory (DFT), second order Møller-Plesset perturbation theory (MP2), and the second-order approximate coupled cluster model (CC2) [34]. These implementations in the DALTON program has formed the basis for many computational developments and applications [35–43]. The CD strategy has subsequently been implemented in the MOLCAS program [44] for multiconfigurational methods (multiconfigurational self-consistent field (MCSCF) [45] and multiconfigurational second-order perturbation theory (CASPT2) [46]) as well as scaled opposite spin MP2 [47] and coupled cluster (CC) methods [44]. The MOLCAS implementation has been crucial for a number of further developments and applications [21, 48–69]. Røeggen and Johansen [30] were the first to report a parallel implementation of the CD that shows a practically linear scaling with the number of compute nodes. The future use of CD based methods depends on the ability to evaluate geometrical derivatives of the molecular energy. In contrast to the numerical approach by O’Neal and Simons [31], analytic energy derivatives based on CD have been discussed recently by Aquilante et al. [52]. The CD is still perceived to be a rather complicated procedure. The aim of this chapter is to demonstrate that CD is a very rich tool and finds many practical applications in electronic structure theory.

The use of the RI representation of the two-electron integral matrix is sometimes referred to as density fitting (DF). Both these acronyms, RI and DF, are somewhat misleading. The density fitting community often anchors the method in the 1973 paper by Whitten [1] on integral approximations, whereas the RI terminology is mostly a descendent of the work by Almlöf and Feyereisen [7, 8]. The most correct description would probably be to denote them as inner projection methods. The concept of inner projections was introduced into quantum chemistry by Löwdin in his 1967–1971 landmark papers on perturbation theory [70, 71]. The CD is a powerful method to determine the optimal basis in the inner projection.

We start our review with some general mathematical considerations regarding the CD. This is then followed by Section 13.3 discussing several of our recent applications of the method in electronic structure theory. Section 13.4 is devoted to accuracy calibration and implementation aspects are discussed in Section 13.5. The chapter ends with our outlooks and conclusions.

13.2. MATHEMATICAL BACKGROUND

In April 1924 a paper [23] by Commandant Benoît was published summarizing some handwritten notes dated in Vincennes on December 2nd 1910 by André-Louis

Cholesky. Commandant Cholesky had developed a method to solve the systems of linear equations appearing in the compensation of geodesic networks, using a particular lower-upper (LU) decomposition [72] of a symmetric positive definite matrix \mathbf{M}

$$\mathbf{M}\mathbf{x} = \mathbf{L}\mathbf{L}^T\mathbf{x} = \mathbf{b} \quad (13-1)$$

where the matrix \mathbf{M} has been decomposed in the product of a lower triangular matrix with strictly positive diagonals, \mathbf{L} , and its transpose. With such decomposition, the solution of the linear system is trivial by Gauss elimination in a two-step procedure: Solve first $\mathbf{L}\mathbf{y} = \mathbf{b}$ for \mathbf{y} , and then $\mathbf{L}^T\mathbf{x} = \mathbf{y}$ for \mathbf{x} .

Cholesky decomposition is easily understood as an iterative procedure where in each iteration a Cholesky vector L_p^J is being subtracted from the updated matrix,

$$\mathbf{M}^{(n+1)} = \mathbf{M}^{(n)} - \mathbf{L}^J(\mathbf{L}^J)^T \quad (13-2)$$

which remains positive definite at all steps in the process. Note that $\mathbf{M}^{(0)} = \mathbf{M}$. Convergence is achieved when the residuals in the diagonal elements are smaller than a predefined threshold, τ . The original matrix can be approximated to almost arbitrary accuracy as

$$\mathbf{M} \approx \sum_{J=1}^K \mathbf{L}^J(\mathbf{L}^J)^T \quad (13-3)$$

with Cholesky vectors defined according to

$$L_i^{J_n} = \frac{M_{ij}^{(n)}}{\sqrt{M_{JJ}^{(n)}}} \quad (13-4)$$

The Cholesky vectors constitute the columns of the \mathbf{L} matrix and, therefore, in order to obtain the required lower triangular form, one needs to carry out the decomposition in such a way that the selected $M_{JJ}^{(n)}$ is always the first non-zero diagonal element in the matrix. For the sake of numerical stability of the algorithm, it is often preferable to choose as pivoting element the maximum diagonal element in each step of the procedure

$$M_{JJ}^{(n)} = \max_i (M_{ii}^{(n)}) \quad (13-5)$$

Consequently, while the CD of a positive definite matrix is unique, there can be different sets of Cholesky vectors depending on the ordering in which the diagonal elements are selected. At any rate, this does not cause any additional difficulty, as the different vector sets span the same subspace. Moreover, the super-matrix of two-electron integrals $M_{\alpha\beta,\gamma\delta} = (\alpha\beta | \gamma\delta)$ is positive semi-definite and the CD exists, but is in general not unique.

The reason why CD is a valuable tool in electronic structure calculations lies in the fact that it provides an efficient way of removing linear dependencies in a given matrix. As a matter of fact, CD can eliminate the zero or almost zero eigenvalues of a matrix without computing the whole matrix, but only calculating the complete diagonal as well as the columns of the decomposed diagonal elements. For a strictly positive matrix, the number K of Cholesky vectors equals the dimension of the matrix N . However, for a positive semi-definite matrix, K is smaller than N , $N - K$ being the number of linear dependencies. As a simple example, let us consider the following matrix

$$\mathbf{A} = \begin{pmatrix} a & c & \alpha a + \beta c \\ c & b & \alpha c + \beta b \\ \alpha a + \beta c & \alpha c + \beta b & \alpha^2 a + \beta^2 b + 2\alpha\beta c \end{pmatrix} \quad (13-6)$$

in which, obviously, the third column is a linear combination of the first two. When \mathbf{A} is decomposed, we obtain only two Cholesky vectors

$$\begin{aligned} \mathbf{A} = & \frac{1}{\sqrt{a}} \begin{pmatrix} a \\ c \\ \alpha a + \beta c \\ 0 \end{pmatrix} \begin{pmatrix} a & c & \alpha a + \beta c \end{pmatrix} \frac{1}{\sqrt{a}} \\ & + \begin{pmatrix} 0 \\ \sqrt{b - \frac{c^2}{a}} \\ \beta \sqrt{b - \frac{c^2}{a}} \end{pmatrix} \begin{pmatrix} 0 & \sqrt{b - \frac{c^2}{a}} & \beta \sqrt{b - \frac{c^2}{a}} \end{pmatrix} \end{aligned} \quad (13-7)$$

At this point, it is important to recall that the updated matrix remains positive definite only when exact arithmetic is used, but this property can be lost if round-off errors are significant. That is, round-off errors might cause matrices, which formally should be positive semi-definite, to have a slightly negative definite part. This is, for instance, the case for the two-electron integral matrix [32], which in practice limits the accuracy of the CD to about 10^{-12} ; still, this is more than enough for practical applications. For matrices that are better conditioned, such as the orbital energy denominators appearing in many-body perturbation theory (MBPT) calculations, it is possible to reach machine precision (i.e. 10^{-16}) in a straightforward manner [73].

To further illustrate the removal of linear or near-linear dependence by Cholesky decomposition, consider a positive definite operator $\hat{M}(\mathbf{r}_1, \mathbf{r}_2)$ with the following matrix representation in a real basis $\{\phi_i(\mathbf{r})\}$,

$$M_{ij} = \int \int \phi_i(\mathbf{r}_1) \hat{M}(\mathbf{r}_1, \mathbf{r}_2) \phi_j(\mathbf{r}_2) d\mathbf{r}_1 d\mathbf{r}_2 \equiv (\phi_i | \phi_j) \quad (13-8)$$

The positive definite operator is here assumed to be a two-electron operator such as the Coulomb operator $\hat{M}(\mathbf{r}_1, \mathbf{r}_2) = |\mathbf{r}_1 - \mathbf{r}_2|^{-1}$, or the attenuated Coulomb operator $\hat{M}(\mathbf{r}_1, \mathbf{r}_2) = A(|\mathbf{r}_1 - \mathbf{r}_2|) |\mathbf{r}_1 - \mathbf{r}_2|^{-1}$ (A is a strictly positive function; e.g., a Gaussian function or complementary error function). It could also be the Dirac delta function

$\hat{M}(\mathbf{r}_1, \mathbf{r}_2) = \delta(\mathbf{r}_1 - \mathbf{r}_2)$. Now, even if the operator is positive definite the matrix representation may be positive semi-definite or nearly so. This occurs whenever the basis is linearly dependent in the metric defined by the operator $\hat{M}(\mathbf{r}_1, \mathbf{r}_2)$. As discussed above, CD of a positive semi-definite matrix leads to a number of Cholesky vectors which is smaller than the dimension of the matrix. The pivoting procedure defined by Eq. (13-5) leads to the concept of the Cholesky basis, which is defined as the subset of the basis set for which the corresponding diagonal elements give rise to Cholesky vectors. We use h_J to denote members of the Cholesky basis. Performing a modified Gram-Schmidt orthonormalization in the \hat{M} -metric of the Cholesky basis leads to the orthonormal Cholesky basis

$$Q_J = N_J \left(h_J - \sum_{K=1}^{J-1} Q_K (h_J | Q_K) \right) \quad (13-9)$$

where the normalization constant is given by

$$N_J = \left[(h_J | h_J) - \sum_{K=1}^{J-1} (h_J | Q_K)^2 \right]^{-\frac{1}{2}} \quad (13-10)$$

and the matrix elements $(\cdot | \cdot)$ are defined in Eq. (13-8). We can now show that the Cholesky vectors can be expressed in terms of the orthonormal Cholesky basis as [49, 52, 58]

$$L_i^J = (\phi_i | Q_J) \quad (13-11)$$

This implies that CD can be used to remove linear dependence in a given basis using any positive definite metric. The original matrix can then be expressed as an inner projection in two equivalent ways

$$\begin{aligned} (\phi_i | \phi_j) &= \sum_J (\phi_i | Q_J)(Q_J | \phi_j) \\ &= \sum_{IJ} (\phi_i | h_I) \tilde{M}_{IJ}^{-1} (h_J | \phi_j) \end{aligned} \quad (13-12)$$

where $\tilde{M}_{IJ}^{-1} = (\tilde{\mathbf{M}}^{-1})_{IJ}$ and

$$\tilde{M}_{IJ} = (h_I | h_J) \quad (13-13)$$

Alternatively, we may expand the linearly dependent basis in the Cholesky basis

$$\phi_i = \sum_J C_i^J h_J \quad (13-14)$$

and obtain yet another equivalent expression

$$(\phi_i | \phi_j) = \sum_{IJ} C_i^I \tilde{M}_{IJ} C_j^J \quad (13-15)$$

The expansion coefficients are determined by a least-squares fitting (in the \hat{M} -metric), leading to the equations

$$\sum_I C_j^I \tilde{M}_{IJ} = (\phi_j | h_J) \quad (13-16)$$

from which the coefficients can be computed. Using that the matrix $\tilde{\mathbf{M}}$ is the sub-block of \mathbf{M} which is represented exactly by the CD, these fitting equations can be recast as [58]

$$\sum_I C_j^I L_I^J = L_j^J \quad (13-17)$$

providing a relation between fitting coefficients and Cholesky vectors.

We close this section by showing an important property of the CD that is rarely discussed in standard textbooks on linear algebra. The decomposition of a projection operator gives orthonormal Cholesky vectors [48], such that an incomplete decomposition is again a projection operator. Consider a projector P and the projection on the complement $Q = 1 - P$, such that $P^2 = P$ and $Q^2 = Q$. In the complete basis $\{|n\rangle\}$ of finite or infinite dimension we have the resolution of identity

$$\sum_n |n\rangle\langle n| = 1 \quad (13-18)$$

and the matrix representations that we assume real

$$\begin{aligned} P_{nm} &= \langle n | P | m \rangle = P_{mn} \\ Q_{nm} &= \langle n | Q | m \rangle = Q_{mn} . \end{aligned} \quad (13-19)$$

The first Cholesky vector

$$L_n^1 = \langle n | P | 1 \rangle \langle 1 | P | 1 \rangle^{-1/2} = P_{n1} P_{11}^{-1/2} \quad (13-20)$$

is easily seen to be normalized. The second Cholesky vector

$$L_n^2 = \left(P_{n2} - \frac{P_{12}^2}{P_{11}} \right) \left(P_{22} - \frac{P_{n1} P_{12}}{P_{11}} \right)^{-1/2} \quad (13-21)$$

is also normalized

$$\sum_n (L_n^2)^2 = \left(P_{22} - \frac{P_{12}^2}{P_{11}} \right)^{-1} \sum_n \left(P_{2n} - \frac{P_{1n}P_{12}}{P_{11}} \right) \left(P_{n2} - \frac{P_{n1}P_{12}}{P_{11}} \right) = 1 \quad (13-22)$$

and orthogonal to the first Cholesky vector

$$\begin{aligned} \sum_n L_n^1 L_n^2 &= P_{11}^{-1/2} \left(P_{22} - \frac{P_{12}^2}{P_{11}} \right)^{-1/2} \sum_n P_{1n} \left(P_{n2} - \frac{P_{n1}P_{12}}{P_{11}} \right) \\ &= P_{11}^{-1/2} \left(P_{22} - \frac{P_{12}^2}{P_{11}} \right)^{-1/2} \left(P_{12} - \frac{P_{11}P_{12}}{P_{11}} \right) = 0 \end{aligned} \quad (13-23)$$

An induction proof is now straightforwardly completed. As P and Q are orthogonal projectors, i.e. $PQ = 0$, any incomplete decomposition of P and Q give Cholesky vectors that are orthonormal. We shall apply this property in Section 13.3.3 to localize occupied and virtual orbitals.

13.3. APPLICATIONS

In this section we give a number of examples of the use of the CD technique in *ab initio* methods. These examples include the approximate representation of two-electron integrals, of course, but also other aspects such as orbital localization and quartic-scaling MP2.

13.3.1. Connection Between Density Fitting and Cholesky Decomposition

Although Beebe and Linderberg [24] noted that the CD technique was an inner projection approximation and Vahtras and co-workers [8] noted that the so-called V approximation in their integral approximation scheme is “an inner projection similar to the Beebe-Linderberg approximation” this has never been explicitly demonstrated and exploited. In this section we will clearly demonstrate that the CD method implicitly generates an auxiliary basis, the orthonormal Cholesky auxiliary basis, which in some respects is no different from those used in standard DF methods. The connection between DF and CD is discussed in detail in the recent review by Pedersen, Aquilante, and Lindh [58].

As discussed in the previous section, the CD procedure is nothing but a modified Gram-Schmidt orthonormalization procedure applied to the positive definite molecular super-matrix, $(\alpha\beta | \gamma\delta)$ and includes in a pivoting algorithm the original atomic orbital (AO) product functions $\gamma\delta$ one by one into the orthonormalization procedure. Let us use this order index, J , to denote a particular AO product as h_J , the parent Cholesky auxiliary basis. The CD procedure contains the two elements — orthogonalization and normalization. The orthonormalized Cholesky auxiliary basis, Q_J , is defined by Eq. (13-9) with the normalization constant given by Eq. (13-10).

We note that the parent Cholesky auxiliary basis $\{h_J\}$ and the orthonormal Cholesky auxiliary basis $\{Q_J\}$ span the same space and that for the latter, by virtue of design, the molecular super-matrix is trivially expressed as $(Q_J | Q_K) = \delta_{JK}$.

This equivalence now allows us to express the approximated two-electron integrals using the DF formalism in two equivalent ways (the first two lines of the equation),

$$\begin{aligned}
 (\alpha\beta | \gamma\delta) &= \sum_{JK} (\alpha\beta | h_J) G_{JK}^{-1} (h_K | \gamma\delta) \\
 &= \sum_{JK} (\alpha\beta | Q_J) \tilde{G}_{JK}^{-1} (Q_K | \gamma\delta) \\
 &= \sum_J (\alpha\beta | Q_J) (Q_J | \gamma\delta)
 \end{aligned} \tag{13-24}$$

where $G_{JK} = (h_J | h_K)$ and $\tilde{G}_{JK} = (Q_J | Q_K) = \delta_{JK}$. The last step is a trivial consequence of the orthonormal Cholesky auxiliary basis and leads us to the identification of the Cholesky vectors as

$$L_{\alpha\beta}^J = (\alpha\beta | Q_J) \tag{13-25}$$

which, apart from a slightly different notation, is identical to Eq. (13-11). We have now established that the CD approach indirectly form a particular auxiliary basis to be used within the DF formalism. This auxiliary basis is similar in many respects to the standard available DF auxiliary basis sets. However, there are three major differences. First, the orthonormal Cholesky auxiliary basis is in principle a two-center type of auxiliary basis. This allows us to, with a single parameter, control the error of the approximated integrals to an arbitrary accuracy, while it also presents some challenges in the calculation of analytic gradients. This problem has been resolved with the atomic CD procedure [49, 62], in which accurate analytic gradients can be expressed with a reduction of accuracy of the approximated integrals that is of no practical consequence [52]. Second, the Cholesky auxiliary basis set is always a subset of the full product space. Third, the auxiliary basis set is a set of (product) basis functions ordered with respect to their significance in the reproduction of the two-electron integrals, i.e. the set can be further truncated on-the-fly in a screening scheme with complete control of the accuracy. That is, it is a compact and efficient auxiliary basis set. Normally, DF auxiliary basis sets are improved by ad hoc uncontraction or addition of primitive Gaussians. This procedure does not control that the additional functions are completely within the space of the original product basis, and can in this way be wasteful. Rather, the quality of the extended DF auxiliary basis sets are checked in subsequent test calculations based on energy criterions (see for example Refs. [74–76]). To summarize, there are good arguments why the CD auxiliary basis sets, in the parent or orthonormal form, are the optimal general auxiliary basis sets. Benchmark results that support this view are presented in Section 13.4.

13.3.2. One-Center CD Auxiliary Basis Sets

In contrast to conventional RI or DF schemes, the CD procedure generates auxiliary basis sets which in general are of two-center type. This allows the standard

CD technique applied to the two-electron integral, which we denote Full-CD, to approximate the conventional result to any degree of accuracy with the adjustment of a single threshold parameter. However, the two-center character of the Full-CD auxiliary basis set makes it difficult to formulate a general analytic expression for derivatives of the two-electron integrals with respect to the nuclear coordinates. As the geometry changes, the set of Full-CD auxiliary basis functions changes as well which may introduce discontinuities on the potential energy surface of the order of magnitude of the decomposition threshold. A brute force way to control this would of course be to reduce the threshold to the extent that this feature is of no practical significance. However, for larger CD thresholds the problem remains. Having established the connection between CD and RI/DF techniques in Section 13.3.1 we can solve this problem in a pragmatic way. For RI/DF techniques analytic expressions for gradients have already been derived and is a consequence of the strict one-center type of auxiliary basis sets used in these techniques – the auxiliary basis set is not a function of the molecular geometry. Still with these limitations the RI/DF approach has been shown to provide an approximation with reasonable accuracy. The question which follows at once is “Can a CD procedure be used to generate meaningful one-center type auxiliary basis sets?”.

In a series of papers, methods for one-center type of CD auxiliary basis sets have been described [49, 58, 62] The first paper developed the one-center CD (1C-CD) and the atomic CD (aCD) auxiliary basis sets. Both of these methods are straightforward modifications of the Full-CD procedure. In the 1C-CD approach only one-center product functions are allowed to enter the Cholesky basis [49]. Thus, a one-center auxiliary basis set is constructed which for all practical purposes, though not strictly, is invariant to the molecular geometry. This is, however, strictly the case for the aCD approach [49] in which the auxiliary basis set is generated from a decomposition of the separate atomic blocks of the molecular two-electron integral matrix. For these two types of auxiliary basis set one remaining deficiency in common with Full-CD and in difference to standard RI/DF auxiliary basis sets remains: a rather large set of primitive Gaussians is used. The so-called atomic compact CD (acCD) auxiliary basis sets [62] offer a significant reduction of these primitive sets without significant loss of accuracy. The hallmark of the acCD procedure is that in the atomic CD procedure the set of primitive Gaussian products itself is subject to a Cholesky decomposition and that the remaining functions are fitted to produce an accurate representation of the parent aCD auxiliary basis set. This compact representation of the aCD auxiliary basis set introduces significant reduction of the primitive space and speeds up the computation of two- and three-center two-electron integrals when the acCD auxiliary basis sets are used in the RI/DF procedure (see Figure 13-1 for a representation of the reduction of the primitive product space in the case of an all-electron atomic natural orbital valence basis set for technetium). In addition, it should be noted that these new one-center auxiliary basis sets are constructed on the fly. That is, with these new procedures, the need for auxiliary basis set libraries is a feature of the past and that RI/DF calculations now can be performed directly for any existing or future valence basis set. The accuracy of the one-center CD auxiliary basis sets is discussed in Section 13.4.

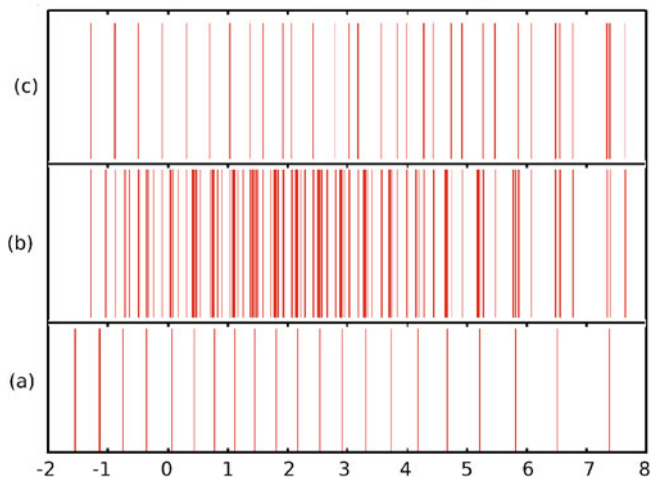


Figure 13-1. Progression of the primitive set of technetium in **a** the valence ANO-RCC *s*-shell and corresponding **b** aCD-4 and **c** acCD-4 auxiliary basis sets. The decimal logarithm of the Gaussian exponent is reported on the horizontal axes (reproduced with the permission of AIP)

Finally, we point out a unique feature of the aCD and acCD auxiliary basis sets. Since the auxiliary functions span the same space (within the decomposition threshold) as the one-center atomic orbital product functions that are to be fitted, only auxiliary functions on the same center as the product functions are needed to produce an accurate fit [62]. That is, the fitting of one-center atomic orbital products becomes increasingly local as the threshold is decreased. This feature of the atomic CD sets implies that local density fitting can be performed without the use of less accurate short-range metrics such as the overlap or attenuated Coulomb metrics discussed by Jung et al. [77]. The situation is different for two-center atomic orbital products where two-center auxiliary functions are needed to obtain an inherently local fit with the accurate long-range Coulomb metric [58]. As discussed in [58], it is possible to get an accurate local two-center fit with a minimum amount of two-center auxiliary functions, namely exactly those that are needed to make the auxiliary set complete (within the decomposition threshold) in the subspace of interest. These observations pave the way for truly local density fitting where each approximate atomic orbital product function is represented in exactly the same way in any molecule: the fit becomes transferable and thus free from (auxiliary) basis set superposition errors. By the same token, this approach eliminates the size-extensivity errors uncovered by Werner and Manby [78] with the explicitly correlated DF-MP2-R12 method.

To illustrate the locality of the atomic CD sets, we follow Jung et al. [77] in considering a simple model problem. Suppose that we wish to fit a spherical unit-charge density s_T using two identical auxiliary basis functions s_1 and s_2 , which are also spherical unit-charge densities. While s_1 is centered at the same point as s_T , s_2 is a distance r away. We now seek the coefficients c_1 and c_2 such that the

approximation $|s_T) \approx c_1|s_1) + c_2|s_2)$ is the best possible in a least-squares sense. This is achieved by solving the fitting equations

$$[c_1 \ c_2] \begin{bmatrix} A & B \\ B & A \end{bmatrix} = [C \ D] \quad (13-26)$$

where $A = (s_1|s_1) = (s_2|s_2)$, $B = (s_1|s_2) = (s_2|s_1)$, $C = (s_1|s_T)$, and $D = (s_2|s_T)$. The solution is given by

$$c_1 = \frac{C}{A} - \frac{B}{A} \frac{AD - BC}{A^2 - B^2} \quad (13-27)$$

$$c_2 = \frac{AD - BC}{A^2 - B^2} \quad (13-28)$$

showing that, in general, there is a non-vanishing contribution to the fit from the distant auxiliary function s_2 . The central question is whether this contribution decays sufficiently fast to allow a local fit involving the function s_1 only. For large distances r , we have [77]

$$B \rightarrow r^{-1} \quad (13-29)$$

$$D \rightarrow r^{-1} \quad (13-30)$$

and therefore

$$c_1 \rightarrow \frac{C}{A} \quad (13-31)$$

$$c_2 \rightarrow \frac{A - C}{A^2} \frac{1}{r} \quad (13-32)$$

This shows that c_2 is a slowly decaying function of the distance, making the fitting procedure inherently nonlocal. However, using the Cholesky approach to auxiliary basis functions for this simple model system, we have $s_1 = s_T$ and therefore $C = A$ and $D = B$. Hence, regardless of the distance r , Eqs. (13-27) and (13-28) become

$$c_1 = 1 \quad (13-33)$$

$$c_2 = 0 \quad (13-34)$$

showing that the fit is manifestly local. Fitting a single function using itself as auxiliary basis is silly, of course, but the example underlines the importance of choosing the auxiliary basis such that it spans the same space, or very nearly so, as the functions to be fitted. Not only will the fit be more accurate, it will render the long-range decay of the fitting coefficients irrelevant [62]. More general discussions, theoretical as well as through numerical examples, of this inherent locality can be found in [58, 62].

13.3.3. Orbital Localization Using Cholesky Decomposition

A key ingredient needed for state of the art electronic structure methods to be efficient is the sparsity of the molecular orbital (MO) coefficient representation of the density matrix. Sparsity is in this context the property of an array to have relatively few, and usually scattered, large elements. Due to the invariance of HF theory with respect to unitary transformations among the occupied (or virtual) orbital space, an infinite number of such representations are possible. Of course, sparsity of the MO coefficients does not necessarily imply that the resulting orbitals are localized. Locality carries the notion of spatial extent of an object, which in this case indicates that the orbitals are confined to few neighboring atoms. Orbital locality implies a degree of sparsity in the MO coefficients but not vice versa. Several localization schemes have been developed for choosing a unitary transformation of the molecular orbitals. Among the most common are the Boys [79], Edmiston-Ruedenberg [80], and Pipek-Mezey [81] procedures, which are all formulated as an optimization problem where a localization functional is maximized with respect to rotations among the orbitals. The orbital localization thus becomes an iterative procedure. An alternative approach to obtain localized orbitals is provided by the Cholesky decomposition of the AO density matrix [48]. This Cholesky localization has several computational advantages over the standard schemes and also some unique features. First, Cholesky decomposition is a numerically stable and fast algorithm that can be made linear scaling for matrices with linear scaling number of non-zero elements [82]. Second, being a non-iterative procedure, complicated optimization techniques are not needed. Third, as no initial orbitals need to be given, the procedure is particularly well suited for determining local MOs directly from density matrix-based HF theory. Fourth, it is the natural choice for obtaining localized orbitals to be used in connection with the local-K exchange screening discussed in Section 13.3.4.

In addition to local occupied orbitals, Cholesky decomposition of *ad hoc* defined density-type matrices can produce local MOs spanning the virtual space, as required by linear-scaling wave function-based electron correlation models. In particular, the corresponding Cholesky MOs are reasonably localized even though they are orthonormal by construction (since the density is a projector, see also Section 13.2). The convenience of using orthonormal orbitals for the virtual space instead of the usual (redundant) projected AOs could increase in the future the popularity of Cholesky localization techniques – probably the only orbital localization scheme that works for both occupied and virtual orbitals, with and without symmetry, and produces very quickly localized orbitals directly from the parent density matrix.

As mentioned above, the HF energy is invariant under any unitary transformation that preserves the mutual orthogonality between the occupied and virtual subspaces. The underlying reason is that the density matrix

$$D_{\alpha\beta} = \sum_i^{\text{occ}} C_{\alpha i} C_{\beta i} \quad (13-35)$$

where the matrix \mathbf{C} contains the molecular orbital coefficients and i denotes occupied MOs, is indeed invariant under rotations of the occupied orbitals. Similarly, the virtual density-like matrix

$$D_{\alpha\beta}^V = (\mathbf{S}^{-1} - \mathbf{D})_{\alpha\beta} = \sum_a^{\text{virt}} C_{\alpha a} C_{\beta a} \quad (13-36)$$

where \mathbf{S} is the overlap matrix in the AO basis and a denotes virtual MOs, is invariant under rotations of the virtual orbitals. Both \mathbf{D} and \mathbf{D}^V matrices are positive semi-definite, their ranks being the number of occupied and virtual orbitals, respectively. It is possible to Cholesky decompose each of these matrices selecting only those diagonals that correspond to atomic orbitals centered on atoms belonging to a pre-defined set of active centers defining a subsystem [43]. Once the decomposition is done in the reduced subspace, the residual matrix is still positive semi-definite and can, therefore, be decomposed without any restriction. In this way, we obtain an active set of orbitals, occupied and virtual, orthogonal to an inactive set that is eliminated, i.e. kept frozen, in the subsequent correlation treatment. Alternatively, one can also decompose completely the two density matrices on an atom-by-atom basis, thus obtaining a set of orthonormal MOs that span the same subspace as the canonical Hartree-Fock set. When the decomposition is completed, the active orbital space is selected from the atomic centers forming the subsystem. Either way, we obtain a localized MO basis spanning a reduced space located on the subsystem. If orbital energies are required, the Fock operator may be diagonalized in the active space.

The great advantage of using a small subsystem space is to concentrate the computational effort where it is in fact required. Indeed, many molecular properties are essentially local in character and, thus, it is reasonable to assume that only the atoms in the neighborhood of a specific site, the subsystem, significantly contribute to the considered property. In Figure 13-2 we represent the orbital spread [83] of the Cholesky orbitals in C_{10}H_2 compared to that of the canonical Hartree-Fock orbitals. It is easily verified that the procedure is able to localize the molecular orbitals, although augmentation (depicted in the right part) introduce a larger degree of delocalization.

For the calculation of intermolecular interaction energies, we start by noting that the canonical Hartree-Fock molecular orbitals are not well suited for this purpose (see Figure 13-3). In fact, they are spread out along the entire organic unit, but have very small components in the vicinity of the interaction area. Thus, the largest amplitudes will give virtually zero contribution to the calculated interaction. On the other hand, the Cholesky orbitals are concentrated in the area of interest. The interaction energy has been calculated for several active spaces and using double zeta correlation consistent basis sets [84]. The smallest subsystem is formed by the neon atom, the $\text{CH}_2=\text{CH}-$ group in front of it and a [3s3p2d1f1g] set of bond functions [85] located at the center of the line connecting the neon atom and the $\text{C}=\text{C}$ double bond. In each successive space an additional CH_2 unit is attached. Our results are depicted in Figure 13-4. This is a very complicated problem, as the interaction

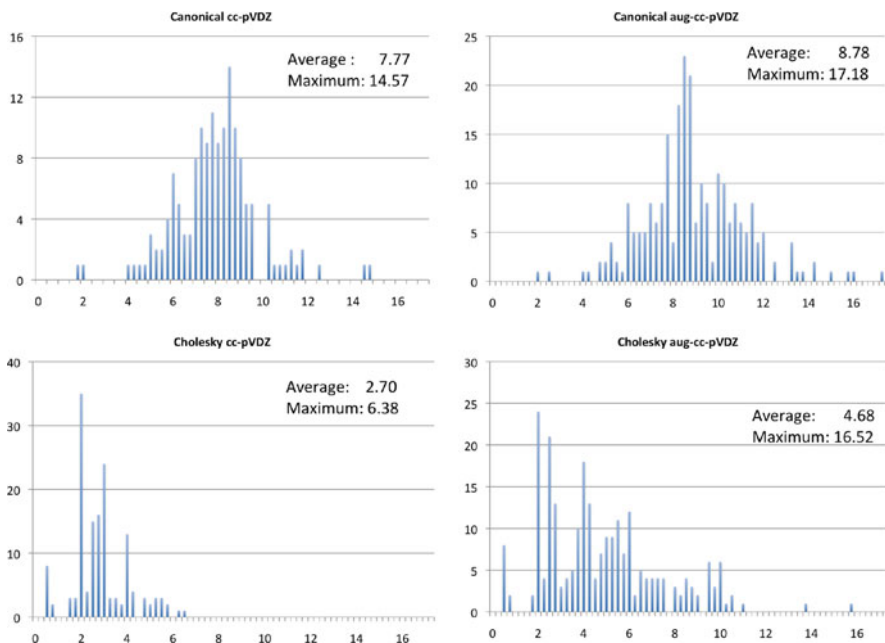


Figure 13-2. Histogram of orbital spreads of canonical (*above*) and Cholesky (*below*) molecular orbitals for $C_{10}H_2$ with cc-pVDZ (*left*) and aug-cc-pVDZ (*right*) basis sets. The abscissa denotes the orbital spread in atomic units and the ordinate the number of molecular orbitals (both occupied and virtual) containing the spread for a step of 0.25 a.u.

is completely described by weak dispersion forces, and augmented basis sets are required. As discussed above, augmentation introduces some delocalization, implying that rather large subsystems are needed to get meaningful results. However, if the interaction is calculated according to

$$\Delta E_{MP2/CCSD(T)} = \Delta E_{CCSD(T)}^{act} - \Delta E_{MP2}^{act} + \Delta E_{MP2}^{exact} \quad (13-37)$$

the convergence towards to the exact value is fast and almost uniform, making it feasible to get accurate results using very reduced spaces.

13.3.4. The LK Algorithm

The use of the Cholesky representation of the two-electron integrals, as proposed by Beebe and Lindenberg [24] and extended by Koch and co-workers [32], does not always yield a satisfactory performance for SCF calculations involving the evaluation of HF-exchange. For large molecules (>100 atoms) and compact basis sets, standard integral-direct algorithms are by far the fastest. The quartic scaling of the evaluation of the exchange Fock matrix \mathbf{K} quickly downgrades the capacity of the straightforward Cholesky and DF SCF implementations [19, 32] for electron-rich

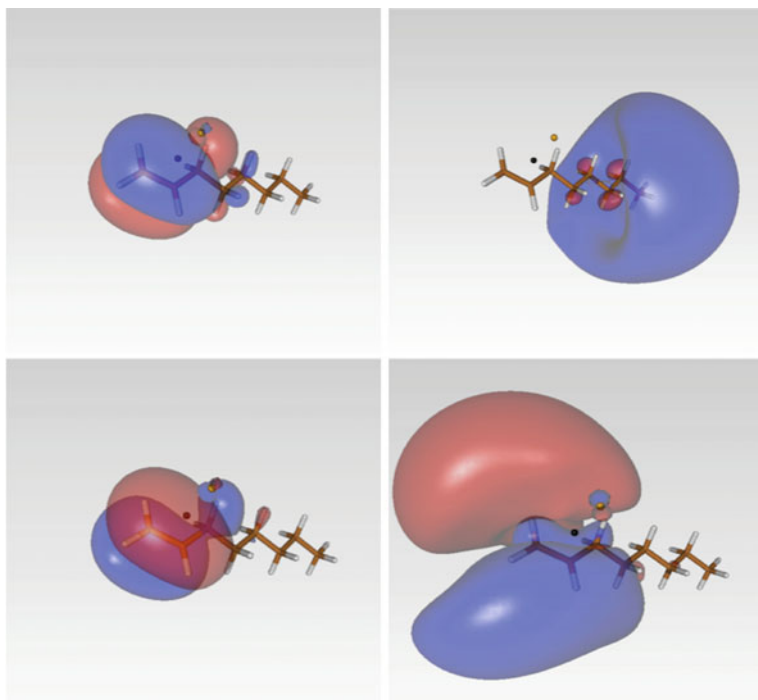


Figure 13-3. Complex octene-neon: HOMO (left) and LUMO (right) in the canonical (above) and Cholesky (below) molecular orbital basis

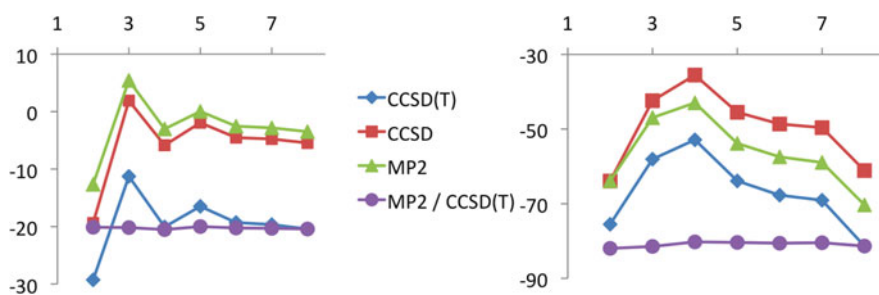


Figure 13-4. Interaction energy (in cm^{-1}) for the neon-octene complex using cc-pVDZ (left) and aug-cc-pVDZ (right) supplemented with midbond functions. The horizontal axis represents the number of $\text{CH}_{(n)}$ groups in the active space

(many occupied orbitals) systems and large basis set. Particularly unpleasant is the dependence of the computational costs on the number of occupied orbitals, as this is not the case for integral-based SCF algorithms. Polly et al. [20] were the first to propose an alternative algorithm for computing the exchange Fock matrix in DF-based SCF with reduced scaling. Although asymptotically linear scaling, this procedure does not yield bounded errors — therefore the accuracy of the result cannot be

controlled solely on the basis of energy thresholds. As discussed previously, it is exactly this error control that makes the Cholesky approximation extremely appealing. Consequently, an alternative solution to this “*exchange problem*” that could maintain the prime characteristic of the method was proposed by some of the present authors [21]. This approach, called *Local K* or simply *LK* algorithm is general in the sense that it does not involve *a priori* assumptions about the size of the system or the nature of its electronic structure. Only the short-range character of the exchange interactions is required for the screening to be effective.

In order to implement an efficient and also error bounded screening on the contribution of a molecular orbital i to the matrix elements of K , the *LK* algorithm makes use of the following chain of inequalities

$$\begin{aligned} |K_{\alpha\beta}^i| = |(\alpha i | \beta i)| &\leq \sum_{\gamma\delta} |C_{\gamma i}| |(\alpha\gamma | \beta\delta)| |C_{\delta i}| \\ &\leq \sum_{\gamma\delta} |C_{\gamma i}| |D_{\alpha\gamma}^{1/2} D_{\beta\delta}^{1/2}| |C_{\delta i}| = Y_{\alpha}^i Y_{\beta}^i \end{aligned} \quad (13-38)$$

where $D_{\alpha\beta} = (\alpha\beta | \alpha\beta)$ are the (exact) diagonal elements of the two-electron matrix in AO basis and the i -th vector \mathbf{Y}^i has elements $Y_{\alpha}^i = \sum_{\gamma} D_{\alpha\gamma}^{1/2} |C_{\gamma i}|$. Clearly, the vector \mathbf{Y}^i will be sparse whenever the corresponding MO coefficient vector \mathbf{C}^i represents a localized orbital. Experience shows that the use of Cholesky orbitals, described in Section 13.3.3, mediates perfectly between the need for a fast localization (to be performed at each SCF cycle) with that of a sufficient sparsity in the resulting \mathbf{Y} vectors.

It is important to notice that in deriving the inequalities Eq. (13-38) we have only used the fact that the two-electron integral matrix in AO basis is positive semi-definite and therefore satisfies the Schwarz inequality. Whenever the contribution to the exchange Fock matrix from a certain number m of Cholesky vectors has been computed, the inequalities can be applied in the very same way to the remainder matrix. In practice this means that the Y vectors can be computed using updated integral diagonals, namely

$$\tilde{D}_{\alpha\beta} = D_{\alpha\beta} - \sum_{J=1}^m (L_{\alpha\beta}^J)^2 \quad (13-39)$$

Due to the inner projection nature of the Cholesky decomposition, these updated integral diagonals are guaranteed to remain nonnegative. Most importantly, the number of significant elements $\tilde{D}_{\alpha\beta}$ will decrease, since more and more Cholesky vectors have already contributed to the exchange Fock matrix. The details of the LK screening are presented and extensively discussed in the original paper [21]. A sketch of the shell-driven LK algorithm is shown in Figure 13-5. (A shell is defined as a set of atomic orbital basis functions on a given center with the same angular momentum.) The need to perform an MO half-transformation of the Cholesky vectors, formally as expensive as the build of \mathbf{K} , is tackled by employing estimates based

Loop over Cholesky vectors

Loop over occupied orbitals (i)

(1) Pre-selection and pre-ordering of the eligible shells

Compute the $Y^{(i)}$ screening vectors from (updated) integral diagonals

Loop over all α -shells

If ($MY^{(i)} \cdot \max(Y_{\alpha}^{(i)}) \geq \tau$) then

Add the α -shell to a list $ML^{(i)}$

EndIf

End Loop

Sort the α -shells in $ML^{(i)}$ by the value $\max(Y_{\alpha}^{(i)})$

(2) Frobenius-norm screened MO transformation

Loop over α -shells in the list $ML^{(i)}$

Loop over all β -shells in the shell-pairs ($\alpha\beta$) of the AO Cholesky vectors

If ($\|L_{\alpha\beta}^J\|_F \cdot \|C_{\beta}^{(i)}\|_F \geq \tau_F$) then

Perform the MO half-transformation $L_{\alpha(i)}^J = \sum_{\beta} L_{\alpha\beta}^J C_{\beta}^{(i)}$

EndIf

End Loop

Remove from $ML^{(i)}$ the α -shells that did not qualify for the MO transformation

End Loop

(3) Evaluation of the exchange Fock matrix $K_{\alpha\beta}^{(i)}$

Loop over α -shells in $ML^{(i)}$

Loop over the β -shells ($\beta \leq \alpha$) in $ML^{(i)}$

If ($\max(Y_{\alpha}^{(i)}) \cdot \max(Y_{\beta}^{(i)}) \geq \tau$) then

Compute $K_{\alpha\beta}^{(i)} = \sum_J L_{\alpha(i)}^J L_{\beta(i)}^J$

Else

Leave β -loop

EndIf

End Loop

End Loop

End Loop

(4) Update integral diagonals

End Loop

Figure 13-5. A sketch of the LK algorithm. For a given occupied orbital i , $MY^{(i)}$ is defined as the maximum element of the vector $Y^{(i)}$ defined in Eq. (13-38), and $ML^{(i)}$ is a list of contributing shells of basis functions

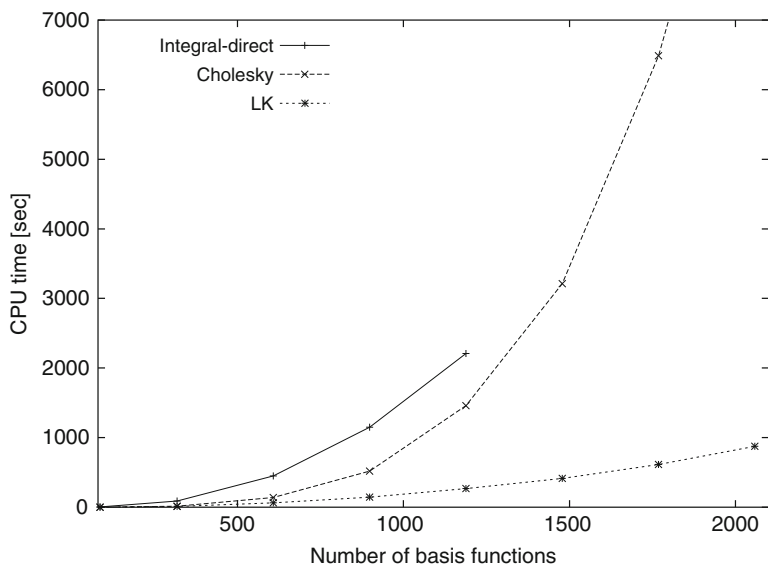


Figure 13-6. Timings for the construction of the exchange Fock matrix for linear alkanes using standard Cholesky, LK-Cholesky and integral-direct. Decomposition threshold $\delta = 10^{-4}$ and cc-pVTZ basis set

on the Frobenius norm of the resulting matrices. The exploitation of the permutational symmetry of the two-electron integrals, as well as the shell pre-ordering, represent some of the key features for the efficiency of the screening. By the nature of the method, the accuracy of the LK screening is absolutely reliable and can be controlled by the choice of the screening thresholds. Moreover, the LK screening is indeed capable of reducing the scaling of the evaluation of the exchange Fock matrix from quartic to quadratic. In Figure 13-6, we can see an example of what that means in terms of performances in Cholesky SCF calculations: with LK it is now possible to perform HF wavefunction optimizations faster than with integral-direct algorithms. Currently, the LK screening is used in MOLCAS for any type of Fock matrix build based on Cholesky vectors. We also stress the importance of the speedup achieved for CASSCF calculations, as documented in the original implementation paper [45]. Here, as an example, we will only report the performances of the LK-CASSCF algorithm for some of the systems described in Ref. [59]. These systems are important intermediates in the reaction of O_2 with a Cu(I)- α -Ketocarboxylate, and the accurate evaluation of the singlet-triplet splitting in each species is essential to the understanding of the mechanism of activation of molecular oxygen by copper coordination complexes [60]. With atomic natural orbital (ANO) basis sets of double- ζ quality, we are in a range of about 280–450 contracted Gaussian basis functions, depending on the system (point group symmetry not employed). In this range, the time spent to generate the DF-vectors is only a small fraction of the total time for any choice of the Cholesky basis (Full-CD, aCD, etc.), which also has no significant effect on the time required by the subsequent

steps. The following timings refer always to wall-time observed on an architecture of the type Intel(R) Xeon(TM) 3.20 GHz with 8 GB RAM and employing the MOLCAS software. For a typical calculation with 300 basis functions, about 2.5 h are required for computing and storing the conventional two-electron integrals. The subsequent CASSCF wavefunction optimization of the singlet ground state takes about 38 minutes per iteration, for an active space of (12-in-12). Using acCD-4, the vector generation is performed in only 3 min, and 3.4 min per iteration are required in the LK-CASSCF step. Considering that with the present CASSCF optimizer in MOLCAS an average of 100 iterations are needed for converging the wavefunction, the observed speed-up for the overall calculation is nearly a factor 12. Moving towards 450 basis functions, the conventional calculations can hardly be afforded due to the large disk-space requirements. With 437 basis functions, the acCD-4 vector generation goes up to 8 min, whereas the LK-CASSCF time per iteration stays within 4 minutes. Already with this relatively small basis set, the overall speed-up compared to the conventional calculation is nearly of two orders of magnitude. Speed-up for larger basis sets is difficult to measure, as the conventional calculation becomes impossible.

We close this section with a final remark. There is not a single notion in the LK algorithm that could distinguish between a Cholesky or any other DF representation of the integrals. In other words, the LK screening is a simple, accurate and general solution to the exchange problem.

13.3.5. Quartic-Scaling MP2

In MP2 theory, the need for the set of integrals $(ai | bj)$, where i, j and a, b label occupied and virtual orbitals, respectively, makes the conventional calculation a fifth-order process. Using Cholesky or DF, we can compute the same set of integrals as follows

$$(ai | bj) = \sum_J L_{ai}^J L_{bj}^J \quad (13-40)$$

where L_{ai}^J are the MO-transformed Cholesky or DF vectors. The MO transformation of these vectors is not the bottleneck of the calculation. With O and V denoting, respectively, the number of occupied and virtual orbitals and M the number of Cholesky vectors, it requires $\sim ON^2M$ operations, while the evaluation of Eq. (13.40) has a computational cost of $\sim O^2V^2M$. Compared to the conventional $\sim ON^4$ computational requirement, the smaller prefactor allows substantial speed-ups. The evaluation of the integrals from Eq. (13-40) is particularly well suited for canonical MP2 calculations, since in this case they can be computed on-the-fly in a batched loop, used to evaluate the energy contribution and never stored on disk [32]. Comparatively, in the Cholesky-based CASPT2 method [46] there is a possibility to avoid the evaluation of the corresponding $(ai | bj)$ -type integrals and reformulate the method directly in terms of Cholesky vectors. However, the existing MOLCAS implementation of CASPT2 still goes through the evaluation of such integrals as in

Eq. (13-40) and stores them on disk. Nonetheless, the present implementation makes possible CASPT2 calculations otherwise beyond the capabilities of the conventional implementation [51, 53–55, 57, 59, 60]. This is achieved because it bypasses completely the AO integral storage bottleneck and also because it produces the needed MO integrals at reduced computational cost and input-output overheads.

Let us analyze in more detail the formal scaling of MP2. The question is whether or not the approach adopted so far in Cholesky and DF (closed-shell) MP2 is the best possible. We shall demonstrate that it is not, and that the scaling of the method can be reduced from fifth to fourth order, with an algorithm that is also perfectly parallelizable. This is achieved by performing the Cholesky decomposition of the MP2 amplitude matrix (with minus sign), namely

$$-t_{ai,bj} = \frac{(ai | bj)}{\varepsilon_a - \varepsilon_i + \varepsilon_b - \varepsilon_j} = \sum_{K=1}^m R_{ai}^K R_{bj}^K. \quad (13-41)$$

The Cholesky decomposition algorithm applied to this matrix requires $\sim OVm^2$ operations plus the evaluation of m columns of the matrix \mathbf{t} . The necessary two-electron integrals can be computed using Cholesky or DF representations as in Eq. (13-40). It is crucial to understand how the value of m scales with system size. Although the matrix \mathbf{t} has a quadratic-scaling dimension (OV), its effective rank m scales only linearly with the size of the system. In fact, it is easy to realize that m is bounded by a linear scaling quantity, $n_r M$, where n_r is the number of Cholesky vectors needed for an exact decomposition of the orbital energy denominator matrix. It is known that this number is very small and, more importantly, independent of the size of the molecule [73]. Therefore the effective rank of \mathbf{t} scales linearly with the system size.

We can now write the expression for the closed-shell canonical MP2 energy as follows

$$\begin{aligned} E_2 &= \sum_{K=1}^m \sum_{aibj} R_{ai}^K R_{bj}^K [2(ai | bj) - (aj | bi)] \\ &= \sum_{\alpha\beta\gamma\delta} \Theta_{\alpha\beta,\gamma\delta} [2(\alpha\beta | \gamma\delta) - (\alpha\delta | \gamma\beta)] \end{aligned} \quad (13-42)$$

where

$$\Theta_{\alpha\beta,\gamma\delta} = \sum_{K=1}^m R_{\alpha\beta}^K R_{\gamma\delta}^K \quad (13-43)$$

and $R_{\alpha\beta}^K$ are the elements of the back-transformed Cholesky vectors of the amplitudes. It is possible to show that Θ is a sparse matrix [86]. Together with the sparsity of the AO two-electron integrals, this implies that for large systems an efficient screening is possible in order to reduce the costs for the evaluation of E_2 . In fact, by applying the Schwarz inequality to both Θ and the integrals, we can show that

the exchange-type term can be computed with an effort that is asymptotically linear. However, due to the fact that Θ needs to be computed from its Cholesky representation, most likely this step becomes quadratic scaling with a low prefactor. In the same way, the Coulomb-type term will require a cubic scaling effort.

In order to efficiently implement Eq. (13-42), the exact AO two-electron integrals need to be computed in a direct fashion and not from their Cholesky or DF representation. The reason for that is the possibility to achieve efficient parallelization of the code. The Cholesky decomposition of \mathbf{t} can be performed separately on each node without any communication. The amplitude matrix \mathbf{t} will be different on each node and corresponds to a partial contribution to the $(ai | bj)$ integrals, which is computed from MO transformed Cholesky vectors distributed among the nodes. On the other hand, since the evaluation of the AO two-electron integrals is at most a quadratic step, it can be performed by each node without jeopardizing the overall efficiency of the calculation. Indeed, since the matrix on each node is only a partial contribution to the total matrix, the application of the Schwarz inequality will result in the evaluation of an even smaller (and different) set of AO integrals on each node. Aquilante and Pedersen [47] have shown an application of a simplified form of this algorithm for the evaluation of the Coulomb-type term only (namely, scaled opposite spin (SOS) MP2).

13.3.6. Calculation of Molecular Gradients

The calculation of the forces acting on the atomic nuclei of molecules is a bread-and-butter task of quantum chemistry. Knowledge of the atomic forces makes it possible to study molecular geometries, such as equilibrium structures and transition states, and is also needed for molecular dynamics simulations. Atomic forces are defined as (minus) the first derivatives of the total electronic energy with respect to nuclear positions. Higher-order energy derivatives with respect to nuclear positions are needed for the calculation of harmonic force constants and vibrational frequencies (second derivatives), anharmonic force constants (third derivatives), and so on. In order to compute atomic forces and higher-order derivatives we must be able to calculate derivatives of the two-electron integrals. Since CD of the two-electron integrals is a numerical procedure, defining analytic derivatives of Cholesky vectors is non-trivial.

O'Neal and Simons [31] have proposed a procedure in which the undifferentiated and differentiated integrals are considered as elements of an extended positive semi-definite matrix, which is Cholesky decomposed. Owing to the fact that most of the first derivative atomic orbital product functions belong to the space spanned by the undifferentiated products, only a modest increase in the number of Cholesky vectors is observed in comparison to the undifferentiated case. Combining this approach with the method specific CD technique (Section 13.3.7) could provide a viable path to reduced scaling evaluation of atomic forces.

An alternative analytic approach was recently proposed by Aquilante, Lindh, and Pedersen [52]. It is based on the connection between CD and DF discussed in Section 13.3.1. The first derivative of Eq. (13-24) can be written as

$$(\alpha\beta | \gamma\delta)^{(1)} = \sum_J C_{\alpha\beta}^J (\gamma\delta | h_J)^{(1)} + \sum_J (\alpha\beta | h_J)^{(1)} C_{\gamma\delta}^J - \sum_{JK} C_{\alpha\beta}^J G_{JK}^{(1)} C_{\gamma\delta}^K \quad (13-44)$$

where

$$C_{\alpha\beta}^J = \sum_K G_{JK}^{-1} (\alpha\beta | h_K) \quad (13-45)$$

and all derivatives are to be evaluated at the nuclear geometry of interest. This expression solely involves derivative integrals that can be evaluated analytically. While Eq. (13-44) takes into account the explicit geometry-dependence of the auxiliary basis functions, any implicit geometry-dependence is neglected. This means that Eq. (13-44) is exact for any auxiliary basis set whose composition is independent of molecular geometry. This is a significant difference as compared to the approach suggested by O'Neal and Simons which has an accuracy depending on the CD threshold.

Predefined auxiliary basis sets are composed of atom-centered functions, which are used regardless of the molecular geometry. Hence, predefined auxiliary basis sets only contain explicit geometry-dependence, making Eq. (13.44) exact for this case [74, 87–91]. Cholesky auxiliary basis sets are generally more complicated. The molecular two-electron integral matrix is a function of geometry. Consequently, its decomposition varies with molecular geometry. In particular, this means that the composition of the Cholesky auxiliary basis set, i.e. the set of linearly independent product functions singled out by the decomposition, varies with geometry. It is, however, reasonable to assume that the Cholesky auxiliary basis set composition is invariant under infinitesimal changes in molecular geometry, making Eq. (13-44) a good approximation. The test calculations reported by Aquilante, Lindh, and Pedersen [52] have not revealed problems associated with the use of Eq. (13-44). On the contrary, it was found that the accuracy (relative to conventional calculations) of equilibrium structures can be controlled by adjusting the decomposition threshold [52].

13.3.7. Method Specific Cholesky Decomposition

Although the CD of the two-electron integral matrix has proven to be very useful in the determination of molecular properties of small to medium-sized molecular systems, there are still several limitations. The major drawback of standard CD comes from the fact that integrals actually not needed are nonetheless calculated. In most cases the goal is not the exact determination of the two-electron integral matrix, but the calculation of some expression such as

$$E = \sum_{\alpha\beta\gamma\delta} V_{\alpha\beta} (\alpha\beta | \gamma\delta) V_{\gamma\delta} = \sum_{pq} V_p M_{pq} V_q = \sum_{pq} Z_{pq} \quad (13-46)$$

where a characteristic matrix \mathbf{Z} is implicitly defined. Instead of directly decomposing the matrix \mathbf{M}

$$M_{pq} = \sum_J L_p^J L_q^J + \Delta_{pq} \quad (13-47)$$

such that all elements of the residual matrix Δ are smaller than a predetermined threshold τ , it is normally more efficient to decompose the characteristic matrix \mathbf{Z} , as in this way the screening introduced by \mathbf{V} is taken into account. Alternatively, we can understand this decomposition considering a positive semidefinite matrix whose dimension is twice that of \mathbf{M}

$$\begin{aligned} \begin{pmatrix} V_p M_{pq} V_q & V_p M_{ps} \\ M_{rq} V_q & M_{rs} \end{pmatrix} &= \sum_J \begin{pmatrix} K_p^J \\ L_r^J \end{pmatrix} \begin{pmatrix} K_q^J \\ L_s^J \end{pmatrix}^T \\ &= \sum_J \begin{pmatrix} V_p \frac{M_{pJ} M_{Jq}}{M_{JJ}} V_q & V_p \frac{M_{pJ} M_{Js}}{M_{JJ}} \\ \frac{M_{rJ} M_{Jq}}{M_{JJ}} V_q & \frac{M_{rJ} M_{Js}}{M_{JJ}} \end{pmatrix} \\ &= \sum_J \begin{pmatrix} V_p L_p^J L_q^J V_q & V_p L_p^J L_s^J \\ L_r^J L_q^J V_q & L_r^J L_s^J \end{pmatrix} \end{aligned} \quad (13-48)$$

The off-diagonal block of the matrix in Eq. (13-48) enters in the expression of the gradient of the energy E

$$G_p = 2 \sum_q M_{pq} V_q = 2 \sum_J L_p^J \sum_q L_q^J V_q + 2 \sum_q \Delta_{pq} V_q \quad (13-49)$$

where the error terms are either zero ($\Delta_{pq} = 0$) or bound by the inequality

$$\begin{aligned} |\Delta_{pq} V_p| &= \frac{|V_p \Delta_{pq} V_q|}{|V_p|} \leq \frac{|V_p \Delta_{pp} V_p|^{1/2} |V_q \Delta_{qq} V_q|^{1/2}}{|V_p|} \\ &= \Delta_{pp}^{1/2} |V_q \Delta_{qq} V_q|^{1/2} \leq \Delta_{pp}^{1/2} T^{1/2} \end{aligned} \quad (13-50)$$

Therefore, the threshold of the decomposition also controls the error in the gradient. Moreover, the double dimension matrix illustrates that if we are only interested in the off-diagonal block, we can keep track of the two diagonals in Eq. (13-48) and choose different thresholds for each block.

The usefulness of the previous discussion becomes apparent when taking into account that the functional in Eq. (13-46) has the form of a variety of matrix contractions that appear in electronic structure computations. In particular, it is related to the calculation of the Coulomb and the exchange terms in Hartree-Fock and DFT calculations [40]. We start by what we denominate *Coulomb decomposition*. The calculation of the Coulomb term in conventional direct SCF methods scales as N^4 in the limit of a complete basis and as N^2 in the limit of a large system if the density

scales linearly with the system size. In contrast, the standard CD scales as N^3 in both limits (due the scaling of the decomposition itself).

The Coulomb energy is

$$E_C = \sum_{\alpha\beta\gamma\delta} D_{\alpha\beta}(\alpha\beta | \gamma\delta) D_{\gamma\delta} \quad (13-51)$$

and thus, according to our previous discussion, the characteristic matrix is

$$M_{\alpha\beta,\gamma\delta}^C = D_{\alpha\beta}(\alpha\beta | \gamma\delta) D_{\gamma\delta} \quad (13-52)$$

which can be Cholesky decomposed to give

$$M_{\alpha\beta,\gamma\delta}^C = \sum_J L_{\alpha\beta}^J L_{\gamma\delta}^J = \sum_{IJ} D_{\alpha\beta}(\alpha\beta | I) S_{IJ}^{-1}(J | \gamma\delta) D_{\gamma\delta} \quad (13-53)$$

where we have expressed the CD in an inner product [70, 71] form to emphasize its relationship with the RI method, as discussed in Sections 13.2 and 13.3.1. The matrix S has elements $S_{IJ} = (I | J)$ where I and J denote functions of the Cholesky basis. The decomposition might eventually be carried out in a reduced space — say, the atomic orbitals centered on a particular atom — to get a smaller Cholesky basis. Once the Cholesky vectors have been computed, the Coulomb energy is evaluated very easily

$$E_C = \sum_J \left(\sum_{\alpha\beta} L_{\alpha\beta}^J \right)^2 \quad (13-54)$$

The Coulomb Fock operator can be calculated in terms of the auxiliary basis or in terms of the CD of $S = KK^T$

$$F_{\alpha\beta}^C = 2 \sum_{IJ} (\alpha\beta | I) S_{IJ}^{-1}(J | \gamma\delta) D_{\gamma\delta} = 2 \sum_{IJ} (\alpha\beta | I) K_{JI}^{-1} \sum_{\gamma\delta} L_{\gamma\delta}^J \quad (13-55)$$

Due to the screening of high angular momentum functions in SCF and DFT methods, the number of Cholesky vectors required to compute the energy given by Eq. (13-54) becomes constant in the limit of a complete basis and therefore the global scaling is N^2 . The scaling of the Fock operator is also N^2 in the limit of a complete basis, but the scaling can become linear if we only calculate the elements with one occupied index and one general, as required for optimizing the energy. In the limit of a large system, the decomposition of the characteristic Coulomb matrix should scale quadratically in the integral calculation and cubically in the decomposition since the number of Cholesky vectors increases linearly.

The exchange contribution is very difficult to calculate with the RI and CD methods [19, 21] since using the vectors from standard CD of the two-electron integral matrix formally shows quartic scaling. Local density fitting [15, 20, 22] can reduce

the scaling but pays the price of loosing strict error control. Recently, Aquilante et al. [21] showed that it is possible to contract the density with the Cholesky vectors with only quadratic scaling, although the global procedure still scales as N^3 because of the scaling of the CD itself. As a matter of fact, the savings derived from the use of the standard CD are a consequence of the fact that the decomposition needs to be done only once, while a direct SCF method needs several calculations of the two-electron integrals. Therefore, it is very convenient to apply a specific decomposition-based technique to calculate the exchange. With opposite signs, the exchange energy and the Fock matrix read

$$E_X = \sum_{\alpha\beta\gamma\delta} D_{\alpha\gamma}(\alpha\beta | \gamma\delta)D_{\beta\delta} \quad (13-56)$$

$$F_{\alpha\beta}^X = \sum_{\gamma\delta} (\alpha\gamma | \beta\delta)D_{\gamma\delta} \quad (13-57)$$

The product of densities entering in Eq. (13-56) is an element of the Kronecker product of the density matrix times itself and therefore its rank is the number of kl -pairs, i.e., $O(O+1)/2$, O being the number of occupied orbitals. Therefore, the direct decomposition of a matrix with elements $D_{\alpha\gamma}(\alpha\beta | \gamma\delta)D_{\beta\delta}$ does not imply any saving as the number of kl -pairs easily becomes larger than the numerical rank of the two-electron matrix. We turn our attention, then, to the exchange Fock operator, which — after Cholesky decomposing the one-electron density matrix — is written as

$$F_{\alpha\beta}^X = \sum_{\gamma\delta k} C_{\gamma}^k(\alpha\gamma | \beta\delta)C_{\delta}^k \quad (13-58)$$

where, as previously shown by us [48], the orbitals C^k are localized. The former expression defines a characteristic matrix for the so-called *Exchange- k* algorithm

$$M_{\alpha\beta,\gamma\delta}^k = C_{\beta}^k(\alpha\beta | \gamma\delta)C_{\delta}^k = \sum_J {}^kL_{\alpha\beta}^J {}^kL_{\gamma\delta}^J \quad (13-59)$$

Let us recall that the *Exchange- k* algorithm builds up a localized auxiliary basis for each occupied orbital and therefore O decompositions of this kind are required for each calculation of the Fock operator in the SCF process. However, in many cases the localized orbitals have a significant overlap and, thus, it is more efficient to use a common auxiliary basis obtained from the decomposition of a composed characteristic matrix

$$\Omega = \begin{pmatrix} C_{\beta}^k(\alpha\beta | \gamma\delta)C_{\delta}^k \cdots C_{\beta}^k(\alpha\beta | \kappa\lambda)C_{\lambda}^l \\ \vdots \qquad \qquad \qquad \vdots \\ C_{\nu}^l(\mu\nu | \gamma\delta)C_{\delta}^k \cdots C_{\nu}^l(\mu\nu | \kappa\lambda)C_{\lambda}^l \end{pmatrix} \quad (13-60)$$

Since the orbitals C^k are localized, they make the characteristic matrix local in the limit of a large system and, consequently, the auxiliary basis becomes independent of the system size and the scaling becomes linear. On the other hand, as only two indices are screened, large basis sets will make the pre-factor larger. As the error in the energy is quadratic in the norm of the gradient, i.e. the Fock operator, the decomposition threshold needs not be very small if we are only interested in the energy.

Once the decomposition is carried out, the contribution of each localized orbital to the exchange Fock operator may be evaluated according to

$$F_{\alpha\gamma}^k = \sum_J {}^k H_{\alpha}^J {}^k H_{\gamma}^J = \sum_J \left(\sum_{\beta} {}^k L_{\alpha\beta}^J \right) \left(\sum_{\delta} {}^k L_{\gamma\delta}^J \right) \quad (13-61)$$

where we have implicitly defined the ${}^k \mathbf{H}^J$ vector. In practice, it is sufficient to decompose simply the two-electron integral matrix, but doing the screening on the diagonal elements on the basis of the characteristic matrices above.

As we have seen, in the *Exchange-k* decomposition only two indices are screened. It is also possible to screen the four indices of the two-electron integral while keeping the linear scaling in the computation of the exchange term in the Fock operator, but at the price of increasing the number of decompositions. This is the basic idea of the *Exchange-kl* algorithm, which can be derived from the expression of the exchange energy in Eq. (13-56) after decomposing the density matrices:

$$D_{\alpha\gamma} D_{\beta\delta} = \sum_k C_{\alpha}^k C_{\gamma}^k \sum_l C_{\beta}^l C_{\delta}^l = \sum_{kl} D_{\alpha\beta}^{kl} D_{\gamma\delta}^{kl} \quad (13-62)$$

This resorting of the density elements motivates the new characteristic matrix $M_{\alpha\beta,\gamma\delta}^{kl}$

$$E_X = \sum_{kl} \sum_{\alpha\beta\gamma\delta} M_{\alpha\beta,\gamma\delta}^{kl} = \sum_{kl} \sum_{\alpha\beta\gamma\delta} D_{\alpha\beta}^{kl} (\alpha\beta | \gamma\delta) D_{\gamma\delta}^{kl} \quad (13-63)$$

The decomposition of this matrix gives a localized auxiliary basis for each kl -pair of occupied orbitals. Therefore, the linearity with the molecular size of the scaling is kept, but the number of decompositions scales in a quadratic manner. Therefore, the method is in general not appropriate for compact systems with a high number of electrons. Parallel to the *Exchange-k* algorithm, in many cases the overlap among the different orbital pairs makes it more efficient to consider a composed characteristic matrix similar to that in Eq. (13-60). While the exchange energy may be directly evaluated in terms of the Cholesky vectors from the decomposition of $M_{\alpha\beta,\gamma\delta}^{kl}$, the Fock matrix with one occupied index can be calculated by adding all the pair contributions in terms of the auxiliary basis denoted by I and J

$$\begin{aligned}
 F_{\alpha k}^X &= \sum_l F_{\alpha k}^l = \sum_{\beta \gamma \delta l} C_{\beta}^l(\alpha \beta | \gamma \delta) D_{\gamma \delta}^{kl} \\
 &= \sum_{IJ\beta l} C_{\beta}^l(\alpha \beta | I) S_{IJ}^{-1} \sum_{\gamma \delta} (J | \gamma \delta) D_{\gamma \delta}^{kl}
 \end{aligned} \tag{13-64}$$

The two approaches to compute the exchange discussed so far suffer from the fact that several decompositions are required. To eliminate this disadvantage, but loosing the linear scaling with the system size, it is possible to add the transition exchange densities into a single exchange density matrix

$$D_{\alpha\beta}^X = N \sum_{kl} D_{\alpha\beta}^{kl} = N \sum_{kl} C_{\alpha}^k C_{\beta}^l \tag{13-65}$$

where N is a normalization constant that can be chosen in several ways, which actually correspond to different thresholds in the decomposition. For instance, the normalization with respect to the number of electrons N_e , such that

$$\sum_{\alpha\beta} \langle \phi_{\alpha} | \phi_{\beta} \rangle D_{\alpha\beta}^X = 1 \tag{13-66}$$

is achieved by choosing N as $2/N_e$. This is a convenient normalization constant for compact systems since $(N_e/2)^2$ terms enter the exchange energy, but in the large system limit only $(N_e/2)$ terms enter and, thus, taking N as $\sqrt{2/N_e}$ is more appropriate. It is even possible to take N simply as unity. In the *Exchange*(n) algorithms (where n is an integer indicating the different normalizations according to $n = 1: N = 1, n = 2: N = \sqrt{2/N_e}, n = 3: N = 2/N_e$) the characteristic matrix can be found by considering the matrix

$$\Omega = \begin{pmatrix} D_{\alpha\beta}^{kl}(\alpha\beta | \gamma\delta) D_{\gamma\delta}^{kl} & \cdots & D_{\alpha\beta}^{kl}(\alpha\beta | \kappa\lambda) D_{\kappa\lambda}^{k'l'} \\ \vdots & & \vdots \\ D_{\mu\nu}^{k'l'}(\mu\nu | \gamma\delta) D_{\gamma\delta}^{kl} & \cdots & D_{\mu\nu}^{k'l'}(\mu\nu | \kappa\lambda) D_{\kappa\lambda}^{k'l'} \end{pmatrix} \tag{13-67}$$

and we observe that the sum of the diagonal elements is precisely the exchange energy. Accordingly, we suggest to decompose the characteristic matrix

$$M_{\alpha\beta, \gamma\delta} = D_{\alpha\beta}^X(\alpha\beta | \gamma\delta) D_{\gamma\delta}^X, \tag{13-68}$$

to get the auxiliary basis. The scaling of such decomposition is the same as the standard CD, but the pre-factor is significantly smaller.

To illustrate the performance of the method, we present in Tables 13-1 and 13-2 the number of Cholesky vectors, i.e. the number of auxiliary basis functions, required to fit the Coulomb and the Exchange contributions for some model systems in the Hartree-Fock method. For the sake of comparison, recall that preoptimized

Table 13-1. Number of Cholesky vectors for water and benzene for Coulomb, *Exchange(3)*, and standard Cholesky decomposition for different basis sets, where N denotes the number of basis functions. The normalization used in the *Exchange(3)* decomposition is $2/N_e$. The number of vectors is presented both using the converged SCF density and the density from the Hückel guess. The decomposition threshold is 10^{-8}

Basis	N	Coulomb		Exchange(3)		CD
		Converged	Hückel	Converged	Hückel	
Water						
aug-cc-pVDZ	41	66	45	94	73	414
aug-cc-pVDZ	41	66	45	94	73	414
aug-cc-pVTZ	92	67	47	130	77	984
aug-cc-pVQZ	172	77	62	134	108	1,750
aug-cc-pV5Z	287	71	89	135	201	2,839
aug-cc-pV6Z	443	70	110	144	342	4,268
aug-cc-pV7Z	643	89	197	259	849	5,779
Benzene						
aug-cc-pVDZ	192	324	242	326	264	2,000
aug-cc-pVTZ	414	305	220	442	394	4,108
aug-cc-pVQZ	756	299	283	577	454	6,867

Table 13-2. Number of Cholesky vectors for different decompositions for an alpha helix glycine chain using aug-cc-pVDZ basis set, where N denotes the number of basis functions. The normalization used in the *Exchange(1)* and *Exchange(2)* decompositions are 1 and $\sqrt{2/N_e}$, respectively. The decomposition threshold is 10^{-8} for *Coulomb* and *Exchange(1-2)* decompositions and 10^{-4} for *Exchange-k* decomposition

Nr. glycines	N	Coulomb	Exchange(1)	Exchange(2)	Exchange-k	CD
1	160	258	736	534	1,524	1,792
2	279	469	1,213	771	3,034	3,071
3	398	688	1,850	1,145	4,562	4,345
5	636	1,132	3,033	1,752	8,054	6,899
10	1,231	2,264	6,262	3,361	18,730	13,195
14	1,707	3,177	8,606	4,311	27,589	—
20	2,421	4,545	12,601	5,994	40,804	—
25	3,016	5,665	15,954	7,369	51,687	—
30	3,611	6,815	—	8,346	62,690	—

standard RI auxiliary basis sets normally contain around 2–4 times the number of basis functions.

13.4. CALIBRATION OF ACCURACY

Several sets of benchmark calculations have been performed in order to establish the accuracy of the Cholesky auxiliary basis sets. In these benchmark papers the accuracy has been assessed as a function of the CD threshold, the AO basis set quality, the wave function model, variations of the CD auxiliary basis set generation and

the impact of auxiliary basis set pruning. In the first investigation Aquilante et al. [49] compared Full-CD, 1C-CD, and aCD auxiliary basis sets with pre-optimized auxiliary basis sets using the test set of Baker and Chan [92]. Results with respect to total energies and activation energies at the HF, DFT and MP2 level of approximation were analyzed. In a second study the 118 closed shell molecules of the G2/97 test set [93] and a small set of 7 transition metal containing elements of the MLBE21/05 database [94] were used to investigate the accuracy of the CD auxiliary basis sets [61]. In this benchmark, accuracies for total energies and dipole moments were presented in association with the HF, DFT and MP2 methods using several AO basis sets. This study also included assessments of the acCD auxiliary basis sets. Finally, in the third study, Boström et al. [69] assessed the accuracy with respect to the CASSCF/CASPT2 vertical excitation energies of 196 valence states of the test suite by Schreiber et al. [95] and 72 Rydberg states of 3 small organic systems. Below we give a brief summary of the findings.

13.4.1. Accuracy of Total Energies

The accuracy of total energies are presented in all of the above mentioned benchmark articles. Aquilante et al. [49] compared on-the-fly CD auxiliary basis sets with the pre-optimized RI-J [76] and RI-C [75] auxiliary basis sets, claiming that the former in contrast to the latter does not show a bias towards a specific quantum chemical method. The additional approximation introduced in the 1C-CD and aCD were also claimed to be negligible. The subsequent benchmark study by Boström and co-workers [61] confirmed these findings. Figure 13-7 shows Full-CD accuracy assessments in combination with the HF, MP2, DFT(BLYP) and DFT(B3LYP) models. Similar accuracies were observed independently of the quantum chemical model, supporting the claim that the CD auxiliary basis sets are unbiased. The accuracies were also seen to improve with tighter CD thresholds. For Full-CD the improvement was almost linear in these log-log-plots. A saturation effect could be

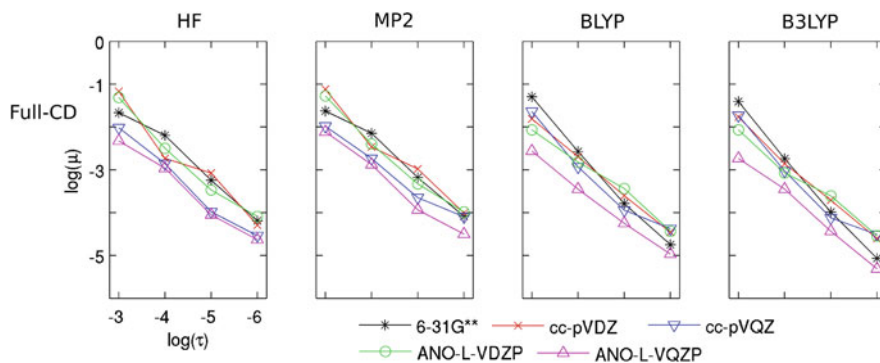


Figure 13-7. Mean absolute errors, μ , in kcal/(mol-electron) of the total energy associated with the Full-CD auxiliary basis set as a function of the Cholesky threshold, τ , in au for different AO basis sets. Each panel shows the result for a specific quantum chemical method

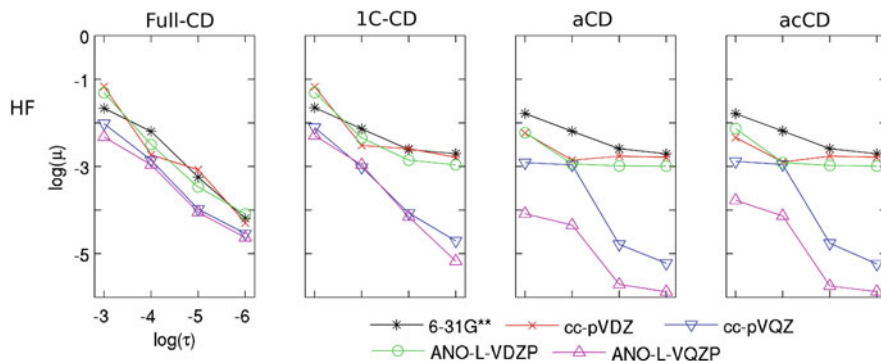


Figure 13-8. Mean absolute errors, μ , in kcal/(mol-electron) of the total energy associated with the HF wave function model vs the Cholesky threshold, τ , in au for different AO basis sets. Each panel shows the result for a specific CD auxiliary basis set

observed for the 1C-CD and atomic CD methods (shown in Figure 13-8) as the CD threshold was reduced. This was especially noted for AO basis sets of lower quality. It was generally found that the higher the quality of the AO basis set, the better the accuracy of the auxiliary basis set, this is particularly true for the aCD and acCD auxiliary basis sets. It was also observed that there is no significant difference between the aCD and acCD auxiliary basis sets. In general, an error of 0.01 kcal/(mol-electron) was found to be associated with a CD threshold of 10^{-4} au. Studies on a few transition metal complexes and additional properties as the dipole moments, and results presented for total CASPT2-energies of ground and excited states further support these findings.

13.4.2. Accuracy of Vertical Transition Energies

In the study by Aquilante et al. [49], the accuracy of activation energies were reported. A favorable cancellation of errors was observed in the computed activation energies corresponding to a reduction by a factor of 2–3 as compared to total energies. In a subsequent benchmark study [69] on CASPT2 vertical excitation energies, optimal with respect to error cancellation, a reduction of the error of roughly one order of magnitude was observed (see Figure 13-9).

Just as for total energies a dependence upon the AO basis set is present, favoring CD auxiliary basis sets generated in connection with higher quality AO basis sets. In Figure 13-9 it is demonstrated that the errors at the CASSCF and CASPT2 levels of theory for all practical purposes are similar. Just as for the G2/97 test it was observed that the Full-CD error decays almost exponentially whereas the gains in moving to smaller thresholds are less pronounced for the acCD and aCD auxiliary basis set. It was also noticed that the difference between the aCD and acCD approximations is insignificant and that the auxiliary basis set pruning gives an acceptable additional error. Computing excitations to Rydberg states can be challenging and special primitive functions are often added to the AO basis sets to correctly describe their diffuse character. To accommodate this, pre-optimized auxiliary basis sets are

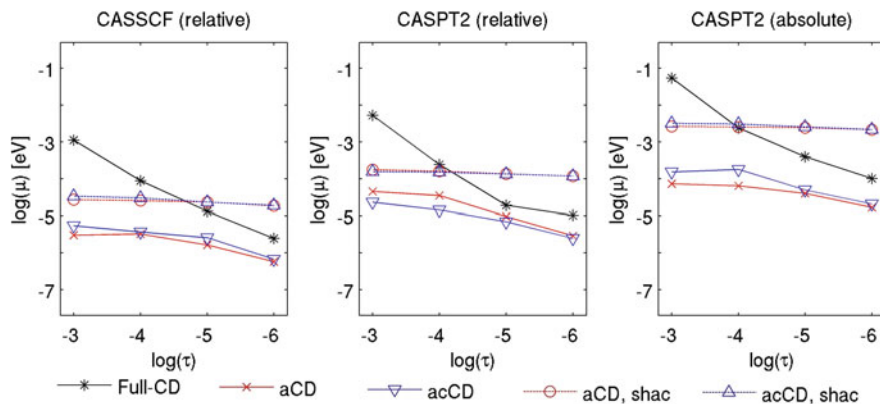


Figure 13-9. Mean absolute errors, μ , in eV of the vertical transition energies for the ANO-RCC-VTZP AO basis set at the CASSCF (left panel) and CASPT2 (center panel) level of theory and in total CASPT2 energies (right panel) as a function of the Cholesky threshold, τ , in au, the CD auxiliary basis set, and auxiliary basis set pruning

normally augmented with primitive auxiliary basis functions to maintain the accuracy established for valence excited states. In the CD auxiliary basis set, however, no special care is needed as long as the parent AO basis set used to generate it is properly augmented for the purpose. The trend observed for valence states was shown to hold for Rydberg states as well.

Qualitative results from benchmarking vertical transition energies showed that a CD threshold of 10^{-3} yields average errors smaller than 0.01 eV in all but some of the Full-CD cases and a CD threshold of 10^{-4} , as recommended for absolute energies above, will lower this to around 0.001 eV and even better in some cases.

13.4.3. Auxiliary Basis Set Pruning

In the study by Boström and co-workers[61] it was noted that the accuracy associated with the atomic CD auxiliary basis sets was better than necessary and that additional reductions of the basis set could be possible without too severe reduction in the accuracy. A method to prune the auxiliary basis set by skipping some higher angular momentum functions (denoted SHAC), a concept originally introduced by Eichkorn et al. [74], has been presented together with the loss of accuracy in utilizing SHAC on a small subset of 24 G2/97 molecules. The results using pruned auxiliary basis sets were also presented alongside the full aCD and acCD results in the CASSCF/CASPT2 benchmark paper. We note that the method of pruning in the study of Boström and co-workers is different from and slightly more sophisticated than the one used in the study by Aquilante et al. [49] In the latter the pruning is done after the atomic CD, while in the former the pruning it is done before the atomic CD.

A rather uniform loss of about one order of magnitude in accuracy (see Figure 13-10) was observed while using the pruned auxiliary basis set to calculate

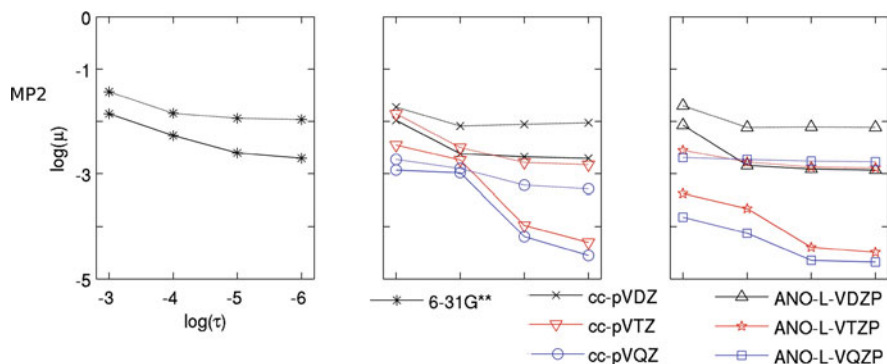


Figure 13-10. Mean absolute errors, μ , of the total MP2 energy in kcal/(mol-electron) evaluated with the aid of an aCD auxiliary basis set as a function of the Cholesky threshold, τ , in au, the AO basis set and auxiliary basis set pruning. The *dashed lines* represents results using auxiliary basis set pruning

relative energies. This can generally be afforded while still maintaining accuracies almost as good as, or in some cases better, than with Full-CD. For total energies the trend is not as clear, but pruning might still be a viable alternative, at least for high quality AO basis sets.

13.5. IMPLEMENTATIONAL ASPECTS

Cholesky decomposition of a positive semi-definite matrix \mathbf{M} is often based on the assumption that the matrix can be stored in memory. This is a reasonable assumption for a number of matrices such as the atomic orbital overlap matrix for which the number of nonzero elements scales linearly with system size (number of atoms). In such cases, the Cholesky decomposition can be performed in linear-scaling time [82]. In many cases, however, the matrix can not be stored in memory. For example, the entire molecular two-electron integral matrix can be stored in core only for the smallest basis sets and molecules. In addition, the semi-definite nature implies that only a fraction of the matrix columns is needed to decompose the matrix to a prescribed accuracy specified by the decomposition threshold. An out-of-core (matrix-direct) algorithm is clearly needed. Using τ to denote the decomposition threshold, an out-of-core algorithm for the decomposition of a positive semi-definite matrix \mathbf{M} can be summarized as follows:

1. Get diagonal elements of the matrix:

$$D_p = M_{pp}$$

$$D_{\max}^{(1)} = \max_p D_p$$

2. Compute reduced set of significant diagonal elements:

$$\mathcal{L}^{(1)} = \left\{ p \mid d \sqrt{D_{\max}^{(1)} D_p} > \tau, d \geq 1 \right\}$$

3. Initialize vector counter: $\mathcal{N} = 0$.
4. Initialize counter: $i = 0$
5. While $D_{\max}^{(i+1)} > \tau$:

- a. Update counter: $i = i + 1$
- b. Compute smallest diagonal that may be treated:

$$D_{\min}^{(i)} = \max \left(sD_{\max}^{(i)}, \tau \right), \quad s \leq 1$$

- c. Compute set of qualified diagonals:

$$\mathcal{Q}^{(i)} = \left\{ q \mid q \in \mathcal{L}^{(i)}, D_q > D_{\min}^{(i)} \right\}$$

- d. Get matrix columns corresponding to qualified diagonals:

$$M_{pq}, \quad p \in \mathcal{L}^{(i)}, q \in \mathcal{Q}^{(i)}$$

- e. Subtract contributions from previous vectors:

$$\Delta_{pq} = M_{pq} - \sum_{J=1}^{\mathcal{N}} L_p^J L_q^J, \quad p \in \mathcal{L}^{(i)}, q \in \mathcal{Q}^{(i)}$$

- f. Compute largest diagonal among qualified:

$$Q_{\max} = \max_{q \in \mathcal{Q}^{(i)}} D_q^{(i)}$$

- g. Initialize counter: $j = 0$
- h. While $j < \dim(\mathcal{Q}^{(i)})$ and $Q_{\max} > D_{\min}^{(i)}$:
 - i. Update counters: $j = j + 1, J = \mathcal{N} + j$
 - ii. Assign Cholesky basis function h_j to $[q]_J$, the index corresponding to Q_{\max}
 - iii. Calculate Cholesky vector:

$$L_p^J = Q_{\max}^{-1/2} \Delta_{p,[q]_J}, \quad p \in \mathcal{L}^{(i)}$$

- iv. Update:

$$\begin{aligned} \Delta_{pq} &\leftarrow \Delta_{pq} - L_p^J L_q^J, \quad p \in \mathcal{L}^{(i)}, q \in \mathcal{Q}^{(i)} \\ D_p &\leftarrow D_p - \left(L_p^J \right)^2, \quad p \in \mathcal{L}^{(i)} \\ Q_{\max} &= \max_{q \in \mathcal{Q}^{(i)}} D_q \end{aligned}$$

- i. Update vector counter: $\mathcal{N} = \mathcal{N} + j$
- j. Compute largest diagonal:

$$D_{\max}^{(i+1)} = \max_{p \in \mathcal{L}^{(i)}} D_p$$

k. Compute reduced set of significant diagonal elements:

$$\mathcal{L}^{(i+1)} = \left\{ p \mid d \sqrt{D_{\max}^{(i+1)} D_p} > \tau, d \geq 1 \right\}$$

Due to the subtraction step (point 5 e), the computational effort is cubic with respect to the dimension of the reduced set (point 2). This implies that the decomposition of the entire molecular two-electron integral matrix scales cubically with the size of the system. As discussed above, the decomposition of the characteristic matrices appearing in method-specific Cholesky decomposition can be done in quadratic or linear time, depending on the characteristic matrix.

In addition to the decomposition threshold τ , two input parameters are used in this algorithm: the screening damping $d \geq 1$ (points 2 and 5k) and the span factor $s \leq 1$ (point 5 b). The screening damping ensures that matrix elements with values below the decomposition threshold have a nonzero Cholesky representation. For decomposition of two-electron integrals, we choose the damping according to $d \approx 10^9 \tau$ for thresholds above 10^{-8} and $d = 1.0$ for lower thresholds. The span factor modifies the pivoting by allowing diagonals to be treated even if the value of the diagonal element is not the largest. It has been introduced in order to minimize the overhead that may be involved in fetching the columns (point 5 d) as well as to minimize the I/O operation necessary for the subtraction (point 5 e) in cases where the Cholesky vectors can not be stored in core. This is normally the case when decomposing two-electron integrals. For two-electron integrals we choose the span factor as $s = 0.01$, i.e. diagonals that are at most 100 times smaller than the largest diagonal may be treated. Since two-electron integrals in the atomic orbital basis are usually computed in shell quadruples, i.e. a subblock of the integral matrix where each of the four atomic orbital indices belongs to a given atomic shell, the span factor allows us to make use of more computed integrals than just the column corresponding to the largest diagonal. This, in turn, minimizes the potentially huge number of integral recalculations that would result from strict pivoting. In order to keep the dimension of the set of qualified diagonals (point 5c) at a reasonable level, it is further restricted to contain at most 100 diagonals. For two-electron integral decompositions, these are chosen from the shell pairs containing the largest diagonals.

The decomposition time is dominated by the subtraction step (point 5 e) in most cases, although the fetching of integral columns may be equally time-consuming. The latter is the case, e.g., for two-electron integral evaluations involving basis sets with a very large number of primitive Gaussian functions. The main bottleneck of the subtraction step is reading the previous vectors from disk, which is needed when available memory is insufficient to store the vectors in core. Two approaches have been implemented to circumvent the I/O bottleneck: a distributed parallel algorithm and a two-step algorithm.

In a parallel execution, the elements of the the reduced sets (points 2 and 5k) are distributed among the processes. Each process fetches the corresponding rows of the matrix (point 5d) and performs the subtraction of previous Cholesky vectors (point 5e). This requires that the Cholesky vector elements corresponding to the set of qualified diagonals (L_q^J in point 5e) are broadcast from the process holding them. This design ensures that the memory requirement per process is minimized and that Cholesky vector I/O can be avoided by increasing the number of computational nodes (thus increasing available memory).

The two-step algorithm, as the name indicates, proceeds in two steps. In the first step, the algorithm outlined above is used to obtain the Cholesky basis (assuming that the matrix is a finite basis set representation of an operator) such that

$$M_{IJ} = \sum_K L_I^K L_J^K$$

Note that this is exact regardless of the chosen decomposition threshold. The only modification of the algorithm is that reduced sets (points 2 and 5k) are computed according to

$$\mathcal{L}^{(i)} = \left\{ p \mid D_p > \tau \right\}$$

That is only those diagonals that may give rise to Cholesky vectors are retained. In the second step, complete Cholesky vectors are computed according to

$$L_p^J = (L_J^J)^{-1/2} \left[M_{pJ} - \sum_{K=1}^{J-1} L_p^K L_J^K \right]$$

where M_{pJ} denotes element p of the column corresponding to Cholesky vector J . By driving the calculation of full Cholesky vectors with a loop over (blocks of) row indices p , I/O is avoided if the vector components corresponding to the Cholesky basis, L^K_J , can be stored in core. If they can not be stored in core, the I/O bottleneck is not removed but significantly reduced. The two-step algorithm can fairly easily be parallelized. The parallel algorithm discussed above can be utilized for the first step, while the loop over row indices in the second step can be parallelized.

In order to illustrate the performance of these algorithms, as implemented in the MOLCAS program package [44], we consider the Cholesky decomposition of the molecular two-electron integral matrix for the three units of 3-butylthiophene shown in Figure 13-11. The atomic orbital basis sets cc-pVTZ and cc-pVQZ correspond to a total of 1,270 and 2,457 basis functions, respectively, for this system. The two-electron integral matrix thus contains approximately 326×10^9 and $4,559 \times 10^9$ elements. Using a single processor on a 2.66 GHz Intel Xeon X5355 Quad Core with 1,900 Mb memory, the Cholesky decomposition of the cc-pVTZ integral matrix with a threshold of 10^{-4} au requires 10.5 h wall time. The Cholesky vectors

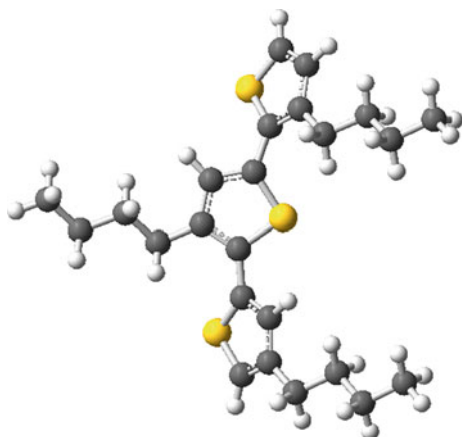


Figure 13-11. System consisting of 3 units of 3-butylthiophene

require 12.4 Gb storage and the CPU time of 1.8 h clearly indicates the I/O bottleneck alluded to above. Using the two-step algorithm, the total decomposition time reduces to 1.2 h wall time and 0.8 h CPU time. Though not entirely removed, the I/O bottleneck is significantly reduced. Using the parallel one-step algorithm for the cc-pVQZ basis set with the same decomposition threshold (10^{-4} au), the speedup (in terms of wall time) is given in Figure 13-12. The speedup is measured for 8, 16, 32, 64, 128, and 256 processors relative to the calculation on 4 processors. All processors are of the above mentioned type connected with Infiniband and 1,900 Mb memory is used on each processor. The Cholesky vectors require 73.5 Gb storage. The calculation on 4 processors requires 70.2 h wall time/32.1 h CPU time, whereas the calculation on 256 processors requires 1.1 h wall time/1.0 h CPU time. These timings show that a major advantage of parallel execution is the reduction of I/O.

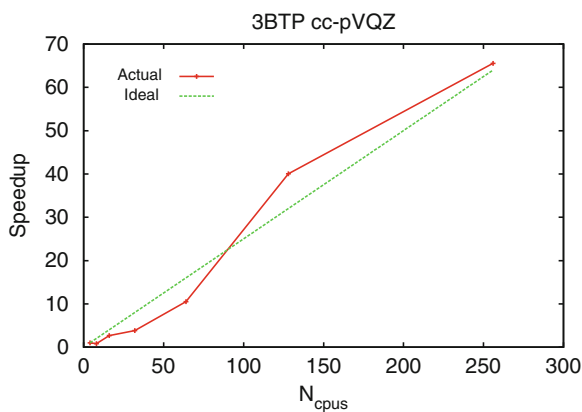


Figure 13-12. Parallel speedup for the cc-pVQZ decomposition

Running the same decomposition with the serial two-step algorithm takes 29.8 h wall time/9.3 h CPU time with 1,900 Mb memory and 8.3 h wall time/6.4 h CPU time with 15,200 Mb memory. Comparing to the timings of the parallel one-step algorithm, it is clear that optimal performance would be achieved by parallelizing the two-step algorithm. This is an on-going project.

Finally, it is worth mentioning that the first step in the two-step algorithm can be regarded as computation of the Cholesky basis to be used with the density fitting approach. The timings for this step are therefore of interest. With the cc-pVTZ basis set, generation of the Cholesky basis requires 9.5 min wall time/7.1 min CPU time, whereas the cc-pVQZ basis set requires 4.7 h wall time/1.3 h CPU time with 1,900 Mb memory and 1.2 h wall time/1.1 h CPU time with 15,200 Mb memory on a single processor.

The calculation of integrals in the CD procedure is in practice not different from that of an ordinary two-electron integral driver. The only significant difference is in the respect that the CD algorithm is expressed in terms of specific basis functions, whereas the most efficient two-electron integrals implementations and algorithms derive their efficiency in not treating the basis functions one at the time but rather to compound all basis functions of a center and with the same total angular momentum into a single entity – a shell. Hence, efficient modern computer codes compile integrals in batches of shell quadruples. This is in conflict with the CD procedure and would, if not handled or considered, make the program compute a significant number of integrals in vain. The effect is of particular significance for generally contracted basis functions (so-called ANO basis set) as compared to the segmented basis sets. The so-called span factor has been introduced to reduce this loss and is of particular importance when dealing with basis sets of the ANO type. In common to a traditional two-electron code a CD implementation requires the standard set of pre-computed intermediates to be computed. After that the CD procedure requires the two electron integral code to be able to compute a shell quadruple on demand and in any order. This is ensured with some minor modifications to any existing integral code to introduce the required modularity of the code.

13.6. OUTLOOK AND PERSPECTIVES

As we have demonstrated in the previous sections, CD is a valuable tool to control the accuracy and associated computational effort with only a single threshold parameter. The advantage using a decomposed form of the two-electron integrals is not apparent in all cases. For instance, using this integral representation in coupled cluster models does not lead directly to lower scaling expressions.

An essential solution to this problem is to perform method specific decomposition (Section 13.3.7), such that the auxiliary basis sets are tailor-made for a given model or even a particular term. As was shown in the previous section, the actual construction of the basis is the smallest part of the calculation. The scaling of the subsequent contractions will benefit from the reduced size as compared to any pre-optimized procedure. In some cases the basis becomes practically constant (e.g. for

the Coulomb energy) and these reductions are almost impossible to obtain using pre-optimized auxiliary basis sets.

Another solution is to exploit the inherent locality of the Cholesky basis (Section 13.3.2) to design a trivially linear-scaling density fitting algorithm which retains the unbiased (i.e., non-method specific) nature and complete error control of full CD [58, 62]. Compared to method specific CD, the local approach will require more auxiliary basis functions (since it is unbiased) but it will be the same auxiliary functions that are used for all contributions (Coulomb, exchange, dynamical and static correlation).

In the limit of large basis, CD is clearly favored as one may save the Cholesky vectors in compact form and in this way save expensive recalculation of two-electron integrals. One should remember that, in the complete basis set limit, the number of two-electron integrals scales as N^4 and to treat 10,000 atomic orbitals will result in roughly 10,000 TByte of two-electron integrals to be processed. This calls for even more compact treatment of the two-electron integrals beyond the $3N^3$ to $8N^3$ scaling attainable by the full CD. The ultimate goal is an N^2 scaling in the limit of a complete basis, and we have already made significant progress in this direction.

The development of correlated methods such as coupled cluster and CASPT2 for energy, gradient and response properties will be needed in order to take full advantage of the developments presented in this chapter. Subsystem based methods are becoming very important in quantum chemistry as the need for accurate electronic structure methods for larger systems is increasing. Techniques based on CD will play a central role in these developments.

13.7. SUMMARY AND CONCLUSIONS

In this review we have presented the original scheme behind Cholesky decomposition [23] of positive semidefinite matrices, which can be considered a special type of Gram-Schmidt orthonormalization or as a special case of LU factorization. In particular, a point is made that the iterative procedure, controlled with a single parameter, completely removes linear dependencies by eliminating zero or near-zero eigenvectors in a controlled manner. Hence, the CD procedure can be considered an effective way to represent large matrices in a compact manner. The CD procedure has in the past been considered a purely numerical procedure used mainly, if not exclusively, for solving positive definite linear equations. In 1977, however, the CD procedure was introduced as a tool for simplifying the handling of two-electron integrals in quantum chemistry by Beebe and Linderberg [24].

For a number of cases, we demonstrate how the CD procedure may be applied to the methods of electronic structure theory. We show that the CD procedure is a special type of resolution-of-the identity or density-fitting scheme. This connection is of particular importance, since it provides an analytic view of CD. From this point of view, it becomes possible to derive, with some limitations, analytic expression for gradients and higher-order derivatives with respect to nuclear geometry. We furthermore demonstrate that the CD procedure forms a reliable and accurate tool

for constructing one-center auxiliary basis sets to be used in the RI/DF formalism. The CD procedure can also be applied to the one-particle occupied density and the virtual pseudo-density matrix to obtain localized MOs (Cholesky MOs) in an effective non-iterative fashion. The Cholesky MOs are instrumental for an effective and fast computation of the exchange contribution to the Fock matrix, the LK algorithm. Special versions of the CD MO localization scheme allow the generation of active orbitals to be used in correlation treatments. The use of these orbitals has demonstrated considerable reduction of the computational effort in the evaluation of, for example, intermolecular interaction energies at the MP2 and CCSD(T) levels of theory. Yet another use of the CD procedure is demonstrated in quartic-scaling MP2. Here the CD procedure is applied directly to the MP2 amplitude matrix. Combined with efficient prescreening, this yields a canonical MP2 approach scaling as N^4 . Finally, we provide yet another case in which the CD procedure is applied to give dramatic reduction as compared to a conventional implementation. In method specific CD, the two-electron integrals are not treated alone but are combined with density matrices such that the resulting Cholesky basis is tailored to accurately represent the contribution (Coulomb or exchange) of interest. This leads to what we have coined *Coulomb decomposition* and three different *Exchange decompositions*. It is demonstrated that the method specific CD procedure leads to dramatic savings as compared to the standard CD procedure applied to the two-electron integrals.

We present results from calibration calculations in which the statistical accuracy of the CD procedure is studied. These assessments are investigated for total energies for a range of wave function models and density functional theory, as well as for vertical excitation energies at the CASSCF and CASPT2 levels of theory. The benchmark calculations were performed for various sets of valence and CD auxiliary basis sets. Accuracies for total energies associated with CD thresholds of 10^{-4} au were found to be of 0.01 kcal/(mol · electron) and for excitation energies the corresponding accuracy was found to be 0.001 eV on average. Furthermore, these studies verify that CD (full as well as atomic) is an unbiased, highly accurate alternative to pre-optimized auxiliary basis sets, albeit at the price of a slightly larger number of auxiliary basis functions. For Full-CD basis sets the Cholesky threshold gives complete control of the accuracy. A good compromise of speed and accuracy is obtained using a threshold of 10^{-4} in connection with absolute energies. For relative energies a reduction in error due to favorable cancellation of errors have been observed and for vertical excitation energies this might even allow for a threshold of 10^{-3} to be used in most cases. For high quality basis sets, pruning gives a significant reduction in auxiliary basis set size with an affordable loss of accuracy. Moreover, the special type of atomic CD auxiliary basis sets, the so-called atomic compact CD (acCD), comes with significant reduction of the number of primitive functions in the auxiliary basis set at virtually no loss of accuracy.

Towards the end of this review, details of the implementational aspects of the CD method are presented. Techniques are presented which take into consideration the fact that the computer representation of numbers is not infinitely accurate. In addition, the fact that effective two-electron integral computation is done in shell-quadruples – a procedure which is not perfect for a straightforward CD

implementation – is considered and compromises are suggested. Finally, a scheme of efficient implementation of a parallel CD procedure is presented together with benchmark results which demonstrate encouraging speed-up with up to 256 CPUs.

Finally an outlook and perspective of the CD method in ab initio quantum chemistry is presented. The authors take the view that the CD procedure offers several advantages in reducing the scaling of well-known quantum chemical methods. To fully exploit CD techniques, however, further work has to be done with respect to implementation.

To conclude, it is our opinion that the CD technique is a much overlooked method that holds a great potential in the field of quantum chemistry. We hope that the current flux of papers on CD technique has changed this general attitude – to our knowledge to this date (February 2010) there has been published in total 22 papers with respect to the CD technique in quantum chemistry, 16 of these over the last three years. We are convinced that the CD procedure has much more to offer if we look more carefully for opportunities.

ACKNOWLEDGMENTS

ASM acknowledges financial support from Spanish FEDER+MEC project CTQ2007-67143-C02-01/BQU. RL and JB would like to thank the Swedish Research Council directly and through the Linnaeus Center of Excellence on Organizing Molecular Matter at Lund University, Sweden, for financial support. TBP acknowledges financial support from the CoE Centre for Theoretical and Computational Chemistry (179568/V30). FA would like to acknowledge funding from the Swiss National Science Foundation (SNF), Grant No. 200020-120007. HK and LB would like to thank the Norwegian Research Council for support (Grant No. 154011/420). The authors thank Eirik Hjertenæs at the Norwegian University of Science and Technology for proof-reading the manuscript.

REFERENCES

1. Whitten JL (1973) *J Chem Phys* 58:4496
2. Baerends EJ, Ellis DE, Ros P (1973) *Chem Phys* 2:41
3. Jafri JA, Whitten JL (1974) *J Chem Phys* 61:2116
4. Sambe H, Felton RH (1975) *J Chem Phys* 62:1122
5. Dunlap BI, Connolly JWD, Sabin JR (1979) *J Chem Phys* 71:3396
6. Dunlap BI, Connolly JWD, Sabin JR (1979) *J Chem Phys* 71, 4993
7. Feyereisen M, Fitzgerald G, Komornicki A (1993) *Chem Phys Lett* 208:359
8. Vahtras O, Almlöf, Feyereisen M (1993) *Chem Phys Lett* 213:514
9. Gallant RT, St-Amant A (1996) *Chem Phys Lett* 256:569
10. Fonseca Guerra C, Snijders JG, te Velde G, Baerends EJ (1998) *Theor Chem Acc* 99:391
11. Dunlap BI (2000) *J Mol Struct Theochem* 501–502:221
12. Sierka M, Hogeckamp A, Ahlrichs R (2003) *J Chem Phys* 118:9136
13. Sodt A, Subotnik JE, Head-Gordon M (2006) *J Chem Phys* 125:194109
14. Sałek P, Høst S, Thøgersen L, Jørgensen P, Manninen P, Olsen J, Jansík B, Reine S, Pawłowski F, Tellgren E, Helgaker T, Coriani S (2007) *J Chem Phys* 126:Art.Nr. 114110

15. Reine S, Tellgren E, Krapp A, Kjærgaard T, Helgaker T, Jansík B, Høst S, Salek P (2008) *J Chem Phys* 129:Art.Nr. 104101
16. Köster AM del Campo JM, Janetzko F, Zuniga-Gutierrez B (2009) *J Chem Phys* 130:Art.Nr. 114106
17. Domínguez-Soria, G Geudtner, JL Morales, P Calaminici, Köster, AM (2009) *J Chem Phys* 131:Art.Nr. 124102
18. Burow AM, Sierka M, Mohamed F (2009) *J Chem Phys* 131:Art.Nr. 214101
19. Weigend F (2002) *Phys Chem Chem Phys* 4:4285
20. Polly R, Werner HJ, Manby FR, Knowles P (2004) *Mol Phys* 102:2311
21. Aquilante F, Pedersen TB, Lindh R (2007) *J Chem Phys* 126:Art.Nr. 194106
22. Sodt AM, Head-Gordon (2008) *J Chem Phys* 128:Art.Nr. 104106
23. Benoît Cdt (1924) *Bull Géodésique* 2:67
24. Beebe NHF, Linderberg J (1977) *Int J Quantum Chem* 12:683
25. Røeggen I, Wisløff-Nilssen E (1986) *Chem Phys Lett* 132:154
26. Røeggen I, Veseth L (2005) *Int J Quantum Chem* 101:201
27. Røeggen I (2006) *J Chem Phys* 124:Art.Nr.184502
28. Røeggen I (2006) *Theor Chem Acc* 116:683
29. Røeggen I (2007) *J Chem Phys* 126:Art.Nr. 204303
30. Røeggen I, Johansen T (2008) *J Chem Phys* 128:Art.Nr. 194107
31. O'Neal DW, Simons J (1989) *Int J Quantum Chem* 36:673
32. Koch, H Sánchez de Merás A, Pedersen TB (2003) *J Chem Phys* 118:9481
33. Pedersen TB, Sánchez de Merás A, Koch H (2004) *J Chem Phys* 120:8887
34. Christiansen O, Koch H, Jörgensen P (1995) *Chem Phys Lett* 243:409
35. García Cuesta I, Pedersen TB, Koch H, Sánchez de Merás AMJ (2004) *Chem Phys Lett* 390:170
36. Pedersen TB, Koch H, Boman L, Sánchez de Merás AMJ (2004) *Chem Phys Lett* 393:319
37. García Cuesta I, Pedersen TB, Koch H, Sánchez de Merás A (2006) *Chem Phys Chem* 7:2503
38. Fernández B, Pedersen TB, Sánchez de Merás A, Koch H (2007) *Chem Phys Lett* 441:332
39. García Cuesta I, Sánchez Marín J, Pedersen TB, Koch H, Sánchez de Merás A (2008) *Phys Chem Chem Phys* 10:361
40. Boman L, Koch H, Sánchez de Merás A (2008) *J Chem Phys* 129:Art.Nr. 134107
41. Pedersen TB, Kongsted J, Crawford TD, Ruud K (2009) *J Chem Phys* 130:Art.Nr. 034310
42. Pedersen TB, Kongsted J, Crawford TD (2009) *Chirality* 21:S68
43. Sánchez de Merás A, Koch H, García Cuesta I, Boman L (2010) *J Chem Phys* 132: Art.Nr. 204105
44. Aquilante F, De Vico L, Ferré N, Ghigo G, Malmqvist PA, Neogrady P, Pedersen TB, Pitoňák M, Reiher M, Roos BO, Serrano-Andrés L, Urban, M Varyazov V, Lindh R (2010) *J Comput Chem* 31:224
45. Aquilante F, Pedersen TB, Roos BO, Sánchez de Merás A, Koch H (2008) *J Chem Phys* 129:Art.Nr. 24113
46. Aquilante F, Malmqvist PÅ, Pedersen TB, Ghosh A, Roos BO (2006) *J Chem Theory Comput* 4:694
47. Aquilante F, Pedersen TB (2007) *Chem Phys Lett* 449:354
48. Aquilante F, Pedersen TB, Sánchez de Merás A, Koch H (2006) *J Chem Phys* 125:Art.Nr. 174101
49. Aquilante F, Lindh R, Pedersen TB (2007) *J Chem Phys* 127:Art.Nr. 114107
50. Öhrn A, Aquilante F (2007) *Phys Chem Chem Phys* 9:470
51. Roos BO, Varyazov V, Conradie J, Taylor PR, Ghosh A (2008) *J Phys Chem B* 112:14099
52. Aquilante F, Lindh R, Pedersen TB (2008) *J Chem Phys* 129:Art.Nr. 034106
53. Pierloot K, Vancoillie S (2008) *J Chem Phys* 128:Art.Nr. 034104
54. Radoń M, Pierloot K (2008) *J Phys Chem A* 112:11824
55. Bozoglian F, Romain S, Ertem MZ, Todorova TK, Sens C, Mola J, Montserrat R, Romero I, Benet-Buchholz J, Fontrodona X, Cramer CJ, Gagliardi L, Llobet A (2009) *J Am Chem Soc* 131:15176
56. Söderhjelm P, Aquilante F, Ryde U (2009) *J Phys Chem B* 113:11085

57. Srnec M, Aquilante F, Ryde U, Rulíšek L (2009) *J Phys Chem B* 113:6074
58. Pedersen TB, Aquilante F, Lindh R (2009) *Theor Chem Acc* 124:1
59. Huber SM, Shahi ARM, Aquilante F, Cramer CJ, Gagliardi L (2009) *J Chem Theory Comput* 5:2967
60. Huber SM, Ertem MZ, Aquilante F, Gagliardi L, Tolman WB, Cramer CJ (2009) *Chem Eur J* 15:4886
61. Boström J, Aquilante F, Pedersen TB, Lindh R (2009) *J Chem Theory Comput* 5:1545
62. Aquilante F, Gagliardi L, Pedersen TB, Lindh R (2009) *J Chem Phys* 130:Art.Nr. 154107
63. Riley KE, Pitoňák M, Černý J, Hobza P (2010) *J Chem Theory Comput* 6:66
64. Pitoňák M, Heßelmann A (2010) *J Chem Theory Comput* 6:168
65. Pitoňák M, Neogfady P, Hobza P (2010) *Phys Chem Chem Phys* 12:1369
66. Vysotskiy VP, Cederbaum LS (2010) *J Chem Phys* 132:Art.Nr. 044110
67. Chwee TS, Carter EA (2010) *J Chem Phys* 132:074104
68. Tabookht Z, López X, de Graaf C (2010) *J Phys Chem A* 114:2028
69. Boström J, Delcey MG, Aquilante F, Serrano-Andrés L, Pedersen TB, Lindh R (2010) *J Chem Theory Comput* 6:P747
70. Löwdin PO (1965) *J Chem Phys* 43:S175
71. Löwdin PO (1970) *Int J Quantum Chem* S4:231
72. Golub GH, Van Loan CF (1996) *Matrix computations*, 3rd edn. Johns Hopkins University Press, Baltimore, MD
73. Koch H, Sánchez de Merás A (2000) *J Chem Phys* 113:508
74. Eichkorn K, Treutler O, Öhm H, Häser M, Ahlrichs R (1995) *Chem Phys Lett* 240:283
75. Weigend F, Köhn A, Hättig C (2002) *J Chem Phys* 116:3175
76. Weigend F (2006) *Phys Chem Chem Phys* 8:1057
77. Jung Y, Sodt A, Gill PMW, Head-Gordon M (2005) *Proc Natl Acad Sci USA* 102:6692
78. Werner HJ, Manby FR (2006) *J Chem Phys* 124:Art.Nr. 054114
79. Boys SF (1960) *Rev Mod Phys* 32:296
80. Edmiston C, Ruedenberg K (1963) *Rev Mod Phys* 35:457
81. Pipek J, Mezey PG (1989) *J Chem Phys* 90:4916
82. Schweizer S, Kussmann J, Doser B, Ochsenfeld C (2008) *J Comput Chem* 29:1004
83. Ziołkowski M, Jansík B, Jørgensen P, Olsen J (2009) *J Chem Phys* 131:Art.Nr. 124112
84. Dunning TH Jr (1989) *J Chem Phys* 90:1007
85. Fernández B, Koch H, Makarewicz J (1999) *J Chem Phys* 111:5922
86. Scuseria GE, Ayala PY (1999) *J Chem Phys* 111:8330
87. Weigend F, Häser M (1997) *Theor Chem Acc* 97:331
88. Hättig C (2003) *J Chem Phys* 118:7751
89. Köhn A, Hättig C *J Chem Phys* 119:5021
90. Deglmann P, May K, Furche F, Ahlrichs R (2004) *Chem Phys Lett* 384:103
91. Rappoport D, Furche F (2005) *J Chem Phys* 122:Art.Nr. 064105
92. Baker J, Chan F (1996) *J Comput Chem* 17:888
93. Curtiss LA, Raghavachari K, Redfern PC, Pople JA (1997) *J Chem Phys* 106:1063
94. Schultz NE, Zhao Y, Truhlar DG (2005) *J Phys Chem A* 109:11127
95. Schreiber M, Silva-Junior M, Sauer SPA, Thiel W (2008) *J Chem Phys* 128:Art.Nr. 134110

CHAPTER 14

LOCAL APPROXIMATIONS FOR AN EFFICIENT AND ACCURATE TREATMENT OF ELECTRON CORRELATION AND ELECTRON EXCITATIONS IN MOLECULES

TATIANA KORONA¹, DANIEL KATS², MARTIN SCHÜTZ²,
THOMAS B. ADLER³, YU LIU³, AND HANS-JOACHIM WERNER³

¹ Faculty of Chemistry, University of Warsaw, PL-02-093 Warsaw, Poland,
e-mail: tania@chem.uw.edu.pl

² Institute of Physical and Theoretical Chemistry, University of Regensburg, D-93040 Regensburg,
Germany, e-mail: danylo.kats@chemie.uni-regensburg.de; martin.schuetz@chemie.uni-regensburg.de

³ Institut für Theoretische Chemie, Universität Stuttgart, D-70569 Stuttgart, Germany, e-mail:
adler@theochem.uni-stuttgart.de; liu@theochem.uni-stuttgart.de; werner@theochem.uni-stuttgart.de

Abstract: Local methods for the description of electron correlation in ground and electronically excited states of molecules, as implemented in the MOLPRO system of ab initio programs, are reviewed. Recent improvements in the performance of the local method resulting from an implementation of the density-fitting technique for all electron-repulsion integrals are discussed. Local fitting approximations lead to linear scaling of CPU time and disk space with molecular size, and allow for a significant increase of the size of molecules and basis sets that can be treated by the local MP2, CCSD, and CCSD(T) ab initio methods. Recent extensions of these methods to open-shell systems, as well as the inclusion of explicitly correlated terms are described. It is demonstrated that the latter lead to a drastic improvement of the accuracy of local methods. A local treatment of electron excitations within the EOM-CCSD and CC2 theories, as well as a local description of first- and second-order molecular properties are also discussed. Finally, we present some illustrative applications of the outlined methods.

Keywords: Local correlation, Coupled cluster, Local CCSD, Local CC2, Density fitting, Explicit correlation

14.1. INTRODUCTION

The accurate treatment of electron correlation in large molecules is one of the major challenges in theoretical chemistry. In the first place, this requires the selection of an appropriate method and a sufficiently complete basis set. The method is determined by the definition of the wave function and the way in which the wave function parameters are optimized, e.g. Hartree-Fock (HF), second-order

Møller-Plesset perturbation theory [1] (MP2), configuration interaction with single and double excitations (CISD), coupled cluster theory [2] with single and double excitations [3] (CCSD), CCSD with a perturbative treatment of triple excitations [4] [(CCSD(T)], higher-order coupled cluster methods with full inclusion of triple and quadruple excitations [5–9] (CCSDT, CCSDTQ), or full configuration interaction (FCI) [10]. All these many-electron wave functions are constructed from antisymmetrized products of one-electron functions called molecular orbitals (MOs), which in turn are linearly expanded in a basis of atomic orbitals (AOs). Normally, Gaussian type orbitals (GTOs) are used as a basis. Each method has an *intrinsic* accuracy (compared with exact results or experiments), which is reached only for a complete (infinitely large) basis set. For a given finite basis set, the best possible result is obtained with FCI. The difference between the results for finite and complete basis sets for a given method is called *basis set incompleteness error* or simply *basis set error*. Thus, the aim is to use a method with the smallest possible intrinsic error in combination with a basis set that minimizes the basis set error. Sometimes, basis set and intrinsic errors partially compensate each other, which may yield a good result for the wrong reason. Even though this is formally undesirable, computational chemistry often relies on such error compensations, since experience has shown that they may be quite systematic.

Unfortunately, the computational cost rises very steeply with the quality of the method and the size of the basis set. Typically, the cost rises with the fourth power of the number of basis functions N_{AO} per atom, but the error in the correlation energy decreases only with $1/N_{\text{AO}}$. Even more severe is the fact that the CPU time scales steeply with molecular size¹ \mathcal{N} , i.e., $t_{\text{cpu}} \propto \mathcal{N}^n$, and the exponent n increases with the computational level, e.g., $n = 5, 6, 7, 8, 10$ for MP2, CCSD, CCSD(T), CCSDT, and CCSDTQ, respectively. This means that for CCSD(T) the CPU time increases by 2 orders of magnitude if the molecular size is doubled. For CCSDTQ, the time increases formally by a factor of 1,024. Thus, there is a scaling wall that cannot be overcome even with the largest supercomputers.

Pictorially, one can summarize the above problems by the scheme in Figure 14-1, where on one axis *ab initio* methods with an increasing complexity are presented, while on the second axis basis sets with improving quality are displayed. If we add a third axis denoting the molecular size, we get a full picture of the main challenges of nonrelativistic quantum chemistry, i.e., one has to move along all three directions (method, basis, size) simultaneously in order to achieve the “chemical heaven”. As explained above, the computational cost rises steeply in each direction.

A major goal of current research in theoretical chemistry is therefore to reduce the bottlenecks in all three directions as far as possible and to climb up closer towards the “chemical heaven”. For example, the convergence of the energy with the size of the basis set can be dramatically improved (without much additional cost) by including terms into the wave function that depend explicitly on the inter-electronic distances r_{ij} . In recent years great advances have been made in making

¹ The molecular size can be measured by e.g. the number of atoms or the number of correlated electrons.

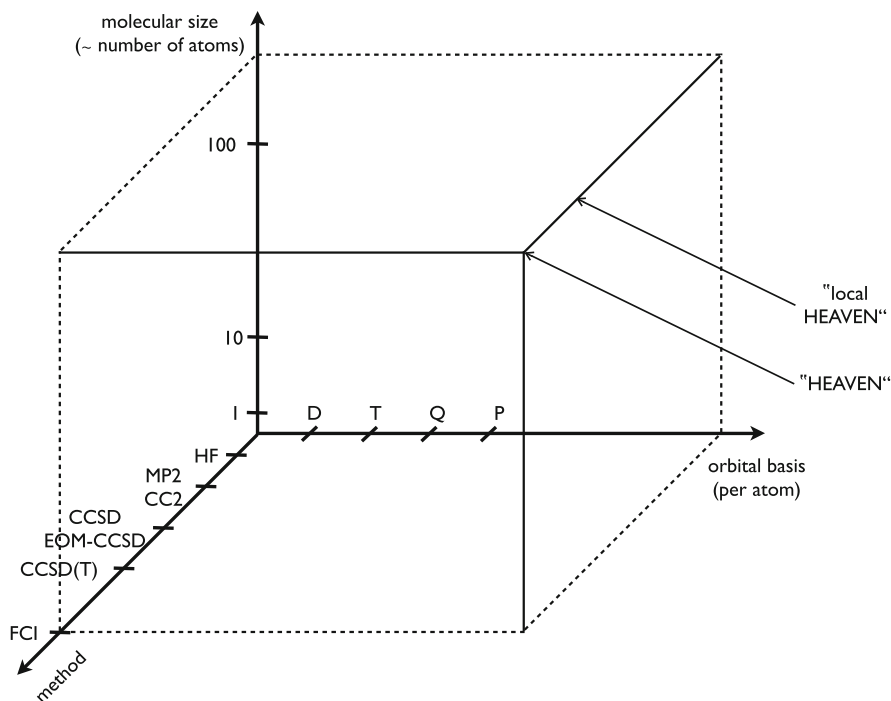


Figure 14-1. A pictorial description of the main challenge of the nonrelativistic computational chemistry

such explicitly correlated methods efficient, numerically stable, and applicable to quite large systems (see, e.g., [11–13] and references therein; reviews can be found in [14] and in another recent volume of this series [15, 16]). Some of these developments will be discussed in Section 14.2.5. The scaling of the cost with the size of the basis set can be reduced by using density fitting approximations for the evaluation and transformation of the two-electron repulsion integrals (ERIs). These methods will be introduced in Section 14.3. And the steep scaling of the computational resources with molecular size can be reduced by local approximations, which are the main subject of this article. The basis for such approximations is the fact that, in non-metallic systems, the correlation energy is a short-range effect that decreases with r_{ij}^{-6} . Thus, by using a local orbital basis, one can systematically neglect the correlation of distant electrons. The steep cost-scaling of conventional methods is mainly due to the fact that traditionally the many-electron wave functions have been constructed using canonical HF orbitals, which are very delocalized over the molecule and do not allow to exploit the locality of electron correlation.

Unavoidably, the introduction of approximations can cause additional errors. For example, the use of density fitting approximations introduces an additional basis set error, depending on the size of the auxiliary fitting basis used. Normally, this error is very small and negligible. Much more severe can be errors caused by local approximations. On the one hand, these can be due to approximations in the wave

function *ansatz* (e.g. neglect of distant pairs or restricting excitations to domains), which affect the intrinsic accuracy of the computational model. On the other hand, local approximations can also be made in the density fitting approach or by neglecting small terms in the coupled cluster equations. These approximations are of more technical nature and should be kept negligibly small. It is therefore very important to benchmark new methods and approximations extensively in order to establish their accuracy and reliability.

In the current article, we restrict ourselves to MP2 and CCSD(T) on the method axis for describing ground electronic states. Provided the electronic structure is well described by single reference methods (i.e., the Hartree-Fock determinant strongly dominates the wave function), CCSD(T) has an excellent intrinsic accuracy (about 5 kJ/mol for energy differences), and has become a “golden standard” in computational quantum chemistry for small molecules. Our aim is to extend the applicability of this method in the other two directions as far as possible, using a combination of local approximations, the density fitting technique, and explicit correlation approaches. Furthermore, we will consider the calculation of electronic excitation energies using local variants of the equation-of-motion CCSD (EOM-CCSD) method (see e.g. Refs. [17–19]) and the simpler CC2 model [20]. These methods provide an adequate treatment (by which we understand errors of 0.2–0.3 eV) for states which are well described by the excitation of a single electron from the electronic ground state.

14.2. LOCAL TREATMENT OF ELECTRON CORRELATION

The basic quantities for the construction of single reference ab initio methods beyond the one-determinantal level (i.e. HF theory) for singlet states are spin-summed orbital replacement operators \hat{E}_{ai}

$$\hat{E}_{ai} = \eta_a^{\alpha\dagger} \eta_i^\alpha + \eta_a^{\beta\dagger} \eta_i^\beta, \quad (14-1)$$

where η_i^σ and $\eta_a^{\sigma\dagger}$ are spin-orbital annihilation and creation operators for $\sigma = \alpha$ or β , respectively. Here and in the following the labels i, j, k, l will denote orbitals that are occupied in the HF reference determinant Φ_0 and a, b, c, d represent unoccupied (virtual) orbitals. The replacement operators \hat{E}_{ai} can be used to define contracted single-, double-, and higher excitation operators,

$$\begin{aligned} \hat{T}_1 &= \sum_{ia} t_a^i \hat{E}_{ai}, \\ \hat{T}_2 &= \frac{1}{2} \sum_{ijab} T_{ab}^{ij} \hat{E}_{ai} \hat{E}_{bj}, \end{aligned} \quad (14-2)$$

where t_a^i and T_{ab}^{ij} are the cluster amplitudes for single and double excitations. In coupled cluster theory the wave function is represented as

$$\Psi_{CC} = e^{\hat{T}} \Phi_0, \quad (14-3)$$

with the cluster operator \hat{T} defined as a sum $\hat{T} = \hat{T}_1 + \hat{T}_2 + \dots$. Normally, \hat{T} is truncated at a certain excitation level; e.g., in CCSD theory $\hat{T} = \hat{T}_1 + \hat{T}_2$.

The number of singles, doubles and triples amplitudes scales as \mathcal{N}^2 , \mathcal{N}^4 , and \mathcal{N}^6 , respectively, with the molecular size \mathcal{N} . As already mentioned in the introduction, the number of elementary floating point operations grows even more steeply, thus strongly limiting the maximum size of molecules that can be treated with a given method using an acceptable amount of computer resources. On the other hand, the local character of electron correlation in molecules has been known since long time, and attempts to exploit this in order to reduce the computation time date back more than 40 years. The first really successful and general scheme of localization approximations was proposed by Pulay [21] and implemented by Sæbø and Pulay for MP perturbation theories and the coupled-electron pair approximation (CEPA) [22, 23]. Their approach has been later generalized for local closed-shell CCSD and CCSD(T) theories by Werner et al. [24–33]. For these methods, linear scaling of the CPU time and disk space with molecular size has been achieved. Local methods have been also introduced and tested for properties other than the energy, like first-order properties and gradients [34–36], static second-order properties [37, 38], and other response properties [39]. More recently, local methods have been extended for computing electronic excitation energies using local EOM-CCSD [40] and (time-dependent) local CC2 response theories [41–44]. Furthermore, extensions to open-shell systems and combinations of local and explicitly correlated methods are currently in progress and will be briefly reviewed in this article. Local correlation methods for periodic systems (to describe surfaces and crystals), which have been developed over the past few years in the context of the CRYSCOR project [45–48], have just been reviewed recently in another book [49] and are therefore not further discussed here.

The locality of electron correlation has also been exploited by several other research groups. Examples are the AO-based methods described by Maslen and Head-Gordon [50], Scuseria and Ayala [51] and Auer and Nooijen [52], the di- and triatomic in molecule schemes of Maslen and Head-Gordon et al. [53–55], and the local coupled cluster doubles algorithms of Subotnik, Head-Gordon et al. [56–60]. Chwee et al. proposed a linear-scaling multireference singles and doubles configuration interaction approach based on local truncation schemes coupled with integral prescreening [61]. It should be noted, however, that this method is not size-consistent, and therefore a linear scaling scheme is of limited use. An efficient local CEPA approach has recently been described by Neese et al. [62, 63], who use pair natural orbitals combined with the density fitting technique for evaluating the integrals. Another class of methods divides the molecule into smaller subsystems for which the CCSD equations are solved separately. This was first proposed in the work of Förner et al. [64] and refined by Li et al. [65]. The latter “cluster-in-molecule” (CIM) approach was recently generalized for the CCSD, CCSD(T), and CC(2,3) models [66]. Related to this is the divide-and-conquer implementation of the CCSD(T) by Flocke and Bartlett [67, 68] based on natural localized hybrid orbitals. In these methods, each localized orbital is associated to one of the subsystems, and the contributions to the correlation energy of each localized

occupied orbital are summed up. Another, related approach has been described by Friedrich and Dolg et al. [69–73], who use the incremental scheme originally proposed by Stoll [74] to sum up the correlation energy contributions of the fragments. Naturally, these methods scale linearly with molecular size, but the problem of these approaches is that the individual fragments must overlap, and this may cause a considerable computational overhead. The full review of all these developments is beyond the scope of this contribution.

In general, two steps lead to linear scaling of local methods: (i) reduction of the configurational space available for excitation operators, and (ii) exploitation of the sparsity of excitation amplitudes resulting from the step (i) in devising efficient computational algorithms for a correlated approach under study. We will now proceed with a description of both steps. For historical reasons we will concentrate on the closed-shell ground state, although most ideas are directly transferable to open-shells and to excited states. The problems specific for open-shell molecules will be outlined in Section 14.2.4, and those for excited states will be described in Section 14.5.

14.2.1. Local Approximations in the Electronic Ground State

The canonical HF orbitals are usually delocalized over the whole molecule. Therefore, as an introductory step to almost all local methods, the HF orbitals must be localized. In the procedure introduced by Pulay [21–23] the occupied orbitals are localized by using one of the available localization algorithms, while the virtual local orbitals are constructed from atomic orbitals (AOs) by projecting them against the occupied orbital space. It should be emphasized that since the localization is just a rotation of orbitals, separately within occupied and virtual orbital spaces, the results obtained with the local sets of occupied and virtual orbitals are identical to those retrieved with canonical orbitals, as long as the method is invariant with respect to transformations within the occupied and virtual orbital spaces (in the virtual space, the non-orthogonality of the projected orbitals must of course be taken into account). The localization of orbitals alone does not offer any computational advantage over methods utilizing the canonical set of HF orbitals. Quite on the contrary, in most cases it somewhat increases the cost of calculations and the complexity of computer codes. For example, the local MP2 equations must be solved iteratively, since in the local basis the Fock matrix is not diagonal.² The localization of orbitals offers, however, a suitable framework for applying approximations which will eventually lead to linear scaling methods.

The localization of the occupied orbitals can be performed according to one of the well-known localization criteria, like the Pipek and Mezey (PM) localization scheme [76], or the Boys procedure [77]. Alternatively, also natural localized molecular orbitals [78] (NLMOs) can be used [67, 79]. The PM localization as well as the NLMO scheme keep the separation of σ and π orbitals in planar molecules [80]

²The iterative solution of LMP2 equations can be avoided if the Laplace transform is applied to the energy denominator, see Ref. [75] and Section 14.5.2.3.

and are therefore the preferred localization methods. The PM algorithm minimizes the number of atoms at which the occupied orbitals are localized. The natural localization scheme constructs LMOs which closely resemble atomic natural orbitals or natural bond orbitals. The advantage of the latter scheme is that it is more stable with respect to basis set variations than the PM localization [79]. In particular, it also yields well localized orbitals if diffuse basis functions are present. In such cases the PM localization sometimes fails to produce well localized orbitals, unless the contributions of diffuse basis functions are eliminated in the localization criterion.

The localized occupied orbitals ϕ_i can be expressed in the atomic orbital (AO) basis χ_μ by a rectangular transformation matrix \mathbf{L} ($N_{\text{AO}} \times N_{\text{occ}}$)

$$\phi_i = \sum_{\mu=1}^{N_{\text{AO}}} \chi_\mu L_{\mu i}. \quad (14-4)$$

The external (virtual) orbital space is spanned by projected atomic orbitals (PAOs) (labeled by the indices p, q, r, s, \dots):

$$\phi_p^{\text{PAO}} = \hat{P} \phi_p^{\text{AO}}, \quad (14-5)$$

where \hat{P} projects out the contributions of the occupied space,

$$\hat{P} = 1 - \sum_{i=1}^{N_{\text{occ}}} |\phi_i\rangle \langle \phi_i| \quad (14-6)$$

so that $\langle \phi_p^{\text{PAO}} | \phi_i \rangle = 0$ for all i, p . In general, the atomic orbitals ϕ_p^{AO} can be represented in the AO basis by a block-diagonal matrix \mathbf{C}^{AO}

$$\phi_p^{\text{AO}} = \sum_{\mu \in A} \chi_\mu C_{\mu p}^{\text{AO}}. \quad (14-7)$$

Each non-zero block of the coefficient matrix \mathbf{C}^{AO} corresponds to one centre and therefore each PAO can be uniquely assigned to a centre as well. In principle, the choice of the atomic orbitals is arbitrary. However, for numerical reasons, it is advisable to remove PAOs that correspond to core orbitals. This is because the MOs which correspond to core orbitals very strongly overlap with the corresponding AOs, and thus the norms of the PAOs resulting from such AOs become very small. It is therefore advantageous to use AOs that separate the core orbitals well from the valence orbitals. The best choice are the canonical AOs. If generally contracted basis sets are used, like the correlation consistent basis sets of Dunning [81], the canonical core and valence orbitals are represented by individual contracted basis functions. One can then project the basis functions directly, in which case \mathbf{C}^{AO} becomes the unit matrix. The use of generally contracted basis functions is therefore recommended for local correlation methods.

In the AO basis, the PAOs are represented by a coefficient matrix \mathbf{P} ,

$$\phi_p^{\text{PAO}} = \sum_{\mu=1}^{N_{\text{AO}}} \chi_{\mu} P_{\mu p}, \quad (14-8)$$

with

$$\mathbf{P} = (\mathbf{1} - \mathbf{L}\mathbf{L}^{\dagger}\mathbf{S}_{\text{AO}})\mathbf{C}^{\text{AO}} = \mathbf{C}_v\mathbf{C}_v^{\dagger}\mathbf{S}_{\text{AO}}\mathbf{C}^{\text{AO}}, \quad (14-9)$$

where the rectangular ($N_{\text{AO}} \times N_{\text{virt}}$) coefficient matrix \mathbf{C}_v represents the canonical virtual orbitals, and \mathbf{S}_{AO} is the overlap matrix between the basis functions χ_{μ} . Thus, the PAOs can be obtained by a transformation

$$\mathbf{Q} = \mathbf{C}_v^{\dagger}\mathbf{S}_{\text{AO}}\mathbf{C}^{\text{AO}} \quad (14-10)$$

from the canonical virtual space. Note that this matrix is rectangular ($N_{\text{virt}} \times N_{\text{AO}}$) and the N_{AO} PAOs are non-orthogonal and linearly dependent. Their overlap matrix

$$\mathbf{S} = \mathbf{P}^{\dagger}\mathbf{S}_{\text{AO}}\mathbf{P} \quad (14-11)$$

has N_{occ} zero eigenvalues. The linear dependencies in the PAO set are removed for individual domains [24, 82], as will be outlined in Section 14.2.2.1.

14.2.1.1. Domain Construction

In the local approach of Pulay and Sæbø [22, 23], which has been adopted and refined in our work, single excitations from a given LMO ϕ_i are restricted to a subset of PAOs (called an *orbital domain* [i]) which are spatially close to the dominant part of ϕ_i . Double excitations from a pair of LMOs ϕ_i and ϕ_j are allowed only to a *pair domain* [ij] which is a union of the corresponding orbital domains [i] and [j]. Domains for triple excitations can be defined analogously [28, 29].

The quality of the local wave functions depends crucially on the proper choice of the orbital domains. In order to select them automatically, two procedures are implemented in MOLPRO [33]: originally and by default, a modification of the method proposed by Boughton and Pulay [80] (BP) is utilized. More recently, a new method has been developed in which the domains are determined on the basis of natural population analysis (NPA) [79]. It has been shown that this scheme is more stable with respect to basis set variations than the BP method. It can be used with PM LMOs as well as with NLMOs.

In both methods for domain selection we assume that all AOs are atom-centered. The construction of PAOs (see Eq. (14-5)) ensures a one-to-one correspondence between AOs and PAOs, which means that each PAO can be attributed to an individual atom. A domain always contains all PAOs at a given subset of atoms, and

thus the problem of defining the domain is reduced to finding an appropriate subset of atoms for a given ϕ_i .

In the BP method this subset is selected for an LMO ϕ_i by the following procedure: first the atoms are ordered according to decreasing Löwdin orbital charges [83]

$$z_A^{(i)} = 2 \left[\sum_{\mu \in A} (\mathbf{S}_{AO}^{1/2} \mathbf{L})_{\mu i} \right]^2. \quad (14-12)$$

Initially, all atoms are added to the domain which have charges larger than 0.5. Next, the so-called completeness check of Boughton and Pulay [80] is performed by computing the quantity

$$f(\phi'_i) = \min \int (\phi_i(\mathbf{r}) - \phi'_i(\mathbf{r}))^2 d\mathbf{r}, \quad (14-13)$$

where (ϕ'_i) is an approximation to the orbital ϕ'_i built only from AOs belonging to the already selected atoms. Expansion coefficients of the approximate orbitals are optimized by minimizing the functional f , which leads to a simple set of linear equations. If (ϕ'_i) is still larger than some prescribed threshold δ , the next atom from the ordered list is added, until the inequality $f(\phi'_i) < \delta$ is fulfilled. The default values for δ are 0.020, 0.015, and 0.010, respectively, for the cc-pVDZ, cc-pVTZ, and cc-pVQZ correlation consistent basis sets of Dunning [81]; the same values can also be used for the corresponding augmented aug-cc-pVnZ basis sets.³ The procedure can be refined by additional criteria. For example, atoms are not added to the domain if the Löwdin atomic charge is smaller than a certain threshold (e.g. 0.03 for H atoms and 0.01 for other atoms). Furthermore, symmetry equivalent atoms are always treated on equal footing.

In the NPA method natural charges [84] are computed for each atom and orbital. These charges are much more stable with respect to basis set variations than the Löwdin (or Mulliken) charges, and can be used directly to select the domains [79]. It is recommended to include all atoms into a domain which have charges larger or equal to 0.03–0.05; the domain sizes are then comparable to those obtained with the BP procedure [79].

Typically, the standard orbital domains obtained by one of the above methods contain only a few atoms: one for lone pairs, two for isolated bonds, and 3–4 for conjugated bonds. In highly symmetrical systems the localization may not be unique, e.g. for benzene the localized π orbitals can freely rotate in the ring, without affecting the localization criterion. In order to make the correlation energy invariant with respect to such rotations of the π orbitals, the domains of these orbitals can be

³ In MOLPRO, the threshold $T_{BP} = 1 - \delta$ is used, i.e. 0.980, 0.985, and 0.990 for double, triple, and quadruple zeta basis sets.

merged into one. Numerical studies show that such domain merging is useful whenever two orbital domains overlap by more than one atom (this is usually the case in conjugated systems), and the domain merging can be performed automatically in such cases. The dimension of orbital domains selected according to these criteria is independent of the size of the molecule, and depends linearly on the size of the AO basis per atom.

The restriction of excitations to domains causes a certain error in the correlation energy; this is denoted *domain error*. This error becomes smaller with increasing basis set and increasing domain sizes. Typically, for a triple-zeta basis and standard domains, the domain error amounts to 1% of the canonical correlation energy obtained with the same basis and method. In order to recover a larger fraction of the correlation energy, it is sometimes useful to extend the orbital domains by an additional shell of atoms. Such cases involve, e.g., studies of the reaction mechanisms [85] or molecular properties [37]. Domain extensions can be performed according to distance or connectivity criteria. When a distance criterion is used, all atoms are added which are within a certain distance from at least one atom belonging to the considered LMO. Alternatively, one can use connectivity criteria and add all atoms which are separated by a maximum number of bonds from any atom in the domain [82]. This has the advantage that it takes into account the longer bond distances when the molecule contains heavier atoms. The connectivity matrix, which holds the minimum number of bonds by which two given atoms are separated, can be determined automatically on the basis of atomic radii and atomic distances. Two atoms are considered to be connected if their distance is smaller than the sum of their atomic radii multiplied by 1.2. Typically, if the standard domains are augmented by the next neighbours, 99.8–99.9% of the canonical correlation energy is recovered. It should be noted, however, that such domain extensions considerably increase the computational cost, since the CPU time increases with the third (LMP2) or fourth [LCCSD(T)] power of the domain sizes.

Another problem, which has been discussed in the literature, is the fact that the domains may change as a function of geometry, and this causes steps on potential energy surfaces [56, 85, 86]. In most cases this problem can be avoided by determining the domains at one structure and then keeping them fixed. In particular, this is the method of choice when computing properties that require only relatively small displacements, like in calculations of gradients or Hessians by finite differences. It has been found that the choice of the geometry at which the domains are determined has very little influence on optimized equilibrium geometries and vibrational frequencies [85]. In geometry optimizations, the domains are frozen once the step-length or gradient falls below a certain threshold. This is similar to density-functional theory (DFT) calculations, in which the grid has to be frozen. Note that analytical energy gradients are always well defined, since they are computed using the domains at the reference structure.

A more severe problem arises when one needs to compute energy differences between structures which have a different electronic structure, for example reaction barriers. An unbalanced choice of domains at the two structures may lead to significant errors in the energy difference. It is then advisable to merge the domains of the two (or more) structures and use the merged ones along the whole reaction path.

This can be done automatically. In LCCSD(T) calculations it is important that not only the domains are frozen but also the pair classes (see next section). A detailed discussion with examples of such cases can be found in Ref. [85].

By the introduction of local domains the number of singles and doubles amplitudes for a given orbital or orbital pair becomes independent of the molecular size. However, the number of all pairs (ij) still scales quadratically with \mathcal{N} . The next step is to reduce the number of pairs, so that overall the number of doubles amplitudes scales linearly.

14.2.1.2. Classification of Orbital Pairs

In order to reduce the number of pairs one can use the fact that the pair correlation energies ε_{ij} decrease quickly with the distance between the orbitals i and j . We therefore classify the pairs according to the distances or number of bonds between the two orbitals. The definition of the orbital distances and connectivities was already defined in the previous section. Note, however, that the distances used for determining the pair classes are always based on the standard domains. Thus, domain extensions do not affect the pair classes. However, if overlapping orbital domains are merged (for example in benzene), the merged domains are used to determine the classes. If domains from two or more structures are merged, the smallest distance for any given pair of atoms is used to determine the pair classes.

In our methods we normally distinguish strong, close, weak, and very distant pairs. Typically, in strong pairs the two orbital domains share at least one atom. Close pairs are separated by 1 or 2 bonds, weak pairs by 3–7 bonds, and very distant pairs by 8 bonds ($\approx 15 a_0$) or more. The very distant pairs are completely neglected. The remaining number of pairs and amplitudes scales linearly with molecular size, which is the prerequisite for achieving linear scaling of the CPU time and other computational resources. All surviving classes are normally fully included in LMP2, i.e., the LMP2 is independent of all distance criteria except for the one defining the neglected pairs.⁴ Independent of the parameters used for classifying the pairs, the number of pairs in each class scales asymptotically linearly with molecular size. Summarizing, local approximations in pair lists (P) and in orbital domains lead to the following modified form of Eq. (14-2):

$$\begin{aligned}\hat{T}_1 &= \sum_i \sum_{r \in [i]} t_r^i \hat{E}_{ri}, \\ \hat{T}_2 &= \frac{1}{2} \sum_{ij \in P} \sum_{rs \in [ij]} T_{rs}^{ij} \hat{E}_{ri} \hat{E}_{sj},\end{aligned}\tag{14-14}$$

with a considerably reduced number of spin-adapted configuration state functions (CSFs).

⁴Optionally, in LMP2 one can introduce as a further class called “distant pairs”, for which the two-electron integrals are approximated by multipole approximations [25, 27]. However for LCCSD calculations this saves little time and is not recommended. This approximation will therefore not be further discussed in the current article.

The distinction of strong, close, and weak pairs comes into play only in LCCSD(T) calculations. Strong pairs are fully included in the LCCSD(T), and their amplitudes are optimized at the LCCSD level. Typically, they account for more than 90% of the correlation energy. The amplitudes of the close and weak pairs are taken from the initial LMP2 calculation and then kept fixed. The amplitudes of the weak pairs are neglected in the LCCSD residuals for the strong pairs, i.e. they are only used to compute the LMP2 contribution to the correlation energy. The close pair amplitudes, however, are taken into account. In the LCCSD part, they are (optionally) included in the amplitude equations for the strong pairs. As will be outlined later, this is possible with relatively little extra cost and significantly improves the accuracy (in particular in LCCSD(T)-F12 calculations). If the close pair amplitudes are neglected in the LCCSD, the pair energies of the strong pairs are usually overestimated. This was the case in earlier versions of our program and turned out to improve the accuracy due to a partial compensation of the domain error when medium size basis sets were used. However, this fortuitous error compensation does not work well for large basis sets (quadruple zeta or larger). Even more problematic are explicitly correlated calculations, in which the basis set and domain errors are almost fully removed (cf. Section 14.2.5). In these cases it is important to minimize the error caused by the pair approximations in order not to spoil the overall accuracy. In some cases this means that the strong and close pair classes must be extended to achieve the very high intrinsic accuracy of this method (cf. Section 14.6).

In the local perturbative triples (T) correction, the *triples* of LMOs i,j,k are neglected unless (i) all three pairs of LMOs belong to *strong* or *close* pairs, and (ii) at least one pair is a strong pair [28, 29]. Furthermore, the strong and close pair amplitudes are taken into account in the triples residual. This will be discussed in Section 14.2.3.

14.2.1.3. Correlation Regions

The concept of pair approximations discussed in the previous section can be extended by correlating only that part of the molecule that is chemically relevant [87]. Each LMO or group of LMOs, together with their associated domains, can be viewed as a subsection of the system and can be individually treated at a specific level of theory. A lower level method, e.g., local second-order Møller-Plesset perturbation theory (LMP2), can be applied to a large part of the molecule or the whole system, and a higher level method, e.g. LCCSD(T), to a smaller subset of LMOs. This is in the same spirit as molecular mechanics/quantum mechanics (QM/MM) hybrid schemes or QM/QM coupling schemes as, e.g., the IMOMO model [88] or the more general ONIOM model [89]. In contrast to these schemes, however, in local region calculations it is not necessary to split the molecule into parts, and one set of HF orbitals is used for the whole system. It has been found that quantities like reaction energies converge quickly with the size of the region that is treated at highest level. Typically, only the atoms that are directly involved in the reaction and their direct neighbours need to be included in the definition of the high-level region. A larger environment is treated by LMP2, and the rest of the molecule remains

uncorrelated. This leads to $\mathcal{O}(1)$ scaling of the computational cost for the correlation calculation, i.e., the CPU time and other resources do not change if, e.g., a side group is added or changed far from the reaction centre. The remaining bottleneck is then the HF calculation. But this means that high-level correlated calculations are possible for systems of the same size as can be done with hybrid DFT methods (including exact exchange). Examples and more details about the definition of the regions can be found in Ref. [87].

14.2.2. Exploiting Localization in Program Algorithms

14.2.2.1. Solving the Amplitude Equations

The amplitudes t_p^{ij} and T_{pq}^{ij} can be determined by solving the amplitude equations for the method under consideration. For LMP2 these are linear and can be written as

$$R_{pq}^{ij} \equiv \langle \tilde{\Phi}_{ij}^{pq} | [\hat{F}, \hat{T}_2] | \Phi_0 \rangle + \langle \tilde{\Phi}_{ij}^{pq} | \hat{H} | \Phi_0 \rangle = 0 \quad \forall p, q \in [ij], \quad (14-15)$$

where \hat{F} is the closed-shell Fock operator

$$\hat{F} = \sum_{rs} \hat{E}_{rs} f_{rs}, \quad (14-16)$$

$$f_{rs} = h_{rs} + \sum_j [2(rs|jj) - (rj|sj)]. \quad (14-17)$$

Here and in the following the ‘‘chemical notation’’ is used for the electron-repulsion integrals, i.e.,

$$(pq|rs) = \int d\mathbf{r}_1 \int d\mathbf{r}_2 \phi_p^*(\mathbf{r}_1) \phi_q(\mathbf{r}_1) r_{12}^{-1} \phi_r^*(\mathbf{r}_2) \phi_s(\mathbf{r}_2). \quad (14-18)$$

We also assume that the orbitals are real. The projection functions $\tilde{\Phi}_{pq}^{ij}$ and the corresponding singly excited configurations $\tilde{\Phi}_i^p$ are defined as

$$\tilde{\Phi}_i^p = \frac{1}{2} \hat{E}_{pi} | \Phi \rangle, \quad (14-19)$$

$$\tilde{\Phi}_{ij}^{pq} = \frac{1}{6} (2\hat{E}_{pi}\hat{E}_{qj} - \hat{E}_{qi}\hat{E}_{jp}) | \Phi_0 \rangle. \quad (14-20)$$

In contrast to the canonical case, these equations must be solved iteratively, since the Fock matrix is non-diagonal in the basis of LMOs and PAOs. Since for optimized HF orbitals the Brillouin condition $f_{ip} = 0$ is satisfied there are no single excitations in the first-order wave function. As mentioned before, these equations are solved for all pairs ij ($i \geq j$) except for the neglected very distant pairs.

In local coupled cluster theory the amplitudes of the singles and of the strong pair doubles are obtained by solving amplitude equations

$$\begin{aligned}
 r_p^i &\equiv \langle \tilde{\Phi}_i^p | e^{-\hat{T}} \hat{H} e^{\hat{T}} | \Phi_0 \rangle = 0 \quad \forall i, \quad \forall p \in [i], \\
 R_{pq}^{ij} &\equiv \langle \tilde{\Phi}_{ij}^{pq} | e^{-\hat{T}} \hat{H} e^{\hat{T}} | \Phi_0 \rangle = 0 \quad \forall ij \in P_s, \quad \forall p, q \in [ij],
 \end{aligned}
 \tag{14-21}$$

where P_s is the list of strong pairs ($i \geq j$), and the PAO indices p, q are restricted to the corresponding domains. Both restrictions strongly reduce the computational effort as compared to canonical CCSD, in which all pairs $i \geq j$ and all virtual orbitals p, q are considered. However, the explicit form of the equations is somewhat complicated by the non-orthogonality of the PAO basis. Furthermore, the sparse block structure of the amplitude matrices T_{pq}^{ij} must be taken into account. This will be discussed in the following section. The cluster operator \hat{T} contains all strong and (optionally) close pairs. The amplitudes of the latter are taken from the initial LMP2 and kept fixed. Weak pairs are entirely neglected in the LCCSD equations.

The amplitudes of the strong pairs are optimized by solving Eq. (14-21) iteratively. Note that the number of equations equals the number of amplitudes to be determined. In each iteration first the residuals r_p^i and R_{pq}^{ij} are calculated. In order to update the amplitudes it is necessary to transform them from the non-orthogonal PAO basis into a pair-specific pseudo-canonical orthogonal basis (denoted in the following by indices a, b)

$$r_a^i = \sum_{p \in [ij]} W_{pa}^{(ij)} r_p^i, \tag{14-22}$$

$$R_{ab}^{ij} = \sum_{pq \in [ij]} W_{pa}^{(ij)} R_{pq}^{ij} W_{qb}^{(ij)}. \tag{14-23}$$

The transformation matrices $W_{pa}^{(ij)}$ are obtained by solving the projected Fock equations

$$\mathbf{f}^{(ij)} \mathbf{W}^{(ij)} = \mathbf{S}^{(ij)} \mathbf{W}^{(ij)} \mathbf{e}^{(ij)}, \tag{14-24}$$

where $\mathbf{f}^{(ij)}$ and $\mathbf{S}^{(ij)}$ are the Fock and overlap matrices, respectively, in the basis of the PAOs of the domain $[ij]$, and $\mathbf{e}^{(ij)}$ is a diagonal matrix holding the orbital energies $\varepsilon_a^{(ij)}$. Due to the fact that the PAO basis is redundant, the overlap matrix $\mathbf{S}^{(ij)}$ may have zero or very small eigenvalues. These are removed using singular value decomposition.⁵ Thus, the resulting transformation matrices $W_{pa}^{(ij)}$ may be rectangular with fewer columns (a) than rows (p). In most cases, however, there are no redundancies in individual domains. The amplitude updates are computed as

⁵ Another possibility of removing linear dependencies consists in eliminating individual basis functions from the domains. In this case the functions which have the largest coefficients in the eigenvectors of $\mathbf{S}^{(ij)}$ corresponding to small eigenvalues are removed. However, this is less satisfactory since it is sometimes difficult to select the deleted functions so that the symmetry of the molecule is not disturbed and that the wave function remains invariant to rotations of the molecule.

$$\Delta t_a^i = -\frac{r_a^i}{\varepsilon_a^{(ii)} - f_{ii}}, \quad (14-25)$$

$$\Delta T_{ab}^{ij} = -\frac{R_{ab}^{ij}}{\varepsilon_a^{(ij)} + \varepsilon_b^{(ij)} - f_{ii} - f_{jj}}. \quad (14-26)$$

Finally, these are back-transformed into the PAO basis

$$\Delta t_p^i = \sum_{a \in [ii]} W_{pa}^{(ii)} \Delta t_a^i, \quad (14-27)$$

$$\Delta T_{pq}^{ij} = \sum_{ab \in [ij]} W_{pa}^{(ij)} \Delta T_{ab}^{ij} W_{qb}^{(ij)}, \quad (14-28)$$

and added to the previous amplitudes. Convergence of this process can be improved by solving in each LCCSD iteration the LMP2-like linear equations

$$0 = r_p^i + \langle \tilde{\Phi}_i^p | [\hat{F}, \Delta \hat{T}_1] | \Phi_0 \rangle, \quad (14-29)$$

$$0 = R_{pq}^{ij} + \langle \tilde{\Phi}_{ij}^{pq} | [\hat{F}, \Delta \hat{T}_2] | \Phi_0 \rangle. \quad (14-30)$$

In case of canonical orbitals, these reduce to the simple update formula (14-26); with localized orbitals, the off-diagonal Fock matrix elements f_{ik} are non-zero and the equations must be solved iteratively (*microiterations*) in the same way as described above. It is sufficient to perform at most 2 microiterations per LCCSD macroiteration in order to speed up convergence. A further improvement can be achieved by applying in the macroiterations the DIIS (direct inversion of the iterative subspace) [90] procedure. Overall, the convergence of solving the LCCSD equations is then almost identical to the standard canonical case. Typically, 8–10 iterations are needed to converge the energy to microhartree accuracy.

Using the converged amplitudes (strong pairs from LCCSD, close and weak pairs from LMP2) one obtains the LCCSD correlation energy as

$$E = 2 \sum_i \sum_{r \in [i]} f_{ir} t_r^i + \sum_{ij} \sum_{rs \in [ij]} \tilde{C}_{rs}^{ij} K_{rs}^{ij}. \quad (14-31)$$

where

$$C_{rs}^{ij} = T_{rs}^{ij} + t_r^i t_s^j, \quad (14-32)$$

$$\tilde{C}_{rs}^{ij} = 2C_{rs}^{ij} - C_{sr}^{ij}, \quad (14-33)$$

and the exchange integrals K_{rs}^{ij} in Eq. (14-31) are defined as

$$K_{rs}^{ij} = (ri|sj). \quad (14-34)$$

The Fock matrix elements f_{ir} vanish if fully optimized HF orbitals are used (Brillouin theorem), and then the first term in Eq. (14-31) does not contribute.

14.2.2.2. Residuals and Summations

When the explicit form of Eq. (14-21) is derived for the local case, two complications arise. First, the PAOs are nonorthogonal, which results in additional multiplications by the \mathbf{S} matrix (defined by Eq. (14-11)) in the residual equations. Secondly, the sparse form of the amplitude vectors t_p^i and matrices T_{pq}^{ij} must be taken into account. This is essential for reducing the computational cost and to achieve linear cost scaling with molecular size. The explicit form of the residual equations has been presented elsewhere [24, 30] and will be not repeated here. These equations are most conveniently expressed in terms of matrix/vector operations, where each matrix or vector is specified by LMO labels (superscripts), and the matrix elements (subscripts) correspond to PAOs. For example, the amplitudes T_{pq}^{ij} and residuals R_{pq}^{ij} are considered as matrices with elements $pq \in [ij]$, i.e., $[\mathbf{T}^{ij}]_{pq} = T_{pq}^{ij}$ and $[\mathbf{R}^{ij}]_{pq} = R_{pq}^{ij}$, respectively. Note that $T_{rs}^{ij} = T_{sr}^{ji}$, and therefore only the amplitudes for $i \geq j$ need to be stored. Similarly, the two-electron integrals can be ordered in matrix form, e.g., $[\mathbf{J}^{kl}]_{pq} = (kl|pq)$ (Coulomb operators) and $[\mathbf{K}^{kl}]_{pq} = (pk|lq)$ (exchange operators) for integrals with two LMO and two PAO labels. In the following, we will distinguish integrals with zero to four external (PAO) labels, and for simplicity these will be denoted 0-external, 1-external, ..., 4-external integrals.

In order to achieve linear scaling, all summations over PAOs in the residual equations should be limited to domains, and only amplitude matrices of strong and (optionally) close pairs contribute in the residual equations. For simplicity, we assume in the following that only amplitudes of strong pairs are included; this does not change any of the conclusions. As an example let us analyse one selected term of the LCCSD doubles residual [30]

$$\mathbf{R}^{ij} = \dots + \sum_k \mathbf{S}(2\mathbf{T}^{ik} - \mathbf{T}^{ki})(\mathbf{K}^{kj} - \frac{1}{2}\mathbf{J}^{kj}). \quad (14-35)$$

Here \mathbf{S} is the overlap matrix of the PAO basis, cf. Eq. (14-11). Since in Eq. (14-35) both pairs (ij) and (ik) are strong, both j and k must be close to i , and therefore the number of (kj) pairs is independent of the molecular size. Therefore, the total number of all matrices \mathbf{K}^{kj} needed for the construction of all local \mathbf{R}^{ij} residual matrices depends asymptotically linearly on \mathcal{N} . Since the pair lists are known a priori, it is possible to create *operator lists* for the \mathbf{K}^{kj} and \mathbf{J}^{kj} matrices (the so-called K - and J -lists) and to restrict the computation of integrals only to those which are really necessary in the LCCSD calculation.

We now examine the matrix multiplications in Eq. (14-35) in more detail. Writing out the indices explicitly we can immediately see that all summations over PAOs are restricted to domains

$$R_{pq}^{ij} = \dots + \sum_k \sum_{r,s \in [ik]} S_{pr} (2T_{rs}^{ik} - T_{sr}^{ik}) (K_{sq}^{kj} - \frac{1}{2} J_{sq}^{kj}) \quad \forall p, q \in [ij], \quad (14-36)$$

and therefore it is clear that the total computational effort for this term scales linearly with molecular size. We still have the choice in which order the summations are executed. One can either do the multiplication by \mathbf{S} for each k , as shown above. This yields the smallest possible dimensions in each matrix multiplication, but the multiplication with \mathbf{S} is done repeatedly. Note that for each k a different subblock of \mathbf{S} is needed, and these blocks are extracted from the full \mathbf{S} before doing the actual matrix multiplication. Thus, in the local algorithms we need lots of gather and scatter operations, but these are simple and efficient since we always deal with blocks of matrices. Alternatively, we could move \mathbf{S} out of the sum over k

$$R_{pq}^{ij} = \dots + \sum_{r \in [i]_{\cup}} S_{pr} \left[\sum_k \sum_{s \in [ik]} (2T_{rs}^{ik} - T_{sr}^{ik}) (K_{sq}^{kj} - \frac{1}{2} J_{sq}^{kj}) \right] \quad \forall p, q \in [ij]. \quad (14-37)$$

Now the intermediate in the square brackets is formed first. Since for each k the range of r is determined by a different domain $[ik]$, the number of rows of the intermediate corresponds to the number of PAOs in the *union* of all domains $[ik]$ for a fixed i . This space is specific for each orbital i and is called the *united pair domain* $[i]_{\cup}$. Since all k are close to i , it follows that the PAO label r must also be close to i , and therefore the dimensions of the united domains are independent of the molecular size, though considerably larger than the dimensions of the individual pair domains. Thus, in the second algorithm we have less matrix multiplications, but the ones with \mathbf{S} have larger dimensions. Still, the number of floating point operations scales linearly with molecular size. The relative computational effort of the two algorithms depends on the definition of the strong pair list and the size of the domains. In most cases, the second one is more efficient.

Similar arguments can be used for all other terms in Eq. (14-21). Finally, it turns out that for a given (kl) it is sufficient to calculate J_{pq}^{kl} for $pq \in [kl]_J$, where $[kl]_J$ denotes a J -operator domain. Similarly, for the exchange matrices we have K_{pq}^{kl} with $pq \in [kl]_K$. The K -operator domains $[kl]_K$ are usually larger than the J -operator domains since there are more types of interactions involving the K -operators. Furthermore, in extended molecules the K -list is always larger than the J -list. The K -operators are also needed in the LMP2, and therefore all weak pairs must be included in the K -list.

From the considerations presented above it is clear that dimensions of the K - and J -operator domains are independent of \mathcal{N} , although they can be substantially larger than the pair domains. Since the number of matrices \mathbf{J}^{kl} and \mathbf{K}^{kl} scales linearly with \mathcal{N} , the total number of integrals with two LMO and two PAO labels scales linearly with \mathcal{N} as well. Thus, not only the CPU time but also the disk space scales linearly. However, in our current implementation there is a small part of the memory requirement that scales quadratically, since we need a few full matrices, e.g., the overlap

matrix in the PAO basis, and some scratch matrices for accumulating intermediates. This has never been a bottleneck so far.

Most other summations involving 0-, 1-, and 2-external integrals can be treated in a similar way as presented above. For all important terms linear scaling is achieved without any additional approximations beyond the definition of the strong pair list and the domain for each pair. In fact, for the local coupled electron pair approximation (LCEPA) and local quadratic configuration interaction (LQCISD) this is exactly true for all terms involving the doubles amplitudes. However, the singles residual contains some terms which do not scale linearly unless interactions of distant singles are neglected [30]. Furthermore, in the LCCSD case there are a few non-linear terms where summations over LMO labels are not bound by pair labels. For example, in the following contribution to the doubles residual

$$R_{rs}^{ij} = \dots - 2 \sum_{kl} \sum_{tu \in [lj]} S_{rt} T_{tu}^{lj} S_{us} \sum_{p \in [k]} t_p^k(pk|li), \quad (14-38)$$

there is no restriction in the range of the index k in the integral $(pk|li)$. However, the orbitals ϕ_k and ϕ_p are spatially close (since ϕ_p belongs to the domain of ϕ_k), and therefore the orbital product $\phi_p(\mathbf{r}_1)\phi_k(\mathbf{r}_1)$ describes a charge distribution close to the domain $[k]$. Because one of these two orbitals is virtual and the second one occupied, the lowest-order contribution to this charge distribution is a dipole. Similarly, the orbitals ϕ_i and ϕ_l are close to each other (recall that (ij) and (lj) are strong pairs with one common index), so their product $\phi_i(\mathbf{r}_2)\phi_l(\mathbf{r}_2)$ describes a charge distribution which is also well confined in space. In the worst case ($l = i$) this distribution contains a monopole (a charge), therefore an R^{-2} distance dependence is expected for the integral $(pk|ii)$. Integrals with $l \neq i$ will decay with R^{-3} . Here R is defined as the minimum distance between ϕ_k and ϕ_i or ϕ_l . Although this decay is quite slow, it will nonetheless allow to achieve linear scaling for extended molecules by neglecting these integrals if R is larger than a certain threshold. The error introduced by this approximation is very small.

A similar R^{-2} decay is observed for a 3-external counterpart of Eq. (14-38),

$$R_{rs}^{ij} = \dots + 2 \sum_{tu \in [ij]} S_{rt} T_{tu}^{ij} \sum_{v \in [k]} t_v^k(vk|us), \quad (14-39)$$

which is part of terms involving the so-called $\mathbf{G}(\mathbf{E})$ operator

$$[\mathbf{G}(\mathbf{E})]_{rs} = \sum_{ku} [2(rs|ku) - (rk|us)] t_u^k. \quad (14-40)$$

Without further approximations, this operator is needed in the full PAO basis; it can be evaluated like a Fock matrix, but this leads to quadratic scaling of the computational cost. As will be demonstrated later, this spoils the overall linear scaling and becomes dominant for extended molecules. We found that making approximations in this term can cause quite large errors, and may even lead to convergence

problems. However, a closer inspection shows that the terms in Eqs. (14-38) and (14-39) have opposite sign and cancel to a large extent. Numerical experiments have shown that it is possible to neglect the terms involving $\mathbf{G}(\mathbf{E})$ together with the ones in Eq. (14-38) (and a similar exchange term) completely. The error caused by this approximation, which restores linear scaling, is quite small; in particular, it is *much* smaller than the difference of the LCCSD and LQCISD correlation energies (in LQCISD these terms are all absent). For a more extensive discussion of all terms in the coupled cluster equations we refer to Ref. [30].

To conclude this section, we note that in most practical applications for medium size molecules linear scaling is not of highest importance. There are some terms in the LCCSD equations which can be made linear, but this causes considerable overhead for smaller systems. An example is

$$\mathbf{R}^{ij} = \dots + \mathbf{S}\mathbf{T}^{ij} \sum_{kl} \mathbf{L}^{kl} \mathbf{T}^{lk} \mathbf{S} \quad (14-41)$$

with $\mathbf{L}^{kl} = 2\mathbf{K}^{kl} - \mathbf{K}^{lk}$. Since there is no link between the labels ij and kl one would formally need L_{rs}^{kl} for all r , leading to quadratic scaling of the number of such integrals. However, it is straightforward to show that these integrals decrease exponentially with the distance between k or l and r [30], and therefore interactions of pairs (ij) and (kl) that are distant from each other can be neglected. Still, a linear scaling algorithm would require to perform all matrix multiplications for each (ij) and (kl) individually. On the other hand, the intermediate $\sum_{kl} \mathbf{L}^{kl} \mathbf{T}^{lk}$ could be precomputed once (accumulated in a full matrix). One could then either multiply this from the right with \mathbf{S} once, leading to a (very) small contribution with cubic (\mathcal{N}^3) scaling, or carry out the multiplication with \mathbf{S} separately for each ij , leading to quadratic scaling. Thus, there are cross-over points below which it may be more efficient to use an algorithm that scales quadratically or even cubically. In our current program we attempt to minimize the overall cost for applications with up to about 50 atoms. Except for very large systems this version is faster than the original linear scaling program described in Ref. [30], even though linear scaling is not enforced for all terms.

14.2.2.3. Terms with 4-External Integrals

In LCCSD theory 4-external electron-repulsion integrals appear only in the doubles residual and in form of contractions with the amplitudes

$$R_{rs}^{ij} = \dots + [\mathbf{K}(\mathbf{C}^{ij})]_{rs} = \dots + \sum_{tu \in [ij]} (rt|su) C_{tu}^{ij}, \quad (14-42)$$

where C_{tu}^{ij} is defined in Eq. (14-32), and $\mathbf{K}(\mathbf{C}^{ij})$ are the so-called external exchange operators [91, 92]. In the local approximation all four indices r, s, t, u correspond to PAOs in the same domain $[ij]$, and therefore the number of transformed integrals

($rt|su$) needed for the calculation of one \mathbf{R}^{ij} matrix is independent of the molecular size. Since the amplitude labels ij are the same as of the residual, the external exchange operators are only needed for strong pairs. Thus, the computational effort and the number of 4-external integrals are independent of the number of close pairs that are included in the residual. The same is true for the contributions of the 3-external integrals (in this case it requires the neglect of some interactions between close pairs and singles, but this causes a negligible error). Thus, the inclusion of close-pair amplitudes in the residuals only affects the number of 0–2 external integrals and therefore only leads to a moderate increase of the CPU time. On the other hand, the accuracy is significantly improved.

From the above it is clear that the number of required 4-external integrals scales linearly with molecular size. The problem is that many strong pair domains overlap, and therefore the same integrals contribute to different pairs. It would therefore be wasteful to compute them for each pair individually. An efficient integral-direct procedure for calculating the minimum number of required 4-external integrals for Eq. (14-42) has been described in Ref. [32]. It is based on the fact that always all PAOs at a given centre are included in a domain. Thus, for a given pair (ij), the set of integrals ($rt|su$) can be represented by a much smaller set of four centres ($RS|TU$) (here centres are denoted by capital letters). By generating for each strong pair a list of all centre quadruplets, and then taking the union of all these, one obtains a list of centre quadruplets representing the minimum number of integrals needed. Obviously, the number of such centre quadruplets also scales linearly with molecular size. This list is used to derive the actual integral transformation and the evaluation of the $\mathbf{K}(\mathbf{C}^{ij})$ from these integrals. Efficient density-fitting techniques to generate these integrals will be outlined in Section 14.3.

14.2.3. Perturbative Triple Excitations

The calculation of the perturbative (T) energy correction for triple excitations is complicated by the fact that in the local basis the Fock matrix is not diagonal, and therefore the perturbation equations have to be solved iteratively. This makes it necessary to store the triples amplitudes, and even if domain approximations are made and the triples list (ijk) is restricted, the computational expense may be large. As mentioned before, the triples domains [ijk] are taken to be the union of the orbital domains [i], [j], and [k]. The triples list is restricted so that the pairs (ij), (ik), or (jk) are strong or close, and at least one of these is strong. The inclusion of the close pair amplitudes, which are taken from the initial LMP2, is important for achieving a sufficient accuracy [29]. As in the LMP2, the couplings due to the PAO-PAO block of the Fock matrix can be eliminated by transforming each triples residual to a pseudo-canonical basis, in complete analogy to the update procedure described in Section 14.2.2.1. Then only couplings by the occupied-occupied off-diagonal elements f_{ij} remain. By neglecting these, the triples correction can be computed non-iteratively without storing the triples amplitudes. This is very efficient and has been denoted (T0)-approximation [28, 29]. In the majority of all applications carried out so far, this approximation works very well. In cases of doubt, one can perform

one iteration [(T1)-approximation], which is still possible without keeping all triples amplitudes in memory [29]. A full iterative local triples program is also available [29]. Even iterative triples approximations beyond (T), such as CCSDT-1b, have been implemented and scale linearly with molecular size [31].

14.2.4. Open-Shell Local Correlation Methods

The closed-shell LMP2 and LCCSD theories can be generalized for open-shell systems in a rather straightforward way, and local LRMP2 (local spin-restricted MP2) and LUCCSD (local spin-unrestricted coupled cluster theory) have recently been implemented [93]. These methods are based on high-spin ROHF (restricted open-shell HF) reference functions. There are a few subtleties that should be mentioned here. First, there are two options to generate the local orbital basis: one can either localize the doubly and singly occupied orbitals separately, since the ROHF reference function is invariant with respect to unitary transformations within these orbital subspaces. Alternatively, one can localize the α - and β -spin orbitals separately. The former option has the advantage that a single set of localized orbitals and a single set of orbital domains results, and these can be used for all spin-orbital excitations. However, it may happen that the few open-shell orbital(s) cannot be well localized. In particular, if there is only a single open-shell orbital (doublet states), there is no freedom for localization at all; the open-shell ROHF orbital may then be more or less localized, depending on the molecule under consideration. The second option (separate localization of α - and β -spin orbitals) often leads to better localization and smaller domains, but since the resulting two sets of LMOs are different, this option requires more transformed integrals and separate orbital domains for α - and β -spin. As will be demonstrated in Section 14.6, the efficiency of both possibilities is comparable, but the second option is often somewhat more accurate. In particular, it will be more suitable for non-iterative perturbative triples approximations, which are currently under development in the Stuttgart group.

Similarly, one can either generate different sets of PAOs for α and β spin, or use the α -spin ones for all excitations (here we assume that the open-shell orbitals are occupied with α -spin electrons). In the latter case, the domains for β -spin excitations need then to be augmented by the open-shell ROHF orbitals. This is certainly much more efficient than using different sets of PAOs; in particular, for LUCCSD(T) one needs only one set of 4-external orbitals and two sets of 3-external integrals (if α - and β -spin orbitals are localized separately).

In the open-shell theories, we use spin-orbital excitation operators $\hat{e}_{ri}^\alpha = \eta_r^{\alpha\dagger} \eta_i^\alpha$ and $\hat{e}_{ri}^\beta = \eta_r^{\beta\dagger} \eta_i^\beta$ rather than the spin-free orbital excitation operators \hat{E}_{ri} . We therefore have different amplitudes for α - and β -spin excitations, and the \hat{T}_1 and \hat{T}_2 cluster operators take the form

$$\hat{T}_1 = \sum_{ri}^{(\alpha)} \tilde{t}_r^i \hat{e}_{ri}^\alpha + \sum_{ri}^{(\beta)} \tilde{t}_r^i \hat{e}_{ri}^\beta, \quad (14-43)$$

$$\hat{T}_2 = \frac{1}{4} \sum_{rsij}^{(\alpha)} \tilde{T}_{rs}^{ij} \hat{e}_{ri}^{\alpha} \hat{e}_{sj}^{\alpha} + \frac{1}{4} \sum_{rsij}^{(\beta)} \tilde{T}_{rs}^{ij} \hat{e}_{ri}^{\beta} \hat{e}_{sj}^{\beta} + \sum_{ri}^{(\alpha)} \sum_{sj}^{(\beta)} T_{rs}^{ij} \hat{e}_{ri}^{\alpha} \hat{e}_{sj}^{\beta}, \quad (14-44)$$

where $\tilde{T}_{rs}^{ij} = -\tilde{T}_{rs}^{ji} = -\tilde{T}_{sr}^{ij} = \tilde{T}_{sr}^{ji}$. Similar permutational symmetries hold for the pure β -spin amplitudes \tilde{T}_{rs}^{ij} . However, the $\alpha\beta$ -amplitudes T_{rs}^{ij} have no permutational symmetries. Thus, there are about 3 times as many unique amplitudes and equations as in the closed-shell case. The corresponding coupled cluster equations for canonical orbitals can be found in Refs. [94, 95]. For the local case they have to be transformed into the PAO basis. Formally, this simply requires to multiply with the \mathbf{S} matrix wherever an amplitude PAO label is not connected with an integral label. The structure of the resulting equations is very similar to the closed-shell case, and all conclusions about the scaling behaviour remain valid.

In the open-shell case the ROHF reference wave function is not an eigenfunction of the standard UMP2 zeroth-order Hamiltonian

$$\hat{H}^{(0)} = \sum_{ij} f_{ij} \hat{e}_{ij} + \sum_{ab} f_{ab} \hat{e}_{ab} + \sum_{ia} f_{ai} (\hat{e}_{ai} + \hat{e}_{ia}), \quad (14-45)$$

where the summations are over spin-orbitals (both spins). The reason is that the Brillouin theorem does not hold for ROHF wave functions, and the Fock-matrix elements f_{ai} are not zero (note that here and in the rest of Section 14.2.4 r,s in f_{rs} correspond to spin-orbital labels, while in Eq. (14-17) orbital labels are used). This prevents the application of simple Rayleigh-Schrödinger perturbation theory. This problem can be circumvented by using a projected Fock operator

$$\hat{g} = \hat{\delta} \hat{f} \hat{\delta} + (1 - \hat{\delta}) \hat{f} (1 - \hat{\delta}), \quad (14-46)$$

where $\hat{\delta} = \sum_i |i\rangle \langle i|$ projects onto the occupied space. This leads to a simplified zeroth-order Hamiltonian

$$\hat{H}^{(0)} = \sum_{ij} f_{ij} \hat{e}_{ij} + \sum_{ab} f_{ab} \hat{e}_{ab}. \quad (14-47)$$

Now the ROHF determinant is an eigenfunction of this operator, and it is straightforward to apply an UMP2-like perturbation theory, which uses ROHF reference functions [96, 97]. It should be noted, however, that single excitations must be included. This method is usually referred to as RMP2, even though it is not strictly spin-adapted.⁶

⁶ A strictly spin-adapted theory can be obtained by projecting out the spin-contamination as described for partially spin-restricted coupled cluster theory in Ref. [94]; the differences of the results to standard RMP2 are usually negligibly small.

14.2.5. Explicitly Correlated Local Correlation Methods

The very slow convergence of the correlation energy with the size of the AO basis set is due to the inability of expansions of orbital products (Slater determinants) to describe the wave function cusp for $r_{12} \rightarrow 0$ properly. Perhaps even more important is an accurate description of the correlation hole for small and medium values of the inter-electronic distances r_{12} . This can be strongly improved by adding terms to the wave function that depend explicitly on r_{12} and allow to satisfy the wave function cusp conditions exactly. Unfortunately, the straightforward inclusion of such terms leads to extremely numerous many-electron integrals, and for a long time this has prevented the development of explicitly correlated methods that can be applied to larger molecules.

In 1985 Kutzelnigg made two important suggestions [98]: first, he proposed to augment the conventional wave functions just by one explicitly correlated term for each pair, rather than to construct the whole wave function using only r_{12} -dependent functions, as was the case in many of the earlier theories. Secondly, he proposed to approximate the many-electron integrals by resolution of identities (RIs); the three- and four-electron integrals can then be split into sums of products of two-electron integrals. The first so-called R12-methods were implemented by Kutzelnigg and Klopper [99–104]. In these methods the RIs were approximated by the AO basis (standard approximation), and in order to obtain numerically accurate results very large AO basis sets were still needed. Thus, the basis set problem now occurred in another context. This problem was solved in 2002 by Klopper and Samson [105], who implemented the first MP2-R12 method in which an auxiliary basis set was used for the RI. This was further improved by the complementary auxiliary basis set (CABS) approach of Valeev [106], in which the RIs are represented by the union of the AO basis and an auxiliary basis. The CABS approach is particularly important for the development of explicitly correlated coupled cluster theories, both for numerical and theoretical reasons. A further very important finding was that the replacement of the linear r_{12} correlation factor [107, 108], as used in the early theories of Kutzelnigg and Klopper, by a short-range non-linear function $F_{12}(r_{12})$ leads to much better results and numerical stability. Several different functional forms were tested [109], and it turned out that a simple Slater function

$$F_{12}(r_{12}) = -\frac{1}{\gamma} e^{-\gamma r_{12}}, \quad (14-48)$$

as originally proposed by Ten-no [107] works at least as well as other choices. This has now become the standard in so-called F12-methods. In most cases, the Slater function is approximated by a linear combination of Gaussians, since this simplifies the evaluation of the integrals.

A detailed presentation of the theory of explicitly correlated MP2 and coupled cluster methods is beyond the scope of the current article. We refer to a recent review in this series [15], in which the explicitly correlated canonical MP2-F12 and CCSD(T)-F12 methods for closed-shell [11, 110, 111] and open-shell [11, 112]

systems as implemented in MOLPRO are described in detail and discussed in the context of other methods. Reviews of other authors can be found in [14, 16]. Here we focus on explicitly correlated local methods [12, 13, 113–115], which do not only improve the basis set convergence, but also reduce the domain error in local correlation methods.

14.2.5.1. The LMP2-F12 and LCCSD(T)-F12 Wave Functions

The doubly-excited cluster operator used in the MP2-F12 and LCCSD(T)-F12 theories is defined as

$$\hat{T}_2 = \frac{1}{2} \left[\sum_{ij \in P_w} \sum_{rs \in [ij]} T_{rs}^{ij} \hat{E}_{ri} \hat{E}_{sj} + \sum_{ij \in P_c} \sum_{\alpha, \beta}^{\text{complete}} T_{\alpha\beta}^{ij} \hat{E}_{\alpha i} \hat{E}_{\beta j} \right], \quad (14-49)$$

with

$$T_{\alpha\beta}^{ij} = \sum_{kl} \langle \alpha\beta | \hat{Q}_{12}^{ij} F_{12} | kl \rangle T_{kl}^{ij}. \quad (14-50)$$

The operator \hat{T}_1 and the first part of \hat{T}_2 are the same as in standard LCCSD, cf. Eq. (14-14), and the bracket notation $\langle \alpha\beta | \cdot | kl \rangle$ denotes, as usual, a two-electron integral in which the labels α and k correspond to the first electron and the labels β and l – to the second electron. In LMP2-F12, the pair list P_w includes all strong, close, and weak pairs, while in LCCSD only strong and optionally close pairs are included (cf. Section 14.2.1.2). The second part in \hat{T}_2 contains the explicitly correlated terms. Formally, this can be viewed as an externally contracted expansion of double excitations in a complete basis set (denoted by indices α, β). Normally, it is sufficient to include strong and close pairs, as indicated by the list P_c . The amplitudes T_{kl}^{ij} can either be optimized or determined from the wave function cusp conditions [107, 116–118] and kept fixed:

$$T_{kl}^{ij} = \frac{3}{8} \delta_{ik} \delta_{jl} + \frac{1}{8} \delta_{jk} \delta_{il}. \quad (14-51)$$

This hardly affects the accuracy and has the advantage that no extra amplitude equations have to be solved for these parameters. F_{12} is the correlation factor defined in Eq. (14-48) where the parameter γ is typically chosen to be $1 a_0^{-1}$. Finally, \hat{Q}_{12}^{ij} is a strong orthogonality projector:

$$\hat{Q}_{12}^{ij} = (1 - \hat{o}_1)(1 - \hat{o}_2) - \sum_{cd \in [ij]} |cd\rangle \langle cd|, \quad (14-52)$$

where $\hat{o} = \sum_i |i\rangle \langle i|$ projects onto the occupied space and the index indicates the coordinates of the electron on which it acts. The projector is needed to keep the explicitly correlated terms strongly orthogonal to the HF reference function and the conventional single and double excitations. In contrast to the canonical case, \hat{Q}_{12}^{ij} is pair specific [12, 115], since the conventional double excitations are restricted to

domains. The indices c, d in Eq. (14-52) denote an orthonormal set of orbitals that span the domain $[ij]$ (cf. Section 14.2.2).

The use of the pair-specific projectors has two important advantages. First, it reduces the number of necessary integrals and makes it possible to devise linear scaling algorithms [12]. Secondly, the double excitations into virtual orbitals *outside* the domain $[ij]$ are not entirely excluded as in standard local correlation methods, but for a pair ij implicitly approximated by

$$\Delta\hat{T}_2 = \sum_{ij \in P_c} \sum_{rs \notin [ij]} \bar{F}_{rs}^{ij} \hat{E}_{ri} \hat{E}_{sj}, \quad (14-53)$$

where $\bar{F}_{rs}^{ij} = \sum_{kl} \langle rs | F_{12} | kl \rangle T_{kl}^{ij}$. This means that instead of fully optimized amplitudes T_{rs}^{ij} the fixed matrix elements \bar{F}_{rs}^{ij} are used. These terms are implicitly taken into account by the F12 treatment and they correct very successfully for the domain error [12, 13, 115].

In the LCCSD(T)-F12 method [13], certain approximations are made in order to keep the extra computational effort as small as possible. In particular, we use the F12a method [11, 111], in which in the LCCSD-F12 equations all terms are neglected that require multiple RI approximations. The only remaining term, which describes the most important couplings between the explicitly correlated and conventional configurations, is independent of the RI basis. Furthermore, we apply the so-called approximation 3*A, in which exchange terms are neglected and the extended Brillouin condition (EBC) is used, i.e. the Fock-matrix elements f_{rx} between orbitals in and outside the orbital basis are assumed to be zero [105, 110]. Despite these approximations very high accuracy can be achieved. Some examples will be presented in Section 14.6. For further details of the theory and implementation we refer to the original publications [11–13, 111] and our recent review [15].

14.3. DENSITY FITTING

The local approximations reviewed so far allow to lower the scaling of the MP2, CCSD, and CCSD(T) methods with respect to the molecular size. However, an important aspect that has not been yet discussed is the evaluation and transformation of the two-electron integrals. Since for large systems the integrals in the AO basis cannot be stored, they have to be computed and used on-the-fly. A detailed description of the algorithms for such *integral-direct* transformations is beyond the scope of the present article, and we refer to our previous papers for details [26, 30, 32, 119]. Here we only note that based on screening techniques and suitable test densities it is possible to achieve linear scaling in all transformation steps. It is important to note that such test densities can be only constructed if the domains are known in advance.

Unfortunately, despite linear scaling, the prefactor of these integral-direct methods is high. It grows at least with the fourth power of the orbital basis size per atom.

In practice, it might even be worse since the expense per integral increases with the number of high angular momentum functions in the basis set.

These bottlenecks can be very strongly reduced by means of the density fitting (DF) technique. DF approximations are widely used in electronic structure theory. Originating from DFT [120–122] their usage spreads today from HF, [123–126] MP2, [127–131] CC2 [132], MP2-F12 [108, 110, 112, 133], up to CCSD [134, 135], DFT-SAPT [136, 137], and SAPT(CC) [138, 139]. The overall scaling of the computational effort for conventional methods with respect to system size is not affected by standard DF, but it significantly reduces the prefactor. Furthermore, for two-electron integrals involving just two external indices it reduces the scaling with respect to the basis set size per atom from formally quartic to cubic. This leads to enormous savings in calculations with large basis sets. If density fitting is combined with local approximations, linear scaling can be achieved. This was first shown for the calculation of the exchange contribution in HF [125] and local MP2 [131]; it has more recently been extended to MP2-R12 [133] and LMP2-F12 [12, 113, 114]. Furthermore, as a first step towards a fully density fitted LCCSD(T) implementation, a linear scaling DF algorithm to evaluate the 4-external integrals in LCCSD was presented already in 2004 [135]. Meanwhile this approach has been extended to treat all integral classes in LCCSD(T) and LCCSD(T)-F12 calculations by density fitting. It leads to dramatic savings in calculations for large molecules, in particular if larger basis sets are used.

14.3.1. Local Density Fitting in LMP2

In LMP2 one only needs the 2-external exchange integrals $K_{rs}^{ij} = (ri|sj)$. These can be written as an integral over two one-electron charge distributions ρ_{ri} and ρ_{sj}

$$(ri|sj) = \int d\mathbf{r}_1 \int d\mathbf{r}_2 \rho_{ri}(\mathbf{r}_1) r_{12}^{-1} \rho_{sj}(\mathbf{r}_2), \quad (14-54)$$

$$\rho_{ri}(\mathbf{r}_1) = \phi_r(\mathbf{r}_1)\phi_i(\mathbf{r}_1). \quad (14-55)$$

The idea of density fitting is to expand the one-electron densities in an auxiliary basis

$$\rho_{ri}(\mathbf{r}) = \phi_r(\mathbf{r})\phi_i(\mathbf{r}) \approx \sum_A d_A^{ri} \chi_A(\mathbf{r}) = \bar{\rho}_{ri}(\mathbf{r}). \quad (14-56)$$

Here the auxiliary basis functions will be labelled by capital letters A, B, C, D . Normally, standard Gaussian basis functions are used. The fitting coefficients d_{ri} can be obtained by minimizing [121, 122]

$$\Delta_{ri} = \int d\mathbf{r}_1 \int d\mathbf{r}_2 \frac{[\rho_{ri}(\mathbf{r}_1) - \bar{\rho}_{ri}(\mathbf{r}_1)][\rho_{ri}(\mathbf{r}_2) - \bar{\rho}_{ri}(\mathbf{r}_2)]}{r_{12}}. \quad (14-57)$$

This leads to

$$d_B^{ri} = \sum_A (ri|A)[\mathbf{J}^{-1}]_{AB} \quad \text{or} \quad \sum_B J_{AB} d_B^{ri} = J_A^{ri}, \quad (14-58)$$

$$K_{rs}^{ij} = \sum_B d_B^{ri}(B|sj) = \sum_{AB} (ri|A)[\mathbf{J}^{-1}]_{AB}(B|sj), \quad (14-59)$$

where

$$J_{AB} = \int d\mathbf{r}_1 \int d\mathbf{r}_2 \frac{\chi_A(\mathbf{r}_1)\chi_B(\mathbf{r}_2)}{r_{12}}, \quad (14-60)$$

$$J_A^{ri} \equiv (ri|A) = \int d\mathbf{r}_1 \int d\mathbf{r}_2 \frac{\phi_r(\mathbf{r}_1)\phi_i(\mathbf{r}_1)\chi_A(\mathbf{r}_2)}{r_{12}}. \quad (14-61)$$

If the MOs are expanded in a basis of GTOs $\{\chi_\mu\}$, the 3-index integrals in the MO basis are obtained by a two-step transformation of the 3-index integrals $(\mu\nu|A)$ in the AO basis

$$(\mu i|A) = \sum_\nu L_{\nu i}(\mu\nu|A), \quad (14-62)$$

$$(ri|A) = \sum_\mu P_{\mu r}(\mu i|A). \quad (14-63)$$

According to the Gaussian product theorem, the size of an integral $(\mu\nu|A)$ decreases exponentially with the square of the distance between the basis functions χ_μ and χ_ν , and therefore the number of non-negligible integrals scales asymptotically as $\mathcal{O}(\mathcal{N}^2)$. In canonical DF-MP2 calculations, in which the occupied and virtual orbitals are delocalized and no sparsity can be exploited, the first and second transformation steps scale as $\mathcal{O}(\mathcal{N}^3)$ and $\mathcal{O}(\mathcal{N}^4)$, respectively. Solving the linear equations (14-58) also behaves as $\mathcal{O}(\mathcal{N}^4)$. The assembly step (Eq. (14-61)) scales as $\mathcal{O}(\mathcal{N}^5)$ and by far dominates the total computational cost in calculations for large molecules. However, all the four steps described above require simple matrix multiplications, and can be performed very efficiently on modern computers. This leads to a low prefactor for the algorithm, and despite the $\mathcal{O}(\mathcal{N}^5)$ scaling quite large molecules (about 40 non-hydrogen atoms) can be handled.

The local approximations have a most profound effect on the assembly step in DF-LMP2: since the number of pairs (ij) scales linearly, and the number of r,s is independent of the molecular size, the computational effort for this step (Eq. (14-59)) is dramatically reduced from $\mathcal{O}(\mathcal{N}^5)$ in the canonical case to just $\mathcal{O}(\mathcal{N}^2)$. Moreover, since the PAOs r must be within a finite range of the LMOs i and j , one needs only those transformed 3-index integrals $(ri|A)$ with r in the *united pair domain* of the associated orbital i . This domain comprises all PAOs that belong to any pair domain $[ij]$ in which orbital i occurs. For large molecules, the size of the united pair domains also become independent of the molecular size, and therefore the number of integrals $(ri|A)$ scales only as $\mathcal{O}(\mathcal{N}^2)$. This reduces the computational effort for solving the linear equations (14-58) from $\mathcal{O}(\mathcal{N}^4)$ to

$\mathcal{O}(\mathcal{N}^3)$. Finally, since the occupied orbitals i are now local, the number of half-transformed integrals $(\mu i|A)$ scales only as $\mathcal{O}(\mathcal{N}^2)$. Using prescreening techniques, the first and second half transformations (Eqs. (14-62) and (14-63)) should then scale only as $\mathcal{O}(\mathcal{N}^2)$. Thus, without further approximations in the fitting basis, the bottleneck for large molecules will be to solve the linear equations in Eq. (14-58). We note that it is numerically more accurate to solve the linear equations (e.g., using LU-decomposition) rather than to invert the \mathbf{J} -matrix.

Linear scaling of all steps can be achieved by using domains also for the fitting basis. The reasoning behind this approximation is that the charge distributions ρ_{ri} are local, and therefore a subset of fitting functions spatially close to this distribution should be sufficient to represent them. This means that we use for each LMO ϕ_i a different fitting domain $[i]_{\text{fit}}$ of functions χ_A . In order to minimize the error of this approximation, one has to use the *robust fitting* formula [131, 135, 140–142]

$$K_{rs}^{ij} \approx \sum_{A \in [i]_{\text{fit}}} d_A^{ri} J_A^{sj} + \sum_{B \in [j]_{\text{fit}}} J_B^{ri} d_B^{sj} - \sum_{A \in [i]_{\text{fit}}} \sum_{B \in [j]_{\text{fit}}} d_A^{ri} J_{AB} d_B^{sj}. \quad (14-64)$$

The fitting coefficients d_B^{ri} are obtained by solving the linear equations

$$\sum_{B \in [i]_{\text{fit}}} J_{AB} d_B^{ri} = J_{ri}^A \quad (\forall A \in [i]_{\text{fit}}). \quad (14-65)$$

Since asymptotically the sizes of the fitting domains $[i]_{\text{fit}}$ as well of the united pair domains $r \in [i]_{\text{U}}$ are independent of the molecular size, the effort for solving the linear equations is proportional to the number of correlated LMOs i ; this leads to linear scaling or even $\mathcal{O}(1)$ scaling if only a region of orbitals is correlated (cf. Section 14.2.1.3). It is easy to see that also the other steps scale linearly. However, since the linear equations have to be solved for each LMO, there is an overhead for small molecules. Local fitting approximations are therefore only useful for extended molecules.

14.3.2. Local Density Fitting in LCCSD(T)

In LCCSD theory all classes of integrals are needed, i.e., 0-external to 4-external. The 2-external exchange integrals $K_{rs}^{kl} = (rk|ls)$ ($rs \in [kl]_{\text{K}}$) are computed as described above for LMP2. The 0- and 1-external integrals can be obtained in the same way with very little extra cost. Since for LCCSD the operator lists kl and operator domains $[kl]_{\text{K}}$ are much larger than in the LMP2 case [30], it is usually not useful to enable local fitting – the cross-over point to linear scaling occurs quite late, and for medium size calculations the overhead exceeds the savings.

The 2-external Coulomb integrals $J_{rs}^{ij} = (rs|ij)$ are first computed in the AO basis as

$$J_{\mu\nu}^{ij} \equiv (\mu\nu|ij) = \sum_A (\mu\nu|A) d_A^{ij}, \quad (14-66)$$

where d_A^{ij} are the fitting coefficients obtained in the generation of the 0-external integrals. The coefficients d_A^{ij} are kept in memory. The outermost loop runs over blocks of $\mu \geq \nu$, and for each block the 3-index integrals

$$(\mu\nu|A) = \int d\mathbf{r}_1 \int d\mathbf{r}_2 \chi_\mu(\mathbf{r}_1) \chi_\nu(\mathbf{r}_1) r_{12}^{-1} \chi_A(\mathbf{r}_2) \quad (14-67)$$

are computed and contracted on-the-fly with the fitting coefficients. Since for each of these blocks the index ij runs fastest, the resulting integrals $(\mu\nu|ij)$ are sorted into the final order (ij runs slowest). In the last step the integrals are transformed into the PAO basis before being written to disk. Currently, for these integrals local fitting is not implemented. However, despite the fact that without local fitting the algorithm scales (in the asymptotic limit) cubically, the CPU time for this part of the transformation is quite short and has never been a bottleneck in the calculations.

As the 0–2 external integrals, the 3- and 4-external integrals are generated by utilizing density fitting. The 3-external integrals $(rs|kt)$ occur in various terms involving contractions with the singles amplitudes, e.g. $\sum_{t \in [j]} (rs|kt) t_t^j$, and with double amplitudes $\sum_{st \in [ij]} (rs|kt) C_{st}^{ij}$, as well as in the expression of the perturbative triples correction. The range of indices r, s, t for each LMO k is independent of the molecular size can be determined in advance (3-ext domains). Thus, in the asymptotic limit, the number of these integrals scales linearly with molecular size. A detailed description of the definition of the 3-ext domains can be found in Ref. [30].

The 4-external integrals $(rt|su)$ just appear in the external exchange operators $\mathbf{K}(\mathbf{C}^{ij})$ (cf. Eq. (14-42)) which contribute only to the doubles residual for pair (ij) . Since the four indices of $(rt|su)$ always belong to the same domain, this set of integrals is significantly more compact than the 3-external integral set, in spite of the additional virtual orbital index.

In the following we outline our algorithm for the 4-external integrals, for which local fitting is most useful. Local fitting for the 3-external integrals proceeds along similar lines. However, since the 3-external domains are quite extended, the savings are smaller than in the 4-external case, and the cross-over point to the standard non-local fitting method occurs only for larger molecular sizes.

As for the 2-external exchange operators, local fitting makes it necessary to use the robust 3-term fitting expression

$$(rs|tu) \approx \sum_{A \in [RS]} d_A^{rs} J_A^{tu} + \sum_{B \in [TU]} J_B^{rs} d_B^{tu} - \sum_{A \in [RS]} \sum_{B \in [TU]} d_A^{rs} (A|B) d_B^{tu}, \quad (14-68)$$

or the symmetric two-term formula [135]

$$(rs|tu) \approx \frac{1}{2} \left[\sum_{A \in [RS]} d_A^{rs} J_A^{tu} + \sum_{B \in [TU]} J_B^{rs} d_B^{tu} \right]. \quad (14-69)$$

A comparison of the performance of the symmetric and robust formulae for the 4-external integrals can be found in table 1 of Ref. [135]. $A \in [RS]$ represents an auxiliary fitting function confined to a fit domain $[RS]$. This domain is related to the charge distributions of the orbital products $\phi_r^{\text{PAO}}(\mathbf{r})\phi_s^{\text{PAO}}(\mathbf{r})$, where r and s denote functions located at the centres R and S , respectively. Thus, the fitting domains are specific to centre pairs. d_A^{rs} are the fitting coefficients obtained by solving the following equations for each centre pair RS

$$\sum_{B \in [RS]} (A|B)d_B^{rs} = J_A^{rs}, \quad \forall A \in [RS]. \quad (14-70)$$

Since this implies that the indices A, B, r, s refer to functions that are spatially close, the computational effort scales linearly with molecular size. In the case that full fitting domains are used (non-local fitting), all terms in Eqs. (14-68) and (14-69) are identical, yielding the usual one-term expression of density fitting. For further details of the algorithm and the choice of the fitting domains we refer to Ref. [135].

14.4. LOCAL PROPERTIES OF FIRST AND SECOND ORDER

Molecular properties calculated from canonical linear response (LR) CCSD theory or its time-dependent (TD) variant for dynamic properties [17, 143, 144] are not very sensitive to the relaxation of orbitals caused by the perturbation. Numerical experience shows that orbital-nonrelaxed and relaxed dipole moments and static dipole polarizabilities are quite similar to each other. The explanation of this fact is based on the recognition that the $\exp(\hat{T}_1)$ operator already accounts for most of the orbital rotations [145].

The situation is different if local approximations are introduced. Since the single excitations are restricted to domains, they cannot account well for the orbital relaxation. In contrast to the canonical case it is therefore essential to include orbital relaxation effects explicitly in calculations of first- and second-order properties. In a benchmark study of Korona et al. [37] dipole moments and static dipole polarizabilities were computed using LCCSD for 16 molecules. It was found that with standard domains the average absolute errors of orbital-relaxed LCCSD relative to the canonical calculations amount to 1.6% for dipole moments and 0.5% for polarizabilities. With extended domains these errors were reduced to 0.9 and 0.3%, respectively.

It should be noted, however, that the explicit inclusion of orbital relaxation in LR-CC theory is not advisable for dynamic properties [143], since an artificial set of poles (resulting from the TD-HF equations) is introduced in this way for real frequencies. The problem of computing accurate dynamic second-order properties using local wave functions requires more investigations.

14.4.1. Analytical Energy Gradients for Local Wave Functions

Local gradients have been so far implemented for the LMP2 [34, 36] and LQCISD [35] methods. Additionally, local static second-order properties have been implemented for the LMP2 method [38]. As discussed above, only orbital-relaxed variants of local properties produce valuable results. The most effective local gradient method available so far is the density-fitted LMP2 gradient implementation described in Ref. [36].

The derivations of the LMP2 and LQCISD gradients described in Refs. [34, 35] use the interchange technique of Handy and Schaefer [146] to replace the dependence on the first-order orbital (and amplitude, in the case of LQCISD) response by corresponding Z -vectors. This is very important, since the number of sets of equations to be solved then becomes *independent* of the number of perturbations. The application of the interchange technique is somewhat obscure though, a much more natural way is to set up an appropriate energy Lagrangian [143, 147], containing all the required equations of the non-variational wave function parameters to be fulfilled (like the Brillouin and locality conditions for the orbitals, and the amplitude equations in the LQCISD case) as constraints. The Lagrangian is required to be stationary with respect to *all* wave function parameters (including the multipliers); the latter correspond exactly to the elements of the Z -vectors of the interchange technique, but appear immediately and much more naturally. The derivation of the formalism of the density-fitted LMP2 gradient described in Ref. [36] follows this second strategy and is very briefly laid out in the following.

For the LMP2 case no multipliers corresponding to the LMP2 amplitude equations have to be determined. It is a simple task to show that the orbital-unrelaxed MP2 Lagrangian (which includes the MP2 amplitude equations as a constraint) is equivalent to the Hylleraas functional,

$$E_2 = 2\langle\Phi_0|\hat{H}|\Phi_1\rangle + \langle\Phi_1|\hat{H}^{(0)} - E^{(0)}|\Phi_1\rangle, \quad |\Phi_1\rangle = \hat{T}_2^{(1)}|\Phi_0\rangle, \quad (14-71)$$

with the multipliers being identical to the contravariant amplitudes. For the closed-shell case we have $\hat{H}^{(0)} \equiv \hat{F}$ with \hat{F} defined in Eq. (14-17) and $E^{(0)} = \langle\Phi_0|\hat{F}|\Phi_0\rangle$ (for a definition of $\hat{H}^{(0)}$ for the open-shell case see Eq. (14-47)). The orbital-relaxed LMP2 Lagrangian is then the Hylleraas functional E_2 , augmented by the Brillouin ($f_{ai} = 0$), localization ($r_{ij} = 0$), and orthonormality conditions for the orbitals, i.e.,

$$\mathcal{L} = E_2 + \sum_{i>j} z_{ij}^{\text{loc}} r_{ij} + \sum_{ai} z_{ai} f_{ai} + \sum_{pq} x_{pq} [\mathbf{C}^\dagger \mathbf{S}_{\text{AO}} \mathbf{C} - \mathbf{1}]_{pq}. \quad (14-72)$$

Equation (14-72) is written in a semi-local (localized occupied, canonical virtual MOs) orbital basis, i.e. $\mathbf{C} = \mathbf{L}||\mathbf{C}_v$, where the $||$ sign means that two matrices are glued together. This mixed representation makes the orthonormality condition particularly simple. The amplitudes can be transformed from local PAOs to canonical virtuals according to

$$T_{ab}^{ij} = \sum_{rs} Q_{ar} T_{rs}^{ij} Q_{sb}^{\dagger} \quad (14-73)$$

with the transformation matrix defined in Eq. (14-10). Note that the transformation specified in Eq. (14-73) connects local and “canonical” amplitudes which eventually live in different vector spaces; the true canonical amplitudes are only obtained if no truncations to excitation domains are introduced. For a detailed discussion of transformation relations between the canonical orbital space and the local redundant orbital subspaces we refer to Ref. [75].

Differentiation of the Lagrangian (cf. Eq. (14-72)) with respect to orbital variations yields equations for the multipliers z_{ij}^{loc} , z_{ai} , and x_{pq} , which can be decoupled from each other (see Ref. [36] for details). The equations to be solved for the z_{ij}^{loc} and z_{ai} are the coupled perturbed localization (Z-CPL) and coupled perturbed HF (Z-CPHF) Z-vector equations of the interchange technique, but now straightforwardly obtained. The Z-CPL equations must be solved before the Z-CPHF equations since the r.h.s. of the latter depends on the z_{ij}^{loc} . Finally the x_{pq} , which depend on both the z_{ij}^{loc} and the z_{ai} , are calculated directly afterwards (no iterative scheme is needed to get the x_{pq}).

Due to the stationarity of the Lagrangian (Eq. (14-72)), its derivative with respect to the perturbations (which is identical to energy gradient) is just the partial derivative with respect to these perturbations. It can be written in the form

$$\mathcal{L}^q = E_2^q = E_2^{(q)} + \sum_{ai} z_{ai} f_{ai}^{(q)} + \sum_{i>j} z_{ij}^{\text{loc}} r_{ij}^{(q)} + \sum_{pq} x_{pq} [\mathbf{C}^{\dagger} \mathbf{S}_{\text{AO}}^q \mathbf{C}]_{pq}, \quad (14-74)$$

and evaluated immediately after all the multipliers are determined. In Eq. (14-74) the subscript (q) indicates that the corresponding quantity is evaluated as usually, but with the AO integrals $h_{\mu\nu}$, $(\mu\nu|\rho\sigma)$, $(S_{\text{AO}})_{\mu\nu}$ replaced by the corresponding *derivative* AO integrals $h_{\mu\nu}^q$, $(\mu\nu|\rho\sigma)^q$, and $(S_{\text{AO}}^q)_{\mu\nu}$, respectively. Equation (14-74) can be rearranged such that all terms to be contracted with a certain *derivative* integral type are collected into a single term, yielding finally for the total (HF plus LMP2) gradient

$$[E_{\text{HF}} + E_2]^q = \sum_{\mu\nu} (d_{\mu\nu} h_{\mu\nu}^q + X_{\mu\nu} (S_{\text{AO}}^q)_{\mu\nu}) + \frac{1}{2} \sum_{\mu\nu\rho\sigma} D_{\mu\nu,\rho\sigma} (\mu\nu|\rho\sigma)^q. \quad (14-75)$$

Here, the effective one- and two-particle density matrices $d_{\mu\nu}$ and $D_{\mu\nu,\rho\sigma}$, as well as the quantity $X_{\mu\nu} = [\mathbf{C}\mathbf{x}\mathbf{C}^{\dagger}]_{\mu\nu}$ are introduced. For a detailed definition of these objects we refer to eqs. (38), (43), and (44) of Ref. [36]. $D_{\mu\nu,\rho\sigma}$ consists of two parts, the non-separable correlation part, which is essentially the back-transform of the local MP2 amplitudes into the AO basis, and the separable HF part. The back-transformation is actually one of the most expensive steps of conventional (non-local) MP2 gradient calculations.

A key feature of the density-fitted LMP2 gradient described in Ref. [36] is the consequent use of density fitting, also for the HF part [125]. Therefore, unfactorized

two-electron derivative integrals $(\mu\nu|\rho\sigma)^q$ never appear. In fact, the only 4-index quantity in the present DF-LMP2 implementation is the compact set of local amplitudes T_{rs}^{ij} . This set is half-contracted with the related fitting coefficients to form the 3-index key quantity

$$V_{ir}^A = \sum_j \sum_{s \in [ij]} \tilde{T}_{rs}^{ij} d_A^{js}, \quad (14-76)$$

immediately after the preceding LMP2 energy calculation, i.e., at the very beginning of the gradient step. Analogous key quantities appear also in density-fitted LCC2 and time-dependent LCC2 response theory (cf. Eq. (14-90) below). The contraction of the non-separable part of the two-particle density matrix with the 4-index electron repulsion derivative integrals of Eq. (14-75) now simplifies to

$$\Delta E_2^q = 4 \sum_A \sum_{\mu\nu} (\mu\nu|A)^q V_{\mu\nu}^A - 2 \sum_{AB} J_{AB}^q \sum_i \sum_{r \in [i]_U} V_{ir}^A d_B^{ir}, \quad (14-77)$$

with $V_{\mu\nu}^A$ representing the V_{ir}^A quantity back-transformed to the AO basis, and $[i]_U$ denotes the *united pair domain* introduced after Eq. (14-37). Hence, instead of a 4-index transformation, just a two-index back-transformation is required, and just 3- and 2-index (rather than the usual 4-index) electron repulsion derivative integrals are needed in the subsequent contraction.

The density-fitted LMP2 gradient program has also been parallelized in a simple way, based on a shared-files approach (the scratch files containing integrals and amplitudes reside on a common shared file system). It is an efficient workhorse to produce optimized geometries of extended molecular systems at the level of local MP2. Since the correlation component of the gradient is not more expensive than the related density-fitted HF part, optimizations at the LMP2 level are also feasible, whenever they are feasible at the corresponding HF level.

14.5. LOCAL METHODS FOR EXCITED STATES

In EOM-CCSD theory the m th electronic excited wave function Ψ^m is generated from the ground state CCSD wave function by an operator \hat{R}^m

$$\Psi^m = \hat{R}^m e^{\hat{T}} \Phi_0, \quad \text{where} \quad \hat{R}^m = \hat{R}_0^m + \hat{R}_1^m + \hat{R}_2^m. \quad (14-78)$$

This operator has the same structure as the cluster operator \hat{T} in the CCSD ground-state wave function. Therefore, at a first glance, all approximations applied before to develop a local approach for the ground state can be directly transferred to treat excited states. In reality, the situation is much less comfortable. The reason for this will be clear if we compare the importance of single and double excitations in the operators \hat{R}^m and \hat{T} . For the ground-state wave function of CCSD theory, $\exp(\hat{T})\Phi_0$, the \hat{T} operator *corrects* the existing HF reference Φ_0 , so the norm of this operator is

an order(s) of magnitude less than 1. Additionally, a relative importance of double excitations is larger than that of singles, since in the MP expansion of the CC wave function the single excitation operators appear for the first time in the second-order wave function. This means that in the development of local methods an accurate treatment of \hat{T}_2 is crucial for a proper account of the electron correlation, while \hat{T}_1 can be treated more approximately.

For excited states dominated by the promotion of a single electron from the ground state⁷ the relative importance of single and double excitations is reversed. The \hat{R}^m operator creates a wave function which has a small (if any) overlap with Φ_0 , so the norm of \hat{R}^m is of the order of 1, and in particular the norm of the \hat{R}_1^m operator is usually well above 0.9. Double excitations contained in \hat{R}_2^m should be, however, included, since errors resulting from a neglect of \hat{R}_2^m can be of order of 1 eV (see the configuration interaction singles (CIS) [148] method, which is equivalent to coupled cluster singles – CCS – for the excitation energies).

Also the MP analysis of the second-order dynamic properties of time-dependent CCSD theory (TD-CCSD) accentuates the difference in the relative importance of single and double substitutions for the ground-state and perturbed excitation operators. For example, the *perturbed* singly-excited operator appears already in zeroth order of MP theory (double excitations are of first order). Knowing that excitation energies of TD-CCSD (and EOM-CCSD) theory are poles of the TD-CCSD linear response function, calculated with the neglect of orbital relaxation, one might expect a large influence of local approximation on the quality of these poles. Fortunately, using a pilot implementation of the local EOM-CCSD method [40], it has been shown that the problem is not so acute as it could be feared, and that for low-lying excited states it is possible to construct local excitation spaces which are sufficient to reproduce nonlocal excitation energies with a good accuracy.

14.5.1. Local EOM-CCSD

In EOM-CCSD theory [19] the excitation energy ω^m is obtained by solving the following equation

$$[e^{-\hat{T}}\hat{H}e^{\hat{T}},\hat{R}^m]\Phi_0 = \omega^m\hat{R}^m\Phi_0, \quad (14-79)$$

where the wave function of the m -th excited state is given in Eq. (14-78) and \hat{T} is the CCSD cluster operator. In practice the Davidson method generalized to non-symmetric matrices [149, 150] is used to solve Eq. (14-79) iteratively, and the main computational effort – similarly to the ground-state case – goes into the calculation of residuals, which should be equal to zero for converged \hat{R}^m and ω^m

⁷Only electronic states dominated by single excitations can be obtained reliably with EOM-CCSD for molecules containing more than 2 electrons. Electronic states dominated by double excitations are also formally available, but their accuracy is questionable.

$$\begin{aligned} v_p^i &= \langle \tilde{\Phi}_p^i | ([e^{-\hat{T}} \hat{H} e^{\hat{T}}, \hat{R}^m] - \omega^m \hat{R}^m) | \Phi_0 \rangle \quad \forall i \in o, \quad \forall p \in v, \\ \mathfrak{V}_{pq}^{ij} &= \langle \tilde{\Phi}_{pq}^{ij} | ([e^{-\hat{T}} \hat{H} e^{\hat{T}}, \hat{R}^m] - \omega^m \hat{R}^m) | \Phi_0 \rangle \quad \forall i \geq j \in o, \quad \forall p, q \in v. \end{aligned} \quad (14-80)$$

It is worth to notice that in the EOM-CCSD approach several excited states can be obtained at the same time.

As outlined above the main challenge of the local methods for excited states is a proper description of single excitations. Contrary to the ground state, one cannot assume any longer that excitations are limited to PAOs that are spatially close to the LMOs, from which the excitation takes place (a prominent example are charge-transfer states). In fact, calculations of excitation energies using standard domains and pair lists from LCCSD yield a very poor description of excited states, even for the lowest ones (the excitation energies are worse than in CIS) [151]. A simple extension of all orbital domains by neighbouring atoms might help for a few lowest valence states, but eventually this *brute force* method will fail for efficiency reasons. It turns out that in order to select more precisely the appropriate orbital domains, the local EOM-CCSD (LEOM-CCSD) method should be state-selective, since for one particular state it is easier to adapt the excitation space appropriately.

14.5.1.1. Local Excitation Space in LEOM-CCSD

Since in EOM-CCSD theory only states dominated by single excitations are of practical interest, it is legitimate to assume that the main features of these states are already described at the level of some simpler theory, like CIS. If the CIS wave function bears the main characteristics of the exact function (i.e. to which regions of a molecule goes the main part of the excitation etc.), one can select a priori orbital domains that are specific for the excited state of interest. Practically this is done by an analysis of the excitations from a given LMO ϕ_i in the corresponding CIS wave function Ψ_{CIS}^m . This can be represented by an excitation into a single orbital

$$\phi_i^* = \sum_a c_a^i \phi_a, \quad (14-81)$$

where c_a^i are the expansion coefficients from Ψ_{CIS}^m . The squared norm of ϕ_i^* has a meaning of a *weight* of the excitation from a given LMO (the sum of all weights is one). LMOs are divided into *important* and *unimportant* ones for a given excited state m , based on their contribution to the excitation. The LMOs are ordered according to their decreasing weights, then a set of important orbitals is created in such a way that LMOs are added as long as the sum of weights of included LMOs is smaller than some prescribed number κ_e (usually $\kappa_e = 0.9975$). The normalized orbitals from Eq. (14-81) (which can be thought of as *natural virtual orbitals* – NVO – for a given excitation) are utilized in the Boughton-Pulay procedure for creating excitation orbital domains, i.e. the orbital ϕ_i^* replaces the old localized ϕ_i in Eq. (14-13). The excitation domain for the orbital ϕ_i (denoted as $[i]^*$) is a union of the orbital domain $[i]$ for the ground state and the part resulting from the Boughton-Pulay procedure for the corresponding NVO. The latter part is added for important

LMOs only. The possibility of excitations into the ground-state orbital domain [i] allows for a relaxation of the hole remaining after the excitation from ϕ_i and makes it possible to minimize the electron repulsion after the excitation on a given molecular fragment took place. The excitation space for singles in LEOM-CCSD is always larger than for the underlying LCCSD method, reflecting the fact that the singles contribution in the excitation operator \hat{R}^m is responsible for the main part of the excitation energy.

An appropriate treatment of double excitations is nonetheless an indispensable part of the LEOM-CCSD approach. Similarly to the ground-state case the pairs (ij) are divided into classes and the excitations are allowed to the union of the excitation domains [i]* and [j]* only. A division into *strong* and *weak* EOM-CCSD pairs is performed, and only excitations from strong pairs are allowed. The usual selection criteria for the EOM-CCSD strong pairs are the following: either the pair should be diagonal, or (i) at least one LMO in a pair should be important, and (ii) the distance of these two LMOs should be less than some prescribed value (the distance between two LMOs is defined as described in Section 14.2.1.1).

14.5.1.2. Treatment of \hat{T}_2 in Local EOM-CCSD

The energies of the excited states in EOM-CCSD theory are obtained from a diagonalization of the similarity-transformed Hamiltonian $e^{-\hat{T}}\hat{H}e^{\hat{T}}$ projected on singly and doubly excited CSFs, denoted here collectively as μ . An important feature of EOM-CCSD is the decoupling of the excitation part of the matrix representation of the similarity-transformed Hamiltonian from the reference determinant. This relies on the fact that the elements $\mathfrak{V}_\mu = \langle \tilde{\Phi}_\mu | e^{-\hat{T}}\hat{H}e^{\hat{T}} | \Phi_0 \rangle$ of this matrix are equal to zero for converged CCSD amplitudes (μ denotes here symbolically indices for single or double excitations). In the space composed of the reference determinant Φ_0 and excited CSFs, $|\mathbf{q}\rangle\langle\mathbf{q}| = |\Phi_0\rangle\langle\Phi_0| \oplus |\mu\rangle\langle\mu|$ we therefore have

$$\langle\mathbf{q}|e^{-\hat{T}}\hat{H}e^{\hat{T}}|\mathbf{q}\rangle = \begin{pmatrix} \langle\Phi_0|e^{-\hat{T}}\hat{H}e^{\hat{T}}|\Phi_0\rangle & \langle\Phi_0|e^{-\hat{T}}\hat{H}e^{\hat{T}}|\mu\rangle \\ \mathbf{0} & \langle\mu|e^{-\hat{T}}\hat{H}e^{\hat{T}}|\mu\rangle \end{pmatrix}, \quad (14-82)$$

so that only the $\langle\mu|e^{-\hat{T}}\hat{H}e^{\hat{T}}|\mu\rangle$ part of Eq. (14-82) needs to be diagonalized in order to obtain energies of excited states. However, since domains and pair lists for the LEOM-CCSD and LCCSD methods are usually not identical, there will be nonzero residual elements \mathfrak{V}_μ for μ which are present in the excitation space for LEOM-CCSD, but absent in LCCSD. One obvious remedy to this problem is a recalculation of the \hat{T} operator in the LEOM-CCSD space. However, this approach has two major drawbacks: first, this procedure should be repeated for each excited state, leading to an increase of the computational cost; secondly, the LCCSD correlation energy will slightly change from one excited state to another. Therefore, a simpler procedure has been devised in order to approximately counterweight double excitations in \hat{R}^m and \hat{T} operators: in the local EOM-CCSD calculation we include LMP2 amplitudes for those pairs (ij), which are strong in local EOM-CCSD, but weak in LCCSD.

We have found that this method allows for a proper balance of these two operators without a substantial increase of the computational cost.

Since the structure of EOM-CCSD residual equations is similar to that for the ground-state case, most arguments related to lowering of the computational effort applies also for this case. Some notable differences include the relative importance of some types of integrals, e.g. the 2-external Coulomb integrals should be treated on the same footing as the 2-external exchange integrals, since both appear in the main, CIS-like, term of the residual equations [152]. Moreover, if for some excited state the excitation is well localized in one part of a molecule, the number of strong excited pairs may be even independent of \mathcal{N} (provided that the requirement to include all diagonal pairs is lifted). In practice, since excited domains are often much larger than orbital domains, such an ideal situation is rarely observed.

14.5.1.3. State-Specific Character of Local EOM-CCSD

The small space constructed during the Davidson iterations is created first by making initial guesses for the excited states and then by calculating updates in each iteration from the energy-weighted residuals. This space contains approximations not only for the desired state, but represents to some extent several other excited states. In the LEOM-CCSD method these states, which are not very well described in the local excitation space tailored for a particular state, are usually shifted to higher energies. It often happens that a state, which is energetically lower than the state under consideration in the canonical EOM-CCSD theory, is represented so poorly in the local space, that the order of excited states in the small Davidson space is changed. In order to locate the selected state, a root-homing algorithm [153] has been implemented by a modification of the nonsymmetric Davidson iterative method. In this algorithm the overlap of the eigenvectors of the small Davidson space with the sample vector (usually the CIS vector) is calculated in each iteration and the vector with the largest overlap is selected for an update.

14.5.2. Local CC2 Response Theory

The CC2 model [20] is the simplest CC-type method which can be applied in the framework of time-dependent CC response theory. It is appropriate to describe electronic excited states which are dominated by single promotions of an electron from the ground state. The computational scaling of CC2 is similar to MP2, but – opposite to MP2 – the CC2 formalism allows for an unambiguous formulation of molecular properties. In particular, excitation energies are defined as poles of the TD-CC2 linear response functions, while transition moments can be retrieved from their residues [143].

A density-fitted version of CC2 response (DF-CC2, also called RI-CC2), utilizing density-fitting techniques for an approximate calculation of ERIs, allows to treat excited states of medium-size molecules (containing about 25 non-hydrogen atoms) [132, 154, 155]. Despite density-fitting the DF-CC2 method has some parts of the code which still scale as $\mathcal{O}(\mathcal{N}^5)$. In order to lower the scaling behaviour of the CC2 model local approximations can be introduced.

In CC2 the singly-excited operator \hat{T}_1 is treated as a quantity of the zeroth MP order [20]. A strong support for such a “privileged” treatment comes from MP theory (the high second MP order of the \hat{T}_1 operator is a result of a fulfillment of the Brillouin’s theorem ($f_{ia} = 0$) by the HF reference determinant, while the response to any one-particle perturbation operator gives a contribution already in the zeroth MP order). Since (as already noted) inclusion of explicit orbital-relaxation constraints into the time-averaged second-order CC2 Lagrangian would lead to additional spurious poles in the linear response functions, it is much preferable to let $\exp(\hat{T}_1)$ taking over this role. Consequently, in the local CC2 (LCC2) response formalism [41–44] local approximations are applied to doubly-excited operators only, while single excitations remain unrestricted, like in the canonical case.

Equations for the CC2 model are most easily described in terms of a *dressed* Hamiltonian operator \hat{H} , which is defined as $\exp(-\hat{T}_1)\hat{H}\exp(\hat{T}_1)$. For the local case the CC2 equations take the form

$$\begin{aligned}\langle\mu_1|\hat{H} + [\hat{H}, \hat{T}_2^{\text{loc}}]|\Phi_0\rangle &= 0, \\ \langle\mu_2^{\text{loc}}|\hat{H} + [\hat{H}, \hat{T}_2^{\text{loc}}]|\Phi_0\rangle &= 0,\end{aligned}\quad (14-83)$$

and

$$\mathbf{A}\mathbf{R}^m = \omega^m\mathbf{M}\mathbf{R}^m, \quad \mathbf{L}^m\mathbf{A} = \omega^m\mathbf{L}^m\mathbf{M}, \quad (14-84)$$

for ground and excited states, respectively, where \mathbf{A} is the LCC2 Jacobian,

$$A_{\mu_i\nu_j} = \begin{pmatrix} \langle\mu_1|[\hat{H}, \hat{\tau}_{\nu_1}] + [\hat{H}, \hat{\tau}_{\nu_1}], \hat{T}_2^{\text{loc}}|\Phi_0\rangle & \langle\mu_1|[\hat{H}, \hat{\tau}_{\nu_2}^{\text{loc}}]|\Phi_0\rangle \\ \langle\mu_2^{\text{loc}}|[\hat{H}, \hat{\tau}_{\nu_1}]|\Phi_0\rangle & \langle\mu_2^{\text{loc}}|[\hat{H}, \hat{\tau}_{\nu_2}^{\text{loc}}]|\Phi_0\rangle \end{pmatrix}, \quad (14-85)$$

and \mathbf{M} the metric matrix (in the canonical space the latter equates to the identity matrix). The $\hat{\tau}_{\nu_i}$ symbols denote one- or two-particle excitation operators for $i = 1, 2$, respectively. Even though no a priori local approximations are imposed on the singles (such that the nominal scaling of the singles terms is $\mathcal{O}(\mathcal{N}^4)$), the locality of the orbital basis still leads to a lower asymptotic scaling due to prescreening in the calculation of the individual singles terms. In practical examples, an overall scaling around $\mathcal{O}(\mathcal{N}^2)$ was observed.

14.5.2.1. Configurational Space for LCC2 Response

As in all other local methods described here, LMOs and PAOs are utilized to span occupied and virtual orbital spaces, respectively. Since in LCC2 no local approximations are introduced for single excitations, ground-state orbital $[i]$ and excitation orbital $[i]^*$ domains are created only for the purpose of defining pair domains $[ij]$ and $[ij]^*$ for double excitations, which are as usual formed as a union of the corresponding orbital domains. These domains can be further modified if necessary (*vide*

infra). For the ground state, the orbital domains and the hierarchy of orbital pairs (ij) are constructed on the base of spatial vicinity criteria, similarly to the LMP2 case (the pairs are called strong in this case if the interorbital distance is smaller than 10 bohr and only such pairs are considered in ground-state CC2 calculations). Orbital excitation domains for a given excited state are initially constructed using the same procedure as in LEOM-CCSD (see Ref. [40] and Section 14.5.1). In this way the quality of the LCC2 calculation is determined by an initial guess of the domains and pair lists. In Ref. [42] a refinement of the orbital excitation domains has been proposed, which is based on an analysis of coupled-perturbed localization equations. This domain extension has been necessary in order to improve the local treatment of CC2 first-order properties. A more robust way of adapting pair domains [43] is based on a Löwdin-like analysis of the yet-unconverged R_{pq}^{ii} amplitudes of a given excited state (in the following we skip the superscript numbering the excited state), i.e. diagonal parts of the doubly-excited amplitudes (where i denotes an LMO, p, q are calculated in the unrestricted orbital basis). Since in the local CC2 response method only double amplitudes are treated locally, this approach allows to establish the domains from an analysis of the object which is to be approximated. The construction of such domains is only possible in case of the Laplace-transformed formulation of LCC2 (*vide infra*). R_{pq}^{ii} is a 3-index object and its calculation for the CC2 case then is not expensive despite its $\mathcal{O}(\mathcal{N}^4)$ formal scaling, since the quantity can be calculated with very rough approximations, like fewer integration points in the Laplace transform and large prescreening thresholds. To this end a quantity d_A^i , defined as

$$d_A^i = \sum_{p \in [A]} \sum_{qrr's} S_{pq}^{1/2} R_{qr}^{ii} S_{rr'} S_{r's}^{1/2}, \quad (14-86)$$

is constructed, which condenses the information about the distribution of the excitation for the LMO i among the atoms A of the molecule. Based on $\sum_A d_A^i$ a set of important orbitals is determined in analogy to the LEOM-CCSD case (but usually a more tight parameter $\kappa_e = 0.999$ is utilized). Then the BP procedure is performed, see Eq. (14-13), where φ_i and φ'_i represent, for a given excited state, the whole double excitation from the LMO i for untruncated and truncated domains of diagonal double amplitudes, respectively, i.e.

$$\varphi'_i(\mathbf{r}) = \sum_{rs \in [ii]^*} \phi_r(\mathbf{r}) \phi_s(\mathbf{r}) R_{rs}^{ii}. \quad (14-87)$$

The domains obtained on the basis of the analysis of the diagonal part of doubles amplitudes are denoted Laplace domains.

It should be stressed that as a consequence of the domain refinement several additional steps apart from the calculation of the next residual should be performed. Since these steps are quite expensive, it is important to reduce the number of such domain re-specifications to a necessary minimum. The additional operations after each of these refinements comprise a modification of the data specifying domains

and pair lists. It should also be mentioned that some intermediates cannot be precalculated before the LCC2 iterations if domain modifications are enabled, even if they formally do not depend on \hat{R}_2^m (or alternatively, they have to be calculated in the full orbital space). After the domains and the pair list are altered, the old vectors from the Davidson trial space are still expressed with reference to the old local excitation space and thus should be projected onto the new configurational space. Usually, domain refinement is carried out only as part of the Davidson refreshment procedure.⁸ Hence, the domain change is performed together with the Davidson refresh if the analysis of the approximate excited states indicates large shifts of the excitations in comparison to the initial local configurational space, i.e., if the overlap between the first Davidson basis vector for a particular state and the actual approximation of that state falls below a certain threshold (usually 0.5).

After the excitation domains are known, double excitations from LMO pairs ϕ_i and ϕ_j are divided into strong and weak, and only excitations from strong pairs are allowed. The strong pair list in the LCC2 case consists of two groups of pairs: the first group comprises all pairs between important orbitals (regardless their interorbital distance), and the second group is composed of pairs, which have at least one unimportant LMO. The additional restriction applied to the pair (ij) from the second group is that a interorbital distance should be smaller than a prescribed threshold (usually 5 bohr). Since the number of important LMOs for a given excited state is independent of the molecular size, the number of strong pairs is governed by the second group which scales linearly with \mathcal{N} . The dimensions of the pair domains are independent of the size of the molecule, so finally the number of doubly-excited configurations grows like $\mathcal{O}(\mathcal{N}^1)$. Single excitations are not restricted in LCC2, so their number scales as $\mathcal{O}(\mathcal{N}^2)$. However, for sizes of molecules which can be treated by LCC2, single excitations so far do not constitute any bottleneck.

14.5.2.2. Notes on the Implementation of DF-LCC2 Response

An efficient formulation of the CC2 equations is based on dressed operators. The dressed electron-repulsion integral is calculated according to the equation

$$(vw|\hat{x}y) = \sum_{\mu\nu\rho\sigma} (\mu\nu|\rho\sigma) A_{\mu\nu}^{\mathbf{p}} A_{\nu w}^{\mathbf{h}} A_{\rho x}^{\mathbf{p}} A_{\sigma y}^{\mathbf{h}}, \quad (14-88)$$

where $A^{\mathbf{p}}$ and $A^{\mathbf{h}}$ are modified matrices of MO coefficients,

$$A^{\mathbf{p}} = [\mathbf{L} | (\mathbf{P} - \mathbf{L} \mathbf{t}_1^\dagger \mathbf{S})], \quad A^{\mathbf{h}} = [(\mathbf{L} + \mathbf{P} \mathbf{t}_1 | \mathbf{P}], \quad (14-89)$$

and v,w,x,y denote general indices (LMOs and PAOs). These matrices, where \mathbf{t}_1 denotes the $N_{\text{AO}} \times N_{\text{occ}}$ matrix of the singles amplitudes, are rectangular with the

⁸ The Davidson refreshment procedure consists of a selection of the best approximation for a desired vector and the removal of all other vectors from the small Davidson space. It is usually performed when the dimension of this space reaches some maximum allowed value.

dimensions $N_{\text{AO}} \times (N_{\text{AO}} + N_{\text{occ}})$. In DF-LCC2 the 4-index integrals are replaced by Eq. (14-68). In the present DF-LCC2 program local fitting domains (see Section 14.3.1) are not yet implemented, so further improvements of the scaling properties can still be expected within this approach.

An efficient utilization of DF requires that a proper factorization of the LCC2 equations is achieved. The complete working equations for DF-LCC2 are given in Ref. [41] (for right eigenvectors of the Jacobian) and Ref. [42] (for left eigenvectors and first-order properties, including transition moments). Here we only briefly analyse one representative term of the residual equations from the former paper. One of the most expensive parts of the product $\sum_{v_2} A_{\mu_1 v_2} U_{v_2}$ (where U_{v_2} is a doubles basis vector spanning the Davidson subspace) is the term

$$W_{ip}^A = \sum_{kq} (2U_{pq}^{ik} - U_{qp}^{ik}) d_{kq}^A, \quad (14-90)$$

where d_A^{kq} is defined according to Eq. (14-58). Without localization the cost of the calculation of this intermediate scales as $\mathcal{O}(N_{\text{AO}}^2 N_{\text{fit}} N_{\text{occ}}^2)$, i.e., with the fifth power of \mathcal{N} . The localization of the double amplitudes reduces this scaling to $\mathcal{O}(\mathcal{N}^2)$, since the number of strong pairs scales linearly with \mathcal{N} , while the dimension of the $[ik]^*$ domains is independent of \mathcal{N} . Furthermore, after introducing local fit domains $\mathcal{O}(\mathcal{N})$ scaling can eventually be achieved.

14.5.2.3. Laplace-Transform LCC2 Response

The canonical equations for the CC2 residuals can be rewritten [132] by utilizing the Löwdin partitioning technique in such a way that any storage of double amplitudes is avoided. The cost of this approach is the introduction of an effective Jacobian in the singly-excited space, which is dependent on the unknown excitation energy for the excited state under consideration,

$$\mathbf{A}^{\text{eff}}(\omega^m)_{\mu_1 v_1} = A_{\mu_1 v_1} + \sum_{\mu_2} A_{\mu_1 \mu_2} D(\omega^m)_{\mu_2}^{-1} A_{\mu_2 v_1}; \quad \mathbf{A}^{\text{eff}}(\omega^m)_{\mathbf{r}_1^m} = \omega^m \mathbf{r}_1^m, \quad (14-91)$$

where μ_n denotes the n -fold excitation index. In this approach the diagonal form of the doubles-doubles Jacobian block $A_{\mu_2 v_2} \equiv \delta_{\mu_2 v_2} \Delta_{\mu_2}$ is utilized. The key quantity in Eq. (14-91) is the diagonal matrix $\mathbf{D}^{-1}(\omega^m)$ containing energy denominators shifted by the (approximate) excitation energy ω^m of the m th excited state

$$D(\omega^m)_{\mu_2}^{-1} = -\frac{1}{\Delta_{\mu_2} - \omega^m} = -\frac{1}{\varepsilon_a + \varepsilon_b - \varepsilon_{\bar{i}} - \varepsilon_{\bar{j}} - \omega^m}, \quad (14-92)$$

where \bar{i}, \bar{j} denote the canonical occupied orbital indices. The utilization of Eq. (14-91) within the initial formulation of the LCC2 response method [41, 42] is not possible because of the nondiagonal character of the Fock matrix in the local basis. However, recently [43, 44, 75] this obstacle has been circumvented by the

utilization of the Laplace transform (LT) for energy denominators [156, 157]. The LT identity $1/x = \int_0^\infty \exp(-xt)dt$ is applied to Eq. (14-92), then the integration over t is replaced by the numerical integration with points t_q and weights w_q of the quadrature (usually just a few n_q points are sufficient in the numerical quadrature)

$$\frac{1}{\Delta_{\mu_2} - \omega^m} = \int_0^\infty e^{-\Delta_{\mu_2}t} e^{\omega^m t} dt \approx \sum_{q=1}^{n_q} w_q e^{-\Delta_{\mu_2}t_q} e^{\omega^m t_q}. \quad (14-93)$$

The replacement of the energy denominator by the product of exponents dependent on a single orbital index opens the possibility for a factorization of the expressions containing this quantity. In particular, Eq. (14-93) serves as a spring-board to develop a fast and robust multi-state LT-DF-LCC2 method. After Eq. (14-93) is inserted into Eq. (14-91) the canonical orbitals from $\mu_2 = (\bar{i}\bar{j}ab)$ can be back-transformed to the local basis of LMOs and PAOs by the utilization of the appropriate transformation/projection matrices [43, 75]. These matrices have the form

$$\begin{aligned} X_{ij}^o(\mathbf{q}) &= \sum_{\bar{i}} \bar{W}_{\bar{i}\bar{i}}^\dagger \exp((\varepsilon_{\bar{i}} - \varepsilon_F)t_q + \frac{1}{4} \ln |w_q|) \bar{W}_{\bar{i}j}, \\ X_{pq}^v(\mathbf{q}) &= \sum_a Q_{pa}^\dagger \exp((- \varepsilon_a + \varepsilon_F)t_q + \frac{1}{4} \ln |w_q|) Q_{aq}, \\ Y_{pq}^v(\mathbf{q}) &= \sum_{rs} V_{pr} X_{rs}^v(\mathbf{q}) V_{sq}^\dagger, \end{aligned} \quad (14-94)$$

and can be shown to be sparse [75]. Here, \bar{W} is the usual unitary transformation matrix specified by the chosen localization criterion which transforms from the canonical occupied orbitals to LMOs, whereas Q transforms from canonical virtual orbitals to PAOs. Although not shown explicitly in Eq. (14-94), V corresponds to a pseudo-inverse of the corresponding block of the PAO overlap matrix, as used for local double excitations. The result of the multiplication of A^{eff} by the right vector \mathbf{r}^m has the form

$$\begin{aligned} \sum_{v_1} A_{\mu_1 v_1}^{\text{eff}} r_{v_1}^m &= \sum_{v_1} A_{\mu_1 v_1} r_{v_1}^m - \sum_{ipjq} \sum_{krls} A_{\mu_1 ipjq} \sum_q \text{sgn}(w_q) \exp(\omega^m t_q) \\ &\quad \times Y_{pr}^v(\mathbf{q}) Y_{qs}^v(\mathbf{q}) \left(\sum_{v_1} A_{rksl} r_{v_1}^m \right) X_{ki}^o(\mathbf{q}) X_{lj}^o(\mathbf{q}). \end{aligned} \quad (14-95)$$

Once the effective Jacobian has been expressed in the local quantities, the usual approximations can be performed to the local configurational space for doubles. Note that since the double part of the LCC2 excitation vector does not enter the small Davidson space and is calculated on-the-fly while obtaining the effective Jacobian, a treatment of several local states simultaneously (each with its own local double space!) becomes easily possible. In many cases such a possibility greatly improves

the convergence of the Davidson iterations. The absence of double CSFs in the Davidson space greatly facilitates the tuning of the domains (in fact, the domain refinement as described above is implemented in the framework of the LT-DF-LCC2 response method only).

For the calculation of transition strengths and (orbital-unrelaxed) first-order properties of the excited states further equations have to be solved [42, 44]. Apart from the right and left eigenvectors of the Jacobian, $\mathbf{R}^m, \mathbf{L}^m$, the Lagrange multipliers Λ and Λ^m for ground and excited state are needed for the first-order properties. Another set of multipliers $\bar{\mathbf{M}}^m(\omega^m)$ is needed for the transition strengths S_{XY}^{0m} , which are calculated as the individual residuals of the linear response function $\langle\langle X; Y \rangle\rangle_{\omega_Y}$,

$$S_{XY}^{0m} = \lim_{\omega_Y \rightarrow \omega^m} (\omega_Y - \omega^m) \langle\langle X; Y \rangle\rangle_{\omega_Y}. \quad (14-96)$$

The multipliers $\bar{\mathbf{M}}^m(\omega^m)$ satisfy the linear equation system

$$0 = \sum_{v_j} \bar{M}_{v_j}^m(\omega^m) (A_{v_j \mu_i} + \omega^m M_{v_j \mu_i}) + \sum_{v_j} F_{\mu_i v_j} R_{v_j}^m \quad (14-97)$$

(the matrix \mathbf{F} is the second derivative of the time-averaged second-order CC2 Lagrangian with respect to the Fourier components of the first-order amplitudes). All these equations including the last one (apart from the right eigenvalue problem yielding \mathbf{R}^m) involve left trial vector \times Jacobian vector-matrix products. Fortunately, the Laplace transform can be applied also here. For simplicity we just consider here the case with the most simple r.h.s., i.e., the equations specifying the Lagrange multipliers for the ground state. These satisfy the linear equation system

$$-\eta_{\mu_i} = \sum_{v_j} \Lambda_{v_j} A_{v_j \mu_i}, \quad \text{where} \quad \eta_{\mu_i} = \langle \Phi_0 | [\hat{H}, \hat{t}_{\mu_i}] | \Phi_0 \rangle. \quad (14-98)$$

After the LT is applied the equation above transforms into

$$\begin{aligned} -\eta_{\mu_1} = & \sum_{v_1} \Lambda_{v_1} A_{v_1 \mu_1} - \sum_{ijpq} \sum_{klrs} \left(\sum_{q=1}^{n_q} \text{sgn}(w_q) X_{ki}^0(\mathbf{q}) X_{lj}^0(\mathbf{q}) \right. \\ & \left. \times (\eta_{ipjq} + \sum_{v_1} \Lambda_{v_1} A_{v_1 ipjq}) Y_{pr}^v(\mathbf{q}) Y_{qs}^v(\mathbf{q}) \right) A_{rksl \mu_1}. \end{aligned} \quad (14-99)$$

The quantity in parenthesis is the negative of the doubly-excited part of Λ . It is calculated on-the-fly and stored for later use in the last iteration. A similar treatment is straightforwardly possible for other doubly-excited operators appearing in the definitions of CC2 first-order properties and transition strengths, including Eq. (14-97) (cf. eq. (22) in Ref. [44]).

Finally, a few words about the quality of local approximations for the CC2 case are appropriate. The agreement with the canonical reference shows that the excitation energies agree usually within 0.1 eV, which is a satisfactory result (the

systematic errors resulting from the approximate treatment of double excitations and the neglect of triple and higher excitations in CC2 are of order of 0.3 eV). On the other hand, the dipole moments and oscillator strengths in the LCC2 are sometimes obtained with an error of 10% or more, in particular if they are small. The situation somewhat improves if domains are extended [42]. Nevertheless some more work is needed for further improvements along this direction.

14.6. EXAMPLE APPLICATIONS

In this section we will first briefly summarize previous applications of our local correlation methods for electronic ground states. All results that have been published so far refer to closed-shell systems. Only very recently, LRMP2 and LUCCSD methods have been implemented (cf. Section 14.2.4). First results obtained with these methods will be presented in Section 14.6.5. Another recent development is the LCCSD(T)-F12 method, in which the local and explicit correlation approaches are combined (cf. Section 14.2.5). Some representative results will be shown in Section 14.6.6. Finally, we will present some typical applications for electronically excited states.

14.6.1. Equilibrium Structures, Vibrational Frequencies, and Other Molecular Properties

We will start with the discussion of properties characterizing molecules at their equilibrium structures. Geometry optimizations can be carried out using analytic gradient methods, which have first been implemented for LMP2 [34], and later also for LQCISD (local quadratic configuration interaction) [35]. A more efficient implementation of LMP2 gradients using density fitting [36] is also available. Optimized equilibrium structures obtained with local methods are in excellent agreement to those obtained with their canonical counterparts. Typically, bond lengths are slightly longer, which has been attributed to reduced intramolecular basis set superposition errors (BSSE) in the local calculations [34–36].

A problem which has often been discussed in the literature [56, 85, 86] is the fact that the domains may change as function of the geometry. This can lead to discontinuities on potential energy surfaces. The easiest way to avoid this problem is to freeze the domains (cf. Section 14.2.1.1). It has been found that optimized structures are very insensitive to the choice of domains, and therefore it is uncritical at which geometry they are selected and frozen [85].

The impact of local approximations on vibrational frequencies has been studied in a number of papers [158–162]. In most cases, the effect of local approximations is small. However, for some modes, e.g., out-of-plane vibrations of mono-substituted benzenes such as phenol, benzaldehyde, and fluorobenzene, striking differences of over 40 cm^{-1} between the frequencies obtained with local and canonical MP2 methods were found, and in all cases the LMP2 values were in better agreement with experimental values [161]. Overall, the errors of LMP2 frequencies were smaller

and more systematic than the MP2 ones [158, 161]. This was attributed to the reduced BSSE in the local calculations.

In the absence of analytical second derivatives harmonic vibrational frequencies can only be computed by finite differences of gradients. The calculation of the gradients for different displacements can be easily parallelized [162]. Using the efficient DF-LMP2 gradient method [36] it is then possible to compute harmonic vibrational frequencies for rather large molecules, e.g. testosterone using the cc-pVTZ basis set [161]. Furthermore, many-dimensional potential energy surfaces can be automatically generated and used to compute accurate anharmonic frequencies, even using the LCCSD(T0) method [162]. The most important outcome of this study was that local correlation methods (with frozen domains) can safely be used for the calculation of larger fractions of multi-dimensional potential energy surfaces; furthermore, it was shown that the non-iterative (T0) approximation works well in such calculations.

Other properties such as dipole moments and dipole polarizabilities [37] have already been discussed in Section 14.4 and will not be repeated here. We note that a pilot implementation of a GIAO-LMP2 method for the calculation of NMR chemical shifts has also been presented [163]. Test calculations showed that the deviations between GIAO-LMP2 and GIAO-MP2 are small, e.g., for ^{13}C typically less than 1 ppm, and that the GIAO-LMP2 approach holds great promise for application to larger molecules.

14.6.2. Reaction Energies and Conformational Energies

In contrast to equilibrium properties, the choice of the domains can have a significant impact on reaction energies, since the electronic structure and the domains may differ in the reactants and products. In some cases it may require some experimentation to achieve a balanced treatment. Normally, the domain error is very similar at the LMP2 and LCCSD levels. The recommended approach is therefore to test the domain approximation by comparing MP2 and LMP2 results before carrying out the much more expensive LCCSD(T) calculations. The accuracy can usually be significantly improved by adding the MP2-LMP2 energy difference to the LCCSD(T) results.

Nevertheless, a well defined computational model is difficult to establish. This is certainly the most severe disadvantage of local correlation methods, even though it often happens that due to the reduction of BSSE local methods yield better results and faster convergence with the quality of the basis set than canonical methods. However, in cases where BSSE helps to improve the accuracy, the opposite can be true as well. These effects have been discussed in detail in a previous review [82].

Extensive studies of reaction energies [38, 82, 131] have shown that on the average the accuracy of reaction energies obtained with CCSD(T) and LCCSD(T0) as compared to experiment is not much different when triple- ζ basis sets are used. Often the basis set error is larger than the error due to local approximations. If larger basis sets are used and one aims at higher accuracy, the domain error becomes more important. It can then be reduced by extending the domains [38,

82, 131], but, as already mentioned in Section 14.2.1.1, this strongly increases the computational cost.

A much better very recent solution to this problem is to combine local and explicitly correlated methods (cf. Section 14.2.5). This simultaneously reduces the domain and basis set errors to an almost negligible amount and makes it possible to compute accurate reaction energies for quite large systems. Some examples will be presented in Section 14.6.6.

Local methods have also been used to study conformational energies of 95 conformers using MP2 and LMP2 methods and correlation consistent basis sets ranging from double- ζ to augmented quintuple- ζ quality [164]. It was found that both methods yield quite similar results, and the differences between MP2 and LMP2 decrease systematically with increasing basis set. Due to reduced intramolecular BSSE effects, the LMP2 results converge more slowly to the basis set limit for most of the smaller systems. However, for larger peptides, the BSSE has a very large effect on the energy difference between extended and helical structures, leading to a very strong basis set dependence of the canonical MP2 results. It was demonstrated for alanine octapeptides that the basis set error exceeds 30 and 20 kJ/mol, respectively, if augmented double- ζ and triple- ζ basis sets were used. On the other hand, the LMP2 results were only slightly affected by the basis set size, and even with augmented double- ζ basis sets reasonably accurate results were obtained.

14.6.3. QM/MM Calculations of Reaction Barriers in Enzymes

Another application of the LCCSD(T0) method was the accurate calculation of activation barriers (enthalpies and free energies) in enzymes, using QM/MM methods. The first such calculations were carried out for chorismate mutase (CM) [165] and *p*-hydroxybenzoate hydroxylase (PHBH) [165, 166]. In these studies the convergence of the results with respect to all parameters (basis set, local approximations) in the calculations were systematically studied. The calculations turned out to be difficult since the electronic structure at the barriers were quite different from the reactants. By comparing MP2 and LMP2 results it was found that the best approach to obtain balanced results is to merge the domains at both structures, using procedures described in Ref. [85]. Furthermore, the distance criterion for selecting close pairs had to be significantly increased over the default values in order to get a converged triples contribution to the barrier height. It should be stressed, however, that these applications are at the limit of what is possible with single-reference methods; the correlation effects are huge: the LCCSD(T) the barriers are reduced by a factor of two as compared to the HF results, and about one third of this effect is due to the triples. Nevertheless, excellent agreement (within 1–2 kcal/mol) with experimental values was achieved for both systems (obtained by taking the average of 10–15 snapshots).

It is noteworthy that accurate results for PHBH were also obtained using the region approach, i.e., by correlating only a small part of the system near the reactive site. Details of these calculations can be found in Ref. [87].

Recently, LMP2 and LCCSD(T0) QM/MM calculations of energy and free energy barriers for acetaldehyde conversion in aldehyde oxidoreductase were carried out [167]. Relative energies were computed for various stationary points along three different reaction pathways. The LCCSD(T0) results were found to be in qualitative agreement with DFT/B3LYP results. For some barriers, however, both MP2 and LMP2 yielded unreasonably high energies. This has been attributed to problems in the description of the Mo = S bond. It was suspected that the Mo(VI) \rightarrow Mo(IV) transition, with a developing Mo d^2 -configuration, could introduce some multireference character that is not captured at the MP2 level.

An interesting application of LCCSD(T0) to transition state theory of polar reactions in solution has recently been published by Harvey [168]. In this work it was concluded that accurate ab initio calculations are now possible for systems with 50–100 atoms, but the prediction of rate constants remains still difficult. This may be due to the remaining intrinsic error of the local coupled cluster method and to deficiencies in the continuum solvent models applied.

14.6.4. Intermolecular Interactions

A very successful area of applications of local correlation methods is the calculation of intermolecular interaction energies. If a calculation of the local interaction energy is performed, intermolecular orbital pairs are recognized automatically and treated as strong pairs, independent on the interorbital distance. Since local methods remove (to a large extent) intermolecular BSSE effects by construction, the application of the counterpoise correction [169] is not recommended in the supermolecular calculations. It was found that uncorrected LMP2 results are in close agreement with CP corrected MP2 ones [24, 170, 171]. This is particularly useful for geometry optimizations and has for example been used to optimize the geometry of water clusters [171] and to determine an improved water potential [172]. More recently, stacking interactions in the benzene dimer [173] and other systems [174–177] were extensively studied using the LMP2 and LCCSD(T0) methods. It can be also noted that with the DF-LCC2 approach it is possible to obtain virtually BSSE-free interaction energies of excited-state noncovalent complexes. In one of the first works devoted to this problem, Ref. [178], it has been confirmed that the elimination of the BSSE by the local principle holds also for excited states (see table I from Ref. [178]).

We can also note that the local character of the LMOs and PAOs makes it possible to split the correlation contributions to interaction energies into various parts, like intramolecular, ionic, dispersion, and exchange-dispersion [171]. However, it should be stressed that the two last contributions do not correspond to the identically named components of symmetry-adapted perturbation theory of intermolecular interactions [179]. This partition has been used to study and analyse aurophilic [180] and other metallophilic interactions [181, 182]. Related energy analyses have also been described by other authors [183, 184]. In addition, this classification is very useful to understand the origins for the BSSE elimination in the local interaction energy. To proceed with the explanation let us place the interacting molecules sufficiently far from each other, so that the effect of polarization of one interacting molecule

(*A*) by another (*B*) can be neglected and therefore one can assume that the set of occupied orbitals for the composite molecule *AB* is just the union of occupied orbitals of *A* and *B*. It is easy to see that the definition of local domains prevents the inclusion of double excitations from the occupied orbitals of *A*, such that one or both electrons are excited to the orbital domain of *B* (excitations of ionic and doubly-ionic types, respectively). On the other side, “mixed” double excitations from one occupied orbital of *A* and one occupied orbital of *B* are not restricted, so e.g. the excitations from *A* to *B* are allowed, giving rise to the excitation classes mentioned above. Ionic and doubly-ionic excitations, which are missing in the local wave function, are mainly responsible for the BSSE in canonical wave functions and are (approximately) eliminated by the counterpoise correction.

The DF-LMP2 gradient program [36] can also be applied to DF-SCS-LMP2 (spin-component scaled LMP2 [185]), which often gives better results for dispersion interactions than MP2. One very recent application of this program is a mixed model potential/QM geometry optimization of the aniline (An) dimer and trimer [186]. The model potential, adapted on-the-fly to QM energies, served to perform a global search on the potential energy surfaces of An₂ or An₃, in order to locate approximately possible structures for the minima. Afterwards, the energetically lowest rough geometries were optimized using the DF-SCS-LMP2 method, employing the aug-cc-pVDZ and aug-cc-pVTZ AO basis sets. The orbital domains were specified at large distances and kept unchanged during the optimization of the dimer and trimer geometries. Several local minima could be identified, which differ by a few kcal/mol. The global minimum of the dimer corresponds to a head-to-tail NH- π arrangement of the two monomers, with both monomers being nearly equivalent. Its interaction energy as found by DF-SCS-LMP2 amounts to 7.2 kcal/mol, which agrees rather well with the DFT-SAPT estimate [186] of 7.7 kcal/mol. The lowest trimer geometry, on the other hand, features two directional NH-N hydrogen bonds. In contrast to the dimer the three chromophores are clearly non-equivalent. As a consequence, three different electronic origins might be visible in the absorption spectrum (provided that corresponding stable minima exist for the excited state(s) and the related Franck-Condon factors are large enough).

14.6.5. Open-Shell Local Coupled Cluster Calculations

In this section we present preliminary results using the new implementation of open-shell local RMP2 and UCCSD methods [93]. To test the accuracy of these methods we have computed ionization potentials (IPs) for molecules containing 2–78 atoms. Some of the larger molecules are shown in Figure 14-2. It is expected that IPs are sensitive to local approximations, since the neutral and ionic states must be treated in a balanced way. Furthermore, since the number of electrons changes, electron correlation effects are significant.

The IPs have been computed at the optimized LMP2 equilibrium structures of the closed-shell molecules. In all calculations the cc-pVTZ basis set (without *d*-functions on hydrogen atoms) has been used. The PM method has been utilized to

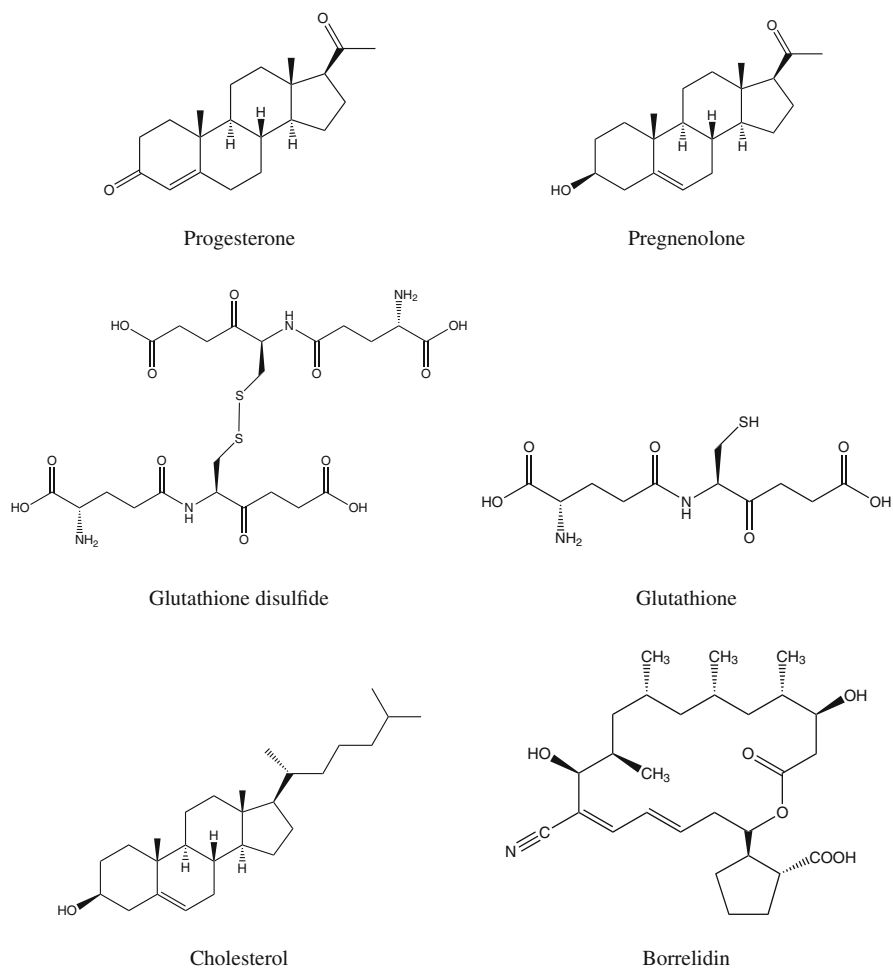


Figure 14-2. Structures of some larger molecules

localize the orbitals, and the domains and pair classes were obtained using default parameters ($T_{BP} = 0.985$, $R_{vd} = 15a_0$.) Table 14-1 shows the results obtained with canonical and local RMP2 methods. In the latter case, the two options for orbital localization described in Section 14.2.4 have been compared: in LRMP2(sd), the orbitals are localized within the closed- and open-shell orbital subspaces, while in LRMP2(ab) they are localized separately for α and β spin-orbitals. It is found that in both cases the differences between the canonical and local methods are very small; the mean absolute deviations are only 0.034 and 0.023 eV, respectively, for the (sd) and (ab) variants. Despite the fact that the domains are usually smaller in the (ab) variant, it yields in nearly all cases more accurate results. It is very satisfying to find that the errors do not increase with molecular size.

Table 14-1. Ionization potentials (in eV) obtained with canonical and local RMP2 methods. The deviations from the canonical values are given in parenthesis. The cc-pVTZ basis set (without *d*-functions on hydrogen atoms) has been used. N_{e1} is the number of correlated electrons, N_{AO} – the number of basis functions

Molecule	N_{e1}	N_{AO}	ROHF	RMP2	LMP2(sd)	LMP2(ab)
Hydrogen chloride (HCl)	7	43	11.697	12.646	12.644 (-0.001)	12.644 (-0.001)
Water (H ₂ O)	7	48	11.105	12.685	12.671 (-0.014)	12.671 (-0.014)
Formaldehyde (HCHO)	11	78	9.685	11.190	11.192 (0.002)	11.190 (0.000)
Hydrazine (NH ₂ NH ₂)	13	96	7.695	8.024	7.989 (-0.035)	8.007 (-0.017)
Methylamine (CH ₃ NH ₂)	13	105	8.412	9.714	9.691 (-0.023)	9.692 (-0.022)
Oxirane (CH ₂ CHO)	17	126	9.279	10.941	10.946 (0.004)	10.943 (0.002)
Dimethyl ether (CH ₃ OCH ₃)	19	144	8.960	10.374	10.381 (0.008)	10.375 (0.001)
Ethanol (C ₂ H ₅ OH)	19	144	9.594	11.062	11.016 (-0.046)	11.026 (-0.037)
Propane (CH ₃ CH ₂ CH ₃)	19	162	11.586	11.825	11.781 (-0.044)	11.794 (-0.031)
Butadiene (CH ₂ CHCHCH ₂)	21	174	8.096	9.126	9.087 (-0.039)	9.092 (-0.034)
Propionyl chloride (CH ₃ CH ₂ COCl)	29	199	9.823	11.403	11.355 (-0.048)	11.367 (-0.036)
Catechol (C ₆ H ₄ (OH) ₂)	41	294	7.479	8.311	8.281 (-0.030)	8.279 (-0.032)
Glutathione (C ₁₀ H ₁₇ N ₃ O ₆ S)	113	757	8.525	9.351	9.319 (-0.032)	9.324 (-0.027)
Androstenedione (C ₁₉ H ₂₆ O ₂)	864	864	8.192	9.573	9.510 (-0.063)	9.535 (-0.037)
Testosterone (C ₁₉ H ₂₈ O ₂)	115	882	8.038	9.440	9.378 (-0.062)	9.408 (-0.032)
Progesterone (C ₂₁ H ₃₀ O ₂)	125	960	8.118	9.513	9.450 (-0.063)	9.476 (-0.037)
Pregnenolone (C ₂₁ H ₃₂ O ₂)	127	978	7.349	8.870	8.828 (-0.042)	8.852 (-0.019)
Testosterone propionate (C ₂₂ H ₃₂ O ₃)	137	1,038	8.156	9.553	9.490 (-0.063)	9.520 (-0.033)
Androstenedione precursor (C ₂₅ H ₃₂ O ₄)	155	1,158	7.096	7.755	7.710 (-0.045)	7.717 (-0.038)
Cholesterol (C ₂₇ H ₄₆ O)	159	1,254	7.230	8.765	8.723 (-0.042)	8.747 (-0.018)
Borrelidin (C ₂₈ H ₄₃ NO ₆)	195	1,437	7.578	8.434	8.416 (-0.018)	8.422 (-0.012)
Glutathione disulfide (C ₂₀ H ₃₂ N ₆ O ₁₂ S ₂)	225	1,496	8.893	8.961	8.934 (-0.027)	8.939 (-0.022)
Mean absolute error					0.034	0.023
Maximum error					-0.063	-0.037

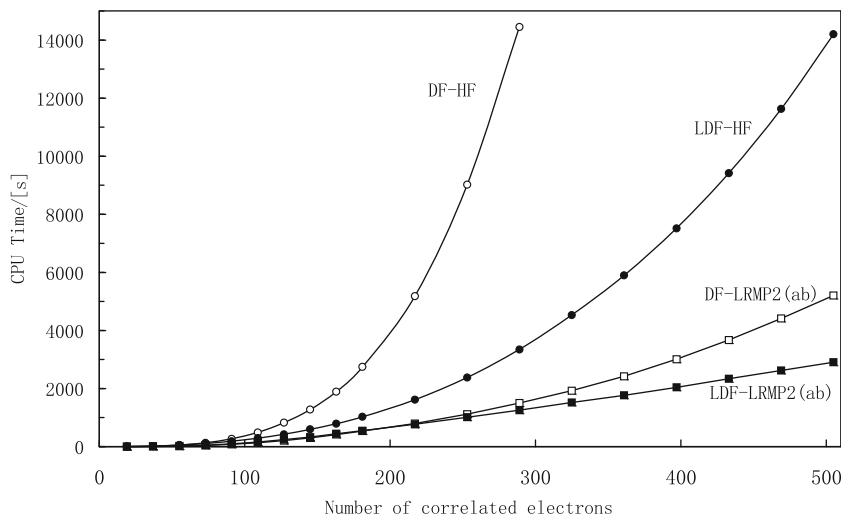


Figure 14-3. Total CPU times for DF-HF and DF-LRMP2 calculations of polyvinyl fluoride radicals. The cc-pVDZ basis set has been used

Figure 14-3 shows the total CPU times (in seconds on Opteron 2380 2.5 GHz processor) of DF-HF and DF-LRMP2 calculations for polyvinyl fluoride chains with a radical position at one end. The DF-HF results are shown with and without local fitting. As expected, the local fitting approximation (LDF) improves the scaling and strongly reduces the CPU time for the large systems, both for HF and for LRMP2. The DF-LRMP2 calculations take much less time than the DF-HF. If LDF is used they show nearly linear scaling behaviour. The computational effort and scaling is very similar for the (ab) and (sd) variants, and therefore the (sd) timings are not shown.

Figure 14-4 demonstrates the scaling of the CPU times for the DF-LUCCSD(sd) method. In this case the times per iteration are shown. The computational effort for LUCCSD is strongly dominated by the calculation of the $\mathbf{G}(\mathbf{E})$ operators (see Eq. (14-40)). Currently, these operators are still computed without local fitting, and therefore there is significant potential for improvement. All remaining terms in the residual take very little time and scale linearly with molecular size. Thus, approximations which make it possible to neglect $\mathbf{G}(\mathbf{E})$ would be very useful. However, such approximations have not yet been implemented and tested for the open-shell LUCCSD method.

In Table 14-2 we present a comparison of ionization potentials computed using UCCSD and LUCCSD. In this case the canonical UCCSD calculations are only possible for the small systems. The results are very similar to the LRMP2 case: the differences between the canonical and local results are uniformly small, and again the (ab) scheme is somewhat more accurate. The effect of weak pair approximations in the LUCCSD method is also demonstrated: if only strong pairs are included in the LUCCSD and the remaining close and weak pairs are treated by LRMP2, the

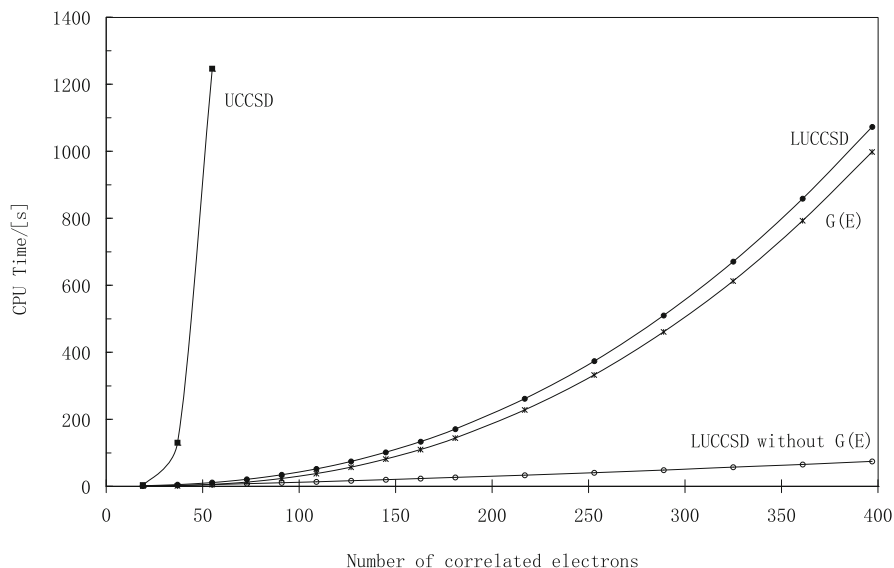


Figure 14-4. CPU times per iteration for DF-HF and DF-LUCCSD calculations polyvinyl fluoride radicals. The cc-pVDZ basis set has been used

errors are approximately twice as large as in the LUCCSD calculation with all pairs. However, the differences to the canonical values are still small; for the (ab) scheme the mean absolute and maximum errors amount to just 0.032 and 0.068 eV, respectively. Further more extensive benchmarks of the open-shell methods are currently in progress and will be presented elsewhere.

Table 14-2. Ionization potentials (in eV) obtained with canonical and local UCCSD methods. The deviations from the canonical values are given in parenthesis. The cc-pVTZ basis set (without *d*-functions on hydrogen atoms) has been used

Molecule	Strong pairs			All pairs	
	UCCSD	LUCCSD(sd)	LUCCSD(ab)	LUCCSD(sd)	LUCCSD(ab)
HCl	12.542	12.544 (0.001)	12.544 (0.001)	12.544 (0.001)	12.544 (0.001)
H ₂ O	12.443	12.433 (-0.010)	12.433 (-0.010)	12.433 (-0.010)	12.433 (-0.010)
HCHO	10.723	10.761 (0.038)	10.753 (0.030)	10.732 (0.009)	10.726 (0.003)
NH ₂ NH ₂	8.190	8.197 (0.007)	8.192 (0.002)	8.159 (-0.030)	8.173 (-0.016)
CH ₃ NH ₂	9.502	9.536 (0.033)	9.546 (0.043)	9.490 (-0.012)	9.490 (-0.012)
CH ₃ CHO	10.493	10.551 (0.058)	10.544 (0.051)	10.505 (0.012)	10.501 (0.008)
CH ₃ OCH ₃	9.983	10.057 (0.074)	10.051 (0.068)	10.002 (0.020)	9.993 (0.011)
C ₂ H ₅ OH	10.632	10.665 (0.033)	10.658 (0.026)	10.603 (-0.029)	10.613 (-0.019)
CH ₃ CH ₂ CH ₃	11.908	11.989 (0.081)	11.949 (0.042)	11.874 (-0.033)	11.884 (-0.023)
CH ₂ CHCH ₂	9.154	9.222 (0.068)	9.201 (0.047)	9.119 (-0.035)	9.122 (-0.032)
Mean absolute error		0.040	0.032	0.019	0.014
Maximum error		0.081	0.068	-0.035	-0.032

14.6.6. Explicitly Correlated Local Coupled Cluster Calculations

In this section the reduction of the basis set and domain errors by the explicit correlation treatment will be demonstrated [187]. All calculations employ fixed amplitudes (Eq. (14-51)), and the correlation factor was chosen to be $\gamma = 1.0a_0^{-1}$. The triples correction was generally computed with the non-iterative (T0) approximation. Table 14-3 shows statistical data for a set of 50 reactions involving closed-shell molecules only. This is the same set as used in Ref. [11], except that 4 reactions involving only very small molecules have been omitted. All calculations have been done with the VTZ-F12 basis set of Peterson [188]; as RI basis and for Coulomb and exchange fitting in the DF-HF calculation we used the cc-pVTZ/JKFIT basis sets of Weigend [124], while in the density fitting of all other integrals the aug-cc-pVTZ/MP2FIT basis sets of Weigend [130] were employed. The orbitals were localized by the PM procedure. In order to improve the localization, the contributions of the most diffuse function of each angular momentum have been removed from the localization criterion.

The table shows the maximum (max) and root mean square (rms) deviations from conventional CCSD and CCSD(T) extrapolated complete basis set (CBS) estimates, obtained by fitting the correlation energy obtained with two basis sets to the formula $E_n = E_{\text{CBS}} + An^{-3}$. In most cases, the aug-cc-pV5Z ($n = 5$) and aug-cc-pV6Z ($n = 6$) basis sets were used in the extrapolations. For some reactions involving larger molecules the calculations with the aug-cc-pV6Z basis were not possible, and in these cases the aug-cc-pVQZ ($n = 4$) and aug-cc-pV5Z basis sets were used (cf. Ref. [11]). For the local LCCSD-F12 and LCCSD(T0)-F12 calculations three cases are compared: in the first case, only strong pairs are included in the LCCSD-F12; in the second case also close pairs were included (these are all pairs in which the two orbitals i and j are separated by 1 or 2 bonds), but the amplitudes of these pairs were determined at the MP2 level and kept fixed in the LCCSD-F12 calculations. In the last case all pairs were fully optimized in the LCCSD(T0)-F12 calculation.

Table 14-3. Maximum and root mean square deviations of total LCCSD-F12 and LCCSD(T0)-F12 reaction energies (in kJ/mol) from CCSD or CCSD(T) extrapolated basis set limits for a benchmark set comprising 50 reactions of smaller molecules.^a All F12 results include the CABS-singles correction of the Hartree-Fock energy

Pairs in LCCSD	LCCSD		LCCSD(T)		LCCSD-F12		LCCSD(T)-F12	
	max	rms	max	rms	max	rms	max	rms
Strong	17.2	4.5	19.5	5.0	3.7	0.9	3.8	1.0
Strong+close ^b	19.8	4.6	22.6	5.1	2.1	0.5	3.5	0.9
All	19.8	4.6	22.6	5.1	2.0	0.5	3.5	1.0
Canonical	12.2	3.3	12.1	3.3	2.9	0.6	2.2	0.5

^a The reactions and CBS reference values can be found in Ref. [11]. In most cases the aug-cc-pV5Z and aug-cc-pV6Z basis sets have been used in the extrapolations.

^b Close pair amplitudes optimized by MP2 and kept fixed.

The following conclusions can be drawn from the results: (i) Without explicit correlation and with all pairs, the LCCSD and LCCSD(T0) results are slightly less accurate than their canonical counterparts (as compared to the canonical CBS values). However, if only strong pairs are included in the LCCSD, the accuracy looks better than for the canonical case, but this is due to an error compensation between the domain error and the error caused by neglecting close pairs in the LCCSD. (ii) In the explicitly correlated calculations, the inclusion of close pairs is essential to obtain high accuracy. In this case the above mentioned error compensation is not possible any more, since the domain error is largely removed. (iii) The errors of the CCSD-F12 and LCCSD-F12 results are reduced by one order of magnitude as compared to the corresponding calculations without explicitly correlated terms. There is no significant difference in the accuracy of the canonical and local F12 results, i.e., the basis and domain errors are both removed in the LCCSD-F12 calculations. (iv) Excellent and comparable results are also obtained with the CCSD(T)-F12 and LCCSD(T0)-F12 methods; here the improvement is somewhat smaller, since the (T) correction is not directly affected by the F12 treatment, and therefore a basis set error remains in the triples correction. The quite similar performance of the canonical and local methods indicates that the (T0) approximation has no significant effect on the accuracy. The rms error relative to the canonical CCSD(T)/CBS results is still just 1 kJ/mol.

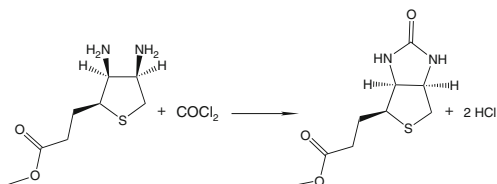
Next we investigate five reactions involving medium size and larger molecules. The reactions are shown in Figure 14-5 and the results are presented in Table 14-4. In these cases it is still possible to obtain MP2/CBS reference values, but corresponding CCSD or CCSD(T) calculations are not feasible. Thus, we can only check the local results by comparing LMP2-F12 and MP2/CBS values. It is likely, however, that the LCCSD and LCCSD(T0) results are of similar accuracy. Comparing the MP2 and MP2/CBS results shows the basis set error, while comparison of the MP2 and LMP2 values shows the domain error. For example, the basis set error is quite large for reaction **II**, while the domain error is particularly large for reaction **V**. In all cases, however, are the MP2-F12, LMP2-F12, and MP2/CBS results in close agreement. This demonstrates that both the basis set as well as the domain errors are eliminated to a large extent. As expected, the differences between the LMP2 and LMP2-F12 results on the one hand, and of the LCCSD(T0) and LCCSD(T0)-F12 ones on the other hand are very similar. This indicates that the basis set and domain errors are removed to a similar extent in the LCCSD(T0)-F12 method. A more extensive investigation of the effect of pair approximations on the LCCSD(T0)-F12 results is in progress and will be published elsewhere.

14.6.7. Excited States

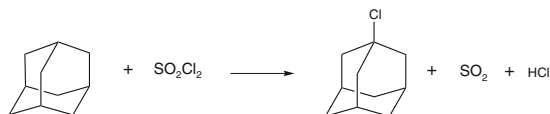
The quality of the local approximations to the electronic excitations has been extensively tested in Refs. [40–44]. It turns out that with an appropriate selection of the local excitation space and the underlying ground-state space the errors in excitation energies for valence states are usually below 0.05 eV. For details of these tests we refer to the above mentioned references.

ID

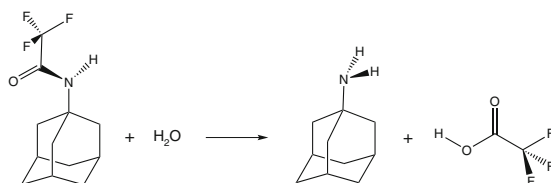
I



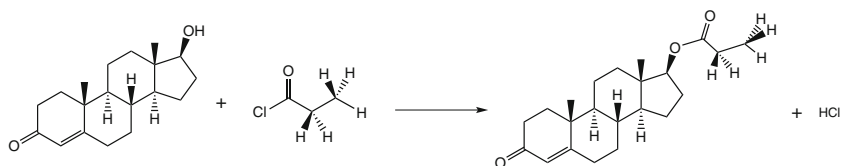
II



III



IV



V

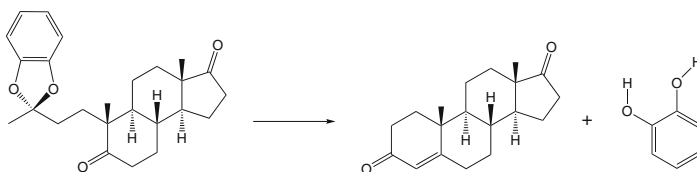
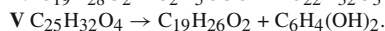
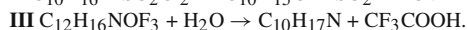
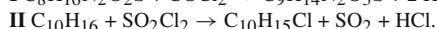
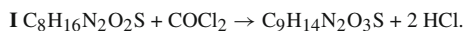


Figure 14-5. Five reactions involving medium sized and large molecules with up to 61 atoms. **I** is one possible step in the synthesis of biotin. **II** represents the functionalization of an adamantane cage at a tertiary C-atom. Reaction **III** shows the synthesis of amantadine which is used in the treatment of the Parkinson disease. In **IV** the testosterone molecule is modified to make it more lipophilic for a longer retention time in the body tissues. **V** represents the last synthetic step to yield androstendione

As an illustrative example for an application, we present results from calculations performed for the 3-(5-(5-(4-(bis(4-(hexyloxy)phenyl)thiophene-2-yl)thiophene-2-yl)-2-cyanoacrylic acid (D21L6), an organic sensitizer for solar-cell applications which was synthesized and measured in Ref. [189]. The D21L6 sensitizer shows an absorption maximum in the visible region at 2.71 eV with a high molar extinction coefficient, which arises from a $\pi \rightarrow \pi^*$ charge transfer (CT) transition, where electron density is shifted down the chain containing the two thiophene groups.

Table 14-4. Total reaction energies (in kJ/mol) for 5 reactions involving medium sized and large molecules. All F12 results include the CABS-singles correction^a of the Hartree-Fock energy. The correlation factor was chosen as $\gamma = 1.0a_0^{-1}$. The MP2/CBS values were extrapolated,^b all other calculations used basis sets of triple- ζ quality^c

ID	MP2	LMP2	MP2-F12	LMP2-F12	MP2/CBS	LCCSD(T)	LCCSD(T)-F12
I	-116.7	-120.0	-114.6	-114.6	-113.1	-126.9	-121.1
II	-90.7	-90.7	-68.9	-68.3	-70.2	-98.6	-76.1
III	49.1	45.9	48.6	47.0	49.5	42.3	43.2
IV	-26.2	-21.3	-19.4	-18.2	-19.2	-26.6	-23.7
V	29.6	16.8	20.3	19.2	19.6	20.8	23.5



^a CABS-singles corrections: I: 0.94, II: 2.63, III: -0.33, IV: 0.89, V: -2.16.

^b Basis sets for extrapolations: I-III: AVQZ/AV5Z; IV: AVTZ/AVQZ; V: VQZ, O = AVQZ/V5Z, O = AV5Z. AVnZ and VnZ, $n = T, Q, 5$ are the abbreviations for aug-cc-pVnZ and cc-pVnZ basis sets, respectively.

^c Basis sets: I-III VTZ-F12; IV: AVTZ, V: AVTZ,H=VTZ.

Weaker peaks appear around 3.5–3.6 and 4.1–4.3 eV (cf. figure 1 in Ref. [189]). The D21L6 comprises 98 atoms and 262 correlated electrons.

In the context of the present work excitation energies, oscillator strengths, and orbital-unrelaxed first-order properties of the lowest six excited states of the D21L6 molecule have been calculated using the LT-DF-LCC2 response method. Due to the CT character (over significant distances) of some of the excited states, the TD-DFT method is bound to fail for this system. The LT-DF-LCC2 calculations were performed with adaptive pair domains, based on the diagonal parts of the doubly-excited amplitudes (this has been denoted as Laplace domains in Ref. [43], cf. Section 14.5.2.1). For the Laplace integration three quadrature points were used, which turned out to be sufficient in previous studies [43]. The cc-pVDZ basis was employed as AO basis set.

Table 14-5 lists excitation energies, along with the norms of the dipole difference vectors and the oscillator strengths. Plots of the density differences (excited vs. ground state density) are displayed in Figure 14-6 for the S_1 and S_3 states, respectively. The spectrum is dominated by the S_1 $\pi \rightarrow \pi^*$ transition, which can be seen from the examination of the oscillator strengths in Table 14-5. The large change in the dipole moment (from 2.62 to 9.78 a.u.) indicates that S_1 has substantial CT character. As can be seen from Figure 14-6, the electron density is indeed shifted down the chain containing the two thiophene units, as was anticipated in the experimental paper [189]. The vertical excitation energy of 2.74 eV is in excellent agreement with the experimentally measured absorption band (2.71 eV), certainly to a large extent due to a fortuitous error cancellation.

Table 14-5. Excitation energies, properties and timings (in minutes) (7 CPUs, Intel(R) Xeon(R) CPU X5560 @ 2.80 GHz) for the D21L6 molecule

State	Char.	ω^a	$ \delta\mu^m ^b$	f^c	r_D^d	$t(U_{rs}^{ij})^e$	$t(W_{ir}^P)^f$	$t(v_r^i)^g$	$t(\text{iter})^h$
S_1	CT	2.737	7.349	1.348	6.5%	7.7	2.9		
S_2	CT	3.541	4.802	0.086	16.9%	17.9	6.2		
S_3	local	3.668	0.075	0.051	16.9%	16.7	6.2	19.9	141.9
S_4	CT	3.909	5.480	0.260	11.7%	12.7	4.5		
S_5	local	4.188	1.049	0.023	13.5%	14.9	5.2		
S_6	local	4.262	1.870	0.120	13.5%	16.1	5.9		

^a Excitation energies ω in eV.

^b Norms (in a.u.) of the dipole difference vectors.

^c Oscillator strength (length gauge); $f = \frac{2}{3}\omega(S_{XX}^{0m} + S_{YY}^{0m} + S_{ZZ}^{0m})$.

^d Ratio of the sizes of the local vs. canonical doubles vectors.

^e Elapsed time for calculation of the doubles vector, eq. (22) in Ref. [43].

^f Elapsed time for calculation of W_{ir}^P , Eq. (14-90).

^g Elapsed time for calculation of v_r^i (only multi-state part), eq. (19) in Ref. [43].

^h Elapsed time for one Davidson iteration.

The S_2 state also has CT character, while the S_3 is a locally excited state (cf. the dipole moment changes in Table 14-5 and Figure 14-6 for the case of the S_3 state). Both states, i.e., notably also the locally excited S_3 , have rather small oscillator strengths in comparison to S_1 . S_4 again is a CT state, while S_5 and S_6 are both locally excited states. The oscillator strengths of S_4 and S_6 are larger than those of S_2 and S_3 , but still much smaller than that of S_1 . The transition to the locally excited S_5 state has the smallest oscillator strength, i.e., is only about half as intense, as the transition to the weak S_3 state. It can be anticipated that the Franck-Condon factors are larger for transitions to locally excited – than to CT states. This increases the overall intensities of the former compared to the latter and relativizes somewhat the picture just drawn, based solely on the electronic oscillator strengths.

Table 14-5 also compiles the ratios r_D (local vs. canonical) of the number of elements of the doubles part of the Jacobian eigenvectors, which range between 7 and 17% for the individual states. Finally, representative timings are given for some key steps of the calculation, which was run on 7 cores of an Intel(R) Xeon(R) CPU X5560 @ 2.80 GHz. A typical Davidson iteration involving all six states takes about 2.4 hours, which makes it possible to investigate molecules of this complexity within a reasonable amount of time at a level clearly superior to TD-DFT.

14.7. OUTLOOK

We have presented the current state of research of the local correlation methods as implemented in the MOLPRO program. Linear scaling LMP2 and LCCSD(T) methods are available since quite long time for closed-shell ground electronic states. Recently, this has been extended to open shell systems. Currently, DF-LRMP2 and DF-LUCCSD methods with high-spin ROHF reference functions are functional,

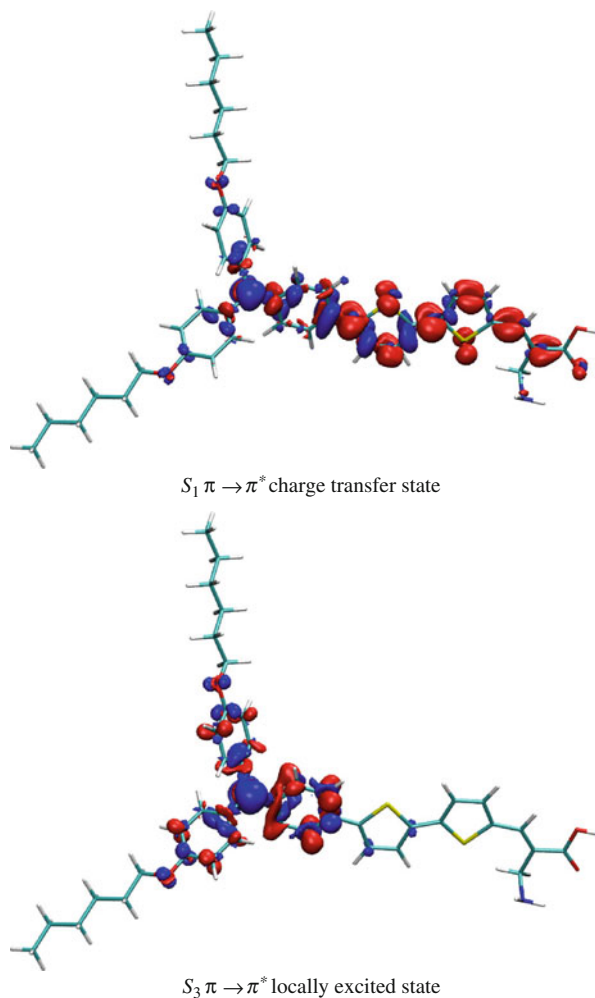


Figure 14-6. Differential densities (with isovalue ± 0.0015) for states S_1 and S_3 of the D21L6 molecule. Red areas show an increase, blue a depletion of density relative to the ground state

and perturbative triple excitations for open-shell systems are under development. Furthermore, efficient DF-LCC2 methods for the calculation of excitation energies in large molecules have been developed and applied.

It has been demonstrated that calculations for ground and excited states of molecules with about 100 atoms are now feasible, using triple zeta or even better basis sets. Local methods have been successfully applied to a large variety of problems, including calculations of equilibrium geometries, harmonic and anharmonic frequencies, reaction energies, conformational energies, reaction barriers in enzymes and in solution, dipole and transition moments as well as dipole polarizabilities.

Until recently, the main limitation of the accuracy of local coupled cluster calculations has been the domain error, in particular if energy differences of molecules with different electronic structure were considered. This problem has now been largely removed by the combination of local and explicit correlation methods. In the new LCCSD(T)-F12 method the errors due to both the domain approximation and basis set incompleteness are reduced to a size that is smaller than the expected intrinsic accuracy of the CCSD(T) method. So far, this very promising method is available only for closed-shell ground states, but extensions to open-shell systems are under development.

A remaining challenge is the application of accurate local correlation methods to large transition metal clusters, which are of great importance in catalysis and biochemistry. In many cases single reference methods are not appropriate to treat such systems. Therefore, the development of efficient local multireference correlation methods is one of our goals for future research.

REFERENCES

1. Møller C, Plesset MS (1934) *Phys Rev* 46:618
2. Čížek J (1966) *J Chem Phys* 45:4256
3. Purvis GD III, Bartlett RJ (1982) *J Chem Phys* 76:1910
4. Raghavachari K, Trucks GW, Pople JA, Head-Gordon M (1989) *Chem Phys Lett* 157:479
5. Kállay M, Surján PR (2000) *J Chem Phys* 113:1359
6. Kállay M, Surján PR (2001) *J Chem Phys* 115:2945
7. Kállay M, Szalay PG, Surján PR (2002) *J Chem Phys* 117:980
8. Hirata S (2003) *J Phys Chem A* 107:9887
9. Olsen J (2000) *J Chem Phys* 113:7140
10. Knowles PJ, Handy NC (1984) *Chem Phys Lett* 111:315
11. Knizia G, Adler TB, Werner HJ (2009) *J Chem Phys* 130:054104
12. Adler TB, Werner HJ, Manby FR (2009) *J Chem Phys* 130:054106
13. Adler TB, Werner HJ (2009) *J Chem Phys* 130:241101
14. Klopper W, Manby FR, Ten-no S, Valeev EF (2006) *Int Rev Phys Chem* 25:427
15. Werner HJ, Adler TB, Knizia G, Manby FR (2010) In: Cársky P, Paldus J, Pittner J (eds) *Recent progress in coupled cluster methods*. Springer, Heidelberg, p 573
16. Tew DP, Hättig C, Bachorz RA, Klopper W (2010) In: Cársky P, Paldus J, Pittner J (eds) *Recent progress in coupled cluster methods*. Springer, Heidelberg, p 535
17. Monkhorst HJ (1977) *Int J Quantum Chem Symp* 11:421
18. Sekino H, Bartlett RJ (1984) *Int J Quantum Chem Symp* 18:255
19. Stanton JF, Bartlett RJ (1993) *J Chem Phys* 98:7029
20. Christiansen O, Koch H, Jørgensen P (1995) *Chem Phys Lett* 243:409
21. Pulay P (1983) *Chem Phys Lett* 100:151
22. Saebø S, Pulay P (1985) *Chem Phys Lett* 113:13
23. Pulay P, Saebø S (1986) *Theor Chim Acta* 69:357
24. Hampel C, Werner HJ (1996) *J Chem Phys* 104:6286
25. Hetzer G, Pulay P, Werner HJ (1998) *Chem Phys Lett* 290:143
26. Schütz M, Hetzer G, Werner HJ (1999) *J Chem Phys* 111:5691
27. Hetzer G, Schütz M, Stoll H, Werner HJ (2000) *J Chem Phys* 113:9443
28. Schütz M, Werner HJ (2000) *Chem Phys Lett* 318:370

29. Schütz M (2000) *J Chem Phys* 113:9986
30. Schütz M, Werner HJ (2001) *J Chem Phys* 114:661
31. Schütz M (2002) *J Chem Phys* 113:8772
32. Schütz M (2002) *Phys Chem Chem Phys* 4:3941
33. Werner HJ, Knowles PJ, Manby FR, Schütz M, Celani P, Knizia G, Korona T, Lindh R, Mitrushenkov A, Rauhut G, Adler TB, Amos RD, Bernhardsson A, Berning A, Cooper DL, Deegan MJO, Dobbyn AJ, Eckert F, Goll E, Hampel C, Heßelmann A, Hetzer G, Hrenar T, Jansen G, Köppl C, Liu Y, Lloyd AW, Mata RA, May AJ, McNicholas SJ, Meyer W, Mura ME, Nicklass A, Palmieri P, Pflüger K, Pitzer R, Reiher M, Shiozaki T, Stoll H, Stone AJ, Tarroni R, Thorsteinsson T, Wang M, Wolf A (2010) Molpro, version 2010.1, a package of ab initio programs. <http://www.molpro.net>
34. El Azhary A, Rauhut G, Pulay P, Werner HJ (1998) *J Chem Phys* 108:5185
35. Rauhut G, Werner HJ (2001) *Phys Chem Chem Phys* 3:4853
36. Schütz M, Werner HJ, Lindh R, Manby FR (2004) *J Chem Phys* 121:737
37. Korona T, Pflüger K, Werner HJ (2004) *Phys Chem Chem Phys* 6:2059
38. Pflüger K (2008) Thesis, University of Stuttgart
39. Russ NJ, Crawford TD (2004) *Chem Phys Lett* 400:104
40. Korona T, Werner HJ (2003) *J Chem Phys* 118:3006
41. Kats D, Korona T, Schütz M (2006) *J Chem Phys* 125:104106
42. Kats D, Korona T, Schütz M (2007) *J Chem Phys* 127:064107
43. Kats D, Schütz M (2009) *J Chem Phys* 131:124117
44. Kats D, Schütz M (2010) *Z Phys Chem* 224:601
45. Pisani C, Busso M, Capecchi G, Casassa S, Dovesi R, Maschio L, Zicovich-Wilson C, Schütz M (2005) *J Chem Phys* 122:094113
46. Maschio L, Usvyat D, Pisani C, Manby FR, Casassa S, Schütz M (2007) *Phys Rev B* 76:075101
47. Maschio L, Usvyat D (2008) *Phys Rev B* 78:073102
48. Usvyat D, Maschio L, Pisani C, Schütz M (2010) *Z Phys Chem* 224:441
49. Schütz M, Usvyat D, Lorenz M, Pisani C, Maschio L, Casassa S, Halo M (2010) In: Manby FR (ed) *Accurate condensed-phase quantum chemistry*. Taylor and Francis Group, Abingdon, p 29
50. Maslen PE, Head-Gordon M (1998) *Chem Phys Lett* 283:102
51. Scuseria GE, Ayala PY (1999) *J Chem Phys* 111:8330
52. Auer AA, Nooijen M (2006) *J Chem Phys* 125:024104
53. Maslen PE, Head-Gordon M (1998) *J Chem Phys* 109:7093
54. Lee MS, Maslen PE, Head-Gordon M (2000) *J Chem Phys* 112:3592
55. Maslen PE, Dutoi AD, Lee MS, Shao YH, Head-Gordon M (2005) *Mol Phys* 103:425
56. Subotnik JE, Head-Gordon M (2005) *J Chem Phys* 123:064108
57. Subotnik JE, Sodt A, Head-Gordon M (2006) *J Chem Phys* 125:074116
58. Sodt A, Subotnik JE, Head-Gordon M (2006) *J Chem Phys* 125:194109
59. Subotnik JE, Sodt A, Head-Gordon M (2008) *J Chem Phys* 128:034103
60. Subotnik JE, Head-Gordon M (2008) *J Phys Condens Matter* 20:294211
61. Chwee TS, Szilva AB, Lindh R, Carter EA (2008) *J Chem Phys* 128:224106
62. Neese F, Hansen A, Liakos DG (2009) *J Chem Phys* 131:064103
63. Neese F, Wennmohs F, Hansen A (2009) *J Chem Phys* 130:114108
64. Förner W, Ladik J, Otto P, Čížek J (1985) *Chem Phys* 97:251
65. Li S, Ma J, Jiang Y (2002) *J Comput Chem* 23:237
66. Li W, Piecuch P, Gour JR, Li S (2009) *J Chem Phys* 131:114109
67. Flocke N, Bartlett RJ (2004) *J Chem Phys* 121:10935
68. Hughes TF, Flocke N, Bartlett RJ (2008) *J Phys Chem A* 112:5994
69. Friedrich J, Hanrath M, Dolg M (2007) *J Chem Phys* 126:154110

70. Friedrich J, Hanrath M, Dolg M (2008) *Chem Phys* 346:266
71. Friedrich J, Dolg M (2008) *J Chem Phys* 129:244105
72. Friedrich J, Dolg M (2009) *J Chem Theory Comput* 5:287
73. Friedrich J, Coriani S, Helgaker T, Dolg M (2009) *J Chem Phys* 131:154102
74. Stoll H (1992) *J Chem Phys* 97:8449
75. Kats D, Usvyat D, Schütz M (2008) *Phys Chem Chem Phys* 10:3430
76. Pipek J, Mezey PG (1989) *J Chem Phys* 90:4916
77. Boys SF (1966) In: Löwdin PO (ed) *Quantum theory of atoms, molecules, and the solid state*. Academic Press, New York, NY, p 253
78. Reed AE, Weinhold F (1985) *J Chem Phys* 83:1736
79. Mata R, Werner HJ (2007) *Mol Phys* 105:2753
80. Boughton JW, Pulay P (1993) *J Comput Chem* 14:736
81. Dunning TH Jr (1989) *J Chem Phys* 90:1007
82. Werner HJ, Pflüger K (2006) *Annu Rep Comput Chem* 2:53
83. Löwdin PO (1950) *J Chem Phys* 18:365
84. Reed AE, Weinstock RB, Weinhold F (1985) *J Chem Phys* 83:735
85. Mata R, Werner HJ (2006) *J Chem Phys* 125:184110
86. Russ NJ, Crawford TD (2004) *J Chem Phys* 121:691
87. Mata R, Werner HJ, Schütz M (2008) *J Chem Phys* 128:144106
88. Humbel S, Sieber S, Morokuma K (1996) *J Chem Phys* 105:1959
89. Dapprich S, Komáromi I, Byun KS, Morokuma K, Frisch MJ (1999) *J Mol Struct THEOCHEM* 461:1
90. Pulay P (1980) *Chem Phys Lett* 73:393
91. Meyer W (1976) *J Chem Phys* 64:2901
92. Hampel C, Peterson KA, Werner HJ (1992) *Chem Phys Lett* 190:1
93. Liu Y, Werner HJ (2010) to be published
94. Knowles PJ, Hampel C, Werner HJ (1993) *J Chem Phys* 99:5219
95. Knowles PJ, Hampel C, Werner HJ (2000) *J Chem Phys* 112:3106
96. Amos RD, Andrews JS, Handy NC, Knowles PJ (1991) *Chem Phys Lett* 185:256
97. Lauderdale WJ, Stanton JF, Gauss J, Watts JD, Bartlett RJ (1991) *Chem Phys Lett* 187:21
98. Kutzelnigg W (1985) *Theor Chim Acta* 68:445
99. Klopper W, Kutzelnigg W (1987) *Chem Phys Lett* 134:17
100. Klopper W, Kutzelnigg W (1990) *J Phys Chem* 94:5625
101. Klopper W (1991) *Chem Phys Lett* 186:583
102. Klopper W, Röhse R, Kutzelnigg W (1991) *Chem Phys Lett* 178:455
103. Kutzelnigg W, Klopper W (1991) *J Chem Phys* 94:1985
104. Termath V, Klopper W, Kutzelnigg W (1991) *J Chem Phys* 94:2002
105. Klopper W, Samson CCM (2002) *J Chem Phys* 116:6397
106. Valeev EF (2004) *Chem Phys Lett* 395:190
107. Ten-no S (2004) *Chem Phys Lett* 398:56
108. May AJ, Manby FR (2004) *J Chem Phys* 121:4479
109. Tew DP, Klopper W (2005) *J Chem Phys* 123:074101
110. Werner HJ, Adler TB, Manby FR (2007) *J Chem Phys* 126:164102
111. Adler TB, Knizia G, Werner HJ (2007) *J Chem Phys* 127:221106
112. Knizia G, Werner HJ (2008) *J Chem Phys* 128:154103
113. Werner HJ, Manby FR (2006) *J Chem Phys* 124:054114
114. Manby FR, Werner HJ, Adler TB, May AJ (2006) *J Chem Phys* 124:094103
115. Werner HJ (2008) *J Chem Phys* 129:101103
116. Kato T (1957) *Commun Pure Appl Math* 10:151

117. Pack RT, Byers Brown W (1966) *J Chem Phys* 45:556
118. Ten-no S (2004) *J Chem Phys* 121:117
119. Schütz M, Lindh R, Werner HJ (1999) *Mol Phys* 96:719
120. Boys SF, Shavitt I, University of Wisconsin (1959) Report WIS-AF-13
121. Whitten JL (1973) *J Chem Phys* 58:4496
122. Baerends EJ, Ellis DE, Ros P (1973) *Chem Phys* 2:41
123. Früchtl HA, Kendall RA, Harrison RJ, Dylla KG (1997) *Int J Quantum Chem* 64:63
124. Weigend F (2002) *Phys Chem Chem Phys* 4:4285
125. Polly R, Werner HJ, Manby FR, Knowles PJ (2004) *Mol Phys* 102:2311
126. Loibl S, Manby FR, Schütz M (2010) *Mol Phys* 108:477
127. Vahtras O, Almlöf J, Feyereisen MW (1993) *Chem Phys Lett* 213:514
128. Feyereisen MW, Fitzgerald G, Komornicki A (1993) *Chem Phys Lett* 208:359
129. Weigend F, Häser M, Patzelt H, Ahlrichs R (1998) *Chem Phys Lett* 294:143
130. Weigend F, Köhn A, Hättig C (2002) *J Chem Phys* 116:3175
131. Werner HJ, Manby FR, Knowles P (2003) *J Chem Phys* 118:8149
132. Hättig C, Weigend F (2000) *J Chem Phys* 113:5154
133. Manby FR (2003) *J Chem Phys* 119:4607
134. Rendell AP, Lee TJ (1994) *J Chem Phys* 101:400
135. Schütz M, Manby FR (2003) *Phys Chem Chem Phys* 5:3349
136. Heßelmann A, Jansen G, Schütz M (2005) *J Chem Phys* 122:014103
137. Bukowski R, Podeszwa R, Szalewicz K (2005) *Chem Phys Lett* 414:111
138. Korona T, Jeziorski B (2008) *J Chem Phys* 128:144107
139. Korona T (2009) *J Chem Theory Comput* 5:2663
140. Dunlap BI (2000) *Phys Chem Chem Phys* 2:2113
141. Dunlap BI (2000) *J Mol Struct THEOCHEM* 529:37
142. Dunlap BI (2000) *J Mol Struct THEOCHEM* 501–502:221
143. Christiansen O, Jørgensen P, Hättig C (1998) *Int J Quantum Chem* 68:1
144. Wheatley RJ (2008) *J Comput Chem* 29:445
145. Thouless DJ (1960) *Nucl Phys* 21:225
146. Handy NC, Schaefer HF III (1984) *J Chem Phys* 81:5031
147. Jørgensen P, Helgaker T (1988) *J Chem Phys* 89:1560
148. Foresman JB, Head-Gordon M, Pople JA, Frisch MJ (1992) *J Phys Chem* 96:135
149. Davidson ER (1975) *J Comput Phys* 17:87
150. Hirao K, Nakatsuji H (1982) *J Comput Phys* 45:246
151. Crawford DT, King RA (2002) *Chem Phys Lett* 366:611
152. Korona T, Werner HJ. Unpublished
153. Butscher W, Kammer WE (1976) *J Comput Phys* 20:313
154. Hättig C, Köhn A (2002) *J Chem Phys* 117:6939
155. Köhn A, Hättig C (2003) *J Chem Phys* 119:5021
156. Almlöf J (1991) *Chem Phys Lett* 181:319
157. Häser M, Almlöf J (1992) *J Chem Phys* 96:489
158. Rauhut G, Azhary AE, Eckert F, Schumann U, Werner HJ (1999) *Spectrochim Acta A* 55:647
159. Rauhut G, Werner HJ (2003) *Phys Chem Chem Phys* 5:2001
160. Hrenar T, Werner HJ, Rauhut G (2005) *Phys Chem Chem Phys* 7:3123
161. Hrenar T, Rauhut G, Werner HJ (2006) *J Phys Chem A* 110:2060
162. Hrenar T, Werner HJ, Rauhut G (2007) *J Chem Phys* 126:134108
163. Gauss J, Werner HJ (2000) *Phys Chem Chem Phys* 2:2083
164. Kaminsky J, Mata RA, Werner HJ, Jensen F (2008) *Mol Phys* 106:1899

165. Claeysens F, Harvey JN, Manby FR, Mata RA, Mulholland AJ, Ranaghan KE, Schütz M, Thiel S, Thiel W, Werner HJ (2006) *Angew Chem* 118:7010
166. Mata RA, Werner HJ, Thiel S, Thiel W (2008) *J Chem Phys* 128:025104
167. Dieterich JM, Werner HJ, Mata RA, Metz S, Thiel W (2010) *J Chem Phys* 132:035101
168. Harvey JN (2010) *Faraday Discuss* 145:487
169. Bernardi F, Boys SF (1970) *Mol Phys* 19:553
170. Saebø S, Pulay P (1993) *Annu Rev Phys Chem* 44:213
171. Schütz M, Rauhut G, Werner HJ (1998) *J Phys Chem A* 102:5997
172. Hartke B, Schütz M, Werner HJ (1998) *J Chem Phys* 239:561
173. Hill JG, Platts JA, Werner HJ (2006) *Phys Chem Chem Phys* 8:4072
174. Hill JG, Platts JA (2007) *J Chem Theory Comput* 3:80
175. Hill JG, Platts JA (2008) *J Chem Phys* 129:134101
176. Hill JG, Platts JA (2008) *Phys Chem Chem Phys* 10:2785
177. Hill JG, Platts JA (2009) *Chem Phys Lett* 479:279
178. Schemmel D, Schütz M (2007) *J Chem Phys* 127:174304
179. Jeziorski B, Moszynski R, Szalewicz K (1994) *Chem Rev* 94:1887
180. Runeberg N, Schütz M, Werner HJ (1999) *J Chem Phys* 110:7210
181. Mognko L, Schweizer M, Rauhut G, Schütz M, Stoll H, Werner HJ (2002) *Phys Chem Chem Phys* 4:1006
182. Riedel S, Pykkø P, Mata RA, Werner HJ (2005) *Chem Phys Lett* 405:148
183. Langlet J, Caillet J, Berges J, Reinhardt P (2003) *J Chem Phys* 118:6157
184. Grimme S, Mueck-Lichtenfeld C, Antony J (2008) *Phys Chem Chem Phys* 10:3327
185. Grimme S (2003) *J Chem Phys* 118:9095
186. Schemmel D, Schütz M (2010) *J Chem Phys* 132:174303
187. Adler TB, Werner HJ (2010) to be published
188. Peterson KA, Adler TB, Werner HJ (2008) *J Chem Phys* 128:084102
189. Yum J, Hagberg DP, Moon S, Karlsson KM, Marinado T, Sun L, Hagfeldt A, Nazeeruddin MK, Grätzel M (2009) *Angew Chem Int Ed* 48:1576

CHAPTER 15

THE LINEAR SCALING SEMIEMPIRICAL LOCALSCF METHOD AND THE VARIATIONAL FINITE LMO APPROXIMATION

ARTUR PANCAKIEWICZ AND VICTOR M. ANISIMOV

FQS Poland, 30-538 Krakow, Poland, e-mail: a.panczakiewicz@fqs.pl; v.anisimov@fqs.pl

Abstract: When dealing with large biological systems speed determines the utility of the computational method. Therefore in order to bring quantum-mechanical (QM) methods to computational studies of biomolecules it is necessary to significantly reduce their resource requirement. In this light semiempirical QM methods are particularly encouraging because of their modest computational cost combined with potentially high accuracy. However, even semiempirical methods are frequently found to be too demanding for typical biological applications which require extensive conformational sampling. Significant speed up is obtained in the linear scaling LocalSCF method which is based on the variational finite localized molecular orbital (VFL) approximation. The VFL provides an approximate variational solution to the Hartree-Fock-Roothaan equation by seeking the density matrix and energy of the system in the basis of compact molecular orbitals using constrained atomic orbital expansion (CMO). Gradual release of the expansion constraints leads to determination of the theoretically most localized solution under small non-orthogonality of CMOs. Validation tests confirm good agreement of the LocalSCF method with matrix diagonalization results on partial atomic charges, dipole moment, conformational energies, and geometry gradients while the method exhibits low computer memory and CPU time requirements. We observe stable dynamics when using the LocalSCF method.

Keywords: CMO, Linear scaling, LMO, NDDO method, Normalization condition, Orthogonality condition, QM MD, SCF method, VFL approximation

Abbreviations

AM1	Austin model 1
AO	Atomic orbital
B3LYP	Becke 3-term correlation, Lee-Yang-Parr exchange functional
CC	Coupled cluster
CI	Configuration interaction
CMO	Constrained expansion molecular orbital

CPU	Central processing unit
DFT	Density functional theory;
HF/6-31G*	Hartree-Fock method using Pople 6-31G* basis set
HOF	Heat of formation
LMO	Localized molecular orbital
LocalSCF	Local self consistent field
MD	Molecular dynamics
MO	Molecular orbital
MP2	Second-order Moller-Plesset perturbation theory
NDDO	Neglect of diatomic differential overlap
NPT	Constant number of particles, pressure, and temperature
NVE	Constant number of particles, volume, and energy
NVT	Constant number of particles, volume and temperature
PBC	Periodic boundary condition
PM3	Parametric method 3
PM5	Parametric method 5
QM	Quantum mechanics
RAM	Random access memory
SBP	Spherical boundary potential
SCF	Self-consistent field
VFL	Variational finite localized molecular orbital approximation

15.1. INTRODUCTION

Application of quantum-mechanical (QM) methods to biological problems is a long standing goal in simulation science. Solving this problem would bring multiple advancements to computational biology including the expansion of the range of biological applications to bond breaking and formation processes and the increase in general physical accuracy. The advanced physical model of the QM methods provides a necessary precondition for that.

Significant progress has been made in reducing the computational cost of various QM methods due to the development of linear scaling algorithms [1, 2]. However the obtained performance is still insufficient to deal with biological macromolecules. Therefore approximate QM methods are necessary in order to bring the QM methodology to the forefront of biomolecular modeling on equal or comparable footing with classical force fields.

In the hierarchy of QM methods semiempirical methods based on neglect of diatomic differential overlap (NDDO) represent the lowest and the fastest level of theory. Their approximate nature and high speed are the two core factors which make them particularly attractive for biological applications. For instance, the chemically accurate hybrid density functional theory (DFT) methods, e.g. B3LYP, have thousand-fold performance overhead over semiempirical methods. This performance bottleneck makes impossible to treat real-size biological systems in presence

of explicit solvent. Therefore targeting large molecular systems having inherently dynamic character will require versatile QM methods beyond the performance capabilities of the current ab initio and DFT methods.

Another important aspect of biomolecular simulation is the ability of the selected method to accurately describe condensed phase phenomena. Since all currently accessible non-empirical QM methods (e.g. Hartree-Fock, DFT, and MP2) are not sufficiently accurate for liquid simulations due to missing or insufficient treatment of electron correlation it requires introducing optimized parameters in order to compensate for the deficiency of the level of theory. Semiempirical QM methods provide the necessary solution in the form of their tunable parametric framework. In this regard they are not much different from classical force fields. However being formulated on the quantum-mechanical platform semiempirical methods add an important additional level of physics into the treatment of atomic interactions over the classical mechanics models.

Despite of the computational advantage of the semiempirical theory, it alone is also insufficient to open the door to biological simulations. Since the pioneering work of Karplus and co-workers [3] biological macromolecules have long been recognized as dynamic entities governed by thermal motions. For the latter to be properly accounted one has to use molecular dynamics (MD). This requirement imposes serious performance restrictions on applicability of high levels of theory. Clearly, additional steps beyond replacing matrix diagonalization by linear scaling algorithms are necessary in order to gain additional computational performance. Recognizing this problem prompted the authors to introduce the variational finite localized molecular orbital approximation (VFL) [4, 5].

15.2. THEORY

15.2.1. Linear Scaling Problem

According to the quantum-mechanical theory the complete description of the molecular system is included in the wave function of the system, which can be found by solving Schrödinger equation. Since straight forward solution of the Schrödinger equation cannot be made for systems of chemical interest, various levels of approximate solutions are introduced. Historically, Hartree-Fock-Roothaan approximation [6–8] provided the first practically useful approach to QM description of molecular systems. In this fundamental method the single-determinant wave function [6] is constructed from 1-electron molecular orbital functions (MO) describing the energy of a single electron in the average field created by all other electrons and nuclei in the system.[6] The MOs are in turn represented by a linear combination of hydrogen-like atomic orbitals (AO) following the Roothaan-Hall approximation [7, 8]. Variationally minimizing the linear coefficients of AOs in their MO expansion leads to determination of the molecular wave function.

The Roothaan-Hall approximation to the Hartree-Fock method introduced the important concept of basis set. The type of AOs, their number per atom, and their analytical form are known as basis set. Minimal basis set conceptually originates

from hydrogen atom solution of the Schrödinger equation. By analogy, one assigns hydrogen-like $1s$, $2s$, $2p_x$, $2p_y$, $2p_z$, etc. atomic orbitals to non-hydrogen atoms. Semiempirical methods utilize valence-electron approximation, thus incorporating inner shells into a parametric core. This leaves 4 valence AOs $2s$, $2p_x$, $2p_y$ and $2p_z$ as the basis for atoms of the second row. Since the concept of basis primarily serves the numerical purposes of providing variational degrees of freedom more sophisticated basis sets have been introduced such as split-valence bases in which valence AOs are expanded in a linear combination of several functions having independent exponents. Extending the basis splitting process to infinity virtually leads to a complete basis set which provides the Hartree-Fock energy limit. Since Hartree-Fock-Roothaan is a variational method, using a finite basis set provides an upper-bound energy estimation to the theoretical energy limit. Expanding the size of the basis will naturally improve the accuracy of the approximation.

Unfortunately Hartree-Fock method provides incomplete description of electron correlation effects, therefore seeking Hartree-Fock limit is not going to improve sufficiently the quality of the wave function. A solution is provided by DFT, post-Hartree-Fock (MP2, CI, CC), and semiempirical methods. The latter, which are of primary concern in this article, use fitting to experimental data in order to avoid otherwise extremely computationally expensive mathematical operations.

Since semiempirical methods are based on the Hartree-Fock-Roothaan theory they experience similar scalability problems as the Hartree-Fock-Roothaan method yet of obviously lesser severity due to the NDDO approximation. Particularly semiempirical methods scale quadratically in memory storage and cubically in CPU-time with the number of atomic orbitals in the matrix diagonalization step of self-consistent field (SCF) calculations.

Another important part of scalability problem in QM methods is efficient handling of long-range Coulomb interactions. In semiempirical methods these calculations scale quadratically in memory storage and CPU time. Solving this problem is mandatory in order to achieve linear scaling calculations. Since the efficient treatment of long-range Coulomb interactions has been achieved in the Fast Multipole Method (FMM) [9] we do not need to worry about this part and instead will focus on the matrix diagonalization problem only.

Several powerful algorithms have recently been developed for the semiempirical framework providing linear scaling alternative to matrix diagonalization [10–12]. The methodological importance of these methods warrants their brief analysis.

It is apparent that the unfavorable scaling of conventional QM methods has the origin in the naturally delocalized character of MOs. Indeed, following the Roothaan-Hall method each MO is expanded over the entire AO-space represented by all atoms in the system thus leading to full delocalization of MOs over the entire system. To combat the delocalization and the inherent unfavorable scaling of the conventional SCF algorithm one needs to reformulate the Hartree-Fock-Roothaan equations in terms of local interactions.

A remarkable approach is to replace MOs by localized molecular orbitals (LMO) and to seek the final density matrix in terms of LMOs [10]. Since LMOs consume lesser space than delocalized MOs and have fewer variational degrees to optimize

the LMO approach provides valuable memory saving and performance improvement over the use of delocalized MOs when dealing with large systems. This elegant idea has been proposed by Stewart and implemented in MOZYME method [10]. In it Jacobi rotations are performed on Fock matrix constructed in the basis of LMOs. The occupied-virtual LMO rotations are carried out to reduce the Fock matrix to block-diagonal form via orthogonalization of occupied to virtual LMOs. Inside the occupied-occupied and virtual-virtual blocks the orthogonalization is not required. During the SCF procedure the LMOs quickly reach the saturation point of about 150 atomic centers and after that they remain roughly constant in size. Since the number of LMOs depends linearly on the number of atoms in the system the method is linear scaling. The small size of LMOs is the determining factor of high performance of the MOZYME method. The main computational overhead in MOZYME comes from slow convergence of the LMO tails.

Another insightful linear scaling approach is presented by the divide-and-conquer method [13] as implemented by Merz and co-workers in semiempirical DivCon program [11]. It utilizes a different powerful resource which can be categorized as a constrained compartmentalization. In this method the entire system is divided on fixed-size compartments which are small enough to be treated via matrix diagonalization. Each part enclosing a group of closely positioned atoms can be viewed as a fixed-size container carrying its own partial density matrix self-consistently optimized in the electric field created by other compartments. Iteratively walking through the list of compartments one can eventually reach the self-consistency point. The full density matrix of the system is assembled from the compartments density matrices. Because the number of compartments is proportional to the number of atoms in the system the method is linear scaling. The main computational cost in the divide-and-conquer method comes from diagonalization and iterating over the large number of compartments. Increasing the compartment size reduces the iteration cost but increases the cost of diagonalization. Reducing the compartment size reduces diagonalization cost but increases the cost of iterations. Assuming that the compartment size is optimized to maximize the computational performance one obtains the theoretical limit of performance of the method.

15.2.2. VFL Approximation

Despite remarkable improvement in performance of QM methods due to the linear scaling formulations the sheer size of biological macromolecules demands faster computations than the linear scaling within the Hartree-Fock-Roothaan framework can provide. A different strategy is necessary in order to further speed up QM calculations. Such approach was proposed by Anikin et al. [4] by suggesting an additional approximation on the top of the Hartree-Fock-Roothaan method and which is termed variational finite localized molecular orbital (VFL) approximation (Figure 15-1) [5].

If in the original Roothaan-Hall formulation the density matrix is expressed in the basis of completely delocalized MOs, in contrast to that, the VFL approximation provides a method to compute approximate density matrix in the basis of compact

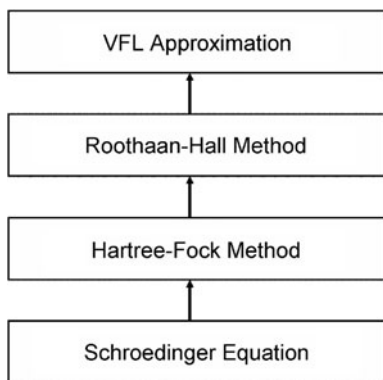


Figure 15-1. Hierarchy of QM approximations toward modeling larger systems

or constrained molecular orbitals (CMO). In VFL the CMO expansion over AOs is fixed and does not change during SCF. Finding the energy and density matrix under the constrained AO expansion is the purpose of the VFL approximation. For example, one may constrain CMO expansion to 5 atomic centers and, based on the VFL approximation, still will be able to variationally determine the density matrix and energy corresponding to such constraint. Obviously, the density matrix constructed under such stringent conditions will deviate significantly from the true density matrix, but important step to realize is the availability of such solution. This opportunity is advantageously utilized in the linear scaling LocalSCF method, which will be discussed in a separate section.

Before starting the derivation of the VFL equations it might be helpful to discuss the concept of CMOs in a greater detail. Since CMOs have limited expansion over AO space they are similar in this aspect to LMOs. However, the distinctive moment of the comparison is that LMO expansion changes during SCF while CMO expansion remains fixed, because it is constrained. The constraint can be trivially implemented by using gradient-based SCF optimization of linear coefficients of CMOs. The non-trivial part is how to maintain orthogonalization and normalization requirements for CMOs.

Normalization counts the number of electrons assigned to MOs. Its numerical value must be unit per MO; any deviation from the unit value will indicate a charge loss or its creation from nowhere leading to computational data making no physical sense. The other property of MOs, the orthogonalization requirement, stems from the concept of independent degrees of freedom like normal vectors \mathbf{i} , \mathbf{j} , \mathbf{k} in the Cartesian coordinate system. If the degrees of freedom are dependent, this is a non-orthogonal case. It is not possible in general to manipulate with dependent variables so the non-orthogonality has to be accounted by employing the inverse overlap matrix.

Orthogonality of MOs can also be obtained via diagonalization but the latter can be applied only when MOs share same AO space, like for example in the divide-and-conquer method. This is not the case of CMOs each having individual AO

expansion; hence, diagonalization is entirely inapplicable in the present circumstances. The possible alternative could be to work with non-orthogonal CMOs but such solution is not very appealing because of high computational cost of manipulation with inverse overlap matrix. Therefore we need to find the way to keep CMOs orthogonal at lesser computational expense.

To maintain orthogonality of CMOs during SCF procedure we can utilize a well-known concept of perturbation theory stating that if we know an approximate solution of the target function and its expansion series in vicinity of that point, then there is a mathematically certain way to improve the initial solution. Correspondingly, if the non-orthogonality of CMOs is small, it can be viewed as a perturbation in the vicinity of the density matrix $\mathbf{P}(0) = \mathbf{C}^* \mathbf{C}^t$ constructed from orthogonal CMOs, where \mathbf{C} is matrix of linear coefficients of CMOs and \mathbf{C}^t its transpose. Next, we can expand the energy of the system, E , into perturbation (Taylor) series around $\mathbf{P}(0)$

$$E[\mathbf{P}] = E[\mathbf{P}(0)] + \partial E / \partial \mathbf{P} \cdot [\mathbf{P} - \mathbf{P}(0)] + 1/2 \cdot \partial^2 E / \partial \mathbf{P}^2 \cdot [\mathbf{P} - \mathbf{P}(0)]^2 + \dots \quad (15-1)$$

The unknown final density matrix, \mathbf{P} , has the following form considering the general case of non-orthogonality of CMOs

$$\mathbf{P} = \mathbf{C} \cdot \mathbf{S}^{-1} \cdot \mathbf{C}^t \quad (15-2)$$

where, \mathbf{S} is overlap matrix between CMOs. Under the condition that non-orthogonality of CMOs is small the \mathbf{S}^{-1} matrix can also be expanded in Taylor series while neglecting second and higher order terms:

$$\mathbf{S}^{-1} = \mathbf{I} - (\mathbf{S} - \mathbf{I}) + \dots \quad (15-3)$$

where, \mathbf{I} is diagonal unit matrix. Combining Eqs. (15-2) and (15-3) one can obtain

$$\mathbf{P} - \mathbf{P}(0) \approx \mathbf{C} \cdot [\mathbf{I} - (\mathbf{S} - \mathbf{I})] \cdot \mathbf{C}^t - \mathbf{P}(0) = -\mathbf{C} \cdot (\mathbf{S} - \mathbf{I}) \cdot \mathbf{C}^t \quad (15-4)$$

This provides the opportunity to solve Eq. (15-1). Under the condition of small non-orthogonality we may neglect the second- and higher-order terms in Eq. (15-1) and compensate the missing parts via a penalty term. This produces energy function which approximately maintains orthogonality of CMOs and which is tolerant to small residual non-orthogonality between CMOs:

$$E \approx E[\mathbf{P}(0)] + \partial E / \partial \mathbf{P} \cdot [\mathbf{P} - \mathbf{P}(0)] + \mathbf{W} \cdot [\mathbf{S} - \mathbf{I}]^2 \quad (15-5)$$

where, \mathbf{W} is a penalty matrix, taken for simplicity as a constant.

Now when orthogonality is properly handled the remaining problem is to ascertain normalization of CMOs during the SCF iterations. This is also a non-trivial

problem considering that CMOs become interdependent due to the normalization requirement and all CMOs have to be determined simultaneously rather than separately. Conventionally linear coefficients of CMOs can be determined under normalization constraints imposed by the cumbersome method of Lagrange multipliers. Although powerful it is a time consuming procedure. Therefore in order to keep computations at maximum speed we are going to handle the normalization constraints via a computationally efficient approximation. Targeting this goal Anikin et al. [4] suggested an elegant solution to incorporate the normalization constraints into the SCF procedure via variational optimization of generalized degrees of freedom instead of directly manipulating with the linear coefficients of CMOs. These degrees of freedom, \mathbf{R} , are formulated in such way so their variation does not break the normalization of CMOs. It can be shown that when CMO variation $\delta\psi_i$ is orthogonal to the old (before SCF) CMO ψ_i^{old} the resulting ψ_i^{new} (after SCF) is automatically normalized in the first order of perturbation theory.

$$\psi_i^{new} = \psi_i^{old} + \delta\psi_i \quad (15-6)$$

$$\delta\psi_i = \sum_{\mu} R_{i\mu} \cdot (\varphi_{\mu} - C_{i\mu} \cdot \psi_i^{old}) \quad (15-7)$$

here φ_{μ} is atomic orbital.

From

$$\langle \psi_i^{old} | \delta\psi_i \rangle = 0 \quad (15-8)$$

it follows that

$$\langle \psi_i^{new} | \psi_i^{new} \rangle \approx 1 \quad (15-9)$$

It means that any variation $\delta\psi_i$, which is orthogonal to its parent, ψ_i^{old} , and which minimizes the energy of the system, also preserves the CMO normalization. Correspondingly we can vary coefficients \mathbf{R} in order to minimize the energy without the fear of breaking the normalization of CMOs. Optimization of matrix coefficients \mathbf{R} is performed by using a steepest descent gradient minimization procedure.

$$R_{i\mu}^{new} = R_{i\mu}^{old} - \alpha \cdot \partial E / \partial R_{i\mu} \quad (15-10)$$

where α is a small constant. Now when ψ_i^{new} are determined we can deduce linear coefficients of the CMO by using the standard Fourier approach:

$$C_{i\mu} = \langle \psi_i^{new} | \varphi_{\mu} \rangle \quad (15-11)$$

The Eqs. (15-5) and (15-7) summarize the VFL approximation. Since VFL is a variational method the incomplete CMO expansion will lead to upper energy bound according to the theory. Obviously, the larger the expansion the closer the result will

be to the conventional Hartree-Fock-Roothaan solution. Molecular properties computed under complete AO expansion would be entirely equivalent to those obtained using canonical MOs. In analogy with the Roothaan-Hall approximation in ab initio methods, which leaves the choice of basis set to the user, the VFL approximation applies no restrictions on the choice of CMO expansion and we are free to choose any non-redundant expansion that suits the task. Once we are concerned with determining the smallest CMO expansion while getting the energy and density matrix as close as possible to the conventional matrix diagonalization we enter the territory of the linear scaling LocalSCF method.

15.2.3. LocalSCF Method

The LocalSCF approach to finding the localized solution to the Hartree-Fock-Roothaan method is based on perturbation expansion of the energy of the system in vicinity of the known approximate density matrix as expressed by Eq. (15-1). Pertaining to LocalSCF, the approximate density matrix, $\mathbf{P}(\mathbf{0})$, is the result of the VFL SCF computation. Despite both the LocalSCF method and VFL approximation rely on perturbation theory, they employ it to achieve different goals. The VFL approximation is concerned with determining the density matrix of the system in the basis of constrained CMOs. In turn the LocalSCF method uses perturbation theory in order to gradually lift the expansion constraints aiming to reach the true density matrix while minimally changing the CMO expansion.

The LocalSCF solution to the density matrix is sought iteratively. Having $\mathbf{P}(\mathbf{0})$ as a starting point we can get improved density matrix $\mathbf{P}(\mathbf{1})$, which we can substitute then instead of $\mathbf{P}(\mathbf{0})$ and repeat the procedure, each time coming closer to the true Hartree-Fock-Roothaan density matrix, \mathbf{P} . This process logically connects the path from the density matrix $\mathbf{P}(\mathbf{0})$ to \mathbf{P} determined on different AO expansions. It is almost like starting an ab initio calculation from STO-3G basis set initially applied to all atoms in the system and finishing the calculation with various parts of the system carrying locally 3–21G or 6–31G basis sets. Of course, this analogy should not be understood literally, but to portray the technical difficulty in deciding on the optimal basis set for each part of a large and complex molecular system.

The expansion procedure in the LocalSCF method assures the energy convergence under gradual release of the CMO expansion constraints. Since the optimal expansion of CMOs is to be determined, one can conveniently initiate computations from an initial guess of 2- and 1-center CMOs corresponding to covalent bonds and lone-pairs of the molecular system under study. The VFL SCF procedure can refine the linear coefficients of these CMOs thus producing the density matrix $\mathbf{P}(\mathbf{0})$. Now we need to improve this density matrix by choosing a better CMO expansion. This step is central to the LocalSCF method. Having the density matrix $\mathbf{P}(\mathbf{0})$ fully relaxed incorporates in it all the information necessary to determine the best possible expansion for individual CMOs, which $\mathbf{P}(\mathbf{0})$ is constructed from. LocalSCF identifies the best expansions based on energy criterion, which is estimated according to the first-order perturbation correction

$$E \approx E(0) + (\partial E(0)/\partial R_{i\mu}) \cdot dR_{i\mu} \quad (15-12)$$

where $E(0)$ is energy of the system before expansion, E is estimated energy after expansion of CMO i on AO μ , and $R_{i\mu}$ is the generalized variational degree of freedom of the considered AO [5].

On the technical side the computer program first creates the list of adjacent AOs for each CMO according to the distance criterion to the already present atomic centers in the CMO. This list represents potential directions for expansion. Then each new AO in the list is tested on the possible energy gain using Eq. (15-12) and only those AOs are retained which produce the energy improvement greater than a threshold value. Such test is carried out for each CMO independently. Then the selected AOs with zeroed linear coefficients are added to the corresponding CMOs. Next the expanded CMOs are subjected to the VFL SCF procedure to relax the energy of the system and to determine new density matrix. The CMO expansion and VFL SCF steps are repeated until the energy of the system is converged. If the expansions are not rushed and performed by one AO at a time and immediately followed by VFL SCF relaxation of linear coefficients the resulting density function will closely approach the true Hartree-Fock-Roothaan density matrix of the system while being constructed from the CMOs having the theoretically smallest AO expansion.

According to validation tests [14] the energy of the system in LocalSCF method converges when CMOs acquire about 30 atomic centers on average. Obviously CMOs in LocalSCF all have different sizes because the expansion decision depends on the local environment of each CMO. At this point atomic partial charges, dipole moment, conformational energies, and geometry gradients are well converged in comparison with the result of the conventional matrix diagonalization calculation [14]. After LocalSCF CMOs reach the saturation point of 30 atomic centers the method becomes linear scaling.

Now having reviewed the technical aspects of the proposed algorithm we can compare the LocalSCF method with other linear scaling techniques formulated in the framework of MO theory. First and the foremost limitation of the conventional linear scaling methods is that they have little control over the localization process. Typically the degree of localization can be controlled by adjusting various cut-offs and thresholds. However this is a dangerous approach potentially leading to uncontrollable numerical errors. This problem is resolved in the LocalSCF method offering full control over the localization process. Instead of adjusting cut-offs the LocalSCF method offers the mechanism of adjustable SCF constraints in the form of tunable CMO expansion. Correspondingly, we can make CMOs shorter or longer and see what effect it produces on the energy and other physical properties of the system. The VFL SCF procedure variationally adjusts the resulting density matrix to the available CMO expansion space thus always finding the best possible density matrix under the given expansion constraint.

Besides stressing the differences it might be additionally illuminating to note the conceptual similarities between the LocalSCF and other linear scaling methods. For instance, one can draw parallels between LocalSCF CMOs and MOZYME

LMOs. They both represent limited expansion over atomic centers. Next, one may spot a similarity between the CMO expansion constraints and the compartment size constraints employed in the divide-and-conquer method. Having these parallels established one may see clearer what kind of conceptual improvement the LocalSCF method actually brings.

As an improvement over the MOZYME the constrained AO-expansion character of CMOs in LocalSCF eliminates the problem of weakly determined LMO tails. The result can immediately be seen in improved stability of SCF convergence in LocalSCF. As an improvement over the divide-and-conquer method the LocalSCF brings the idea of customization of compartment size to the level of individual CMOs. This leads to drastic reduction in the necessary computer memory. Finally one more analogy can be portrayed. The LocalSCF method and the VFL approximation redefine the large-scale molecular problem in terms of controlled AO expansion. This is reminiscent of using different basis sets in *ab initio* methods. However, this time the extent of MO expansion over atomic centers is itself a variable parameter which explains the notion that VFL is an approximate extension of the Roothaan-Hall method (see Figure 15-1).

Since LocalSCF is an approximate method, its main strength of using compact CMOs is also its main weakness. According to validation tests [14] LocalSCF underestimates the heat of formation (which is the analog of potential energy in semiempirical methods) by 5–10 kcal/mol per 1,000 atoms. No such problem exists in MOZYME which operates with larger LMOs. The conservative expansion procedure of LocalSCF trained to keep CMOs as compact as possible takes too much CPU time to reach the 150-center AO expansion, making such computation impractical. However reaching this goal may not be entirely necessary, because biological simulations are primarily concerned with relative energy differences, which are typically more accurate.

Additional limitation of the LocalSCF method is related to the condition of reaching the state of saturated CMO expansion, i.e. when CMO expansion stabilizes versus adding new AO to the existing expansion and to removing the least contributing AO from the existing expansion. There are two practically important different saturation conditions, one, taking place when dealing with a rigid-geometry system, and the second condition existing when the system is subjected to geometry changes.

When atoms are fixed in space their position uniquely determines the final result of the CMO expansion. The situation of moving atoms brings additional factors influencing the expansion process. This condition is partially present in geometry optimization calculations but it is mostly distinctive in molecular dynamics simulations. The moving atoms find themselves in a constantly changing neighborhood forcing their CMOs to additionally grow in size vs. the rigid geometry calculation. For instance, in liquid simulations (solvent) molecular fragments can travel on substantial distances in space visiting different parts of the macromolecular system at different time moments. The mobile molecular units carry in their CMOs the atomic orbitals of those atomic centers which they visited some time ago along the simulation path but which no longer satisfy the proximity test. This requires periodically

inspecting the CMO expansion and deleting those atomic centers which no longer make a sensible energetic contribution to the given CMO.

What we have in the end is the constantly fluctuating expansion space of the CMOs associated with labile molecular fragments. The processes of CMO growth and compactization eventually reach a dynamic equilibrium resulting in the density matrix which cannot be reproduced in a rigid geometry computation started from the same structure snapshot. In this we have a new phenomenon pertaining to molecular dynamics and geometry optimization jobs in LocalSCF calculations which carry a history of CMO expansion/compactization. As a consequence, single-point energy calculation performed on the final structure after geometry optimization is done would report a less favorable energy of the system than the geometry optimization job came up with. To avoid such confusion LocalSCF dumps density matrix to a computer file after each geometry change. Obviously, single-point calculation restarted from the saved density matrix would produce exactly the same energy as the value reported in the geometry optimization job or molecular dynamics step.

Taking into account this important difference it is necessary to avoid a potential mistake in attempting to compare the energy taken from a rigid geometry calculation with the energy obtained from a flexible geometry calculation. The only sensible energy comparison would correspond to “rigid with rigid” and “flexible with flexible” modes. Similarly in MD simulations the snapshot energies have to be all taken either from the MD output or all recomputed for rigid geometry snapshots extracted from the MD trajectory. Alternatively, one may save the density matrix for each trajectory snapshot to ensure the consistency between the sing-point and dynamic calculations.

15.2.4. SCF Convergence Criteria

In the LocalSCF computer program the SCF calculation otherwise known as single-point calculation is a complex hierarchical procedure (see Figure 15-2). It consists of two iterative levels – micro-SCF and macro-SCF. Each of them is controlled by its own set of convergence criteria.

15.2.4.1. Micro-SCF Iterations

The micro-SCF computations perform gradient optimization of linear coefficients of CMOs using the VFL SCF procedure under constrained CMO expansion. The linear coefficients of CMOs are optimized iteratively. During the micro-SCF iterations the algorithm checks five termination criteria. Unless specifically mentioned it is enough to satisfy any one of the termination criteria in order to finish the micro-SCF iterations.

First termination criterion, dQ_{thr} , monitors the change in diagonal elements of the density matrix between iterations. Since in the semiempirical theory the diagonal elements of the density matrix correspond to atomic charges the current termination criterion actually checks the maximum change in atomic charges between the two consecutive iterations. The SCF procedure will stop when the maximum

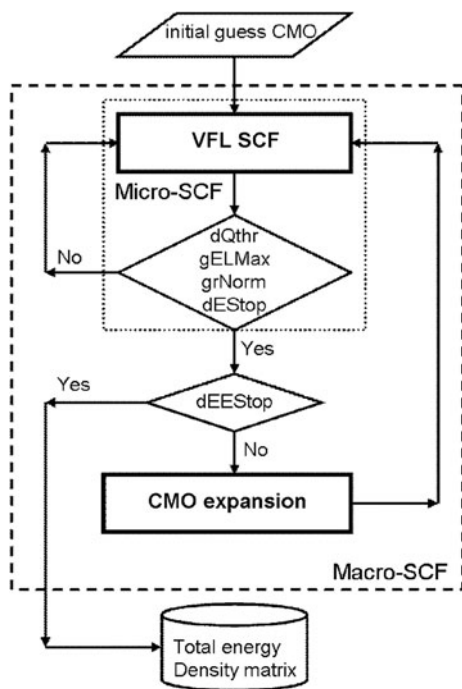


Figure 15-2. Schematic representation of SCF calculation in LocalSCF

change drops below the value of the parameter $dQthr$ set to 0.0003 electron units by default.

Second termination criterion, $gELMax$, looks after the maximum component of the derivative of the energy of the system over generalized variational degrees of freedom, R , corresponding to individual LMO coefficients. This condition will be satisfied when the derivative drops below $gELMax$ set to 0.002 eV/Å by default.

$$|\partial E / \partial R_{i\mu}| < gELMax \quad (15-13)$$

Third termination criterion, $grNorm$, watches for the gradient norm to become smaller than the $grNorm$ parameter set to 0.0005 eV/Å by default.

$$\|\partial E / \partial R\| < grNorm \quad (15-14)$$

Fourth termination criterion, $dEStop$, will be satisfied when the energy change between two successive micro-iterations drops below the default threshold value of 0.0001 kcal/mol. The purpose of this criterion is to terminate micro-SCF iterations when the energy change becomes negligibly small but gradient tests are still not satisfied.

$$\Delta E^{total} < dEStop \quad (15-15)$$

The dQthr and gELMax termination criteria are always on guard regardless of the computation mode. However, the grNorm and dEStop criteria are applied to starting geometry only referred to as single-point calculation. Since the gELMax criterion is more difficult to satisfy than the grNorm and dEStop, it automatically implies that the calculations involving geometry optimization and molecular dynamics will be executed under tighter SCF convergence criteria, which is necessary in order to ensure sufficient accuracy of geometry gradients.

Fifth micro-SCF convergence criterion, which is hardcoded, fulfills the role of a fault tolerant switch. The micro-SCF iterations will be stopped if the maximum value of the overlap matrix in the basis of molecular orbitals S_{ij} ($i \neq j$) exceeds the value of 0.07. Normally the overlap integrals should be an order of magnitude smaller. If this cannot be satisfied during the micro-SCF iterations their continuation makes no sense. If this happens the program will exit the micro-SCF iterations and seek help in the CMO expansion procedure.

15.2.4.2. Macro-SCF Iterations

The VFL SCF procedure and the CMO expansion step jointly define a macro-SCF iteration loop (see Figure 15-2). In the begin of the calculation the initial guess CMOs have too short expansion so applying the VFL micro-SCF iterations to them can not produce the final density matrix. The CMOs need to be expanded using the LocalSCF algorithm and then again subjected to the VFL micro-SCF iterations in order to refine their linear coefficients. The macro-SCF convergence criteria determine how many such repetitive cycles of VFL SCF and CMO expansion will be necessary to determine the total energy and density matrix with desirable accuracy.

The outcome of the CMO expansion at the given macro-SCF step depends on the expansion criterion, ThrDer1, which is a threshold parameter for derivative of the energy of the system over the variational parameter R corresponding to a linear coefficient of AO. The CMO expansion on a new atomic center will be accepted when the expansion gradient for that center is greater than 0.04 eV, which is a default value. Choosing smaller value for the ThrDer1 parameter will result in admitting more atomic centers to the CMO thus quickly increasing its size, and hence, the memory requirement and calculation time. On the other hand, a larger ThrDer1 value may equally produce a negative effect of too slowly growing CMOs and too slowly converging density matrix.

Additional parameter controlling the process of CMO expansion is orthogonality criterion, SijCrt. The algorithm tolerates small non-orthogonality between CMOs. This does not deteriorate quality of the computational results but facilitates faster calculations. The non-orthogonality of CMOs is not supposed to exceed the SijCrt value set to 0.001 by default. In case this criterion is exceeded the problematic CMO will be subjected to an additional cycle of expansion which will improve its orthogonality to other CMOs. Requesting a smaller non-orthogonality threshold than the default value improves the density matrix. However, setting too small value for the

SijCrt parameter may lead to a negligible improvement in the energy but quickly raising computational demand.

Final decision to stop the macro-SCF iterations depends on comparison of the energy change between two consecutive macro-iterations against dEESStop parameter. The macro-SCF iterations will be continued until the energy change between the CMO expansions drops below dEESStop value set to 0.5 kcal/mol by default.

15.2.5. Quantum-Mechanical Molecular Dynamics

Refocusing the target of QM calculations from small molecules to large systems brings new challenges besides of dealing with the increased number of basis functions. Due to their internal flexibility biomolecules possess huge number of local energy minima and, as a result, the detailed knowledge of the electronic structure of a single local minimum provides insufficient information to predict physical properties of the macromolecule. Therefore geometry optimization developed as the major computational approach in quantum chemical studies of small molecules becomes insufficient when dealing with macromolecules. Henceforth, switching from small molecules to very large systems results not only in the increase in the number of atoms but also brings in the requirement to perform extensive conformation sampling of biomacromolecules so the expected physical properties of the system can be obtained as a statistical average along the dynamics trajectory. As a result, targeting the feasibility of QM calculation of biological macromolecules goes far beyond reaching the linear scaling regimen but requires additional drastic reduction in computational cost in order to enable molecular dynamics simulations at QM level.

A molecular system evolving in time has electronic and nuclear degrees of freedom to account for. In the original Schrödinger equation the movement of all electrons and atomic nuclei in the system is described via single wave function. However considering a significant disparity between the masses of electron and proton with the ratio of 1,836 in favor of proton it is reasonable to decouple the motion of electrons and atomic nuclei thus reducing the complexity of the original equation. This is the essence of the Born-Oppenheimer approximation laying the foundation of the modern QM methods.

Based on the Born-Oppenheimer approximation we can assume atomic nuclei in biomolecule moving according to the classical Newton dynamics while modeling the electron density by quantum mechanical wave function adiabatically adjusting it to the instantaneous nuclei configuration. This is called SCF dynamics. In contrast to the classical mechanics MD where the potential energy function is also treated at classical level, the QM MD uses QM level of theory to compute potential energy of the system. This brings additional accuracy to the computational model vs classical approach due to the more fundamental description of electrostatic interactions.

In majority of the technical aspects, except the calculation of the potential energy and geometry gradients, QM MD relies on the same mathematical apparatus originally developed for classical force field MD [15]. In it molecular dynamics trajectory is a result of numerical time integration of the Newton equation

$$F_i = m_i \ddot{r}_i \quad (15-16)$$

where F_i is the total force acting on atom i ; m_i is atomic mass; and \ddot{r}_i is acceleration. Force is determined as negative gradient of the energy, E , over atomic coordinate vector, r_i

$$F_i = -\partial E / \partial r_i \quad (15-17)$$

Giving the initially static atoms a kick in the form of randomly oriented velocities initiates the dynamics. After the initial perturbation subsides and the system relaxes from the internal geometric strain it eventually reaches the thermal equilibrium. This marks the begin of the production run after which one can start saving the dynamics trajectory for subsequent analysis. From now on the dynamics can run forever in the absence of non-conservative forces assuming that the computer code is free from accumulation of numerical errors.

15.3. VALIDATION

15.3.1. Linear Scaling

Scalability of the LocalSCF method was tested on protein structures 1G5A (9,896 atoms), 1HZH (20,462 atoms), 3E2P (61,504 atoms), and 1AON (119,574 atoms) downloaded from the protein databank [16]. These particular proteins were selected based on their roughly doubling number of atoms along the series. The largest selected protein contains a representative number of atoms which is quite exceeding the average number of atoms typically targeted by classical force fields. Since the purpose of the test is to demonstrate linear scalability of the LocalSCF method and its actual resource requirement any other set of proteins would work equally well. Using real proteins in the test provides realistic estimation of what to expect from the computational method in practical applications.

The downloaded proteins were cleaned up by removing solvent molecules and adding hydrogen atoms. The protonation state of titratable amino acids was determined at physiological pH. Since these are model gas-phase calculations no counter-ions were added to the systems. Single-point LocalSCF [17] calculations (LocalSCF ver 2.0 Rev 2007.08.27 EM64T) were performed under default program settings on Intel Core 2 Duo 3.0 GHz, 4 GB RAM desktop working under Linux (Ubuntu 9.04) operating system. Long-range Coulomb interactions were treated via FMM method [18]. Plot of CPU time and required memory over number of atoms are presented in Figures 15-3 and 15-4 for PM3 [19] and PM5 [20, 21] Hamiltonians.

These data show remarkable linear scaling capability of LocalSCF both for CPU time and memory. Single-point calculation of the largest considered protein (GroEL-GroES chaperonin complex; PDB id 1AON) required 1.6 GB RAM and took 2 h and 10 min. Thus semiempirical QM calculations of such and even larger biological systems are now readily affordable on desktop computers. The accuracy of the linear scaling algorithm will be discussed in a separate section.

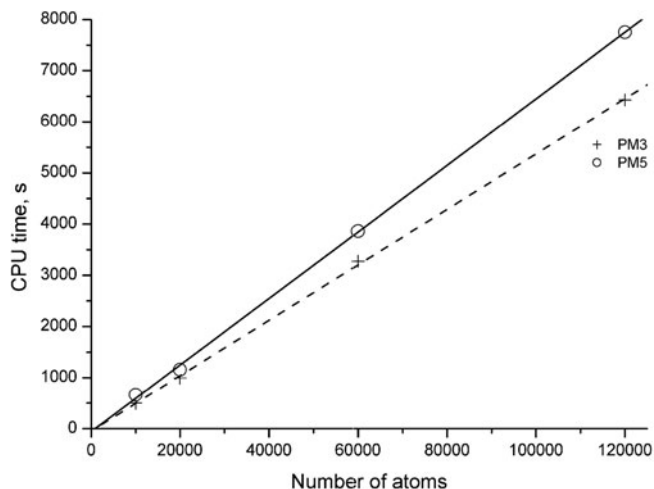


Figure 15-3. LocalSCF scaling of CPU time over number of atoms for PM3 and PM5 Hamiltonians

Additional degree of speed up can be obtained via utilization of multiple processing capabilities of the modern computer hardware. To test parallel scalability of LocalSCF program we took GroEL-GroES chaperonin complex. Calculations were performed using AM1 [22] Hamiltonian; exchange interactions were neglected beyond 6 Å distance; CMO expansion threshold derivative ThrDer1 was set to 0.05 eV; the maximum gradient tolerance gELMax was set to 0.05 eV. Long-range electrostatics was treated via FMM method using default program settings. Calculations were performed on a symmetric multiprocessor architecture SGI Altix

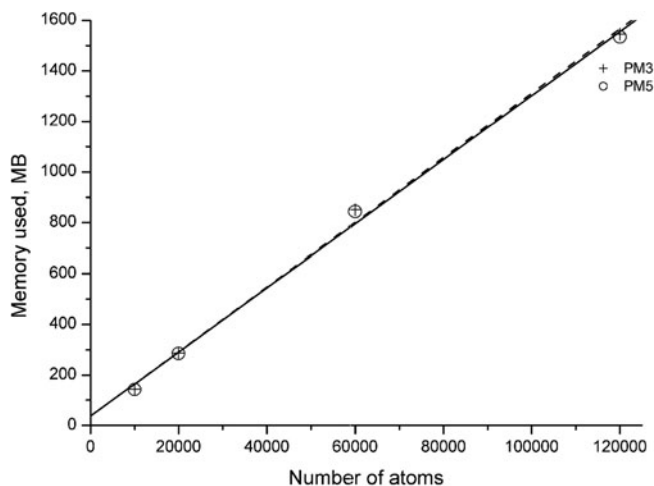


Figure 15-4. LocalSCF scaling of required memory over number of atoms for PM3 and PM5 Hamiltonians

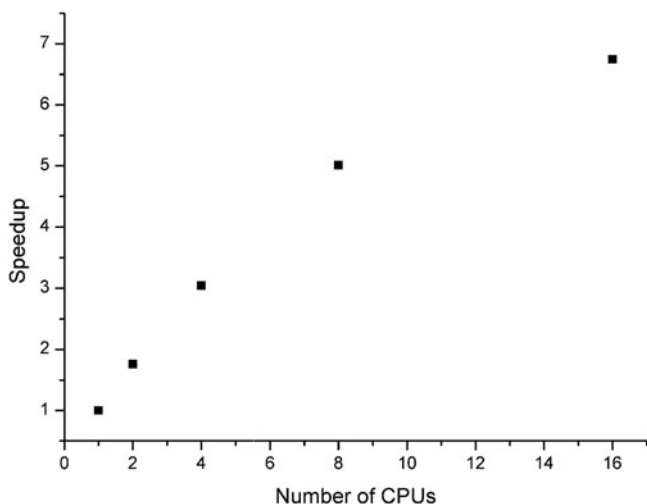


Figure 15-5. Scalability of parallel LocalSCF calculation of GroEL-GroES chaperonin complex

3,700 computer equipped with Intel Itanium2 1.5 GHz CPUs and 256 GB RAM, running under GNU Linux. Calculation time was measured for 5 cycles of all-atom geometry optimization and the speedup factor as a function of the number of utilized CPUs is presented in Figure 15-5.

Considering the general complexity of parallelization of quantum-mechanical codes the presented scalability is quite satisfactory. The scalability is almost linear up to 8 processors and shows less efficient CPU utilization when the number of processors reaches 16. After that point adding more processors to the job is likely not going to further speedup the calculation in the present software implementation.

15.3.2. Accuracy of the Linear Scaling Algorithm

The linear scalability of the LocalSCF method is a direct consequence of using CMOs in contrast to delocalized MOs employed in conventional SCF methods. Although the individual CMOs have different size in terms of their AO expansion, they are significantly shorter than conventional MOs and less extended than MOZYME LMOs. This fact may raise a concern how reliable are the computational results obtained on such short CMOs and from the LocalSCF calculations in general?

To study this matter we performed gas-phase AM1 calculations of proinsulin (PDB id 1EFE) protein containing 60 amino acids and representing the system of 1,034 atoms. This is a large system for running semiempirical matrix diagonalization calculations but still affordable as fitting into 1 Gb memory limit so calculations on this system by using MOPAC program [20] would not be too difficult. The protonation state of the titratable amino acids was determined at pH=7 and resulted in

the total charge of +1 electron units for the protein. The protein consists of 6 positively charged amino acids (ARG, LYS) and 5 negatively charged amino acids (ASP, GLU). The two histidines present in the protein were modeled in neutral state. The original protein structure was designated as conformation A. The conformation B was obtained by rotating sidechain of TYR26 by 30 degrees toward the hydrophobic protein core.

TYR26 is located at the boundary of the hydrophobic core of proinsulin and has sufficient rotational degree of freedom which won't create unfavorable short contacts to other amino acids due to the applied sidechain rotation. At the same time the proximity of TYR26 to other amino acids will make the conformational change in TYR26 sidechain visible on potential energy profile of the protein. By introducing this small conformational perturbation to TYR26 sidechain we model energetically accessible structural changes which protein samples during the course of molecular dynamics simulation. Now we want to know how well the energy difference between the two protein conformations as computed by matrix diagonalization will be reproduced by the linear scaling LocalSCF method and its underlying VFL approximation. The structurally different parts of the overlaid conformations A and B are displayed in Figure 15-6 with the rest of the systems hidden from the view.

Matrix diagonalization calculations of the two protein conformations were performed by using MOPAC with default settings. Initial attempts to perform MOPAC

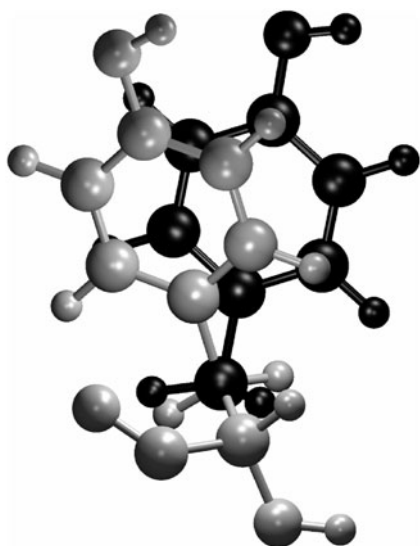


Figure 15-6. The structurally different parts of overlaid conformations A and B of proinsulin. The A (native) conformation is shown in gray. The B conformation having TYR26 sidechain rotated by 30 degrees toward protein hydrophobic core is shown in black

SCF calculations were unsuccessful due to convergence problems. As our computational practice demonstrates, gas-phase matrix diagonalization calculations of proteins having high content of ionizable amino acids (ARG, LYS, GLU, ASP) show systematic convergence problems. These problems worsen with the increasing number of ionized amino acids in the system and with the increasing number of atoms, and are related to insufficient quality of the generic initial guess. Therefore the density matrix computed by the final LocalSCF method had to be supplied as an initial guess to the MOPAC jobs. After that MOPAC jobs converged in 9 SCF iterations. Using final LocalSCF density matrix as initial guess made the MOPAC calculation looking artificially faster than it would be in the normal case when starting from the generic initial guess. Therefore MOPAC calculation time was projected to 50 SCF iterations in order to obtain a more realistic time estimate. Although the number 50 is based on a pure guesswork its value is absolutely unimportant because even for the absolutely artificial case of MOPAC converging in 9 iterations the LocalSCF computation would still be faster by factor of 10 than the superficial matrix diagonalization (see Table 15-1).

LocalSCF calculations were performed in two modes. One was performed with default program settings, as discussed above, and the second one with tight SCF convergence criterion. These calculation modes are denoted in Table 15.1 with labels *def* and *acc*, respectively. In the accurate mode all the SCF parameters except for the diagonal density matrix elements (dQthr) were intentionally set to such small values so these conditions cannot be satisfied. This forced the VFL SCF micro-iteration convergence to the remaining criterion of dQthr = 0.0003 electron units. The number of CMO expansion steps was limited to 5 and the expansion criterion thrDer1 was set to the negligibly small value of 10^{-8} . In the factual absence of the energy criterion all the possible CMO expansions found by the proximity criterion were

Table 15-1. Comparison of LocalSCF in default (def) and accurate (acc) modes with matrix diagonalization (MOPAC) on proinsulin conformations A and B using AM1 Hamiltonian

Property	MOPAC	LocalSCF (def)	LocalSCF (acc)
HOF ^a , kcal/mol	-4,509.82	-4,498.29	-4,509.27
E _{conf} ^b , kcal/mol	-8.78	-8.83	-8.78
ΔQ ^{a,c} , a.u.	N/A	0.004	0.004
Dipole moment ^a , D	241.45	239.55	239.44
ΔGradient ^{a,d} , kcal/(mol*Å)	N/A	0.34	0.04
MO size ^{a,e}	1,034	23	85
Memory ^a , MB	1,061	25	30
CPU time ^f , s	5,652	46	123

^aConformation A.

^bE_{conf} = HOF_A - HOF_B.

^cRoot mean square difference in atomic charges using MOPAC charges as reference.

^dRoot mean square difference in geometry gradients using MOPAC gradients as reference.

^eAverage size of MOs by the number of atomic centers in their AO expansion.

^fMOPAC calculation time is projected to 50 SCF iterations.

accepted. We also tightened the orthogonality criterion to 10^{-8} and increased the cut-off for exchange interactions and for the product of Fock matrix with CMOs to 20 Å.

For the analysis of accuracy of the LocalSCF method we selected heat of formation (HOF), conformational energy, partial atomic charges, dipole moment, and geometry gradients, with the results summarized in Table 15-1. As it was mentioned before, LocalSCF in default mode underestimates the absolute value of heat of formation. In this example the heat of formation is underestimated by 11.53 kcal/mol. However, all other properties are reasonably well reproduced in the default calculation mode. The conformational energy, partial atomic charges and dipole moment are in good agreement with the corresponding matrix diagonalization results. Satisfactory agreement is also obtained for geometry gradients with root means square difference of only 0.34 kcal/(mol*Å).

The LocalSCF CMOs in proinsulin, when obtained in default mode comprise 23 atomic centers on average. For comparison the size of delocalized MOs in the matrix diagonalization calculation of proinsulin is 1,034 atomic centers. The use of short CMOs in LocalSCF is the primary reason for underestimation of the absolute value of the heat of formation. Since absolute energy values are of limited use in biomolecular calculations and because the relative properties are accurately reproduced, the default settings in LocalSCF represent a reasonable balance of accuracy vs. performance. The most significant advantage of the obtained speedup is making feasible QM MD calculations of large systems, which will be discussed in a separate section.

The LocalSCF method does not preclude the user from accessing the matrix diagonalization energy limit. In the situations when absolute value of energy or highly accurate geometry gradients are needed one can resort to somewhat larger CMOs. The computational results corresponding to such (accurate) mode are presented in Table 15-1. In the accurate mode the average CMO size grew up to 85 atomic centers. This immediately improved the agreement in the absolute value of heat of formation from 11.53 to 0.55 kcal/mol. Similarly the root mean square difference in geometry gradients dropped from 0.34 to 0.04 kcal/(mol*Å). This is obtained at the cost of 2.7-times slower calculations than the default LocalSCF mode, which is acceptable considering very high performance of the method. The calculation time of the accurate LocalSCF mode is still better by the factor of 46 in comparison to the matrix diagonalization calculation. This is a remarkable speed up considering the fact that the system consisting of 1,034 atoms is quite small by biophysical standards. Since the LocalSCF method is linear scaling the level of speed up will be even more impressive when going to real-size biological systems encountering tens of thousands of atoms.

The performed validations tests using just two protein conformations do not sufficiently evaluate the conformational energy profile of the protein. Although running LocalSCF calculations over an extensive set of protein snapshots is a trivial matter, there are obvious technical difficulties in collecting the reference data using matrix diagonalization due to high computational cost of such calculations. As a compromise, we performed a validation test on 20 proinsulin conformations [14].

In contrast to the use of a completely dry protein as in the above calculations the new computations included 100 water molecules placed in vicinity of the ionized residues of the proinsulin. This greatly improved stability of the QM calculations. Indeed, zwitter-ionic forms of amino acids are unstable in gas-phase resulting in artificially high polarization making meaningless such QM calculations. Attempts to relax gas-phase structure by means of QM calculation produce a number of computational artifacts, including disruption of covalent bonds due to hydrogen atom abstraction by anionic centers. Our experience of applications of QM methods to biological systems suggests that proteins in gas-phase cannot have the same ionization state as they have in water. This is not a limitation of the QM methods but rather a valuable lesson. It shows the limits of the classical mechanical models where the notion of protein ionization state originally came from.

According to the performed calculations on the 20 proinsulin snapshots, AM1 and PM3 conformational energy differences were 0.41 and 0.29 kcal/mol, respectively [14]. Dipole moment differences were within 0.1 Debye in both cases. The RMS difference on partial atomic charges was about 0.0003 electron units. The obtained better agreement with the matrix diagonalization data in comparison to our previous tests should be attributed to the water solvation of ionized protein sites and to the use of slightly better SCF convergence criteria.

Now when the general performance and accuracy of the LocalSCF method have been sufficiently established on the relatively small system consisting of a thousand of atoms we may consider performing validation tests on larger systems. Since in typical biomolecular simulation the simulation box often consists of tens of thousands of atoms we need to prepare a comparable system by the number of atoms. For that purpose we placed proinsulin in a water box with the walls extending on at least 10 Å in each direction from the nearest protein atom. The system was neutralized by adding a chloride counterion. 20 snapshots of this system consisting of 20,058 atoms were generated using classical force field MD [14]. Since running matrix diagonalization on such large system is beyond the reach of the readily available computer hardware, the reference data were obtained by running LocalSCF calculation while treating all Coulomb integrals explicitly. Since such calculation scales quadratically with the number of atoms it cannot be used in massive calculations. However, high accuracy of this computation mode and relatively low computational demand make it suitable to generate the reference data to test the quality of the faster LocalSCF calculation modes.

For large systems the LocalSCF program includes the capability to treat long-range Coulomb interactions via the linear scaling FMM method. For the system of 20,058 atoms the FMM provides 9-fold speed up when using AM1 Hamiltonian. Total memory requirement is 256 and 283 MB when using AM1 and PM3 Hamiltonians, respectively. Since the modern desktop computers are equipped with gigabytes of memory we have sufficient room to treat hundreds of thousands of atoms at QM level on a commodity computer using the LocalSCF method.

Following is a brief analysis of the obtained results for the 20,058 atoms' system. The accuracy of calculation of partial atomic charges still remained high with

the root mean square difference of 0.0016 electron units for AM1 and 0.0003 for PM3 Hamiltonian. The difference in dipole moment increased to 1.1 and 0.2 Debye for AM1 and PM3, respectively, with PM3 again showing better numerical agreement with the reference data. More noticeable differences were accumulated in conformational energy. AM1 showed 5.4 kcal/mol difference while PM3 resulted in 1.9 kcal/mol difference against the reference data. Although reaching a better numerical accuracy in conformational energy would be desirable the obtained values are still quite satisfactory considering that the comparable MOZYME calculations gave 25.5 and 23.8 kcal/mol differences for AM1 and PM3 Hamiltonians, respectively.

Overall, the QM energy calculations of the 20,058 atoms system taking only about 1 h of a single-processor time make feasible massive exploration of biological problems based on QM principles. This marks a turning point on the front line of biological simulations where for a long time only classical mechanics methods were practically affordable.

15.3.3. Validation of QM Molecular Dynamics

Making feasible all-atom quantum-mechanical calculations of large molecular systems is an important step toward better understanding the physics of biological macromolecules. The all-QM approach to biological systems is particularly important in the light of recent studies showing significant differences between classical mechanical and QM description of electrostatic interactions [23]. The charge transfer effects, which are omitted in the classical mechanics model, influence the structural dynamics profile of biomolecules and must be taken into account when targeting the accurate picture at atomic resolution. The net amino acid charges determined from QM MD trajectory show their dependence on particular amino acid environment. This disagrees with the practice of assignment of unified unit charges to amino acids in classical mechanics, based on mean field approximation. Such unification is a sound approach when dealing with isotropic bulk liquids where the mean field approximation has a solid theoretical ground but becomes problematic for biomolecules which are highly anisotropic systems. The fixed-charge electrostatic model and the mean field approximation average out important atomistic details, which are anisotropic by definition, and uncovering which is the sole purpose of biomolecular simulations.

The global character of charge transfer also places certain limits on the range of applicability of hybrid QM/MM schemes representing a rapidly growing theoretical approach to biomolecular simulation [24]. To account for charge transfer effects the entire macromolecular system including protein and solvent should be treated at QM level.

The feasibility of treating large systems entirely at QM MD level is an important advantage of the LocalSCF method. Though, this is still largely unexplored area. There is no sufficient information on how large systems can be treated at QM MD level and what length of simulation time can be approached. These questions will be addressed although at limited degree in the present article.

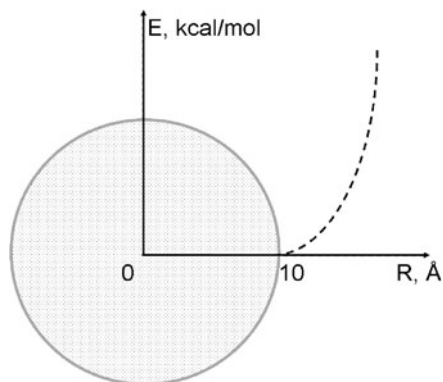


Figure 15-7. Schematic representation of the half-shoulder spherical boundary potential. The energy due to the potential is shown by dashed line. It is zero inside the sphere of radius of 10 Å and has harmonic shape outside the droplet walls

For the purpose of this study we built a spherical water droplet having the radius of 10 Å. This system contained 144 water molecules or 432 atoms. To prevent the water molecules leaving the droplet due to their kinetic energy during the dynamics run we added a half-shoulder harmonic spherical boundary potential (SBP) with force constant of 10 kcal/(mol*Å). The SBP potential has zero value inside the sphere of the radius of 10 Å while it gently pushes back the water molecules attempting to cross the spherical boundary. The potential is applied to non-hydrogen atoms only in order to minimize its influence on rotational degrees of freedom of water molecule. The schematic picture of the SBP potential is given in Figure 15-7.

Using the droplet model to represent water solvation has obvious disadvantages over the use of periodic boundary condition (PBC). However the SBP model is simple to implement and it is computationally more attractive than the PBC model. This is the reason why we selected the SBP model for validation of the following QM MD calculations.

The water droplet can be simulated using various types of dynamics. First in the list is constant volume – constant energy NVE molecular dynamics, generating microcanonical ensemble of configurations. NVE is the simplest form of molecular dynamics, which can be obtained by direct solution of the Newton second law equations separately written for each dynamic particle in the system Eq. (15-16). It describes a closed system so no mass or heat exchange with the environment is possible. Since the particles are bound by potential forces that keep them sticking together the volume occupied by the system remains constant during the simulation after reaching the equilibrium state. Though, strictly speaking the rigorous definition of volume requires the presence of walls, like in PBC conditions. No mechanism is available in the NVE dynamics to maintain constant temperature of the system. The NVE Hamiltonian (H) consists of kinetic (K) and potential (U) energy terms each being a function of N particles having coordinates r

$$H = K(r^N) + U(r^N) \quad (15-18)$$

The microcanonical ensemble generated by NVE dynamics is not consistent with experimental measurements which are typically performed at constant temperature condition. Therefore practically more useful is isochoric-isothermic molecular dynamics, abbreviated as NVT, which keeps temperature fluctuating around the target value, T_0 . The most popular scheme to achieve temperature stabilization while generating a canonical ensemble is the Nose-Hoover algorithm [25] which extends the Hamiltonian by adding a virtual degree of freedom, s , associated with thermostat (aka thermostat coordinate), and which is considered as a dynamic variable

$$H = \frac{1}{2} \sum_i^N m_i (s \cdot \dot{r}_i)^2 + U(r^N) + \frac{1}{2} Q \dot{s}^2 + (3N + 1) k_B T_0 \ln(s) \quad (15-19)$$

where Q is a thermostat coupling parameter (aka thermostat mass), k_B is Boltzmann's constant. In this equation the particle velocities (determining temperature) are scaled by the parameter s at each time step and the degree of coupling of the real particles with the thermostat is determined by the parameter Q .

With the NVT dynamics and uniform velocity rescaling it may happen that due to accumulation of numerical errors the thermostat may start redirecting the kinetic energy from high-frequency modes to the rigid-body rotation and translation degrees of freedom of the droplet, which are not coupled to the internal degrees of freedom of the systems. When happened it would break the momentum conservation thus leading to the "flying ice cube" problem [26]. This is a serious problem when attempting hundreds of picoseconds long NVT simulation of a droplet system under SBP boundary condition. To avoid such problem one would need to apply thermostat equations to internal velocities which provide an explicit mechanism to maintain momentum conservation. Working with internal velocities vs. real ones brings additional computational overhead. A simpler solution is to resort to Langevin dynamics given by the modified Newton equation

$$m_i \ddot{r}_i = - \frac{\partial E(r^N)}{\partial r_i} - \gamma_i m_i \dot{r}_i + R(t) \sqrt{2m_i \gamma_i k_B T_0} \quad (15-20)$$

where $R(t)$ is an uncorrelated Gaussian distribution with zero-mean, and γ_i time-independent friction parameters. The random collisions of the real atoms with imaginary solvent molecules eliminate the possibility for an unphysical kinetic energy distribution over the degrees of freedom. It also introduces solvent viscosity into the dynamic equations. Langevin dynamics is a popular method of choice when dealing with molecular clusters in the absence of PBC conditions. On the negative side of the Langevin dynamics is its time-irreversible and non-deterministic character but its numerical stability and the simple way to account for the solvent viscosity outweigh the deficiencies.

Correspondingly we performed 1 ns Langevin dynamics of the water droplet under the SBP condition. During the simulation the temperature was maintained at

300 K and the friction parameter was set to 10 ps^{-1} . The dynamics equations were integrated with the timestep of 1 fs. No constraints were applied to bonds involving hydrogen atoms. First 100 ps of the simulation were considered as equilibration while the remainder of the trajectory was saved for analysis. QM simulations were performed using PM5 Hamiltonian. The 1 ns QM MD simulation took 20 days to run on two cores of an Intel Core 2 Duo 3.0 GHz desktop.

The volume of the system was computed based on the sphere radius defined by the most distant oxygen atom from the center of the sphere. During the simulation the volume of the droplet oscillated around the average value of $4,955.10 \text{ \AA}^3$. This corresponds to water density of 0.85 g/cm^3 which, as we can see, is underestimated by PM5.

Important indicator of stability of the simulation method is conservation of the virial of the system. In the presence of only conservative forces, which is our case, the following relation known as the virial theorem must hold

$$2\langle K \rangle + \langle U \rangle = 0 \quad (15-21)$$

The potential energy of the water droplet, $U = U_{\text{int}} + U_{\text{ext}}$, has internal and external components. The internal term is as follows

$$U_{\text{int}} = \sum_i F_{\text{int},i} \cdot r_i = - \sum_i \frac{\partial E}{\partial r_i} \cdot r_i \quad (15-22)$$

where E is the computed QM energy, $F_{\text{int},i}$ is internal force acting on particle i due to other particles. The external component of the potential energy is created by the SBP potential

$$U_{\text{ext}} = \frac{k_0}{2} \sum_i (|r_i| - R_0)^2 \text{ when } |r_i| > R_0; \text{ otherwise } U_{\text{ext}} = 0 \quad (15-23)$$

$$F_{\text{ext}} = -\nabla U_{\text{ext}} = -k_0 \sum_i \left(1 - \frac{R_0}{|r_i|}\right) \cdot r_i \quad (15-24)$$

where R_0 is the radius of the sphere where the restraining force is initiated; F_{ext} is external force with the force constant k_0 ; r_i is atomic coordinate vector. Equation (15-23) and (15-24) assume the origin of the coordinate system being placed at the center of mass of the droplet.

The plot of virial of the system along dynamics trajectory is displayed in Figure 15-8.

Trajectory average of the virial gives the value of -0.6 kcal/mol , which is very close to the expected value of zero thus pointing to stable dynamics.

Having defined the volume of the system we can compute internal pressure inside the droplet based on the virial expression [27, 28]

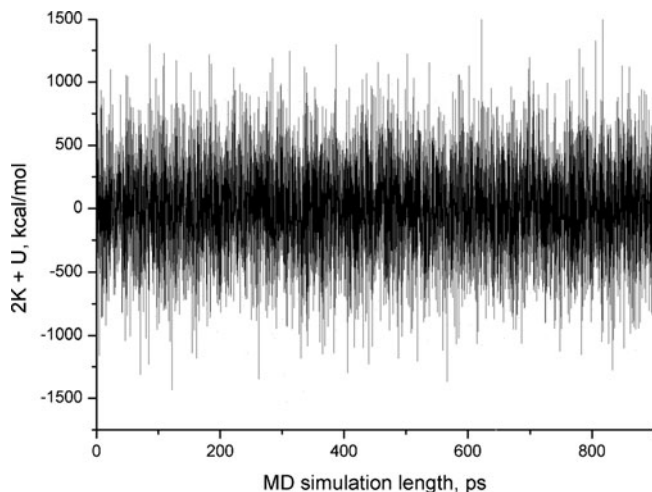


Figure 15-8. Conservation of virial during PM5 MD simulation of water droplet

$$P = \rho k_B T + \frac{1}{3V} \left\langle \sum_i F_i \cdot r_i \right\rangle \quad (15-25)$$

where ρ is number density of particles; k_B is Boltzmann's constant; V is volume of the droplet; F_i is total force acting on particle i due to other particles and soft walls. Equation (15-25) can be rewritten in terms of kinetic and potential energy of the droplet

$$P = \frac{1}{3V} (2K + U) \quad (15-26)$$

Averaging over the dynamics trajectory gives the pressure value of 5.7 atm, which is relatively close to the normal pressure of 1 atm. Using a larger system would make the pressure determination more reliable.

Since the SBP boundary condition introduces distinct volume one may use it to derive a true constant temperature-pressure NPT dynamics. Following the standard approach [29] it is possible to consider volume as another dynamic variable and formulate the corresponding dynamic equations. However, exploring this venue goes beyond the limits of the current article.

15.4. CONCLUDING REMARKS

Linear scaling LocalSCF method provides a valuable alternative to matrix diagonalization when dealing with large molecular systems. It shows about 50-fold speedup over matrix diagonalization already on such small system as 1,034 atoms proinsulin. As a result, QM calculations of hundreds of atoms systems can be readily conducted

on commodity computers. Validation tests confirm good accuracy of the linear scaling computations on partial atomic charges, dipole moments, conformational energies and geometry gradients.

The most significant value of the linear scaling LocalSCF method is the feasibility of running QM MD of biological systems thus advancing the computational biophysics beyond the fixed charge approximation. The presented spherical boundary potential is a computationally economical approach for explicit treatment of water in QM biomolecular dynamics. The 1 fs integration time step makes feasible accumulating hundreds of picoseconds or even nanosecond long trajectories on the modern hardware by utilizing parallel processing capabilities.

The performed water dynamics using PM5 Hamiltonian showed the need to further improve the condensed phase properties of water. The accumulated speedup due to the linear scaling LocalSCF method provides the necessary technical means to succeed in such effort and to move on with the development of accurate biologically oriented semiempirical Hamiltonians.

REFERENCES

1. Goedecker S (1999) Linear scaling electronic structure methods *Rev Mod Phys* 71:1085–1123
2. Goedecker S, Scuseria GE (2003) Linear scaling electronic structure methods in chemistry and physics *Comp Sci Eng* 5:14–21
3. McCammon JA, Gelin BR, Karplus M (1977) Dynamics of folded proteins *Nature* 267:585–590
4. Anikin NA, Anisimov VM, Bugaenko VL et al. (2004) LocalSCF method for semiempirical quantum-chemical calculation of ultralarge biomolecules *J Chem Phys* 121:1266–1270
5. Anisimov VM, Bugaenko VL (2009) QM/QM docking method based on the variational finite localized molecular orbital approximation *J Comp Chem* 30:784–798
6. Szabo A, Ostlund NS (1996) *Modern quantum chemistry*, Dover, New York, NY
7. Roothaan CCJ (1951) New developments in molecular orbital theory *Rev Mod Phys* 23:69–89
8. Hall GG (1951) The molecular orbital theory of chemical valency. VIII. A method of calculating ionization potentials *Proc Roy Soc, London A*205:541–552
9. Greengard LF (1988) *The rapid evaluation of potential fields in particle systems*, MIT Press, Cambridge, MA
10. Stewart JJP (1996) Application of localized molecular orbitals to the solution of semiempirical self-consistent field equations *Int J Quant Chem* 58:133–146
11. Dixon SL, Merz KM Jr (1996) Semiempirical molecular orbital calculations with linear system size scaling *J Chem Phys* 104:6643–6649
12. Lee T-S, York DM, Yang W (1996) Linear-scaling semiempirical quantum calculations for macromolecules *J Chem Phys* 105:2744–2750
13. Yang W, Lee T-S (1995) A density-matrix divide-and-conquer approach for electronic structure calculations of large molecules *J Chem Phys* 103:5674–5678
14. Anisimov VM, Bugaenko VL, Bobrikov VV (2006) Validation of linear scaling semiempirical localSCF method *J Chem Theory Comput* 2:1685–1692
15. Tuckerman ME, Martyna GJ (2000) Understanding modern molecular dynamics: Techniques and applications *J Phys Chem B* 104:159–178
16. Berman HM, Westbrook J, Feng Z, et al. (2000) The protein data bank *Nucl Acids Res* 28:235–242
17. Bugaenko VL, Bobrikov VV, Andreyev AM, et al. (2005) LocalSCF, Fujitsu Ltd, Tokyo

18. White CA, Head-Gordon M (1994) Derivation and efficient implementation of the fast multipole method *J Chem Phys* 101:6593–6605
19. Stewart JJP (1989) Optimization of parameters for semiempirical methods I. Method. *J. Comp. Chem.* 10:209–220
20. Stewart JJP (2002) Mopac 2002, Fujitsu Ltd, Tokyo
21. Stewart JJP (2007) Optimization of parameters for semiempirical methods V: Modification of NDDO approximations and application to 70 elements *J Mol Model* 13:1173–1213
22. Dewar MJS, Zoebisch EG, Healy EF, et al. (1985) Development and use of quantum mechanical molecular models. 76. AM1: A new general purpose quantum mechanical molecular model *J Am Chem Soc* 107:3902–3909
23. Anisimov VM, Bugaenko VL, Cavasotto CN (2009) Quantum mechanical dynamics of charge transfer in ubiquitin in aqueous solution *Chem Phys Chem* 10:3194–3196
24. Altoè P, Stenta M, Bottoni A, et al. (2007) A tunable QM/MM approach to chemical reactivity, structure and physico-chemical properties prediction *Theor Chem Acc* 118:219–240
25. Hoover WG (1985) Canonical dynamics: Equilibrium phase-space distributions *Phys Rev A* 31:1695–1697
26. Harvey SC, Tan RKZ, Cheatham III TE (1998) The flying ice cube: Velocity rescaling in molecular dynamics leads to violation of energy equipartition *J Comp Chem* 19:726–740
27. Hummer G, Gronbeck-Jensen N, Neumann M (1998) Pressure calculation in polar and charged systems using Ewald summation: Results for the extended simple point charge model of water *J Chem Phys* 109:2791–2797
28. Winkler RG (2002) Virial pressure of periodic systems with long range forces *J Chem Phys* 117:2449–2450
29. Martyna GJ, Tuckerman ME, Tobias DJ et al. (1996) Explicit reversible integrators for extended systems dynamics *Mol Phys* 87:1117–1157

CHAPTER 16

DENSITY MATRIX METHODS IN LINEAR SCALING ELECTRONIC STRUCTURE THEORY

ANDERS M. N. NIKLASSON

Theoretical Division, Los Alamos National Laboratory, Los Alamos, NM 87545, USA; Applied Materials Physics, Department of Materials Science and Engineering, Royal Institute of Technology, SE-100 44 Stockholm, Sweden, e-mail: amn@lanl.gov

Abstract: We review some recursive Fermi operator expansion techniques for the calculation of the density matrix and its response to perturbations in tight-binding, Hartree-Fock, or density functional theory, at zero or finite electronic temperatures. Thanks to the recursive formulation, the expansion order increases exponentially with the number of iterations and the computational cost scales only linearly with the system size for sufficiently large sparse matrix representations. The methods are illustrated using simple models that are suitable for small numerical experiments.

Keywords: Eigenvalue problem, Electronic structure theory, Density functional theory, Density matrix, Linear scaling

16.1. INTRODUCTION

Computational materials science, chemistry and biology, are rapidly being transformed by a quest for accuracy, speed, and reduced complexity. The development is driven by the continuous increase of available computer capacity, where traditional techniques become obsolete when they fail to fully utilize improved processing power. The bottle neck is the scaling of the arithmetic cost with the number of atoms. Typically, the cost of first principles calculations that are based on tight-binding, Hartree-Fock [1], or density functional theory [2, 3], scales with the cube, $\mathcal{O}(N^3)$, of the system size N . To increase the number of atoms by a factor of 10 therefore requires an improvement of the computational capacity by a factor of 1,000. Only by reducing the scaling of the arithmetic cost is it possible to take full advantage of increased processing power. A new computational paradigm has therefore emerged in electronic structure theory, where no significant part of a calculation is allowed to increase more than linearly, $\mathcal{O}(N)$, with the system size. The linear scaling paradigm holds the promise of a revolution in atomistic simulation,

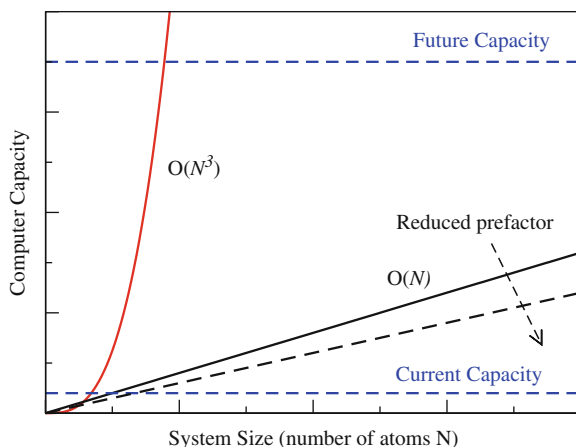


Figure 16-1. A computational forecast of reduced complexity $\mathcal{O}(N)$ algorithms for electronic structure calculations. Linear scaling electronic structure theory in large scale calculations will increase in importance as the computational capacity continues to improve in comparison to conventional $\mathcal{O}(N^3)$ methods

allowing reliable large scale calculations involving millions of atoms that are based directly on the first principles of quantum mechanics. The high expectations are clearly seen in the recent developments of high-performance linear scaling electronic structure codes such as Siesta, Conquest, FreeON, Ergo, Latte, Open-MX, Femteck, and Onetep [4–11].

Looking at a computational forecast, it is easy to predict that only methods that can maintain efficiency with increased processing power will be of interest in future large-scale first principles simulations. Figure 16-1 shows the schematic picture of the required computer capacity as a function of system size. With the current capacity, most linear scaling algorithms has an advantage, but for self-consistent density functional or Hartree-Fock based $\mathcal{O}(N)$ methods, this advantage is still fairly small because of the large computational prefactor associated with most linear scaling algorithms. However, as the trend in computational development continues, with cheaper and faster processors, the importance of linear scaling electronic structure theory will become paramount, regardless of prefactor complexity.

Probably one of the first practical methods in linear scaling electronic structure theory goes back to the Green's function recursion method by Haydock [12–14] based on the pioneering work of Lanczos [15]. However, it was not until over a decade later [16–30] when linear scaling electronic structure theory became a more independent discipline of broader general interest. There are several excellent reviews of linear scaling methods [31–36]. The purpose of this chapter is to present a fairly recent class of recursive Fermi-operator expansion methods for the solution of the quantum mechanical eigenvalue problem [28, 30, 37, 38, 39–44] that are based on, or related to, density matrix purification [28, 45] or the corresponding sign-matrix methods [37, 46, 47]. In contrast to Chebyshev or Green's

function expansion schemes [21, 22, 26, 48, 49] these methods do not allow a general operator expansion, instead they are tailored specifically only for the Fermi function at finite electronic temperatures or the corresponding step function at zero temperatures. The recursive Fermi operator expansion methods reviewed in this chapter provide a very rapid convergence, similar to fix point iterations used for solving non-linear equations, and they have a linear scaling cost for non-metallic systems with a fairly small prefactor also for three-dimensional structures. They have been implemented as stand alone techniques or as options in a number of different self-consistent linear scaling electronic structure codes, such as FreeON [6], Ergo [50, 51], Latte [8], Siesta [42], and Conquest [5]. The recursive Fermi operator expansion approach also forms the basis of a density matrix perturbation theory [52] that can be used as an efficient $\mathcal{O}(N)$ alternative to Rayleigh-Schrödinger or Green's function perturbation theory for the calculation of static response properties [53–57]. Apart from the recursive Fermi operator expansion methods there are a number of alternative $\mathcal{O}(N)$ techniques based on constrained functional minimization with respect to the density matrix [17, 18, 29, 58–60] or the wavefunctions [19, 20, 23, 61–66]. These methods will not be discussed here.

The computational tasks in first principles electronic structure theory can generally be divided in two parts: (a) the construction of the effective single-particle Hamiltonian, i.e. the Fockian or the Kohn-Sham Hamiltonian, and (b) the solution of the single-particle eigenvalue problem. Thanks to the efficiency of the fast Fourier transform [67, 68], fast multipole methods [69–72], quantum chemical tree-codes [73, 74], and reduced complexity schemes for exchange calculations [75–78], the Hamiltonian can be calculated, using localized basis-set representations, with a cost that scales only linearly with the system size for sufficiently large problems. The second part, the eigenvalue problem, is less straightforward to solve within $\mathcal{O}(N)$ complexity and a broad variety of different approaches exist that are more or less efficient for different systems. The linear scaling ability can here be analyzed from Kohn's concept of nearsightedness [58, 79]. An electronic system at elevated electronic temperatures, or with a gap, can be described by Wannier functions that decay exponentially as a function of interatomic distance [80, 81]. At each point in space, only the contribution inside some system-size-independent local interaction zone has to be included in the electronic description. Because of this electronic locality the complexity of the solution scales only linearly with the system size, which allows, at least in principle, calculations of the solution, defined by the eigenvalue problem, which scale only linearly with the total number of atoms. For metallic systems the Wannier functions decay only algebraically and the localization is effectively lost. It should be noted that using local interaction zones through an *ad hoc* cut and paste or divide and conquer approach often leads to a very slow convergence with the size of the local zones and to uncontrolled errors, in particular for complex non-homogeneous materials. By using special tailored boundary conditions of the local interaction zones, it is possible to reduce the errors [25, 82, 83, 84]. However, instead of using a “cut and paste” approach, the matrix sparsity of operator representations within a local basis set can be explored. If only matrix elements above some threshold tolerance are included, which is set by, for example, the requirement of rigorous

matrix norm errors [85–87], efficient linear scaling complexity can be reached for Fermi operator expansion methods in which sparse matrix-matrix operations, such as additions and multiplications [88], can be performed in $\mathcal{O}(N)$ within a well controlled accuracy. This is the basic approach followed by the methods reviewed in this chapter.

16.2. THE EIGENVALUE PROBLEM

The key electronic structure problem addressed in this chapter is the quantum mechanical eigenvalue equation,

$$\mathbf{H}\mathbf{v}_i = \varepsilon_i\mathbf{v}_i, (i = 1, 2, \dots) \quad (16-1)$$

which determines the electronic solution. Here \mathbf{H} is the effective single-particle Hamiltonian matrix in tight-binding, Hartree-Fock, or density functional theory, with matrix elements

$$H_{ij} = \int d\mathbf{r}\phi_i(\mathbf{r}) \left(-\frac{1}{2}\nabla^2 + U(\mathbf{r}) \right) \phi_j(\mathbf{r}), \quad (16-2)$$

where $-\frac{1}{2}\nabla^2$ is the kinetic energy operator and $U(\mathbf{r})$ is an effective single-particle potential [89]. $U(\mathbf{r})$ is typically determined by the electronic density as well as the external nuclear potential. This leads to the requirement of a self-consistent solution that can be found by an iterative procedure, where the Hamiltonian is constructed and the eigenvalue problem is solved repeatedly. The column eigenvectors \mathbf{v}_i have components $\{v_i(j)\}_{j=1}^N$ with eigenvalues ε_i . Throughout this chapter we will assume that the underlying basis-set representation, $\{\phi_i(\mathbf{r})\}_{i=1}^N$, is local and orthogonal. In the case of, for example, a nonorthogonal Gaussian basis set representation, it is easy to transform the generalized eigenvalue problem to the orthogonal standard form [90] using the inverse Cholesky or Löwdin factors, \mathbf{Z} , of the overlap matrix,

$$S_{ij} = \int d\mathbf{r}\phi_i(\mathbf{r})\phi_j(\mathbf{r}). \quad (16-3)$$

In a nonorthogonal (no) representation the eigenvalue problem, Eq. (16-1), has the general form,

$$\mathbf{H}^{\text{no}}\mathbf{v}_i^{\text{no}} = \varepsilon_i\mathbf{S}\mathbf{v}_i^{\text{no}}. \quad (16-4)$$

By using the inverse factorization of \mathbf{S} , where

$$\mathbf{Z}^T\mathbf{S}\mathbf{Z} = \mathbf{I}, \quad (16-5)$$

the general nonorthogonal eigenvalue problem can be transformed by the congruence transformation [94],

$$\mathbf{Z}^T \mathbf{H}^{\text{no}} \mathbf{Z} \mathbf{Z}^{-1} \mathbf{v}_i^{\text{no}} = \varepsilon_i \mathbf{Z}^T \mathbf{S} \mathbf{Z} \mathbf{Z}^{-1} \mathbf{v}_i^{\text{no}}. \quad (16-6)$$

With $\mathbf{H} = \mathbf{Z}^T \mathbf{H}^{\text{no}} \mathbf{Z}$ and $\mathbf{v}_i = \mathbf{Z}^{-1} \mathbf{v}_i^{\text{no}}$ the standard eigenvalue problem in Eq. (16-1) is recovered. The inverse Cholesky factors can be calculated in a number of different ways such that the cost scales only linearly with system size for sufficiently large sparse problems [91–98]. In this chapter we assume that $S_{ij} = \delta_{ij}$ or that a congruence transformation has been performed.

Solving the eigenvalue problem in Eq. (16-1) by a conventional diagonalization method [90] usually has a computational cost that scales $\mathcal{O}(N^3)$. Because of the expensive cubic scaling of the arithmetic cost a straightforward diagonalization for the solution of the eigenvalue equations is thus prohibitively expensive for large quantum problems. A key observation behind most linear scaling electronic structure schemes is that the *individual* eigenvalues and eigenvectors in Eq. (16-1) are not needed. In fact, typically, only the sum of the occupied eigenvalues (the single-particle band structure energy),

$$E_s = \sum_{i \in \text{occ}} \varepsilon_i, \quad (16-7)$$

and the density,

$$n(\mathbf{r}) = \sum_{i \in \text{occ}} |\Psi_i(\mathbf{r})|^2, \quad (16-8)$$

are required, where the electronic eigenfunctions $\Psi_i(\mathbf{r})$ are given from the basis functions and the eigenvectors, i.e.

$$\Psi_i(\mathbf{r}) = \sum_j v_i(j) \phi_j(\mathbf{r}). \quad (16-9)$$

This observation leads to a tremendous simplification. In particular, the single-particle density matrix,

$$\mathbf{P} = \sum_{i \in \text{occ}} \mathbf{v}_i \mathbf{v}_i^T, \quad (16-10)$$

or its real space representation

$$P(\mathbf{r}, \mathbf{r}') = \sum_{i \in \text{occ}} \Psi_i(\mathbf{r}) \Psi_i(\mathbf{r}') = \sum_{k,l} P_{k,l} \phi_k(\mathbf{r}) \phi_l(\mathbf{r}'), \quad (16-11)$$

provides a very useful tool for most calculations. For example, once the density matrix is known, the electron density is determined by the diagonal part of the real space representation,

$$n(\mathbf{r}) = P(\mathbf{r}, \mathbf{r}), \quad (16-12)$$

and the single-particle energy is given by the matrix trace,

$$E_s = \text{Tr}[\mathbf{PH}] = \sum_{i \in \text{occ}} \varepsilon_i. \quad (16-13)$$

As will be discussed in this chapter, the density matrix can be constructed from a Fermi operator expansion of the Hamiltonian without calculating the individual eigenvalues and eigenfunctions. By exploiting quantum locality, which gives rise to sparse matrix representations of the density matrix in a local basis, efficient electronic structure calculations can be performed, which have a computational cost that scales only linearly with the system size. Density matrix formalism has become a key ingredient of linear scaling electronic structure theory.

16.3. QUANTUM LOCALITY AND DISORDER

Electronic locality or nearsightedness, which manifests itself in sparse matrix representations of the density matrix in a local basis set, is a key feature necessary for most $\mathcal{O}(N)$ methods. There are a number of studies of the locality of the electronic solutions in materials, which can be measured by the localization of the density matrix $P(\mathbf{r}, \mathbf{r}')$ as a function of interatomic separation [48, 79, 80, 99–102]. Two different types of underlying localization mechanisms are usually discussed: (a) the formation of a gap at the chemical potential and, (b) fractional occupation of the single-particle states at finite electronic temperatures. These two mechanisms of electronic localization have been discussed rather extensively in a number of articles and reviews. In molecular systems the existence of a gap is the most important property for localization since the electronic temperature then typically has very little effect. However, there is a third localization mechanism that has received little attention in connection to linear scaling electronic structure theory. The third mechanism is localization due to disorder. This mechanism, which in its strong limit is related to the famous Anderson localization proposed over 50 years ago [103], is fairly easy to illustrate. Let's start with a simple periodic one-dimensional free electron Hamiltonian matrix,

$$\mathbf{H} = -\frac{1}{2} \begin{pmatrix} -2 & 1 & 0 & 0 & \dots & 1 \\ 1 & -2 & 1 & 0 & \dots & 0 \\ 0 & 1 & -2 & 1 & \dots & 0 \\ \vdots & \vdots & \vdots & \vdots & \ddots & \vdots \\ 1 & 0 & \dots & 0 & 1 & -2 \end{pmatrix}. \quad (16-14)$$

This Hamiltonian yields a density matrix at $T_e = 0$ that has a slow algebraic decay. By introducing a random perturbation of the diagonal elements,

$$\mathbf{R} = \begin{pmatrix} r_{1,1} & 0 & 0 & 0 & \dots \\ 0 & r_{2,2} & 0 & 0 & \dots \\ 0 & 0 & r_{3,3} & 0 & \dots \\ \vdots & \vdots & \vdots & \vdots & \ddots \end{pmatrix}, \tag{16-15}$$

where $r_{i,i}$ are uniformly distributed random values in the interval $[-1, 1]$, it is possible to create the perturbed Hamiltonian

$$\mathbf{H}' = \mathbf{H} + \alpha \mathbf{R}. \tag{16-16}$$

The amount of disorder is controlled by the size of α . If $\alpha = 0$ the density matrix has a free electron behavior, whereas a localization occurs for values of α above some threshold. Disorder automatically provides an intrinsic decoherence of the quantum state to a more localized “classical” density matrix. The effect may be understood from the perspective of phase cancellation. The perturbation creates random phase shifts in the wavefunctions, which lead to cancellations of their long-range decay through destructive interference. In numerical experiments, the localization from randomness is a simple and practical way to construct Hamiltonians, which have localized density matrices that can be calculated with $\mathcal{O}(N)$ complexity. Figure 16-2 shows the decay of the density matrix elements for the one-dimensional free electron Hamiltonian, Eq. (16-14), with 400 states of which 30 are occupied. For the free electron density matrix the magnitude of the matrix elements have a slow algebraic long-ranged asymptotic decay, which is typical for metals. If the random noise

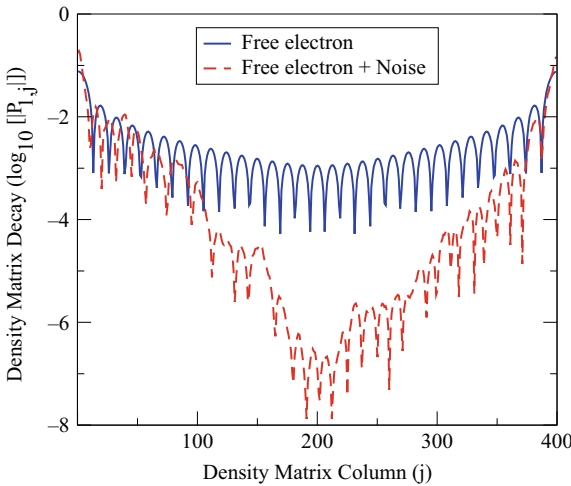


Figure 16-2. The decay of the density matrix elements for the one-dimensional free electron Hamiltonian, Eq. (16-14), with 400 states of which 30 are occupied, with the diagonal noise term in Eq. (16-15) for $\alpha = 0$ or 0.125 in Eq. (16-16)

with $\alpha = 0.125$ is introduced, we find an exponential decay, which provides a localized “nearsighted” solution. The number of non-zero matrix elements above some small numerical threshold will therefore only scale linearly with the system size. This linear scaling property also holds for three-dimensional structures, though the number of non-zero elements per matrix row will be larger. As pointed out previously, quantum locality and matrix sparsity is often critical for efficient linear scaling calculations, which in practice limits the $\mathcal{O}(N)$ Fermi operator expansion methods discussed in this paper to non-metallic materials and local basis set representations. For metallic systems, sufficient locality is in practice reached only at extreme temperatures.

16.4. FERMI OPERATOR EXPANSION

The Hamiltonian and the density matrix at zero electronic temperature, $T_e = 0$, can be expanded in their spectral decompositions,

$$\mathbf{H} = \sum_i \varepsilon_i \mathbf{v}_i \mathbf{v}_i^T \quad (16-17)$$

and

$$\mathbf{P} = \sum_i \theta(\mu_0 - \varepsilon_i) \mathbf{v}_i \mathbf{v}_i^T. \quad (16-18)$$

Here θ is the Heaviside step function and μ_0 is the chemical potential, which separates the occupied states from the unoccupied. From Eqs. (16-17) and (16-18) we find that the density matrix is given as a matrix function of the Hamiltonian,

$$\mathbf{P} = \theta(\mu_0 \mathbf{I} - \mathbf{H}), \quad (16-19)$$

where \mathbf{I} is the identity matrix. Often a specific electronic occupation, N_{occ} , is required, which is given by the trace of the density matrix,

$$Tr[\mathbf{P}] = N_{occ}. \quad (16-20)$$

This canonical condition can be fulfilled by adjusting the chemical potential μ_0 such that it correctly separates the right number of occupied states from the unoccupied. In the more general case, at finite electronic temperatures, $T_e \geq 0$, the step function in Eq. (16-19) is replaced by the Fermi-Dirac function,

$$\mathbf{P} = \left[e^{\beta(\mathbf{H} - \mu_0 \mathbf{I})} + \mathbf{I} \right]^{-1}, \quad (16-21)$$

where $\beta = 1/(k_B T_e)$. Thus, the density matrix can be calculated by a Fermi operator expansion, either at $T_e = 0$, for integer occupation of the states, or at $T_e > 0$, for fractional occupation. An artificial electronic temperature of a few 1,000 K is

sometimes included in molecular dynamics simulations. The temperature smearing of the electronic occupation also helps to improve the self consistency convergence when parts of a system is metallic.

The Fermi operator expansion approach is probably the most straightforward way of calculating electronic structure properties that is able to avoid a full solution of the Hamiltonian eigenvalue problem. By utilizing nearsightedness, which, as discussed above, manifests itself in terms of the exponential decay of $P(\mathbf{r}, \mathbf{r}')$ as a function of $|\mathbf{r} - \mathbf{r}'|$, reduced complexity scaling can be achieved. Because of nearsightedness, both the Hamiltonian and the density matrix will be sparse for non-metallic materials in a local basis set representation. The number of nonzero matrix elements above some numerical threshold then scales only linearly with the number of atoms for sufficiently large problems. By exploring this matrix sparsity, the density matrix can be constructed directly from the Hamiltonian through an expansion of the Fermi function of \mathbf{H} , with a computational cost that scales only linearly with the system size. The only essential operations needed are basic matrix-matrix or matrix-vector multiplications, additions and subtractions. These can all be performed with linear scaling complexity for sufficiently large sparse matrices [88, 104–106]. In the recursive Fermi operator expansion non-zero off-diagonal matrix elements will propagate throughout the calculation and create fill in that reduces matrix sparsity, in particular after each matrix-matrix multiplication. By applying thresholding it is possible to keep the matrix sparse also for complex three dimensional structures within well controlled error bars [40, 85–87].

16.4.1. Chebyshev Expansion

Some of the first linear scaling Fermi operator expansion methods were based on the Chebyshev expansion of the the Fermi function [21, 26, 27, 107–109], where the density matrix is given by the *serial* expansion,

$$\mathbf{P} = c_0 T_0(\mathbf{H}) + c_1 T_1(\mathbf{H}) + c_2 T_2(\mathbf{H}) + \dots \quad (16-22)$$

The c_i coefficients are determined from the condition that

$$(e^{\beta(x-\mu_0)} + 1)^{-1} \approx c_0 T_0(x) + c_1 T_1(x) + c_2 T_2(x) + \dots \quad (16-23)$$

The Hamiltonian must be rescaled such that its eigenvalues are in the interval on convergence, $[-1, 1]$. The Chebyshev polynomials $T_i(\mathbf{H})$ can be constructed from the recurrence relation

$$T_{i+1}(\mathbf{H}) = 2\mathbf{H}T_i(\mathbf{H}) - T_{i-1}(\mathbf{H}), \quad (16-24)$$

where

$$T_0(\mathbf{H}) = \mathbf{I}, \quad (16-25)$$

and

$$T_1(\mathbf{H}) = \mathbf{H}. \quad (16-26)$$

Only sparse matrix-matrix or matrix-vector operations are needed, which all can be performed with linear scaling complexity and in parallel for sufficiently large sparse systems. Another major advantage with the Chebyshev expansion is its numerical stability and its reduced size of Gibbs oscillations that occurs at any finite polynomial expansion order, especially at low electronic temperatures. The technical problem with Gibbs oscillations can be reduced further by including damping that modifies the values of the expansion coefficients, c_i , as in the kernel polynomial method [26, 110]. The Chebyshev method is a grand canonical expansion for a constant chemical potential μ_0 , which has to be known in advance or be adjusted iteratively through multiple expansions to give a density matrix \mathbf{P} that has a given electronic occupation within a canonical ensemble.

16.4.2. Green's Function Expansion

The Chebyshev Fermi operator expansion is a fast and efficient technique that can be applied also to very large problems. However, sometimes very high-order polynomials are needed, which is computationally expensive. For this case Goedecker proposed a rational Fermi operator expansion [22], which constructs the density matrix from a complex contour integration of the Green's function,

$$\mathbf{G}(z_i) = (\mathbf{H} - z_i \mathbf{I})^{-1}, \quad (16-27)$$

for a discrete set of numbers z_i along some path in complex plane. The density matrix is given by the *serial* expansion

$$\mathbf{P} = \sum_i w_i \mathbf{G}(z_i), \quad (16-28)$$

where w_i and z_i are determined from

$$(e^{\beta(\varepsilon - \mu_0)} + 1)^{-1} \approx \sum_i \frac{w_i}{\varepsilon - z_i}. \quad (16-29)$$

The Green's functions $\mathbf{G}(z_i)$ can be calculated using iterative matrix solvers that can utilize matrix sparsity in matrix-matrix or matrix-vector operations to achieve linear scaling complexity in the computational cost for sufficiently large sparse systems. To achieve a specific occupation of \mathbf{P} additional optimization of μ_0 is required.

Related Green's function expansion methods that are combined with the concept of local interaction zones have been developed for a number of linear scaling electronic structure schemes, e.g. [12, 24, 25, 49, 82, 111, 112, 83], of which some can

handle even fairly complex metallic problems such as embedded nanoclusters and substitutional alloys.

16.4.3. Recursive Fermi-Operator Expansion at $T_e > 0$

The Green's function and Chebyshev Fermi operator expansion techniques presented above are based on *serial* expansions of the Fermi function. Alternatively, the density matrix at finite electronic temperatures can be constructed by a *recursive* Fermi operator expansion [41] in m steps,

$$\mathbf{P} = \left[e^{\beta(\mathbf{H} - \mu_0 \mathbf{I})} + I \right]^{-1} \approx f_m(f_{m-1}(\cdots f_0(\mathbf{H}) \cdots)). \quad (16-30)$$

In contrast to most of the Fermi-operator or Green's expansions, of which there are many flavors [21, 27, 48, 49, 107, 113–117], the *recursive* expansion in Eq. (16-30) leads to a very high-order approximation in only a few number of iterations. Here we will use a recursive Fermi-operator expansion based on the Pade' polynomial

$$f_n(x) = x^2/[x^2 + (1-x)^2] \quad (16-31)$$

in Eq. (16-30) for $n > 0$ [41]. The function is shown in Figure 16-3. It is smooth and monotonically increasing for $x \in [0,1]$. After an initialization of the Hamiltonian, where

$$\mathbf{X}_0 = f_0(\mathbf{H}) = \frac{1}{2} \mathbf{I} - (\mathbf{H} - \mu_0 \mathbf{I})\beta/2^{2+m}, \quad (16-32)$$

the recursive Pade' expansion,

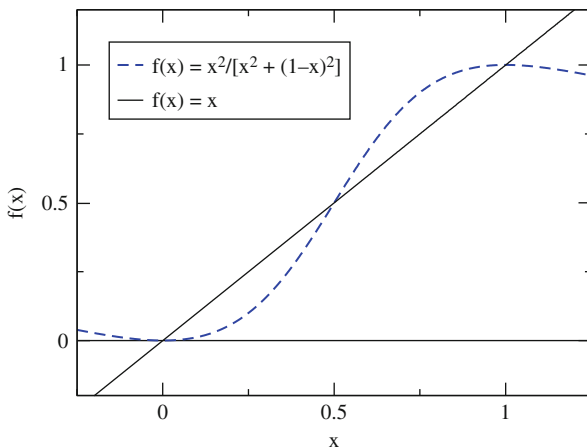


Figure 16-3. The Pade' expansion polynomial, Eq. (16-31), used in the Fermi operator expansion scheme in Eq. (16-38)

$$\mathbf{X}_n = \mathbf{X}_{n-1}^2 / [\mathbf{X}_{n-1}^2 + (\mathbf{I} - \mathbf{X}_{n-1})^2], \quad n = 1, 2, \dots, m \quad (16-33)$$

provides a very efficient Fermi operator expansion in the calculation of the temperature dependent density matrix \mathbf{P} . The recursive Fermi operator expansion is derived from the approximation of the matrix exponential [118],

$$e^x = (e^{x/n})^n = \left(\frac{e^{x/(2n)}}{e^{-x/(2n)}} \right)^n, \quad (16-34)$$

which after a first order Taylor expansion gives

$$e^x = \lim_{n \rightarrow \infty} \left(\frac{2n+x}{2n-x} \right)^n. \quad (16-35)$$

Inserting this expression in the Fermi function gives the recursive expansion after a few algebraic manipulations [41, 44].

The problem of finding the chemical potential μ_0 in Eq. (16-30) such that the correct occupation is achieved,

$$\text{Tr}(\mathbf{P}) = N_{\text{occ}}, \quad (16-36)$$

can be solved by a Newton-Raphson optimization using the analytic derivative of the density matrix with respect to μ_0 ,

$$\frac{\partial \mathbf{P}}{\partial \mu_0} = \beta \mathbf{P}(\mathbf{I} - \mathbf{P}). \quad (16-37)$$

The recursive Fermi operator expansion of the temperature dependent density matrix, which automatically finds the chemical potential by a Newton-Raphson optimization [41, 44], is given by the following algorithm:

$$\begin{aligned}
 & m = \text{Number of recursive iterations} \\
 & \beta = 1/(k_B T_e) \\
 & \mu_0 = \text{Initial guess of } \mu_0 \\
 & \text{while Occupation Error} > \text{Tolerance} \\
 & \quad \mathbf{X}_0 = \frac{1}{2} \mathbf{I} - (\mathbf{H} - \mu_0 \mathbf{I}) \beta / 2^{2+m} \\
 & \quad \text{for } n = 1 : m \\
 & \quad \quad \text{solve } [\mathbf{X}_{n-1}^2 + (\mathbf{I} - \mathbf{X}_{n-1})^2] \mathbf{X}_n = \mathbf{X}_{n-1}^2 \\
 & \quad \text{end} \\
 & \quad \mathbf{P} = \mathbf{X}_m \\
 & \quad \text{Occupation Error} = |\text{Tr}(\mathbf{P}) - N_{\text{occ}}| \\
 & \quad \mu_0 = \mu_0 + [N_{\text{occ}} - \text{Tr}(\mathbf{P})] / \text{Tr}[\beta \mathbf{P}(\mathbf{I} - \mathbf{P})] \\
 & \text{end.}
 \end{aligned} \quad (16-38)$$

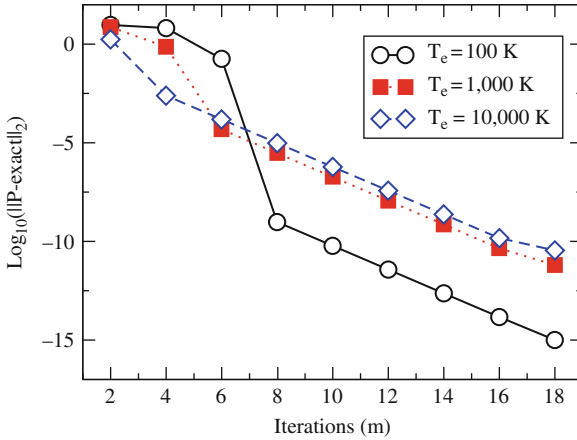


Figure 16-4. The convergence error of the grand canonical Fermi operator expansion (inner loop of Eq. (16-38)) as a function of the number of recursion steps m for a Hamiltonian with 400 uniformly distributed eigenvalues in the interval $[-2, 2]$. The chemical potential $\mu_0 = -1$ without any optimization

The outer loop for the Newton-Raphson optimization of μ_0 should be straightforward to apply also in Chebyshev or Green's function expansions.

In the recursive Fermi-operator expansion algorithm in Eq. (16-38), a system of linear equations arising from the Pade' polynomials in Eq. (16-33) is solved in each iteration. The numerical problem is well-conditioned and symmetric positive definite, where the solution from the previous cycle \mathbf{X}_{n-1} typically is close to \mathbf{X}_n . A linear conjugate-gradient solver is therefore very efficient [41]. The Fermi operator expansion algorithm can be formulated based on matrix-matrix operations and does not require a diagonalization of the Hamiltonian. It is therefore possible to reach a reduced complexity $\mathcal{O}(N)$ scaling of the computational cost as a function of system size if linear scaling sparse matrix algebra is used.

The algorithm is rapidly convergent and the number of recursive iterations can often be kept low with $m < 10$. Thanks to the particular smooth form of the Pade' polynomial, Gibb's like oscillations for finite expansion orders are avoided. Figure 16-4 shows the convergence properties as a function of the number of recursion steps m for a Hamiltonian with 400 uniformly distributed eigenvalues in the interval $[-2, 2]$. The expansion was performed within a grand canonical ensemble with a fix chemical potential $\mu_0 = -1$, which corresponds to the inner part of the expansion algorithm in Eq. (16-38), without the additional Newton-Raphson optimization.

16.4.4. Recursive Fermi-Operator Expansion at $T_e = 0$ by Purification

The recursive Fermi operator expansion in Eq. (16-38) can be used also at $T_e = 0$, however in this limit, where the Fermi function becomes equivalent to the Heaviside

step function, there exist other more efficient schemes that are based on the idea behind density matrix purification [28, 45] or the corresponding sign-function expansion [47, 119]. A density matrix at $T_e = 0$ is idempotent, i.e.

$$\mathbf{P} = \mathbf{P}^2, \quad (16-39)$$

because of the “pure” integer occupation, with all eigenvalues being either 0 or 1. This means that the zero temperature density matrix acts as a projector on the occupied subspace. McWeeny [46] used this idempotency criterion to numerically improve an approximate density matrix, $\tilde{\mathbf{P}}$, to a more pure ensemble, \mathbf{P} , through “purification”,

$$\mathbf{P} = f_{\text{McW}}(\tilde{\mathbf{P}}) = 3\tilde{\mathbf{P}}^2 - 2\tilde{\mathbf{P}}^3. \quad (16-40)$$

It is easy to see how the McWeeny purification improves the idempotency from the graph in Figure 16-5. Eigenvalues close to 0 or 1 will be projected toward the fix points at 0 and 1. By iteratively repeating the McWeeny purification the eigenvalues successively get closer to the fix points. Similar ideas for spectral projections have been used to construct matrix sign functions, with the only significant difference that the eigenvalues of the sign matrix are at -1 and 1 instead of 0 and 1 . Palser and Manolopolous used the idea behind McWeeny purification to construct the zero temperature density matrix from the Hamiltonian with linear scaling complexity [28]. This was performed either in a grand canonical or a canonical ensemble, i.e. with a fix chemical potential or with a predefined occupation.

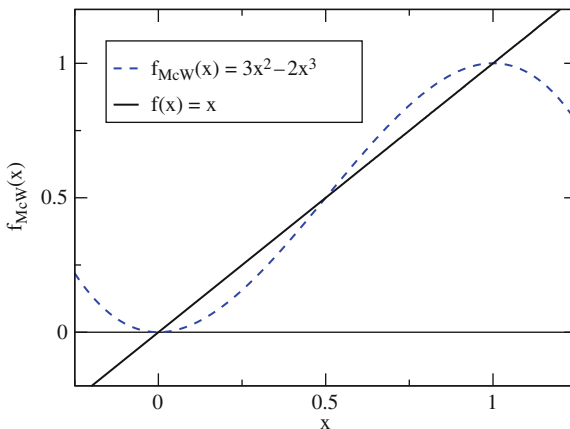


Figure 16-5. The McWeeny purification polynomial with stationary fix points at $x = 0$ and $x = 1$. The McWeeny purification, Eq. (16-40), provides a spectral projection moving eigenvalues close to 0 or 1 toward the fix points at 0 and 1

16.4.4.1. Grand Canonical McWeeny Purification

In the grand canonical McWeeny purification scheme by Palser and Manolopolous [28], the Fermi operator expansion at $T_e = 0$ is given *recursively*,

$$\mathbf{P} = \theta(\mu_0 \mathbf{I} - \mathbf{H}) = \dots (f_{McW}(\dots f_{McW}(f_0(\mathbf{H})) \dots)) \dots, \quad (16-41)$$

with the initial normalization

$$\mathbf{X}_0 = f_0(\mathbf{H}) = \alpha \frac{1}{2}(\mu_0 \mathbf{I} - \mathbf{H}) + \frac{1}{2} \mathbf{I}, \quad (16-42)$$

where

$$\alpha = \min\{(\varepsilon_{\max} - \mu_0)^{-1}, (\mu_0 - \varepsilon_{\min})^{-1}\}. \quad (16-43)$$

Here ε_{\max} and ε_{\min} are estimates of the highest and lowest eigenvalues of \mathbf{H} . These estimates of the spectral bounds can be calculated using, for example, Gersgorin circles or a couple of Lanczos iterations. In the initialization, Eq. (16-42), the Hamiltonian eigenvalue spectrum, $\{\varepsilon_i\}$, is rescaled to the interval of convergence, $[0, 1]$, in reverse order with the highest (unoccupied) eigenvalue close to 0 and the lowest (occupied) eigenstate close to 1. The chemical potential is shifted to the inflection point of the purification polynomials, i.e. $\mu_0 \rightarrow 1/2$. After this normalization, the McWeeny polynomial,

$$\mathbf{X}_{n+1} = 3\mathbf{X}_n^2 - 2\mathbf{X}_n^3, \quad (16-44)$$

gradually projects the eigenvalues toward 0 for the unoccupied and toward 1 for the occupied states, thereby creating a successively more “purified” approximation of the density matrix. At convergence,

$$\mathbf{P} = \lim_{n \rightarrow \infty} \mathbf{X}_n, \quad (16-45)$$

and the density matrix is idempotent, i.e. $\mathbf{P} = \mathbf{P}^2$. The scheme is rapidly convergent with the polynomial order increasing exponentially with the number of iterations. Only sparse matrix-matrix operations are needed, which can be performed with $\mathcal{O}(N)$ scaling. Each iteration requires two sparse matrix-matrix multiplications, which is the most expensive part of the calculation. After 30 multiplications (15 iterations) the polynomial expansion order is 3^{15} , i.e. over 14 million. The McWeeny polynomial is a continuously increasing function in $[0, 1]$ and there are no Gibbs oscillations occurring because of finite order truncations. As in the Chebyshev expansion scheme, this method also requires prior knowledge of the chemical potential μ_0 .

16.4.4.2. Canonical McWeeny Purification

In general, the exact location of the chemical potential μ_0 is unknown and we need to iteratively adjust μ_0 such that the correct required occupation is achieved within a canonical ensemble, for example, by using the Newton-Raphson scheme in the outer loop of the algorithm in Eq. (16-38). In a canonical generalization Palser and Manolopolous [28] modified the McWeeny polynomial such that the trace is conserved in each purification step. In this way, the extra step of adjusting the chemical potential is avoided. First the Hamiltonian is normalized to the interval $[0, 1]$ with the trace set to the correct value,

$$\mathbf{X}_0 = f_0(\mathbf{H}) = \alpha(\bar{\mu}\mathbf{I} - \mathbf{H}) + (N_{occ}/N)\mathbf{I}, \quad (16-46)$$

where

$$\alpha = N^{-1} \min\left(\frac{N_{occ}}{\varepsilon_{\max} - \bar{\mu}}, \frac{N - N_{occ}}{\bar{\mu} - \varepsilon_{\min}}\right), \quad (16-47)$$

and

$$\bar{\mu} = Tr[\mathbf{H}]/N, \quad (16-48)$$

such the $Tr[\mathbf{X}_0] = N_{occ}$. Thereafter, trace conserving canonical purification is performed with

$$\mathbf{X}_{n+1} = \begin{cases} \frac{(1+c_n)\mathbf{X}_n^2 - \mathbf{X}_n^3}{c_n}, & c_n \geq 1/2, \\ \frac{(1-2c_n)\mathbf{X}_n + (1+c_n)\mathbf{X}_n^2 - \mathbf{X}_n^3}{1-c_n}, & c_n < 1/2, \end{cases} \quad (16-49)$$

where

$$c_n = \frac{Tr[\mathbf{X}_n^2 - \mathbf{X}_n^3]}{Tr[\mathbf{X}_n - \mathbf{X}_n^2]}. \quad (16.50)$$

In each purification step the trace is conserved and at convergence the density matrix is idempotent with the correct occupation. The rather expensive additional adjustment of the chemical potential is thus avoided.

The canonical purification scheme is a highly efficient technique that typically has a rapid convergence without requiring any prior knowledge of the chemical potential. Only matrix-matrix operations are needed in each iteration. In comparison to alternative $\mathcal{O}(N)$ method, such as the constrained functional minimization by Li, Nunes and Vanderbilt, and Daw [17, 18], the canonical purification is simple, fast and robust [43, 120]. However, at low or high partial occupation, i.e. when N_{occ}/N is close to 0 or 1, the canonical purification scheme is fairly slow to converge [28, 30]. The 3rd order McWeeny polynomial is also less optimal, since, for example, a 4th

order polynomial can be calculated with the same number of matrix-matrix multiplications, which would lead to a faster increase of the expansion order. Higher-order generalizations of the McWeeny polynomial has therefore been suggested [30, 38, 121, 122]. Unfortunately, using higher-order polynomials requires additional intermediate memory storage, which can be a limiting factor in large scale calculations.

16.4.4.3. Occupation Correcting Fermi Operator Expansion

To avoid the problems with a slow convergence at low or high partial occupation and the suboptimal order of the McWeeny purification polynomial, Niklasson proposed a simplified approach to the Fermi operator expansion at $T_e = 0$ [30]. Instead of using the 3rd order McWeeny polynomial or its modifications and higher-order generalizations, a set of two 2nd order spectral projection polynomials are applied,

$$f(x) = \begin{cases} x^2, \\ 2x - x^2. \end{cases} \quad (16-51)$$

This set of functions are shown in Figure 16-6. A fix combined set of these polynomials, either $(2x - x^2)^2$ or $(2x^2 - x^4)$, had previously been used by Mazzotti [39] to improve idempotency between iterations in a variational optimization for the calculation of the density matrix [17, 18]. Two important observations can be made about the spectral projection polynomials in Eq. (16-51): (a) any recursive combination of the two polynomials expands the step function for $x \in [0, 1]$, i.e.

$$\theta(\mu_0 - x) = \lim_{n \rightarrow \infty} f_n(f_{n-1}(\dots(f_0(x)\dots))), \quad (16-52)$$

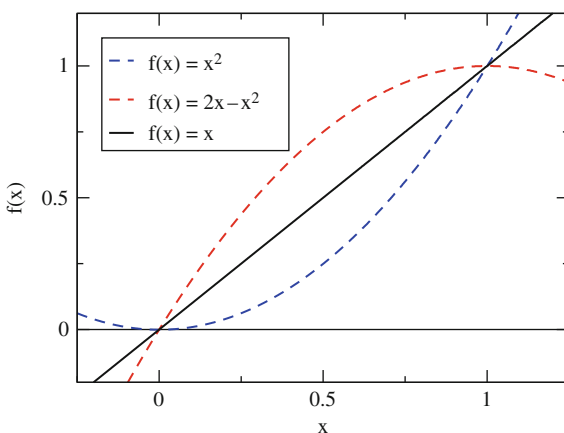


Figure 16-6. The 2nd order Fermi operator expansion polynomials used by Niklasson in the occupation correcting Fermi-operator expansion at $T_e = 0$ [30]

with the step $\mu_0 \in [0,1]$, and $b)$ the trace of a matrix with all eigenvalues $\varepsilon_i \in [0,1]$ is modified by the polynomials such that

$$\begin{aligned} \text{Tr}[\mathbf{X}^2] &\leq \text{Tr}[\mathbf{X}], \\ \text{Tr}[2\mathbf{X} - \mathbf{X}^2] &\geq \text{Tr}[\mathbf{X}]. \end{aligned} \quad (16-53)$$

From these two observations it is easy to construct an efficient Fermi operator expansion for $T_e = 0$ [30]. Start with a normalization of the Hamiltonian,

$$\mathbf{X}_0 = f_0(\mathbf{H}) = \frac{\varepsilon_{\max} \mathbf{I} - \mathbf{H}}{\varepsilon_{\max} - \varepsilon_{\min}}, \quad (16-54)$$

which rescales the eigenvalue spectrum of \mathbf{H} in reverse order in $[0, 1]$, with the lowest occupied states close to 1 and the highest unoccupied states close to 0. Thereafter the density matrix is given by $\mathbf{P} = \lim_{n \rightarrow \infty} \mathbf{X}_n$, where

$$\mathbf{X}_{n+1} = \begin{cases} \mathbf{X}_n^2, & \text{if } \mathcal{A}, \\ 2\mathbf{X}_n - \mathbf{X}_n^2, & \text{if not } \mathcal{A}. \end{cases} \quad (16-55)$$

With the condition \mathcal{A} chosen properly, the step function is expanded at the same time as the eigenvalues are projected toward 1 or 0 such that the required occupation is given at convergence. As the condition \mathcal{A} we may use, for example,

$$\mathcal{A}: |\text{Tr}[\mathbf{X}_n^2] - N_{occ}| < |\text{Tr}[2\mathbf{X}_n - \mathbf{X}_n^2] - N_{occ}|. \quad (16-56)$$

This simply means that the expansion sequence is chosen to project the eigenvalues such that the occupation is improved after each iteration. A variety of alternative conditions can also be applied. At convergence the density matrix is idempotent with the correct occupation. Only one sparse matrix-matrix multiplication per iteration is required, which reduces intermediate memory requirements and provides a very rapid convergence. After 30 multiplications the polynomial expansion order is over one billion. As an efficient convergence criteria we may use the change in the occupation, i.e. the idempotency error,

$$|\text{Tr}[\mathbf{X}_{n+1} - \mathbf{X}_n]| = |\text{Tr}[\mathbf{X}_n(\mathbf{I} - \mathbf{X}_n)]|, \quad (16-57)$$

between every second iteration. Figure 16-7 shows the expansion after 8 alternating iterations starting with x^2 and Figure 16-8 shows the propagation of the eigenvalues as a function of iterations.

16.4.4.4. Occupation Resetting Fermi Operator Expansion

As an alternative to canonical McWeeny purification, where the occupation is constant, and to the 2nd order occupation correcting Fermi operator expansion, where the occupation reaches the correct value only at convergence, a third approach was developed [40, 43]. In this case the occupation is allowed to fluctuate in some steps,

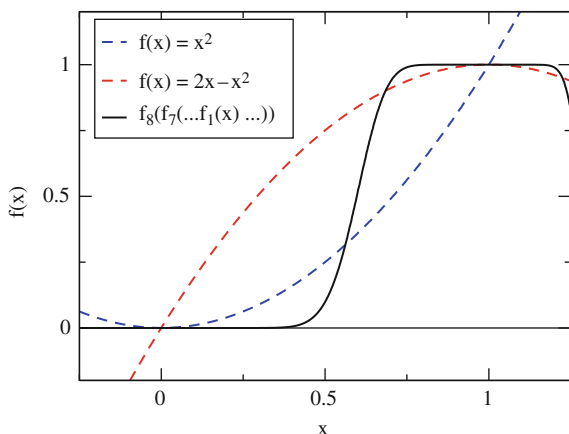


Figure 16-7. The approximate step function in the recursive 2nd order Fermi-operator expansion after 8 iterations

but is reset to the correct value in other iterations. In the trace-resetting purification scheme by Niklasson, Tymczak and Challacombe [40], a pair of 4th order purification polynomials are used,

$$\begin{aligned} \mathcal{F}(x) &= x^2(4x - 3x^2), \\ \mathcal{G}(x) &= x^2(1 - 2x + x^2), \end{aligned} \tag{16-58}$$

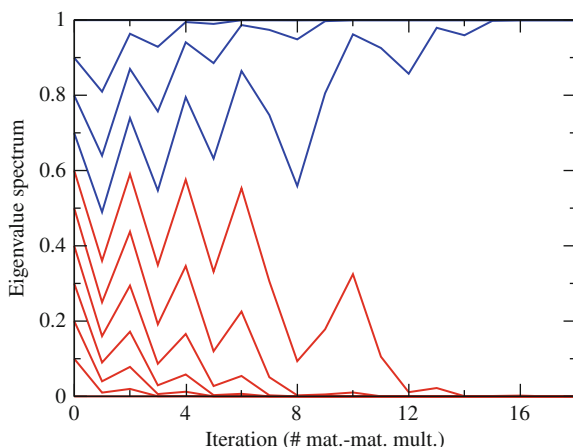


Figure 16-8. The propagation of the eigenvalue spectrum in the recursive 2nd order occupation correcting Fermi-operator expansion as a function of iterations or matrix–matrix multiplications is shown. If \mathbf{X}^2 is used the eigenvalues move toward 0 and if $2\mathbf{X} - \mathbf{X}^2$ is applied the eigenvalues increase until convergence is reached at the fix points at 0 and 1. The alternating recursive expansion is reflected in the oscillatory behavior of the spectrum

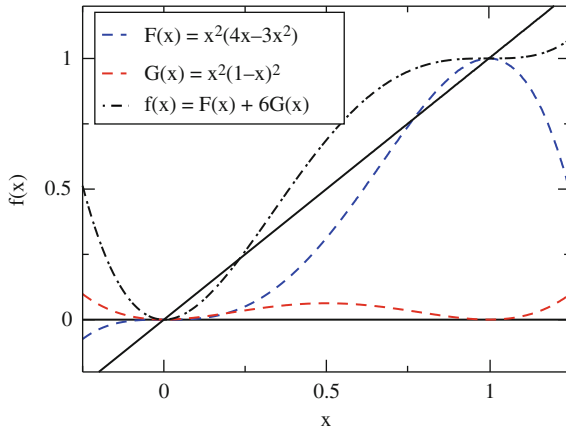


Figure 16-9. Combinations of trace (occupation) resetting purification polynomials

that are shown in Figure 16-9. After an initialization that transforms the eigenvalue spectrum of \mathbf{H} in reversed order in $[0, 1]$,

$$\mathbf{X}_0 = (\varepsilon_{\max} \mathbf{I} - \mathbf{H}) / (\varepsilon_{\max} - \varepsilon_{\min}), \tag{16-59}$$

a combination of the two polynomials,

$$\mathbf{X}_{n+1} = f_n(\mathbf{X}_n) = \mathcal{F}(\mathbf{X}_n) + \gamma_n \mathcal{G}(\mathbf{X}_n), \tag{16-60}$$

where

$$\gamma_n = (N_{\text{occ}} - \text{Tr}[\mathcal{F}(\mathbf{X}_n)]) / \text{Tr}[\mathcal{G}(\mathbf{X}_n)], \gamma_n \in [0,6], \tag{16-61}$$

can be used to expand the step function. After each iteration the trace of \mathbf{X}_{n+1} is automatically set to the required occupation, N_{occ} . However, this trace setting mechanism is possible only within a limited range of $\gamma_n \in [0,6]$. With an unrestricted γ_n , $f_n(\mathbf{X}_n)$ may map eigenvalues of \mathbf{X}_n outside of the interval $[0, 1]$, which could lead to instabilities. In this case, i.e. when γ_n in Eq. (16-61) is out of bound, the 2nd order occupation correcting projection polynomials in Eq. (16-55) are applied, such that

$$\mathbf{X}_{n+1} = \begin{cases} \mathbf{X}_n^2, & \text{if } \gamma_n < 0, \\ 2\mathbf{X}_n - \mathbf{X}_n^2, & \text{if } \gamma_n > 6. \end{cases} \tag{16-62}$$

In this step the trace of \mathbf{X}_{n+1} is no longer conserved. However, toward convergence $\gamma_n \in [0,6]$ and the occupation is always reset to the correct value.

An advantage with the trace resetting scheme above, compared to the 2nd order occupation correcting purification scheme, is the ability to deal with degeneracy and fractional occupation. Figure 16-10 shows the modified Fermi expansion for

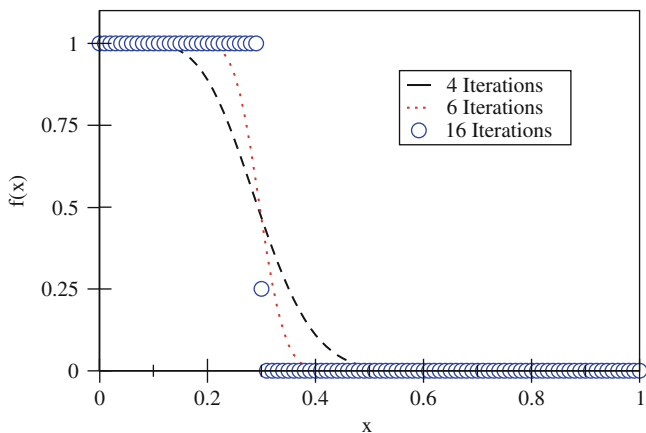


Figure 16-10. Convergence of trace (occupation) resetting purification for a system with a fractional occupation of 30.25

a Hamiltonian with 100 uniformly distributed eigenvalues in $[0, 1]$ with the fractional occupation $N_{\text{occ}} = 30.25$. At convergence, an additional step is automatically formed for the last fractionally occupied state at 0.25. The same convergence for fractional occupation can also be achieved with the canonical scheme by Palser and Manolopolous. The occupation resetting Fermi operator expansion has the same rapid convergence as the 2nd order occupation correcting expansion scheme, but the calculation of the 4th order polynomials requires more intermediate memory storage in the calculation.

16.4.5. Convergence and Accuracy

In a number of tests of linear scaling methods the efficiency of different techniques have been analyzed simply by running examples for various materials systems. Without a detailed analysis this is not always very useful. Figure 16-11 and Figure 16-12 show the energy convergence of two different examples (A and B) based on the same model systems for the canonical Fermi operator expansion scheme by Palser and Manolopolous (PM) and the 2nd order occupation correcting expansion by Niklasson. As a simple model system we used the Hamiltonian

$$\mathbf{H} = -\frac{1}{2} \frac{\partial^2}{\partial x^2} + \alpha \sin(\beta x), \quad (16-63)$$

with periodic boundary conditions. Both examples clearly show that the error is well controlled by a simple threshold τ below which all matrix elements are set to 0 after each matrix-matrix multiplication in order to preserve sparsity. By reducing the matrix threshold τ the error is systematically reduced, similar to the change of the numerical accuracy by a modification of the machine precision. An important feature is that the error is stable even when the calculation proceeds beyond the point

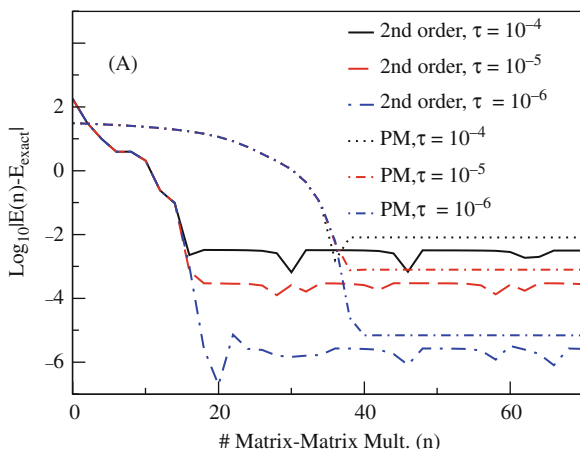


Figure 16-11. Example A: Energy convergence for the canonical Fermi operator expansion scheme by Palser and Manolopolous (PM) and the 2nd order occupation correcting expansion by Niklasson. All matrix elements below the numerical threshold τ were set to 0 after each matrix–matrix multiplication to improve sparsity

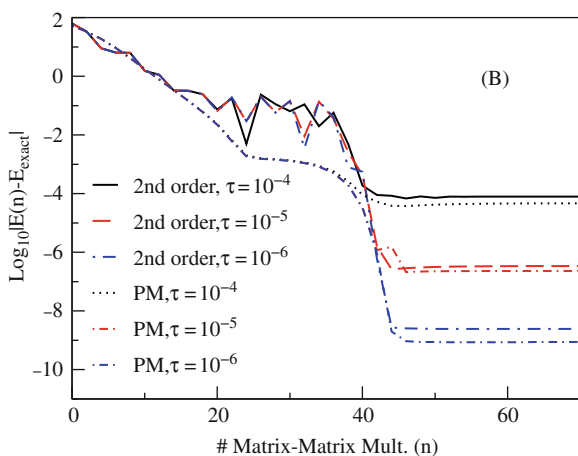


Figure 16-12. Example B: Energy convergence for the canonical Fermi operator expansion scheme by Palser and Manolopolous (PM) and the 2nd order occupation correcting expansion by Niklasson. All matrix elements below the numerical threshold τ were set to 0 after each matrix–matrix multiplication to improve sparsity

of convergence. The fluctuations seen in the energy for the 2nd order expansion scheme are due to the alternating choice of the projection polynomials. Most of the oscillations have been removed by showing only every second iteration. In example (A), Figure 16-11, the 2nd order expansion method seems superior to the PM scheme, since the computational cost is only about half and the accuracy is slightly better. In example (B), Figure 16-12, the computational cost has increased for the

2nd order expansion method, whereas it is about the same for the PM scheme. The overall converged accuracy is improved compared to example (A). Without a more detailed analysis it would not be clear which method actually is the better for yet another system. The differences can be understood mainly from two factors: (a) the size of the gap and (b) the relative filling, i.e. the occupation factor N_{occ}/N . In example (A) the occupation factor is 10%, whereas it is 50% in example (B), which also has a substantially smaller gap. As mentioned above, the canonical PM scheme is significantly slower in the case of high or low occupation factors when the trace conserving purification polynomials become close to linear [28, 30]. At around 50% occupation the PM and the 2nd order schemes have a very similar performance. The higher general accuracy of example (B) is due to the fact that the smaller gap gives rise to a less localized system. This means a lower matrix sparsity and that more matrix elements are included in the expansion, which here leads to a higher accuracy. Comparing the converged accuracy between the PM and the 2nd order scheme is difficult, because in the two different expansions a slightly different number of small matrix elements are removed for the same threshold value. Removing more matrix elements gives a sparser representation with faster calculations, but the accuracy is lower. Instead of the simple thresholding performed here, the more accurate and well-controlled adjustable threshold strategies that recently have been proposed by Rubensson et al. can be performed [85–87].

Figure 16-13 shows an example of the convergence for a single water molecule using a hybrid Hartree-Fock DFT functional and a Gaussian basis set, with or without the simple thresholding. Even for a small molecule with a full final density matrix does the thresholding affect the accuracy, since elements tend to be smaller

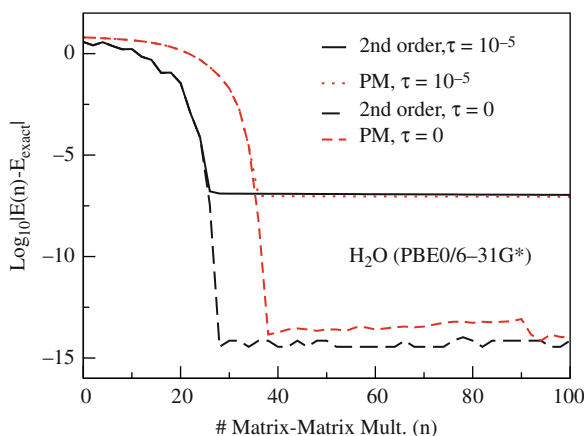


Figure 16-13. Energy convergence for a single water molecule (PBE0/6-31G*) for the canonical Fermi operator expansion scheme by Palser and Manolopolous (PM) and the 2nd order occupation correcting expansion by Niklasson. All matrix elements below the numerical threshold τ were set to 0 after each matrix–matrix multiplication

during the initial expansion. Without thresholding the accuracy is of the same order as given by an “exact” diagonalization.

The Fermi operator expansion order required for a given accuracy is dependent on the inverse gap, such that a small gap needs a higher-order Fermi operator expansion. For the Chebychev expansion the number of iterations necessary to reach a given accuracy is inversely proportional to the gap [107], whereas the required number of iterations for the recursive schemes scales only with the logarithm of the inverse gap [30]. The efficiency in the limit of small gap systems is determined by the derivative of the expansion polynomial at the inflection point that separates the occupied eigenvalue spectrum from the unoccupied part [30], which seems to favor a Pade’ form of the expansions polynomials.

The main source of the error in a recursive Fermi operator expansion scheme is in general not the approximate nature of the step function or the Fermi function expansion, i.e. the eigenvalue distribution, but the accumulated commutation error,

$$[\mathbf{H},\mathbf{P}] = \mathbf{HP} - \mathbf{PH}, \quad (16-64)$$

which never is exactly zero because of numerical thresholding or other errors. The commutator reflects the error in the underlying wavefunctions and excludes errors due to an inexact eigenvalue distribution. Figure 16-14 shows an example of the convergence of the idempotency error ($\text{Error}(n) = \text{Tr}[\mathbf{X}_n(\mathbf{I} - \mathbf{X}_n)]$) vs. the accumulation of commutation error ($\text{Error}(n) = \|[\mathbf{H},\mathbf{X}_n]\|_2$) for the single water molecule using the hybrid Hartree-Fock DFT functional with a Gaussian basis set. The idempotency error is very well controlled and the commutation error increases initially but reaches a constant value when the expansion reaches idempotency [40].

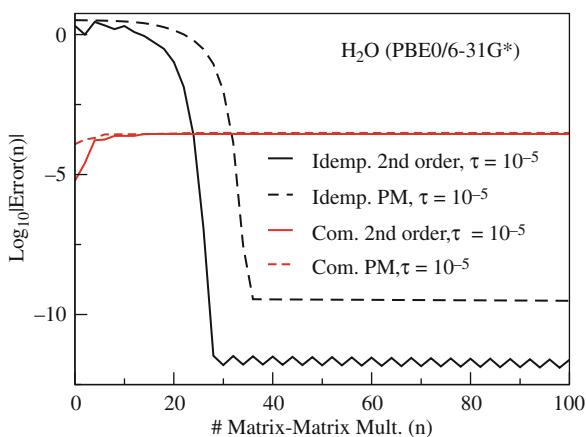


Figure 16-14. The idempotency (Idem.) convergence and commutation error accumulation (Com.) for a single water molecule (PBE0/6-31G*) using the canonical Fermi operator expansion scheme by Palser and Manolopolous (PM) and the 2nd order occupation correcting expansion by Niklasson. All matrix elements below the numerical threshold τ were set to 0 after each matrix–matrix multiplication

16.4.6. Iterative Refinement Techniques

If an approximate solution for the density matrix $\tilde{\mathbf{P}}$ is given, either from a previous self-consistent field cycle or from an approximate calculation with a large numerical threshold, there are at least three options to improve the solution: (1) adjust or rescale $\tilde{\mathbf{P}}$ to fulfill, for example, idempotency and the correct occupation, (2) use $\tilde{\mathbf{P}}$ as an initial guess in a variational approach to optimize the density matrix, or (3) simply recalculate a new density matrix from scratch using a sufficient numerical accuracy.

16.4.6.1. Adjusting and Rescaling

Let $\mathbf{X}_0 = \tilde{\mathbf{P}}$. Thereafter the occupation correcting purification can be used:

$$\mathbf{X}_{n+1} = \begin{cases} \mathbf{X}_n^2, & \text{if } \mathcal{A}, \\ 2\mathbf{X}_n - \mathbf{X}_n^2, & \text{if not } \mathcal{A}. \end{cases} \quad (16-65)$$

As condition \mathcal{A} we can use Eq. (16-56). Alternative purification based on the original McWeeny polynomial can of course also be applied, where

$$\mathbf{X}_{n+1} = 3\mathbf{X}_n^2 - 2\mathbf{X}_n^3. \quad (16-66)$$

The purification schemes above will converge quickly if the approximate $\tilde{\mathbf{P}}$ is close to idempotency. On the other hand, if $\tilde{\mathbf{P}}$ is too far away from idempotency, with some eigenvalues to far below 0 or above 1, the purification approach may diverge. Other alternatives to improve the approximate density matrix include a simple rescaling $\tilde{\mathbf{P}} \rightarrow \alpha\tilde{\mathbf{P}}$ or a constant shift $\tilde{\mathbf{P}} \rightarrow \tilde{\mathbf{P}} + \alpha\mathbf{I}$ to adjust to the required occupation. Notice that the purification, rescaling, or shifting only adjust the eigenvalues of $\tilde{\mathbf{P}}$. Commutation errors are not affected.

16.4.6.2. Variational Optimization

If $\tilde{\mathbf{P}}$ has the correct trace and is idempotent the purification or rescaling above will not give any improvements. If the main cause of the error is a non-vanishing commutation, $[\mathbf{H}, \tilde{\mathbf{P}}] \neq \mathbf{0}$, a more complex improvement besides the adjustment of the eigenvalue spectrum is needed. In this case the source of the error is due to the particle-hole hole-particle transitions [121, 39],

$$\mathbf{G} = \tilde{\mathbf{P}}\tilde{\mathbf{H}}\tilde{\mathbf{Q}} + \tilde{\mathbf{Q}}\tilde{\mathbf{H}}\tilde{\mathbf{P}}, \quad (16-67)$$

where $\tilde{\mathbf{Q}} = \mathbf{I} - \tilde{\mathbf{P}}$ is the virtual (hole) density matrix. Only if $\tilde{\mathbf{P}}$ commutes with \mathbf{H} , would \mathbf{G} vanish. By adjusting $\mathbf{X}_0 = \tilde{\mathbf{P}}$ with \mathbf{G} , the approximate density matrix \mathbf{X}_{n+1} can iteratively be improved,

$$\mathbf{X}_{n+1}(\lambda) = \mathbf{X}_n + \lambda\mathbf{G}_n. \quad (16-68)$$

The approach assumes that $\tilde{\mathbf{P}}$ and $\tilde{\mathbf{Q}}$ are projectors and idempotent. Between each iteration a purification step as in Eq. (16-65) is therefore needed. The key problem in this approach is to calculate the optimal values of λ . Using a small constant value of λ may work, but it could lead to a slow convergence, or in the worst case to divergence. If the minimization of the single particle energy, i.e. some form of $Tr[\mathbf{HX}_{n+1}(\lambda)]$, is used to find the optimal value of λ , under the condition of approximate idempotency as in the constrained functional minimization approach by Li, Nunes and Vanderbilt, and Daw [17, 18], the penalty functional approach by Kohn, Haynes and Payne [58, 59], or the “curvy-step” method by Helgaker et al. [29, 60, 123], the cost of calculating the optimal value of λ is fairly high. If $\tilde{\mathbf{P}}$ is too far away from the exact solution, the variational optimization approaches may lead to instabilities, because of non-linearities in the idempotency constraints.

16.4.6.3. Recalculation

Probably the easiest and most straightforward approach to improve $\tilde{\mathbf{P}}$ is simply to perform a full recalculation using, for example, the occupation correcting Fermi operator expansion. In the case of a commutation error it is hard to beat a full recalculation with a recursive Fermi operator expansion method, which requires less intermediate memory and relative few matrix-matrix multiplications compared to a variational optimization, even when its initial guess is good. At finite electronic temperatures there are probably no practical alternatives.

16.5. LINEAR SCALING DENSITY MATRIX PERTURBATION THEORY

The recursive Fermi-operator expansion approach provides a very efficient framework for calculating the density matrix response due to time independent perturbations in the Hamiltonian [52]. This density matrix perturbation theory can be formulated without including individual eigenfunctions and eigenvalues and has the ability to reach linear scaling complexity for sufficiently large sparse matrix problems. The linear scaling density matrix perturbation theory is a very efficient and surprisingly simple alternative to Rayleigh-Schrödinger or Green’s function perturbation theory for the calculation of static response properties with a fix chemical potential. Linear scaling density matrix perturbation theory can be used in a number of applications, for example, calculating static polarizabilities [124] and hyperpolarizabilities [54], the Born effective charge and the optical dielectric constant for crystals [54], spin-spin coupling constants, and analytic force gradients [125]. A number of alternative formulations for reduced complexity calculations of the density matrix response, including frequency dependent properties, have also recently been developed, which are given through iterative solutions of Sylvester-like equations [123, 126–131]. Linear scaling calculation of frequency dependent properties through the real-time evolution of the nonadiabtic response is also an interesting alternative [132–135].

16.5.1. Density Matrix Response by Recursion

If the time-independent Hamiltonian \mathbf{H} is expanded in a perturbation parameter λ ,

$$\mathbf{H}(\lambda) = \mathbf{H}^{(0)} + \lambda\mathbf{H}^{(1)} + \lambda^2\mathbf{H}^{(2)} + \dots, \quad (16-69)$$

the corresponding adiabatic density matrix response expansion at $T_e = 0$ is given by

$$\mathbf{P}(\lambda) = \mathbf{P}^{(0)} + \lambda\mathbf{P}^{(1)} + \lambda^2\mathbf{P}^{(2)} + \dots, \quad (16-70)$$

where

$$\mathbf{P}^{(m)} = \frac{1}{m!} \frac{\partial^m}{\partial \lambda^m} \theta[\mu\mathbf{I} - \mathbf{H}(\lambda)]|_{\lambda=0}. \quad (16-71)$$

The problem of calculating the derivative over the step function for non-commuting perturbations in \mathbf{H} can be solved through the recursive expansion of the step function. In each recursion step the perturbations are kept up to some specific order. With the recursive sequence of intermediate, approximate density matrices,

$$\mathbf{X}_n(\lambda) = \mathbf{X}_n^{(0)} + \lambda\mathbf{X}_n^{(1)} + \lambda^2\mathbf{X}_n^{(2)} + \dots, \quad (16-72)$$

the updated approximate response matrices are given by

$$\mathbf{X}_{n+1}^{(m)} = \frac{1}{m!} \frac{\partial^m}{\partial \lambda^m} f_n[\mathbf{X}_n(\lambda)]|_{\lambda=0}, \quad (16-73)$$

where $f_n(\mathbf{X}_n)$ are the recursive Fermi operator expansion polynomials. In the second order occupation correcting expansion, this sequence is generated recursively from

$$\mathbf{X}_{n+1}^{(m)} = \mathbf{X}_n^{(m)} + \sigma_n \left[\mathbf{X}_n^{(m)} - \sum_{i=0}^m \mathbf{X}_n^{(i)} \mathbf{X}_n^{(m-i)} \right], \quad (m = 0, 1, 2, \dots). \quad (16-74)$$

Here $\sigma_n = \pm 1$ depending on the condition \mathcal{A} , which can be chosen to minimize the error in occupation of the updated approximation of the density matrix, i.e.

$$\sigma_n = \begin{cases} +1 & \text{if } |\text{Tr}[\mathbf{X}_n^{(0)2}] - N_{occ}| > |\text{Tr}[2\mathbf{X}_n^{(0)} - \mathbf{X}_n^{(0)2}] - N_{occ}|, \\ -1 & \text{else.} \end{cases} \quad (16-75)$$

The initial set of normalized intermediates $\{\mathbf{X}_0^{(m)}\}$ is determined by Eq. (16-73) for the initial normalization in Eq. (16-54), such that

$$\mathbf{X}_0^{(m)} = \frac{1}{m!} \frac{\partial^m}{\partial \lambda^m} \left[\frac{\varepsilon_{\max}\mathbf{I} - \mathbf{H}(\lambda)}{\varepsilon_{\max} - \varepsilon_{\min}} \right] |_{\lambda=0}, \quad (16-76)$$

At convergence it is easy to see that the recursive sequence in Eq. (16-74) fulfill the generalized idempotency conditions,

$$\begin{aligned}
 \mathbf{P}^{(0)}\mathbf{P}^{(0)} &= \mathbf{P}^{(0)} \\
 \mathbf{P}^{(0)}\mathbf{P}^{(1)} + \mathbf{P}^{(1)}\mathbf{P}^{(0)} &= \mathbf{P}^{(1)} \\
 \mathbf{P}^{(0)}\mathbf{P}^{(2)} + \mathbf{P}^{(2)}\mathbf{P}^{(0)} + \mathbf{P}^{(1)}\mathbf{P}^{(1)} &= \mathbf{P}^{(2)} \\
 \dots, &
 \end{aligned}
 \tag{16-77}$$

that are given from finite order truncations of

$$\mathbf{P}(\lambda)^2 = \mathbf{P}(\lambda).
 \tag{16-78}$$

The occupation is given by $Tr[\mathbf{P}^{(0)}] = N_{occ}$ and $Tr[\mathbf{P}^{(i)}] = 0$ for $i > 0$. Also the important commutation relations:

$$\begin{aligned}
 [\mathbf{P}^{(0)}, \mathbf{H}^{(0)}] &= 0 \\
 [\mathbf{P}^{(0)}, \mathbf{H}^{(1)}] + [\mathbf{P}^{(1)}, \mathbf{H}^{(0)}] &= 0 \\
 [\mathbf{P}^{(0)}, \mathbf{H}^{(2)}] + [\mathbf{P}^{(2)}, \mathbf{H}^{(0)}] + [\mathbf{P}^{(1)}, \mathbf{H}^{(1)}] &= 0 \\
 \dots, &
 \end{aligned}
 \tag{16-79}$$

can be shown to be fulfilled throughout the recursive iterations. These are the finite order generalizations of

$$[\mathbf{P}(\lambda), \mathbf{H}(\lambda)] = 0.
 \tag{16-80}$$

By using the identity matrix \mathbf{I} as a perturbation, the recursive density matrix perturbation theory above can be used to calculate derivatives of the approximate step function. Figure 16-15 shows the recursive approximation of the Heaviside

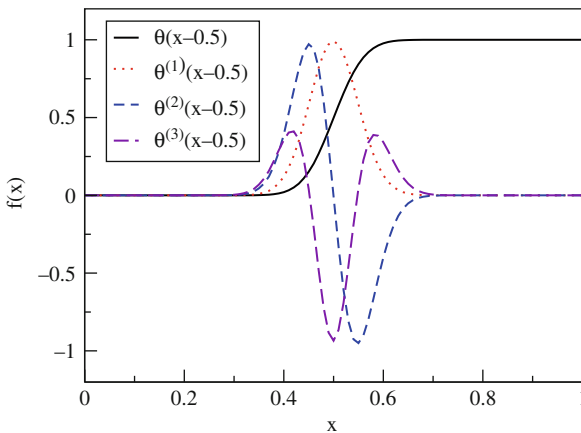


Figure 16-15. The recursive approximation of the Heaviside step function and its first three derivatives (rescaled) as approximated by 10 iterations with the second order occupation correction perturbation scheme, Eq. (16-74)

step function $\theta(x - 0.5)$ and its first three rescaled derivatives, $\theta^{(n)}(x - 0.5)$ ($n = 1, 2, 3$), after 10 iterations, using the second order perturbation scheme in Eq. (16-74). The Hamiltonian is here simply a diagonal matrix with a uniform distribution of eigenvalues in $[0, 1]$. The functions are smooth, without any oscillatory Gibb's errors in the step function approximation. This is particularly important in the calculations of the derivatives that otherwise would show significant errors.

The perturbation scheme above includes time-independent perturbations only at zero temperatures around a fix chemical potential. This grand canonical perturbation approach works well for non-metallic materials that have gaps and when the perturbation does not cause any states to cross the chemical potential. Higher-order canonical perturbation theory at finite temperatures, which would allow states to cross the Fermi level, is more complicated, involving free energies with an entropy dependent response. A separate article will be published elsewhere [136].

16.5.2. Calculating Response Properties From the $n + 1$ and $2n + 1$ Rules

The density matrix perturbation theory can be used to calculate the adiabatic response functions of a quantum observable, \mathbf{A} , to any order in the perturbation parameter λ ,

$$\langle \mathbf{A}(\lambda) \rangle = \text{Tr}[\mathbf{A}(\lambda)\mathbf{P}(\lambda)] = a^{(0)} + \lambda a^{(1)} + \lambda^2 a^{(2)} + \dots \quad (16-81)$$

The expansion of the energy,

$$E(\lambda) = \text{Tr}[\mathbf{H}(\lambda)\mathbf{P}(\lambda)] = E^{(0)} + \lambda E^{(1)} + \lambda^2 E^{(2)} + \dots, \quad (16-82)$$

can be calculated using the “ $n + 1$ ” density matrix response formula

$$E^{(m)} = \sum_{j=1}^m \frac{j}{m} \text{Tr}[\mathbf{P}^{(m-j)}\mathbf{H}^{(j)}]. \quad (16-83)$$

Here the energy response of order $m = n + 1$ is calculated from density matrix derivatives of order n and lower. For particular lower order expansions, when only a first order perturbation is included, i.e. when

$$\mathbf{H}(\lambda) = \mathbf{H}^{(0)} + \lambda \mathbf{H}^{(1)}, \quad (16-84)$$

more efficient expressions have been derived analogous to Wigner's $2n + 1$ rule [52, 55, 137–139]:

$$E^{(1)} = \text{Tr}[\mathbf{P}^{(0)}\mathbf{H}^{(1)}], \quad (16-85)$$

$$E^{(2)} = \frac{1}{2} \text{Tr}[\mathbf{P}^{(1)}\mathbf{H}^{(1)}], \quad (16-86)$$

$$E^{(3)} = \text{Tr}[(\mathbf{P}^{(1)}\mathbf{P}^{(0)} - \mathbf{P}^{(0)}\mathbf{P}^{(1)})\mathbf{P}^{(1)}\mathbf{H}^{(1)}], \quad (16-87)$$

$$E^{(4)} = \frac{1}{2}Tr[(2\mathbf{I} - \mathbf{P}^{(0)})\mathbf{P}^{(2)}\mathbf{P}^{(0)}\mathbf{P}^{(1)} - \mathbf{P}^{(0)}\mathbf{P}^{(1)}\mathbf{P}^{(2)}(\mathbf{I} + \mathbf{P}^{(0)})]\mathbf{H}^{(1)}. \quad (16-88)$$

16.5.3. Example

To illustrate the density matrix perturbation theory we may use an example with the model Hamiltonian,

$$\mathbf{H}(\lambda) = \mathbf{H}^{(0)} + \lambda\mathbf{H}^{(1)}, \quad (16-89)$$

where

$$\mathbf{H}^{(0)} = -\frac{1}{2} \frac{\partial^2}{\partial x^2} + V_a(x), \quad (16-90)$$

and

$$\mathbf{H}^{(1)} = \lambda[V_b(x) - V_a(x)]. \quad (16-91)$$

The potentials $V_a(x)$ and $V_b(x)$ are given by two shifted Gaussians,

$$V_a(x) = -e^{-(x-x_a)^2}, \quad (16-92)$$

$$V_b(x) = -e^{-(x-x_b)^2}, \quad (16-93)$$

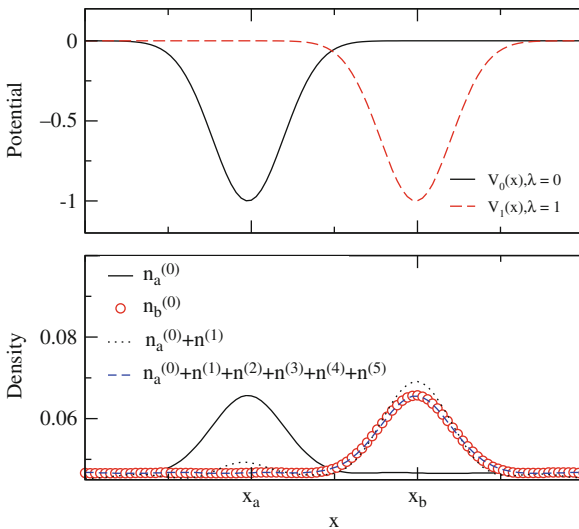


Figure 16-16. The potentials $V_a(x)$ and $V_b(x)$, Eqs. (16.92) and (16.93), are shown in the upper panel. In the lower panel the densities, $n_{a,b}^{(0)}(x) = P_{a,b}^{(0)}(x,x)$, calculated for $\lambda = 0$ and $\lambda = 1$, together with the expanded density derived from the perturbation theory, $n^{(m)}(x) = P^{(m)}(x,x)$ are shown

as shown in the upper panel of Figure 16-16. The kinetic energy operator is given by the finite difference scheme in Eq. (16-14) with periodic boundary conditions. The total number of states $N = 100$ with $N_{\text{occ}} = 5$ occupied states. The density $n_b^{(0)}(x)$ for the exact solution at $\lambda = 1$ is shown in comparison to the first order expansion $n_a^{(0)}(x) + n^{(1)}(x)$ as well as the fifth order expression, $n^a(x) + \sum_{i=1}^5 n^{(i)}(x)$, which is more or less identical to the exact solution.

The recursive linear scaling density matrix perturbation theory can also be used to calculate local perturbations to “infinite” order [52], which allows an exact cut and past approach, where weakly interacting molecular subsystems can be calculated separately and thereafter be glued together by the perturbation scheme. This approach may enable highly efficient parallel calculations of large composite nanosystems. The effects of local perturbations could also be calculated using the recursive perturbation scheme. This avoids, for example, calculating small energy changes as differences between total energies of large systems.

16.6. SUMMARY

In this chapter we have reviewed some recursive Fermi operator expansions methods for the calculation of the density matrix and its response in linear scaling electronic structure theory. Thanks to the recursive formulation these methods have a rapid convergence, where the expansion order increases exponentially with the number of operations. The recursive formulations can be used both for finite and zero temperature expansions and can be performed with a cost that scales only linearly with the system size for sufficiently large sparse matrix representations.

The linear scaling paradigm in electronic structure theory, where no significant part of a calculation is allowed to grow more than linearly with the system size, is a great challenge that typically requires more than efficient computer science. It often demands physically motivated insights or reformulations of the basic quantum description. Thanks to these requirements, linear scaling theory is a rich field that may provide novel spin-offs also in other areas of research.

ACKNOWLEDGMENTS

I would like to thank my collaborators that have contributed, directly or indirectly to this work, including Igor Abrikosov, Anders Bergman, Nicolas Bock, Marc Cawkwell, Matt Challacombe, Eric Chisolm, Erik Holmström, Karoly Nemeth, Anders Odell, Travis Peery, Emanuel Rubensson, Heinrich Röder, Pawel Salek, CJ Tymczak, Valery Weber, and John Wills. In particular, I would like to thank the pleasant atmosphere at the Ten Bar International Science Cafe and Travis Peery for many stimulating discussions. We gratefully acknowledge the support of the U.S. Department of Energy through the LANL LDRD/ER program for this work.

REFERENCES

1. Roothaan CCJ (1951) Rev Mod Phys 23:69
2. Hohenberg P, Kohn W (1964) Phys Rev 136 B:864

3. Kohn W, Sham LJ (1965) *Phys Rev* 140:1133
4. Soler JM, Artacho E, Gale JD, Garcia A, Junquera J, Ordejon P, Sanchez-Portal D (2002) *J Phys: Condens Matter* 14:2745
5. Bowler DR, Choudhury R, Gillan MJ, Miyazaki T (2006) *Phys Stat Sol B* 243:898
6. Bock N, Challacombe M, Gan CK, Henkelman G, Nemeth K, Niklasson AMN, Odell A, Schwegler E, Tymczak CJ, Weber V, FREEON (2008) Los Alamos National Laboratory (LA-CC 01-2; LA-CC-04-086) Copyright University of California., URL <http://www.nongnu.org/freeon/>
7. Rudberg E, Rubensson E, Salek P, ERGO (2006) Version 1.1: a quantum chemistry program for large-scale self consistent field calculations
8. Cawkwell M et al., LATTE (2009) A first principles self-consistent tightbinding program for large-scale atomistic simulations
9. Ozaki T, Kino H (2005) *Phys Rev B* 72:045121
10. Tsuchida E, Tsukada M (1998) *J Phys Soc Jpn* 67:3844
11. Hine ND, Haynes PD, Mostofi AA, Skylaris C-K, Payne MC (2009) *Comput Phys Comm* 180:1041
12. Haydock R, Heine V, Kelley MJ (1975) *J Phys C* 8:2591
13. Haydock R (1980) *Comput Phys Commun* 20:11
14. Haydock R (1980) *Solid State Phys* 35:3547
15. Lanczos C (1950) *J Res Nat Bur Stan B* 45:255
16. Yang W (1992) *Phys Rev Lett* 66:1438
17. Li XP, Nunes RW, Vanderbilt D (1993) *Phys Rev B* 47:10891
18. Daw MS (1993) *Phys Rev B* 47:10895
19. Mauri F, Galli G, Car R (1993) *Phys Rev B* 47:9973
20. Ordejón P, Drabold DA, Grumbach MP, Martin RM (1993) *Phys Rev B* 48:14646
21. Goedecker S, Colombo L (1994) *Phys Rev Lett* 73:122
22. Goedecker S (1995) *J Comp Phys* 118:261
23. Kim J, Mauri F, Galli G (1995) *Phys Rev B* 52:1640
24. Wang Y, Stocks GM, Shelton WA, Nicholson DMC, Szotek Z, Temmerman WM (1995) *Phys Rev Lett* 75:2867
25. Abrikosov IA, Niklasson AMN, Simak SI, Johansson B, Ruban AV, Skriver HL (1996) *Phys Rev Lett* 76:4203
26. Silver RN, Roder H (1994) *Int J Mod Phys C* 5:735
27. Silver RN, Roder H, Voter AF, Kress JD (1996) *Int J Comput Phys* 124:115
28. Palser AHR, Manolopoulos DE (1998) *Phys Rev B* 58:12704
29. Helgaker T, Larsen H, Olsen J (2000) *Chem Phys Lett* 327:397
30. Niklasson AMN (2002) *Phys Rev B* 66:155115
31. Galli G (1996) *Cur Op Sol State Mat Sci* 1:864
32. Ordejón P (1998) *Comput Mater Sci* 12:157
33. Goedecker S (1999) *Rev Mod Phys* 71:1085
34. Scuseria G (1999) *J Phys Chem* 103:4782
35. Wu SY, Jayanthi CS (2002) *Phys Rep* 358:1
36. Goedecker S, Scuseria GE (2003) *Comput Sci Eng* 5:14
37. Beylkin G, Coult N, Mohlenkamp MJ (1999) *J Comp Phys* 152:32
38. Holas A (2001) *Chem Phys Lett* 340:552
39. Mazziotti DA (2003) *Phys Rev E* 68:066701
40. Niklasson AMN, Tymczak CJ, Challacombe M (2003) *J Chem Phys* 118:8611
41. Niklasson AMN (2003) *Phys Rev B* 68:233104
42. Xiang HJ, Liang WZ, Yang J, Hou JG, Zhu Q (2005) *J Chem Phys* 123:124105
43. Jordan DK, Mazziotti DA (2005) *J Chem Phys* 122:084114

44. Niklasson AMN (2008) *J Chem Phys* 129:244107
45. McWeeny R (1956) *Proc R Soc London Ser A-Math* 235:496
46. Kenney CS, Laub AJ (1991) *SIAM J Matrix Anal Appl* 12:273
47. Kenney CS, Laub AJ (1995) *IEEE Trans Auto Cont* 40:1330
48. Goedecker S (1999) *Rev Mod Phys* 71:1085
49. Bernstein N (2001) *Europhys Lett* 55:52
50. Bondesson L, Rudberg E, Lu Y, Salek P (2007) *J Phys Chem* 111:10320
51. Rudberg E, Rubensson EH, Salek P (2008) *J Chem Phys* 128:184106
52. Niklasson AMN, Challacombe M (2004) *Phys Rev Lett* 92:193001
53. Weber V, Niklasson AMN, Challacombe M (2004) *Phys Rev Lett* 92:193002
54. Xiang HJ, Yang J, Hou JG, Zhu Q (2006) *Phys Rev Lett* 97:266402
55. Weber V, Niklasson AMN, Challacombe M (2005) *J Chem Phys* 123:44106
56. Niklasson AMN, Weber V, Challacombe M (2005) *J Chem Phys* 123:44107
57. Niklasson AMN, Tymczak CJ, Challacombe M (2006) *Phys Rev Lett* 97:123001
58. Kohn W (1996) *Phys Rev Lett* 76:3168
59. Haynes PD, Payne MC (1999) *Phys Rev B* 59:12173
60. Shao Y, Saravanan C, Head-Gordon M (2003) *J Chem Phys* 118:6144
61. Mauri F, Galli G (1994) *Phys Rev B* 50:4316
62. Ordejón P, Drabold DA, Martin RM, Grumbach MP (1995) *Phys Rev B* 51:1456
63. Liu S, Perez-Jorda JM, Yang W (2000) *J Chem Phys* 112:1634
64. Fattebert JL, Gygi F (2006) *Phys Rev B* 73:115124
65. Weber V, VandeCondele J, Hutter J, Niklasson AMN (2008) *J Chem Phys* 128:084113
66. Weber V and Hutter J (2008) *J Chem Phys* 128:064107
67. Cooley JW, Tukey JW (1965) *Math Comput* 19:297
68. Frigo M, Johnson SG (2005) *Proc IEEE* 93:216
69. Greengard L, Rokhlin V (1987) *J Comp Phys* 73:325
70. Greengard L, Rokhlin V (1990) *Comp Phys* 4:142
71. Challacombe M, White C, HeadGordon M (1997) *J Chem Phys* 107:9708
72. Rudberg E, Salek P (2006) *J Chem Phys* 125:084106
73. Greengard L (1994) *Science* 265:909
74. Challacombe M, Schwegler E, Almlöf J (1996) *J Chem Phys* 104:4685
75. Schwegler E, Challacombe M (1996) *J Chem Phys* 105:2726
76. Burant JC, Scuseria GE, Frisch MJ (1996) *J Chem Phys* 105:8969
77. Challacombe M, Schwegler E (1997) *J Chem Phys* 106:5526
78. Ochsenfeld C, White CA, Head-Gordon M (1998) *J Chem Phys* 109:1663
79. Prodan E, Kohn W (2005) *Proc Natl Acad Sci USA* 102:11635
80. Kohn W (1959) *Phys Rev* 115:809
81. Kohn W (1964) *Phys Rev A* 133:A171
82. Smirnov AV, Johnson DD (2001) *Phys Rev B* 64:235129
83. Zeller R (2008) *J Phys: Condens Matter* 20:294215
84. Cankurtaran BO, Gale JD, Ford MJ (2008) *J Phys: Condens Matter* 20:294208
85. Rubensson EH, Salek P (2005) *J Comput Chem* 26:1628
86. Rubensson EH, Rudberg E, Salek P (2008) *J Chem Phys* 128:074106
87. Rubensson EH, Rudberg E, Salek P (2008) *J Comput Chem* 30:974
88. Gustavson FG (1978) *ACM Trans Math Soft* 4:250
89. Parr RG, Yang W (1989) *Density-functional theory of atoms and molecules*, Oxford University Press, Oxford
90. Golub G, van Loan CF (1996) *Matrix Computations*, Johns Hopkins University Press, Baltimore, MD

91. Benzi M, Meyer CD (1995) *SIAM J Sci Comput* 16:1159
92. Millam JM, Scuseria GE (1997) *J Chem Phys* 106:5569
93. Challacombe M (1999) *J Chem Phys* 110:2332
94. Benzi M, Kouhia R, Tuma M (2001) *Comp Meth App Mech Eng* 190:6533
95. Ozaki T (2001) *Phys Rev B* 64:195110
96. Schweizer S, Kussmann J, Doser B, Ochsenfeld C (2008) *J Comput Chem* 29:1004
97. Niklasson AMN (2004) *Phys Rev B* 70:193102
98. Rubensson EH, Bock N, Holmström E, Niklasson AMN (2008) *J Chem Phys* 128:104105
99. Baer R, Head-Gordon M (1997) *Phys Rev Lett* 79:3962
100. Goedecker S (1998) *Phys Rev B* 58:3501
101. Ismail-Beigi S, Arias TA (1999) *Phys Rev Lett* 82:2127
102. Hastings MB (2004) *Phys Rev Lett* 93:126402
103. Anderson PW (1958) *Phys Rev* 109:1492
104. Press WH, Teukolsky SA, Vetterling WT, Flannery BP (1992) *Numerical recipes in FORTRAN*. Cambridge University Press, Port Chester, NY
105. Challacombe M (2000) *Comput Phys Commun* 128:93
106. Saravanan C, Shao C, Baer R, Ross PN, Head-Gordon M (2003) *J Comput Chem* 24:618
107. Goedecker S, Teter M (1995) *Phys Rev B* 51:9455
108. Voter AF, Kress JD, Silver RN (1996) *Phys Rev B* 53:12733
109. Liang WZ, Baer R, Saravanan C, Shao YH, Bell AT, Head-Gordon M (2004) *J Comp Phys* 194:575
110. Weisse A, Wellein G, Alvermann A, Fehske H (2006) *Rev Mod Phys* 78:275
111. Pessoa S (2002) *Phys Rev B* 46:14570
112. Bergman A, Holmström E, Niklasson AMN, Nordström L, Frota-Pessoa S, Eriksson O (2004) *Phys Rev B* 70:174446
113. Matsubara T (1955) *Prog Theor Phys* 14:351
114. Goedecker S (1993) *Phys Rev B* 48:17573
115. Liang WZ, Saravanan C, Shao Y, Baer R, Bell AT, Head-Gordon M (2003) *J Chem Phys* 119:4117
116. Ozaki T (2007) *Phys Rev B* 75:035123
117. Ceriotti M, Kühne TD, Parrinello M (2008) *J Chem Phys* 129:024707
118. Moler C, Loan CV (2003) *SIAM Rev* 45:3
119. Nemeth K, Scuseria GE (2000) *J Chem Phys* 113:6035
120. Daniels AD, Scuseria GE (1999) *J Chem Phys* 110:1321
121. Mazzioni DA (2001) *J Chem Phys* 115:8305
122. Niklasson AMN, Tymczak CJ, Roder H (2002) *Phys Rev B* 66:155120
123. Larsen H, Helgaker T, Olsen J, Jorgensen P (2001) *J Chem Phys* 115:9685
124. Weber V, Niklasson AMN, Challacombe M (2004) *Phys Rev Lett* 92:193002
125. Niklasson AMN, Weber V (1996) *J Chem Phys* 127:44107
126. Ochsenfeld C, Head-Gordon M (1997) *Chem Phys Lett* 270:399
127. Ochsenfeld C, Kussmann J, Koziol F (2004) *Angewandte Chemie* 43:4485
128. Izmaylov AF, Brothers EN, Scuseria GE (2006) *J Chem Phys* 125:224105
129. Coriani S, Host S, Jasník B, Thøgersen L, Olsen J, Jorgensen P, Reine S, Pawłowski F, Helgaker T, Salek P (2007) *J Chem Phys* 126:154108
130. Lucero MJ, Niklasson AMN, Tretiak S, Challacombe M (2008) *J Chem Phys* 129:064114
131. Tretiak S, Isborn CM, Niklasson AMN, Challacombe M (2009) *J Chem Phys* 130:054111
132. Yokojima S, Chen GH (1998) *Chem Phys Lett* 292:379
133. Yabana K, Bertsch GF (1999) *Int J Quantum Chem* 75:55
134. Tsolakidis A, Sanches-Portal D, Martin R (2002) *Phys Rev B* 66:235416

135. Wang F, Yam CY, Chen GH, Fan K (2007) *J Chem Phys* 126:134104
136. Niklasson AMN et al. Unpublished
137. Helgaker T, Jorgensen P, Olsen J (2002) *Molecular electronic-structure theory*, 1st ed. Wiley, New York, NY
138. McWeeny R (1962) *Phys Rev* 126:1028
139. Kussmann J, Ochsenfeld C (2007) *J Chem Phys* 127:204103

CHAPTER 17

LINEAR SCALING FOR METALLIC SYSTEMS BY THE KORRINGA-KOHN-ROSTOKER MULTIPLE-SCATTERING METHOD

RUDOLF ZELLER¹

¹ *Peter Grünberg Institut and Institute for Advanced Simulation, Forschungszentrum Jülich GmbH, D-52425 Jülich, e-mail: ru.zeller@fz-juelich.de*

Abstract: A Green function (GF) linear-scaling technique based on the Korringa-Kohn-Rostoker (KKR) multiple scattering method is presented for Hohenberg-Kohn-Sham density functional calculations of metallic systems. Contrary to most other methods the KKR-GF method does not use a basis-set expansion to solve the Kohn-Sham equation for the wavefunctions, but directly determines the Kohn-Sham Green function by exploiting a reference system concept. An introduction to the KKR-GF method is given and it is shown how linear-scaling is obtained by the combined use of a repulsive reference system, which leads to sparse matrix equations, iterative solution of these equations and a spatial truncation of the Green function in the sense of Kohn's principle of near-sightedness of electronic matter. The suitability of the technique for metallic systems with thousands of atoms is illustrated by model calculations for large supercells and its usefulness for computing on massively parallel supercomputers is discussed.

Keywords: Condensed matter, Electronic structure, Metallic systems

17.1. INTRODUCTION

In the last decades Hohenberg-Kohn-Sham density functional theory [1, 2] has emerged as a powerful tool for the quantum mechanical description of chemical and physical properties of materials. Instead of the many electron wavefunction density functional theory uses the electronic density as the basic variable and provides single-particle equations to determine this density. In spite of this considerable simplification systems with many atoms still present a serious computational challenge if standard techniques are used to solve the single-particle equations because the computing time increases proportionally to the third power of the number of electrons in the system. In recent years considerable effort has been spent to develop

algorithms for density functional calculations which avoid this bottleneck in several or all parts of the computer codes.

Most of these sophisticated algorithms are based on a locality principle which is valid in density functional calculations for local properties that are affected insignificantly by long range potential contributions. For instance, the density in neutral systems is such a property that can be calculated accurately if long range potential contributions are neglected. Then ideally one can expect for systems large enough that the computational effort scales linearly with system size because the density around each atom can be calculated separately so that the total effort scales with the number of atoms.

One of these algorithms which has been developed recently in our institute in Jülich will be introduced in this chapter and its usefulness will be discussed and illustrated. The algorithm based on the KKR-GF method was intended initially for metallic systems, but can be used also for systems with bandgap as semiconductors and insulators. The KKR-GF method solves the single-particle density-functional equations for all electrons including the tightly bound core electrons without the need of a pseudopotential approximation. Its particular strength is its applicability to non-periodic situations, for instance to solve the embedding problem of impurity atoms in bulk crystals and atoms or cluster of atoms on surfaces or at interfaces. Because the KKR-GF method is not so widely known,¹ it will be explained in some detail, particularly emphasizing the characteristic differences between a Green function and a wavefunction formalism. It will be shown how sparse matrix equations can be obtained by a screening transformation, that these matrix equations can be solved by iteration in highly parallel manner, how the locality principle can be used by truncating the Green function for large distances and that linear scaling can be obtained for the computational effort. A model system will be presented for the investigation of the effects of iteration and truncation on accuracy of calculated total energies. The model system is also used to study how large the system must be so that linear scaling with its large prefactor is more advantageous than standard KKR-GF calculations with cubic scaling.

17.2. PRELIMINARIES

Here the main equations of density functional theory are introduced, linear scaling strategies are explained and the particular problem with metallic systems is discussed.

17.2.1. Density Functional Theory

Density functional theory provides a mapping of the interacting many electron system with external potential $v_{ext}(\mathbf{r})$ to an auxiliary non-interacting system with potential $v_{eff}(\mathbf{r})$ such that the ground-state electron densities of both systems are identical. The effective potential can be written as

¹ A relatively recent description of important issues can be found in [3].

$$v_{\text{eff}}(\mathbf{r}) = v_{\text{ext}}(\mathbf{r}) + e^2 \int_{\infty} \frac{n(\mathbf{r}')}{|\mathbf{r} - \mathbf{r}'|} d\mathbf{r}' + v_{\text{xc}}[n(\mathbf{r})](\mathbf{r}), \quad (17-1)$$

where the infinity sign indicates integration over all space. The second term on the right hand side of (17-1) is the classical Coulomb potential due to the electron density $n(\mathbf{r})$ and the last term is the exchange-correlation potential defined as a density functional $v_{\text{xc}}[n(\mathbf{r})]$ for which approximations exist in various degree of sophistication. The electron density for the auxiliary non-interacting system can be calculated as

$$n(\mathbf{r}) = 2 \sum_i |\varphi_i(\mathbf{r})|^2 \quad (17-2)$$

from normalized Kohn-Sham wavefunctions (orbitals) $\varphi_i(\mathbf{r})$, which obey a single-particle Schrödinger equation

$$\left[-\nabla_{\mathbf{r}}^2 + v_{\text{eff}}(\mathbf{r}) \right] \varphi_i(\mathbf{r}) = E_i \varphi_i(\mathbf{r}). \quad (17-3)$$

To simplify the appearance of the equations in this chapter Rydberg atomic units $\hbar^2/2m = 1$ will be used and only equations for non-spin-polarized systems will be given. The generalization to spin-polarized (magnetic) systems is straightforward. Thus for a system with N electrons the density (17-2) is calculated by a finite sum over the $N/2$ orbitals with lowest values of E_i and spin degeneracy is taken into account by the factor 2.

Because the effective potential is defined by the density and the density depends by (17-2) and (17-3) on the effective potential, the density functional equations (17-1–17-3) must be solved in a self-consistent manner. Self-consistency is usually achieved by iteration. Starting from an initial guess for the density one calculates the effective potential by (17-1), solves for the orbitals by (17-3), calculates a new density by (17-2), chooses a judicious combination of the densities as input for the next iteration and iterates until input and output densities of one iteration cycle agree sufficiently well. For large systems the self-consistent solution requires very large computer resources, not only because the equations must be solved repeatedly, but also because they are expensive to solve for systems with many atoms if standard solution techniques are used with their cubically scaling computational effort.

17.2.2. Linear Scaling Strategies

Usually, during self-consistency iterations the calculation of the orbitals (17-3) is more time consuming than calculation of density (17-2) and effective potential (17-1). If the orbitals are calculated in standard manner by using an expansion in a set of basis functions, an algebraic eigenvalue problem must be solved, where the matrix to be diagonalized has a dimension proportional to the number of atoms.

Compared to the $O(N^3)$ work² to solve the eigenvalue problem, the calculation of density and classical Coulomb potential require only $O(N^2)$ work. The calculation of the exchange-correlation potential $v_{xc}[n(\mathbf{r})]$ can be even less demanding, for instance the work scales as $O(N)$ for the local density approximation (LDA) or the quasi-local generalized gradient approximation (GGA).

In this chapter only the problem to obtain linear scaling for the treatment of (17-2) and (17-3) will be considered assuming that the problem for the Coulomb potential is solved, for instance by multigrid, wavelet or fast multipole methods. Although multigrid and wavelet methods eventually can be used to obtain linear scaling for (17-2) and (17-3), most of the recently developed linear scaling algorithms are based on a locality principle for the density which was formulated by Kohn et al. [4, 5]. It is valid, for instance in density functional calculations, for local properties as the density that do not depend on the potential far away.

The locality principle or the nearsightedness of electronic matter as it has been called by Kohn means that in systems without long range electric fields (and for fixed chemical potential) the density change at a point r_0 , which is caused by a potential change in a finite region far away (outside a sphere with radius R around r_0), is small and decays to zero if R increases to infinity. As a consequence it should be possible to determine the density around an atom from the potential in a large enough local region surrounding this atom, whereas the potential outside this region is neglected.

The concept of nearsightedness is exploited directly in divide and conquer approaches [6, 7]. Here one calculates the density by a standard method for a local region, which contains the atoms of interest and enough surrounding buffer atoms so that the potential outside the buffer region can be neglected. The effort obviously scales linearly because the system can be decomposed into $O(N)$ parts treated independently. The calculated densities are then patched together and calculation of the effective potential (17-1), which anyhow usually requires only an insignificant part of the computing time, is treated in the normal way. The number of atoms, for which the calculated density is used, can be chosen as one as in the locally self-consistent multiple scattering (LSMS) method [8] and in the locally self-consistent Green function (LSGF) method [9, 10], which are based on the KKR and the related linear muffin-tin orbital (LMTO) method, or as more than one as in the original method of Yang [6]. It has been discussed in detail by Smirnov and Johnson [11] that for metallic systems the size of the buffer region puts limitations on the accuracy that can be achieved. In principle the accuracy can be increased with larger buffer regions, but the cost is high because the effort increases with the third power of the number of atoms in the buffer region. Thus additional techniques to accelerate the calculations are needed.

Because $O(N^3)$ steps in the calculation of the orbitals mainly arise from the extent of the orbitals over the entire system and/or from their necessary orthogonalization, the obvious idea is to avoid these steps by calculating directly the density matrix

²The symbol $O(N^\alpha)$ denotes as usual an increase proportional to N^α for large values of N .

$$\rho(\mathbf{r}, \mathbf{r}') = 2 \sum_i \varphi_i^*(\mathbf{r}) \varphi_i(\mathbf{r}') \quad (17-4)$$

from which the density $n(\mathbf{r}) = \rho(\mathbf{r}, \mathbf{r})$ immediately follows.

In the density matrix the nearsightedness of electronic matter is observable as a decay of $\rho(\mathbf{r}, \mathbf{r}')$ with increasing distance $|\mathbf{r} - \mathbf{r}'|$. The decay is exponential in systems with bandgap and algebraic in metals. However, because nearsightedness alone is not enough for an efficient linear scaling method, usually three other key factors are exploited in density matrix based linear scaling algorithms. Localized basis functions are used to obtain sparse matrices in the basis set representation of the Hamiltonian, iterative solution techniques are applied to exploit sparse matrix operations and efficient parallelization is intended for use of supercomputers. Efficient parallelization is particularly necessary because linear scaling methods with their large overhead are more advantageous than cubically scaling methods only for systems containing hundred or thousands of atoms. This system size makes the use of massively parallel supercomputers indispensable.

17.2.3. Metallic Systems

Metallic systems present a significant challenge for the development of linear scaling techniques. One problem is that the density matrix (17-4) does not decay exponentially as in insulators or semiconductors, but only algebraically as

$$\rho(\mathbf{r}, \mathbf{r}') \sim \frac{\cos(k_F |\mathbf{r} - \mathbf{r}'|)}{|\mathbf{r} - \mathbf{r}'|^2} \quad (17-5)$$

and is thus less nearsighted in metals than in insulators and semiconductors. To solve this problem it has been suggested to apply an artificial temperature $T \neq 0$ to the electron system, because temperature introduces an exponential factor into the density matrix decay. For example, for the free electron gas, which is a simple metallic system, the density matrix behaves for large distance $|\mathbf{r} - \mathbf{r}'|$ as [12, 13]

$$\rho(\mathbf{r}, \mathbf{r}', T) \sim \frac{\cos(k_F |\mathbf{r} - \mathbf{r}'|)}{|\mathbf{r} - \mathbf{r}'|^2} \exp(-\gamma |\mathbf{r} - \mathbf{r}'|), \quad (17-6)$$

where k_F is the Fermi wave vector and γ is proportional to T/k_F . Here the important question (which will be answered to some extent in the model study in Section 17.4.4) is whether the exponential decay caused by temperature is large enough for temperatures which are reasonably small so that reliable results can be calculated. Another problem for metallic systems is the missing gap between occupied and unoccupied states so that an unambiguous choice of the states contributing to the density matrix is nontrivial. Nevertheless, some success of linear scaling techniques has already been reported for metallic systems [14, 15].

17.3. THE KKR-GF METHOD

The KKR method was introduced for solution of the single-particle Schrödinger in crystals with periodic potential by Korringa [16] in 1947 and by Kohn and Rostoker [17] in 1954. The method was originally formulated and understood within multiple scattering theory [18] which describes the interference of electron waves scattered at potentials centered at the atomic positions. In this theory the solution of the Schrödinger equation (17-3) is decoupled into two parts. First the solution is found for single-scattering events at the potentials around each atomic site and then the multiple scattering problem is solved with the constraint that the incident wave on a site is determined by the sum of the outgoing waves at all other sites. In this sense the method is even older as quantum mechanics, since it was already introduced by Lord Rayleigh [19] in 1892 in his paper “On the influence of obstacles arranged in rectangular order upon the properties of a medium”, where he studies the conductivity for heat or electricity in two or three dimensions in a uniform medium interrupted by cylindrical or spherical obstacles.

A historical handicap for the KKR method was the belief that the method is valid only for situations where the potential is spherical within non-overlapping muffin-tin spheres around each scattering site and zero in the interstitial region between the spheres. The belief that this restriction is necessary was caused by the original derivation of the KKR method in a multiple scattering picture, where a wave is scattered at obstacles and freely propagates between them. The property of free propagation was used to reexpand outgoing waves from scattering sites into incoming waves at other sites. This multiple scattering picture obviously breaks down if the scattering events are not clearly separated so that a scattering event at one site is not finished before the wave enters the scattering region at another site. A breakthrough for the KKR method was the demonstration by several authors³ in the 1980s that the assumption of free propagation between scattering events is not necessary to derive the KKR equations. Later it also was demonstrated that the full potential KKR method leads to calculated total energies and forces, which are as accurate as they are calculated by other density functional methods (see Section 17.3.4), and now it is commonly accepted that the full potential KKR method is valid for potentials of general shape.

Another handicap of the original wavefunction formulation was the computational complexity caused for the KKR method. To determine the eigenvalues E_i in (17-3) it was necessary to find the zeros of a determinant of a matrix which depends in a highly non-linear fashion on the relevant variables. To find $O(N)$ eigenvalues required to calculate many determinants each with $O(N^3)$ effort. The overall $O(N^4)$ scaling made the original KKR method quite uncompetitive compared to basis set methods with $O(N^3)$ scaling. Here another breakthrough was provided by the Green function formulation of the KKR method, which reduces the work to the solution of linear equations with $O(N^3)$ effort.

³ An elementary derivation using a Green function formalism as presented below is given in [20].

17.3.1. Properties of the Green Function

Since the 1960s and 1970s the KKR method is understood as a technique to determine directly the classical [21, 22] Green function for the Kohn-Sham equation (17-3). This Green function, which should not be confused with the single-particle Green function of many-body theory, is defined as the solution of

$$\left[-\nabla_{\mathbf{r}}^2 + v_{eff}(\mathbf{r}) - E \right] G(\mathbf{r}, \mathbf{r}'; E) = -\delta(\mathbf{r} - \mathbf{r}') \quad (17-7)$$

with the boundary condition $G(\mathbf{r}, \mathbf{r}'; E) \rightarrow 0$ for $|\mathbf{r} - \mathbf{r}'| \rightarrow \infty$. Obviously (17-7) is more complicated than the corresponding wavefunction equation (17-3). On the other hand the Green function is more powerful, for instance it can be used to solve the embedding problem of defect atoms in infinite bulk crystals [3, 23, 24] and to obtain the linear scaling algorithm presented below.

In (17-7) the energy E is a complex variable and as function of this variable the Green function is an analytical function⁴ except for singularities on the real energy axis. Here the Green function can have poles corresponding to discrete eigenvalues of the Hamilton operator $\hat{H} = -\nabla_{\mathbf{r}}^2 + v_{eff}(\mathbf{r})$ and branch cut singularities corresponding to the continuous spectrum. In principle, the Green function can be obtained by

$$G(\mathbf{r}, \mathbf{r}'; E + i\varepsilon) = \sum_i \frac{\varphi_i^*(\mathbf{r})\varphi_i(\mathbf{r}')}{E + i\varepsilon - E_i} + \int_{-\infty}^{\infty} \frac{\varphi^*(\mathbf{r}; E')\varphi(\mathbf{r}'; E')}{E + i\varepsilon - E'} dE' \quad (17-8)$$

from the eigenfunctions of the Hamilton operator, which are determined by (17-3). In this spectral representation the sum is over the discrete eigenstates and the integral is over the continuous eigenstates. The lower limit of this and subsequent energy integrals is chosen usually as minus infinity, actually it depends on the material and is finite because the spectrum of the Hamilton operator \hat{H} is bounded from below. From (17-8) and the identity

$$\lim_{y \rightarrow 0^+} \frac{1}{x + iy} = P \frac{1}{x} - i\pi \delta(x), \quad (17-9)$$

where P denotes the principal value, one can deduce that the Green function is connected with the density matrix $\rho(\mathbf{r}, \mathbf{r}')$ by

$$\rho(\mathbf{r}, \mathbf{r}') = -\frac{2}{\pi} \text{Im} \int_{-\infty}^{E_F} G(\mathbf{r}, \mathbf{r}'; E + i\varepsilon) dE \quad (17-10)$$

⁴For an elementary introduction to classical Green functions and their analytical properties the textbook of Economou [21] is a good source.

and with the density $n(\mathbf{r}) = \rho(\mathbf{r}, \mathbf{r})$ by

$$n(\mathbf{r}) = -\frac{2}{\pi} \text{Im} \int_{-\infty}^{E_F} G(\mathbf{r}, \mathbf{r}; E + i\varepsilon) dE. \quad (17-11)$$

Here the Fermi level E_F must be determined by the condition that the density $n(\mathbf{r})$ integrated over all space gives the required number of electrons, which for instance in neutral systems must agree with the sum of the atomic numbers. The local density of states within a volume V can be calculated from the Green function as

$$\rho_V(E) = -\frac{2}{\pi} \text{Im} \int_V G(\mathbf{r}, \mathbf{r}; E + i\varepsilon) d\mathbf{r}. \quad (17-12)$$

In (17-8) and (17-10), (17-11) and (17-12) the notation $E + i\varepsilon$ means that the integrals are along the real axis, E is real and ε is a small real positive quantity chosen to avoid the Green function singularities on the real axis. Note that $\varepsilon \rightarrow 0^+$ gives results which differ from the ones obtained by $\varepsilon \rightarrow 0^-$ because branch cut singularities lead to different side limits as discussed in [21].

17.3.2. Calculation of the Green Function

For the calculation of the Green function neither the defining equation (17-7) nor the spectral representation (17-8) is convenient. Standard techniques for partial differential equations are difficult to apply for the numerical solution of (17-7) because the source term $\delta(\mathbf{r} - \mathbf{r}')$ diverges for $\mathbf{r} \rightarrow \mathbf{r}'$. The problem for the application of the spectral representation (17-8) is that all (in principle, infinitely many) eigenfunctions must be calculated because the weight of their contribution only slowly decays inversely proportional to energy. It is much more convenient to use the concept of reference systems and to transform (17-7) into an integral equation

$$G(\mathbf{r}, \mathbf{r}'; E) = G^r(\mathbf{r}, \mathbf{r}'; E) + \int_{-\infty}^{\infty} G^r(\mathbf{r}, \mathbf{r}''; E) [v_{\text{eff}}(\mathbf{r}'') - v^r(\mathbf{r}'')] G(\mathbf{r}'', \mathbf{r}'; E) d\mathbf{r}'' \quad (17-13)$$

or by changing the order of G^r and G in the integrand into the integral equation

$$G(\mathbf{r}, \mathbf{r}'; E) = G^r(\mathbf{r}, \mathbf{r}'; E) + \int_{-\infty}^{\infty} G(\mathbf{r}, \mathbf{r}''; E) [v_{\text{eff}}(\mathbf{r}'') - v^r(\mathbf{r}'')] G^r(\mathbf{r}'', \mathbf{r}'; E) d\mathbf{r}'' . \quad (17-14)$$

Here G^r is the Green function and v^r the potential of a reference system. The equivalence of (17-7) and (17-13) can be verified by applying the operator $-\nabla_{\mathbf{r}}^2 + v^r(\mathbf{r}) - E$ on both sides of (17-13) from the left and using that the reference Green function G^r satisfies (17-7) if the effective potential is replaced by the reference potential. The equivalence of (17-7) and (17-14) can be verified similarly by applying the operator $-\nabla_{\mathbf{r}}^2 + v_{\text{eff}}(\mathbf{r}) - E$ on both sides of (17-14) from the left.

The concept of reference Green functions can be used to find the Green function of a complicated systems successively from Green functions of simpler systems. For instance, the Green function for adsorbate atoms on a surface can be calculated

by starting from the Green function of free space, where the reference potential $v^0(\mathbf{r})$ vanishes, calculating first the Green function of an ideal bulk crystal using its three-dimensional periodicity, then calculating the Green function of a crystal with a surface using two-dimensional periodicity and finally using the surface Green function as reference Green function for the adsorbate system. In each step the region, where the potential changes, is exactly embedded in a simpler system and the integral equation is restricted in space to the region, where the potential changes. In this way all interactions, for instance between the adsorbate atoms and the substrate are included and the use of substitute geometries as supercells or clusters is avoided.

The essential problem in the numerical application of (17-13) or (17-14) is to find a useful representation for the Green function, which depends on two points in space and on energy, which together are seven variables. Here multiple scattering theory provides the key idea to obtain such a representation. In multiple scattering theory the reference system is free space with vanishing potential $v^0(\mathbf{r}) = 0$. The Green function for free space is analytically known and given by

$$G^0(\mathbf{r}, \mathbf{r}'; E) = -\frac{1}{4\pi} \frac{\exp(i\sqrt{E}|\mathbf{r} - \mathbf{r}'|)}{|\mathbf{r} - \mathbf{r}'|} \quad (17-15)$$

which is symmetric in the space variables $G^0(\mathbf{r}, \mathbf{r}'; E) = G^0(\mathbf{r}', \mathbf{r}; E)$. It can be written (see appendix) in an almost separable form as

$$G^0(\mathbf{r}, \mathbf{r}'; E) = \sum_L^\infty H_L(\mathbf{r}_>; E) J_L(\mathbf{r}_<; E), \quad (17-16)$$

where $H_L(\mathbf{r}; E)$ and $J_L(\mathbf{r}; E)$ are products of spherical Hankel functions of the first kind and spherical Bessel functions with real spherical harmonics. The symbols $\mathbf{r}_>$ and $\mathbf{r}_<$ mean that $\mathbf{r}_>$ is the vector \mathbf{r} or \mathbf{r}' with larger length and $\mathbf{r}_<$ the one with smaller length. The sum in (17-16) converges slowly if the vectors \mathbf{r} and \mathbf{r}' have large lengths. Thus it cannot be used for the numerical purpose to solve (17-13) or (17-14) in entire space. In multiple scattering theory the problem arising from the large length of \mathbf{r} or \mathbf{r}' is solved by dividing space into a collection of space-filling non-overlapping cells and by introducing cell-centered coordinates by the replacement $\mathbf{r} \rightarrow \mathbf{R}^n + \mathbf{r}$ and $\mathbf{r}' \rightarrow \mathbf{R}^{n'} + \mathbf{r}'$ as schematically shown in Figure 17-1. Usually the cell centers \mathbf{R}^n are chosen at the nuclear positions where the Coulomb potential diverges.

By use of the addition theorem of spherical Hankel functions (see Appendix) the free space Green function in cell-centered coordinates can be written in the form

$$\begin{aligned} G^0(\mathbf{r} + \mathbf{R}^n, \mathbf{r}' + \mathbf{R}^{n'}; E) &= \delta_{nm'} \sum_L^\infty H_L(\mathbf{r}_>; E) J_L(\mathbf{r}_<; E) \\ &+ \sum_{LL'}^\infty J_L(\mathbf{r}; E) G_{LL'}^{0, nm'}(E) J_{L'}(\mathbf{r}'; E). \end{aligned} \quad (17-17)$$

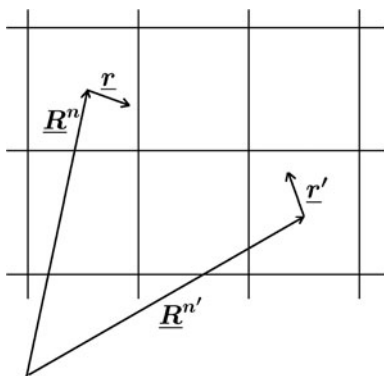


Figure 17-1. Schematic view of the partitioning into cells with \mathbf{R}^n and $\mathbf{R}^{n'}$ denoting cell centers and \mathbf{r} and \mathbf{r}' cell-internal coordinates

In this expression the variables \mathbf{r} and \mathbf{r}' are restricted to the cells around \mathbf{R}^n and $\mathbf{R}^{n'}$ and thus are vectors with small length.

For the validity of the KKR-GF method the crucial discovery was that the Green function for a general potential can be expressed in analogy to (17-17) as⁵

$$G(\mathbf{r} + \mathbf{R}^n, \mathbf{r}' + \mathbf{R}^{n'}; E) = \delta_{nn'} \sum_L^\infty S_L^n(\mathbf{r}_{>}; E) R_L^n(\mathbf{r}_{<}; E) + \sum_{LL'}^\infty R_L^n(\mathbf{r}; E) G_{LL'}^{nn'}(E) R_L^{n'}(\mathbf{r}'; E). \quad (17-18)$$

The Green function matrix elements $G_{LL'}^{nn'}(E)$ can be calculated from the Green function matrix elements of the reference system (denoted by an upper index r) by

$$G_{LL'}^{nn'}(E) = G_{LL'}^{r,nn'}(E) + \sum_{n''L''L'''}^\infty G_{LL''}^{r,nn''}(E) \Delta t_{L''L'''}^{n''n'}(E) G_{L''L'''}^{n''n'}(E). \quad (17-19)$$

Here $\Delta t_{L''L'''}^{n''n'}(E)$ is a difference of single-cell t matrices determined from potential and reference potential restricted to cell n . For numerical calculations the infinite angular momentum sums in (17-18) and (17-19) must be truncated to a finite number of terms. Usually values $l \leq l_{max} = 3$ are used. In (17-19) this leads to matrices with dimension $N(l_{max} + 1)^2$ which is determined by l_{max} and the number N of atoms. The matrix Δt has not two, but one site index n'' indicating that it is block diagonal,

⁵ Several different notations have been used in the historical development of the KKR-GF method. In this chapter the most concise one introduced in [25] is used.

all t matrix elements which couple different sites vanish. The equations to calculate t matrices and single-scattering wavefunctions $R_L^n(\mathbf{r}; E)$ and $S_L^n(\mathbf{r}; E)$ are given in Appendix.

It is here important to realize that the KKR expression (17-18), which solves (17-7) for the classical Green function of the Kohn-Sham equation (17-3), couples different atomic sites only through the Green function matrix elements (17-19) and that these elements do not depend on the cell-internal coordinates \mathbf{r} and \mathbf{r}' . First this means that all other quantities as t matrices and single-scattering wavefunctions can be calculated independently for each cell with a naturally linear scaling effort and in a perfect parallel manner. Second this means that a better spatial resolution in the cells with finer radial meshes for \mathbf{r} and \mathbf{r}' increases the effort to solve the single-cell equations which scales linearly, but not the effort to solve the matrix equation (17-19) which scales cubically. Thus the KKR-GF method can be considered as a two-scale approach where one first uses a fine radial resolution around the atoms and then on an atomic scale solves a linear algebra problem (17-19).

17.3.3. Complex Energy Integration

Whereas in wavefunction methods the density is calculated as a sum (17-2) over Kohn-Sham orbitals, in the KKR-GF method the density is calculated as an integral (17-11), which in cell-centered coordinates can be written as

$$n(\mathbf{r} + \mathbf{R}^n) = -\frac{2}{\pi} \text{Im} \int_{-\infty}^{E_F} G(\mathbf{r} + \mathbf{R}^n, \mathbf{r} + \mathbf{R}^n; E + i\varepsilon) dE. \quad (17-20)$$

Here the integration is along the real energy axis in the limit $\varepsilon \rightarrow 0^+$. In principle, this integral can be evaluated by calculating the Green function for a suitable set of energy mesh points. In practice however, this integration is difficult because near the real energy axis the Green function is as strongly structured as typical density of states which can be expected from the relation (17-12) between Green function and density of states. For an efficient evaluation of (17-20) it is important to use that G is an analytical function of E , if E does not coincide with singularities on the real E axis, so that (17-20) can be evaluated by contour integration [26] in the upper half plane. A useful contour, where away from the real axis all structures of the Green function are broadened by the imaginary part of E , is schematically shown in Figure 17-2.

On the contour special care is needed near the end point E_F which is real so that a finer mesh of energy points should be used there. An elegant way to avoid the real valued end point E_F and to construct a physically motivated set of mesh points on the vertical part of the contour at E_F is to use the finite-temperature density functional formalism [27]. Then (17-20) is replaced by

$$n(\mathbf{r} + \mathbf{R}^n) = -\frac{2}{\pi} \text{Im} \int_{-\infty}^{\infty} f(E - E_F, T) G(\mathbf{r} + \mathbf{R}^n, \mathbf{r} + \mathbf{R}^n; E) dE, \quad (17-21)$$

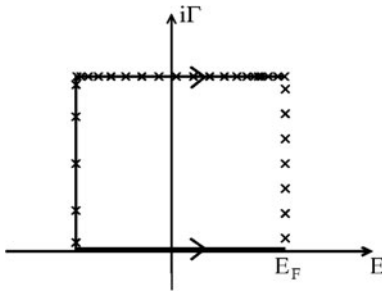


Figure 17-2. Integration contour in the complex energy plane with mesh points indicated by crosses. The points vertically above E_F are the Matsubara energies and the unequally spaced points on the lines of the contour are Gaussian integration points. The thick line along the real axis indicates the original integration of path of (17-20)

where the upper bound of the integration is now infinity and $f(E - E_F, T)$ is the Fermi-Dirac function for chemical potential E_F and temperature T . The horizontal part of the contour can now be shifted to large values of $\text{Im}E$ provided that the residues at the poles of the Fermi-Dirac function are taken into account [28]. The poles of the Fermi-Dirac function (the Matsubara energies) are at $E_j = E_F + (2j - 1)i\pi k_B T$ for all integer values of j and the one closest to E_F in the upper half plane is at $i\pi k_B T$. A convenient contour starts on the negative real energy axis in the energy gap above the core and below the valence states and goes to infinity parallel to the real energy axis with distance $2J\pi k_B T$ from the real axis, where J denotes the number of Matsubara energies at which the residues must be calculated. Note that on the horizontal part of the contour the Fermi-Dirac function has the same values as on the real axis because the Fermi-Dirac function is periodic with period $2i\pi k_B T$. Because both the Green function and the Fermi-Dirac function are rather smooth on the contour, the contour integration error for total energies can be made smaller than 10^{-7} meV with about 30–50 mesh points (including the number of Matsubara energies used). Since the contour in Figure 17-2 includes only contributions of valence states, the contributions of core states must be added separately.

In a certain sense the introduction of the Fermi-Dirac function in (17-21) is similar to the broadening concept usually introduced to improve the Brillouin zone sampling. Note however that the broadening along the horizontal part of the contour is much larger than in conventional broadening schemes and the contributions of the residues at the Matsubara energies are exactly taken into account.

17.3.4. Total Energy and Forces

In density functional theory the total energy is given as a functional $E_{tot}[n(\mathbf{r})]$ of the density $n(\mathbf{r})$, which can be written as

$$E_{tot}[n(\mathbf{r})] = T_s[n(\mathbf{r})] + \int_V n(\mathbf{r})v_{ext}(\mathbf{r})d\mathbf{r} + E_H[n(\mathbf{r})] + E_{xc}[n(\mathbf{r})], \quad (17-22)$$

where V is either the volume of the lattice unit cell in infinite periodic systems (then E_{tot} is defined as the total energy per unit cell) or the volume of all space in real space calculations. In (17-22) the second term on the right hand side is the contribution arising from the external potential provided by the nuclei, E_H is the classical electron-electron interaction (Hartree energy) and E_{xc} the exchange-correlation functional. These three terms are calculated in the usual way from the density $n(\mathbf{r})$. The first term T_s is the kinetic energy functional of non-interacting electrons, which can be calculated either directly from the Green function by

$$T_s[n(\mathbf{r})] = -\frac{2}{\pi} \text{Im} \int_V \left[\int_{-\infty}^{E_F} \lim_{\mathbf{r}' \rightarrow \mathbf{r}} \nabla_{\mathbf{r}}^2 G(\mathbf{r}, \mathbf{r}'; E + i\varepsilon) dE \right] d\mathbf{r} \quad (17-23)$$

or more conveniently from the density of states (17-12) as

$$T_s[n(\mathbf{r})] = \int_{-\infty}^{E_F} E \rho_V(E) dE - \int_V n(\mathbf{r}) v_{eff}(\mathbf{r}) d\mathbf{r}. \quad (17-24)$$

The total energy functional (17-22), which is extremal against charge conserving density variations, can be generalized into the functional

$$\tilde{E}_{tot}[n(\mathbf{r})] = E_{tot}[n(\mathbf{r})] - E_F \left[\int_V n(\mathbf{r}) d\mathbf{r} - N \right] \quad (17-25)$$

which is extremal also if the density variations do not conserve charge. The generalization is important, for instance for impurity calculations [29] where charge neutrality cannot be guaranteed since the fixed Fermi level is determined by the host crystal, and also convenient for the model study below because self-consistency iterations for the large supercells are not necessary.

Total energies calculated by the full potential KKR-GF method exhibit comparable accuracy as total energies calculated by other density functional methods. This has been shown, for instance, for lattice constants and bulk moduli of metals and semiconductors in benchmark calculations [3, 30] both by the KKR-GF and the full potential linear augmented plane wave (FLAPW) method which is generally considered as one of most accurate methods for density functional calculations. The differences between these two methods are rather small if the calculations with both methods are done with sufficiently high accuracy.

The calculation of forces is rather straightforward [31] in the KKR-GF method because the Hellmann-Feynman theorem [32, 33] can be applied. The derivative of (17-22) with respect to the atomic position \mathbf{R}^n is the force \mathbf{F}^n on the nucleus given by

$$\mathbf{F}^n = -\frac{\partial E_{tot}}{\partial \mathbf{R}^n} - \int_V \frac{\delta E_{tot}}{\delta n(\mathbf{r})} \frac{\partial n(\mathbf{r}; \mathbf{R}^n)}{\partial \mathbf{R}^n} d\mathbf{r}. \quad (17-26)$$

Here the first term (evaluated at constant density) is the Hellmann-Feynman force caused by the electric field of all electrons and all other nuclei. The second term

describes a correction if the Kohn-Sham equations are solved only approximately. It vanishes for the exact solution because then the derivative $\delta E_{tot}/\delta n(\mathbf{r})$ is a constant equal to E_F and the derivative of $\int_V n(\mathbf{r})d\mathbf{r} = N$ is zero. In the full potential KKR-GF method contributions of the valence electrons to the correction term are rather small because an almost exact solution is obtained except for approximation by the angular momentum cutoff. Because the core electrons are treated usually in spherical approximation, their contributions must be corrected leading to an “ionic” Hellmann-Feynman theorem [34] which can be written as

$$\mathbf{F}^n = -Z^n \left. \frac{\partial v_M(\mathbf{r})}{\partial \mathbf{r}} \right|_{\mathbf{r}=\mathbf{R}^n} - \int_n n_c(\mathbf{r}) \frac{\partial v_{eff}(\mathbf{r})}{\partial \mathbf{r}} d\mathbf{r}, \quad (17-27)$$

where the first term contains the nuclear charge Z^n and the electrostatic Madelung potential $v_M(\mathbf{r})$ and the correction term [31] contains the core density in cell n and the derivative of the effective potential.

The reliability of force calculations within the full potential KKR-GF method has been demonstrated by calculating displacements around defect atoms and by calculating phonon dispersion curves. For impurities in Cu and Al, where the size difference of impurity and host atoms induces displacements of the surrounding host atoms, good agreement was found [31] for the displacement calculated by minimization of the calculated total energy or by the condition of zero forces. Comparison [31, 35] of the calculated displacements with measured ones obtained by extended x-ray absorption fine structure (EXAFS) experiments shows good agreement in trend and value within the experimental error bars. Displacements in semiconducting materials are usually larger because of the more open structures. In calculations for donor-acceptor pairs in Si and Ge equilibrium positions calculated by the full-potential KKR-GF method are essentially the same as the ones obtained by a pseudopotential method [36] and electric field gradients calculated at the displaced positions for Cd-donor pairs are found in good agreement to measured ones [37]. Phonon dispersion curves can be calculated also successfully by the full-potential KKR-GF method [3, 38]. The dynamical matrix is obtained from force constants calculated at six shells of neighbour atoms around a central displaced atom. Whereas the phonon dispersion curves for Al [3] are in good agreement with experiment, the ones for Fe [38] are not so good probably caused by inadequacy of the used LDA exchange-correlation potential.

17.3.5. Temperature Error

Whereas a finite temperature is usually introduced as a device to improve the Brillouin zone sampling, for the linear scaling algorithm presented below an electronic temperature $T \neq 0$ is of crucial importance for the convergence of the applied iterative solution techniques. For higher temperature the convergence is faster but the temperature error also increases according to

$$E_{tot}(T) = E_{tot}(0) + \alpha_2 T^2 + \alpha_4 T^4 + \dots \quad (17-28)$$

Here terms with odd order in T vanish because the derivative of the Fermi-Dirac function is an even function. It has been pointed out by Smirnov and Johnson [11] that too large temperature can lead to unacceptable results, particularly for magnetic systems. Therefore it would be nice if the quadratic term in (17-28), which has the largest contribution for small T , could be eliminated. The obvious idea, calculations for two different temperatures and elimination of the quadratic term by subtraction, is not useful because very large numbers must be subtracted requiring such high accuracy that no gain can be expected. In the KKR-GF method the numerical subtraction of large numbers is avoided by using an appropriate linear combination of two Fermi-Dirac functions for different temperatures. For instance $\tilde{f}(E - E_F, T) = (9f(E - E_F, T) - f(E - E_F, 3T))/8$ leads exactly to $\tilde{E}_{tot}(T) = E_{tot}(0) - 9\alpha^4 T^4 + \dots$ where the T^2 term is eliminated.

The improvement is illustrated for the elemental metals Cu and Pd in Figure 17-3, where the symbols indicate the results calculated with the T^2 and T^4 schemes. Below $T = 1600$ K the results calculated with the T^4 scheme are considerably better than the ones for the T^2 scheme. The results in Figure 17-3 are very similar to the results shown in Ref. [39] which were obtained by a linear combination of Fermi-Dirac functions for T and $2T$. The choice $3T$ used here seems to be more advantageous because the Matsubara energies for $3T$ are a subset of the ones for T . No additional residues must be calculated and no new point $E_F + 2i\pi k_B T$ relatively near to the real axis is introduced compared with Ref. [39]. Note that the subtraction of two Fermi-Dirac functions leads to a function which changes sign along the horizontal part of the integration contour. However, contrary to the difficulty, which negative occupancies represent for basis set methods, in the KKR-GF method the sign change is easily treated in the construction of integration rules [39].

It should be realized that the good fits seen in Figure 17-3 require very accurate self-consistency convergence, highly accurate contour integration and a very dense \mathbf{k} point mesh for the Brillouin zone integration. Otherwise additional T

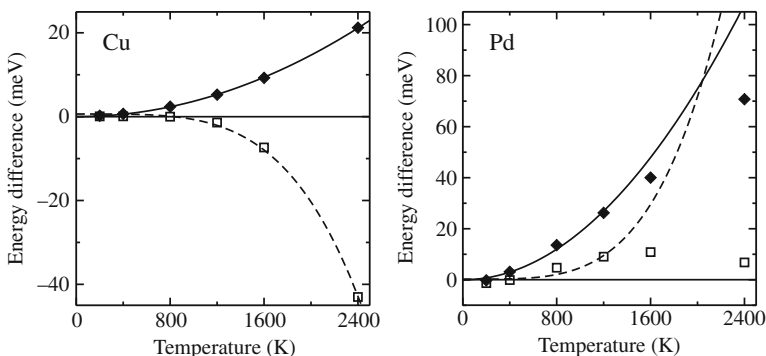


Figure 17-3. Difference $\Delta E_{tot}(T) = E_{tot}(T) - E_{tot}(0)$ as function of temperature for the T^2 (solid symbols) and T^4 (open symbols) broadening schemes. The lines are fits to the data points from $T = 200$ K to $T = 2400$ K for Cu and from $T = 200$ K to $T = 1200$ K for Pd. They were fitted with two parameter according to $\Delta E_{tot}(T) = \alpha_0 + \alpha_2 T^2$ or $\Delta E_{tot}(T) = \alpha_0 + \alpha_4 T^4$

dependencies due to inaccuracies arise and good fits are impossible. For the results displayed in Figure 17-3 the averaged error between input and output potentials of the last self-consistency iteration was smaller than 10^{-9} Ryd, the contour integration error for the total energy was smaller than 10^{-8} Ryd and 5,984 sampling points were used in the irreducible part of the Brillouin zone for simple cubic unit cells with four atoms. (Note that these simple cubic cells are the building blocks for the large supercells used in Section 17.4.4.) Sampling with 19,600 points gave results which are indistinguishable from the ones in Figure 17-3. Such high accuracy would be too expensive for large systems and thus the easy elimination of the T^2 term, which is possible in the KKR-GF method without more work, is rather important.

17.4. LINEAR SCALING IN THE KKR-GF METHOD

It was explained above that in KKR-GF method a considerable part of the computations, the solution of the single-scattering equations around each atom with accurate spatial resolution, scales linearly and can be parallelized easily. Only the matrix equation (17-19) requires cubically scaling work.

One strategy to arrive at linear scaling is the divide and conquer approach with use of the KKR-GF method to calculate the density in the local regions containing the considered atoms as it is done in the locally self-consistent multiple scattering (LSMS) method [8]. Recently capability and high parallel efficiency of such an approach has been demonstrated in an ab initio computation of the free energy of a nanoscale Fe system of 1,024 atoms [40] using the LSMS method together with Wang-Landau sampling [41]. A performance with 1.836 Petaflop/s was achieved on 223,232 cores of the Cray XT5 system Jaguar in Oak Ridge and the Gordon Bell Prize 2009 was awarded for this work.

However, as explained in Section 17.2.2, the use of nearsightedness alone as used in a divide and conquer approach seems to be not enough to obtain a highly accurate linear scaling method. The advantages of sparse matrix representations and iterative solution techniques should also be exploited. The KKR-GF linear scaling algorithm developed over the last two years in Jülich achieves this goal by a tight-binding transformation for (17-19) and by using the quasi-minimal residual method [42, 43] for the iterative solution. How this is done in practice is explained below as well as how truncation of the Green function at large distance leads to linear scaling.

17.4.1. Repulsive Reference System

In the standard KKR-GF method with free space as reference system the Green function matrix elements decay slowly with distance between sites \mathbf{R}^n and $\mathbf{R}^{n'}$. The slow decay of matrix elements arises from the slow decay of the free space Green function with distance $|\mathbf{r} - \mathbf{r}'|$ which is observable in (17-15) if the imaginary part of \sqrt{E} is small. In 1984 Andersen and Jepsen [44] realized that in the limit $E \rightarrow 0$ the Green function matrix elements of the reference system (which are called also structure constants) could be made short-ranged by a screening transformation that was the foundation of the very efficient tight-binding linear-muffin-tin-orbital (TB-LMTO) method. Later Andersen et al. [45] realized that screening is possible also

for the energy dependent structure constants (which is another name for the Green function matrix elements) of the KKR method and invented the screened KKR method which because of its relation to the TB-LMTO method also is called the tight-binding (TB) KKR method. The problem to devise a generally useful recipe to calculate the energy dependent screened structure constants was then solved by the concept of a repulsive reference system [46] and the similar concept of a background hard sphere solid [47] that is applied in the third generation MTO method.

The physical motivation for a repulsive reference system is simple to understand if one considers the free space Green function (17-15) for negative real values of E . Then the free space Green function decays exponentially with distance $|\mathbf{r} - \mathbf{r}'|$ associated with exponentially small Green function matrix element $G_{LL'}^{0,nn'}(E)$ if the distance between sites \mathbf{R}^n and $\mathbf{R}^{n'}$ is large. Since the zero of energy E is arbitrary, it can be changed by adding the same constant to E and $v_{eff}(\mathbf{r})$ in (17-3) or (17-7) and calculations with exponentially decaying Green function matrix elements are possible, at least in principle. The problem with a constant potential of the necessary height of a few Ryd is a large increase of the numerical effort because the angular momentum convergence becomes less rapid. This is mainly caused by the necessity to use a spherical harmonic like expansion for a potential with a large discontinuous step at the complicated non-spherical cell boundaries.

Instead of using a reference system with a uniformly shifted potential a more useful reference system, which does not destroy the good angular momentum convergence, is obtained by applying the shift only within non-overlapping spheres around the atomic positions \mathbf{R}^n . A reference system with exponentially decaying matrix elements [46], which can be calculated accurately with moderate effort, consists of an infinite array of repulsive potentials confined to non-overlapping muffin-tin spheres and a zero potential in the interstitial region between the spheres (as shown in Figure 17-4). Because the KKR-GF method also works for projection potentials acting only on selected angular momentum components, the

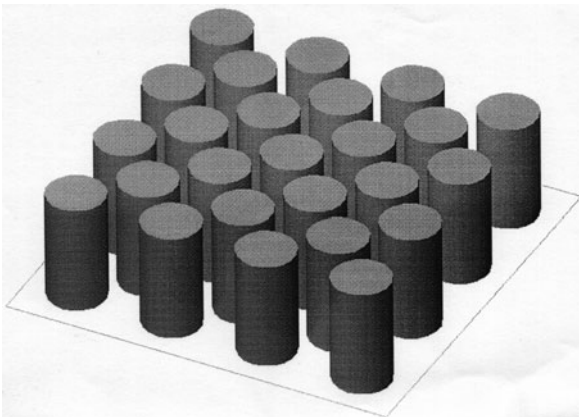


Figure 17-4. Schematic view (in two dimensions) of a repulsive reference system with muffin-tin potentials of constant height. Reprinted from Ref. [48]

t matrix contributions of the reference system can be set to zero for $l > l_{max}$ without introducing any approximation and with maintaining the angular momentum convergence of the physical system.

Application of first-order perturbation theory indicates that eigenstates are shifted to higher energy by an amount which is given by the product of potential strength and volume filling. Actually the shift of the eigenstates shows a saturation effect [46], for instance in a face-centered-cubic lattice sites with volume filling of 74% the lowest eigenstate is at 0.7 Ry for potentials of 1 Ry height, at 1.35 Ry for potentials of 2 Ry height and a 2.25 Ry for potentials of 4 Ry height. These values refer to a constant projection potential with $l_{max} = 3$. Non-constant or infinite repulsive projection potentials in the spheres could be used similarly without affecting the good angular momentum convergence.

The Green function matrix elements of a repulsive reference system can be obtained straightforwardly in real space by solving

$$G_{LL'}^{r,m'}(E) = G_{LL'}^{0,m'}(E) + \sum_{n''L''L'''} G_{LL''}^{0,m''}(E) t_{L''L'''}^{r,n''}(E) G_{L''L'}^{r,n''n'}(E), \quad (17-29)$$

where t^r denotes the reference t matrix. Due to the rapid decay of $G_{L''L'}^{r,n''n'}(E)$ with distance $|\mathbf{R}^{n''} - \mathbf{R}^{n'}|$, only a finite number of sites n'' appreciably contribute to the sum over n'' in (17-29) and the contribution of more distant sites can be neglected. With this neglect (17-29) is a matrix equation of dimension $N_{cl}(l_{max} + 1)^2$ which for each site n' can be solved independently. Here N_{cl} is the number of sites in the cluster of repulsive potentials used around site $\mathbf{R}^{n'}$.

The influence of the neglect on calculated total energies, lattice constants and bulk moduli has been investigated in Ref. [49] for the metals Al, Cu and Pd as typical examples for simple, noble, and transition metals. The results were obtained both by the traditional and the TB-KKR method with an angular-momentum cutoff $l_{max}=3$. If a cluster of only nearest-neighbor atoms ($N_{cl} = 13$ sites) is used to calculate the Green function matrix elements of the repulsive reference system, the error for the total energy is already less than 50 meV per atom. If larger cluster are used, the error rapidly decreases, for $N_{cl} = 55$ the error is below 1 meV and for $N_{cl} = 225$ below 1 μ eV. Typical errors for lattice constants and bulk moduli are of the order of 0.2 pm and 1 GPa, if potentials on central, nearest and next-nearest neighbor sites ($N_{cl} = 19$) are used, and 0.01 pm and 0.05 GPa for $N_{cl} = 79$.

Although the real space calculation of the short range Green function matrix elements of the repulsive reference system is already a simplification compared to the usually cumbersome Ewald procedure necessary for periodic systems, the crucial advantage in the TB-KKR method is that in (17-19) exponentially small elements of the reference Green function matrix can be neglected. This has the consequence that this matrix becomes a sparse matrix and solution techniques for sparse systems of linear equations can be applied.

This feature has been and is extensively used for systems consisting of layers with two-dimensional periodicity as multilayers, surfaces, interfaces, finite slabs,

or half-infinite crystals, where two-dimensional Fourier transformation directly yields band matrices with small bandwidth. This leads to efficient $O(N)$ algorithms already for small number of layers as demonstrated for the TB-KKR method in Ref. [48]. Note that here the essentially one-dimensional problem obtained by Fourier transformation leads to linear scaling.

For two- or three-dimensional systems the TB-KKR Green function method also leads to banded matrices, however the bandwidth increases as $O(N^{1/2})$ or $O(N^{2/3})$ and band matrix algorithms lead to $O(N^2)$ or $O(N^{7/3})$ scaling. With appropriate sophisticated reordering of atoms by algorithms as Cuthill-McKee, minimum degree or nested dissection the work may be reduced to $O(N^{3/2})$ and $O(N^2)$, but only for very large values of N . Therefore, it seems to be much easier to solve (17-19) by iteration which directly leads to $O(N^2)$ scaling as explained below.

It is here important to point out that the sparsity introduced by the artificial auxiliary reference system is not caused by the nearsightedness of the physical system. It is also important to point out that the transformation is exact and that the resulting tight-binding KKR method works for all kind of materials with or without bandgap.

17.4.2. Iterative Solution

If for large systems direct solution methods for linear equations become unfeasible because of the cubically scaling computational work and because of memory requirements, iterative solver must be applied. The iterative solution of the KKR matrix equation (17-19) has been applied before [50, 51]. For systems with up to 2048 atoms Smirnov and Johnson [51] found that the computational effort is reduced to $O(N^{2+\epsilon})$ with ϵ between 0.0 and 0.2 which means almost quadratic scaling. For the larger systems studied below it will shown that true $O(N^2)$ scaling can be achieved.

The equation for straightforward iteration of (17-19) can be written as

$$G_{LL'}^{i+1,nn'}(E) = G_{LL'}^{r,nn'}(E) + \sum_{n''L''L'''} G_{LL''}^{r,nn''}(E) \Delta t_{L''L'''}^{n''}(E) G_{L''L'}^{i,n''n'}(E), \quad (17-30)$$

where i is the iteration index and G^i is the approximation for the Green function after iteration i . An important feature of (17-30) is that each atom n' (and each angular momentum component L' and each E mesh point on the contour) can be treated independently. Therefore iterative solution in the KKR-GF method is ideally suited for parallel computing with hundreds or thousands of processors. The independent treatment of each atom is in the spirit of the divide and conquer approach discussed above, however, whereas the divide and conquer approach usually implies an approximation due to the neglect of potential contributions from the outside of the buffer region, here the independent treatment is exact provided that the iterations have converged. The computational work in (17-30) consists of matrix vector multiplications where the matrix has $N(l_{max} + 1)^2$ rows and each row has $N_{cl}(l_{max} + 1)^2$ non-zero elements. Thus for one site n' and one angular momentum index L' the

work scales as $N_{it}N_{cl}N(l_{max} + 1)^4$ and for all n' and L' as $N_{it}N_{cl}N^2(l_{max} + 1)^6$, where N_{it} is the number of iterations averaged over all sites and angular momentum components. This work is smaller than the work for direct solution, which is proportional to $N^3(l_{max} + 1)^6$, provided that the product $N_{it}N_{cl}$ is smaller than N which gives a rough estimate of the crossover value for N above which iterations are more advantageous than direct solution.

Unfortunately, straightforward iteration of (17-30), which corresponds to Born iteration in scattering theory, usually diverges, in particular near the real energy axis where singularities of the Green function obviously prevent convergence. For complex values of E , which are used in the contour integration to obtain the density, convergence for the iterative solution can be achieved, if straightforward iteration is replaced by judicious mixing of input and output Green function matrix elements obtained by (17-30). Here Anderson mixing [52], which can be related to Broyden's second method [53], can be used successfully [54]. A disadvantage of this mixing scheme is that the required memory increases with iteration number since information of all previous iterations is used and must be kept. It seems that standard iterative solvers for linear equations with lower memory requirements are more suitable. With the substitutions $A = 1 - G^r(E)\Delta t(E)$, $X = G(E)$ and $B = G^r(E)$ equation (17-19) can be written as $AX = B$, which is the standard form for linear equations. Here A is the so-called TB-KKR matrix, which for complex E has complex eigenvalues so that only some of the standard iterative solvers can be applied. As in earlier work [50, 51] the quasi-minimal-residual (QMR) method [42, 43] was found to be very suitable.

For the solution of (17-19) Anderson's mixing and the QMR method gave convergent results for all systems studied so far. In particular, the QMR method in its transpose free form seems to be rather robust within the KKR-GF method. Starting from a zero vector as initial guess, the relative residual norm almost always decreases during the QMR iterations and any desired accuracy could be obtained. In a study [54] for Cu and Pd supercells with 16,384 atoms in face-centered-cubic geometry it was observed that the error of the calculated total energy decreases at least as fast as the specified tolerance criterion for the relative residual norm $\|r\|$ and that about a fixed number of QMR iterations is needed to reduce the error by one order of magnitude. The total energy error is a few meV per atom, if the bound for the residual norm is set at $\|r\| = 10^{-3}$ and a few tenths of meV for $\|r\| = 10^{-4}$. This indicates that for accurate total energies only moderate accuracy of the QMR iterations is required.

17.4.3. Green Function Truncation

Because of the auxiliary repulsive reference system (17-19) can be solved iteratively by sparse matrix techniques with a computing effort that scales quadratically with system size. The question at this points is how nearsightedness can be exploited to achieve an even better scaling. Note that the quadratic scaling was obtained without assuming any property of the physical system, it arises in the KKR-GF method only by the choice that the reference system is repulsive. Contrary to that nearsightedness

is a property of the physical system. To understand how nearsightedness can be applied in the KKR-GF method it is useful to consider the connection between the Green function and the finite-temperature density matrix

$$\rho(\mathbf{r},\mathbf{r}',T) = -\frac{2}{\pi} \text{Im} \int_{-\infty}^{\infty} f(E - E_F, T) G(\mathbf{r}, \mathbf{r}'; E) dE \quad (17-31)$$

which is a generalization of (17-10). From this relation and the property that the Green function decays faster for energies E with larger imaginary part, it is clear that the decay of $\rho(\mathbf{r},\mathbf{r}',T)$ for large distances is mainly determined by the decay of $G(\mathbf{r}, \mathbf{r}'; E_F + i\pi k_B T)$ at the first Matsubara energy. Thus small values of the finite-temperature density matrix for large distances $|\mathbf{r} - \mathbf{r}'|$ corresponds to small values of the Green function for similar distances and, because the single-scattering wave-functions in (17-18) are only multiplicative factors, to small values of the Green function matrix elements G_{LL}^{mn} .

If small Green function matrix elements are set to zero outside a truncation region containing N_{tr} atoms around the considered atom, only $O(N_{tr}N)$ elements are non-zero in the Green function matrix compared to $O(N^2)$ non-zero elements without truncation. This reduces the computational effort by a factor N_{tr}/N if multiplication with zero elements is avoided by appropriate storage techniques. The total effort necessary for all sites is then proportional to $N_{it}N_{cl}N_{tr}N$. This number increases linearly with N for large systems because N_{cl} and N_{tr} are fixed and N_{it} approaches a constant value for large N (see Section 17.4.5). The resulting equations are very similar to the ones in LSMS divide and conquer approach, however, as a consequence of the repulsive reference system and the iterative solution, here the work increases proportionally to $N_{it}N_{cl}N_{tr}N$ whereas it increases in the LSMS method as $O(N_{tr}^3N)$ much faster with increasing size of the region where physical potential is not neglected. Another difference between the linear scaling algorithm proposed here and the LSMS method is the potential used outside of the truncation region. Here it is the potential of the reference system and in the LSMS method it is set to zero.

17.4.4. Model Study

The two key questions for the usefulness of a linear scaling algorithm are: how is the accuracy affected by the size of the truncation region and how many atoms are needed so that despite of its overhead the linear scaling algorithm is more advantageous than standard methods with cubic scaling. To study these issues it would be desirable to have a model system with the following properties. The system should be metallic, large enough so that the effects of the Green function truncation can be assessed and simple enough so that the computer resources for the study are reasonably small. The model systems chosen here, large supercells consisting of identical atoms arranged on the positions of a face-centered-cubic lattice, satisfy these properties as discussed below. It is also desirable if accurate benchmark results without truncation are available. For the present KKR-GF linear scaling algorithm

benchmark results are particularly easily obtained because of the clear separation between the calculation of single-scattering quantities and the solution of the matrix equation (17-19). Only the matrix equation is affected by truncation or iteration, the single-scattering quantities are calculated exactly in the same manner in linear scaling or standard calculations.

The supercells were constructed from simple cubic unit cells with four atoms by repeating the small cells 32 times in all three space directions. They contained $4 \times 32^3 = 131,072$ atoms arranged according to the face-centered-cubic geometry of the elemental metals Cu and Pd. If these large metallic supercells are treated in a standard way by basis set expansions, the number of eigenstates to be calculated would be 131,072 times the number of valence electrons per spin at each sampling point in the Brillouin zone. Obviously the calculation of 720,896 eigenstates for Cu or 655,360 eigenstates for Pd would require enormous computer resources. In the KKR-GF method it is straightforward to utilize the fact that all atoms in the supercells are equivalent. To study the effects of truncation and iteration only the density for one atom in the supercell must be calculated. This represents an enormous reduction of the computational effort compared to realistic systems with inequivalent atoms. Actually, the model study only requires one processor, for instance of a desktop computer, whereas systems with many inequivalent atoms require the power of supercomputers.

To assess the error for the total energy it is necessary to calculate the total energy of the supercells without truncation. Because all atoms are equivalent, such a calculation is feasible, however, it would require about 7 GB of storage for the non-zero elements of the sparse reference Green function matrix and the self-consistent determination of the effective potential and the total energy would be rather expensive. Here the concept of equivalent \mathbf{k} point meshes (explained in Ref. [55]) is of great help. The Brillouin zone (BZ) integration for the periodically repeated supercells, here done with one special point in the irreducible part of the BZ zone chosen as $\mathbf{k} = (1/4, 1/4, 1/4)$ in units of the reciprocal lattice constant, gives results for the on-site blocks of the Green function (and thus for the density, the self-consistent potential and the total energy) which are exactly identical to the ones obtained by calculations for the small cubic unit cell containing four atoms, if 5,984 \mathbf{k} points in the irreducible part of the BZ zone are used for the small cell.

Some details of the calculation were as follows. The lattice constant of supercells was chosen as 11.568 nm for Cu and 12.447 nm for Pd which is 32 times the experimental lattice constant. The repulsive potentials in the reference system had a height of 8 Ryd and clusters with $N_{cl} = 13$ atoms were used to calculate the matrix elements of the reference Green function. The LDA in Vosko-Wilk-Nusair parametrization [56]) was used for the exchange-correlation potential and the points on the energy contour were chosen such that the complex energy integration did not lead to larger errors than 10^{-7} meV for the calculated total energies.

The truncation regions were constructed by using more and more neighbour shells around the central atom so that always one more shell was included in the close-packed (110) direction. The smallest truncation region included two and the largest truncation region eighteen neighbour atoms in that direction leading to

Table 17-1. Error per atom (in meV) for the total energy as function of the number of atoms in the truncation region for three temperatures $T = 400, 800$ and $1,600$ K for large Cu and Pd supercells

N_{tr}	ΔE_{400}^{Cu}	ΔE_{800}^{Cu}	$\Delta E_{1,600}^{Cu}$	ΔE_{400}^{Pd}	ΔE_{800}^{Pd}	$\Delta E_{1,600}^{Pd}$
55	65.4	54.8	39.0	109.4	112.5	118.1
177	1.3	0.8	-4.9	35.2	33.2	24.6
381	-1.1	-3.2	-6.4	-2.7	-1.2	-4.2
767	0.0	-2.4	-5.5	9.7	10.7	9.1
1,289	-1.1	-2.5	-3.4	-2.1	-2.0	0.3
2,093	3.4	3.0	2.9	-2.0	-3.4	-3.1
3,055	3.0	2.6	2.6	2.8	2.6	1.7
4,321	2.5	1.8	1.7	0.0	1.2	1.7

N_{tr} values between 55 and 34,251. The calculated total energy error is shown in Table 17-1 for small and in Figure 17-5 for large truncation regions for three different temperatures $T = 400, 800$ and $1,600$ K. For the small truncation region with 55 atoms the error can be as large as 0.1 eV (comparable errors were found in Ref. [11]), whereas it is smaller than 2 meV for truncation regions with more than a few thousand atoms. With increasing size of the truncation region the error can be made as small as wanted [39, 54]. Note that the errors displayed in Table 17-1 and Figure 17-5 contain a small contribution arising from the choice $||r|| = 10^{-4}$ as tolerance criterion for the relative residual norm in the QMR iterations, whereas the previous results in Refs. [39, 54] were obtained with $||r|| = 10^{-8}$ and are thus slightly better.

The errors shown in Figure 17-5 illustrate that higher temperature is not very useful for the calculation of better total energies, at least not for truncation regions with less than 10,000 atoms. This indicates that the zero-temperature algebraical

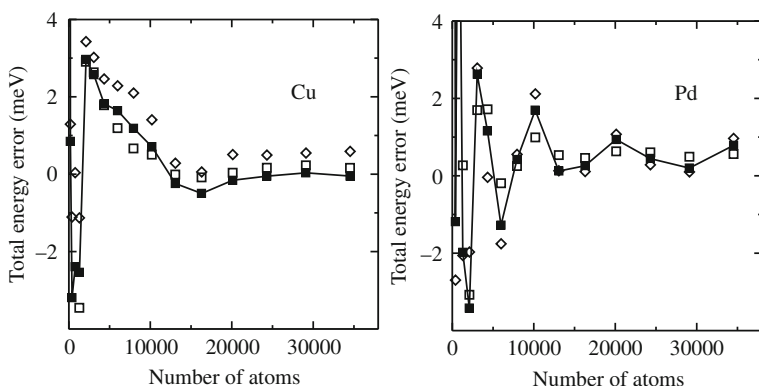


Figure 17-5. Error per atom for the total energy as function of the number of atoms contained in the truncation region. Solid and open squares are for $T = 800$ and $1,600$ K, diamonds for $T = 400$ K. The lines, which connect the results for $T = 800$ K, serve as guide for the eye

decay of the Green function (and density matrix) dominates the additional exponential decay caused by temperatures small enough such that according to Figure 17-3 not too large total energy deviations are introduced.

17.4.5. Scaling Behaviour

For applications of the KKR-GF linear scaling algorithm it is important for which system size it becomes competitive to standard KKR-GF calculations. Obviously one can expect that the crossover size will be reached for relatively large systems and that it depends on the accuracy which one tries to achieve. The results presented here were obtained using a tolerance criterion for the relative residual norm of $\|r\| = 10^{-4}$ which gives a total energy accuracy that seems to be sufficient for practical purposes. Instead of using supercells of different size the scaling behaviour can be studied also by using one supercell (here with 131,072 atoms) and varying the size of the truncation region in the supercell. In [54] it was studied how the number of QMR iterations for the energy point closest to the real energy axis increases with system size. It is probably more meaningful to consider sum of the number N_{mv} of matrix vector products necessary for all points on the integration contour. The total effort proportional to $N_{mv}N_{cl}N_{tr}N$ must be compared to the effort proportional $N_E N^3$ for direct solution in the standard KKR-GF method, where N_E is number of energy points on the contour.

Results for N_{mv} averaged over the $(l_{max} + 1)^2 = 16$ angular-momentum components are shown in Figure 17-6 for different temperatures. The values of N_{mv} increase with increasing truncation region and can be fitted to an exponential behaviour of the form

$$N_{mv} = N_{mv}^{\infty} - \alpha \exp(-\gamma N_{tr}^{1/3}). \tag{17-32}$$

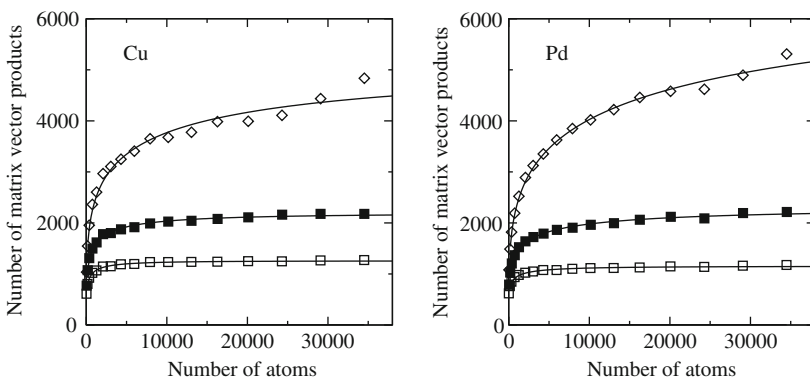


Figure 17-6. Total number (summed over all energy points) of matrix-vector multiplications averaged over the 16 angular momentum components as function of the number N_{tr} of atoms contained in the truncation region. The lines are fitted to an exponential behaviour as described in the text. The open and solid squares are for $T = 800$ K and $T = 1,600$ K, the diamonds for $T = 400$ K

with three temperature dependent parameters N_{mv}^∞ , α and γ where the constant N_{mv}^∞ determines the estimated number of matrix vector products needed for infinitely large systems. Note that $N_{tr}^{1/3}$ is proportional to the radius of the truncation region. Figure 17-6 clearly shows that the necessary number of matrix vector multiplications increases approximately inversely proportional to temperature so that the computational effort considerably decreases for higher temperature. For an efficient parallelization over the energy integration points on the contour, which is used in the Jülich KKR programs since many years [57], it is useful to know how the contributions to N_{mv} are distributed over the energy points. It was found that about 30, 40 and 50% of the work is required at the first Matsubara energy for $T = 1,600$ K, $T = 800$ K and $T = 400$ K.

For small systems the $O(N^2)$ scaling iterative solution is less favourable than the $O(N^3)$ scaling direct solution because of the different prefactors $N_{mv}N_{cl}$ and N_E . The crossover size can be estimated by $N = N_{mv}N_{cl}/N_E$, which shows for $T = 400$ K, $T = 800$ K or $T = 1,600$ K that for more than about 500, 400 or 300 atoms iterative solution becomes more favourable. However, issues of computational implementation are not included in these numbers. Direct solution usually exploits efficient matrix operations, whereas matrix vector operations are used in the parallel iterative solution, but iterative solution requires less communication on distributed memory computers because no large matrices must be stored. The speedup for iterative solution, estimated as $NN_E/N_{mv}N_{cl}$, is shown in Figure 17-7 using the calculated numbers N_{mv} from Figure 17-6. Note that the truncation of the Green function to obtain linear scaling does not introduce any overhead. For example, if a truncation region with a thousand atoms is sufficient, the speedup shown in Figure 17-7 should multiplied by the number of atoms in the system divided by thousand illustrating the gain which can be achieved by linear scaling for large systems with thousands of atoms.

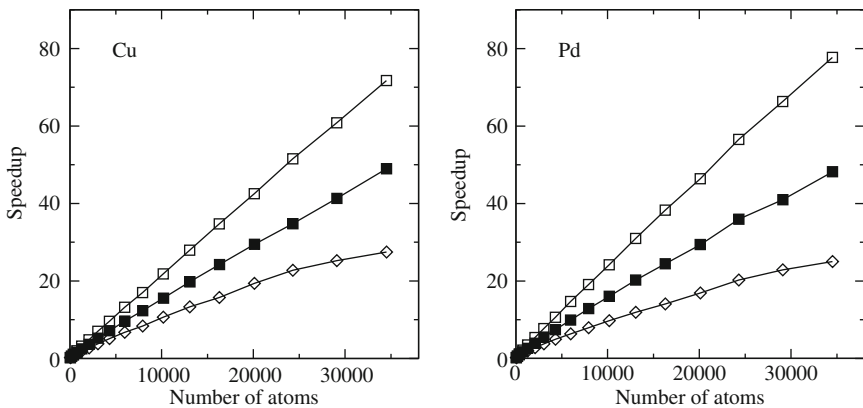


Figure 17-7. Estimates for the speedup obtainable by iteration compared to direct solution. The solid and open squares are for $T = 800$ K and $T = 1600$ K, the diamonds for $T = 400$ K

17.5. CONCLUSIONS AND OUTLOOK

It was shown that the KKR-GF method can be used successfully for accurate density-functional calculations for large metallic systems with linear-scaling computational effort. The key factors for the success are: (1) the clear separation in the KKR method between quantities, which are calculated with fine spatial resolution around the atoms with naturally linear scaling effort, and the combination of these atomic quantities by a linear matrix equation, (2) the generation of sparse matrices by use of a repulsive reference system, (3) finite temperature complex energy integration for the density, (4) robust iterative solutions by the QMR method and (5) high parallel efficiency because the work is almost perfectly decomposed with respect to the atoms.

It was estimated that iterative solution can become more advantageous than direct solution for metallic systems with more than a few hundred atoms and that linear scaling can be used for accurate total energy calculations for metallic systems with more than a few thousand atoms. These estimates are based on the present experience. It can be expected by a variety of techniques that iterative solution can be made faster and truncation more efficient. For instance, it seems that for large distance mostly the $l = 0$ angular momentum components are required in the Green function matrix of the physical system so that already for shorter distances than used so far elements with $l > 0$ can be neglected leading to more zero elements in the Green function matrix. Instead of starting from zero vectors as done now, the iterations may be started from a good estimate either obtained by extrapolation along the energy contour or from the previous self-consistency cycle. Investigation of these issue is in progress as well as investigation of several preconditioners to accelerate the iterative solution.

It should be remarked finally that the linear scaling KKR-GF algorithm is not restricted to non-relativistic systems. It can be extended straightforwardly to solve the Dirac equation so that relativistic effects can be studied in large systems. It should also be remarked that the linear scaling KKR-GF algorithm gives access to spatial and energy resolved quantities as the local density of states, whereas density matrix based methods usually provide only integrated quantities as the total energy.

ACKNOWLEDGMENTS

It is my pleasure to thank all people for the discussions I had, in particular on linear scaling and on the use of general potentials in the KKR-GF method. Because it is impossible to include all appropriate references, I apologize for using mainly references associated to the work in Jülich.

APPENDIX

By using Gegenbauer's addition theorem [58] for Hankel functions the free space Green function can be written in an almost separable form as

$$G^0(\mathbf{r}, \mathbf{r}'; E) = -i\sqrt{E} \sum_{l=0}^{\infty} \sum_{m=-l}^{m=l} h_l^{(1)}(r_{>}\sqrt{E}) j_l(r_{<}\sqrt{E}) Y_{lm}(\hat{\mathbf{r}}) Y_{lm}(\hat{\mathbf{r}}'), \quad (17-33)$$

where the individual terms are products of \mathbf{r} dependent and \mathbf{r}' dependent functions. Here Y_{lm} , $h_l^{(1)}$ and j_l are real spherical harmonics, spherical Hankel functions of the first kind and spherical Bessel functions. Expression (17-33) is in a separated form with respect to the angular variables $\hat{\mathbf{r}} = \mathbf{r}/r$ and $\hat{\mathbf{r}}' = \mathbf{r}'/r'$. For the radial variables separation is not complete because of the restriction $r_{<} = \min(r, r')$ and $r_{>} = \max(r, r')$ and thus (17-33) is called semi-separable. Often a shorthand notation is introduced by using a combined index $L = lm$ and by defining products of Hankel and Bessel functions with real spherical harmonics by $H_L(\mathbf{r}; E) = -i\sqrt{E} h_l^{(1)}(r\sqrt{E}) Y_{lm}(\hat{\mathbf{r}})$ and $J_L(\mathbf{r}; E) = j_l(r\sqrt{E}) Y_{lm}(\hat{\mathbf{r}})$. Then (17-33) can be written in a more compact form as

$$G^0(\mathbf{r}, \mathbf{r}'; E) = \sum_L^{\infty} H_L(\mathbf{r}_{>}; E) J_L(\mathbf{r}_{<}; E), \quad (17-34)$$

where $\mathbf{r}_{>}$ is the vector \mathbf{r} or \mathbf{r}' with larger length and $\mathbf{r}_{<}$ the one with smaller length. The multiple-scattering expression (17-17) for the Green function in cell-centered coordinates is then obtained by using the addition theorem of spherical Hankel functions in the form

$$H_L(\mathbf{r} + \mathbf{R}^n - \mathbf{R}^{n'}; E) = \sum_{L'}^{\infty} G_{LL'}^{0, nm'}(E) J_{L'}(\mathbf{r}; E), \quad (17-35)$$

which is valid for $r < |\mathbf{R}^n - \mathbf{R}^{n'}|$, with the free space Green function matrix elements

$$G_{LL'}^{0, nm'}(E) = 4\pi(1 - \delta_{nm'}) \sum_{L''} i^{l-l'+l''} C_{LL'L''} H_{L''}(\mathbf{R}^n - \mathbf{R}^{n'}; E). \quad (17-36)$$

Here $\delta_{nm'}$ indicates that the free space Green function matrix elements vanish for $\mathbf{R}^n = \mathbf{R}^{n'}$ and $C_{LL'L''}$ are Gaunt coefficients defined as

$$C_{LL'L''} = \int_{4\pi} Y_L(\hat{\mathbf{r}}) Y_{L'}(\hat{\mathbf{r}}) Y_{L''}(\hat{\mathbf{r}}) d\hat{\mathbf{r}} \quad (17-37)$$

which vanish for $l'' > l + l'$ so that the sum in (17-36) contains a finite number of terms.

In the past confusion for the validity of the full-potential KKR-GF method was caused by the spatial restrictions necessary in (17-34) and (17-35). The restriction $r < |\mathbf{R}^n - \mathbf{R}^{n'}|$ necessary in (17-35) means that the distance from the center of a cell to the point farthest away on the boundary of this cell must be smaller than

the distance between centers of adjacent cells. This restriction is not serious, it can always be satisfied if necessary by introducing additional cells not occupied by atoms (empty cells). The restriction for the arguments in Hankel and Bessel functions in (17-33) and (17-34) means that (17-35) can be applied directly only for $r > r'$, whereas for $r < r'$ it must be used for $H_L(\mathbf{r}' - \mathbf{R}^n + \mathbf{R}^{n'}; E)$. This makes the double sum in (17-17) conditionally convergent and convergent results are only obtained if L and L' are put to infinity in correct order. The spatial restriction has also imposed doubt on the validity of the Green function expression (17-18) for general potentials. It is however elementary to show [20, 25] that (17-18) with appropriately defined quantities directly follows from expression (17-17) if all sums are restricted to a finite number of terms. For practical calculations the question of convergence for high angular momentum contributions seems to be unimportant as the good agreement of calculated total energies and forces with those obtained by other density functional methods and experiment illustrates (see Section 17.3.4). Mathematically, convergence has been demonstrated for the so-called empty lattice with a constant non-zero potential [59] and more generally for the full potential by rather sophisticated techniques [20, 60].

The regular and irregular single-scattering wavefunctions $R_L^n(\mathbf{r}; E)$ and $S_L^n(\mathbf{r}; E)$ are defined by integral equations

$$R_L^n(\mathbf{r}; E) = J_L^n(\mathbf{r}; E) + \int_n G^0(\mathbf{r}, \mathbf{r}'; E) v_{\text{eff}}^n(\mathbf{r}') R_L^n(\mathbf{r}'; E) d\mathbf{r}' \quad (17-38)$$

and

$$S_L^n(\mathbf{r}; E) = \sum_{L'} \beta_{LL'}^n(E) H_{L'}(\mathbf{r}; E) + \int_n G^0(\mathbf{r}, \mathbf{r}'; E) v_{\text{eff}}^n(\mathbf{r}') S_L^n(\mathbf{r}'; E) d\mathbf{r}', \quad (17-39)$$

where the matrix

$$\beta_{LL'}^n(E) = \delta_{LL'} - \int_n S_L^n(\mathbf{r}; E) v_{\text{eff}}^n(\mathbf{r}) J_{L'}(\mathbf{r}; E) d\mathbf{r} \quad (17-40)$$

is defined implicitly by the irregular wavefunctions. The single-cell t matrix is defined by

$$t_{LL'}^n(E) = \int_n J_L(\mathbf{r}; E) v_{\text{eff}}^n(\mathbf{r}) R_{L'}^n(\mathbf{r}; E) d\mathbf{r}. \quad (17-41)$$

Details about the numerical treatment of the single-cell equations (17-38), (17-39), (17-40) and (17-41) can be found in [61, 62].

In periodic systems the atomic positions can be written as $\mathbf{R}^n = \mathbf{R}^\mu + \mathbf{s}^m$ where \mathbf{R}^μ denotes lattice vectors and \mathbf{s}^m positions of the atoms in the unit cell. Then (17-19) has the form

$$G_{LL'}^{\mu m, \mu' m'}(E) = G_{LL'}^{r, \mu m, \mu' m'}(E) + \sum_{\mu'' m'' L'' L'''}^{\infty} G_{LL''}^{r, \mu m, \mu'' m''}(E) \Delta t_{L'' L'''}^{m''}(E) G_{L'' L'}^{\mu'' m'', \mu' m'}(E), \quad (17-42)$$

where due to the translational lattice invariance the t matrix difference does not depend on μ and the Green function matrix elements depend only on the difference vector $\mathbf{R}^{\mu} - \mathbf{R}^{\mu'}$. The infinite sum over μ'' can be treated by lattice Fourier transformation

$$G_{LL'}^{mm'}(\mathbf{k}; E) = \sum_{\mu}^{\infty} G_{LL'}^{\mu m, \mu' m'}(E) e^{-i\mathbf{k}(\mathbf{R}^{\mu} - \mathbf{R}^{\mu'})} \quad (17-43)$$

and an analogous equation for the reference Green function matrix elements. Because of the translational invariance the index μ' in (17-43) can be chosen arbitrarily, for instance as $\mu' = 0$. After Fourier transformation the equation

$$G_{LL'}^{mm'}(\mathbf{k}; E) = G_{LL'}^{r, mm'}(\mathbf{k}; E) + \sum_{m'' L'' L'''}^{\infty} G_{LL''}^{r, mm''}(\mathbf{k}; E) \Delta t_{L'' L'''}^{m''}(E) G_{L'' L'}^{m'' m'}(\mathbf{k}; E), \quad (17-44)$$

which has the same form as (17-19), must be solved at a set of \mathbf{k} points in reciprocal space. The results are used to approximate

$$G_{LL'}^{\mu m, \mu' m'}(E) = \frac{1}{\Omega_{BZ}} \int G_{LL'}^{mm'}(\mathbf{k}; E) e^{i\mathbf{k}(\mathbf{R}^{\mu} - \mathbf{R}^{\mu'})} d\mathbf{k}, \quad (17-45)$$

the Fourier transformation back to real space, by a sampling procedure. Here Ω_{BZ} is the volume of the Brillouin zone and only elements with $\mu = \mu'$ and $m = m'$ are needed for the density.

REFERENCES

1. Hohenberg P, Kohn W (1964) Phys Rev 136:B864
2. Kohn W, Sham LJ (1965) Phys Rev 140:A1133
3. Papanikolaou N, Zeller R, Dederichs PH (2002) J Phys Condens Matter 16:2799
4. Prodan E, Kohn W (2005) Proc Natl Acad Sci USA 102:11635
5. Kohn W (1996) Phys Rev Lett 76:3168
6. Yang W (1991) Phys Rev Lett 66:1438
7. Goedecker S (1999) Rev Mod Phys 71:1085
8. Wang Y, Stocks GM, Shelton WA, Nicholson DM, Szotek Z, Temmerman WM (1995) Phys Rev Lett 75:2867
9. Abrikosov IA, Niklasson AM, Simak SI, Johansson B, Ruban AV, Skriver HL (1996) Phys Rev Lett 76:4203
10. Abrikosov IA, Simak SI, Johansson B, Ruban AV, Skriver HL (1983) Phys Rev B 56:9319
11. Smirnov AV, Johnson DD (2001) Phys Rev B 64:235129
12. Goedecker S (1998) Phys Rev B 58:3501

13. Ismail-Beigi S, Arias TA (1999) *Phys Rev Lett* 82:2127
14. Skylaris C-K, Haynes PD, Mostofi AA, Payne MC (2005) *J Phys Condens Matter* 17:5757
15. Ozaki T (2005) *Phys Rev B* 74:245101
16. Korringa J (1947) *Physica* 13:392
17. Kohn W, Rostoker N (1954) *Phys Rev* 94:1111
18. Lax M (1951) *Rev Mod Phys* 23:287
19. Lord Rayleigh (1892) *Philos Mag* 34:481
20. Zeller R (1987) *J Phys C Solid State Phys* 20:2347
21. Economou EN (1979) *Green's functions in quantum physics*. Springer, Berlin
22. Bruus H, Flensberg K (2004) *Matter physics: an introduction*. Oxford University Press, Oxford
23. Zeller R, Braspenning PJ (1982) *Solid State Commun* 42:701
24. Braspenning PJ, Zeller R, Lodder A, Dederichs PH (1984) *Phys Rev B* 29:703
25. Zeller R (2004) *J Phys Condens Matter* 16:6453
26. Zeller R, Deutz J, Dederichs PH (1982) *Solid State Commun* 44:993
27. Mermin ND, *Phys Rev* (1965) 137:A1441
28. Wildberger K, Lang P, Zeller R, Dederichs PH (1995) *Phys Rev B* 52:11502
29. Drittler B, Weinert M, Zeller R, Dederichs PH (1989) *Phys Rev B* 39:930
30. Asato M, Settels A, Hoshino T, Asada T, Blügel S, Zeller R, Dederichs PH (1999) *Phys Rev B* 60:5202
31. Papanikolaou N, Zeller R, Dederichs PH, Stefanou N (1997) *Phys Rev B* 55:4157
32. Hellmann H (1937) *Einführung in die Quantenchemie*. Deuticke, Leipzig
33. Feynman RP (1939) *Phys Rev* 56:340
34. Harris J, Jones RO, Müller JE (1981) *J Chem Phys* 75:3904
35. Papanikolaou N, Zeller R, Dederichs PH, Stefanou N (1997) *Comput Math Sci* 8:131
36. Settels A, Schroeder K, Korhonen T, Papanikolaou N, Aretz M, Zeller R, Dederichs PH (2000) *Solid State Commun* 113:239
37. Settels A, Korhonen T, Papanikolaou N, Zeller R, Dederichs PH (1999) *Phys Rev Lett* 83:4369
38. Korhonen T, Settels A, Papanikolaou N, Zeller R, Dederichs PH (2000) *Phys Rev B* 62:452
39. Zeller R (2008) *Philos Mag* 88:2807
40. Eisenbach M, Zhou C-G, Nicholson DM, Brown G, Larkin J, Schulthess TC (2009) In: *Proceedings of the conference on High Performance Computing Networking, Storage and Analysis, ACM 2009*, <http://doi.acm.org/10.1145/1654059.1654125>
41. Wang F, Landau DP (2001) *Phys Rev Lett* 86:2050
42. Freund RW, Nachtigal NM (1991) *Numer Math* 60:315
43. Freund RW (1993) *SIAM J Sci Comput* 14:470
44. Andersen OK, Jepsen O (1984) *Phys Rev Lett* 53:2571
45. Andersen OK, Postnikov AV, Yu S, Savrasov S (1992) In: Butler WH, Dederichs PH, Gonis A, Weaver RL (eds) *Application of multiple scattering theory to materials science, MRS symposia proceedings no. 253*. Materials Research Society, Pittsburgh, PA, p 37
46. Zeller R, Dederichs PH, Újfalussy B, Szunyogh L, Weinberger P (1995) *Phys Rev B* 52:8807
47. Andersen OK, Jepsen O, Krier G (1994) In: Kumar V, Andersen OK, Mookerjee A (eds) *Lectures on methods of electronic structure calculations*. World Scientific, Singapore
48. Wildberger K, Zeller R, Dederichs PH (1997) *Phys Rev B* 55:10074
49. Zeller R (1997) *Phys Rev B* 55:9400
50. Nachtigal NM, Shelton WA, Stocks GM (1994) *Combining the QMR method with first principles electronic structure codes*. ORNL technical report, ORNL/TM-12873
51. Smirnov AV, Johnson DD (2002) *Solid State Commun* 148:74
52. Anderson DG (1965) *J Assoc Comput Mach* 12:547
53. Eyert V (1996) *J Comput Phys* 124:271

54. Zeller R (2008) *J Phys Condens Matter* 20:294215
55. Chetty N, Weinert M, Rahman TS, Davenport JW (1995) *Phys Rev B* 52:6313
56. Vosko SH, Wilk L, Nusair M (1980) *Can J Phys* 58:1200
57. Zeller R (1993) *Int J Mod Phys C* 4:1109
58. Danos M, Maximon LC (1965) *J Math Phys* 6:766
59. Zeller R (1988) *Phys Rev B* 38:5993
60. Newton RG (1992) *J Math Phys* 33:44
61. Drittler B, Weinert M, Zeller R, Dederichs PH (1991) *Solid State Commun* 79:31
62. Drittler B (1991) Dissertation. Rheinisch-Westfälische Technische Hochschule Aachen

INDEX

A

- AcCD, *see* Atomic compact CD (acCD)
ACD, *see* Atomic CD (aCD)
Active orbital, 166, 314, 340
Adaptive frozen orbital (AFO), 26–27
Adjustable density matrix assembler (ADMA),
98, 136–143, 139, 142, 151, 153–155,
160–163, 165, 167–170
method, 136–143, 151, 160, 167
ADMA, *see* Adjustable density matrix
assembler (ADMA)
AFO, *see* Adaptive frozen orbital (AFO)
Analytical gradient, 67, 77, 80, 123
Annihilation operator, 27, 348
Atomic CD (aCD), 309–311, 319, 330–333,
340
Atomic compact CD (acCD), 310–311, 320,
330–332, 340
Atomic orbitals, (AOs), 2, 4, 7, 9, 21, 55,
67–68, 70–74, 78, 80, 84–85, 93, 98,
100, 102, 130, 136, 139–140, 148–149,
158, 160–161, 169, 178–183, 190, 265,
308, 311, 313–314, 317, 322, 325, 333,
335–336, 339, 346, 350–353, 411–412,
414, 416, 418–419
Auxiliary basis, 10, 32, 78–79, 201, 237–239,
241, 302, 308–312, 323, 326–328, 332,
339–340, 367, 370
Auxiliary basis sets, 32, 78–79, 201, 232, 236,
238, 241, 251, 302, 309–312, 323,
329–333, 338–340, 367

B

- Basis functions, 1–4, 6–7, 9–13, 21, 23–26,
31–32, 58, 70, 73–74, 76–80, 83, 100,
108, 123, 137, 149, 158–159, 161,
200–201, 203, 205, 212, 214–217,
220–221, 228–229, 233–234, 236–242,
244–246, 249–251, 256–257, 265–267,

- 270–274, 276–278, 289, 292, 295–297,
309–312, 317–320, 323, 328–329, 332,
334, 336, 338–340, 346, 351–352, 358,
370–371, 394, 423, 443, 477, 479

- Basis set incompleteness error, 256, 346
Basis set superposition error (BSSE), 10–11,
53, 70–71, 311, 388–392
Biomolecular simulation, 411, 430–431
Bloch-type equation, 89, 92
Border region problem, 165
Boys localization scheme, 70, 166, 313, 350
Brillouin condition, 357, 369
Brillouin theorem, 84, 89, 360, 366
BSSE, *see* Basis set superposition error (BSSE)

C

- CABS, *see* Complementary auxiliary basis set
(CABS)
CAFI, *see* Configuration analysis for fragment
interaction (CAFI)
Calibration of CD auxiliary basis sets, 329–333
Canonical angles, 269
Canonical orbitals, 66, 68–69, 105, 350, 359,
366, 376, 386
Capping hydrogen atom, 164–165, 169
Carbon nanotube, 85–88, 214
CASPT2, *see* Second-order multicon-
figurational perturbation theory
(CASPT2)
CASSCF, 319–320, 330–332, 340
Cauchy-Schwarz inequality, 271
Cauchy-Schwarz screening, 268, 271
Cavity, 17, 44–46
CBS, *see* Complete basis set (CBS)
1C-CD, 241, 310, 330–331
CD, *see* Cholesky decomposition (CD)
Charge density fitting, 99
Charge transfer (CT), 33, 46–47, 51–52, 399,
400–402, 431

- Chebyshev expansion, 284–287, 447–448, 453
- Cholesky basis, 306, 310, 319, 325, 334, 336, 338–340
- Cholesky decomposition (CD), 238, 240–241, 248, 251, 266, 293, 301–341
- Cholesky molecular orbital, 313–314, 317, 340
- Cholesky orbital localization, 53, 132, 308, 313–315, 393
- CI, *see* Configuration interaction (CI)
- Close pair, 355–356, 358, 360, 364, 368, 390, 397–398
- Cluster-in-molecule (CIM), 99, 349
- Compartmentalization, 153, 413
- Complementary auxiliary basis set (CABS), 367
- Complete active space self-consistent field, 177
- Complete basis set (CBS), 339, 345–346, 368, 397, 412
- Computational artifacts, 430
- Computational cost, 28–32, 34–35, 43, 60, 102–103, 105–106, 111, 115, 117, 120, 122, 200, 209–211, 220–221, 232, 236, 259, 263, 293, 316, 320–321, 346, 354, 357, 360, 362, 371, 380–381, 390, 410, 413, 415, 423, 429, 443–444, 447–448, 460
- Conductor-like screening model (COSMO), 98
- Configuration analysis for fragment interaction (CAFI), 52–53
- Configuration interaction (CI), 35, 37, 66, 83–84, 197, 200
 CIS, 37–38, 52, 59, 378–379, 381
 CIS(D), 37, 50
- Configuration space, 86, 89
- Conformational energy, 429–431
- Conjugated caps, 99, 165
- Constrained expansion, 409
- Constrained molecular orbitals, 414, 416–420, 422–423, 425, 428–429
- Continuous set of gauge transformations (CSGT), 17, 55–56
- Correlation cusp, 367
- Correlation hole, 367
- COSMO, *see* Conductor-like screening model (COSMO)
- Coulomb matrix, 7, 228, 233–234, 236–237, 239–242, 244–247, 266–267, 272–275, 293, 295, 325
- Counterpoise correction, 391–392
- Counterpoise (CP), 53
- Coupled-cluster (CC), 32, 34–35, 51, 108, 111, 200, 303, 349, 370, 374, 378, 381, 412
 CC2, 303, 348–349, 370, 381–388
 CCSD, 32, 108–109, 117, 120–123, 346, 348–349, 358, 369–370, 377–381, 383, 397–398
 CCSD[T], 109–111
 CCSD(T), 32, 109–111, 120–122, 200, 315, 340, 346, 348–349, 369, 389, 397–398, 403
 theory, 32, 108, 346, 348, 357, 365–366
- Coupled-perturbed localization, 383
- CP, *see* Counterpoise (CP)
- Creation operator, 27, 348
- CSGT, *see* Continuous set of gauge transformations (CSGT)
- Cusp condition, 367–368
- Cutoff region, 190–191, 197
- Cutoff technique, 175–176, 196
- D**
- DC-CCSD, 116, 120
- DC-CCSD(T), 110, 120
- DC-DFT, 99–105
- DC-DM MP2, 105–107, 111
- DC-HF, 99–105, 107, 111–118, 120–122
- DC-MP2, 111, 116–118, 120, 205
- DC-R-CCSD(T), 111
- DeFT, 99
- Density fitting (DF), 10, 74, 78, 80–81, 99, 158, 237, 244, 303, 308–309, 311, 316, 319–322, 325, 338–339, 347–349, 364, 369–374, 376, 381, 385, 388, 397
- Density functional theory, 11, 19, 32–33, 98, 132–133, 148, 158–160, 229, 236, 263–298, 303, 340, 354, 410, 439, 442, 475–477, 486
- Density matrix
 based localization, 178–180, 182, 444–445
 hermiticity of, 89
 idempotency of, 89, 179, 282, 452, 455
 purification, 264, 284–286, 288–289, 293–294, 440, 452
- Derivative integrals, 303, 323, 376–377
- DF-LCC2, 384–387, 391, 400, 402
- DF-LCCSD, 370
- DF-LCCSD(T), 370
- DF-LMP2, 78, 80, 371, 377, 389, 392
- DF-LRMP2, 395, 401
- DF-LUCCSD(T), 365
- DF, *see* Density fitting (DF)
- DFT, 1, 3–4, 11, 32–33, 35–36, 51, 56–57, 98–100, 102, 114, 159–160, 166, 176, 197, 200, 202–203, 205, 212–213, 220–221, 229–230, 236, 238, 242, 245,

- 247, 303, 324–325, 330, 354, 357, 370, 391–392, 401, 410–412, 461–462
- DIIS, 13, 18, 103–104, 247, 266–267, 359
- Dipole moment, 7, 56, 74, 167, 202, 242, 330–331, 374, 388–389, 400–401, 409, 418, 428–431, 436
- Dipole polarizability, 374, 389, 402
- Direct inversion in the iterative subspace (DIIS), 13, 18, 103–104, 267, 295, 359
- Distant pair, 71, 73–74, 348, 355, 357
- Divide-and-conquer (DC) method, 97–124, 130, 159–160, 162, 165, 199, 202, 349, 413, 419
- DM-Laplace MP2, 99
- Domain, 70–73, 78, 80–81, 99, 148, 153, 201, 232, 248, 348, 352–356, 358, 360–365, 368–369, 371–374, 376–377, 379–385, 387–390, 392–393, 397–398, 400, 403
- Dressed integral, 382, 384
- Dressed operator, 382, 384
- Dual-buffer DC-based correlation, 111, 117
- Dynamic electron correlation, 33, 158
- Dynamic polarizability, 17, 124
- E**
- EDA, *see* Energy density analysis (EDA)
- Effective Jacobian, 385–386
- EFP, 44, 46–48, 60
- Electric embedding, 164, 168
- Electron correlation, 11, 17, 32–33, 38, 65–67, 69–71, 78, 80, 83–85, 92, 94, 97, 99, 158, 200, 217, 229, 313, 345–403, 411–412
- Electron excited state, 35–38, 124, 132–134, 331, 377–388, 391–392, 398–402
- Electrostatic potentials (ESP), 19, 21, 24–25, 28–30, 39, 41–42, 44–45, 51, 53, 55–56, 59, 167–168, 170, 202, 212
- Elimination of linear dependence, 305–306
- Elongation cutoff technique, 176, 196
- Elongation method, 98, 175–197
- Embedding schemes, 163–164, 168
- Energy decomposition analysis, 25, 52
- Energy density analysis (EDA), 107, 123
- Energy-weighted density matrix, 85–87, 89
- Enzyme, 18, 50, 60, 123, 176, 390, 402
- Ergo, 264–265, 267, 275, 277, 279, 289, 292–294, 440–441
- ERI, 13–14, 190–196, 233, 239–240, 355, 365, 368–369
- Erroneous rotation, 264–265, 268–269, 289–290
- Error control, 264, 269, 280, 286, 317, 326, 339
- ESP-DIM, 30
- ESP-PC, 28, 41–42, 53
- ESP, *see* Electrostatic potentials (ESP)
- Exchange-correlation matrix, 15, 267, 276–280, 294–295
- Exchange matrix, 67–68, 72, 228–229, 249–250, 264, 266–267, 271–272, 275–276, 280, 293, 295
- Excitation energy, 27–28, 36–37, 50, 378, 380, 385, 400
- Excited state, 34–38, 56, 59, 124, 132–134, 331–332, 350, 377–388, 391–392, 398, 400–402
- Expansion criterion, 422, 428
- Explicit correlation, 348, 388, 397–398
- Explicitly correlated coupled cluster (F12-CC), 367
- Explicitly correlated perturbation theory (F12-MP2), 367–368, 370, 398
- F12 ansatz, 367, 369, 397–398, 400
- F**
- Factorization of equations, 385
- Fast multipole method, 1, 112, 159, 176, 190, 272, 412, 441, 478
- Fermi-Dirac function, 285, 446, 486, 489
- FILM, 53
- FLMO, 93–94
- Floating-point operation, 349, 361
- Fluctuating expansion, 420
- FMO3, 19–20, 28–30, 39, 204–205
- FMO/F, 54
- FMO/FX, 55
- FMO-LCMO, 54
- FMO-MO, 28, 54
- FMO, *see* Fragment molecular orbital (FMO)
- FMO/XF, 55
- Fock matrix, 7, 23, 26, 39, 44, 54–55, 68, 76, 102, 104, 115–116, 158–159, 177, 181–182, 190–191, 227–229, 232, 241, 245–246, 256, 258, 277, 288, 302, 315–317, 319, 326–327, 340, 350, 357, 359–360, 362, 364, 366, 369, 385, 413, 429
- Fock operator, 21, 26, 314, 325–327, 357, 366
- Forward error, 287–289
- Fragment-based quantum chemical method, 157–170
- Fragment molecular orbital (FMO), 17–60, 99, 114, 162–163, 165, 176, 203–206, 214
- Frozen orbital, 26, 182
- Fullerene, 87–88, 99, 220

G

- GAMESS-US, 31, 99, 111, 123
 Gauge-including atomic orbital (GIAO),
 55–56, 169, 389
 Gaussian basis set, 3, 9, 11, 79, 244, 265, 291,
 442, 461–462
 Gaussian integrals, 264, 270
 Gaussian product theorem, 371
 Gaussian type linear combination of atomic
 orbital basis set (GT-LCAO), 265
 Generalized degrees of freedom, 416
 Generalized gradient approximation (GGA),
 109, 200, 277, 478
 Generalized hybrid orbitals, 164, 166–167, 169
 Geometry optimization, 91, 112, 123, 200–206,
 212–218, 221, 223, 354, 388, 391–392,
 419–420, 422–423, 426
 GGA, *see* Generalized gradient approximation
 (GGA)
 GIAO, *see* Gauge-including atomic orbital
 (GIAO)
 Gibbs oscillations, 285, 448, 453
 Gradient, 36, 39–43, 45–46, 50, 67, 77, 80,
 98, 109, 122–123, 135, 162, 200–206,
 211–217, 220–221, 223, 250, 267, 277,
 282–283, 309–310, 322–324, 327, 339,
 349, 354, 375–377, 388–389, 414, 416,
 418, 420–425, 428–429, 436, 451, 464,
 478, 488
 Gradient minimization, 416
 Green's function, 27–28, 440–441, 448–449,
 451, 464
 GT-LCAO, *see* Gaussian type linear com-
 bination of atomic orbital basis set
 (GT-LCAO)

H

- Hamiltonian, 20–21, 24, 32, 44, 48–50, 54, 57,
 83–84, 86–90, 102, 130–133, 158–159,
 163–164, 182, 189, 266, 293–294, 366,
 380, 382, 424–425, 430–434, 436,
 441–442, 444–447, 449, 451–454, 456,
 459, 464–465, 467–468, 479
 Hartree-Fock exchange, 3–5, 11, 15, 258, 267,
 270, 275–277, 297
 matrix, 267, 275
 Hartree-Fock method, 32, 34, 328–329,
 365–366, 411–412
 HiCu, *see* Hierarchical cubature (HiCu)
 Hierarchical cubature (HiCu), 278
 HOMO-LUMO gap, 54, 73, 228, 269, 285,
 288, 291, 297
 HOP, *see* Hybrid orbital projectors (HOP)
 Hybrid orbital projectors (HOP), 26–27

I

- Idempotency, 89–92, 106, 143, 178–179,
 282–284, 452, 455–456, 462–464, 466
 IFIE, *see* Interfragment interaction energy
 (IFIE)
 IMH, *see* Intermolecular Hückel model (IMH)
 Incremental correlation method, 99
 Integral screening, 103, 271
 Interaction energy, 25, 29, 45, 52–53, 58,
 86–88, 314, 316, 391–392
 Interfragment interaction energy (IFIE), 51,
 53, 59
 Intermolecular Hückel model (IMH), 87–88
 Intermolecular interaction, 53, 391–392
 Internal pressure, 434
 Inverse Cholesky decomposition, 266
 Inverse overlap matrix, 414–415
 Ionization potential (IP), 392, 394–396
 Iteration, 49, 54, 70, 76–77, 89–92, 104–105,
 115–116, 164, 182, 229, 249, 282, 286,
 288–289, 297–298, 304, 320, 358–359,
 365, 381, 384, 387, 395–396, 401, 413,
 415, 420–423, 428, 441, 449–451,
 453–460, 462, 464, 466–467, 476–477,
 487, 490, 493–494, 496–500

J

- Jacobian, 382, 385–387, 401

K

- Kohn-Sham matrix, 84, 158–159, 229, 232,
 265–268, 270, 277, 280–283, 288–289

L

- Lagrange multiplier, 47, 387, 416
 Langevin dynamics, 433
 Laplace MP2, 92, 99
 Laplace transform, 68–69, 84–89, 92, 105,
 350, 383, 385–388
 LCCSD, 67, 80, 355–356, 358–360, 362–363,
 365, 368, 370, 372, 374, 379–380, 389,
 397–398
 LCCSD(T), 67, 80, 354–356, 368–370,
 372–374, 388–390, 401, 403
 Lego approach, 98
 LEOM-CCSD, 379–381, 383
 LK algorithm, 315–320, 340
 LMO based Fock matrix, 181–182, 357, 413
 LMO basis SCF procedures, 413
 LMP2, 52–53, 67, 70–77, 79–81, 201,
 354–359, 361, 364–365, 370–372,
 375–377, 380, 383, 388–392, 398, 401
 Local approximation, 345–403

- Local correlation, 66–67, 69–71, 74, 78, 80–81, 94, 99, 117, 162, 201, 259, 345–403
- Local fitting, 312, 372–374, 385, 395
- Localization method, 70, 72, 351
- Localized hybrid orbitals, 164, 349
- Localized molecular orbital (LMO), 17–18, 93, 162, 176–178, 180, 350, 352–354, 356, 360–362, 372–373, 379, 380, 383–384, 409–436
- Localized occupied orbital, 74, 351
- Localized orbitals, 26, 52, 67–70, 72–74, 76, 80, 131, 162, 166–167, 177, 313, 317, 326–327, 349, 351, 359, 365
- Local self-consistent field, 166
- Local-spin-density approximation, 277
- Long-range interactions, 157–170, 235
- Lowdin partitioning, 385
- LRMP2, 365, 388, 393–395, 401
- LSDA, 277
- LT-DF-LCC2, 386–387, 400
- LUCCSD(T), 365
- M**
- Macro-SCF iteration, 422–423
- Method specific Cholesky decomposition (MSCD), 322–329, 335, 339–340
- MP2, *see* Second-order Moller-Plesset (MP2)
- Multilayer, 34–35, 37, 492
- Multipole expansion, 10, 14, 46, 159, 197, 235–236, 241–242, 268, 272–275
- Multipole moments, 56, 191, 273, 275
- N**
- NEO, 17, 57
- Newton equation, 423, 433
- NMR, 17, 55–56, 157, 169–170, 389
- Normalization, 306, 308, 328–329, 409, 414–416, 453, 456, 465
- Numerical grids, 139, 142, 278
- O**
- Occupied subspace, 252, 263, 265, 268–269, 280, 282, 286, 288–291, 293–294
- One-center Cholesky decomposition, 241, 310, 340
- One-electron Hamiltonian matrix, 24, 89, 266
- Open-shell, 32, 34–35, 123, 223, 349–350, 365–367, 375, 392–396, 401–403
- Optimal expansion, 417
- Orbital
- domain, 73, 201, 352–355, 364–365, 379, 381–383, 392
 - free effective embedding potential, 167
 - relaxation, 374, 378, 382
- Orthogonality criterion, 422, 429
- Orthonormal Cholesky basis, 306
- Ortogonalization, 179–180, 308, 413–414, 478
- Oscillator strength, 388, 400–401
- Overlap matrix, 68, 178–179, 181, 183, 266, 289, 293, 314, 333, 352, 358, 360, 389, 414–415, 422, 442
- P**
- Pair domain, 73, 352, 361, 364, 371, 372, 377, 382–384, 400
- Pair Interaction Energies (PIE), 51–52, 58
- Pair Interaction Energy Decomposition Analysis (PIEDA), 25, 52
- PAO, *see* Projected Atomic Orbital (PAO)
- Parallel Cholesky decomposition algorithm, 321
- Parallelization, 77, 99, 124, 200–201, 250, 298, 322, 426, 479, 499
- Parametrized minimization, 283–284
- Partition matrix, 98, 100
- Path Integral MD (PIMD), 50–51
- PCM, *see* Polarizable continuum model (PCM)
- Perturbation theory, 30–32, 34, 56, 65–81, 84, 88, 97, 199, 200, 201, 303, 305, 346, 356, 366, 391, 410, 415–417, 441, 464, 466, 468, 469, 492
- PIEDA, *see* Pair Interaction Energy Decomposition Analysis (PIEDA)
- PIE, *see* Pair Interaction Energies (PIE)
- PIMD, *see* Path Integral MD (PIMD)
- Pipek-Mezey localization scheme, 350
- Poisson-Boltzmann equation, 98
- Polarizability, 47, 56–57, 124, 164
- Polarizable continuum model (PCM), 44–46, 59, 60, 169
- Polynomial evaluation, 286–287
- Polynomial expansion, 264, 282, 284–287, 289, 448, 453, 456
- Potential energy surface, 231, 310, 354, 388–389, 392
- Prescreening technique, 227, 372
- Primitive Gaussian integrals, 270
- Projected Atomic Orbital (PAO), 72, 73, 351, 352, 357–366, 371, 373, 374, 375, 379, 382, 384, 386, 391

Properties, 9, 18–19, 56, 59, 90, 91–92, 103, 113–114, 124, 130, 132–134, 136–141, 142–143, 148–149, 151–152, 157, 162, 167–170, 175, 187, 199, 200, 202, 212, 213, 221, 238, 241, 302, 314, 323, 331, 339, 349, 354, 374–377, 378, 381, 383, 387–401, 418, 423, 429, 436, 441, 447, 451, 464, 467, 475–476, 478, 480, 481–482, 495, 835

Pseudobond approach, 166, 169

Pseudo-inverse, 386

Purification, 89, 91, 92, 264, 284–286, 287–289, 293, 294, 440, 451–459, 461, 463–464

Q

QCP, *see* Quantum Capping Potential (QCP)

QM/MM, 12, 159, 163–167, 169, 170, 176, 231–232, 259, 356, 390–391, 431

QM/QM, 356

QSAR, *see* Quantitative Structure-Activity Relationship (QSAR)

Quadrature, 6, 8, 12, 85, 93, 106, 229, 293, 302, 386, 400

Quadrupole moment, 56, 113–114

Quantitative Structure-Activity Relationship (QSAR), 58–59

Quantum Capping Potential (QCP), 166

Quantum Monte-Carlo, 38–39

Quasi-one-dimensional systems, 197

R

R12 ansatz, 367

RDM, 27–28

Reaction barrier, 354, 390, 402

Reaction energy, 356, 389–390, 397, 400, 402

Recursive inverse factorization, 266

Regional localization scheme, 176

Regional localized molecular orbital, 176–177

Regional molecular orbital, 177

Region approach, 390

Removal capping atoms, 183

Renormalized coupled cluster, 32

Resolution of identity (RI), 10, 31, 67, 78–79, 201, 236–241, 245, 251, 302, 307

RESP, 55

RHF, 18, 21, 23–24, 28, 30, 33–35, 38, 51, 57, 59, 183–187, 190, 193, 228, 252, 256–257

RI, *see* Resolution of identity (RI)

Robust fitting, 372

ROHF, 34, 365–366, 401–402

See also Hartree-Fock method

S

Saturated CMO expansion, 419

Saturation point, 413, 418

Scaling

- behaviour, 158, 271, 292, 327, 366, 381, 498–499
- linear, 7, 28, 49, 65–81, 92–93, 98–99, 112, 116, 122–124, 129–143, 147–155, 158–159, 175–197, 201, 206, 227–259, 263–267, 269, 275–276, 282, 289, 298, 302–303, 313, 316, 321, 327–328, 333, 339, 349–350, 355, 360, 362–363, 369–370, 395, 401, 409–436, 439–469, 475–503
- reduce, 316, 322

SCF, *see* Self-consistent field (SCF)

Schwarz inequality, 271, 317, 321–322

Screening of integrals, 268

SCS-LMP2, 392

Second-order Moller-Plesset (MP2), 30–35, 37–38, 51–53, 57, 60, 65–81, 88, 92–93, 99, 105–107, 109, 116–118, 120, 122–123, 176, 197, 200–202, 205, 212, 217–220, 222, 231, 303, 308, 320–322, 330, 333, 340, 345–346, 348, 350, 356, 365, 367, 369–370, 375–377, 381, 388–392, 397–398, 400, 411–412, 466

Second-order multiconfigurational perturbation theory (CASPT2), 303, 320–321, 330–332, 339–340

Self-consistent field (SCF), 12, 18–20, 24–25, 28, 33, 47, 50, 54–55, 66, 80, 91, 98–100, 102–105, 109, 112–116, 123, 136, 149, 166–167, 176–178, 181–183, 189–191, 195–197, 227–259, 264–269, 272, 282, 288–290, 293, 297–298, 303, 315–317, 319, 324–326, 329, 412–423, 426, 428, 430, 463

- rotations, 269

Short-range interactions, 73, 158, 163

Similarity-transformed Hamiltonian, 380

Single-point calculation, 420, 422, 424

Singular value decomposition, 358

Slater-type correlation factor (F12), 367–368, 397, 400

Sparse matrix, 92, 141, 263, 266, 279, 282, 289–292, 321, 442, 444, 448, 451, 453, 456, 469, 476, 479, 490, 492, 494

Spherical boundary potential, 410, 432, 436

Spin adaptation, 37, 67–68, 355, 366

Spin contamination, 366

State specific, 381

Strong pair, 71, 73–77, 355–362, 364, 380,
384–385, 391, 395–398

T

Taylor series, 242, 415
TDDFT, 19, 35–36, 51, 56–57, 400
Temperature-lowering technique, 105
Termination criterion, 420–421
Tessera, 17, 44
Thermostat, 433
Time-dependent Hartree-Fock (TDHF)
method, 124
Transition moment, 381, 385, 402
Transition strength, 387
Two-electron repulsion integral (ERI), 246,
347
Two-step decomposition, 304

U

Unrestricted Hartree-Fock (UHF), 123

V

Van der Waals interaction, 51, 163–164
Variational finite localized molecular orbital
approximation, 410–411
Varying fractional occupation number (VFON)
method, 105
Vibration frequency, 213, 322, 354, 388–389
Virial theorem, 434
VISCANA, 58
VLS, 58

W

Weak pair, 71, 73–77, 355–356, 358–359, 361,
368, 395